

This item is held in Loughborough University's Institutional Repository (<https://dspace.lboro.ac.uk/>) and was harvested from the British Library's EThOS service (<http://www.ethos.bl.uk/>). It is made available under the following Creative Commons Licence conditions.



For the full text of this licence, please go to:
<http://creativecommons.org/licenses/by-nc-nd/2.5/>

A GRID-TRANSPARENT NUMERICAL METHOD FOR COMPRESSIBLE VISCOUS FLOWS ON MIXED UNSTRUCTURED GRIDS

by

Andreas C. Haselbacher

B. Eng. (Hons.) Aeronautical Engineering, Loughborough University (1994)

A Doctoral Thesis

Submitted in partial fulfilment of the requirements for the award of

Doctor of Philosophy of the Loughborough University

September 1999

A GRID-TRANSPARENT NUMERICAL METHOD FOR COMPRESSIBLE VISCOUS FLOWS ON MIXED UNSTRUCTURED GRIDS

by

Andreas C. Haselbacher

Submitted to the Department of Aeronautical and Automotive Engineering on
September 10, 1999, in partial fulfilment of the requirements for the degree of
Doctor of Philosophy

Abstract

The goal of the present work is the development of a numerical method for compressible viscous flows on mixed unstructured grids.

The discretisation is based on a vertex-centred finite-volume method. The concept of grid transparency is developed as a framework for the discretisation on mixed unstructured grids. A grid-transparent method does not require information on the cell types. For this reason, the numerical method developed in the present work can be applied to triangular, quadrilateral, and mixed grids without modification.

The inviscid fluxes are discretised using the approximate Riemann solver of Roe. A limited linear-reconstruction method leads to monotonic capturing of shock waves and second-order accuracy in smooth regions of the flow.

The discretisation of the viscous fluxes on triangular and quadrilateral grids is first studied by reference to Laplace's equation. A variety of schemes are evaluated against several criteria. The chosen discretisation is then extended to the viscous fluxes in the Navier-Stokes equations. A careful study of the various terms allows a form to be developed which may be regarded as a thin-shear-layer approximation. In contrast to previous implementations, however, the present approximation does not require knowledge of normal and tangential coordinate directions near solid surfaces.

The effects of turbulence are modelled through the eddy-viscosity hypothesis and the one-equation model of Spalart and Allmaras.

The discrete equations are marched to the steady-state solution by an explicit Runge-Kutta method with local time-stepping. The turbulence-model equation is solved by a point-implicit method. To accelerate the convergence rate, an agglomeration multigrid method is employed. In contrast to previous implementations, the governing equations are entirely rediscritised on the coarse grid levels.

The solution method is applied to various inviscid, laminar, and turbulent flows. The performance of the multigrid method is compared for triangular and quadrilateral grids. Care is taken to assess numerical errors through grid-refinement studies or comparisons with analytical solutions or experimental data.

The main contributions of the present work are the careful development of a solution method for compressible viscous flows on mixed unstructured grids and the comparison of the impact of triangular, quadrilateral, and mixed grids on convergence rates and solution quality.

Keywords: Unstructured Grids, Navier-Stokes Equations, Finite-Volume Method, Upwind Schemes, Multigrid Method, Turbulence Modelling

1991 Mathematics Subject Classification: 76M25 65C20 76D05 76N10

Thesis Supervisor: Prof. James J. McGuirk

Title: Professor of Aerodynamics

Thesis Supervisor: Dr. Gary J. Page

Title: Lecturer

In memory of my mother (1938-1996)

When I write, the story is always uppermost in my mind, and I feel that everything must be sacrificed to it. All the elegant passages, all the so-called beautiful writing—if they are not truly relevant to what I am trying to say, then they have to go. It's all in the voice. You're telling a story, after all, and your job is to make people want to go on listening to your tale. The slightest distraction or wandering leads to boredom, and if there's one thing we all hate in a book, it's losing interest, feeling bored, not caring about the next sentence. In the end, you don't only write the books you need to write, but you write the books you would like to read yourself.

Paul Auster, The Red Notebook

Whenever I complete a book, I'm filled with a feeling of immense disgust and disappointment. It's almost a physical collapse. I'm so disappointed by my feeble efforts that I can't believe I've actually spent so much time and accomplished so little. It takes years before I'm able to accept what I've done—to realise that this was the best I could do. But I never look at the things I've written. The past is the past, and there's nothing I can do about it anymore. The only thing that counts is the project I'm working on now.

Paul Auster, ibid.

Acknowledgements

First and foremost, I would like to express my gratitude to Prof. James McGuirk and Dr. Gary Page for their support and guidance during my studies. It was during the undergraduate lectures of Prof. McGuirk and the final-year project with Prof. McGuirk and Dr. Page that I became fascinated with the flow of fluids and its numerical simulation. I feel honoured that they offered me the opportunity to carry out postgraduate studies and I hope that this thesis fulfills their expectations.

My postgraduate studies would not have been possible without generous financial support by the Department of Aeronautical and Automotive Engineering and through an Overseas Research Student Award of the Committee of Vice-Chancellors and Principals of the Universities of the United Kingdom under grant ORS/94026007.

A number of people have influenced my views on topics contained in this thesis. In particular, I would like to acknowledge helpful discussions with Dr. William Coirier on the discretisation of the viscous fluxes on unstructured grids and Riemann solvers, Dr. Shi Zeng on multigrid methods, Dr. Paul Batten on Riemann solvers, Dr. Phil Tattersall on the wind-tunnel corrections for the RAE 2822 aerofoil computations, and with Dr. Andrew Manners, Mr. Damon Horrocks, and Dr. Dachun Jiang on general topics. I would also like to thank Dr. Jiří Blažek, my office mate for the past two years, for many interesting discussions and comments on a draft of the first chapter.

Since the development of a grid-generation method was not a goal of this thesis, I had to rely on other means of obtaining grids. In this context, I am grateful to Dr. Eribert Benz for permission to use the grid-generation package CENTAUR and to Dr. Laurence Wigton for generating two grids for the RAE 2822 aerofoil.

I would like to thank Prof. Michael Giles of Oxford University and Dr. Weeratunge Malalasekera of Loughborough University for examining this thesis.

Having written software myself, I believe that I am in a position to appreciate, at least partially, the effort which goes into writing a software package, and the pleasure and frustration connected with it. For this reason, I feel obliged to thank Donald

Knuth, Leslie Lamport, Paul Turner, Robert Moniot, and others for providing high-quality software such as L^AT_EX, xmgr, xfig, and ftnchek for free.

I would like to thank my father for his support during my postgraduate studies and comments on drafts of this thesis.

Last but not least, I would like to thank Katrin for simply being there.

Contents

List of Tables	xii
List of Figures	xiv
Nomenclature	xxv
 I INTRODUCTION AND MATHEMATICAL MODEL	 1
1 Introduction	2
1.1 Background	2
1.1.1 Aim of Present Work	4
1.1.2 Classification of Grid Types	4
1.2 Pioneering Efforts on Unstructured Grids	21
1.3 The State-of-the-Art on Unstructured Grids	23
1.3.1 Spatial Discretisation	24
1.3.2 Solution of Discrete Equations	40
1.4 Summary and Appraisal of Previous Work	49
1.5 Objectives of Present Work	49
1.6 Outline of Thesis	50
References	51
 2 Mathematical Model	 72
2.1 Assumptions	72
2.2 The Governing Equations for Inviscid Flow	73
2.3 The Governing Equations for Laminar Flow	73
2.4 The Governing Equations for Turbulent Flow	75
2.4.1 The Reynolds-Averaged Navier-Stokes Equations	76
2.4.2 Turbulence Model	78
2.5 Boundary Conditions	82

References 83

II NUMERICAL METHOD 84

3 Unigrid Numerical Method 85

3.1 Introduction 85

3.2 Finite-Volume Discretisation 85

3.3 Control-Volume Definition 87

3.3.1 Median Dual 88

3.3.2 Containment Dual 88

3.3.3 Comparison 89

3.4 Data Structure 92

3.5 Grid Transparency 94

3.6 Flux Quadrature 96

3.7 Discretisation of Inviscid Fluxes 99

3.7.1 First-Order Discretisation 100

3.7.2 Second-Order Discretisation 100

3.7.3 Numerical Flux Function 117

3.8 Discretisation of Viscous Fluxes 121

3.9 Discretisation of Spalart-Allmaras Turbulence Model 121

3.9.1 Computation of Distance Function 121

3.9.2 Treatment of Transition Terms 122

3.10 Initial Conditions 125

3.11 Boundary Conditions 125

3.11.1 Fluid-Solid Boundary Conditions 126

3.11.2 Fluid-Fluid Boundary Conditions 130

3.12 Solution Algorithm 135

3.12.1 Euler and Navier-Stokes Equations 135

3.12.2 Spalart-Allmaras Turbulence Model Equation 137

3.13 Implementation Details 139

3.13.1 Time-Step Calculation 139

3.13.2 Convergence Monitoring 140

3.14 Closure	140
References	141
4 The Discretisation of Viscous Fluxes on Unstructured Grids	145
4.1 Introduction	145
4.2 Laplace's Equation	147
4.2.1 Conditions on Discretisation	147
4.2.2 Discussion of Conditions	153
4.2.3 Review of Previous Work	157
4.2.4 Non-Canonical Discretisations	161
4.2.5 Canonical Discretisations	167
4.3 The Case for Canonical Discretisations	176
4.4 Navier-Stokes Equations	177
4.4.1 Canonical Discretisation	177
4.4.2 Galerkin Finite-Element Discretisation	182
4.5 Conclusions and Outlook	191
References	193
5 Multigrid Numerical Method	198
5.1 Introduction	198
5.2 Full Approximation Storage (FAS) Scheme	200
5.3 Coarsening Algorithm	202
5.3.1 Selection of Seed Vertices	202
5.3.2 Agglomeration of Control Volumes	203
5.3.3 Movement of Seed Vertices	205
5.4 Coarse-Grid Discretisation	211
5.4.1 Inviscid Fluxes	212
5.4.2 Viscous Fluxes	212
5.4.3 Boundary Conditions	212
5.5 Cycling Strategy	212
5.6 Intergrid-Transfer Operators	215
5.6.1 Restriction Operator	215
5.6.2 Prolongation Operator	216

5.6.3	Interpolation Operator	217
5.7	Closure	217
	References	217
III VALIDATION AND APPLICATION OF METHOD		220
6	Validation of Method for Inviscid Flows	221
6.1	Introduction	221
6.2	Supersonic Free Vortex	222
6.2.1	Analytical Solution	222
6.2.2	Grid-Refinement Study	223
6.2.3	Conclusions	231
6.3	Bump in Channel	233
6.3.1	Subsonic Case	234
6.3.2	Transonic Case	248
6.3.3	Supersonic Case	260
6.3.4	Conclusions	270
6.4	NACA 0012 Aerofoil	271
6.4.1	Subsonic Case	272
6.4.2	Transonic Case	273
6.4.3	Conclusions	274
6.5	Closure	274
	References	275
7	Application of Method to Laminar Flows	287
7.1	Introduction	287
7.2	Flat-Plate Boundary Layer	287
7.2.1	Theoretical Solution	288
7.2.2	Numerical Solutions	289
7.2.3	Conclusions	298
7.3	NACA 0012 Aerofoil	302
7.3.1	Grid-Refinement Study	306
7.3.2	Assessment of Multigrid Acceleration	322

7.3.3	Conclusions	325
7.4	Closure	328
	References	328
8	Application of Method to Turbulent Flows	329
8.1	Introduction	329
8.2	ONERA Bump Case C	330
8.2.1	Numerical Solutions	332
8.2.2	Assessment of Thin-Shear-Layer Approximation	340
8.2.3	Assessment of Multigrid Acceleration	346
8.3	RAE 2822 Aerofoil Case 10	348
8.3.1	Wind-Tunnel Corrections	348
8.3.2	Numerical Solution	350
8.3.3	Assessment of Thin-Shear-Layer Approximation	352
8.3.4	Assessment of Multigrid Acceleration	355
8.4	Conclusions	355
	References	358
IV	CONCLUSIONS AND RECOMMENDATIONS	362
9	Conclusions and Recommendations	363
9.1	Summary of Results	363
9.1.1	Inviscid Flow	363
9.1.2	Laminar Flow	363
9.1.3	Turbulent Flow	364
9.2	Achievements and Findings	365
9.3	Recommended Future Work	366
9.3.1	Development of Solution Methods for Mixed Grids	366
9.3.2	Automatic Generation and Adaptation of Mixed Grids	367
	References	372

List of Tables

2.1	Values of constants for air at moderate temperatures	75
2.2	Values of constants for Spalart-Allmaras turbulence model	82
3.1	Stage coefficients of Runge-Kutta scheme for first- and second-order schemes	136
5.1	Parameters determining the type of cycle in cycling algorithm depicted in Fig. 5.8	215
6.1	Summary of grid characteristics used in computational study for subsonic and transonic bump flow calculations	235
6.2	Summary of characteristics of the 5 grid levels used in assessment of agglomeration multigrid scheme for subsonic and transonic bump flow .	245
6.3	Summary of first-order results for agglomeration multigrid scheme applied to subsonic bump flow	245
6.4	Summary of second-order results for agglomeration multigrid scheme applied to subsonic bump flow	248
6.5	Summary of first-order results for multigrid scheme applied to transonic bump flow	257
6.6	Summary of second-order results for multigrid scheme applied to transonic bump flow	257
6.7	Summary of grid characteristics used in computational study for supersonic bump flow calculations	260
6.8	Summary of grid characteristics of the 5 grid levels used in assessment of multigrid scheme for supersonic bump flow	267
6.9	Summary of first-order results for supersonic bump calculations with multigrid scheme	267
6.10	Summary of second-order results for supersonic bump calculations with multigrid scheme	267

6.11 Summary of grid characteristics of the 5 grid levels used in assessment of agglomeration multigrid scheme for inviscid flow around NACA 0012 aerofoil 272

6.12 Summary of second-order results for calculations with multigrid scheme of subsonic flow around NACA 0012 aerofoil 273

6.13 Summary of second-order results for calculations with multigrid scheme of transonic flow around NACA 0012 aerofoil 274

7.1 Summary of grid characteristics for numerical study of laminar flow over a flat plate 290

7.2 Summary of grid characteristics used in grid-refinement study for subsonic laminar flow about NACA 0012 aerofoil 303

7.3 Summary of characteristics for the 5 grid levels used in assessment of agglomeration multigrid scheme for laminar flow around NACA 0012 aerofoil 325

7.4 Summary of results for multigrid scheme applied to laminar flow about NACA 0012 aerofoil 325

8.1 Summary of grid characteristics for numerical study of turbulent flow over ONERA bump 332

8.2 Comparison of separation and re-attachment positions on lower wall for turbulent flow over ONERA bump 336

List of Figures

1.1	Illustration of challenging flow phenomena by way of an aerofoil	3
1.2	Illustration of grid types and their relationships	6
1.3	Curvilinear grid of C-topology for NACA 0012 aerofoil	7
1.4	Illustration of chimera grid for generic two-element aerofoil	10
1.5	Triangular grid for three-element aerofoil	12
1.6	Typical appearance of simplicial grids for viscous flow simulations . . .	13
1.7	Cartesian grid for NACA0012 aerofoil	15
1.8	Comparison of interface between quadrilateral and triangular cells in zonal and mixed grids	19
1.9	Illustration of generation of prismatic grid by marching along suitably defined normal vectors from a surface triangulation	20
1.10	Section through prismatic-tetrahedral grid	21
1.11	Illustration of two choices for defining control volumes on unstructured grids	25
1.12	Three approaches to reconstructing the linear solution variations neces- sary to obtain second-order accuracy with a vertex-based scheme	29
1.13	Illustration of the upwind scheme of Frink	31
1.14	Typical reconstruction stencils for vertex-based scheme for interior and boundary vertices	32
1.15	Reconstruction stencils for the higher-order scheme of Barth	33
1.16	Illustration of methods for the generation of coarse grid levels for multi- grid methods on unstructured grids	48
3.1	Median dual on triangular and mixed grids	89
3.2	Containment dual on triangular grids	89
3.3	Median dual and containment dual on triangulated quadrilateral grid . .	90
3.4	Effect of diagonal edges on median dual and containment dual for trian- gulated quadrilateral grid	91

3.5	Illustration of data structure	93
3.6	Grid-transparent stencil on quadrilateral and mixed grid	95
3.7	Grid-transparent stencils on quadrilateral and mixed grid through sub- division of non-simplicial cells with virtual edges	96
3.8	Simplification of original flux quadrature for median-dual control volumes	98
3.9	Simplification of original flux quadrature for median-dual control volumes at boundary	99
3.10	Definition of normal vectors used in derivation of Green-Gauss gradient reconstruction	103
3.11	Nomenclature for Green-Gauss gradient reconstruction at boundary . .	105
3.12	Nomenclature for Green-Gauss gradient reconstruction on quadrilateral grid	107
3.13	Illustration of construction of Green-Gauss gradient reconstruction for quadrilateral grids with trapezoidal rule around union of cells as a sum over dual edges and virtual edges	108
3.14	Comparison of stencils obtained with Green-Gauss reconstruction of x - derivative for uniform quadrilateral grid	108
3.15	Virtual edges are inserted into quadrilateral cells on boundaries to in- crease the support of least-squares gradient reconstruction	112
3.16	Function used to illustrate difference between Barth-Jespersen and Venkatakr- ishnan limiter functions	118
3.17	Illustration of computation of distance function for Spalart-Allmaras tur- bulence model	122
3.18	Schematic illustration of implementation of transition terms in Spalart- Allmaras turbulence model	123
3.19	Introduction of left and right solution states on boundaries	126
3.20	Illustration of strong imposition of slip-wall boundary condition	128
3.21	Nomenclature used in derivation of freestream boundary condition for lifting flows	133
4.1	Definition of nomenclature used in Eq. (4.2.1)	148
4.2	Illustration of possible spurious solution modes on quadrilateral grids . .	151

4.3	Grid-transparent stencils for Laplacian on uniform triangular and quadrilateral grids	153
4.4	Examples of quadrilateral grid and triangular grid on which positivity and consistency cannot be achieved simultaneously	154
4.5	Examples of quadrilateral grid and triangular grid near boundaries where positivity and accuracy cannot be achieved simultaneously	156
4.6	Examples of grids near boundaries where positivity and accuracy cannot be achieved simultaneously and consistency is impossible to achieve	156
4.7	Obtaining gradients at control-volume faces by averaging averaging vertex-gradients across control-volume face or averaging cell-gradients along control-volume face	162
4.8	Stencils obtained when averaging node-gradients across control-volume faces for equilateral triangular grid and uniform quadrilateral grid	164
4.9	Averaging gradients at edges is equivalent to reconstructing a gradient at edge mid-point using Green-Gauss theorem	166
4.10	Stencils obtained when averaging cell-gradients along control-volume faces for equilateral triangular grids and uniform quadrilateral grid	168
4.11	Definition of geometric terms for canonical discretisation with Scheme 2	170
4.12	Definition of angle θ_{0i}	172
4.13	Definition of integration path for diamond-path reconstruction	173
4.14	Explanation of nomenclature for alternative interpretation of canonical Scheme 3	175
4.15	Piecewise linear shape function	183
4.16	Definition of nomenclature used in derivation of Galerkin finite-element discretisation	184
4.17	Definition of normal vectors for Dirichlet region	189
4.18	Definition of equivalent control-volume face for discretisation of diffusion equation by Galerkin finite-element method	191
4.19	Illustration of correspondence between Galerkin finite-element discretisation, finite-volume discretisation with Dirichlet regions, and Scheme 1	192

5.1	Illustration of step in agglomeration algorithm to ensure coarsening ratio of four on quadrilateral grid	204
5.2	Structural diagram of coarsening algorithm	206
5.3	Illustration of isotropic agglomeration for triangular grid	207
5.4	Illustration of isotropic agglomeration for quadrilateral grid	208
5.5	Histograms of coarsening ratio on triangular and quadrilateral grids . .	209
5.6	Illustration of movement of seed vertices on coarse grid levels for fine grid consisting of quadrilateral cells	210
5.7	Illustration of V-, W-, and F-cycles for 4 grid levels	213
5.8	Structural diagram of cycling algorithm	214
6.1	Solution domain and boundary conditions for supersonic free vortex flow	223
6.2	41×11 grids used for grid-refinement study for free-vortex flow	225
6.3	Results for first-order scheme for free-vortex flow	228
6.4	Results for second-order scheme with Green-Gauss reconstruction for free-vortex flow	229
6.5	Results for second-order scheme with least-squares reconstruction for free-vortex flow	230
6.6	Solution domain and boundary conditions for flow over bump in channel	233
6.7	Triangular and quadrilateral grids used for subsonic and transonic bump flow calculations	235
6.8	Contours of pressure for first-order solutions on triangular and quadrilateral grid for subsonic bump flow	236
6.9	Contours of pressure for second-order solutions on triangular and quadrilateral grid for subsonic bump flow	237
6.10	Comparison of pressure coefficient for first- and second-order solutions on triangular and quadrilateral grids for subsonic bump flow	239
6.11	Comparison of entropy parameter for first- and second-order solutions on triangular and quadrilateral grids for subsonic bump flow	240
6.12	Triangulated quadrilateral grids obtained from grid shown in Fig. 6.7 . .	241
6.13	Detail view of effect of diagonal edges on control-volume shape near trailing edge of bump	242

6.14	Comparison of pressure coefficient for median and containment dual for second-order solutions on triangulated quadrilateral grids for subsonic bump flow	243
6.15	Comparison of entropy parameter for median and containment dual for second-order solutions on triangulated quadrilateral grids for subsonic bump flow	244
6.16	Comparison of multigrid performance for first-order schemes on triangular and quadrilateral grids for subsonic bump flow	246
6.17	Comparison of multigrid performance for second-order schemes on triangular and quadrilateral grids for subsonic bump flow	247
6.18	Contours of pressure for first-order solutions on triangular and quadrilateral grids for transonic bump flow	249
6.19	Contours of pressure for second-order solutions with Barth-Jespersen and Venkatakrishnan limiter functions and Ollivier-Gooch reconstruction on triangular grid for transonic bump flow	250
6.20	Contours of pressure for second-order solutions with Barth-Jespersen and Venkatakrishnan limiter functions and Ollivier-Gooch reconstruction on quadrilateral grid for transonic bump flow	251
6.21	Comparison of pressure coefficient for second-order solutions on triangular and quadrilateral grids for transonic bump flow	252
6.22	Comparison of entropy parameter for second-order solutions on triangular and quadrilateral grids for transonic bump flow	253
6.23	Convergence histories for second-order schemes with Barth-Jespersen and Venkatakrishnan limiter functions on quadrilateral grid for transonic bump flow	254
6.24	Comparison of pressure coefficient for median and containment dual for second-order solutions on triangulated quadrilateral grids for transonic bump flow	255
6.25	Comparison of entropy parameter for median and containment dual for second-order solutions with Venkatakrishnan limiter function on triangulated quadrilateral grids for transonic bump flow	256

6.26	Comparison of multigrid convergence for first-order schemes on triangular and quadrilateral grids for transonic bump flow	258
6.27	Comparison of multigrid convergence for second-order schemes on triangular and quadrilateral grids for transonic bump flow	259
6.28	Triangular and quadrilateral grids used for supersonic bump flow calculations	260
6.29	Contours of pressure for first-order solutions on triangular and quadrilateral grids for supersonic bump flow	261
6.30	Contours of pressure for second-order solutions on triangular and quadrilateral grids for supersonic bump flow	262
6.31	Comparison of pressure coefficient for first- and second-order solutions on triangular and quadrilateral grids for supersonic bump flow	263
6.32	Comparison of entropy parameter for first- and second-order solutions on triangular and quadrilateral grids for supersonic bump flow	264
6.33	Comparison of pressure coefficient for median and containment dual for second-order solutions on triangulated quadrilateral grids for supersonic bump flow	265
6.34	Comparison of entropy parameter for median and containment dual on triangulated quadrilateral grids for supersonic bump flow	266
6.35	Comparison of multigrid convergence for first-order schemes on triangular and quadrilateral grids for supersonic bump flow	268
6.36	Comparison of multigrid convergence for second-order schemes on triangular and quadrilateral grids for supersonic bump flow	269
6.37	Solution domain and boundary conditions for inviscid flow over NACA 0012 aerofoil	277
6.38	Triangular grid used for inviscid flow over NACA 0012 aerofoil	278
6.39	Contours of pressure for second-order solution of subsonic flow around NACA 0012 aerofoil	279
6.40	Pressure coefficient and entropy parameter for second-order solution of subsonic flow around NACA 0012 aerofoil	280
6.41	The 5 grid levels used in assessment of agglomeration multigrid scheme for flow around NACA 0012 aerofoil	281

6.42	Comparison of multigrid convergence for second-order scheme with V- and W-cycles for subsonic flow around NACA 0012 aerofoil	282
6.43	Contours of pressure for second-order solution of transonic flow around NACA 0012 aerofoil	283
6.44	Pressure coefficient and entropy parameter for second-order solution of transonic flow around NACA 0012 aerofoil	284
6.45	Comparison of present solution for transonic flow around NACA 0012 aerofoil with other published results	285
6.46	Comparison of multigrid convergence for second-order scheme with V- and W-cycles for transonic flow around NACA 0012 aerofoil	286
7.1	Solution domain and boundary conditions for laminar flow over a flat plate at zero incidence	289
7.2	Grids used for laminar flow over flat plate	291
7.3	Comparison of theoretical solution for skin-friction coefficient with solutions obtained on triangular, quadrilateral, and mixed grids	292
7.4	Comparison of numerical solution on triangular grid for u - and v -velocities with theoretical solution at four stations along flat plate	293
7.5	Comparison of numerical solution on quadrilateral grid for u - and v -velocities with theoretical solution at four stations along flat plate	294
7.6	Comparison of numerical solution on mixed grid for u - and v -velocities with theoretical solution at four stations along flat plate	295
7.7	Comparison of convergence on triangular, quadrilateral, and mixed grids in terms of normalised CPU time for laminar flow over flat plate	296
7.8	Comparison of theoretical solution for skin-friction coefficient with solutions obtained on triangular, quadrilateral, and mixed grids	297
7.9	Comparison of numerical solution with thin-shear-layer approximation on triangular grid for u - and v -velocities with theoretical solution at four stations along flat plate	299
7.10	Comparison of numerical solution with thin-shear-layer approximation on quadrilateral grid for u - and v -velocities with theoretical solution at four stations along flat plate	300

7.11 Comparison of numerical solution with thin-shear-layer approximation on mixed grid for u - and v -velocities with theoretical solution at four stations along flat plate	301
7.12 Solution domain and boundary conditions for laminar flow about NACA 0012 aerofoil	303
7.13 Primal and dual medium triangular grids used in grid-refinement study for laminar subsonic flow about NACA 0012 aerofoil	304
7.14 Primal and dual medium quadrilateral grids used in grid-refinement study for laminar subsonic flow about NACA 0012 aerofoil	305
7.15 Mach countours and streamlines with finite-volume discretisation of viscous fluxes on fine level quadrilateral grid	307
7.16 Behaviour of pressure coefficient and skin-friction coefficient with grid refinement on quadrilateral grids	308
7.17 Mach number contours and streamlines with finite-volume discretisation of viscous fluxes on fine level triangular grid	309
7.18 Behaviour of pressure coefficient and skin-friction coefficient with grid refinement on triangular grids with finite-volume discretisation of viscous fluxes	310
7.19 Mach number contours and streamlines with finite-element discretisation of viscous fluxes on fine level triangular grid	311
7.20 Behaviour of pressure coefficient and skin-friction coefficient with grid refinement on triangular grids with finite-element discretisation of viscous fluxes	312
7.21 Behaviour of lift and drag coefficients with grid refinement for quadrilateral and triangular grids	314
7.22 Break-up of drag coefficient into pressure and skin-friction drag coefficients for quadrilateral and triangular grids	315
7.23 Behaviour of separation and reattachment positions with grid refinement for quadrilateral and triangular grids	316
7.24 Comparison of behaviour of lift and drag coefficients with grid refinement for quadrilateral grids for full viscous fluxes and thin-shear-layer approximation	317

7.25	Relative importance of terms in Expressions (4.4.4a) and (4.4.4b) along normal at $x = 0.2$ on upper surface for fine level quadrilateral grid . . .	318
7.26	Relative importance of terms in Expressions (4.4.4a) and (4.4.4b) along normal at $x = 0.7$ on upper surface for fine level quadrilateral grid . . .	319
7.27	Behaviour of separation and reattachment positions with grid refinement for full viscous fluxes and thin-shear-layer approximation on quadrilateral grids	320
7.28	Comparison of behaviour of lift and drag coefficients with grid refinement for triangular grids for full viscous fluxes and thin-layer approximation .	321
7.29	Behaviour of separation and reattachment positions with grid refinement for full viscous fluxes and thin-shear-layer approximation on triangular grids	322
7.30	The 5 grid levels used in assessment of agglomeration multigrid scheme for laminar flow around NACA 0012 aerofoil on triangular grid	323
7.31	The 5 grid levels used in assessment of agglomeration multigrid scheme for laminar flow around NACA 0012 aerofoil on quadrilateral grid	324
7.32	Comparison of multigrid convergence on triangular and quadrilateral grids for laminar flow about NACA 0012 aerofoil	326
8.1	Solution domain and boundary conditions for ONERA bump	331
8.2	Triangular, quadrilateral, and mixed grids used for computation of turbulent flow over ONERA bump	333
8.3	Pressure and Mach number contours for turbulent flow over ONERA bump	335
8.4	Comparison of numerical interferogram of solution on mixed grid and experimental interferogram of interaction region for turbulent flow over ONERA bump	336
8.5	Comparison of numerical solution with experimental values of normalised pressure on upper and lower channel walls for ONERA bump	337
8.6	Locations of comparisons of numerical solution for u -velocity profiles and turbulent shear stress with experimental values superimposed on computed Mach number contours on mixed grid for ONERA bump	338

8.7	Comparison of numerical solutions and experimental values for u -velocity on lower wall for ONERA bump	339
8.8	Comparison of numerical solutions and experimental values for turbulent shear stress $-\widetilde{u''v''}$ on lower wall for ONERA bump	341
8.9	Comparison of convergence on triangular, quadrilateral, and mixed grids in terms of normalised CPU time for ONERA bump	342
8.10	Pressure and Mach number contours for turbulent flow over ONERA bump with thin-shear-layer approximation	343
8.11	Comparison of numerical solution with experimental values of normalised pressure on upper and lower channel walls for ONERA bump	344
8.12	Relative importance of terms in Expressions (4.4.4a) and (4.4.4b) along normal at $x = 0.19$ to solid wall	345
8.13	Relative importance of terms in Expressions (4.4.4a) and (4.4.4b) along normal at $x = 0.27$ to solid wall	347
8.14	Solution domain and boundary conditions for RAE 2822 aerofoil.	351
8.15	Primal grid used for computation of turbulent flow past RAE 2822 aerofoil	352
8.16	Pressure and Mach number contours for turbulent flow past RAE 2822 aerofoil	353
8.17	Comparison of numerical solution with experimental values of pressure and skin-friction coefficient for RAE 2822 aerofoil	354
8.18	Locations of comparisons of numerical solution for u -velocity profiles with experimental values superimposed on computed Mach-number contours for RAE 2822 aerofoil	355
8.19	Comparison of numerical solutions and experimental values for normalised u -velocity on upper surface of RAE 2822 aerofoil	356
8.20	Illustration of the effect of the transition term by comparison of velocity profiles at $x/c = 0.01$ and $x/c = 0.1$ for RAE 2822 aerofoil	358
8.21	Comparison of numerical solution with experimental values of pressure and skin-friction coefficient for RAE 2822 aerofoil	359
9.1	Possible use of virtual edges to improve discretisations at interfaces . . .	366
9.2	Representation of the leading edge of an aerofoil by triangular and quadrilateral faces	369

9.3 Possible use of several cell types in future grid-generation methods . . . 370

9.4 Possible use of several cell types in future adaptation algorithms 371

Nomenclature

The symbols used in the present work were chosen according to the following guidelines:

1. Upper- and lower-case Latin and Greek characters in normal typeface represent scalar quantities.
2. Upper- and lower-case Latin and Greek characters in bold typeface represent vector quantities; a vector component is denoted by the corresponding character in normal typeface with a Latin subscript.
3. Upper-case Latin and Greek characters in sans-serif typeface represent tensor or matrix quantities; a tensor or matrix element is denoted by the corresponding character in normal typeface with two Latin or Greek subscripts.
4. The Einstein summation convention is employed for tensors with repeated Latin indices.

These guidelines are ignored in some cases to ensure compatibility with symbols commonly employed in the literature. Infrequently used symbols are not listed below. SI units are used throughout.

Latin Characters

A	area
A_{Ω_0}	area of control volume at vertex 0
a	speed of sound
C_D	drag coefficient per unit width, defined by Eq. (7.3.1b)
C_L	lift coefficient per unit width, defined by Eq. (7.3.1a)
C_M	moment coefficient per unit width squared, defined by Eq. (6.4.3c)
C_p	specific heat at constant pressure, $C_p = 1004.64 \text{ J/(kg K)}$; pressure coefficient, defined by Eqs. (6.3.1) and (6.4.2)
C_{Suth}	constant in Sutherland's viscosity law, $C_{\text{Suth}} = 110.0 \text{ K}$
C_v	specific heat at constant volume, $C_v = 717.6 \text{ J/(kg K)}$

c	chord of aerofoil
c_{b1}	constant in Spalart-Allmaras turbulence model, $c_{b1} = 0.1355$
c_{b2}	constant in Spalart-Allmaras turbulence model, $c_{b2} = 0.622$
c_{t1}	constant in Spalart-Allmaras turbulence model, $c_{t1} = 1$
c_{t2}	constant in Spalart-Allmaras turbulence model, $c_{t2} = 2$
c_{t3}	constant in Spalart-Allmaras turbulence model, $c_{t3} = 1.2$
c_{t4}	constant in Spalart-Allmaras turbulence model, $c_{t4} = 0.5$
c_{v1}	constant in Spalart-Allmaras turbulence model, $c_{v1} = 7.1$
c_{v2}	constant in Spalart-Allmaras turbulence model, $c_{v2} = 5.0$
c_{w1}	constant in Spalart-Allmaras turbulence model, given by Eq. (2.4.30)
c_{w2}	constant in Spalart-Allmaras turbulence model, $c_{w2} = 0.3$
c_{w3}	constant in Spalart-Allmaras turbulence model, $c_{w3} = 2$
d	distance to nearest solid wall in Spalart-Allmaras turbulence model
d_0	degree of vertex 0
E	total internal energy
E_p	error norm, $p = 1, 2, \infty$
F_0	forcing function for control volume 0, defined by Eq. (5.2.11)
f_{t1}	function in Spalart-Allmaras turbulence model, defined by Eq. (2.4.32)
f_{t2}	function in Spalart-Allmaras turbulence model, defined by Eq. (2.4.31)
f_{v1}	function in Spalart-Allmaras turbulence model, defined by Eq. (2.4.22)
f_{v2}	function in Spalart-Allmaras turbulence model, defined by Eq. (2.4.25)
f_{v3}	function in Spalart-Allmaras turbulence model, defined by Eq. (2.4.26)
f_w	function in Spalart-Allmaras turbulence model, defined by Eq. (2.4.27)
g	function in Spalart-Allmaras turbulence model, defined by Eq. (2.4.28)
g_t	function in Spalart-Allmaras turbulence model, defined by Eq. (2.4.33)
H	total enthalpy
h	static enthalpy; measure of grid spacing
\mathbf{l}	identity tensor, $I_{ij} = \delta_{ij}$
\mathbf{i}	unit vector in x -direction
\mathbf{j}	unit vector in y -direction
k	turbulence kinetic energy

\mathbf{k}	unit vector, $\mathbf{k} = \mathbf{i} \times \mathbf{j}$
M	Mach number, $M = V/a$
M	transformation matrix, $\mathbf{q} = M\mathbf{p}$, defined by Eq. (3.7.5)
N	number of vertices
\mathbf{n}	normal vector, $\mathbf{n} = n_x\mathbf{i} + n_y\mathbf{j}$
n	coordinate direction aligned with freestream direction
n_x	component in x -direction of normal vector
n_y	component in y -direction of normal vector
$O(\cdot)$	on the order of (\cdot)
p	pressure, given by Eq. (2.2.4)
\mathbf{p}	primitive state vector, $\mathbf{p} = \{\rho, u, v, p\}^t$
Pr	Prandtl number, defined as $Pr = \mu C_p / \kappa$
Pr_t	turbulent Prandtl number, defined as $Pr_t = \mu_t C_p / \kappa_t$
\mathbf{q}	conservative state vector, $\mathbf{q} = \{\rho, \rho u, \rho v, \rho E\}^t$; heat-flux vector, defined by Eq. (2.3.6)
$\tilde{\mathbf{q}}$	approximate solution in multigrid method
$\hat{\mathbf{q}}$	coarse-grid solution vector in multigrid method
q	component of velocity vector normal to a given unit vector
R	residual
R_s	Riemann invariant, defined by Eq. (3.11.16b)
R_t	Riemann invariant, defined by Eq. (3.11.16a)
R_+	Riemann invariant, defined by Eq. (3.11.16c)
R_-	Riemann invariant, defined by Eq. (3.11.12)
R	specific gas constant, $R = C_p - C_v$, $R = 287.04 \text{ J/(kg K)}$
r	function in Spalart-Allmaras turbulence model, defined by Eq. (2.4.29); component of velocity vector tangential to a given unit vector; radial coordinate
\mathbf{r}	position vector, $\mathbf{r} = x\mathbf{i} + y\mathbf{j}$
Re	Reynolds number
S	strain tensor, defined by Eq. (2.3.3)
s	coordinate direction normal to freestream direction
T	static temperature

\mathbf{T}	stress tensor, defined by Eq. (2.3.2)
\mathbf{t}	tangential vector; $\mathbf{t} = t_x \mathbf{i} + t_y \mathbf{j}$
t	time coordinate
t_x	component in x -direction of tangential vector
t_y	component in y -direction of tangential vector
Δt	time step
u	component in x -direction of velocity vector
V	velocity magnitude, $V = \ \mathbf{v}\ $
v	component in y -direction of velocity vector
\mathbf{v}	velocity vector, $\mathbf{v} = u\mathbf{i} + v\mathbf{j}$
x	space coordinate in horizontal direction
y	space coordinate in vertical direction

Greek Characters

α	angle of attack of aerofoil; angle between flow direction and normal vector at inflow boundary
α_k	k th stage coefficient in Runge-Kutta method
β	Prandtl-Glauert parameter, $\beta = \sqrt{1 - M_\infty^2}$
γ	ratio of specific heats, $\gamma = C_p/C_v$, $\gamma = 1.4$
δ_{ij}	Kronecker delta, $\delta_{ij} = 1$ if $i = j$, $\delta_{ij} = 0$ if $i \neq j$
ε	variable used in Venkatakrishnan limiter function; small number, $\varepsilon \ll 1$
η	coordinate direction aligned with control-volume face
θ	angular coordinate
κ	coefficient of heat conduction; von Kármán's constant, $\kappa = 0.41$; coefficient in MUSCL interpolation, $-1/6 \leq \kappa \leq 1$
κ_t	eddy coefficient of heat conduction
λ	second coefficient of viscosity, $\lambda = -\frac{2}{3}\mu$; limiter function, defined by Eq. (3.7.67) or (3.7.68)
μ	dynamic laminar viscosity, defined by Eq. (2.3.8)
μ_t	dynamic eddy viscosity, defined by Eq. (2.4.21)

ν	kinematic laminar viscosity
$\tilde{\nu}$	eddy-viscosity variable in Spalart-Allmaras turbulence model
ξ	coordinate direction aligned with edge $0i$
π	$\pi = 3.14159265\dots$
ρ	density
Σ	entropy parameter, defined by Eqs. (6.3.2) and (6.4.4)
σ	constant in Spalart-Allmaras turbulence model, $\sigma = 2/3$
ϕ	generic variable; velocity potential, $\mathbf{v} = \nabla\phi$
χ	variable in Spalart-Allmaras turbulence model, defined by Eq. (2.4.23)
Ω	vorticity, $\Omega = \nabla \times \mathbf{v}$
Ω	magnitude of vorticity, $\Omega = \ \Omega\ $
Ω_0	control volume at vertex 0
Ω'_0	region formed by cells meeting at vertex 0
$\Omega_{0'}$	coarse-grid control volume containing fine-grid control volume at vertex 0
$\tilde{\Omega}$	magnitude of vorticity in Spalart-Allmaras turbulence model
ω	general vector of edge weights
ω	general edge weight

Calligraphic Characters

$\mathcal{C}_{0'}^H$	set of control volumes on grid h contained in control volume $0'$ on grid H
\mathcal{E}_0	set of edges incident to vertex 0
\mathcal{I}_h^H	restriction operator
\mathcal{I}_H^h	prolongation operator
$\bar{\mathcal{I}}_h^H$	interpolation operator
\mathcal{T}_0	set of triangles meeting at vertex 0

Operators

$D(\cdot)/Dt$	substantial derivative, $D(\cdot)/Dt = \partial(\cdot)/\partial t + \mathbf{v} \cdot \nabla(\cdot)$
$\nabla(\cdot)$	gradient operator, $\nabla(\cdot) = \partial(\cdot)/\partial x \mathbf{i} + \partial(\cdot)/\partial y \mathbf{j}$
$ (\cdot) $	magnitude of scalar (\cdot)
$\ (\cdot)\ $	magnitude of vector (\cdot)

$\mathbf{a} \cdot (\cdot)$	scalar product of vector \mathbf{a} with vector (\cdot)
$\mathbf{a} \times (\cdot)$	vector product of vector \mathbf{a} with vector (\cdot)
$\mathbf{a} \otimes (\cdot)$	tensor product of vector \mathbf{a} with vector (\cdot)
$\lceil (\cdot) \rceil$	ceiling function
$\lfloor (\cdot) \rfloor$	floor function
$\text{neg}(\cdot)$	negative projection operator, defined by Eq. (3.12.13)

Subscripts

ac	aerodynamic centre
eff	effective value, given by sum of laminar and turbulent values
i	evaluated at vertex i ; i th component of vector; evaluated at inner radius
ij	ij th component of tensor
L	left state
o	evaluated at outer radius
R	right state
ref	reference quantity
$wall$	evaluated at wall
0	evaluated at vertex 0; evaluated at stagnation state
$0i$	relating to edge directed from vertex 0 to vertex i
$0'$	evaluated in coarse-grid control volume containing fine-grid vertex 0
∞	evaluated at freestream state

Superscripts

H	on grid level with characteristic grid spacing H
h	on grid level with characteristic grid spacing h
m	evaluated at m th stage of Runge-Kutta method
t	transpose
$'$	fluctuating part of Reynolds-decomposed variable
$''$	fluctuating part of Favre-decomposed variable

Overbars

$\overline{(\cdot)}$	averaged part of Reynolds-decomposed variable (\cdot) ; average value in control volume, defined by Eq. (3.2.2); modified quantity, unmodified quantity without overbar
$\widetilde{(\cdot)}$	averaged part of Favre-decomposed variable (\cdot) ; approximate solution, defined by Eq. (5.2.2)
$\widehat{(\cdot)}$	Roe-averaged variable, defined by Eqs. (3.7.71a)–(3.7.71d)

Acronyms

ACR	Average Convergence Rate, defined by Eq. (6.3.3)
ADI	Alternating Direction Implicit
AMG	Algebraic Multigrid
CFD	Computational Fluid Dynamics
CFL	Courant-Friedrichs-Levy
CM	Convergence Measure, defined by Eq. (3.13.7)
CPU	Central Processing Unit
DNS	Direct Numerical Simulation
ENO	Essentially Non-Oscillatory
GMRES	Generalised Minimum Residual
HOT	Higher-Order Terms
ILU	Incomplete Lower-Upper (Factorisation)
LED	Local Extremum Diminishing
LES	Large-Eddy Simulation
LU	Lower-Upper (Factorisation)
LU-SGS	Lower-Upper Symmetric Gauss-Seidel
MUSCL	Monotone Upstream-Centred Schemes for Conservation Laws
RANS	Reynolds-Averaged Navier-Stokes Equations
SCT	Scaled CPU Time
TSL	Thin Shear-Layer
TVD	Total Variation Diminishing
WU	Work Unit

PART I

**INTRODUCTION AND
MATHEMATICAL MODEL**

Chapter 1

Introduction

The background and the aim of the present study are described. Different grid types are classified in order to expose their advantages and disadvantages. For the present study, unstructured grids are chosen because of their suitability for discretising complex geometries and adapting to flowfield features. Previous work on unstructured grids is reviewed and discussed. Attention is focussed on the spatial discretisation and iterative solution methods. Finally, the objectives of the current study are formulated based on the aim and the review of previous work.

1.1 Background

The field of aeronautical engineering is characterised by a wide variety of complex flow phenomena. Taking an aerofoil at high-lift and cruise configurations as an example, flow phenomena such as shock waves and their interaction with boundary layers, separation bubbles, transition from laminar to turbulent flow, and wakes arise, as illustrated in Fig. 1.1.

Attempts to study such flows analytically using the partial differential equations governing fluid flow have met with very limited success. The complexity of these equations means that only the simplest flow fields of interest to engineers are accessible to rigorous theoretical analysis. For example, a boundary layer developing or a shock wave impinging on a flat plate can be studied analytically with relative ease when considered in isolation. When trying to analyse their interaction, however, great difficulties appear. Consequently, the great majority of engineering studies in aerodynamics used to be experimental in nature. The advent of the high-speed digital computer and its rapid development have opened up a further avenue for studying aerodynamic phenomena. It entails the numerical solution of the governing equations and has become known as Computational Fluid Dynamics (CFD).

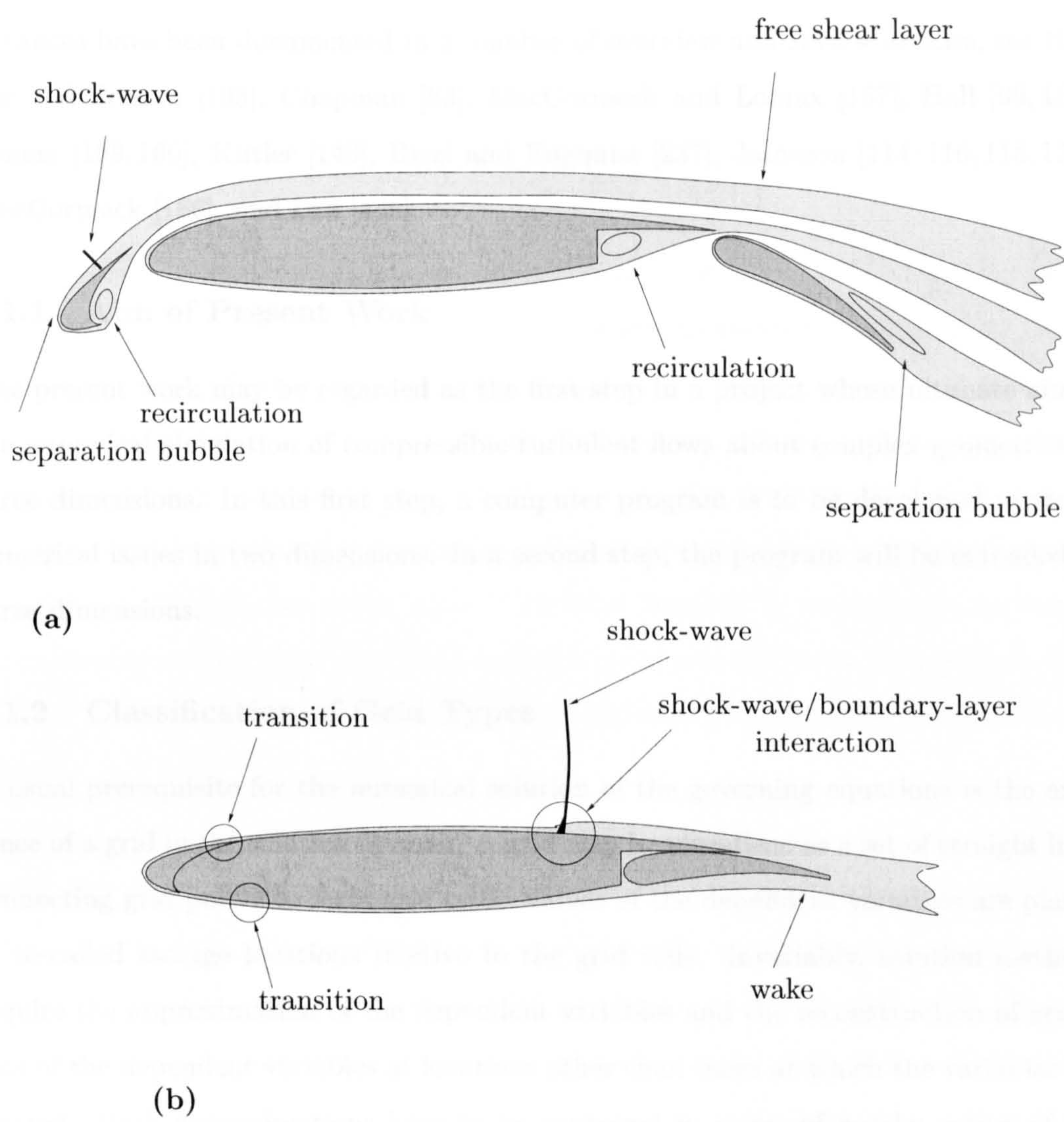


Figure 1.1: Illustration of challenging flow phenomena by way of an aerofoil in (a) high lift and (b) cruise configuration.

CFD enjoys a number of potential advantages over the experimental approach: It reduces lead time in design and development, it is non-intrusive and provides more comprehensive flow-field information, it can simulate hypothetical and hazardous flow conditions, and it is becoming increasingly cost-effective.

During the past decade, CFD has reached a certain level of maturity and flexibility. It can be used with a relatively high degree of confidence for a wide range of problems of engineering interest. While CFD is not yet capable of delivering highly accurate absolute results for all such problems, it usually predicts trends and relative results well (e.g., the change in the flow field due to a change in geometry).

A variety of advances have contributed to the present state-of-the-art in CFD. These

advances have been documented in a number of overview and review articles, see Harlow and Fromm [103], Chapman [63], MacCormack and Lomax [167], Hall [99, 100], Lomax [159, 160], Kutler [143], Rizzi and Engquist [237], Jameson [114–116, 118, 120], MacCormack [166], and Lax [146].

1.1.1 Aim of Present Work

The present work may be regarded as the first step in a project whose ultimate aim is the numerical simulation of compressible turbulent flows about complex geometries in three dimensions. In this first step, a computer program is to be developed to study numerical issues in two dimensions. In a second step, the program will be extended to three dimensions.

1.1.2 Classification of Grid Types

A usual prerequisite for the numerical solution of the governing equations is the existence of a grid in the solution domain. A grid may be visualized as a set of straight lines connecting grid points to form grid cells. Values of the dependent variables are placed at so-called storage locations relative to the grid cells. Invariably, solution methods require the approximation of the dependent variables and the reconstruction of gradients of the dependent variables at locations other than those at which the variables are located. Both approximations have to be expressed in terms of nearby values of the dependent variables. In order to do so, information must be provided to the solution method about which storage locations are nearby a given storage location in the grid. It is this information which is referred to as grid structure (or simply structure). As will be discussed below, grid structure may be provided to the solution method either implicitly or explicitly, or by a combination of both.

Several basic types of grids have been developed. It is instructive to classify these grid types according to the precise way in which grid structure becomes apparent. The classification will demonstrate that each grid type has distinct features and accompanying advantages and disadvantages which directly influence the suitability with respect to the aim given in Subsection 1.1.1. A multitude of additional grid types may be generated by blending features of the existing grid types with the aim of maximising the advantages and minimising the disadvantages. Because of the blending, the classifica-

tion of these additional grid types can become somewhat arbitrary. The classification of grid types presented below is depicted schematically in Fig. 1.2. Detailed information on the various grid types may be found in Thompson et al. [274].

Structured Grids. In structured grids, grid points are placed at the intersections of coordinate lines of a coordinate system which spans the solution domain. As a result, interior grid points have a fixed number of neighbouring grid points and naturally map into a grid-point matrix. This allows the grid points to be referred to by indices. Neighbouring grid points are identified by simply incrementing or decrementing the respective grid-point index. In other words, the underlying coordinate system implicitly lends structure to the grid, hence the name. The label ‘implicit’ is employed to emphasize that the very nature of the grid itself implies a structure which can be exploited. Two types of structured grids can be distinguished, depending on the underlying coordinate system.

Rectilinear Grids. Defining the coordinate system by straight lines leads to rectilinear grids. Due to their simple construction, rectilinear grids were the grids used in early applications of CFD, see, e.g., Reyhner [231] and Purvis and Burkhalter [226]. For non-rectangular solution domains, coordinate lines intersect boundaries at possibly irregular intervals. Consequently, cut boundary cells exist along the boundaries. These cells can complicate the imposition of boundary conditions and require special attention to ensure that stability, consistency, and accuracy of the numerical scheme are maintained. For inviscid flows, Keith Clarke et al. [137] demonstrated that accurate results can be obtained. For viscous flows, however, Frymier et al. [91] found that obtaining accurate solutions is difficult. This has prevented more widespread use of rectilinear grids.

(Single-Block) Curvilinear Grids. The problems of the rectilinear-grid approach can be avoided if coordinate lines coincide with the boundaries, leading to curvilinear grids as pioneered by Thompson et al. [273]. An example of a curvilinear grid for the NACA 0012 aerofoil is shown in Fig. 1.3. For simple geometries (such as aerofoils or wings in cruise configuration), curvilinear grids can be of high quality. Grid quality is usually assessed in terms of the skewness of grid lines and local variations of cell area. As demonstrated

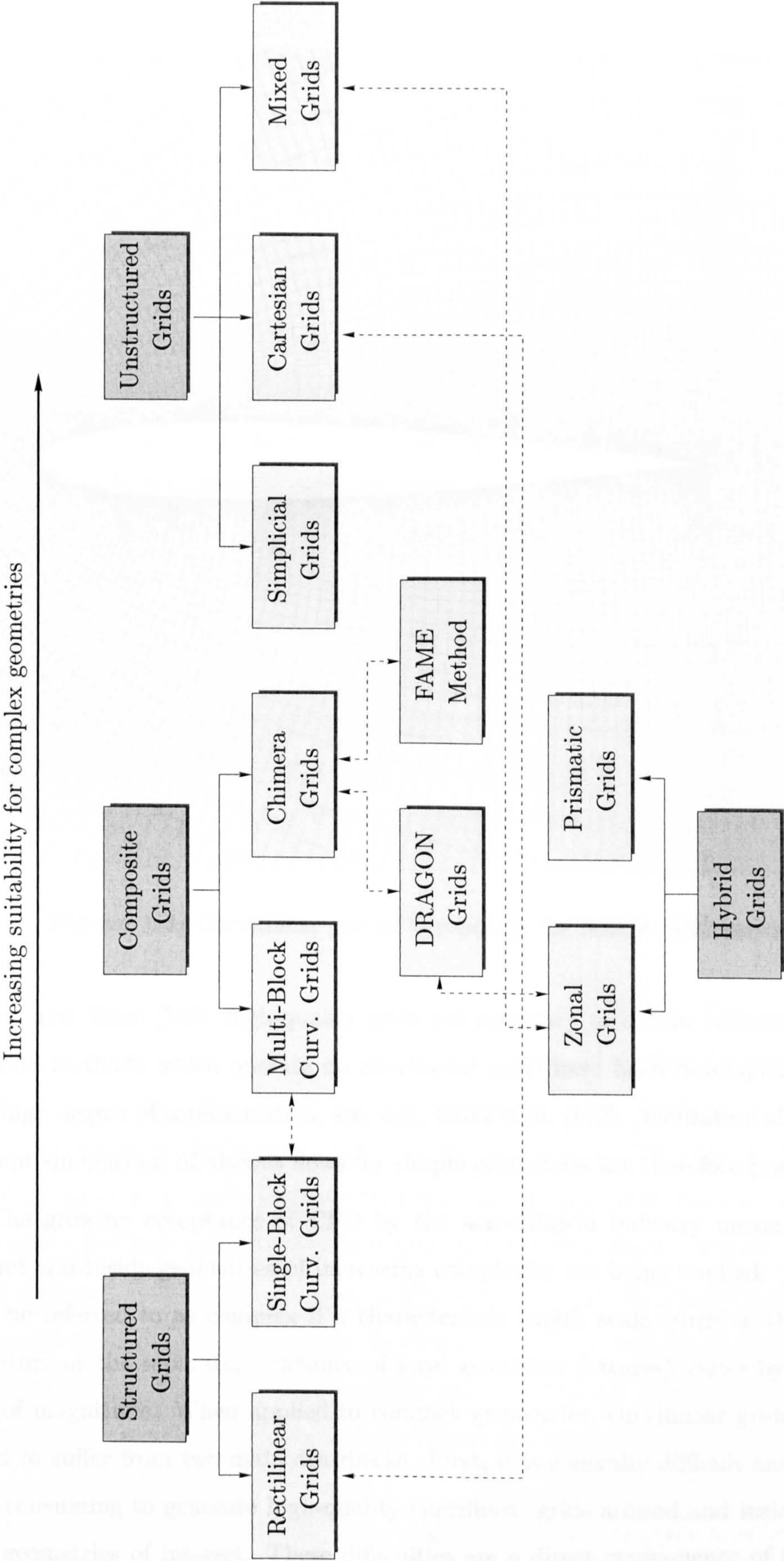


Figure 1.2: Illustration of grid types and their relationships.

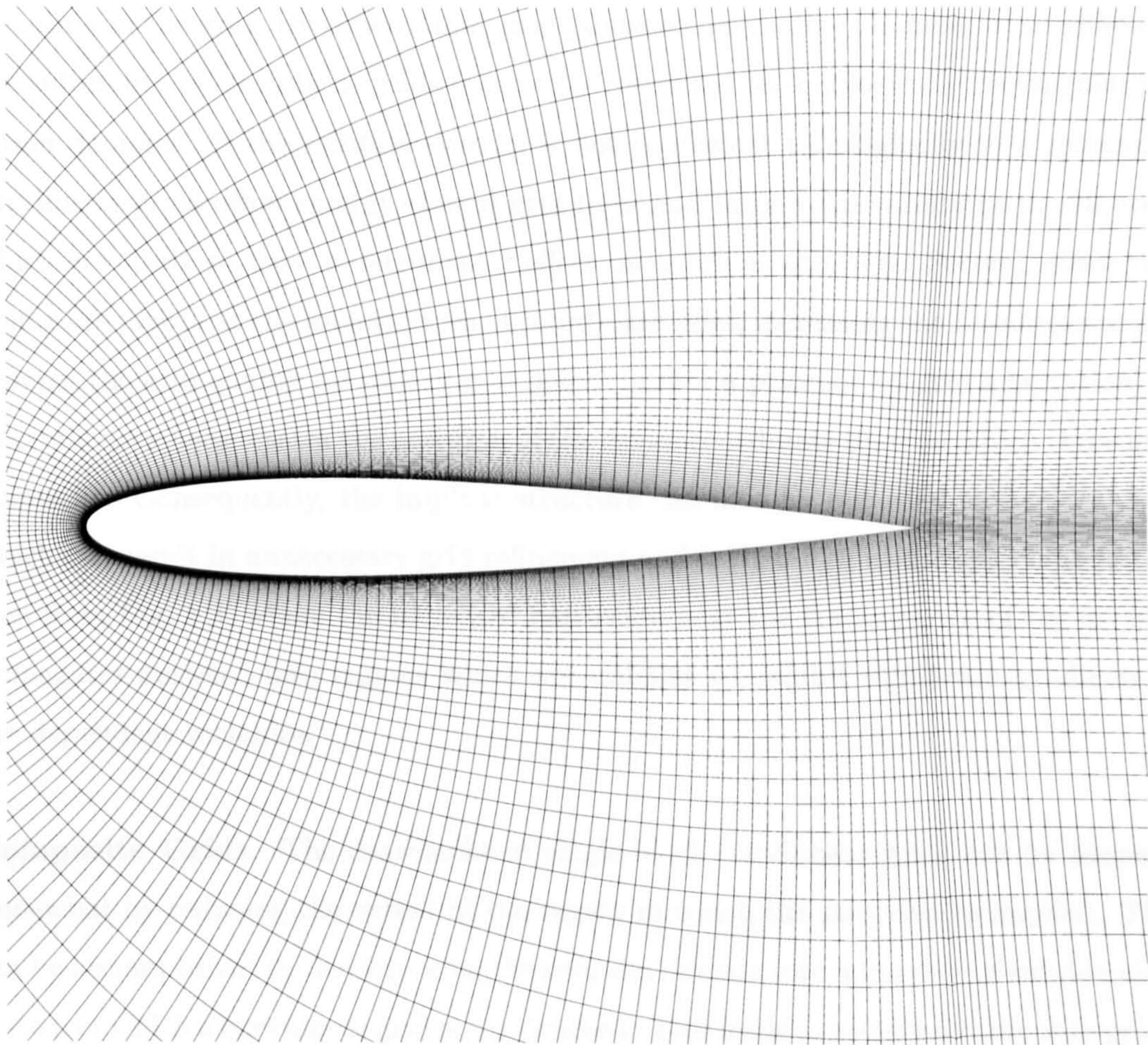


Figure 1.3: Curvilinear grid of C-topology for NACA 0012 aerofoil.

by Lee and Tsuei [149], high-quality grids are necessary to obtain accurate solutions. Solution methods which operate on curvilinear grids have been developed and tuned to a high degree of sophistication, see, e.g., Kroll et al. [142]. Accurate and reasonably efficient simulations of viscous flows for simple geometries are therefore possible.

The growing acceptance of CFD by the aeronautical industry means that flows around and inside geometries of increasing complexity are being studied. A geometry may be referred to as complex if a characteristic length scale (such as the radius of curvature or the separation distance of local geometric features) varies by several orders of magnitude. When applied to complex geometries, curvilinear grids have been found to suffer from two main drawbacks. First, it is generally difficult and extremely time-consuming to generate high-quality curvilinear grids around and inside the complex geometries of interest. These difficulties are a direct consequence of the implicit

structure in the grid. By constraining grid points to have a fixed number of neighbours, the suitability of curvilinear grids is actually restricted to topologically rectangular solution domains. If the solution domain is not equivalent topologically to a rectangle, curvilinear grids often exhibit skewed grid lines and large local variations in cell area, which are likely to have a detrimental effect on solution accuracy. Second, since grid points are placed at the intersections of coordinate lines, increasing the resolution or improving the grid quality by adding grid points (either a priori or by grid adaptation) in a certain area necessitates the addition of the entire coordinate lines on which these grid points lie. Consequently, the implicit structure can also be regarded as being global, which can result in unnecessary grid refinement and is therefore inefficient. This can be seen from Fig. 1.3, where the increased resolution near the trailing edge of the aerofoil propagates outward into regions which are unlikely to exhibit significant gradients of the dependent variables.*

Composite Grids. The drawbacks of single-block curvilinear grids can be lessened somewhat by reducing the extent of the region in which the structure is implicit. This can be accomplished by decomposing the solution domain into a number of subdomains, in each of which a curvilinear grid is constructed. This leads to so-called composite grids. Two main approaches have been suggested.

Multi-Block Curvilinear Grids. Lee and Rubbert [150] and Weatherill and Forsey [295] developed the multi-block method, which divides the solution domain into contiguous blocks. A curvilinear grid is generated in each block. The connectivity between the blocks is specified explicitly in so-called connectivity tables. The basic premise is that it will be easier to generate high-quality curvilinear grids in each block separately than to generate one high-quality curvilinear grid in the entire solution domain. The multi-block approach is probably the most widely used grid type for complex geometries in the aeronautical industry nowadays. As shown by many contributions and exemplified by Vatsa et al. [283], high-quality results can be obtained for complex geometries. However, the multi-block approach suffers from the disadvantage that the generation

*In this particular case, the clustering of grid points near the aerofoil surface improves the resolution of the wake behind the trailing edge due to the adoption of a C-topology and is therefore beneficial for viscous flow simulations.

of a satisfactory block topology for complex geometries is difficult to automate and can therefore be very time-consuming.

Chimera Grids. The chimera method of Benek et al. [40] generates curvilinear grids separately for components of the geometry. In contrast to the multi-block method, the component grids are allowed to overlap, as depicted schematically in Fig. 1.4. Flow-field information is transferred between the grids by special interpolation procedures. The connectivity between the component grids is specified indirectly by the interpolation stencils in the overlap regions. Conservative interpolation methods are required in order to prevent significant errors, especially if the overlap regions are crossed by shock waves, see, e.g., Pärt-Enander and Sjögreen [221]. The chimera method is particularly well-suited for flows with boundaries in relative motion. Detailed descriptions of the chimera method may be found in Steger and Benek [265] and Steger [264]. Strengths and weaknesses of chimera grids were assessed by Belk [39]. The suitability of the chimera approach for complex geometries was demonstrated by Buning et al. [54] by simulating the flow over the space shuttle orbiter complete with solid rocket boosters and external tank.

The chimera method has spawned two additional approaches. With the Feature-Associated Mesh Embedding (FAME) method, Albone [8] takes the association of structured grids with geometry components a step further. Distinct geometric and flow features are classified into types and associated with a suitable grid topology (such as C, H, or O). A multiply embedded Cartesian background grid is used. As with the chimera method, information is transferred between grids through interpolation. Kao and Liou [133] developed DRAGON (Direct Replacement of Arbitrary Grid-Overlapping by Non-structured) grids, in which the overlapping regions are re-ceded and the resulting cavities are triangulated. In this way, the difficulties associated with interpolation are avoided at the expense of introducing another type of grid cell.

Unstructured Grids. The multi-block method may be regarded as a framework which encompasses two special cases. First, by using a single block only, the original structured-grid approach as described above is recovered. Second, each individual grid cell may be taken as a block. As any implicit structure has been removed, and the

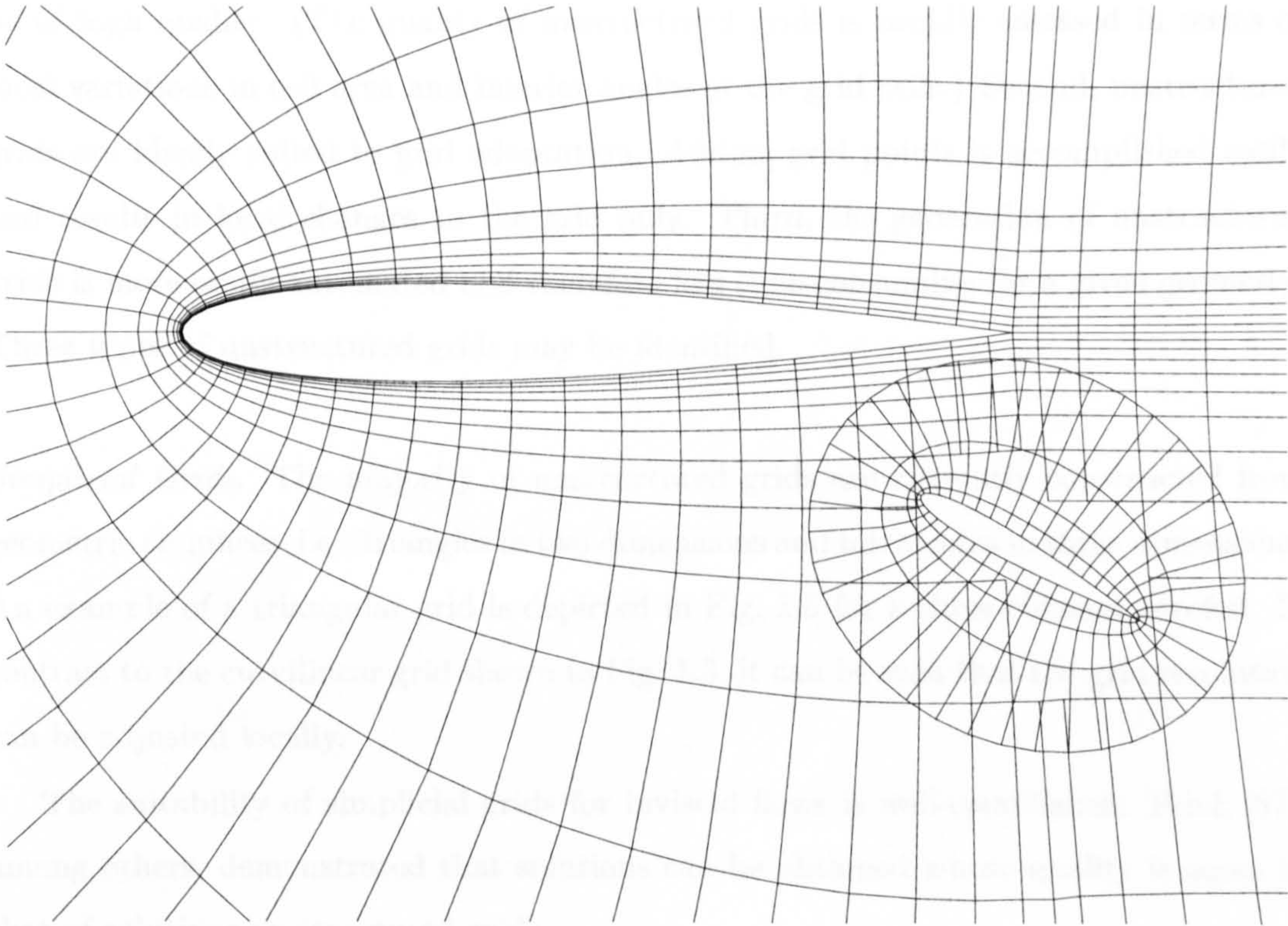


Figure 1.4: Illustration of chimera grid for generic two-element aerofoil.

complete structure has to be specified explicitly, this is usually referred to as an unstructured grid. (This point of view leads to the interpretation of multi-block and chimera grids as being locally, i.e., on the scale of each block or component grid, structured, but globally, i.e., on the scale of the solution domain, unstructured.)

Since the explicit specification of grid structure is completely local, the number of grid cells meeting at a grid point is not restricted to a constant number, as in structured grids. For the same reason, unstructured grids may in principle consist of an arbitrary combination of cell types. Cells may be categorised into types according to the number of edges or faces from which they are constructed.[†] The local nature of unstructured grids leads to three key benefits: First, unstructured grids for complex geometries can

[†] Although it is common to refer to triangular and quadrilateral grids as unstructured and structured grids, respectively, it should be noted that the distinction between structured and unstructured grids is in principle *not* dependent on the cell type. Any structured grid can be treated as an unstructured grid by the solution method (there may be good reasons for doing so, e.g., grid adaptation [3,129,291]), but not every unstructured grid can be treated in a structured manner. It follows that referring to a given grid as ‘structured’ or ‘unstructured’ is not strictly correct. Nevertheless, ‘triangular grids’ are understood to be unstructured triangular grids, and ‘structured grids’ will stand for structured quadrilateral grids in the following.

be of high quality. (The quality of unstructured grids is usually assessed in terms of local variations in cell area and interior angles of the grid cells.) Second, unstructured grids are ideally suited to grid adaptation. Adding grid points is accomplished easily and results in local changes to the grid only. Third, the generation of unstructured grids is more easily automated and therefore less time-consuming for a given geometry. Three types of unstructured grids may be identified.

Simplicial Grids. The majority of unstructured grids are currently constructed from geometric simplices, i.e., triangles in two dimensions and tetrahedra in three dimensions. An example of a triangular grid is depicted in Fig. 1.5 for a three-element aerofoil. In contrast to the curvilinear grid shown in Fig. 1.3, it can be seen that the grid resolution can be adjusted locally.

The suitability of simplicial grids for inviscid flows is well-established. Frink [87], among others, demonstrated that solutions can be obtained whose quality is equal to that of solutions on structured grids.

The application of simplicial grids to viscous flows requires the generation of highly stretched triangular and tetrahedral cells. Triangular grids for high-Reynolds number flows are of the form shown in Fig. 1.6(a), which can be regarded as a compressed and sheared equilateral triangular grid, or as a triangulated quadrilateral grid; the corresponding tetrahedral grid is shown in Fig. 1.6(b).[†] The key observation is that simplicial grids cannot be stretched without skewing the cells, in contrast to quadrilateral and hexahedral grids.

In order to obtain accurate results for viscous flows, it is imperative that numerical diffusion is minimised. Carpentier et al. [60] and Carpentier [58,59] studied the modified equation for a second-order upwind finite-volume discretisation of the linear convection equation on a triangular grid such as that shown in Fig. 1.6 and a quadrilateral grid. The analysis showed that numerical diffusion was substantially higher on the triangular grid than on the quadrilateral grid. Numerical experiments verified this observation. This conclusion is consistent with the comments by Hall [100] and Ramakrishnan et

[†]The shape of the triangular cells is supported by the analyses of Babuška and Aziz [18] and Rippa [236], which indicate that the error of a piecewise linear approximation on a triangular cell is directly proportional to its largest angle. See also Handscomb [102]. The corresponding analysis for tetrahedral grids was presented by Křížek [141].

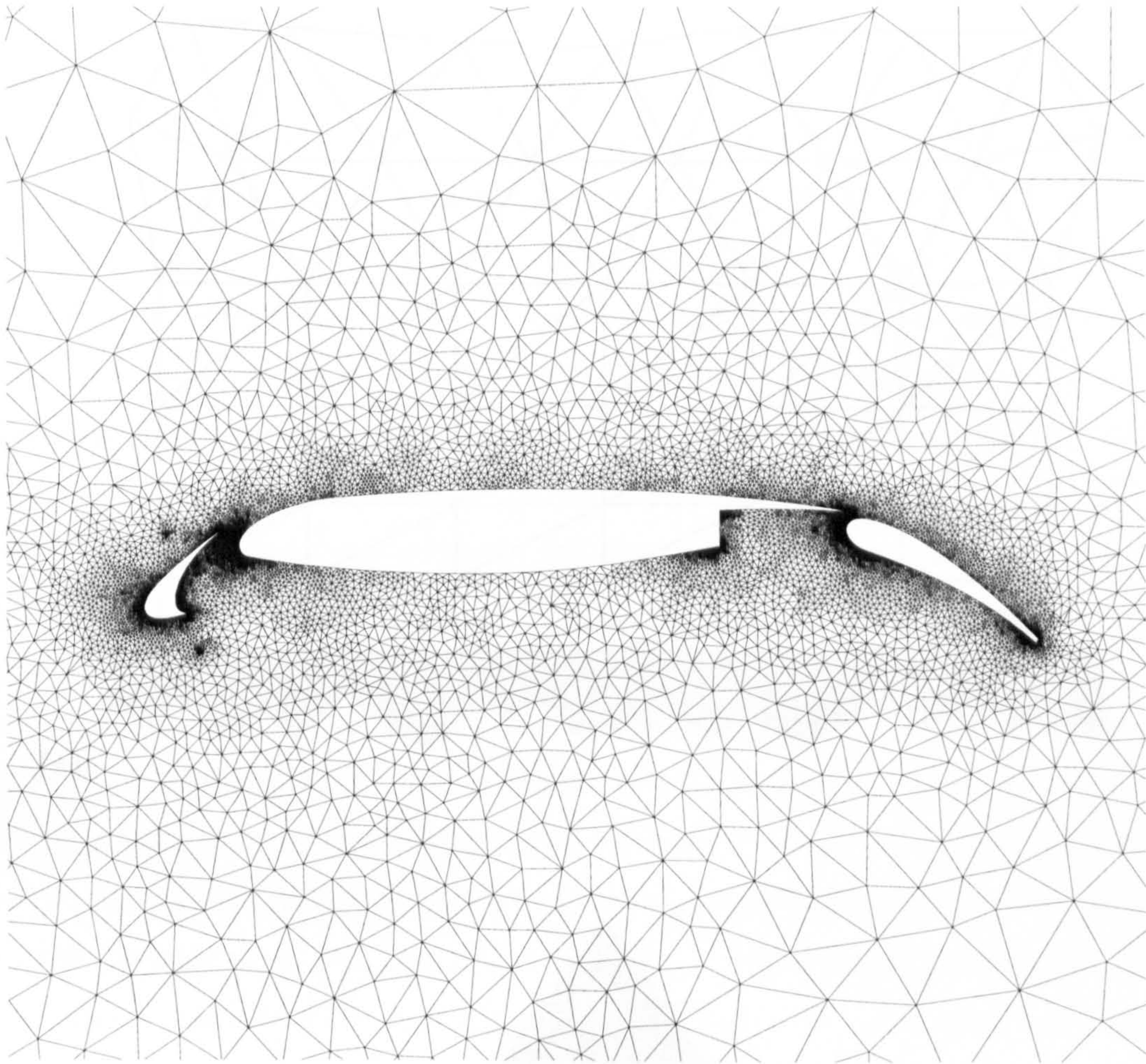


Figure 1.5: Triangular grid for three-element aerofoil.

al. [228], who stated that solutions obtained on simplicial grids were found to be less accurate than those on curvilinear grids. In cases where good agreement was obtained, e.g., Frink [88, 89], it may have been partly due to increased local grid resolution. Of course, it can be argued that local refinement is a legitimate use of an inherent advantage of unstructured grids to reduce potentially larger local errors. Nevertheless, doubts remain over the suitability of simplicial grids for viscous flows. The comparison of multi-block and triangular grids by Sbresny and Baier [246] is also interesting in this regard.

Mixed Grids. As shown above, the shapes of appropriately stretched triangles and tetrahedra in viscous regions are such that they may be merged to form layers of quadrilaterals and prisms (obtained by extruding triangular faces), see, e.g., Merriam [188] and

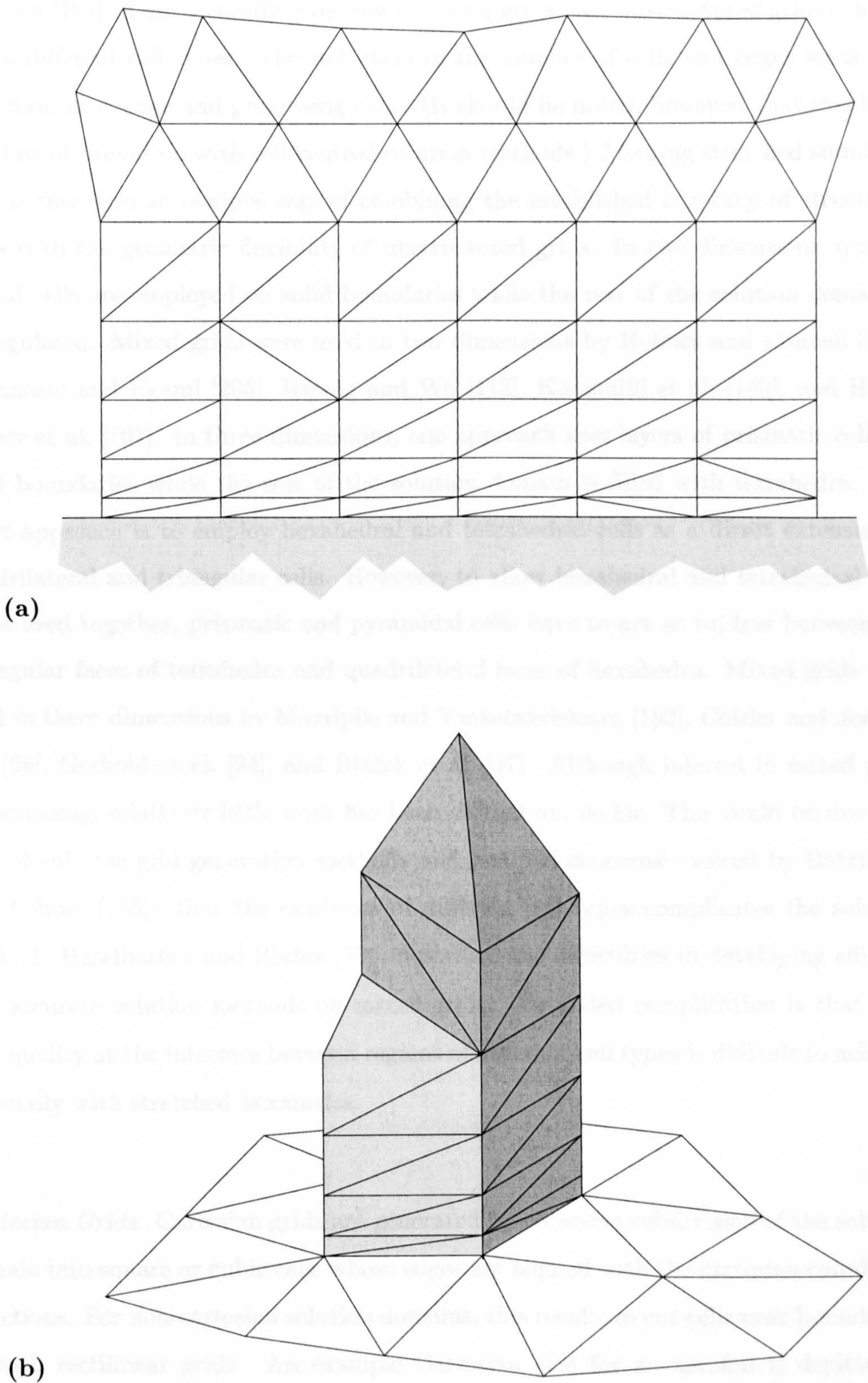


Figure 1.6: Typical appearance of simplicial grids for viscous flow simulations. **(a)** Triangular grid and **(b)** tetrahedral grid. Note the resemblance to subdivided quadrilateral and prismatic grids.

Marcum [169]. This naturally gives rise to mixed grids, i.e., unstructured grids consisting of different cell types. The reduction in the number of cells and edges leads to a reduction in storage and processing time. (It should be noted, however, that this leads to a loss of resolution with cell-centred solution methods.) Merging stretched simplicial cells is therefore an obvious way of combining the established accuracy of structured grids with the geometric flexibility of unstructured grids. In two dimensions, quadrilateral cells are employed on solid boundaries while the rest of the solution domain is triangulated. Mixed grids were used in two dimensions by Holmes and Connell [109], Nakahashi and Egami [205], Hwang and Wu [112], Koomullil et al. [140], and Haselbacher et al. [107]. In three dimensions, one approach uses layers of prismatic cells on solid boundaries while the rest of the solution domain is filled with tetrahedra. Another approach is to employ hexahedral and tetrahedral cells as a direct extension of quadrilateral and triangular cells. However, to allow hexahedral and tetrahedral cells to be used together, prismatic and pyramidal cells have to act as bridges between the triangular faces of tetrahedra and quadrilateral faces of hexahedra. Mixed grids were used in three dimensions by Mavriplis and Venkatakrishnan [183], Coirier and Jorgenson [66], Gerhold et al. [94], and Blažek et al. [47]. Although interest in mixed grids is increasing, relatively little work has been carried out so far. This could be due to a lack of suitable grid generation methods and justified concerns—voiced by Baker [20] and Löhner [155]—that the existence of different cell types complicates the solution method. Haselbacher and Blažek [106] described the difficulties in developing efficient and accurate solution methods on mixed grids. An added complication is that high grid quality at the interface between regions of different cell types is difficult to achieve, especially with stretched hexahedra.

Cartesian Grids. Cartesian grids are generated by recursive subdivision of the solution domain into square or cubic cells whose edges are aligned with the cartesian coordinate directions. For non-cartesian solution domains, this results in cut cells near boundaries, as with rectilinear grids. An example Cartesian grid for an aerofoil is depicted in Fig. 1.7. Since the generation of Cartesian grids is comparatively simple and easily automated, they are well-suited for preliminary design tools based on potential flow analyses, see, e.g., the TRANAIR code of Young et al. [303]. Coirier and Powell [67]

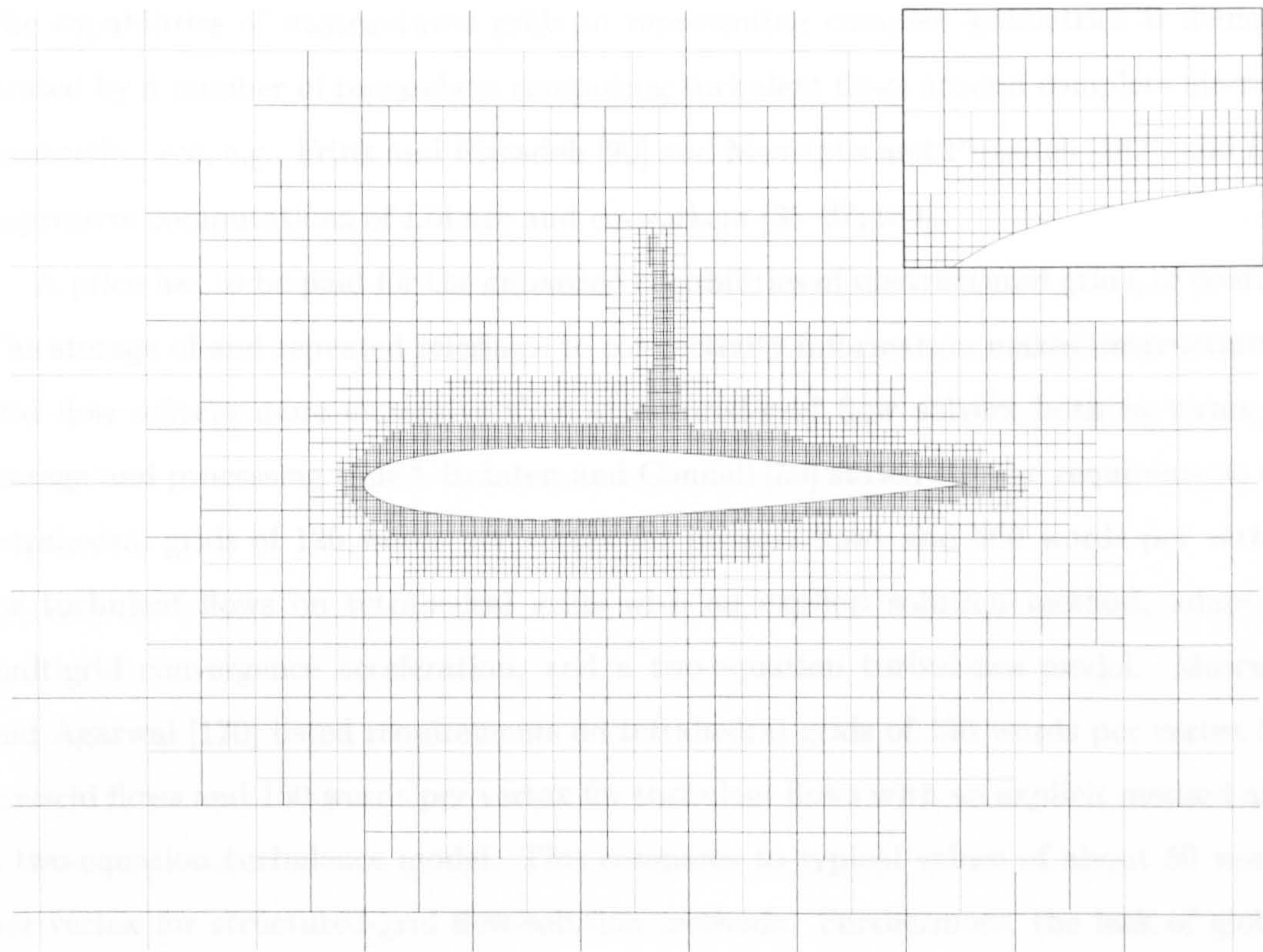


Figure 1.7: Cartesian grid for NACA 0012 aerofoil. Inset shows cut cells near aerofoil surface.

demonstrated through comparisons with curvilinear grids that accurate results can be obtained for the Euler equations. Allmaras and Baron [9] and Berger [41] studied numerical issues regarding accuracy and conservation at the refinement interfaces where hanging nodes and edges exist. The application of Cartesian grids to viscous flows has lagged behind that to inviscid flows, because the cut boundary cells can lead to a serious degradation of accuracy, as demonstrated by Coirier [65], and because the usual isotropic refinement procedures lead to excessive, and therefore inefficient, refinement for anisotropic features such as shear layers. To circumvent these problems, Cartesian grids may be combined with boundary-conforming grids, see, e.g., Melton et al. [187], Karman [134], Bishop and Noack [45], Smith and Leschziner [255], and Delanaye et al. [76]. Further information on Cartesian-grid approaches may be found in Aftosmis [5], Powell [225] and Quirk [227]. Recent research on Cartesian grids has focussed on anisotropic refinement in order to reduce the total number of cells generated, see Berger and Aftosmis [42].

The capabilities of unstructured grids in representing complex geometries is demonstrated by a number of researchers computing turbulent flows around complete aircraft geometries, see, e.g., Frink and Pirzadeh [90] and Mavriplis and Pirzadeh [182], and the impressive computations of Löhner and co-workers [35–37, 189].

A price has to be paid for the enhanced capabilities of unstructured grids, of course. The storage of and repeated reference to connectivity information makes unstructured-grid flow solvers more expensive than structured-grid flow solvers both in terms of storage and processing time.[§] Braaten and Connell [50] stated storage requirements on tetrahedral grids of 120 words per vertex for inviscid flows and 300 words per vertex for turbulent flows on tetrahedral grids with an explicit solution method, adaptive multigrid convergence acceleration, and a two-equation turbulence model. Marcum and Agarwal [170] listed requirements on tetrahedral grids of 130 words per vertex for inviscid flows and 150 words per vertex for turbulent flows with an explicit method and a two-equation turbulence model. This compares to typical values of about 50 words per vertex for structured-grid flow-solution methods. Furthermore, the lack of global grid structure means that efficient solution techniques such as Alternating Direction Implicit (ADI) methods [38] cannot be applied.

It may appear that the increased storage and processing time are a great price to pay for the enhanced capabilities. However, there are two reasons why unstructured grids are an attractive proposition for the computation of flows around complex geometries: First, it is easier and less time-consuming to generate an unstructured grid for a given complex geometry than a multi-block grid. An unstructured grid allows for an increased resolution of regions of interest with a smaller number of grid points covering the entire solution domain than a multi-block grid. Second, the reduction in time required for grid generation and the reduction in the number of grid points will compensate for or even outweigh the increased computational cost of obtaining a flow solution. Evidence which testifies to the validity of these arguments, at least for inviscid flows, was collected by Michal and Halt [190].

Hybrid Grids. The above discussion established that the advantages of unstructured

[§]This does not strictly apply to Cartesian-grid flow-solution methods because quantities such as face areas and control volumes do not have to be stored as they can be inferred directly from the data structure.

grids correspond to the disadvantages of structured grids and vice versa. Given their diametrically opposed characteristics, this is not surprising, of course. It is therefore reasonable to try to maximise the advantages and minimise the disadvantages by hybridising the two approaches, leading to so-called hybrid grids. It is clear from the preceding discussion that hybrid grids share some features with multi-block and chimera grids. The difference is that hybrid grids may be regarded as introducing some means of grid structure into unstructured grids, whereas multi-block and chimera grids attempt the opposite. Two types of hybrid grids can be distinguished.

Zonal Grids. Zonal grids attempt to combine the advantages of structured and unstructured grids by using the most suitable type in certain zones of the solution domain. Typically, structured grids are used near solid boundaries and unstructured grids in the rest of the solution domain. As first demonstrated by Nakahashi and Obayashi [206], this provides the opportunity to solve the Navier-Stokes equations on the structured grid and the Euler equations on the unstructured grid and to tailor the solution methods accordingly. The implementation of Nakahashi and Obayashi allowed overlapping of the structured and unstructured grids, but avoided interpolation since the grid points coincided in the interface regions.

Weatherill [292, 293] suggested the creation of zones with triangular grids only in regions where quadrilateral cells were of poor quality and where grid adaptation was carried out. This approach was also employed in three dimensions by Peace and Shaw [222] and Shaw et al. [252]. In three dimensions, the treatment of the interface between structured and unstructured grids is complicated by the fact that prismatic and pyramidal cells need to be used as bridges between triangular and quadrilateral cell faces.

Zonal grids may also be regarded as multi-block grids where unstructured grids are generated in some blocks, see, e.g., the SAUNA CFD system described by Shaw et al. [253], Shaw [250] and Shaw and Peace [251]. Zonal grids were also used in the UNSFLO code of Giles [96], by Mathur et al. [172], Hefazi et al. [108], Soestrisno et al. [257, 258], Berglind [43] and Tsung et al. [275].

The drawbacks of zonal grids are that the interface between the structured and unstructured zones requires special treatment and that the constant number of layers of quadrilateral or hexahedral cells may lead to poor grid quality near the interface.

Figure 1.8 compares the interface for zonal and mixed grids in two dimensions.

Prismatic Grids. A further way of combining features of structured and unstructured grids is through the use of prismatic grids originally introduced by Nakahashi [203,204] and developed further by Kallinderis [130]. Prismatic cells are generated by marching from surface triangulations in layers along appropriately defined normal directions, as shown schematically in Fig. 1.9. The resulting grid may be regarded as unstructured in each layer and structured in the direction normal to the surface. The advantages of prismatic grids are that considerable savings in storage and processing time may be realised because of the structure in the normal direction, see Parthasarathy et al. [220]. The structure in the normal direction may also be exploited in the derivation of implicit schemes, as done by Pandya and Hafez [218].

Because prismatic grids contain fewer and less skewed cells for a given number of grid points near solid walls, they are generally regarded as more suitable for viscous flow simulations than tetrahedral grids. A drawback of prismatic grids is that they cannot be used for multiply-connected domains and that they require the same number of triangular faces on opposing boundaries. Furthermore, adapting prismatic grids requires subdivision of all cells in the normal direction.

The drawbacks of prismatic grids led to the development of prismatic-tetrahedral grids by Kallinderis et al. [131], Parthasarathy et al. [220] and Khawaja et al. [135]. Prismatic cells are used only adjacent to solid boundaries regions while tetrahedra are used to fill the rest of the solution domain. To prevent prismatic layers from crossing each other, they need to be pulled back in regions of concave curvature, as illustrated by the section through a prismatic-tetrahedral grid in Fig. 1.10. This is a potential drawback of prismatic-tetrahedral grids, as the thickness of the prismatic region is smallest where thickening of boundary layers is expected to occur.

Prismatic-tetrahedral grids may be regarded as a subset of mixed grids. As with mixed grids, obtaining high grid quality at the interface can be difficult, as it depends on the surface triangulation, initial marching step, stretching ratio and the number of prismatic layers.

Prismatic cells may also be used near solid boundaries to circumvent the difficulties associated with cut cells in the cartesian-grid approach, see Melton et al. [187], Karman

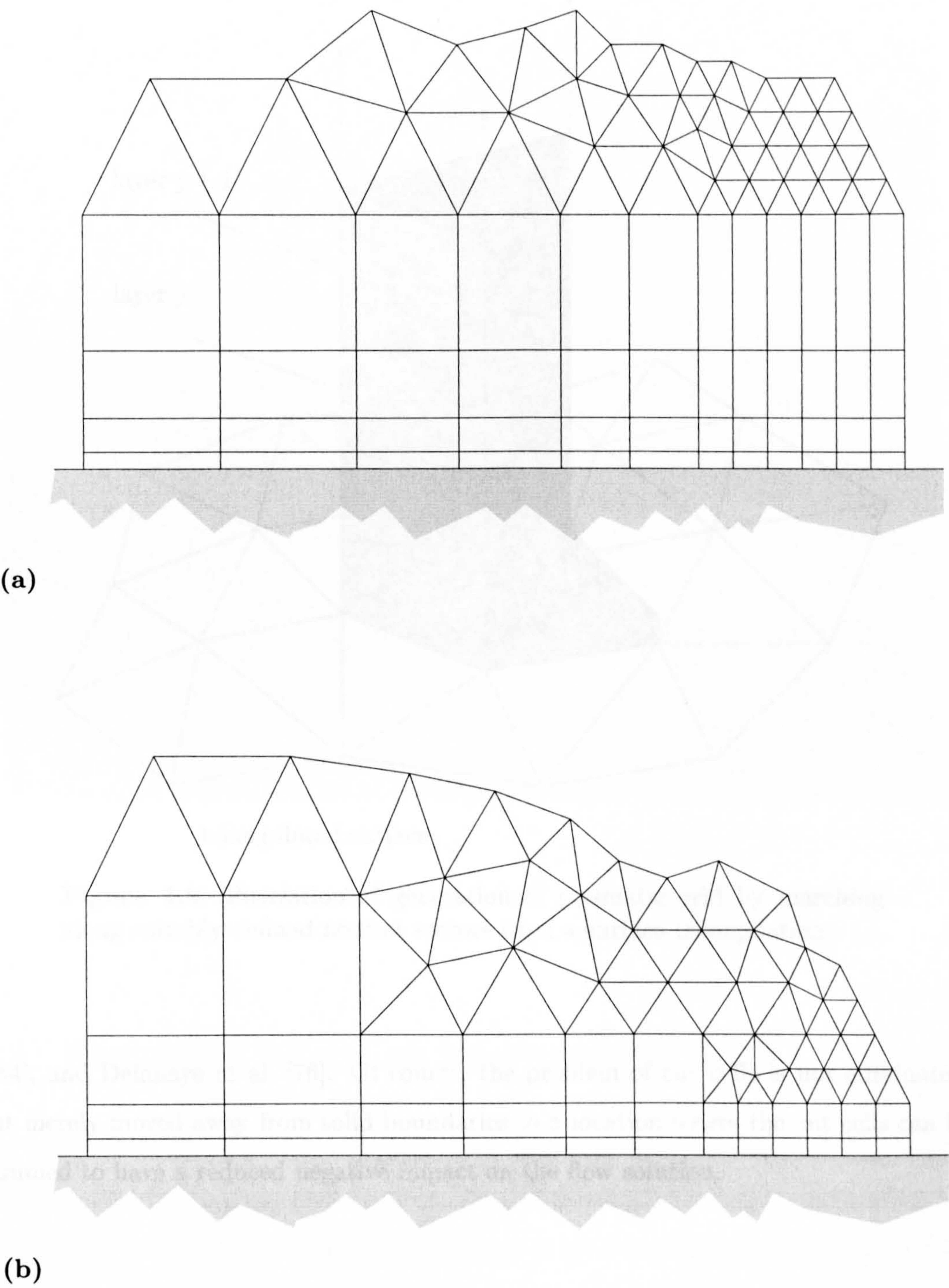


Figure 1.8: Comparison of interface between quadrilateral and triangular cells in (a) zonal grid and (b) mixed grid. Note that the number of layers of quadrilateral cells remains constant in the zonal grid, which can lead to quadrilateral cells of low aspect ratio.

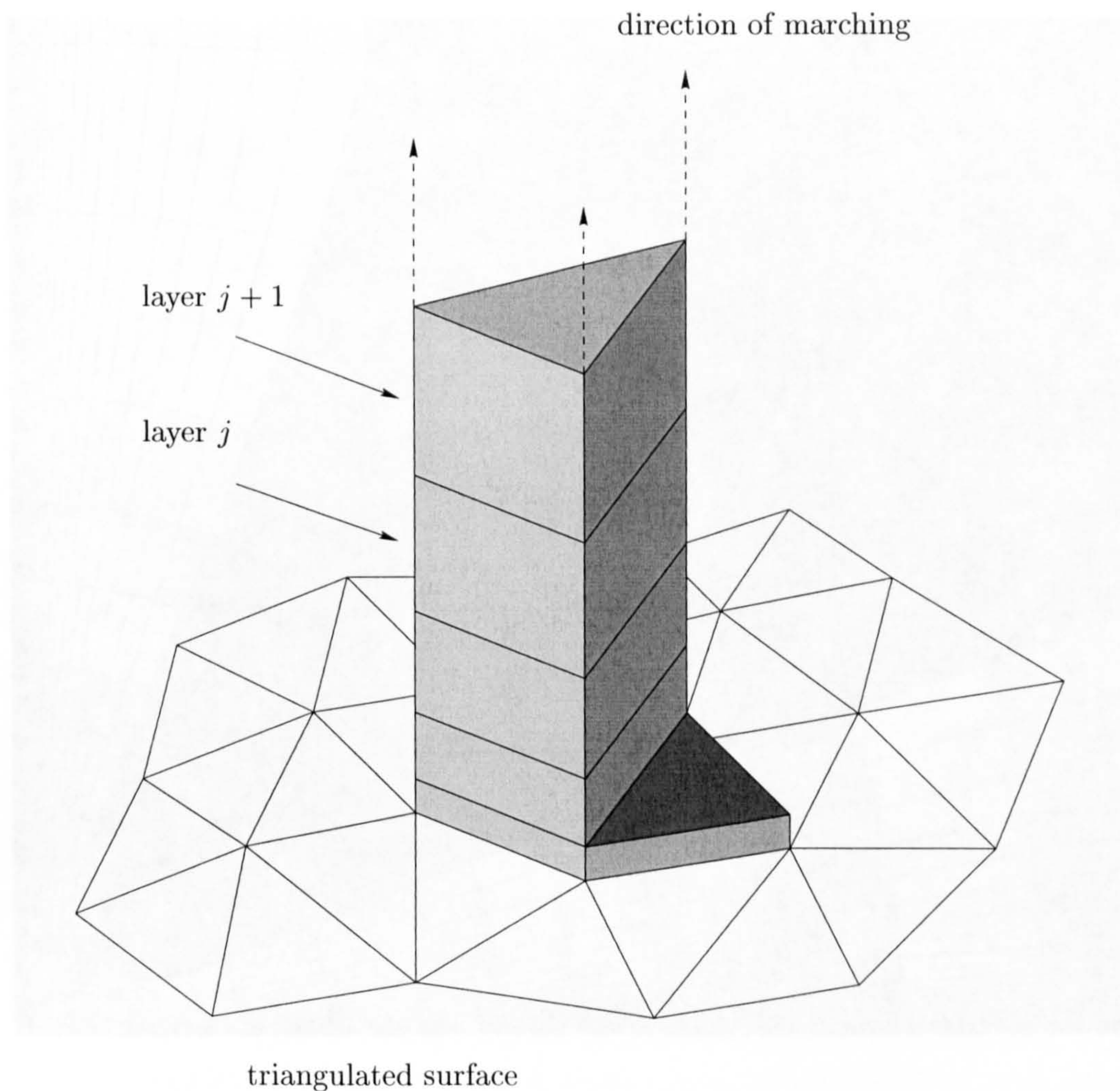


Figure 1.9: Illustration of generation of prismatic grid by marching along suitably defined normal vectors from a surface triangulation.

[134], and Delanaye et al. [76]. Of course, the problem of cut cells is not eliminated, but merely moved away from solid boundaries to a location where the cut cells can be assumed to have a reduced negative impact on the flow solution.

Chosen Grid Type: Unstructured Grids. Unstructured grids were chosen for the present work because they offer virtually unlimited flexibility in discretising complex geometries and in adapting to flow-field features. In the following, the term ‘unstructured grids’ will stand for simplicial and mixed grids; Cartesian grids will only be considered if relevant.

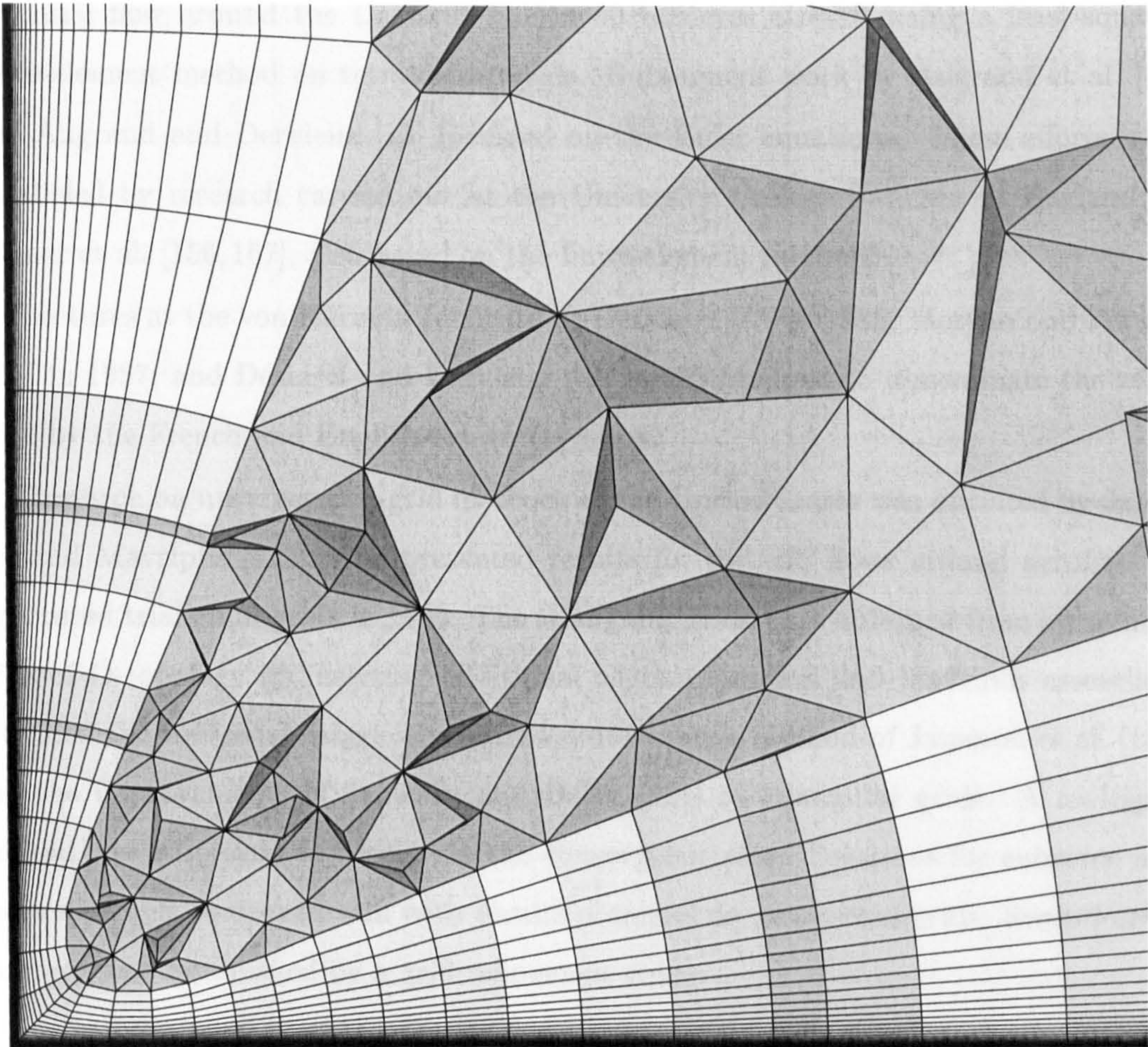


Figure 1.10: Section through prismatic-tetrahedral grid. Note how prismatic layers are pulled towards corner. Generated by method described in [135].

1.2 Pioneering Efforts on Unstructured Grids

The prospect of being able to compute flows around and through arbitrarily complex geometries lead to an intensive research effort in developing solution methods for unstructured grids. It is interesting and instructive to review briefly some of the pioneering efforts.

Early work by French research groups at the Institut National de Recherche en Informatique et Automatique (INRIA) and at Avions Marcel Dassault-Bréguet Aviation (AMD-BA) concentrated on finite-element methods, which traditionally used unstructured grids. As early as 1982, Bristeau et al. [52] presented solutions for transonic

potential flow around the Dassault Falcon 50 business aircraft using a least-squares finite-element method on tetrahedral grids. Subsequent work by Angrand et al. [14] and Angrand and Dervieux [13] focussed on the Euler equations. These efforts were paralleled by research carried out at the University College Swansea in England by Löhner et al. [156,157], also based on the finite-element method.

Lectures at the von Kármán Institute by Dervieux [78] in 1985, Morgan and Peraire [197] in 1987, and Désidéri and Dervieux [79] in 1988 helped to disseminate the early work by the French and English research groups.

Research on unstructured-grid methods in the United States was initiated by Jameson and Mavriplis [123], who presented results for inviscid flows around aerofoils on structured triangular grids in 1985. The triangular grids were obtained from structured grids of O-topology by inserting additional edges. Jameson and Mavriplis essentially extended the well-established cell-centred finite-volume method of Jameson et al. [124] and the improvements of Jameson and Baker [121] to triangular grids. A multigrid method was employed to accelerate the convergence rate. Solutions for subsonic and transonic cases compared well with results obtained on structured grids. Second-order accuracy was established by a grid-refinement study.

In January 1986, Jameson et al. [125] presented inviscid calculations around the Boeing 747 complete with engine pylons and cowlings on tetrahedral grids. The concept of Delaunay triangulation was employed to generate the tetrahedral grid for a given set of points. The solution variables were stored at the vertices of the grid. The control volume at a vertex was defined by the union of the cells meeting at that vertex. Jameson et al. showed that the centred finite-volume discretisation is equivalent to a Galerkin finite-element approximation with linear basis functions. The solution method of Jameson et al. [124] and Jameson and Baker [121] was employed. Subsequently, Jameson and Baker [122] presented improvements to the method.

The contribution of Jameson et al. [125] was important for three reasons.[†] First, it attracted considerable attention because it was the first one to demonstrate solutions of the Euler equations on unstructured grids for a complete aircraft geometry. Second,

[†]The importance of the work of Jameson et al. may also be judged by the fact that it was described in the New York Times [210] as well as non-scientific journals such as Aviation Week and Space Technology [17] and Aerospace America [151]. Weatherill [294] presented an interesting description of the background to the work reported in [125].

it was developed into the AIRPLANE code, which was heavily used by the American aircraft industry and NASA and therefore demonstrated that the concept of unstructured grids was a practical one. Third, as a result of the first two reasons, the work of Jameson et al. [125] served as a catalyst for much of the work which followed. An application for the McDonnell-Douglas MD-11 complete with engine pylons and cowlings as well as winglets was presented by Vassberg and Dailey [282]. Biswas et al. [46] applied the AIRPLANE code to the prediction of an unstarted inlet of a supersonic transport aircraft.

In 1987, Stoufflet et al. [270] presented inviscid calculations around the space shuttle orbiter and the Hermes spacecraft. The inviscid fluxes were computed using the approximate Riemann solver of Osher and Solomon [215]. Monotonic second-order accurate solutions were obtained through a limited extrapolation based on the work of van Leer [280]. The grids were adapted to shock waves through cell subdivision based on Mach-number differences. Real gas effects were modelled assuming local chemical equilibrium. An inexact Newton method was used for the solution update.

Toward the end of the 1980's, the basic capabilities of unstructured grids had been demonstrated and the focus shifted towards the development of more sophisticated solution methods. The subsequent research effort was helped by the large body of knowledge accumulated by researchers using the finite-element method. The equivalence of the finite-element and finite-volume methods under certain conditions [22, 113, 247] allows formulae developed in the finite-element framework to be used in finite-volume discretisations and vice versa. Their equivalence is also responsible for the designations 'Mixed Element-Volume' and 'Finite-Volume-Galerkin' used by French research groups.

1.3 The State-of-the-Art on Unstructured Grids

The following two subsections review the current state-of-the-art on spatial discretisation and solution methods in detail. The review concentrates on contributions based on the finite-volume method, but occasionally reference is made to contributions from the finite-element method because of the above-mentioned similarities between the two approaches. The review does not consider grid generation and adaptation, solution methods for unsteady flows, and parallelisation.

The two subsections are followed by a short summary and appraisal which is used to establish the objectives of the current work. The review and summary are independent of each other. Therefore, the summary may be read without having to read the review.

Further information on the development and current state-of-the-art of unstructured-grid methods—in particular on the topics not considered herein—can be found in the review and overview articles by Batina [33], Mavriplis [175,179], Venkatakrishnan [284], Baker [20], Aftosmis [4], and Morgan and Peraire [198]. A comprehensive exposition of a variety of topics related to unstructured-grid methods may be found in the lecture notes by Sonar [259–261] and the proceedings of an AGARD course [7].

1.3.1 Spatial Discretisation

The review of spatial discretisation methods is divided into the description of previous work on the definition of control volumes and the discretisation of the inviscid and viscous fluxes. The term ‘inviscid fluxes’ denotes the spatial fluxes appearing in the Euler equations, whereas the term ‘viscous fluxes’ denotes the spatial fluxes appearing due to viscosity and conductivity in the Navier-Stokes equations.

Control-Volume Definition. The adoption of the finite-volume method requires the definition of a control volume over which the governing equations are integrated. There are two main choices for the definition of control volumes on unstructured grids. The first choice is the cell-centred scheme in which the grid cells are taken as control volumes and the solution variables are stored at the centroids of the grid cells, as illustrated in Fig. 1.11(a). The second choice is usually referred to as the vertex-based scheme and defines control volumes at each vertex from dual cells and stores the solution variables at the vertices of the grid. A variety of dual cells can be defined, of which the median dual, depicted in Fig. 1.11(b), is probably the most common. The median dual is constructed by joining centroids of grid cells with midpoints of the edges.

The relative merits of the two schemes have been debated for some time, without a clear consensus on the superior choice having emerged. This might be because very few dedicated comparisons have been carried out. Relevant discussions and investigations are widely dispersed in the literature; only the most important contributions are mentioned here. The debate usually addresses the numerical effort required to evaluate

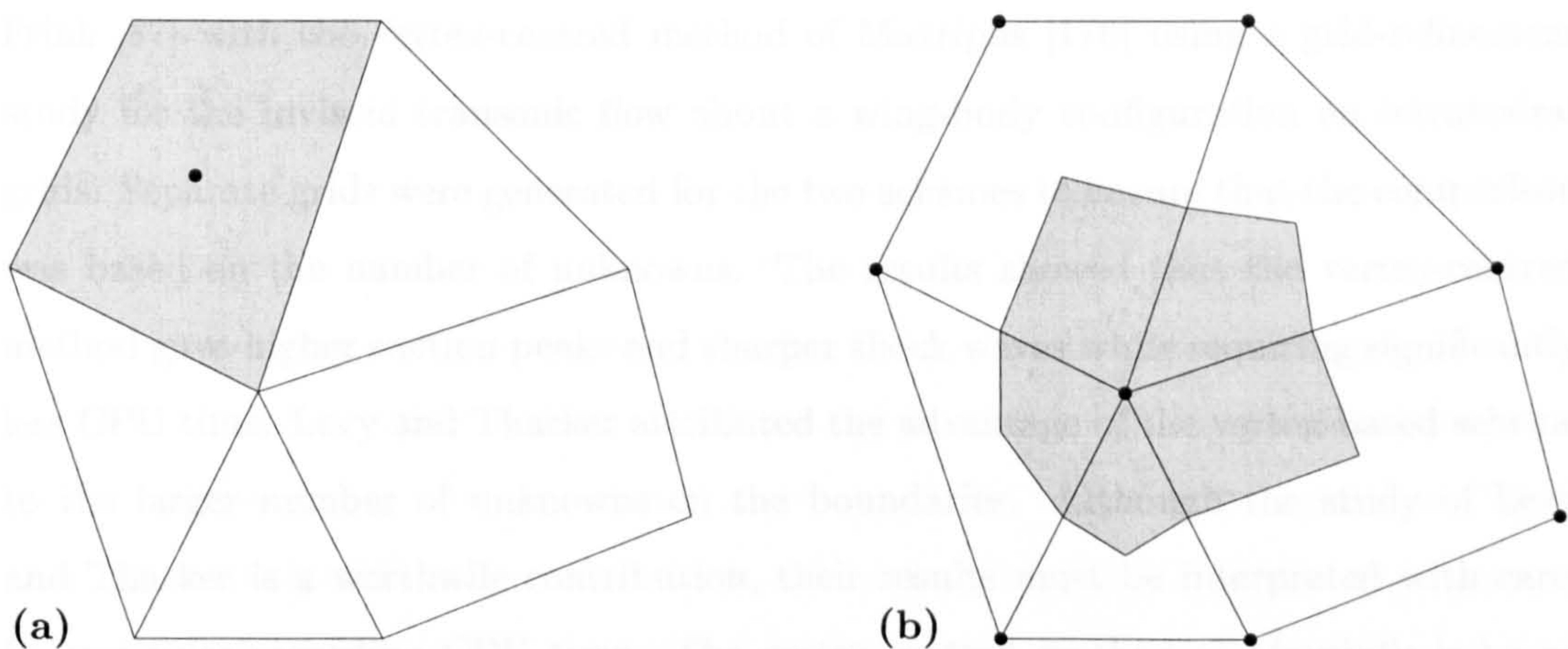


Figure 1.11: Illustration of two choices for defining control volumes on unstructured grids. **(a)** Cell-centred scheme and **(b)** vertex-based scheme. Control volumes are shown shaded and locations of solution variables are denoted by the symbol ‘•.’

the fluxes on a given grid and the accuracy with which the fluxes are discretised.

On a given simplicial grid in two (three) dimensions, there are approximately twice (six to seven times) as many cells as vertices. Therefore, the vertex-based scheme requires considerably less storage than the cell-centred scheme if used on the same simplicial grid. On quadrilateral and hexahedral grids, the storage required by the two schemes is approximately identical.

To compute the fluxes on a given tetrahedral grid, Barth [25] showed that the vertex-based scheme requires less operations than the cell-centred scheme. On hexahedral grids, the number of operations is approximately the same.

Some authors, e.g., Anderson [11] and Venkatakrishnan [285], suggested that the cell-centred scheme will be more accurate because of the larger number of cells than vertices in a given simplicial grid. Conversely, Mavriplis [175] argued that the solution variables are more strongly coupled to neighbouring solution variables in vertex-based schemes, which may contribute to higher accuracy. On quadrilateral and hexahedral grids, the above arguments do not apply as the number of cells and vertices are approximately identical. Perhaps more importantly, the above arguments also do not apply if quadrilateral, hexahedral or prismatic cells are used near solid walls in the simulation of viscous flows, because the resolution normal to the wall is roughly the same.

The only contribution which is based on carefully obtained numerical results is the recent study of Levy and Thacker [153]. They compared the cell-centred method of

Frink [87] with the vertex-centred method of Mavriplis [176] using a grid-refinement study for the inviscid transonic flow about a wing-body configuration on tetrahedral grids. Separate grids were generated for the two schemes to ensure that the comparison was based on the number of unknowns. The results showed that the vertex-centred method gave higher suction peaks and sharper shock waves while requiring significantly less CPU time. Levy and Thacker attributed the advantage of the vertex-based scheme to the larger number of unknowns on the boundaries. Although the study of Levy and Thacker is a worthwhile contribution, their results must be interpreted with care, in particular regarding CPU time. The vertex-centred method of Mavriplis is based on matrix artificial dissipation [272] and agglomeration multigrid, whereas the cell-centred method of Frink employs the approximate Riemann solver of Roe [238] and an implicit method with inexact linearisation. Both of these differences will favour the vertex-centred method in terms of CPU time.

Since unstructured grids are usually non-uniform, it is important to consider the accuracy of a given scheme on distorted grids. It is well-established that the vertex-based scheme incurs smaller errors on nonuniform quadrilateral grids than the cell-centred scheme, see, e.g., the analyses by Roe [239, 240] and Morton and Paisley [200]. It is reasonable to assume that this will be the case on nonuniform triangular grids also. The accuracy of vertex-based solution methods on triangular grids was investigated by Roe [239], Giles [95], and Baker [21]. Turkel [276] showed how the accuracy of cell-centred schemes on non-uniform grids may be improved. Unfortunately, the improved schemes are more prone to instabilities; see the remarks in Roe [240] and Morton and Paisley [200].

Despite the study of Levy and Thacker [153], which represents the first careful comparison, there is not sufficient convincing numerical evidence to designate either the vertex-based or the cell-centred scheme the better approach. Most comparisons are based on heuristic arguments or theoretical analyses which may not apply or be of little relevance in practice. For this reason, the decision on which scheme to use is probably based on subjective points of view. The vertex-based scheme appears to be more widely-used, probably due to the influential work of Barth and co-workers [22, 25, 31].

Inviscid Fluxes. Several researchers employed the central-difference scheme with

scalar dissipation of Jameson et al. [124], see, e.g., Holmes and Connell [109] and Smith [256]. Good results were obtained although the construction of the dissipative terms is not based on physical grounds and reliant on user-specified and problem-dependent empirical parameters. As shown by Haselbacher and Blažek [106], the construction of the dissipative terms is more problematic on mixed grids than on simplicial grids.

In contrast to central-difference schemes, upwind schemes apply an appropriate amount of dissipation to each characteristic component of the Euler equations. Typically, approximate Riemann solvers such as those of Roe [238] or Osher and Solomon [215] are employed in a one-dimensional fashion in the direction normal to a control-volume face.^{||} First-order upwind schemes are easily implemented on unstructured grids as they only depend on solution states from nearest neighbours. Vijayasundaram [289] was among the first to present results obtained with first-order upwind schemes on unstructured triangular grids.

The use of upwind schemes of higher than first order requires the reconstruction of polynomial solution variations from solution states. Computing the inviscid fluxes using a reconstructed polynomial of order k gives spatial accuracy of order $k + 1$. A succinct overview of higher-order schemes was given by Barth [29].

Linear Reconstruction ($k = 1$). Fézoui [83] developed an early second-order accurate upwind scheme for vertex-based solution methods. Gradients of the solution variables were calculated at a vertex as the arithmetic mean of the gradients in the triangles meeting at that vertex. This is illustrated schematically in Fig. 1.12(a), where the shading denotes the area on which gradients are computed for the linear reconstruction at the control-volume face between vertices i and j . The extrapolated states at a control-volume face were limited such that they were bounded by the solution states at the vertices whose control volumes are joined by that face.

Later implementations computed the gradients at a vertex as a linear combination of a divided difference centred on an edge incident to that vertex and upwind and downwind gradients. These schemes may be regarded as extensions to unstructured grids of the one-dimensional MUSCL (Monotonic Upstream-centred Scheme for Conserva-

^{||}This may lead to misinterpretation of flow features which are not aligned with control-volume faces. Genuinely multi-dimensional upwind schemes were reviewed by Paillère and Deconinck [216]. Such schemes will not be considered in the present work.

tion Laws) method of van Leer [280] originally developed on structured grids. Two basic schemes may be identified. First, the upwind-cell formulation used by Stoufflet et al. [270], Rostand and Stoufflet [242], Désidéri and Dervieux [79], and Jameson [117] as shown schematically in Fig. 1.12(b) for two dimensions. Second, the dummy-node formulation employed by Whitaker et al. [300], Cabello et al. [55], and Lyra [165] as illustrated in Fig. 1.12(c). Both schemes require modification near boundaries and extra storage compared to the approach of Fézoui [83]. In practice, many methods employ variations or combinations of these two basic methods, see, e.g., Arminjon and Dervieux [15], Richter [232], Luo et al. [162], and Riemslag and Dick [234].

The three approaches shown in Fig. 1.12 were not regarded as entirely satisfactory since monotonicity was enforced in a one-dimensional manner as on structured grids, although the stencils on unstructured grids are inherently multi-dimensional. This mismatch arose because it had not yet been established how to extend the Total-Variation-Diminishing (TVD) concept of Harten [104] to unstructured grids. Furthermore, with the exception of the work by Fézoui, no unique gradients were defined in each control volume. These deficiencies were resolved by Barth and Jespersen [31], who developed a method which reconstructs gradients and enforced monotonicity in a multi-dimensional manner. The Green-Gauss theorem was employed to compute gradients at each vertex. Monotonicity was enforced by limiting the gradients at a vertex such that the extrapolated face-values were bounded by the value at that vertex and the values at the neighbouring vertices. Their method has become widely used in both two and three dimensions, see, e.g., Whitaker [299], Anderson and Bonhaus [12], Ashford [16], Meister [185], Haselbacher et al. [107], and Galle [92]. Subsequently, Barth [24] also suggested weighted and unweighted least-squares and data-dependent techniques for the reconstruction of gradients.

The limiter function of Barth and Jespersen typically leads to stalled convergence after an initial reduction of the residuals. Venkatakrishnan [285] found that the limiter function was reacting to machine-level noise in regions where the solution variables were nearly constant. An improved limiter function was proposed which does not inhibit convergence behaviour at the expense of a possible loss of monotonicity near large gradients.

A detailed study by Aftosmis et al. [6] showed the least-squares reconstruction to be

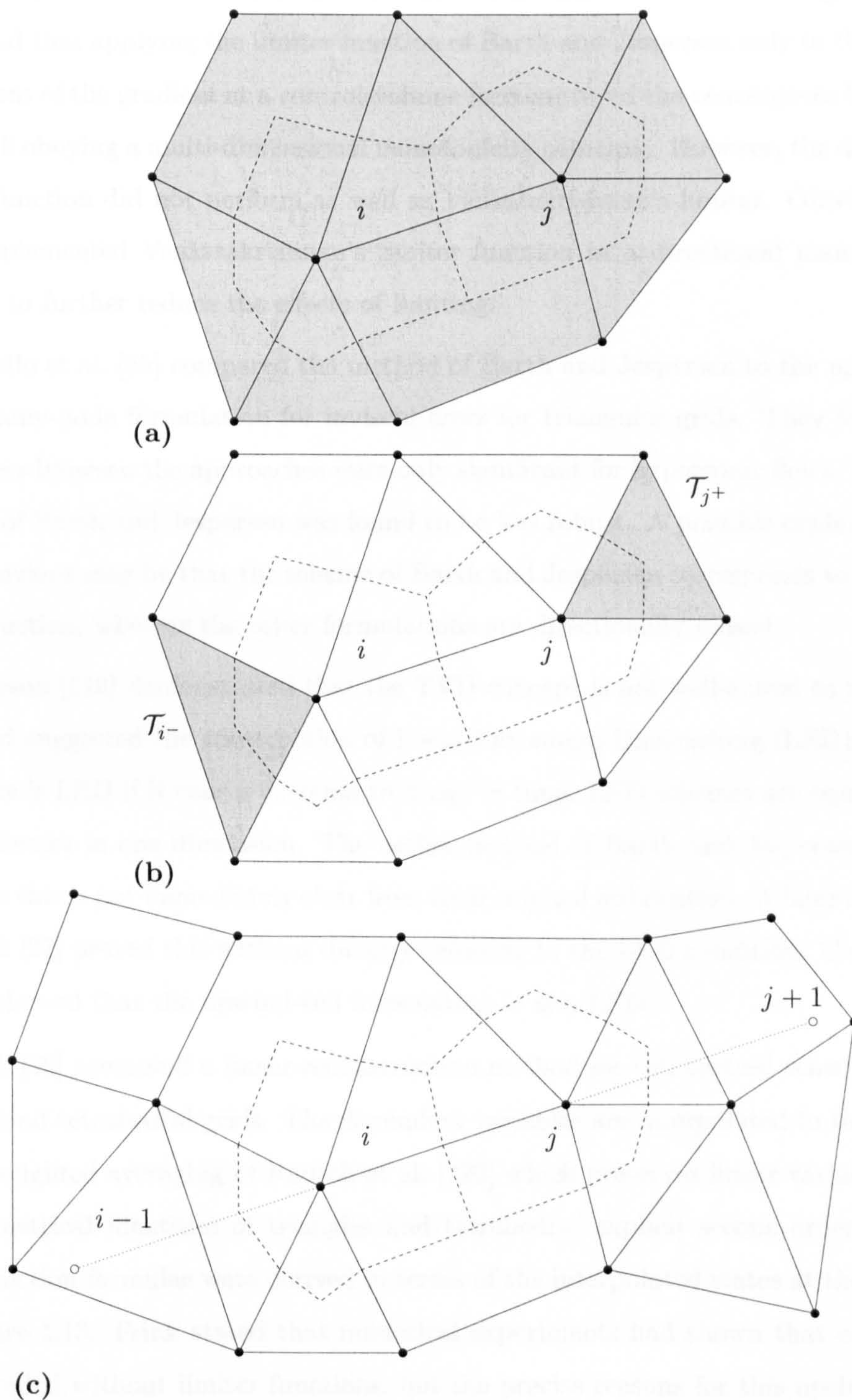


Figure 1.12: Three approaches to reconstructing the linear solution variations necessary to obtain second-order accuracy with a vertex-based scheme. **(a)** Gradients computed at vertices, **(b)** upwind-cell formulation, and **(c)** dummy-node formulation. Shading denotes area over which gradients are computed. Dashed lines denote outline of median-dual control volume.

significantly more accurate than Green-Gauss reconstruction on distorted grids. They also found that applying the limiter function of Barth and Jespersen only to the normal component of the gradient at a control-volume face improved the convergence behaviour while still obeying a multi-dimensional monotonicity principle. However, the directional limiter function did not perform as well as Venkatakrishnan's limiter. Ollivier-Gooch [212] implemented Venkatakrishnan's limiter function in a directional manner in an attempt to further reduce the effects of limiting.

Cabello et al. [55] compared the method of Barth and Jespersen to the upwind-cell and dummy-node formulation for inviscid flows for triangular grids. They found that differences between the approaches were only significant for hypersonic flows, where the method of Barth and Jespersen was found to be less robust. A possible explanation for this behaviour may be that the scheme of Barth and Jespersen corresponds to a centred reconstruction, whereas the other formulations are directionally biased.

Jameson [119] demonstrated that the TVD concept is not well-suited to triangular grids and suggested the construction of Local-Extremum-Diminishing (LED) schemes. A scheme is LED if it causes extrema to decay in time. LED schemes are equivalent to TVD schemes in one dimension. The earlier method of Barth and Jespersen is LED, although this is not immediately clear from their original publication. A later derivation by Barth [27] proved this without directly referring to the LED condition. Cournède et al. [70] showed that the upwind-cell formulation is also LED.

Frink [88] presented a linear-reconstruction method for cell-centred schemes on triangular and tetrahedral grids. The dependent variables are interpolated to the vertices by the weighted averaging of Rausch et al. [229] which preserves linear variations. Using geometrical identities of triangles and tetrahedra, explicit second-order accurate reconstruction formulae were derived in terms of the interpolated states at the vertices, see Figure 1.13. Frink stated that numerical experiments had shown that oscillations were avoided without limiter functions, but the precise reasons for this upshot remain unknown. Mitchell [192] later showed that the interpolation formulae derived by Frink may be regarded as a weighted combination of centred and upwind interpolations. Recent comments by Frink and Pirzadeh [90] indicated that some problems remain with the averaging procedure for viscous flows. Other upwind methods for cell-centred schemes were presented by Knight [138], Anderson [11], Grismer et al. [98], and Strang

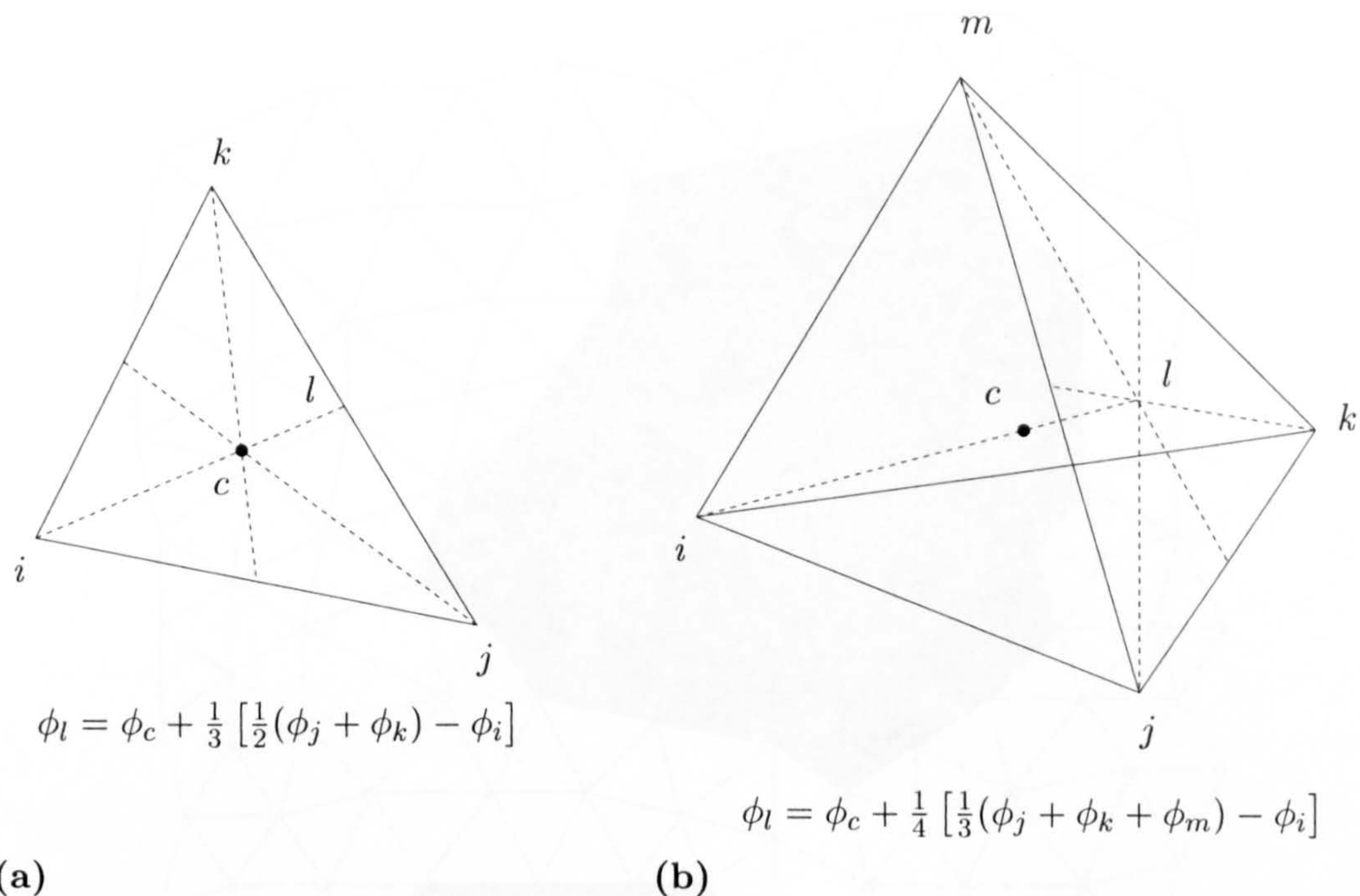


Figure 1.13: Illustration of the upwind scheme of Frink [88] for cell-centred methods on (a) triangular and (b) tetrahedral grids.

et al. [271].

Additional work on linear-reconstruction methods was carried out by Durlofsky et al. [81], Berzins and Ware [44], Batten et al. [34], and Hubbard [110,111].

Higher-Order Reconstruction ($k > 1$). Barth and Frederickson [30] developed a method for the reconstruction of polynomials of arbitrarily high order for cell-averaged data on general unstructured grids. They introduced the property of k -exactness to classify reconstruction schemes which reconstruct polynomials of degree k or less exactly. In order to reconstruct exactly a polynomial of degree k in d dimensions, a stencil of at least $\prod_{i=1}^d (k + i)/d!$ non-coplanar points is required. Barth and Frederickson extended the stencil beyond the minimum required for a given order of accuracy to guard against pathological behaviour of the reconstruction operator. Typical stencils for a vertex-based scheme are shown in Fig. 1.14. The resulting non-square linear system was solved using Gram-Schmidt decomposition. In order to obtain the desired order of accuracy, the integration around the control-volume boundary was carried out by Gaus-

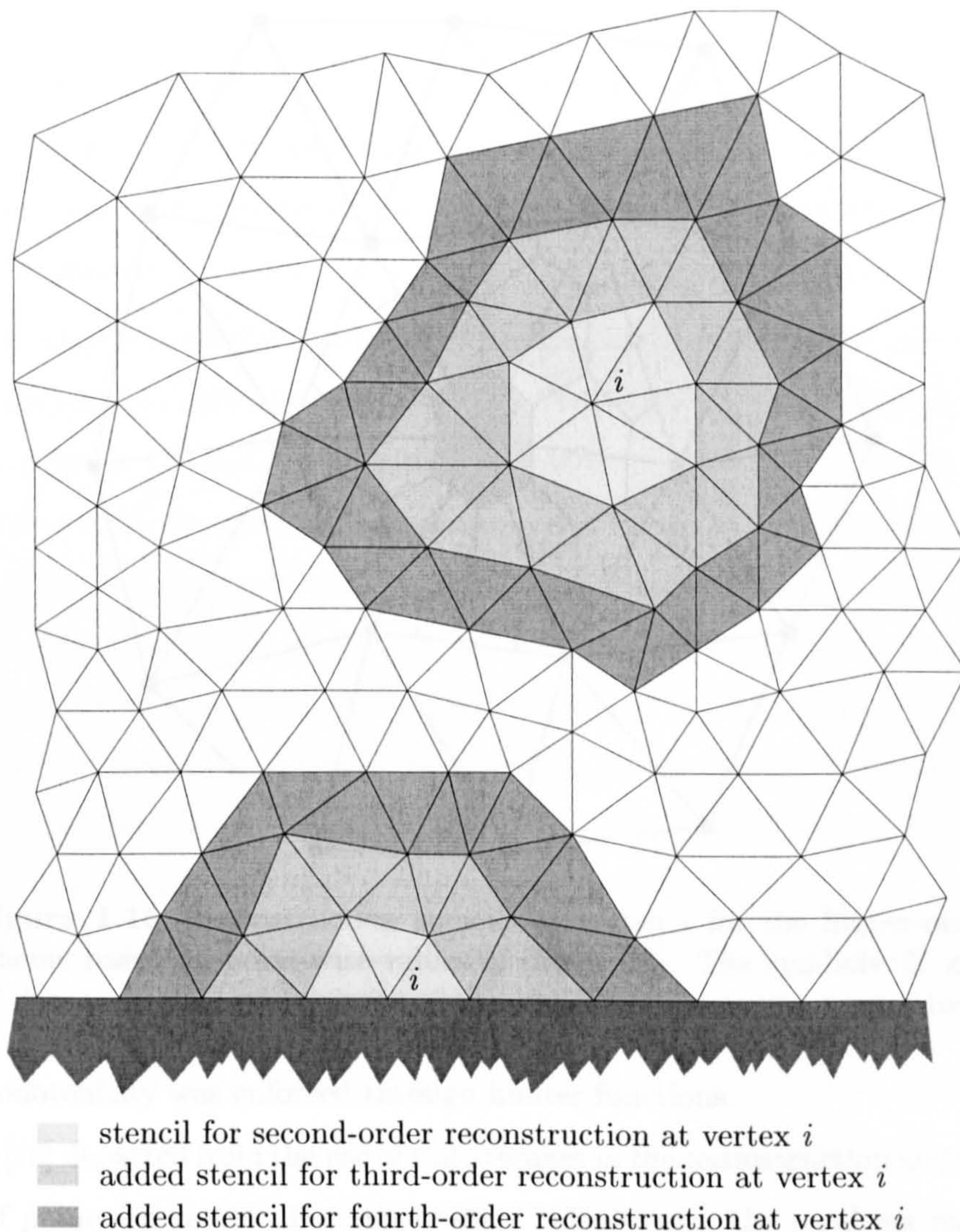


Figure 1.14: Typical reconstruction stencils at vertex i for vertex-based scheme for interior and boundary vertices.

sian quadrature of appropriate order. As may be expected, an order of $\lceil (k+1)/2 \rceil$ was found to be sufficient. The method was applied to the (shockfree) Ringleb flow [235] for which smooth solutions were obtained by quadratic reconstruction on highly distorted triangular grids.

Polynomial reconstruction algorithms based on cell-averaged values were also studied by Mitchell and Walters [193]. In contrast to the work by Barth and Jespersen and Barth and Frederickson, the reconstruction was not carried out within a control volume, but around control-volume faces. The resulting method is thus closer in concept to the MUSCL method and its early extensions to unstructured grids as described

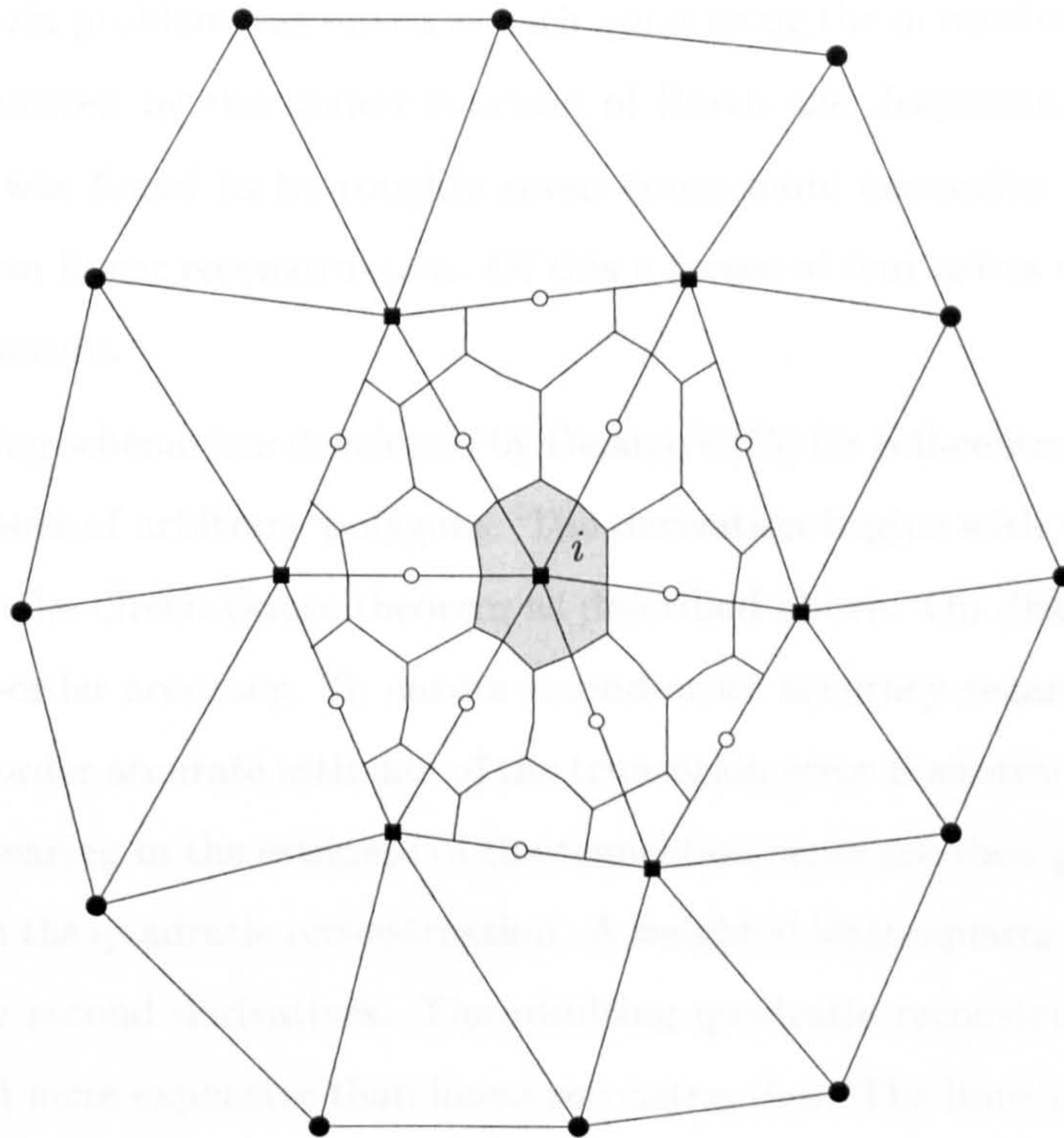


Figure 1.15: Reconstruction stencils at vertex i for the higher-order scheme based on point-wise values of Barth [26]. The symbols ‘ Ξ ’ and ‘ \circ ’ denote original grid points and the additional unknowns, respectively.

above. Monotonicity was enforced through limiter functions.

Barth [26] departed from the use of cell averages in the reconstruction and considered the use of pointwise values. For steady-state calculations, the resulting mass matrix may be lumped without sacrificing spatial accuracy [57]. Additional unknowns are introduced at edge midpoints as shown in Fig. 1.15. This has the advantage that the physical domain of support is well-defined and unchanged between linear and quadratic reconstruction.

Barth constructed two different representations of the solution from the pointwise values. The first representation is the quadratic interpolant on the cell. The second representation is the reconstruction polynomial which is determined such that the difference between it and the quadratic interpolant is minimised in a least-squares sense at all flux-quadrature points. Assuming that the grid is composed of equilateral triangles, this leads to a stencil of 19 points for original grid points and of nine points for newly introduced points in the interior of the solution domain. For boundary grid points, enough points are available to reconstruct the five derivatives. The resulting

non-square matrix problem was solved at each point using the normal equations. Monotonicity was enforced by the limiter function of Barth and Jespersen. The quadratic reconstruction was found to be roughly seven times more expensive in terms of processing time than linear reconstruction. Of this a factor of four arises due to the larger number of unknowns.

An interesting scheme was developed by Delanaye [75] for cell-centred discretisations on grids composed of arbitrary polygons. The derivation begins with the linear reconstruction using the Green-Gauss theorem as described above. On distorted grids, this only gives first-order accuracy. To ensure second-order accuracy regardless of grid distortion, a first-order accurate estimate of the truncation error is subtracted. The second derivatives appearing in the estimate of the truncation error are then grouped together with those from the quadratic reconstruction. A weighted least-squares approach is used to compute the second derivatives. The resulting quadratic reconstruction method is about one third more expensive than linear reconstruction. The limiting procedure was modified to ensure high accuracy in regions of smooth flow.

The higher-order schemes described above suffer from various disadvantages. The rapidly increasing extent of the stencil results in a storage penalty and can lead to problems for shock waves in close proximity. Boundaries have to be represented by curves of higher degree than the simple piecewise straight segments used for second-order schemes. Furthermore, higher-order methods lead to larger spectral radii and hence slower convergence rates. (This problem might be mitigated if, for a given level of accuracy, the coarser grids allow correspondingly larger time steps to be taken.) Approaches based on least-squares methods are prone to ill-conditioning of the coefficient matrix on highly stretched grids.

The first difficulty, i.e., the rapidly increasing extent of the stencil, is circumvented in the approach developed by Halt and Agarwal [101] for cell-centred discretisations in two dimensions. Building upon the work of Allmaras and Giles [10], Halt and Agarwal solved additional equations for derivatives or moments of the governing equations instead of reconstructing the solution from average values. Accuracy of up to fourth order was obtained for Ringleb's flow. The method involving moments was found to be more robust and accurate, but also more expensive. Both methods were significantly more accurate than the approach of Barth and Frederickson. Halt and Agarwal also assessed

the efficiency of the two approaches by comparing storage and processing time against the error achieved for a given convergence tolerance. They found that higher-order methods were more efficient by an order of magnitude for relatively low error tolerances compared to first-order methods. In particular, the use of quadratic polynomials seemed to be the optimum choice for the test case considered. The approach of Halt and Agarwal was developed further by Boschitsch and Quackenbush [49].

Additional work on higher-order methods was carried out by Mitchell [192], Venkatakrishnan and Chakravarthy [287], and Debiez [74].

Essentially Non-Oscillatory (ENO) Schemes. In contrast to the higher-order methods described above, the reconstruction stencils in ENO schemes [105] are not fixed. Instead, the reconstruction selects the stencil whose values support the least oscillatory polynomial. This leads to higher accuracy near discontinuities and eliminates the need for limiter functions. Due to the strong non-linearity of the stencil selection process, ENO schemes typically exhibit convergence problems. The application of ENO schemes to unstructured grids was studied by Vankeirsbilck and Deconinck [279], Abgrall and Lafon [1], Sonar [261], Friedrichs [86], and Abgrall et al. [2]. A comprehensive exposition of ENO schemes on unstructured grids may be found in the book of Sonar [262].

Ollivier-Gooch [213,214] modified the weighted least-squares reconstruction of Barth [24] by introducing a dependency on the smoothness of the function to be reconstructed. The resulting method was shown to satisfy a relaxed form of the ENO conditions. Applications to two-dimensional inviscid external flows indicated savings in processing time of about 15-20% relative to weighted least-squares reconstruction with limiter functions. Detailed comparisons showed third- and fourth-order schemes to be approximately five and seven times more expensive in terms of processing time, and three and four times more demanding in terms of required storage than the second-order scheme of Barth and Jespersen with least-squares reconstruction.

Viscous Fluxes. The discretisation of the viscous fluxes by a finite-volume method requires the approximation of gradients of the dependent variables at the control-volume faces.

On unstructured grids, the approximation of gradients is relatively difficult because

identifiable coordinate directions do not exist. These difficulties manifest themselves in discretisation stencils for the viscous fluxes being ill-behaved in terms of consistency, accuracy, coupling, and positivity. The last property is important because the Laplacian (to which the viscous fluxes reduce for incompressible flow and constant viscosity) satisfies a maximum principle.

Although many researchers compute high-Reynolds-number flows on unstructured grids, only two studies have addressed the discretisation of the viscous fluxes on unstructured grids in any detail. For simplicity, both studies concentrated on Laplace's equation.

Barth [22] demonstrated that the Galerkin finite-element discretisation with linear triangular elements will satisfy a discrete maximum principle if and only if the grid is a Delaunay grid. More restrictive conditions apply in three dimensions, see Barth [23] and Letniowski [152]. These results are of theoretical interest, but of relatively little practical value since Delaunay grids are not ideally suited to the computation of high-Reynolds-number viscous flows.

Coirier [65] studied various schemes on adaptively-refined Cartesian grids. The study was motivated by the observation that calculations with non-positive schemes lead to non-monotone solutions and poor convergence behaviour when computing low Reynolds-number flows. Refined Cartesian grids constitute particularly severe test cases, as it is impossible to have smoothly varying grid cells near refinement boundaries. The results obtained by Coirier have a wider significance, however, since adaptation methods on other grid types may lead to hanging nodes and edges also. Coirier investigated six schemes, four of which employed the Green-Gauss theorem and two of which employed polynomial reconstruction. He showed that accuracy and positivity were difficult to obtain simultaneously.

A more detailed review of the discretisation of the viscous fluxes may be found in Subsection 4.2.3.

Turbulence Models on Unstructured Grids. Soon after the pioneering efforts of Jameson et al. [125] and Stoufflet et al. [270] had demonstrated the capabilities of unstructured grids, attention was turned to the solution of turbulent flows. It is convenient to discuss the modelling of turbulent flows according to the class of turbulence

model employed.

Algebraic Models. As may be expected, the earliest computations of turbulent flows on unstructured grids employed algebraic turbulence models such as those of Cebeci and Smith [61] and Baldwin and Lomax [19]. The non-local nature of algebraic models requires lines, approximately normal to solid boundaries, along which a local turbulence length scale is extracted. On structured grids, one family of coordinate lines may be used for that purpose. On unstructured grids, such lines do not exist and must be constructed explicitly.

In 1987, Weatherill et al. [296] appear to have presented the earliest implementation of the Baldwin-Lomax turbulence model on unstructured grids. Structured grids of O-topology were generated around solid boundaries and triangulated with an imposed connectivity. This resulted in layers of *structured* triangular cells, which allowed the extraction of the local turbulence length scale. The rest of the solution domain was triangulated using the Delaunay criterion. Application of the method to a transonic flow around an aerofoil resulted in reasonable agreement with experimental data.

Apparently unaware of the work by Weatherill et al., Rostand [241] implemented the Baldwin-Lomax and Cebeci-Smith turbulence models on unstructured triangular grids for hypersonic compression ramp flows. Lines which were approximately normal to the boundary were constructed explicitly, along which the eddy viscosity was computed. Mavriplis [174] subsequently refined and generalised this process for multi-element aerofoil geometries by constructing locally structured background grids using hyperbolic grid-generation techniques. Further work on the implementation of algebraic turbulence models on unstructured grids was carried out by Pan and Cheng [217] and Marcum and Weatherill [171].

One-Equation Models. The Spalart-Allmaras [263] one-equation turbulence model was developed partly with the intention that it should be simple to implement on unstructured grids. It may be regarded as semi-local, since it requires only the distance to the nearest solid wall, but not quantities such as the friction velocity or the boundary-layer thickness. As a result, it has become widely used in recent years, see, e.g., Anderson and Bonhaus [12], Barth and Linton [32], Mavriplis and Venkatakrishnan [183], Frink [89],

Khawaja et al. [136], Haselbacher et al. [107], Crumpton et al. [73], Galle [92], and Blažek et al. [47].

Two-Equation Models. Soon after the first implementations of algebraic models, attention shifted toward the use of two-equation models. The reasons for this shift were the well-known shortcomings of algebraic turbulence and their troublesome implementation on unstructured grids. Holmes and Connell [109] presented results using the high-Reynolds number version of the $k - \epsilon$ model [301] in 1989. The implementation of this model is considerably simpler since it is necessary to store only those points which are connected to grid points on solid walls. Subsequently, a number of authors presented results obtained with the high-Reynolds number $k - \epsilon$ model, see, e.g., Stolcis and Johnston [268], Kwon and Hah [144], and Luo et al. [163]. In 1991, Mavriplis and Martinelli [181] published results computed with high- and low-Reynolds-number versions of the $k - \epsilon$ model. The mean flow equations were solved by a multi-stage Runge-Kutta scheme, whereas the turbulence model equations were solved using a point-implicit method for reasons of stability and robustness. Convergence of the mean-flow equations was accelerated by a multigrid method, but the turbulence field was kept frozen on the coarse grid levels. Low-Reynolds number $k - \epsilon$ models were also used by Marcum and Agarwal [170], Marcum and Weatherill [171], and Braaten and Connell [50].

Subsequently, Stolcis and Johnston [269] and Mohammadi [195] employed the $k - \epsilon$ model in conjunction with one-equation models near solid boundaries in order to reduce the required grid density and processing time.

Reynolds-Stress Models. Stolcis [267] and Cantariti and Johnston [56] implemented Reynolds-stress models with wall functions on unstructured grids. Wang et al. [290] presented results obtained with an algebraic Reynolds-stress model.

Large-Eddy Simulation (LES). The use of LES in conjunction with unstructured grids is a current area of research. The earliest work appears to be that of Jansen [126] in 1995, who computed the flow about the NACA 4412 aerofoil at maximum lift coefficient with a Galerkin/least-squares finite-element method on tetrahedral grids. Agreement with experimental values was found to be relatively poor in the separation region.

Discretisation of the transition strip used in the experiment and modelling the wind-tunnel walls in subsequent work brought some improvement in subsequent work, see Jansen [127]. An overview of these pioneering efforts was given by Jansen [128].

Knight et al. [139] presented results for the decay of incompressible isotropic turbulence obtained with a cell-centred finite-volume method on tetrahedral grids. The inviscid fluxes were computed with Roe's approximate Riemann solver [238] with second-order accurate gradient reconstruction using the methods of Frink [88] or Ollivier-Gooch [214]. Comparison of the numerical results with experimental data revealed considerable discrepancies, in particular for the turbulence energy spectrum. Okong'o and Knight [211] subsequently published results for channel and boundary layer flows, for which reasonable agreement was obtained. Urbin et al. [277] extended the method of Knight et al. to third-order accuracy with the approach of Ollivier-Gooch [214], and considered the interaction of a supersonic boundary layer with a compression corner. The numerical results were in reasonable agreement with experimental data for mean quantities.

Miet et al. [191] and Ducros et al. [80] also presented results obtained with LES on unstructured grids.

Regarding the spatial discretisation methods used so far in LES on unstructured grids, questions must be raised about the use of second- and third-order upwind schemes. This is because Mittal and Moin [194] demonstrated that a fifth-order upwind scheme order was more dissipative than a second-order centred scheme. The results of Garnier et al. [93] and Bui [53] are also relevant in this context. This could mean that finite-element methods may get more attention in the future, since they allow easier construction of higher-order centred discretisations on unstructured grids than finite-volume methods.

Disregarding the relatively poor agreement between LES and experiments achieved so far on unstructured grids, it is clear that the trend of applying LES to increasingly complex flows means that LES on unstructured grids will become more widespread in the future. In fact, the ability of unstructured grids to adjust the grid spacing locally is one way of reducing the extreme grid-resolution requirements by aggressive stretching away from solid walls, as already argued by Jansen [126]. Because the grid stretching near solid walls in LES is several orders of magnitude lower than in RANS simulations, tetrahedral grids may turn out to give adequate solution quality. However, using the

same arguments as in Subsection 1.1.2, mixed grids could still be attractive for LES using node-based solution methods.

1.3.2 Solution of Discrete Equations

In general, most methods for the solution of the discrete equations originally developed on structured grids can be applied to unstructured grids with few modifications. The following paragraphs deal with solution methods for steady flows only, where the time-derivative is retained to allow the solution to be obtained through time-marching. Space-marching methods for unstructured grids have been developed by McGrory et al. [168], Nakahashi and Saitoh [207], Nakahashi et al. [208], Löhner [154], and Morino and Nakahashi [199].

A dedicated review of solution methods on unstructured grids, especially implicit and multigrid methods, was presented recently by Mavriplis [180].

Explicit Methods. Due to their simple implementation and low storage requirements, explicit solution methods are widely used, in particular the multi-stage Runge-Kutta method introduced by Jameson et al. [124]. A further advantage of the Runge-Kutta method is that the stage coefficients can be tuned to optimise the high-frequency damping characteristics [281].

Runge-Kutta schemes were used by Jameson et al. [125], Mavriplis [173], Barth and Jespersen [31], Holmes and Connell [109], Nakahashi and Egami [205], Frink [87], Cabello et al. [55], Ollivier-Gooch [212], Gerhold et al. [94], Crumpton et al. [73], Haselbacher et al. [107], Galle [92], Blažek et al. [47], Haselbacher and Blažek [106], and many others.

The use of the Lax-Wendroff method [147] on unstructured grids is not common. The only known applications are due to Kallinderis and co-workers [130, 131, 135, 136, 219, 220] and Marcum and Marcum and co-workers [170, 171].

The main disadvantage of explicit methods is that they suffer from poor convergence rates with increasing grid refinement and stretching. Even with techniques such as local time-stepping [124], enthalpy damping [124] (for inviscid flows only), and implicit residual smoothing [121], convergence rates can still be poor. As a result, implicit solution methods are used or explicit solution methods are employed in conjunction

with a multigrid method.

Implicit Methods. One class of implicit methods is obtained by using the Euler backward method. The linearisation of the residual with respect to the state vector introduces the Jacobian matrix. The inversion of the resulting matrix equation gives rise to the inexact Newton method for large but finite time steps and the Newton method for infinitely large time steps. If the linearisation of the residual is exact, Newton's method is unconditionally stable and exhibits quadratic convergence if the initial iterate is in some sense close to the solution [266]. Because of this property, the use of implicit schemes obtained by the backward Euler method is a very active area of research.

A drawback of implicit methods is that the storage required for the Jacobian matrix is considerable. For example, the solution of the Navier-Stokes equations with a one-equation turbulence model on triangular grids with a vertex-based discretisation requires approximately 175 (475) words per vertex to store non-zero entries of the Jacobian matrix for first-order (second-order) discretisations. The corresponding figures for tetrahedral grids are approximately 504 (1980) words per vertex for first-order (second-order) discretisations. To put these figures into context, it is noted that the storage of the Jacobian matrix alone exceeds the required storage for an explicit method with multigrid.

The linear system can be solved by direct or iterative methods.

Direct Methods. Venkatakrishnan and Barth [286] and Slack et al. [254] employed lower-upper (LU) factorisation in two dimensions. They used reordering procedures such as the reverse Cuthill-McKee algorithm [244, p. 75] to reduce the bandwidth and the operation count. Direct methods are very robust, but suffer from prohibitively large storage requirements and long processing times, precluding their use for practical three-dimensional applications.

Iterative Methods. Using iterative methods for the solution of the linear system is more attractive due to lower demands on storage and processing time. Classical relaxation methods such as the point Gauss-Seidel method were employed by Fézoui and Stoufflet

[84], Anderson [11], Anderson and Bonhaus [12], Frink [88], and Ashford [16]. These methods depend on diagonal dominance for stability which introduces a restriction on the maximum time step. Frink [88] compared the Gauss-Seidel method to a three-stage Runge-Kutta method with local time-stepping and implicit residual averaging for three-dimensional viscous flow simulations. The implicit method converged six times faster in terms of processing time, but required four times more storage than the Runge-Kutta method.

The application of Krylov-subspace methods [244] to unstructured grids is an active area of research. In particular, the Generalised Minimum Residual (GMRES) method of Saad and Schultz [245] is widely used, see, e.g., Venkatakrishnan and Mavriplis [288], Whitaker [299], Barth and Linton [32], Nielsen et al. [209], Koomullil et al. [140], and Delanaye [75].

Preconditioning [244] is critical to achieving robust and fast convergence with Krylov-subspace methods. In general, it can be said that the more powerful the preconditioning matrix, i.e., the more closely it approximates its inverse, the larger the storage required. Venkatakrishnan and Mavriplis [288] investigated a number of preconditioners in conjunction with the GMRES method for inviscid and turbulent flows and concluded that Incomplete Lower-Upper (ILU) factorisation with no additional fill-in [244] performed best. The use of preconditioning methods such as ILU factorisation requires additional storage which is twice that of the Jacobian matrix. Part of this additional storage, however, may be reused to store data needed by the Krylov-subspace methods. Meister [186] compared several Krylov-subspace and preconditioning methods in terms of convergence behaviour for inviscid and laminar flows. With simple blockdiagonal preconditioning, the Transpose-Free Quasi-Minimum Residual (TFQMR) method of Freund [85] was found to converge fastest. With ILU preconditioning, the Bi-Conjugate Gradient Stabilised (BiCGSTAB) method of van der Vorst [278] exhibited the lowest convergence rates. Since the ILU preconditioner leads to faster convergence at the expense of substantially higher memory requirements compared to the blockdiagonal preconditioner, Meister found that the appropriate combination of Krylov-subspace and preconditioning methods depends on whether the solution to a given problem is to be reached with minimal computational time or storage.

The effect of reordering methods on the convergence rate of the GMRES method

with ILU preconditioning was examined by Dutto [82]. The effect of ordering was found to be significant, but the best ordering method was problem-dependent.

Although the iterative solution of the system of discrete equations is more efficient than the direct solution, the cost in terms of storage and processing time is still high. The use of first-order discretisations in computing the Jacobian matrix reduces the storage requirements, but it also precludes attaining the quadratic convergence associated with Newton's method. However, Barth and Linton [32] noted that for reconstruction procedures without limiter functions, higher-order Jacobians can be formed by multiplying the first-order Jacobian with the higher-order reconstructed state vector. Another approach to reduce storage is to use so-called Newton-Krylov methods, in which Fréchet derivatives [266] are used to compute the matrix-vector products, thus bypassing the storage of the Jacobian matrix at the expense of an increased number of residual evaluations. Fréchet derivatives are also useful if the numerical scheme contains complicated or non-differentiable functions which may occur in upwind schemes, limiter functions, and turbulence-model equations. A drawback of Newton-Krylov methods is that powerful preconditioning methods such as ILU factorisation require the Jacobian matrix to be available explicitly. Hence the real benefit of Newton-Krylov methods are not the reduced storage requirements, but that quadratic convergence can be achieved in conjunction with preconditioning.

Nielsen et al. [209] investigated a variety of numerical issues in Newton-Krylov methods for two- and three-dimensional inviscid external flows. The GMRES method was employed with ILU preconditioning and reverse Cuthill-McKee ordering. A comparison of the Newton-Krylov method to a multigrid method with three grid levels for a two-dimensional transonic flow showed that the Newton-Krylov method was slower in terms of processing time. By employing an interpolated coarse-grid solution obtained with the point Gauss-Seidel method as an initial iterate, the Newton-Krylov method compared favourably with the multigrid method. The multigrid method requires considerably less storage, however.

Slack et al. [254] compared a number of explicit and direct and iterative implicit solution methods for transonic inviscid flow over a circular-arc bump in a channel using both first-order and second-order discretisations. Preconditioned iterative implicit solution methods were found to offer better performance with grid refinement than explicit

solution methods.

The only way in which implicit methods can be made competitive with multigrid methods is if both storage and inversion of the Jacobian matrix can be avoided. This can be achieved by the Lower-Upper Symmetric Gauss-Seidel (LU-SGS) method of Yoon and Jameson [302], originally developed on structured grids, which decomposes the Jacobian matrix into strictly lower triangular, diagonal, and strictly upper triangular factors. Through an approximate splitting of the positive and negative projections of the Jacobian and updating on hyperplanes $i + j = \text{constant}$, where i and j denote the usual structured-grid indices, only scalar inversions and forward and backward substitutions are required to advance the solution. This results in a method which is unconditionally stable and requires little additional CPU time per update step compared to an explicit method.

The extension of the LU-SGS method to unstructured grids required special re-ordering procedures for the construction of the hyperplanes. Soestrisno et al. [257, 258] constructed these planes by sorting grid cells into groups of neighbours of neighbours. Sharov and Nakahashi [249] modified that method by coloring the vertices in each hyperplane such that no two vertices of the same color are connected by an edge. Their method gives the usual hyperplanes $i + j = \text{constant}$ on structured grids. Sharov and Nakahashi stated that the time taken for one LU-SGS iteration is less than that for a two-step explicit method. Further applications of the LU-SGS method were presented by Kano and Nakahashi [132], Sharov and Nakahashi [248], and Chen and Wang [64].

By using the LU-SGS method as a preconditioner to Krylov-subspace methods with numerical evaluation of the Jacobian matrix, a matrix-free implicit method may be derived, as pointed out by Luo et al. [164]. They demonstrated accelerations of about one order of magnitude compared to an explicit method for inviscid and laminar flows. The effectiveness of the method of Luo et al. for turbulent flows remains to be demonstrated.

Multigrid Methods.* Multigrid methods [51] use a sequence of successively coarser grids to accelerate the convergence rate of an iterative method. The task of the iterative method is reduced to damping high-frequency error components only. Because

*Multigrid methods are not a solution method as such, because they require an explicit or implicit method to remove high-frequency error components. The basic issues, however, are not directly dependent on the smoothing method. It is therefore convenient to treat multigrid methods separately.

little additional storage is required, multigrid methods are very attractive. The application of multigrid methods to unstructured grids required the development of new techniques for the construction of coarse grid levels. In contrast to structured grids, coarse unstructured grid levels cannot be generated by simply deleting alternate grid lines in each coordinate direction. Since the generation of a suitable fine grid is frequently a burden on the user, it is imperative that the construction of the coarse grid levels is as automatic as possible. Furthermore, it is desirable that the construction of the coarse grid levels is not dependent on a grid generator so that it can operate on grids of unknown origin. Several approaches have been developed, which differ primarily in the degree to which they can be automated.

Mavriplis [178] provided a detailed discussion and comparison of the various approaches, see also Rienslagh and Dick [233] and Chan et al. [62].

Successive Refinement. Perez [224] suggested the generation of a nested sequence of grids by successive subdivision of triangular cells into four smaller triangular cells, as shown in Fig. 1.16(a). This procedure is easily automated and allows a very simple construction of intergrid transfer operators through injection and averaging. Unfortunately, it was found that the resulting finer grid levels were of relatively poor quality. This disadvantage is avoided in the approach of Barth [28], which encodes, in the form of a directed acyclic graph [184], the sequence of structural changes of an incremental Delaunay triangulation. This procedure allows the extraction of valid intermediate triangulations as coarse grid levels. The use of successive refinement suffers from the drawback that it must be closely coupled with the grid-generation procedure and that the surface definition is required. Because of its similarities with grid adaptation through cell subdivision, successive refinement is ideally suited to the coupling of multigrid with grid adaptation, as done by Connell and Braaten [68], Parthasarathy and Kallinderis [219], and Braaten and Connell [50].

Regeneration. Löhner and Morgan [158] and Mavriplis [173] proposed the use of independently generated grids, as depicted in Fig. 1.16(b). Intergrid transfer operators are easily implemented using linear interpolation. The weights for the linear interpolation are commonly computed and stored in a pre-processing step. The computation of the

weights requires efficient search algorithms in order to identify overlapping cells. The obvious disadvantage of this approach is that the generation of the sequence of grids is non-automatic and therefore a burden on the user. Independently generated grid levels were used by Bonhaus [48], Peraire et al. [223], Mavriplis [176,177], Leclercq and Stoufflet [148], and Crumpton and Giles [71].

Vertex Removal. Guillard [97] suggested the selection of a subset of vertices of a given grid and the subsequent construction of a Delaunay triangulation, resulting in vertex-nested grids, as illustrated schematically in Fig. 1.16(c). The selection of a subset of vertices is easily automated. The heuristic vertex-selection algorithm presented by Guillard results in coarsening ratios of approximately four. A drawback of the vertex-removal approach is that special care has to be taken to ensure that vertices critical to the description of the geometry are retained. Guillard retained those vertices whose neighbouring edges form the largest absolute included angle on a given grid level. Even so, for successively coarser grid levels, the solution domain is only approximately conserved. The method of Guillard was used by Morano and Dervieux [196] and Riemsdijk and Dick [234].

Ollivier-Gooch [212] presented a method which removes a subset of vertices of a given grid through edge contraction. This also results in vertex-nested grids levels but, in contrast to the method by Guillard, it does not require a grid generator. The subset of vertices to be removed is determined such that the remaining vertices form a maximal independent set [184]. Edge-swapping is carried out to minimise the maximum angle between edges. Again, special care must be exercised to preserve boundary integrity.

Crumpton and Giles [72] developed a method in which a coarse tetrahedral grid is generated by collapsing edges of a given fine grid. The two vertices connected by an edge are thus replaced by a new vertex at the midpoint of the edge to be collapsed. In contrast to the vertex-removal methods of Guillard and Ollivier-Gooch, the fine and coarse grids are not vertex-nested. To ensure that vertices are removed evenly in the grid, the vertices are colored such that each edge links vertices of different color. For each color, the shortest edge at a given vertex is collapsed. For edges which point toward or lie on a boundary surface, the collapsing algorithm retains that vertex which lies on more boundary surfaces, thus retaining salient features of the geometry. However,

even with these measures, the grid quality was relatively poor, which may affect the performance of the multigrid method. The method of Crumpton and Giles [72] was extended to mixed grids by Müller and Giles [202] and Müller [201].

Control-Volume Agglomeration. An automatic and geometry-preserving coarse-grid construction can be derived by realising that coarser grids need not actually exist for finite-volume discretisations. Instead, coarse grid levels can be constructed by agglomerating control volumes of a given fine grid, as shown in Fig. 1.16(d) for a vertex-based scheme. This approach was developed independently by Lallemand [145] and Smith [256] for vertex-based and cell-centred methods, respectively. In the case of vertex-based schemes, the process is initiated by selecting, in common with the methods described above, a set of so-called seed vertices which remain on the coarse grid level. Control volumes associated with non-selected vertices are then agglomerated with the control volumes associated with seed vertices.

The agglomeration multigrid method suffers from two main problems. First, the discretisation of diffusive fluxes on coarse grid levels is not trivial. Second, it is not immediately clear how to define prolongation operators which are more accurate than trivial injection.

Mavriplis and Venkatakrishnan [183] applied the agglomeration multigrid method to mixed grids in three dimensions. Although the number of applications of the agglomeration multigrid method is increasing slowly, it has been applied mainly by research teams at INRIA and Mavriplis and Venkatakrishnan.

Algebraic Multigrid (AMG). The techniques described above allow the generation of a sequence of coarse grids for use in a geometric multigrid method. In contrast, algebraic multigrid methods [243] do not construct coarse grid levels explicitly. Instead, the coarsening is dependent on the discretisation. The application of AMG to unstructured grids is not widespread. Early work was carried out by Lonsdale [161] and Webster [297] to solve the incompressible Navier-Stokes equations. AMG methods for compressible flows were presented by Raw [230] and Weiss et al. [298].

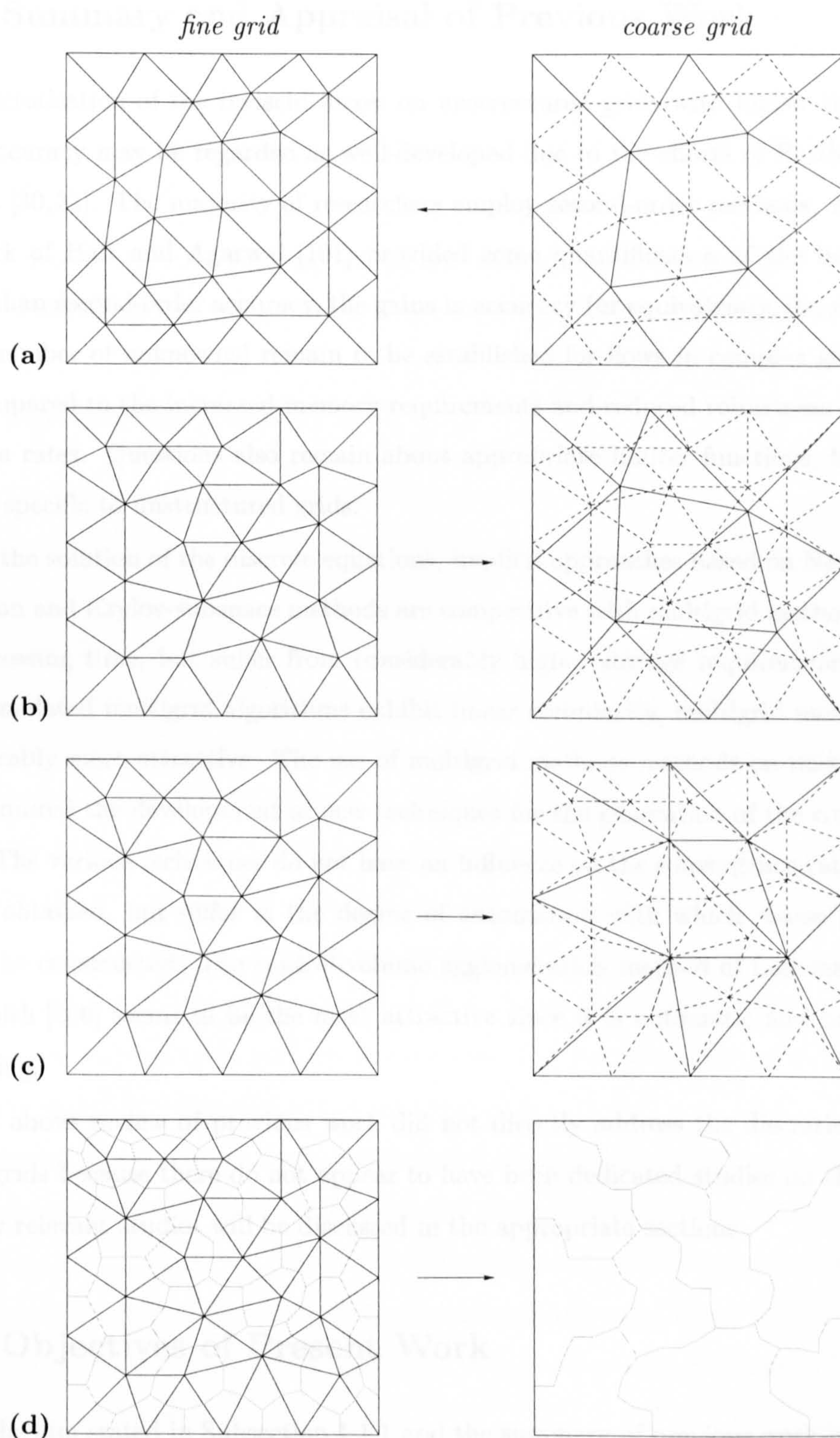


Figure 1.16: Illustration of methods for the generation of coarse grid levels for multigrid methods on unstructured grids. **(a)** Successive refinement, **(b)** regeneration, **(c)** vertex removal, and **(d)** control-volume agglomeration for a vertex-based method.

1.4 Summary and Appraisal of Previous Work

The discretisation of the inviscid fluxes on unstructured grids with higher than first-order accuracy may be regarded as well-developed due to the efforts of Barth and co-workers [30,31]. The majority of researchers employ second-order methods. Although the work of Halt and Agarwal [101] provided some quantification of the benefits of higher than second-order accuracy, the gains in accuracy (or equivalently, the reduction in the number of unknowns) remain to be established for flows in complex geometries and compared to the increased memory requirements and reduced robustness and convergence rates. Questions also remain about appropriate limiter functions, but these are not specific to unstructured grids.

For the solution of the discrete equations, implicit approaches based on Newton linearisation and Krylov-subspace methods are competitive with multigrid methods based on processing time, but suffer from considerably higher storage requirements. Since well-formulated multigrid algorithms exhibit linear complexity, multigrid methods are considerably more attractive. The use of multigrid methods on unstructured grids required the development of new techniques for the generation of the coarse grid levels. The various techniques do not have an influence on the convergence rates which can be obtained, but differ in the degree of automation with which coarse grid levels can be constructed. The control-volume agglomeration method of Lallemand [145] and Smith [256] seems to be the most attractive since it is automatic and boundary-preserving.

The above review of previous work did not directly address the discretisation on mixed grids because there do not appear to have been dedicated studies on this topic. The few relevant studies will be discussed in the appropriate sections.

1.5 Objectives of Present Work

Given the aim stated in Subsection 1.1.1 and the summary of previous work in Section 1.4, the objectives of the present work are:

1. To investigate the use of mixed grids in order to resolve regions dominated by viscous effects.

2. To construct spatial discretisations specifically suited to the computation of viscous flows on mixed grids.
3. To develop an agglomeration multigrid method based on rediscretisation on the coarse grid levels.
4. To demonstrate the performance of the methods developed under 1., 2., and 3. by conducting careful numerical studies on inviscid and viscous test problems.

1.6 Outline of Thesis

The rest of this thesis is organised into eight chapters.

The governing equations for inviscid, laminar, and turbulent flows are presented in Chapter 2.

The numerical method for single-grid calculations is described in Chapter 3. The concept of grid-transparency is introduced to establish a framework for the development of discretisation methods on mixed grids. Particular attention is paid to the performance of the numerical method on different cell types.

The discretisation of viscous fluxes on unstructured grids is addressed in Chapter 4. Laplace's equation is chosen as a model equation for the viscous terms in the Navier-Stokes equations. Various schemes are studied and compared against a number of criteria. The chosen discretisation is extended to the viscous terms in the Navier-Stokes equations. An approximate, grid-transparent form of the viscous terms is derived which may be regarded as a thin-shear-layer approximation.

Chapter 5 is dedicated to the implementation of an agglomeration multigrid method in order to accelerate convergence of the single-grid method described in Chapter 3. In contrast to previous work, the current implementation emphasizes the geometric aspects of the multigrid process by rediscretising the equations on the coarse grid levels. The agglomeration process, intergrid transfer operators, and several implementation issues are described in detail.

The solution method is applied to inviscid flow problems in Chapter 6. Both triangular and quadrilateral grids are used. The exact solution for supersonic vortex flow is chosen to assess the order of accuracy of the method. The flow over a circular-arc bump in a channel is used to illustrate the characteristics of various reconstruction schemes

and limiter functions both in terms of solution quality and convergence histories. The performance of the agglomeration multigrid method is investigated both for the flow over the circular-arc bump and the flow over a NACA 0012 aerofoil.

Solutions for laminar flow problems are listed in Chapter 7. The chosen test cases are the flow over a flat plate and the separated flow over the NACA 0012 aerofoil. Triangular, quadrilateral, and mixed grids are used. Several discretisations for the viscous fluxes are compared. The performance of the agglomeration multigrid method is studied.

Chapter 8 presents results for turbulent flow. The test cases are the ONERA bump Case C [77] and the RAE 2822 aerofoil Case 10 [69].

Chapter 9 summarises the present work, draws conclusions, and recommends areas for future work.

References

- [1] Abgrall R. and Lafon F.C., *ENO Schemes on Unstructured Meshes*, in: *Computational Fluid Dynamics Lecture Series 1993-04*, von Kármán Institute for Fluid Dynamics, March 1993
- [2] Abgrall R., Lantéri S., and Sonar T., *ENO Approximations for Compressible Fluid Dynamics*, *Z. Angew. Math. Mech.*, Vol. 79, No. 1, pp. 3-28, 1999
- [3] Aftosmis M.J., *Upwind Method for Simulation of Viscous Flow on Adaptively Refined Meshes*, *AIAA J.*, Vol. 92, No. 2, pp. 268-277, 1994
- [4] ———, *Emerging CFD Technologies and Aerospace Vehicle Design*, in: *Surface Modelling, Grid Generation, and Related Issues in Computational Fluid Dynamic (CFD) Solutions*, NASA CP 3291, pp. 359-384, March 1995
- [5] ———, *Solution Adaptive Cartesian Grid Methods for Aerodynamic Flows with Complex Geometries*, in: *Computational Fluid Dynamics Lecture Series 1997-02*, von Kármán Institute for Fluid Dynamics, March 1997
- [6] Aftosmis M.J., Gaitonde D., and Tavares T.S., *Behaviour of Linear Reconstruction Techniques on Unstructured Meshes*, *AIAA J.*, Vol. 33, No. 1, pp. 2038-2049, 1995
- [7] *Special Course on Unstructured Grid Methods for Advection Dominated Flows*, AGARD Report 787, May 1992
- [8] Albane C.M., *An Approach to Geometric and Flow Complexity Using Feature-Associated Mesh Embedding, Strategy and First Results*, in: *Numerical Methods for Fluid Dynamics III*, Morton K.W. and Baines M.J. (Eds.), Clarendon Press, Oxford, 1988, pp. 215-235
- [9] Allmaras S.R. and Baron J.R., *Embedded Mesh Solutions of the 2-D Euler Equations: Evaluation of Interface Formulations*, AIAA Paper 86-0509, 24th Aerospace Sciences Meeting, Reno, NV, January 1986

- [10] Allmaras S.R. and Giles M.B., *A Second Order Flux Split Scheme for the Unsteady 2-D Euler Equations on Arbitrary Meshes*, AIAA Paper 87-1119, 8th Computational Fluid Dynamics Conference, Honolulu, HI, June 1987
- [11] Anderson W.K., *A Grid-Generation and Flow-Solution Method for the Euler Equations on Unstructured Grids*, J. Comp. Phys., Vol. 110, pp. 23-38, 1994
- [12] Anderson W.K. and Bonhaus D.L., *An Implicit Upwind Algorithm for the Computation of Turbulent Flows on Unstructured Grids*, Comp. Fl., Vol. 23, No. 1, pp. 1-21, 1994
- [13] Angrand F. and Dervieux A., *Some Explicit Triangular Finite Element Schemes for the Euler Equations*, Int. J. Num. Meth. Fl., Vol. 4, pp. 749-764, 1984
- [14] Angrand F., Dervieux A., Loth L., and Vijayasundaram G., *Simulation of Euler Transonic Flows by Means of Explicit Finite-Element Schemes*, Research Report No. 250, INRIA, October 1983
- [15] Arminjon P. and Dervieux A., *Construction of TVD-like Artificial Viscosities on Two-Dimensional Arbitrary FEM Grids*, J. Comp. Phys., Vol. 106, pp. 176-198, 1993
- [16] Ashford G.A., *An Unstructured Grid Generation and Adaptive Solution Technique for High-Reynolds Number Compressible Flows*, Ph.D. Thesis, University of Michigan, Ann Arbor, Michigan, 1996
- [17] Aviation Week and Space Technology, Vol. 124, No. 3, p. 117, January 20, 1986
- [18] Babuška I. and Aziz A.K., *On the Angle Condition in the Finite Element Method*, SIAM J. Numer. Anal., Vol. 13, No. 2, pp. 214-226, 1976
- [19] Baldwin B.S. and Lomax H., *Thin-Layer Approximation and Algebraic Model for Turbulent Separated Flow*, AIAA Paper 78-257, 1978, 16th Aerospace Sciences Meeting, Huntsville, AL, January 1978
- [20] Baker T.J., *Prospects and Expectations for Unstructured Methods*, in: *Surface Modelling, Grid Generation, and Related Issues in Computational Fluid Dynamic (CFD) Solutions*, NASA CP 3291, pp. 273-287, March 1995
- [21] ———, *Irregular Meshes and the Propagation of Solution Errors*, in: *Proc. 15th Int. Conf. on Numerical Methods in Fluid Dynamics*, Monterey, CA, June 1996, Kutler P. et al. (Eds.), Lecture Notes in Physics, Vol. 490, Springer Verlag, Germany, pp. 596-601, 1997
- [22] Barth T.J., *On Unstructured Grids and Solvers*, in: *Computational Fluid Dynamics Lecture Series 1990-03*, von Kármán Institute for Fluid Dynamics, March 1990
- [23] ———, *Numerical Aspects of Computing High-Reynolds Number Flows on Unstructured Meshes*, AIAA Paper 91-0721, 29th Aerospace Sciences Meeting and Exhibit, Reno, NV, January 1991
- [24] ———, *A 3D Upwind Euler Solver for Unstructured Meshes*, AIAA Paper 91-1548, 10th Computational Fluid Dynamics Conference, Honolulu, HI, June 1991
- [25] ———, *Aspects of Unstructured Grids and Finite-Volume Solvers for the Euler and Navier-Stokes Equations*, in: *Special Course on Unstructured Grid Methods for Advection Dominated Flows*, AGARD Report 787, pp. 6-1 to 6-61, May 1992

- [26] ———, *Recent Developments in High-Order k -Exact Reconstruction on Unstructured Meshes*, AIAA Paper 93-0668, 31st Aerospace Sciences Meeting, Reno, NV, January 1993
- [27] ———, *Aspects of Unstructured Grids and Finite-Volume Solvers for the Euler and Navier-Stokes Equations*, in: *Computational Fluid Dynamics Lecture Series 1994-05*, von Kármán Institute for Fluid Dynamics, March 1994
- [28] ———, *Randomized Multigrid*, AIAA Paper 95-0207, 33rd Aerospace Sciences Meeting and Exhibit, Reno, NV, January 1995
- [29] ———, *Numerical Methods for Gasdynamic Systems on Unstructured Meshes*, in: *An Introduction to Recent Developments in Theory and Numerics for Conservation Laws*, Kröner D. et al. (Eds.), *Lecture Notes in Computational Science and Engineering*, Vol. 5, Springer Verlag, pp. 195-285, 1999
- [30] Barth T.J. and Frederickson P.O., *Higher Order Solution of the Euler Equations on Unstructured Grids Using Quadratic Reconstruction*, AIAA Paper 90-0013, 28th Aerospace Sciences Meeting, Reno, NV, January 1990
- [31] Barth T.J. and Jespersen D.C., *The Design and Application of Upwind Schemes on Unstructured Meshes*, AIAA Paper 89-0366, 27th Aerospace Sciences Meeting, Reno, NV, January 1989
- [32] Barth T.J. and Linton S.W., *An Unstructured-Mesh Newton Solver for Compressible Fluid Flow and Its Parallel Implementation*, AIAA Paper 95-0221, 33rd Aerospace Sciences Meeting and Exhibit, Reno, NV, January 1995
- [33] Batina J.T., *Unstructured Grid Methods—Lessons Learned*, in: *Proc. 4th Int. Symp. on Computational Fluid Dynamics*, Vol. 1, University of California, Davis, pp. 91-96, September 1991
- [34] Batten P., Lambert C., and Causon D.M., *Positively Conservative High-Resolution Convection Schemes for Unstructured Meshes*, *Int. J. Num. Meth. Eng.*, Vol. 39, pp. 1821-1838, 1996
- [35] Baum J.D. and Löhner R., *Numerical Simulation of Pilot/Seat Ejection from an F-16*, AIAA Paper 93-0783, 31st Aerospace Science Meeting and Exhibit, Reno, NV, January 1993
- [36] Baum J.D., Luo H., and Löhner R., *Numerical Simulation of a Blast Inside a Boeing 747*, AIAA 93-3091, 24th Fluid Dynamics Conference, Orlando, FL, July 1993
- [37] ———, *Numerical Simulation of Blast in the World Trade Center*, AIAA Paper 95-0085, 33rd Aerospace Sciences Meeting and Exhibit, Reno, NV, January 1995
- [38] Beam R.M. and Warming R.F., *An Implicit Finite-Difference Algorithm for Hyperbolic Systems in Conservation Form*, *J. Comp. Phys.*, Vol. 22, pp. 87-109, 1976
- [39] Belk D.M., *The Role of Overset Grids in the Development of the General Purpose CFD Code*, in: *Surface Modelling, Grid Generation, and Related Issues in Computational Fluid Dynamic (CFD) Solutions*, NASA CP 3291, pp. 193-204, March 1995
- [40] Benek J.A., Buning P.G., and Steger J.L., *A 3-D Chimera Grid Embedding Technique*, AIAA Paper 85-1523, 7th Computational Fluid Dynamics Conference, Cincinnati, OH, July 1985

- [41] Berger M.J., *On Conservation at Grid Interfaces*, SIAM J. Numer. Anal., Vol. 24, pp. 967-984, 1987
- [42] Berger M.J. and Aftosmis M.J., *Aspects (and Aspect Ratios) of Cartesian Mesh Methods*, Proc. 16th Int. Conf. on Numerical Methods in Fluid Dynamics, Arachon, in: Lecture Notes in Physics, Vol. 515, Bruneau C.H. et al. (Eds.), Springer, 1999
- [43] Berglind T., *A Hybrid Structured-Unstructured Grid Method for Aerodynamic Flow Simulation*, AIAA Paper 95-0051, 33rd Aerospace Sciences Meeting and Exhibit, Reno, NV, January 1995
- [44] Berzins M. and Ware J.M., *Positive Cell-Centered Finite-Volume Discretisation Methods for Hyperbolic Equations on Irregular Meshes*, Appl. Num. Math., Vol. 16, pp. 417-438, 1995
- [45] Bishop D.G. and Noack R.W., *An Implicit Flow Solver with Upwind Differencing for Three-Dimensional Hybrid Grids*, AIAA Paper 95-1707, 12th Computational Fluid Dynamics Conference, San Diego, CA, June 1995
- [46] Biswas R., Thomas S.D., and Cliff S.E., *An Edge-Based Solution-Adaptive Method Applied to the AIRPLANE code*, AIAA Paper 96-0553, 34th Aerospace Sciences Meeting and Exhibit, Reno, NV, January 1996
- [47] Blažek J., Irmisch S., and Haselbacher A., *Unstructured Mixed-Grid Navier-Stokes Solver for Turbomachinery Applications*, AIAA Paper 99-0664, 37th Aerospace Sciences Meeting and Exhibit, Reno, NV, January 1999
- [48] Bonhaus D.L., *An Upwind Multigrid Method for Solving Viscous Flows on Unstructured Triangular Meshes*, M.Sc. Thesis, George Washington University, August 1993
- [49] Boschitsch A.H. and Quackenbush T.R., *Efficient High-Order Compact Scheme for Deforming Unstructured Meshes*, AIAA Paper 96-0415, 34th Aerospace Sciences Meeting and Exhibit, Reno, NV, January 1996
- [50] Braaten M.E. and Connell S.D., *Three-Dimensional Unstructured Adaptive Multigrid Scheme for the Navier-Stokes Equations*, AIAA J., Vol. 34, No. 2, pp. 281-290, 1996
- [51] Brandt A., *Multigrid Techniques: 1984 Guide with Applications to Fluid Dynamics*, GMD-Studien No. 85, Gesellschaft für Mathematik und Datenverarbeitung MBH, Bonn, Germany, May 1984
- [52] Bristeau M.O., Glowinski R., Périaux J., Perrier P., and Pironneau O., *Transonic Flow Simulations by Finite-Element and Least-Squares Methods*, in: *Finite Elements in Fluids*, Vol. 4, Gallagher R.H., Wiley, pp. 453-482, 1982
- [53] Bui T.T., *A Parallel, Finite-Volume Algorithm for Large-Eddy Simulation of Turbulent Flows*, NASA/TM-1999-206570, January 1999
- [54] Buning P., Chu I.T., Obayashi S., Rizk Y.M., and Steger J.L., *Numerical Simulation of the Integrated Space Shuttle Vehicle in Ascent*, AIAA 88-4359, AIAA Computational Flight Mechanics Conference, Minneapolis, MN, August 1989
- [55] Cabello J., Morgan K., and Löhner R., *A Comparison of Higher-Order Schemes in a Finite-Volume Solver for Unstructured Grids*, AIAA Paper 94-2293, 25th Fluid Dynamics Conference, Colorado Springs, CO, June 1994

- [56] Cantariti F.J.-J. and Johnston L.J., *High-Lift Navier-Stokes Computations on Unstructured Grids Using a Differential Reynolds-Stress Model*, in: *Numerical Methods for Fluid Dynamics V*, Eds. Morton K.W. and Baines M.J., Clarendon Press, pp. 319-325, 1995
- [57] Carey G.F. and Oden J.T., *Finite Elements: Computational Aspects*, The Texas Finite Element Series, Vol. III, Prentice-Hall, Eaglewood Cliffs, 1984
- [58] Carpentier R., *Comparaison entre des schémas 2D de type Roe sur maillage régulier triangle ou quadrangle. I: calcul au sommet - pentes centrées*, INRIA Technical Report No. 2824, March 1996
- [59] ———, *Comparaison entre des schémas 2D de type Roe sur maillage régulier triangle ou quadrangle. II: calcul au sommet - le $\beta\gamma$ schéma*, INRIA Technical Report No. 3360, February 1998
- [60] Carpentier R., Glinsky N., and Larroturou B., *Schémas décentrées d'ordre deux opérant sur des quadrangles ou des triangles: une comparaison*, in: *Operation of Segmented Solid Rocket Motors for Space Launchers*, Proc. 1st CNES-ONERA Colloquium, Chatillon, France, December 8/9, 1992
- [61] Cebeci T. and Smith A.M.O., *Analysis of Turbulent Boundary Layers*, Vol. XV in: *Series in Applied Mathematics and Mechanics*, Academic Press, 1974
- [62] Chan T.F., Go. S., and Zikatanov L., *Multilevel Methods for Elliptic Problems on Unstructured Grids*, in: *Computational Fluid Dynamics Lecture Series 1997-02*, von Kármán Institute of Fluid Dynamics, March 1997
- [63] Chapman D.R., *Computational Aerodynamics Development and Outlook*, AIAA J., Vol. 17, No. 12, pp. 1293-1313, December 1979
- [64] Chen R.F. and Wang Z.J., *An Improved LU-SGS Scheme with Faster Convergence for Unstructured Grids of Arbitrary Topology*, AIAA Paper 99-0935, 37th Aerospace Sciences Meeting and Exhibit, Reno, NV, January 1999
- [65] Coirier W.J., *An Adaptively-Refined, Cartesian, Cell-Based Scheme for the Euler and Navier-Stokes Equations*, NASA TM-106754, October 1994
- [66] Coirier W.J. and Jorgenson P.C.E., *A Mixed Volume Grid Approach for the Euler and Navier-Stokes Equations*, NASA TM-107135, January 1996
- [67] Coirier W.J. and Powell K.G., *An Accuracy Assessment of Cartesian-Mesh Approaches for the Euler Equations*, J. Comp. Phys., Vol. 117, pp. 121-131, 1995
- [68] Connell S.D. and Braaten M.E., *Three-Dimensional Unstructured Adaptive Multigrid Scheme for the Navier-Stokes Equations*, AIAA J., Vol. 34, No. 2, pp. 281-290, 1996
- [69] Cook P.H., McDonald M.A., and Firmin M.C.P., *Aerofoil RAE 2822 — Pressure Distributions, and Boundary Layer and Wake Measurements*, AGARD AR-138, pp. A6-1 to A6-77, 1979
- [70] Cournède H., Debiez C., and Dervieux A., *A Positive MUSCL scheme for Triangulations*, INRIA Report 9465, July 1998
- [71] Crumpton P.I. and Giles M.B., *Aircraft Computations Using Multigrid and an Unstructured Parallel Library*, AIAA Paper 95-0210, 33rd Aerospace Sciences Meeting and Exhibit, Reno, NV, January 1995

- [72] ———, *Implicit Time-Accurate Solutions on Unstructured Dynamic Grids*, AIAA Paper 95-1671, 12th Computational Fluid Dynamics Conference, San Diego, CA, June 1995 Also: *Int. J. Num. Meth. Fl.*, Vol. 25, No. 11, pp. 1285-1300, December 1997
- [73] Crumpton P.I., Moinier P., and Giles M.B., *An Unstructured Algorithm for High-Reynolds-Number Flows on Highly-Stretched Grids*, in: *Numerical Methods for Laminar and Turbulent Flows*, Taylor C. and Cross J.T. (Eds.), Pineridge Press, pp. 561-572, 1997
- [74] Debiez C., *Approximation décentrées à faible dissipation pour des problèmes hyperboliques*, INRIA Report 2811, February 1996
- [75] Delanaye M., *Polynomial Reconstruction Finite Volume Schemes for the Compressible Euler and Navier-Stokes Equations on Unstructured Adaptive Grids*, Ph.D. Thesis, Université de Liège, September 1996
- [76] Delanaye M., Aftosmis M.J., Berger M., Liu Y., and Pulliam T.H., *Automatic Hybrid-Cartesian Grid Generation for High-Reynolds Number Flows around Complex Geometries*, AIAA Paper 99-0777, 37th Aerospace Meeting and Exhibit, Reno, NV, January 1999
- [77] Déleroy J., Copy C., and Reisz J., *Analyse au vélocimètre laser bidirectionnelle d'une interaction choc-couche limite turbulente avec décollement étendu*, ONERA Technical Report 37/7078 AY 014, August 1980
- [78] Dervieux A., *Steady Euler Simulations Using Unstructured Grids*, in: *Computational Fluid Dynamics Lecture Series 1985-04*, von Kármán Institute of Fluid Dynamics, March 1985
- [79] Désidéri J.-A. and Dervieux A., *Compressible Flow Solvers Using Unstructured Grids*, in: *Computational Fluid Dynamics Lecture Series 1988-05*, von Kármán Institute of Fluid Dynamics, March 1988. Also: revised and reprinted as INRIA Technical Report 1732, 1992
- [80] Ducros F., Nicoud F., and Schönfeld T., *Large Eddy Simulations of Compressible Flows on Hybrid Meshes*, in: *Proc. 11th Symp. on Turbulent Shear Flows*, Lesieur M. et al. (Eds.), pp. 28-1 to 28-6, 1997
- [81] Durlofsky L.J., Engquist B., and Osher S., *Triangle-Based Adaptive Stencils for the Solution of Hyperbolic Conservation Laws*, *J. Comp. Phys.*, Vol. 98, pp. 64-73, 1992
- [82] Dutto L.C., *The Effect of Ordering on Preconditioned GMRES Algorithm, for Solving the Compressible Navier-Stokes Equations*, *Int. J. Num. Meth. Eng.*, Vol. 36, pp. 457-497, 1993
- [83] Fézoui F., *Résolution des équations d'Euler par un schema de van Leer en éléments finis*, INRIA Technical Report 358, January 1985
- [84] Fézoui F. and Stoufflet B., *A Class of Implicit Upwind Schemes for Euler Simulations with Unstructured Meshes*, *J. Comp. Phys.*, Vol. 84, pp. 174-206, 1989
- [85] Freund R.W., *A Transpose-Free Quasi-Minimum Residual Algorithm for Non-Hermitian Linear Systems*, *SIAM J. Sci. Comp.*, Vol. 14, No. 2, pp. 470-482, 1993

- [86] Friedrichs O., *Weighted Essentially Non-Oscillatory Schemes for the Interpolation of Mean Values on Unstructured Grids*, J. Comp. Phys., Vol. 144, pp. 194-212, 1998
- [87] Frink N.T., *Upwind Scheme for Solving the Euler Equations on Unstructured Tetrahedral Meshes*, AIAA J., Vol. 30, No. 1, pp. 70-77, 1992
- [88] ———, *Recent Progress Towards a Three-Dimensional Unstructured Navier-Stokes Solver*, AIAA Paper 94-0061, 32nd Aerospace Sciences Meeting, Reno, NV, January 1994
- [89] ———, *Tetrahedral Unstructured Navier-Stokes Method for Turbulent Flows*, AIAA J., Vol. 36, No. 6, pp. 1975-1982, 1998. Also: *Assessment of an Unstructured-Grid Method for Predicting 3-D Turbulent Viscous Flows*, AIAA Paper 96-0292, 34th Aerospace Sciences Meeting and Exhibit, Reno, NV, January 1996
- [90] Frink N.T. and Pirzadeh S.Z., *Tetrahedral Finite-Volume Solutions to the Navier-Stokes Equations on Complex Configurations*, NASA TM-1998-208961, December 1998. Also presented at: 10th Int. Conf. on Finite Elements in Fluids, Tucson, AZ, January 1998
- [91] Frymier P.D., Hassan H.A., and Salas M.D., *Navier-Stokes Calculations Using Cartesian Grids: I. Laminar Flows*, AIAA J., Vol. 26, No. 10, pp. 1181-1188, 1988
- [92] Galle M., *Ein Verfahren zur numerischen Simulation kompressibler, reibungsbehafteter Strömungen auf hybriden Netzen*, DLR Forschungsbericht 99-04, DLR Braunschweig, Januar 1999
- [93] Garnier E., Sagaut P., Mossi M., Comte P., and Deville M., *On the Use of Shock-Capturing Schemes for Large-Eddy Simulation*, in: *Numerical Methods for Fluid Dynamics VI*, M.J. Baines (Ed.), Institute of Computational Fluid Dynamics, Oxford University Computing Laboratory, pp. 319-325, 1998
- [94] Gerhold T., Friedrich O., Evans J., and Galle M., *Calculation of Complex Three-Dimensional Configurations Using the DLR- τ -Code*, AIAA Paper 97-0167, 35th Aerospace Sciences Meeting and Exhibit, Reno, NV, January 1997
- [95] Giles M.B., *Accuracy of Node-Based Solutions on Irregular Meshes*, in: *Proc. 11th Int. Conf. on Numerical Methods in Fluid Dynamics*, Williamsburg, VA, June/July 1988, Dwoyer D.L. et al. (Eds.), Lecture Notes in Physics, Vol. 323, Springer Verlag, Germany, pp. 273-277, 1989
- [96] ———, *UNSFLO: A Numerical Method for the Calculation of Unsteady Flow in Turbomachinery*, Gas Turbine Laboratory Report No. 205, Massachusetts Institute of Technology, May 1991
- [97] Guillard H., *Node-Nested Multigrid with Delaunay Coarsening*, INRIA Report No. 1898, March 1993
- [98] Grismer M.J., Strang W.Z., Tomaro R.F., and Witzeman F.C., *Cobalt: A Parallel, Implicit, Unstructured Euler/Navier-Stokes Solver*, Adv. Eng. Sci. Software, Vol. 29, No. 3-4, pp. 365-371, 1998
- [99] Hall M.G., *Computational Fluid Dynamics - A Revolutionary Force in Aerodynamics*, AIAA Paper 81-1014, 5th Computational Fluid Dynamics Conference, Palo Alto, CA, June 1981

- [100] ———, *On Innovation In Aerodynamics*, Aeron. J., No. 1000, Vol. 100, pp. 463-470, 1996
- [101] Halt D.W. and Agarwal R.K., *Compact Higher-Order Characteristic-Based Euler Solver for Unstructured Grids*, AIAA J., Vol. 30, No. 8, pp. 1993-1999, 1992
- [102] Handscomb D.C., *Errors of Linear Interpolation on a Triangle*, Report No. 95/09, Oxford University Computing Laboratory, Numerical Analysis Group, Oxford University, United Kingdom, June 1995
- [103] Harlow F.H. and Fromm J.E., *Computer Experiments in Fluid Dynamics*, Sci. Am., Vol. 212, No. 3, pp. 104-110, March 1965
- [104] Harten A., *High-Resolution Schemes for Conservation Laws*, J. Comp. Phys., Vol. 49, pp. 357-393, 1983
- [105] Harten A., Engquist B., Osher S., and Chakravarthy S.R., *Uniformly High-Order Accurate Essentially Non-Oscillatory Schemes III*, J. Comp. Phys., Vol. 71, pp. 231-303, 1987
- [106] Haselbacher A. and Blažek J., *On the Accurate and Efficient Discretisation of the Navier-Stokes Equations on Mixed Grids*, AIAA Paper 99-3363, 14th Computational Fluid Dynamics Conference, Norfolk, VA, June/July 1999
- [107] Haselbacher A., McGuirk J.J., and Page G.J., *Finite-Volume Discretisation Aspects for Viscous Flows on Mixed Grids*, AIAA J., Vol. 37, No. 2, pp. 177-184, 1999. Also: AIAA Paper 97-1947, 13th Computational Fluid Dynamics Conference, Snowmass, CO, June/July 1997
- [108] Hefazi H., Chin V., and Chen L.T., *Two-Dimensional Euler Zonal Method Using Composite Structured and Unstructured Meshes*, J. Aircraft, Vol. 31, No. 3, pp. 651-658, May-June 1994
- [109] Holmes D.G. and Connell S.D., *Solution of the Two-Dimensional Navier-Stokes Equations on Unstructured Adaptive Grids*, AIAA Paper 89-1932, 9th Computational Fluid Dynamics Conference, Buffalo, NY, June 1989
- [110] Hubbard M.E., *Multidimensional Slope Limiters for MUSCL-Type Finite Volume Schemes*, Numerical Analysis Report 2/98, Department of Mathematics, University of Reading, January 1998
- [111] ———, *Multidimensional Slope Limiters for MUSCL-Type Finite Volume Schemes II - on Improving Existing Unstructured Grid Techniques*, Numerical Analysis Report 8/98, Department of Mathematics, University of Reading, December 1998
- [112] Hwang C.J. and Wu S.J., *Adaptive Finite-Volume Upwind Approach on Mixed Triangular-Quadrilateral Meshes*, AIAA J., Vol. 31, No. 1, pp. 61-67, 1993
- [113] Idelsohn S.R. and Oñate E., *Finite Volumes and Finite Elements: Two Good Friends*, Int. J. Num. Meth. Eng., Vol. 37, pp. 3323-3341, 1994
- [114] Jameson A., *The Evolution of Computational Methods in Aerodynamics*, J. Appl. Mech., Vol. 50, pp. 1052-1070, December 1983
- [115] ———, *Successes and Challenges in Computational Aerodynamics*, AIAA Paper 87-1184, 8th Computational Fluid Dynamics Conference, Honolulu, HI, June 1987
- [116] ———, *Computational Aerodynamics for Aircraft Design*, Science, Vol. 245, pp. 361-371, July 1989

- [117] ———, *Artificial Diffusion, Upwind Biasing, Limiters and their Effect on Accuracy and Convergence in Transonic and Hypersonic Flows*, AIAA Paper 93-3359, 11th Computational Fluid Dynamics Conference, Orlando, July 1993
- [118] ———, *Numerical Wind Tunnel — Vision or Reality*, AIAA Paper 93-3021, 24th Fluid Dynamics Conference, Orlando, July 1993
- [119] ———, *Positive Schemes and Shock Modelling for Compressible Flows*, Int. J. Numer. Meth. Fl., Vol. 20, pp. 743-776, 1995
- [120] ———, *The Present Status, Challenges, and Future Developments in Computational Fluid Dynamics*, in: *Progress and Challenges in CFD Methods and Algorithms*, AGARD-CP-578, pp. 1-1 to 1-38, April 1996
- [121] Jameson A. and Baker T.J., *Solution of the Euler Equations for Complex Geometries*, AIAA Paper 83-1929, 6th Computational Fluid Dynamics Conference, Danvers, MA, July 1983
- [122] ———, *Improvements to the Aircraft Euler Method*, AIAA Paper 87-0452, 25th Aerospace Sciences Meeting and Exhibit, Reno, NV, January 1987
- [123] Jameson A. and Mavriplis D.J., *Finite-Volume Solution of the Two-Dimensional Euler Equations on a Regular Triangular Mesh*, AIAA Paper 85-0435, 23rd Aerospace Sciences Meeting, Reno, NV, January 1985. Also: AIAA J., Vol. 24, No. 4, pp. 611-618, 1986
- [124] Jameson A., Schmidt W., and Turkel E., *Numerical Solution of the Euler Equations by Finite-Volume Methods using Runge-Kutta Time-Stepping Schemes*, AIAA Paper 81-1259, 14th Fluid and Plasma Dynamics Conference, Palo Alto, CA, June 1981
- [125] Jameson A., Baker T.J., and Weatherill N.P., *Calculation of Inviscid Transonic Flow over a Complete Aircraft*, AIAA Paper 86-0103, 24th Aerospace Sciences Meeting, Reno, NV, January 1986
- [126] Jansen K., *Preliminary Large-Eddy Simulations of Flow Around a NACA 4412 Airfoil Using Unstructured Grids*, in: *Annual Research Briefs 1995*, Center for Turbulence Research, NASA Ames/Stanford University, CA, pp. 61-72, 1995
- [127] ———, *Large-Eddy Simulation of Flow Around a NACA 4412 Airfoil Using Unstructured Grids*, in: *Annual Research Briefs 1996*, Center for Turbulence Research, NASA Ames/Stanford University, CA, pp. 225-232, 1996
- [128] ———, *Large-Eddy Simulation Using Unstructured Grids*, in: *Advances in DNS/LES*, Liu C. et al. (Eds.), Proc. 1st AFOSR Int. Conf. on DNS/LES, Greyden Press, Columbus, 1997, pp. 117-128
- [129] Kallinderis Y., *Adaptation Methods for Viscous Flows*, Ph.D. Thesis, Massachusetts Institute of Technology, May 1989
- [130] ———, *A New Finite-Volume Navier-Stokes Scheme on Three-Dimensional Semi-Structured Prismatic Elements*, AIAA Paper 92-2697, 10th Applied Aerodynamics Conference, Palo Alto, CA, June 1992
- [131] Kallinderis Y., Khawaja A., and McMorris H., *Hybrid Prismatic/Tetrahedral Grid Generation for Complex Geometries*, AIAA Paper 95-0211, 33rd Aerospace Sciences Meeting and Exhibit, Reno, NV, January 1995

- [132] Kano S. and Nakahashi K., *Navier-Stokes Computations of HSCT Off-Design Aerodynamics Using Unstructured Hybrid Grids*, AIAA Paper 98-0232, 36th Aerospace Sciences Meeting and Exhibit, Reno, NV, January 1998
- [133] Kao K.H. and Liou M.-S., *Advance in Overset Grid Schemes-From Chimera to DRAGON Grids*, AIAA J., Vol. 33, No. 10, pp. 1809-1815, 1995
- [134] Karman S.L., *SPLITFLOW: A 3D Unstructured Cartesian/Prismatic Grid CFD Code for Complex Geometries*, AIAA Paper 95-0343, 33rd Aerospace Sciences Meeting and Exhibit, Reno, Nevada, 1995
- [135] Khawaja A., McMorris H., and Kallinderis Y., *Hybrid Grids for Viscous Flows around Complex 3-D Geometries including Multiple Bodies*, AIAA Paper 95-1685, 12th Computational Fluid Dynamics Conference, San Diego, CA, June 1995
- [136] Khawaja A., Kallinderis Y., and Parthasarathy V., *Implementation of Adaptive Hybrid Grids for 3-D Turbulent Flows*, AIAA Paper 96-0026, 34th Aerospace Sciences Meeting and Exhibit, Reno, NV, January 1996
- [137] Keith Clarke D., Salas M.D., and Hassan H.A., *Euler Calculations for Multi-element Airfoils Using Cartesian Grids*, AIAA J., Vol. 24, No. 3, pp. 353-358, 1986
- [138] Knight D.D., *A Fully Implicit Navier-Stokes Algorithm Using an Unstructured Grid and Flux-Difference Splitting*, Appl. Num. Math., Vol. 16, pp. 101-128, 1994. Erratum: Appl. Num. Math., Vol. 17, p. 187, 1995
- [139] Knight D.D., Zhou G., Okong'o N., and Shukla V., *Compressible Large-Eddy Simulation Using Unstructured Grids*, AIAA Paper 98-0535, 36th Aerospace Sciences Meeting and Exhibit, Reno, NV, January 1998
- [140] Koomullil R.P., Soni B.K., and Huang C.-T., *Navier-Stokes Simulations on Hybrid Grids*, AIAA Paper 96-0768, 34th Aerospace Sciences Meeting and Exhibit, Reno, NV, January 1996
- [141] Křížek M., *On the Maximum Angle Condition for Linear Tetrahedral Elements*, SIAM J. Numer. Anal., Vol. 29, No. 2, pp. 513-520, April 1992
- [142] Kroll N., Radespiel R., and Rossow C.-C., *Accurate and Efficient Flow Solvers for 3D Applications on Structured Meshes*, in: *Computational Fluid Dynamics Lecture Series 1994-05*, von Kármán Institute for Fluid Dynamics, March 1994
- [143] Kutler P., *A Perspective of Theoretical and Applied Computational Fluid Dynamics*, AIAA J., Vol. 23, No. 3, pp. 328-341, 1985
- [144] Kwon O.J. and Hah C., *Simulation of Three-Dimensional Turbulent Flows on Unstructured Meshes*, AIAA J., Vol. 33, No. 6, pp. 1081-1089, June 1995
- [145] Lallemand M.-H., *Schémas décentrées multigrilles pour la résolution des équations d'Euler en éléments finis*, Ph.D. Thesis, L'université de Provence, March 1988
- [146] Lax P.D., *Computational Fluid Dynamics at the Courant Institute*, in: *Computational Fluid Dynamics Review 1995*, Hafez M.M. and Oshima K. (Eds.), Wiley, pp. 1-5, 1995
- [147] Lax P.D. and Wendroff B., *Systems of Conservation Laws*, Comm. Pure Appl. Math., Vol. 13, No. 2, pp. 217-237, May 1960

- [148] Leclercq M.P. and Stoufflet B., *Characteristic Multigrid Method Application to Solve the Euler Equations with Unstructured and Unnested Grids*, J. Comp. Phys., Vol. 104, pp. 329-346, 1993
- [149] Lee D. and Tsuei Y.M., *A Formula for Estimation of Truncation Errors of Convection Terms in a Curvilinear Coordinate System*, J. Comp. Phys., Vol. 98, pp. 90-100, 1992
- [150] Lee K.D. and Rubbert P.E., *Transonic Flow Computations using Grid Systems with Block Structure*, in: *Proc. 7th Int. Conf. on Numerical Methods in Fluid Dynamics*, Lecture Notes in Physics, Vol. 141, Reynolds W.C. and MacCormack R.W. (Eds.), pp. 266-271, 1981
- [151] Lerner E.J., *More Accurate Simulations of Whole Aircraft*, Aerospace America, pp. 12-13, July 1986
- [152] Letniowski F.W., *Three-Dimensional Triangulations for Finite-Element Approximations to a Second-Order Diffusion Operator*, SIAM J. Sci. Stat. Comput., Vol. 13, No. 3, pp. 765-770, 1992
- [153] Levy D.W. and Thacker M.D., *Comparison of Unstructured Cell- and Node-Based Schemes for the Euler Equations*, AIAA Paper 99-3185, 17th AIAA Applied Aerodynamics Conference, Norfolk, VA, June/July 1999
- [154] Löhner R., *Computational Aspects of Space Marching*, AIAA Paper 98-0617, 36th Aerospace Sciences Meeting and Exhibit, Reno, NV, January 1998
- [155] ———, private communication, January 13, 1999
- [156] Löhner R., Morgan K., and Zienkiewicz O.C., *The Solution of Non-Linear Hyperbolic Equations Systems by the Finite-Element Method*, Int. J. Num. Meth. Fl., Vol. 4, pp. 1043-1063, 1984
- [157] Löhner R., Morgan K., Peraire J., and Zienkiewicz O.C., *Finite-Element Methods for High-Speed Flows*, AIAA Paper 85-1531, 7th Computational Fluid Dynamics Conference, Cincinnati, OH, July 1985
- [158] Löhner R. and Morgan K., *Unstructured Multigrid Methods*, in: *Proc. 2nd European Conf. on Multigrid Methods*, Köln, Germany, Hackbusch W. and Trottenberg U. (Eds.), Lecture Notes in Mathematics, Vol. 1228, Springer, 1985
- [159] Lomax H., *Some Prospects for the Future of Computational Fluid Dynamics*, AIAA J., Vol. 20, No. 8, pp. 1033-1043, 1982
- [160] ———, *CFD in the 1980's from One Point of View*, AIAA Paper 91-1526, 10th Computational Fluid Dynamics Conference, Honolulu, HI, June 1991
- [161] Lonsdale R.D., *An Algebraic Multigrid Solver for the Navier-Stokes Equations on Unstructured Meshes*, Int. J. Num. Meth. Heat Fl. Flow, Vol. 3, pp. 3-14, 1993
- [162] Luo H., Baum J.D., and Löhner R., *An Improved Finite-Volume Scheme for Compressible Flows on Unstructured Grids*, AIAA Paper 95-0348, 33rd Aerospace Sciences Meeting and Exhibit, Reno, NV, January 1995
- [163] ———, *Computation of Compressible Flows Using a Two-Equation Turbulence Model on Unstructured Grids*, AIAA Paper 97-0430, 35th Aerospace Sciences Meeting and Exhibit, Reno, Nevada, January 1995
- [164] ———, *A Fast, Matrix-free Implicit Method for Compressible Flows on Unstructured Grids*, J. Comp. Phys., Vol. 146, pp. 664-690, 1998

- [165] Lyra P.R.M., *Adaptive Algorithms for Fluid Dynamics and Heat Conduction*, Ph.D. Thesis, University of Swansea, Wales, October 1994
- [166] MacCormack R.W., *A Perspective on a Quarter Century of CFD Research*, AIAA Paper 93-3291, 11th Computational Fluid Dynamics Conference, July 1993
- [167] MacCormack R.W. and Lomax H., *Numerical Solution of Compressible Viscous Flows*, Ann. Rev. Fl. Mech., Vol. 11, pp. 289-316, 1979
- [168] McGrory W.D., Walters R.W., and Löwner R., *Three-Dimensional Space-Marching Algorithm on Unstructured Grids*, AIAA J., Vol. 29, No. 11, pp. 1844-1849, 1991
- [169] Marcum D.L., *Generation of Unstructured Grids for Viscous Flow Applications*, AIAA Paper 95-0212, 33rd AIAA Aerospace Sciences Meeting and Exhibit, January 1995
- [170] Marcum D.L. and Agarwal R.K., *Finite-Element Navier-Stokes Solver for Unstructured Grids*, AIAA J., Vol. 30, No. 3, pp. 648-654, 1992
- [171] Marcum D.L. and Weatherill N.P., *Turbulence Models for Unstructured Finite Element Calculations*, Int. J. Num. Meth. Fl., Vol. 20, pp. 803-817, 1995
- [172] Mathur S.R., Madavan N.K., and Rajagopalan R.K., *A Hybrid Structured-Unstructured Grid Method for Unsteady Turbomachinery Flow Computations*, AIAA Paper 93-0387, 31st Aerospace Sciences Meeting and Exhibit, Reno, NV, January 1993
- [173] Mavriplis D.J., *Multigrid Solution of the Two-Dimensional Euler Equations on Unstructured Triangular Meshes*, AIAA J., Vol. 26, No. 7, pp. 824-831, 1988
- [174] ———, *Algebraic Turbulence Models for Unstructured and Adaptive Meshes*, AIAA J., Vol. 29, No. 12, pp. 2086-2093, 1991
- [175] ———, *Unstructured Mesh Algorithms for Aerodynamic Calculations*, in: Proc. 13th Int. Conf. on Numerical Methods in Fluid Dynamics, Lecture Notes in Physics, Vol. 414, pp. 57-77, Springer Verlag, Heidelberg, Germany, 1992
- [176] ———, *Three-Dimensional Unstructured Multigrid for the Euler Equations*, AIAA J., Vol. 30, No. 7, pp. 1753-1761, 1992
- [177] ———, *A Three-Dimensional Multigrid Reynolds-Averaged Navier-Stokes Solver for Unstructured Meshes*, ICASE Report No. 94-29, May 1994
- [178] ———, *Multigrid Techniques for Unstructured Meshes*, in: Computational Fluid Dynamics Lecture Series 1995-02, von Kármán Institute for Fluid Dynamics, March 1995
- [179] ———, *Unstructured Grid Techniques*, Ann. Rev. Fluid Mech., Vol. 29, pp. 473-514, 1997
- [180] ———, *On Convergence Acceleration Techniques for Unstructured Meshes*, AIAA Paper 98-2966, 29th Fluid Dynamics Conference, Albuquerque, NM, June 1998
- [181] Mavriplis D.J. and Martinelli L., *Multigrid Solution of Compressible Turbulent Flow on Unstructured Meshes Using a Two-Equation Model*, ICASE Report No. 91-11, January 1991
- [182] Mavriplis D.J. and Pirzadeh S., *Large-Scale Parallel Unstructured Mesh Computations For 3D High-Lift Analysis*, AIAA Paper 99-0537, 37th AIAA Aerospace Sciences Meeting and Exhibit, Reno, NV, January 1999

- [183] Mavriplis D.J. and Venkatakrishnan V., *A Unified Multigrid Solver for the Navier-Stokes Equations on Mixed Element Meshes*, ICASE Report No. 95-53, July 1995. Also: *Int. J. Comp. Fl. Dyn.*, Vol. 8, No. 4, pp. 247-263, August 1997
- [184] McHugh J.A., *Algorithmic Graph Theory*, Prentice-Hall, 1990
- [185] Meister A., *Zur zeitgenauen numerischen Simulation reibungsbehafteter, kompressibler, turbulenter Strömungsfelder mit einer impliziten Finite-Volumen-Methode vom Box-Typ*, DLR-Forschungsbericht 96-08, DLR Göttingen, May 1996
- [186] ———, *Comparison of Different Krylov Subspace Methods Embedded in an Implicit Finite-Volume Scheme for the Computation of Viscous and Inviscid Flow Fields on Unstructured Grids*, *J. Comp. Phys.*, Vol. 140, pp. 311-345, 1998
- [187] Melton J., Pandya S., and Steger J.L., *3D Euler Flow Solutions Using Unstructured Cartesian and Prismatic Grids*, AIAA Paper 93-0331, 31st Aerospace Sciences Meeting and Exhibit, Reno, NV, January 1993
- [188] Merriam M.L., *An Efficient Advancing Front Algorithm for Delaunay Triangulation*, AIAA Paper 91-0792, 29th AIAA Aerospace Sciences Meeting, Reno, NV, January 1991
- [189] Mestreau E., Löhner R., and Aita S., *TGV Tunnel-Entry Simulations Using a Finite-Element Code with Automatic Remeshing*, AIAA Paper 93-0890, 31st Aerospace Sciences Meeting and Exhibit, Reno, NV, January 1993
- [190] Michal T. and Halt D., *Development and Application of an Unstructured Grid Flow Solver for Complex Fighter Aircraft Configurations*, AIAA Paper 95-1785, 13th Applied Aerodynamics Conference, San Diego, CA, June 1995
- [191] Miet P., Laurence D., and Nitrosso B., *Large Eddy Simulation with Unstructured Grids and Finite Elements*, Technical Report No. 96NB00124, Electricité de France, Clamart, December 1995
- [192] Mitchell C.R., *Improved Reconstruction Schemes for the Navier-Stokes Equations on Unstructured Meshes*, AIAA Paper 94-0642, 31st Aerospace Sciences Meeting, Reno, NV, January 1994
- [193] Mitchell C.R. and Walters R.W., *k-Exact Reconstruction Algorithms for the Navier-Stokes Equations on Arbitrary Grids*, AIAA Paper 93-0536, 1993
- [194] Mittal R. and Moin P., *Suitability of Upwind-Biased Finite-Difference Schemes for Large-Eddy Simulation of Turbulent Flows*, *AIAA J.*, Vol. 35, No. 8, pp. 1415-1417, August 1997
- [195] Mohammadi B., *Complex Turbulent Compressible Flow Computation Using A Two-Layer Approach*, *Int. J. Num. Meth. Fl.*, Vol. 15, pp. 747-771, 1992
- [196] Morano E. and Dervieux A., *Looking for $O(N)$ Navier-Stokes Solutions on Non-Structured Meshes*, ICASE Report 93-26, June 1993
- [197] Morgan K. and Peraire J., *Finite Element Methods for Compressible Flows*, in: *Computational Fluid Dynamics Lecture Series 1987-04*, von Kármán Institute for Fluid Dynamics, March 1987
- [198] Morgan K. and Peraire J., *Unstructured Grid Finite-Element Methods for Fluid Mechanics*, *Rep. Prog. Phys.*, Vol. 61, No. 6, pp. 569-638, June 1998

- [199] Morino H. and Nakahashi K., *Space-Marching Method on Unstructured Hybrid Grid for Supersonic Viscous Flow*, AIAA Paper 99-0661, 37th Aerospace Meeting and Exhibit, Reno, NV, January 1999
- [200] Morton K.W. and Paisley M.F., *A Finite Volume Method with Shock Fitting for the Steady Euler Equations*, J. Comp. Phys., Vol. 80, pp. 168-203, 1989
- [201] Müller J.-D., *Coarsening 3-D Hybrid Meshes for Multigrid Methods*, presented at: 9th Copper Mountain Multigrid Conf., April 1999
- [202] Müller J.-D. and Giles M.B., *Edge-Based Multigrid Schemes for Hybrid Grids*, in: *Numerical Methods for Fluid Dynamics VI*, M.J. Baines (Ed.), Institute of Computational Fluid Dynamics, Oxford University Computing Laboratory, pp. 425-432, 1998
- [203] Nakahashi K., *A Finite-Element Method on Prismatic Elements for the Three-Dimensional Navier-Stokes Equations*, in: *Proc. 11th Int. Conf. on Numerical Methods in Fluid Dynamics*, Dwoyer D.L. et al. (Eds.), Lecture Notes in Physics, Vol. 323, Springer, pp. 434-438, 1989
- [204] ———, *Prismatic Grid Method*, in: *Computational Fluid Dynamics Review 1995*, Hafez M.M. and Oshima K. (Eds.), Wiley, pp. 87-105, 1995
- [205] Nakahashi K. and Egami K., *Automatic Euler Solver using the Unstructured Upwind Method*, Comp. Fl., Vol. 19, No. 3/4, pp. 273-286, 1991
- [206] Nakahashi K. and Obayashi S., *FDM-FEM Zonal Approach for Viscous Flow Computations over Multiple Bodies*, AIAA Paper 87-0604, 25th Aerospace Sciences Meeting, Reno, NV, January 1987
- [207] Nakahashi K. and Saitoh E., *Space-Marching Method on Unstructured Grids for Supersonic Flow with Embedded Subsonic Regions*, AIAA Paper 96-0418, 34th Aerospace Sciences Meeting and Exhibit, Reno, NV, January 1996
- [208] Nakahashi K., Saitoh E., and Sharov D., *Three-Dimensional Space-Marching Method on Unstructured Grids*, in: *Proc. 15th Int. Conf. on Numerical Methods in Fluid Mechanics*, Kutler P. et al. (Eds.), Springer Verlag, Lecture Notes in Physics, Vol. 490, pp. 629-634, 1997
- [209] Nielsen E.J., Anderson W.K., Walters R.W., and Keyes D.E., *Application of Newton-Krylov Methodology to a Three-Dimensional Unstructured Euler Code*, AIAA Paper 95-1733, 12th Computational Fluid Dynamics Conference, San Diego, CA, June 1995
- [210] *Calculating Airflow*, New York Times, Vol. CXXXV, No. 46668, p. C3, Col. 5, January 28, 1986
- [211] Okong'o N. and Knight D.D., *Compressible Large-Eddy Simulation Using Unstructured Grids: Channel and Boundary Layer Flows*, AIAA Paper 98-3315, 34th AIAA/ASME/SAE/ASEE Joint Propulsion Conference and Exhibit, Cleveland, OH, July 1998
- [212] Ollivier-Gooch C.F., *Multigrid Acceleration of an Upwind Euler Solver on Unstructured Meshes*, AIAA J., Vol. 33, No. 10, pp. 1822-1827, 1995
- [213] ———, *A New Class of ENO Schemes Based on Unlimited Data-Dependent Least-Squares Construction*, AIAA Paper 96-0887, 34th Aerospace Sciences Meeting and Exhibit, Reno, NV, January 1996

- [214] ———, *High-Order ENO Schemes for Unstructured Meshes Based on Least-Squares Reconstruction*, AIAA Paper 97-0540, 35th Aerospace Sciences Meeting and Exhibit, Reno, NV, January 1997
- [215] Osher S. and Solomon F., *Upwind Difference Schemes for Hyperbolic Systems of Conservation Laws*, Math. Comp., Vol. 38, No. 158, pp. 339-374, 1982
- [216] Paillère H. and Deconinck H., *A Review of Multidimensional Upwind Residual Distribution Schemes for the Euler Equations*, in: *Computational Fluid Dynamics Review 1995*, Hafez M.M. and Oshima K. (Eds.), Wiley, pp. 141-160, 1995
- [217] Pan D. and Cheng J.-C., *Upwind Finite-Volume Navier-Stokes Computations on Unstructured Triangular Meshes*, AIAA J., Vol. 31, No. 9, pp. 1618-1625, 1993
- [218] Pandya S.A. and Hafez M.M., *A Semi-Implicit Finite-Volume Scheme for Solution of Euler Equations on 3-D Prismatic Grids*, AIAA Paper 93-3431, 11th Applied Aerodynamics Conference, Monterey, CA, August 1993
- [219] Parthasarathy V. and Kallinderis Y., *Directional Viscous Multigrid Using Adaptive Meshes*, AIAA J., Vol. 33, No. 1, pp. 69-78, 1995
- [220] Parthasarathy V., Kallinderis Y., and Nakajima K., *Hybrid Adaptation Method and Directional Viscous Multigrid with Prismatic Tetrahedral Meshes*, AIAA Paper 95-0670, 33rd Aerospace Sciences Meeting and Exhibit, Reno, NV, January 1995
- [221] Pärt-Enander E. and Sjögren B., *Conservative and Non-Conservative Interpolation between Overlapping Grids for Finite-Volume Solutions of Hyperbolic Problems*, Comp. Fl., Vol. 23, No. 3, pp. 551-574, 1994
- [222] Peace A.J. and Shaw J., *The Modelling of Aerodynamic Flows by Solution of the Euler Equations on Mixed Polyhedral Grids*, Int. J. Num. Meth. Eng., Vol. 35, No. 10, pp. 2003-2029, 1992
- [223] Peraire J., Peiró J., and Morgan K., *A 3D Finite-Element Multigrid Solver for the Euler Equations*, AIAA Paper 92-0449, 30th Aerospace Sciences Meeting and Exhibit, Reno, NV, January 1992. Also: Int. J. Num. Meth. Eng., Vol. 36, pp. 1029-1044, 1993
- [224] Perez E., *Finite-Element and Multigrid Solution of the Two-Dimensional Euler Equations on a Non-Structured Mesh*, INRIA Report 442, September 1985
- [225] Powell K.G., *The Adaptive, Cut-Cell Cartesian Approach (Warts and All)*, in: *Proc. ICASE/LaRC Workshop on Adaptive Grid Methods*, South J.C. et al. (Eds.), NASA CP 3316, pp. 59-77, October 1995
- [226] Purvis J.W. and Burkhalter J.E., *Prediction of Critical Mach Number for Store Configurations*, AIAA J., Vol. 17, No. 11, pp. 1170-1177, 1979
- [227] Quirk J.J., *An Alternative to Unstructured Grids for Computing Flows around Arbitrary Complex Two-Dimensional Bodies*, Comp. Fl., Vol. 13, No. 1, pp. 125-142, 1994
- [228] Ramakrishnan S.V., Szema K.Y., Chen C.L., Shankar V.V., and Chakravarthy S.R., *Experiments with Unstructured Grid Computations*, in: *Progress and Challenges in CFD Methods and Algorithms*, AGARD-CP-578, pp. 8-1 to 8-8, April 1996

- [229] Rausch R.D., Batina J.T., and Yang H.T.Y., *Spatial Adaptation of Unstructured Meshes for Unsteady Aerodynamic Flow Computations*, AIAA J., Vol. 30, No. 5, pp. 1243-1251, 1992
- [230] Raw M.J., *Robustness of Coupled Algebraic Multigrid for the Navier-Stokes Equations*, AIAA Paper 96-0297, 34th Aerospace Sciences Meeting and Exhibit, Reno, NV, January 1996
- [231] Reyhner T.A., *Cartesian Mesh Solution for Axisymmetric Transonic Potential Flow Around Inlets*, AIAA Paper 76-421, 9th Fluid and Plasma Dynamics Conf., San Diego, CA, July 1976
- [232] Richter R., *Schémas de capture de discontinuités en maillage non-structuré avec adaptation dynamique*, Ph.D. Thesis, Ecole Polytechnique Fédérale de Lausanne, November 1993
- [233] Rienslagh K. and Dick E., *Implementation Aspects of the Multigrid Formulation of Finite-Volume Algorithms on Unstructured Grids*, in: *Contributions to Multigrid*, Proc. 4th European Multigrid Conference, Amsterdam, July 6-9, 1993, Hemker P.W. and Wesseling P. (Eds.), CWI Tract 103, Centrum voor Wiskunde en Informatica, Amsterdam, pp. 181-192, 1993
- [234] ———, *A Multigrid Method with Unstructured Adaptive Grids for Steady Euler Equations*, J. Comp. Appl. Math., Vol. 67, pp. 73-93, 1996
- [235] Ringleb F., *Lösungen der Differentialgleichung einer adiabatischen Strömung*, Z. Angew. Math. Mech., Vol. 20, No. 4, pp. 185-198, 1940
- [236] Rippa S., *Long and Thin Triangles can be Good for Linear Interpolation*, SIAM J. Numer. Anal., Vol. 29, No. 1, pp. 257-270, 1992
- [237] Rizzi A. and Engquist B., *Selected Topics in the Theory and Practice of Computational Fluid Dynamics*, J. Comp. Phys., Vol. 72, pp. 1-69, September 1987
- [238] Roe P.L., *Approximate Riemann Solvers, Parameter Vectors, and Difference Schemes*, J. Comp. Phys., Vol. 43, pp. 357-372, 1981
- [239] ———, *Error Estimates for Cell-Vertex Solutions of the Compressible Euler Equations*, ICASE Report No. 87-6, January 1987
- [240] ———, *The Influence of Mesh Quality on Solution Accuracy*, in: *Computational Fluid Dynamics Lecture Series 1989-04*, von Kármán Institute for Fluid Dynamics, March 1989
- [241] Rostand P., *Algebraic Turbulence Models for the Computation of Two-Dimensional High-Speed Flows Using Unstructured Grids*, ICASE Report No. 88-63, November 1988
- [242] Rostand P. and Stoufflet B., *TVD Schemes to Compute Compressible Viscous Flows on Unstructured Meshes*, in: *Proc. 2nd Int. Conf. Nonlinear Hyperbolic Problems*, Aachen, March 1988, Notes on Numerical Fluid Mechanics, Vol. 24, Ballhaus J. and Jeltsch R. (Eds.), Vieweg, 1988, pp. 510-520
- [243] Rüge J.W. and Stüben K., *Algebraic Multigrid*, in: *Multigrid Methods*, McCormick S.F. (Ed.), Society for Industrial and Applied Mathematics, pp. 73-130, 1987
- [244] Saad Y., *Iterative Methods for Sparse Linear Systems*, PWS Publishing Company, Boston, 1996

- [245] Saad Y. and Schultz M.H., *GMRES: A Generalised Minimum Residual Algorithm for Solving Nonsymmetric Linear Systems*, SIAM J. Sci. Stat. Comput., Vol. 7, pp. 856-869, 1986
- [246] Sbresny H. and Baier R.-D., *Untersuchung von unstrukturierten und blockstrukturierten Rechenverfahren zur Simulation der Strömung durch Schaufelgitter mit Filmkühlung*, Forsch. Ingenieurwesen, Vol. 63, pp. 146-157, 1997
- [247] Selmin V., *The Node-Centred Finite-Volume Approach: Bridge between Finite Differences and Finite Elements*, Comp. Meth. Appl. Mech. Eng., Vol. 102, pp. 107-138, January 1993
- [248] Sharov D. and Nakahashi K., *Low-Speed Preconditioning and LU-SGS scheme for 3-D Viscous Computations on Unstructured Grids*, AIAA 98-0614, 36th Aerospace Sciences Meeting and Exhibit, Reno, NV, January 1998
- [249] ———, *Reordering of Hybrid Unstructured Grids for Lower-Upper Symmetric Gauss-Seidel Computations*, AIAA J., Vol. 36, No. 3, pp. 484-486, 1998
- [250] Shaw J.A., *Hybrid Grids*, Technical Memorandum 426, Aircraft Research Association, Bedford, March 1998
- [251] Shaw J.A. and Peace A.J., *Simulating Three-Dimensional Aeronautical Flows on Mixed Block-Structured/Semi-Unstructured/Unstructured Grids*, Technical Memorandum 428, Aircraft Research Association, Bedford, April 1998
- [252] Shaw J.A., Peace A.J., and Weatherill N.P., *A Three-Dimensional Structured-Unstructured Method: Motivation, Basic Approach and Initial Results*, in: *Computational Aeronautical Fluid Dynamics*, Fezoui L. et al. (Eds.), Clarendon Press, pp. 157-201, 1994
- [253] Shaw J.A., Peace A.J., May N.E., and Pocock M.F., *Verification of the CFD Simulation System SAUNA for Complex Aircraft Simulations*, Technical Memorandum 401, Aircraft Research Association, Bedford, April 1994
- [254] Slack D.C., Whitaker D.L., and Walters R.W., *Time Integration Algorithms for the Two-Dimensional Euler-Equations on Unstructured Grids*, AIAA J., Vol. 32, No. 6, pp. 1158-1166, 1994
- [255] Smith R.J. and Leschziner M.A., *Automatic Grid Generation for Complex Geometries*, Aeron. J., No. 991, Vol. 100, pp. 7-14, 1996
- [256] Smith W.A., *Multigrid Solution of Transonic Flow on Unstructured Grids*, in: *Recent Advances and Applications in Computational Fluid Dynamics*, FED-Vol. 103, ASME Winter Annual Meeting, Baysal O. (Ed.), pp. 145-152, November 1990
- [257] Soestrisno M., Imlay S.T., and Roberts D.W., *A Zonal Implicit Procedure for Hybrid Structured-Unstructured Grids*, AIAA Paper 94-0645, 32nd Aerospace Sciences Meeting and Exhibit, Reno, NV, January 1994
- [258] ———, *Development of 3-D Zonal Implicit Procedure for Hybrid Structured-Unstructured Grids*, AIAA Paper 96-0167, 34th Aerospace Sciences Meeting and Exhibit, Reno, NV, January 1996
- [259] Sonar T., *Finite-Volume Approximations on Unstructured Grids*, in: *Computational Fluid Dynamics Lecture Series 1996-06*, von Kármán Institute for Fluid Dynamics, March 1996

- [260] ———, *Adaptivity and Residual Control in Numerical Simulations of Compressible Fluid Flows*, in: *Computational Fluid Dynamics Lecture Series 1996-06*, von Kármán Institute for Fluid Dynamics, March 1996
- [261] ———, *ENO Schemes and Recovery Techniques on Unstructured Grids*, in: *Computational Fluid Dynamics Lecture Series 1996-06*, von Kármán Institute for Fluid Dynamics, March 1996
- [262] ———, *Mehrdimensionale ENO-Verfahren*, Teubner, Stuttgart, 1997
- [263] Spalart P.R. and Allmaras S.R., *A One-Equation Turbulence Model for Aerodynamic Flows*, La Recherche Aéronautique, No. 1, pp. 5-21, January 1994
- [264] Steger J.L., *Thoughts on the Chimera Method of Simulation of Three-Dimensional Viscous Flows*, in: *Computational Fluid Dynamics Symposium on Aeropropulsion*, NASA CP 3078, pp. 1-10, April 1990
- [265] Steger J.L. and Benek J.A., *On the Use of Composite Grid Schemes in Computational Aerodynamics*, *Comp. Meth. Appl. Mech. Eng.*, Vol. 64, pp. 301-320, 1987
- [266] Stoer J. and Bulirsch R., *Introduction to Numerical Analysis*, 2nd Ed., Springer, 1992
- [267] Stolcis L., *Navier-Stokes Solution of Compressible Fluid Flows Using Advanced Turbulence Models and Unstructured Grids*, in: *Numerical Methods for Fluid Dynamics V*, Morton K.W. and Baines M.J. (Eds.), Clarendon Press, pp. 591-597, 1995
- [268] Stolcis L. and Johnston L.J., *Compressible-Flow Calculation Using a Two-Equation Turbulence Model and Unstructured Grids*, in: *Proc. 7th Int. Conf. on Numerical Methods for Laminar and Turbulent Flow*, Taylor C. et al. (Eds.), Pineridge Press, pp. 852-862, 1991
- [269] ———, *Near-Wall Turbulence Models and Numerical Solution of the Reynolds-Averaged Navier-Stokes Equations Using Unstructured Grids*, in: *Proc. 13th Int. Conf. on Numerical Methods in Fluid Dynamics*, Napolitano M. and Sabetta F. (Eds.), Springer, pp. 200-204, 1992
- [270] Stoufflet B., Périaux J., Fezoui F., and Dervieux A., *Numerical Simulation of 3-D Hypersonic Euler Flows Around Space Vehicles Using Adapted Finite Elements*, AIAA Paper 87-0560, 25th Aerospace Sciences Meeting, Reno, NV, January 1987
- [271] Strang W.Z., Tomaro R.F., and Grismer M.J., *The Defining Methods of Cobalt₆₀: A Parallel, Implicit, Unstructured Euler/Navier-Stokes Flow Solver*, AIAA Paper 99-0786, 37th Aerospace Sciences Meeting and Exhibit, Reno, NV, January 1999
- [272] Swanson R.C. and Turkel E., *On Central-Difference and Upwind Schemes*, *J. Comp. Phys.*, Vol. 101, No. 2, pp. 292-306, August 1992
- [273] Thompson J.F., Thames F.C., and Mastin C.W., *Automatic Numerical Generation of Body-Fitted Curvilinear Coordinate System for Field Containing Any Number of Arbitrary Two-Dimensional Bodies*, *J. Comp. Phys.*, Vol. 15, pp. 299-319, 1974
- [274] Thompson J.F., Soni B.K., and Weatherill N.P. (Eds.), *Handbook of Grid Generation*, CRC Press, 1999

- [275] Tsung F.-L., Loellbach J., Kwon O., and Hah C., *A Three-Dimensional Structured/Unstructured Hybrid Navier-Stokes Method for Turbine Blade Rows*, NASA TM-106813, December 1994. Also: AIAA Paper 94-3369, 30th Joint Propulsion Conference and Exhibit, Indianapolis, IN, June 1994
- [276] Turkel E., *Accuracy of Schemes with Nonuniform Meshes for Compressible Fluid Flows*, Appl. Num. Math., Vol. 2, pp. 529-550, December 1986. Also: ICASE Report No. 85-43, September 1985
- [277] Urbin G., Knight D.D., and Zheltovodov A.A., *Compressible Large Eddy Simulation Using Unstructured Grid: Supersonic Turbulent Boundary Layer and Compression Corner*, AIAA Paper 99-0427, 37th Aerospace Sciences Meeting and Exhibit, Reno, NV, January 1999
- [278] van der Vorst H.A., *Bi-CGSTAB: A Fast and Smoothly Converging Variant of Bi-CG for the Solution of Non-Symmetric Linear Systems*, SIAM J. Sci. Stat. Comp., Vol. 13, No. 2, pp. 631-644, 1992
- [279] Vankeirsbilck P. and Deconinck H., *Higher-Order Upwind Finite-Volume Schemes with ENO Properties for General Unstructured Meshes*, in: *Special Course on Unstructured Grid Methods for Advection Dominated Flows*, AGARD Report 787, May 1992, pp. 7-1 to 7-54
- [280] van Leer B., *Towards the Ultimate Conservative Difference Scheme, V. A Second-Order Sequel to Godunov's Method*, J. Comp. Phys., Vol. 32, pp. 101-136, 1979
- [281] van Leer B., Tai C.-H., and Powell K.G., *Design of Optimally Smoothing Multi-Stage Schemes for the Euler Equations*, AIAA Paper 89-1933, 9th Computational Fluid Dynamics Conference, Buffalo, NY, June 1989
- [282] Vassberg J.C. and Dailey K.B., *AIRPLANE: Experiences, Benchmarks and Improvements*, AIAA Paper 90-2988, 8th Applied Aerodynamics Conference, Portland, OR, August 1990
- [283] Vatsa V.N., Sanetrik M.D., and Parlette E.B., *Block-Structured Grids for Complex Aerodynamic Configurations: Current Status*, in: *Surface Modelling, Grid Generation, and Related Issues in Computational Fluid Dynamic (CFD) Solutions*, NASA CP 3291, March 1995, pp. 163-177
- [284] Venkatakrishnan V., *A Perspective on Unstructured Grid Flow Solvers*, AIAA Paper 95-0667, 33rd Aerospace Sciences Meeting and Exhibit, Reno, NV, January 1995. Also: AIAA J., Vol. 34, No. 3, pp. 533-547, March 1996
- [285] ———, *Convergence to Steady-State Solutions of the Euler Equations on Unstructured Grids with Limiters*, J. Comp. Phys., Vol. 118, No. 1, pp. 120-130, April 1995
- [286] Venkatakrishnan V. and Barth T.J., *Application of Direct Solvers to Unstructured Meshes for the Euler and Navier-Stokes Equations using Upwind Schemes*, AIAA Paper 89-0364, 27th Aerospace Sciences Meeting, Reno, NV, January 1989
- [287] Venkatakrishnan V. and Chakravarthy S.R., *Towards Higher-Order Accuracy on Unstructured Grids*, in: *Proc. 15th Int. Conf. on Numerical Methods in Fluid Mechanics*, Kutler P. et al. (Eds.), Lecture Notes in Physics, Vol. 490, Springer Verlag, pp. 249-254, 1997

- [288] Venkatakrishnan V. and Mavriplis D.J., *Implicit Solvers on Unstructured Meshes*, J. Comp. Phys., Vol. 105, No.1, pp. 83-91, 1993
- [289] Vijayasundaram G., *Transonic Flow Simulations Using an Upstream Centered Scheme of Godunov in Finite Elements*, J. Comp. Phys., Vol. 6, pp. 416-433, 1986
- [290] Wang Q., Massey S.J., Abdol-Hamid K.S., and Frink N., *Solving Navier-Stokes Equations with Advanced Turbulence Models on Three-Dimensional Unstructured Grids*, AIAA Paper 99-0156, 37th Aerospace Sciences Meeting and Exhibit, Reno, NV, January 1999
- [291] Warren G.P., *Application of Multigrid and Adaptive Grid Embedding to the Two-Dimensional Flux-Split Euler Equations*, Comm. Appl. Num. Math., Vol. 8, pp. 771-784, 1992
- [292] Weatherill N.P., *Grid Generation: Structured, Unstructured, Or Both?*, in: *Computational Methods in Aeronautical Fluid Dynamics*, Stow P. (Ed.), The Institute of Mathematics and its Applications Conference Series, New Series, Vol. 25, Oxford Science Publishing, Clarendon Press, Oxford, pp. 345-365, 1990
- [293] ———, *Mixed Structured-Unstructured Meshes for Aerodynamic Flow Simulations*, Aeron. J., No. 934, Vol. 94, pp. 111-123, April 1990
- [294] ———, *The Delaunay Triangulation—From the Early Work in Princeton*, in: *Frontiers of Computational Fluid Dynamics 1994*, Caughey D.A. and Hafez M.M. (Eds.), pp. 83-100, Wiley, 1994
- [295] Weatherill N.P. and Forsey C.R., *Grid Generation and Flow Calculations for Aircraft Geometries*, J. Aircraft, Vol. 22, No. 10, pp. 855-860, 1985
- [296] Weatherill N.P., Johnston L.J., Peace A.J., and Shaw J.A., *A Method for the Solution of the Reynolds-Averaged Navier-Stokes Equations on Triangular Grids*, in: *Proc. 7th GAMM Conf. on Numerical Methods in Fluid Mechanics*, Deville M. (Ed.), Notes on Numerical Fluid Mechanics, Vol. 20, Vieweg, pp. 418-425, 1988
- [297] Webster R., *An Algebraic Multigrid Solver for Navier-Stokes Problems*, Int. J. Numer. Meth. Fl., Vol. 18, No. 8, pp. 761-780, April 1994
- [298] Weiss J.M., Maruszewski J.P., and Smith W.A., *Implicit Solution of Preconditioned Navier-Stokes Equations Using Algebraic Multigrid*, AIAA J., Vol. 37, No. 1, pp. 29-36, January 1999
- [299] Whitaker D.L., *Three-Dimensional Unstructured Grid Euler Computations Using a Fully-Implicit, Upwind Method*, AIAA Paper 93-3337, 11th Computational Fluid Dynamics Conference, Orlando, FL, July 1993
- [300] Whitaker D.L., Grossman B., and Löhrner R., *Two-Dimensional Euler Computations on a Triangular Mesh Using an Upwind Finite-Volume Scheme*, AIAA Paper 89-0479, 27th Aerospace Sciences Meeting, Reno, NV, January 1989
- [301] Wilcox D.C., *Turbulence Modeling for CFD*, 2nd Ed., DCW Industries Inc., La Cañada, California, 1998
- [302] Yoon S. and Jameson A., *Lower-Upper Symmetric-Gauss-Seidel Method for the Euler and Navier-Stokes Equations*, AIAA J., Vol. 26, No. 9, pp. 1025-1026, September 1988

- [303] Young P.D., Melvin R.G., Bieterman M.B., Johnson F.T., Samant S.S., and Bussoletti J.E., *A Locally Refined Rectangular Grid Finite Element Method: Application to Computational Fluid Dynamics and Computational Physics*, J. Comp. Phys., Vol. 92, pp. 1-66, 1991

Chapter 2

Mathematical Model

The governing equations for inviscid, laminar, and turbulent flows are presented in integral form. Assumptions, auxiliary relations, and empirical constants are listed. The effects of turbulence are modelled through the eddy-viscosity hypothesis and the Spalart-Allmaras one-equation model. Boundary conditions are listed.

2.1 Assumptions

Throughout the current study, air is assumed to be the working fluid. The mathematical model is based on the following assumptions:

1. The fluid is a continuum. For this assumption to be justified, it is required that the Knudsen number Kn [13]

$$Kn \equiv \frac{\lambda}{L} \approx \frac{M}{Re} \ll 1,$$

where λ is the mean free path, L is a local characteristic length scale of the flow, M is the Mach number and Re is the Reynolds number.

2. The fluid may consist of multiple chemical species but it is chemically inert and of a single phase. For air, this requires that the temperature $T \leq 2500$ K.
3. The fluid may be treated as an ideal gas, i.e., intermolecular forces are negligible. As a result, the fluid is thermally and calorically perfect. For air, this requires that the temperature $T \leq 800$ K.
4. The fluid may be treated as a Newtonian fluid, i.e., the fluid is isotropic and the stress and strain fields are linearly related.

In the following sections, the governing equations are stated for an arbitrary control volume Ω with bounding surface $\partial\Omega$ and outward unit normal vector \mathbf{n} . The term

'control volume' is retained although the current study is restricted to two dimensions.

2.2 The Governing Equations for Inviscid Flow

The flow of a compressible inviscid, i.e., frictionless and non-conducting, fluid is described by the Euler equations. They may be written as the equation for conservation of mass,

$$\frac{\partial}{\partial t} \int_{\Omega} \rho dA + \oint_{\partial\Omega} \rho \mathbf{v} \cdot \mathbf{n} ds = 0, \quad (2.2.1)$$

the equations for conservation of momentum,

$$\frac{\partial}{\partial t} \int_{\Omega} \rho \mathbf{v} dA + \oint_{\partial\Omega} (\rho \mathbf{v} \otimes \mathbf{v} + p\mathbf{l}) \cdot \mathbf{n} ds = 0, \quad (2.2.2)$$

and the equation for conservation of energy,

$$\frac{\partial}{\partial t} \int_{\Omega} \rho E dA + \oint_{\partial\Omega} \rho \mathbf{v} H \cdot \mathbf{n} ds = 0, \quad (2.2.3)$$

where t represents time, ρ the density, \mathbf{v} the velocity vector, p the pressure, \mathbf{l} the identity tensor, E the specific total internal energy and H the specific total enthalpy of the fluid.

The pressure is linked to the total internal energy by the equation of state. For a thermally and calorically perfect gas, the equation of state is given by

$$p = R\rho T = (\gamma - 1)\rho \left(E - \frac{1}{2} \mathbf{v} \cdot \mathbf{v} \right), \quad (2.2.4)$$

where R is the gas constant, T is the temperature and $\gamma = C_p/C_v$ is the ratio of specific heats. For a calorically perfect gas, the specific heats are constant. The specific heats are related to the gas constant by $R = C_p - C_v$.

2.3 The Governing Equations for Laminar Flow

The flow of a compressible viscous fluid is described by the Navier-Stokes equations. The equation expressing conservation of mass, Eq. (2.2.1), is unchanged.

The equations for conservation of momentum become

$$\frac{\partial}{\partial t} \int_{\Omega} \rho \mathbf{v} dA + \oint_{\partial\Omega} (\rho \mathbf{v} \otimes \mathbf{v} + p\mathbf{l}) \cdot \mathbf{n} ds = \oint_{\partial\Omega} \mathbf{T} \cdot \mathbf{n} ds, \quad (2.3.1)$$

where \mathbf{T} is the viscous stress tensor. For a Newtonian fluid, the most general form of

the viscous stress tensor can be shown to be [1],

$$\mathbf{T} = 2\mu\mathbf{S} + \lambda|\nabla \cdot \mathbf{v}, \quad (2.3.2)$$

where μ and λ are the first and second coefficients of viscosity, respectively, and \mathbf{S} is the strain tensor,

$$\mathbf{S} = \frac{1}{2}[\nabla \mathbf{v} + (\nabla \mathbf{v})^t]. \quad (2.3.3)$$

By requiring that the mechanical and thermodynamical pressures are identical (Stokes' hypothesis [12]), it follows that $3\lambda + 2\mu = 0$, or,

$$\mathbf{T} = 2\mu\mathbf{S} - \frac{2}{3}\mu|\nabla \cdot \mathbf{v}. \quad (2.3.4)$$

Having eliminated the second coefficient of viscosity, μ is now simply referred to as the (coefficient of) viscosity.

The energy equation is

$$\frac{\partial}{\partial t} \int_{\Omega} \rho E dA + \oint_{\partial\Omega} \rho \mathbf{v} H \cdot \mathbf{n} ds = \oint_{\partial\Omega} (\mathbf{T} \cdot \mathbf{v} - \mathbf{q}) \cdot \mathbf{n} ds, \quad (2.3.5)$$

where \mathbf{q} is the heat flux vector. Fourier's law of heat conduction is assumed to apply,

$$\mathbf{q} = -\kappa \nabla T, \quad (2.3.6)$$

where κ is the coefficient of heat conduction and T is the temperature. The coefficient of heat conduction is related to the viscosity through the Prandtl number

$$\text{Pr} = \frac{\mu C_p}{\kappa}. \quad (2.3.7)$$

The variation of viscosity with temperature is given by Sutherland's law [12],

$$\frac{\mu}{\mu_{\text{ref}}} = \left(\frac{T}{T_{\text{ref}}} \right)^{\frac{3}{2}} \frac{T_{\text{ref}} + C_{\text{Suth}}}{T + C_{\text{Suth}}}, \quad (2.3.8)$$

where μ_{ref} is the value of viscosity at the reference temperature T_{ref} and C_{Suth} is a medium-dependent constant.

The values of the various empirical constants are listed in Table 2.1, for air at moderate temperatures as a working fluid.

Table 2.1: Values of constants for air at moderate temperatures.

constant	value	units
C_p	1004.64	J/kg K
R	287.04	J/kg K
γ	1.4	-
C_{Suth}	110.0	K
Pr	0.72	-

2.4 The Governing Equations for Turbulent Flow

Turbulent flows are characterised by random fluctuations of the dependent variables in space and time [10]. Since the Knudsen number of the smallest characteristic turbulent length scale is much greater than unity, turbulent flows may in principle be computed by solving the Navier-Stokes equations. This deterministic approach is usually referred to as Direct Numerical Simulation (DNS) [5]. The suitability of DNS for high-Reynolds-number flows is limited due to the disparities between the largest and smallest length and time scales which need to be resolved. This may be illustrated by the estimate of the required number of grid points (and hence memory) of a DNS of a turbulent channel flow [11]

$$N_{\text{DNS}} \approx (0.08 \text{Re}_h)^{9/4},$$

where Re_h is the Reynolds number based on the mean velocity and the channel height. The storage capacity of presently available computers means that DNS is only a viable approach for flows of low Reynolds number.

Since the ranges of length and time scales exceed those allowed by affordable computer capacity, some scales must be discarded and their effect on the retained scales modelled. In Large-Eddy Simulations (LES) [4], only the largest turbulent scales are computed directly, while the smaller scales are modelled. Although this restriction reduces the required memory and processing time considerably, the reduction is not large enough to make LES a practical tool for the computation of high-Reynolds-number flows yet. A purely deterministic approach is therefore abandoned for high-Reynolds-number engineering calculations, and a statistical approach is adopted instead.

2.4.1 The Reynolds-Averaged Navier-Stokes Equations

In the statistical approach, attention is focused on average values of turbulent quantities. The goal is the derivation of equations governing the evolution of these average values.

Decomposition and Averaging. This goal is achieved in two steps. First, the flow variables are decomposed into mean and fluctuating parts. For statistically stationary fluctuations, this leads to,

$$\phi(\mathbf{r}, t) = \bar{\phi}(\mathbf{r}) + \phi'(\mathbf{r}, t) \quad (2.4.1)$$

where \mathbf{r} is the position vector. Second, the governing equations with the decomposed variables are averaged such that

$$\overline{\phi'} = 0. \quad (2.4.2)$$

The average is taken as

$$\bar{\phi}(\mathbf{r}) = \frac{1}{\Delta t} \int_t^{t+\Delta t} \phi(\mathbf{r}, t) dt, \quad \tau_{\text{turb}} \ll \Delta t \ll \tau_{\text{mean}} \quad (2.4.3)$$

where τ_{turb} and τ_{mean} denote the time scales of the turbulent and mean flow motion. In the present work, it is tacitly assumed that these time scales are well separated such that the average in Eq. (2.4.3) is well defined.

For compressible flows, the density-weighted average of Favre [3] is more convenient since it avoids the appearance of correlations involving density fluctuations in the time-averaged equations. The Favre-average is defined by

$$\phi(\mathbf{r}, t) = \tilde{\phi}(\mathbf{r}) + \phi''(\mathbf{r}, t) \quad (2.4.4)$$

such that

$$\overline{\rho \phi''} = 0. \quad (2.4.5)$$

In other words,

$$\bar{\rho} \tilde{\phi} = \overline{\rho \phi}. \quad (2.4.6)$$

For ease of exposition, the equations in this section will be presented in their differential form using cartesian tensor notation. The Einstein summation convention is assumed to apply to repeated indices.

In the following, the effect of turbulent fluctuations on viscosity and conductivity is ignored.

By decomposing density and pressure according to Eq. (2.4.1) and the remaining flow variables according to Eq. (2.4.4), and averaging using Eqs. (2.4.2) and (2.4.5), the Reynolds-Averaged Navier-Stokes (RANS) equations are derived.

The continuity equation is given by

$$\frac{\partial \bar{\rho}}{\partial t} + \frac{\partial \bar{\rho} \tilde{u}_j}{\partial x_j} = 0. \quad (2.4.7)$$

The momentum equations are

$$\frac{\partial \bar{\rho} \tilde{u}_i}{\partial t} + \frac{\partial}{\partial x_j} (\bar{\rho} \tilde{u}_i \tilde{u}_j + \bar{p} \delta_{ij}) = \frac{\partial}{\partial x_j} \left(\bar{T}_{ij} - \bar{\rho} u_i'' u_j'' \right), \quad (2.4.8)$$

where δ_{ij} is the Kronecker delta.

The energy equation reads

$$\begin{aligned} \frac{\partial}{\partial t} \left(\bar{\rho} \tilde{E} + \frac{1}{2} \bar{\rho} u_i'' u_i'' \right) + \frac{\partial}{\partial x_j} \left(\bar{\rho} \tilde{H} \tilde{u}_j + \tilde{u}_j \frac{1}{2} \bar{\rho} u_i'' u_i'' \right) = \\ \frac{\partial}{\partial x_j} \left[\tilde{u}_i \left(\bar{T}_{ij} - \bar{\rho} u_i'' u_j'' \right) - \bar{q}_j - \bar{\rho} h'' u_j'' + \overline{u_i'' T_{ij}} - \frac{1}{2} \overline{\rho u_j'' u_i'' u_i''} \right]. \end{aligned} \quad (2.4.9)$$

In the momentum and energy equations, \bar{T}_{ij} is given by

$$\bar{T}_{ij} = \mu \left[\left(\frac{\partial \tilde{u}_i}{\partial x_j} + \frac{\partial \tilde{u}_j}{\partial x_i} \right) - \frac{2}{3} \frac{\partial \tilde{u}_m}{\partial x_m} \delta_{ij} \right] + \mu \left[\left(\frac{\partial \overline{u_i''}}{\partial x_j} + \frac{\partial \overline{u_j''}}{\partial x_i} \right) - \frac{2}{3} \frac{\partial \overline{u_m''}}{\partial x_m} \delta_{ij} \right]. \quad (2.4.10)$$

In Eq. (2.4.10), the second term is commonly neglected since it is expected to be much smaller than $-\bar{\rho} u_i'' u_j''$ in Eq. (2.4.8). This assumption is valid for non-hypersonic flows.

In the energy equation, the turbulence kinetic energy \tilde{k} appears as

$$\tilde{k} = \frac{1}{2} \overline{u_i'' u_i''}, \quad (2.4.11)$$

and is used to redefine the total internal energy and total enthalpy as

$$\tilde{E} \leftarrow \tilde{E} + \tilde{k}, \quad (2.4.11a)$$

$$\tilde{H} \leftarrow \tilde{H} + \tilde{k}. \quad (2.4.11b)$$

To simplify the energy equation, it is common to neglect the terms

$$\overline{u_i'' T_{ij}} - \frac{1}{2} \overline{\rho u_j'' u_i'' u_i''}.$$

With these definitions and simplifications, the energy equation may be written as

$$\frac{\partial \bar{\rho} \tilde{E}}{\partial t} + \frac{\partial}{\partial x_j} (\bar{\rho} \tilde{H} \tilde{u}_j) = \frac{\partial}{\partial x_j} \left[\tilde{u}_i \left(\bar{T}_{ij} - \bar{\rho} u_i'' u_j'' \right) - \bar{q}_j - \bar{\rho} h'' u_j'' \right]. \quad (2.4.12)$$

The equation of state is given by

$$\bar{p} = R \bar{\rho} \tilde{T}. \quad (2.4.13)$$

Closure Problem. The essential consequence of the averaging process is that the resulting system of equations is no longer closed due to the appearance of unknown double correlations, i.e., the elements of the Reynolds-stress tensor $-\bar{\rho} u_i'' u_j''$ and the Reynolds enthalpy flux $-\bar{\rho} h'' u_j''$.

In principle, additional transport equations for the Reynolds-stress tensor and the Reynolds enthalpy flux may be derived. The difficulty is that these equations contain unknown triple correlations and that the transport equations for the triple correlations comprise unknown quadruple correlations. This situation is referred to as the closure problem since the number of equations never balances the number of unknowns.

2.4.2 Turbulence Model

The purpose of a turbulence model is to provide a set of algebraic and/or differential equations which provide sufficient information to overcome the closure problem. A large number of turbulence models of varying degrees of sophistication have been developed, see Rodi [7] and Wilcox [11].

Because the focus of the present work is on the development of numerical algorithms, it is deemed sufficient to restrict attention to a one-equation turbulence model based on the eddy-viscosity hypothesis of Boussinesq [11]. The turbulence model considered contains most of the terms encountered in more sophisticated turbulence models.

Eddy-Viscosity Hypothesis. In direct analogy to the constitutive equation for the viscous stresses, Eq. (2.3.4), the Reynolds-stress tensor is written as

$$-\bar{\rho} u_i'' u_j'' = 2\mu_t \tilde{S}_{ij} - \frac{2}{3}\mu_t \frac{\partial \tilde{u}_m}{\partial x_m} \delta_{ij} - \frac{2}{3}\bar{\rho} \tilde{k} \delta_{ij}, \quad (2.4.14)$$

where μ_t is the turbulent or eddy viscosity. The last term on the right-hand side is required to give the correct trace of the Reynolds-stress tensor.

Similarly, the Reynolds enthalpy flux is modelled by the gradient-diffusion hypothesis,

$$-\bar{\rho} h'' u_i'' = \kappa_t \frac{\partial \tilde{T}}{\partial x_i}, \quad (2.4.15)$$

where κ_t is the eddy coefficient of heat conduction, which is related to the eddy viscosity through the turbulent Prandtl number

$$\text{Pr}_t = \frac{\mu_t C_p}{\kappa_t}. \quad (2.4.16)$$

By introducing Eqs. (2.4.14) and (2.4.15) into the Reynolds-averaged momentum and energy equations, the following equations are obtained,

$$\frac{\partial \bar{\rho} \tilde{u}_i}{\partial t} + \frac{\partial}{\partial x_j} (\bar{\rho} \tilde{u}_i \tilde{u}_j + \bar{p}_t \delta_{ij}) = \frac{\partial}{\partial x_j} \left(2\mu_{\text{eff}} \tilde{S}_{ij} - \frac{2}{3} \mu_{\text{eff}} \frac{\partial \tilde{u}_m}{\partial x_m} \delta_{ij} \right), \quad (2.4.17a)$$

$$\frac{\partial \bar{\rho} \tilde{E}}{\partial t} + \frac{\partial}{\partial x_j} (\bar{\rho} \tilde{H} \tilde{u}_j) = \frac{\partial}{\partial x_j} \left[\tilde{u}_i \left(2\mu_{\text{eff}} \tilde{S}_{ij} - \frac{2}{3} \mu_{\text{eff}} \frac{\partial \tilde{u}_m}{\partial x_m} \delta_{ij} \right) + \kappa_{\text{eff}} \frac{\partial \tilde{T}}{\partial x_j} \right], \quad (2.4.17b)$$

where the static pressure is redefined to include the kinetic energy of the normal Reynolds stresses,

$$\bar{p}_t = \bar{p} + \frac{2}{3} \bar{\rho} \tilde{k}, \quad (2.4.18)$$

and where effective values of the viscosity and conductivity are defined by

$$\mu_{\text{eff}} = \mu + \mu_t, \quad (2.4.18a)$$

$$\kappa_{\text{eff}} = \kappa + \kappa_t. \quad (2.4.18b)$$

Through the eddy-viscosity and gradient-diffusion hypotheses, the task of a turbulence model has been reduced from providing expressions for the Reynolds-stress tensor and heat flux to furnishing an expression for the eddy viscosity and a value for the turbulent Prandtl number.

The weaknesses of the eddy-viscosity hypothesis are discussed by Wilcox [11].

The eddy-viscosity and gradient-diffusion hypotheses allow the governing equations for turbulent flow to be written in the same form as those for laminar flow with time-averaged variables and effective viscosity and conductivity. Therefore, the time-average notation is dropped for the remainder of this work.

Spalart-Allmaras Turbulence Model. The turbulence model of Spalart and All-

maras [9] consists of a single partial differential equation for an eddy-viscosity variable $\tilde{\nu}$

$$\frac{\partial}{\partial t} \int_{\Omega} \rho \tilde{\nu} dA + \oint_{\partial\Omega} \rho \tilde{\nu} \mathbf{v} \cdot \mathbf{n} ds = \frac{1}{\sigma} \oint_{\partial\Omega} \rho (\nu + \tilde{\nu}) \nabla \tilde{\nu} \cdot \mathbf{n} ds + \int_{\Omega} S(\rho \tilde{\nu}) dA \quad (2.4.19)$$

where the source term is given by

$$\begin{aligned} S(\rho \tilde{\nu}) &= \rho c_{b1} (1 - f_{t2}) \tilde{\Omega} \tilde{\nu} && \text{Production} \\ &+ \frac{1}{\sigma} \left[\rho c_{b2} \nabla \tilde{\nu} \cdot \nabla \tilde{\nu} - (\nu + \tilde{\nu}) \nabla \tilde{\nu} \cdot \nabla \rho \right] && \text{Diffusion} \\ &- \rho \left(c_{w1} f_w - \frac{c_{b1}}{\kappa^2} f_{t2} \right) \left(\frac{\tilde{\nu}}{d} \right)^2 && \text{Destruction} \\ &+ \rho f_{t1} \Delta V^2. && \text{Transition} \end{aligned} \quad (2.4.20)$$

The model described below differs slightly from that described in [9]. It incorporates modifications suggested by Spalart [8] to ensure that $\tilde{\Omega}$ (see below) remains positive.

The eddy-viscosity variable $\tilde{\nu}$ is related to the turbulent viscosity μ_t by

$$\mu_t = f_{v1} \rho \tilde{\nu} \quad (2.4.21)$$

where the function f_{v1} is given by

$$f_{v1} = \frac{\chi^3}{\chi^3 + c_{v1}^3} \quad (2.4.22)$$

and where χ is defined as the ratio of the eddy-viscosity variable to the kinematic laminar viscosity,

$$\chi = \frac{\tilde{\nu}}{\nu}. \quad (2.4.23)$$

The various terms in the source term are described in the following.

Production Term. In the production term,

$$\tilde{\Omega} = \Omega f_{v3} + \frac{\tilde{\nu}}{\kappa^2 d^2} f_{v2} \quad (2.4.24)$$

where Ω is the magnitude of the vorticity $\boldsymbol{\Omega} = \nabla \times \mathbf{v}$, κ is von Kármán's constant and d is the normal distance to the closest solid surface. The function f_{v2} is given by

$$f_{v2} = \left(1 + \frac{\chi}{c_{v2}} \right)^{-3}, \quad (2.4.25)$$

and the function f_{v3} is defined as

$$f_{v3} = \frac{(1 + \chi f_{v1})(1 - f_{v2})}{\chi}. \quad (2.4.26)$$

Diffusion Term. Spalart and Allmaras [9] originally defined their turbulence model in non-conservative form. In the above description, the model was cast in conservation form. By changing from the non-conservative to the conservative form, the second term involving the scalar product of the gradients of the eddy-viscosity variable and the density is introduced. This term is likely to be large only in shock-wave/boundary-layer interaction regions.

Destruction Term. In the destruction term, the function f_w is given by

$$f_w = g \left(\frac{1 + c_{w3}^6}{g^6 + c_{w3}^6} \right)^{1/6}, \quad (2.4.27)$$

where

$$g = r + c_{w2}(r^6 - r) \quad (2.4.28)$$

and

$$r = \frac{\tilde{\nu}}{\tilde{\Omega} \kappa^2 d^2}. \quad (2.4.29)$$

The value of c_{w1} is determined from the other constants to ensure correct representation of the logarithmic region, where production is assumed to balance destruction. This gives

$$c_{w1} = \frac{c_{b1}}{\kappa^2} + \frac{1 + c_{b2}}{\sigma}. \quad (2.4.30)$$

Transition Term. The additional source term allows transition locations to be specified. The associated functions are defined by

$$f_{t2} = c_{t3} \exp(-c_{t4} \chi^2) \quad (2.4.31)$$

and

$$f_{t1} = c_{t1} g_t \exp \left[-c_{t2} \frac{\Omega_t^2}{\Delta V^2} (d^2 + g_t^2 d_t^2) \right]. \quad (2.4.32)$$

The function g_t is given by

$$g_t = \min \left(0.1, \frac{\Delta V}{\Omega_t \Delta s_t} \right) \quad (2.4.33)$$

where ΔV is the difference in velocity magnitude between the field point and the transition point, Ω_t is the vorticity at the transition point, Δs_t is the grid spacing at the

Table 2.2: Values of constants for Spalart-Allmaras turbulence model.

constant	value	constant	value
Pr_t	0.9	c_{w2}	0.3
c_{v1}	7.1	c_{w3}	2.0
c_{v2}	5.0	σ	0.6667
κ	0.41	c_{t1}	1.0
c_{b1}	0.1355	c_{t2}	2.0
c_{b2}	0.622	c_{t3}	1.2
c_{w1}	3.2391	c_{t4}	0.5

transition point, and d_t is the distance between the field point and the transition point.

The constants are summarised in Table 2.2.

Comparisons of the Spalart-Allmaras model with variants of the $k - \varepsilon$ and $k - \omega$ models carried out by Menter [6] and Bardina et al. [2] have shown that the Spalart-Allmaras model is an attractive alternative in terms of accuracy, robustness and required computational resources.

2.5 Boundary Conditions

For inviscid flows, the slip condition must be enforced at solid walls

$$(\mathbf{v} \cdot \mathbf{n})_{\text{wall}} = 0. \quad (2.5.1)$$

For viscous flows, the no-slip condition at solid walls requires that

$$\mathbf{v}_{\text{wall}} = 0. \quad (2.5.2)$$

The solid walls may be adiabatic

$$(\mathbf{q} \cdot \mathbf{n})_{\text{wall}} = 0, \quad (2.5.3)$$

or isothermal, where the wall temperature is specified,

$$T = T_{\text{wall}}. \quad (2.5.4)$$

For turbulent flows, the eddy viscosity is zero on solid walls, i.e.,

$$\tilde{\nu}_{\text{wall}} = 0. \quad (2.5.5)$$

References

- [1] Aris R., *Vectors, Tensors, and the Basic Equations of Fluid Mechanics*, Dover, 1989
- [2] Bardina J.E., Huang P.G., and Coakley T.J., *Turbulence Modeling Validation, Testing and Development*, NASA TM 110446, April 1997
- [3] Favre A., *Equations des gaz turbulents compressibles*, Journal de Mécanique, Vol. 4, No. 3, pp. 361-390, 1965
- [4] Ferziger J.L., *Large-Eddy Simulation*, in: *Simulation and Modeling of Turbulent Flows*, Gatski T.B. et al. (Eds.), Oxford University Press, 1996, pp. 109-154
- [5] Leonard A., *Direct Numerical Simulation of Turbulent Flows*, in: *Simulation and Modeling of Turbulent Flows*, Gatski T.B. et al. (Eds.), Oxford University Press, 1996, pp. 79-108
- [6] Menter F.R., *A Comparison of Some Recent Eddy-Viscosity Turbulence Models*, J. Fl. Eng., Vol. 118, pp. 514-519, 1996
- [7] Rodi W., *Turbulence Models and Their Application in Hydraulics*, IAHR Monograph, 3rd Ed., A.A. Balkema, Rotterdam, 1993
- [8] Spalart P.R., *Improvements in Spalart-Allmaras Model*, dated March 1993, private communication, November 13, 1996
- [9] Spalart P.R. and Allmaras S.R., *A One-Equation Turbulence Model for Aerodynamic Flows*, La Recherche Aéronautique, No. 1, pp. 5-21, 1994
- [10] Tennekes H. and Lumley J.L., *A First Course in Turbulence*, MIT Press, 1972
- [11] Wilcox D.C., *Turbulence Modeling for CFD*, 2nd Ed., DCW Industries Inc., La Cañada, California, 1998
- [12] White F.M., *Viscous Fluid Flow*, McGraw-Hill, 2nd Ed., 1991
- [13] Zierep J., *Theoretische Gasdynamik*, 4th Ed., G. Braun, Karlsruhe, 1991

PART II

NUMERICAL METHOD

Chapter 3

Unigrid Numerical Method

The discretisation of the governing equations is described. The definition of control volumes and the data structure are discussed. The concept of grid-transparency is introduced in order to guide the discretisation on mixed grids. The numerical inviscid fluxes are listed and the boundary conditions described.

3.1 Introduction

As indicated in Chapter 1, the current work is based upon the use of the agglomeration multigrid method. In the present implementation of the agglomeration multigrid method, the equations on a given grid level are discretised in the same manner as on the finest grid level. Therefore, it is expedient to consider the finest grid level as the only one and to describe the numerical method as if it applied to a single grid level only, hence the term ‘unigrid numerical method.’

The discretisation is based on the integral form of the governing equations, thereby ensuring conservation and the correct shock jump conditions. Following Jameson et al. [23], the time-dependent form of the governing equations is employed as a means of reaching steady-state solutions. The temporal and spatial discretisations are separated, which allows them to be studied separately and matched to each other. This procedure also eliminates a possible dependency of the steady-state solution on the time step.

3.2 Finite-Volume Discretisation

The integral form of the governing equations is discretised by subdividing the solution domain into non-overlapping control volumes Ω_i . The definition of the control volumes is discussed in the next section. The control volumes are assumed to be invariant with respect to time. It is convenient to describe the discretisation by considering the generic

conservation equation,

$$\frac{\partial}{\partial t} \int_{\Omega_i} \mathbf{q}_i dA + \oint_{\partial\Omega_i} \mathbf{f}(\mathbf{q}) \cdot \mathbf{n} ds = \oint_{\partial\Omega_i} \mathbf{g}(\mathbf{q}, \nabla \mathbf{q}) \cdot \mathbf{n} ds + \int_{\Omega_i} \mathbf{s}(\mathbf{q}, \nabla \mathbf{q}) dA. \quad (3.2.1)$$

In each control volume, the average value of the state vector is defined by

$$\bar{\mathbf{q}}_i(t) = \frac{1}{A_{\Omega_i}} \int_{\Omega_i} \mathbf{q}(\mathbf{r}, t) dA, \quad (3.2.2)$$

so that Eq. (3.2.1) may be written as

$$A_{\Omega_i} \frac{d\bar{\mathbf{q}}_i}{dt} + \oint_{\partial\Omega_i} \mathbf{f}(\mathbf{q}) \cdot \mathbf{n} ds = \oint_{\partial\Omega_i} \mathbf{g}(\mathbf{q}, \nabla \mathbf{q}) \cdot \mathbf{n} ds + \int_{\Omega_i} \mathbf{s}(\mathbf{q}, \nabla \mathbf{q}) dA. \quad (3.2.3)$$

For a generic polygonal control volume consisting of n_{f_i} straight-line segments, the contour integrals are rewritten to give

$$A_{\Omega_i} \frac{d\bar{\mathbf{q}}_i}{dt} + \sum_{j=1}^{n_{f_i}} \int_{\partial\Omega_{ij}} \mathbf{f}(\mathbf{q}) \cdot \mathbf{n} ds = \sum_{j=1}^{n_{f_i}} \int_{\partial\Omega_{ij}} \mathbf{g}(\mathbf{q}, \nabla \mathbf{q}) \cdot \mathbf{n} ds + \int_{\Omega_i} \mathbf{s}(\mathbf{q}, \nabla \mathbf{q}) dA, \quad (3.2.4)$$

where $\partial\Omega_{ij}$ represents the control-volume face separating the control volumes Ω_i and Ω_j . The flux integrals are approximated by Gaussian quadrature with n_G quadrature points (giving an accuracy of $O(h^{2n_G})$), and the source term is assumed to be constant over the control volume to give

$$A_{\Omega_i} \frac{d\bar{\mathbf{q}}_i}{dt} + \sum_{j=1}^{n_{f_i}} \frac{\Delta s_{ij}}{2} \left\{ \sum_{l=1}^{n_G} \omega_l [\mathbf{f}(\mathbf{q}) \cdot \mathbf{n} - \mathbf{g}(\mathbf{q}, \nabla \mathbf{q}) \cdot \mathbf{n}]_{ij, \tilde{s}_l} \right\} = \mathbf{s}(\bar{\mathbf{q}}_i, (\nabla \bar{\mathbf{q}})_i) A_{\Omega_i}. \quad (3.2.5)$$

In Eq. (3.2.5), Δs_{ij} is the length of the control-volume face separating control volumes Ω_i and Ω_j , and \tilde{s} represents the parameterised coordinate along the control-volume face. The values of the weights ω_l and the coordinates of the quadrature points \tilde{s}_l can be found in numerical analysis textbooks, see, e.g., Stoer and Bulirsch [40].

The above derivation defines a generic finite-volume method. In the following, the formal spatial accuracy will be limited to second order. Therefore, only Gaussian quadrature of order one, i.e., the midpoint rule, will be used. Equation (3.2.5) can then be written

$$A_{\Omega_i} \frac{d\bar{\mathbf{q}}_i}{dt} + \sum_{j=1}^{n_{f_i}} [\mathbf{f}(\mathbf{q}) \cdot \mathbf{n} - \mathbf{g}(\mathbf{q}, \nabla \mathbf{q}) \cdot \mathbf{n}]_{ij} \Delta s_{ij} = \mathbf{s}(\bar{\mathbf{q}}_i, (\nabla \bar{\mathbf{q}})_i) A_{\Omega_i}. \quad (3.2.6)$$

Further discretisation requires the evaluation of the inviscid and viscous fluxes at the control volume faces, which is described in Sections 3.7 and 3.8, respectively.

Remark 3.1: The numerical solution of Eq. (3.2.6) necessitates assigning to the average

value \bar{q}_i a location inside the control volume Ω_i . For an arbitrary solution variation, the Taylor-series expansion gives

$$\bar{q}_i = \frac{1}{A_{\Omega_i}} \left[\int_{\Omega_i} q dA - (\nabla \bar{q})_i \cdot \int_{\Omega_i} (\mathbf{r} - \mathbf{r}_i) dA + \text{HOT} \right],$$

where \mathbf{r}_i is the position vector of the centroid of control volume Ω_i , and HOT is the abbreviation for ‘higher-order terms.’ Disregarding the trivial case of vanishing $(\nabla \bar{q})_i$, Eq. (3.2.2) strictly holds only if \bar{q}_i is stored at the centroid of the control volume.

Remark 3.2: In the following, grids will be referred to as uniform and non-uniform. A uniform grid consists of cells of identical areas. A non-uniform grid, which consists of cells of differing areas, may be regular or irregular. A grid is regular if the local variation in cell area is small enough not to cause substantial errors. This is usually achieved by variations in area between neighbouring cells less than approximately 10-20%. An irregular grid exhibits large variations in cell areas.

3.3 Control-Volume Definition

In the present work, cells of the dual grid are chosen as control volumes. To define the dual grid, it is helpful to refer to a given unstructured grid as the primal grid. A dual grid can then be defined through the following properties:

1. Each cell of the dual grid is associated with a vertex of the primal grid.
2. Each edge of the dual grid is associated with an edge of the primal grid.
3. Each vertex of the dual grid is associated with a cell of the primal grid.

Because of the association of cells of the dual grid, i.e., the control volumes, with the vertices of the primal grid, the latter are chosen as the storage locations for the solution variables.

Remark 3.3: By storing variables at the vertices of the primal grid and constructing control volumes from a dual grid, Eq. (3.2.2) is satisfied on a uniform grid only. On non-uniform grids, the average value defined by Eq. (3.2.2) must be regarded as a pointwise value. This has two consequences. First, the average value will be coupled

to neighbouring values by the mass matrix. For steady flows, the mass matrix may be lumped without sacrificing spatial accuracy [7]. Second, the difference between pointwise values and average values can be shown to represent a second-order error [25] and is thus of importance only for methods of order three and higher. Since the current work concentrates on steady flows and employs second-order methods only, the overbar will be dropped in the following.

The above list of properties allows a number of dual grids to be constructed. Two choices were explored in the present work. They are identical for primal grids composed of equilateral triangles.

3.3.1 Median Dual

On triangular grids, the median dual is constructed from median segments, i.e., by connecting the centroids of the triangles to the edge mid-points, as shown in Fig. 3.1(a). On quadrilateral grids, the median dual is defined by connecting midpoints of opposing edges. The median dual for mixed grids is shown in Fig. 3.1(b). It is noted that the median-dual edges are composed of two straight segments.

Remark 3.4: The median dual arises naturally as a control volume if the spatial discretisation produced by the Galerkin Finite-Element Method with linear triangular elements is expressed in finite-volume form [3, 21, 36]. As will become apparent below, the median dual results in geometrical relationships which simplify many discretisation formulae.

3.3.2 Containment Dual

The containment dual is constructed by connecting the centres of the containment circles. The containment circle is defined as the smallest circle containing a triangle. For acute triangles, the containment circle is identical to the circumcircle, making the containment dual identical to the Dirichlet region, as depicted in Fig. 3.2(a). For obtuse triangles, the containment circle is equivalent to a circle centred on the longest edge of the triangle. The containment-dual control volume is shown in Fig. 3.2(b) for a grid composed partially of obtuse triangles.

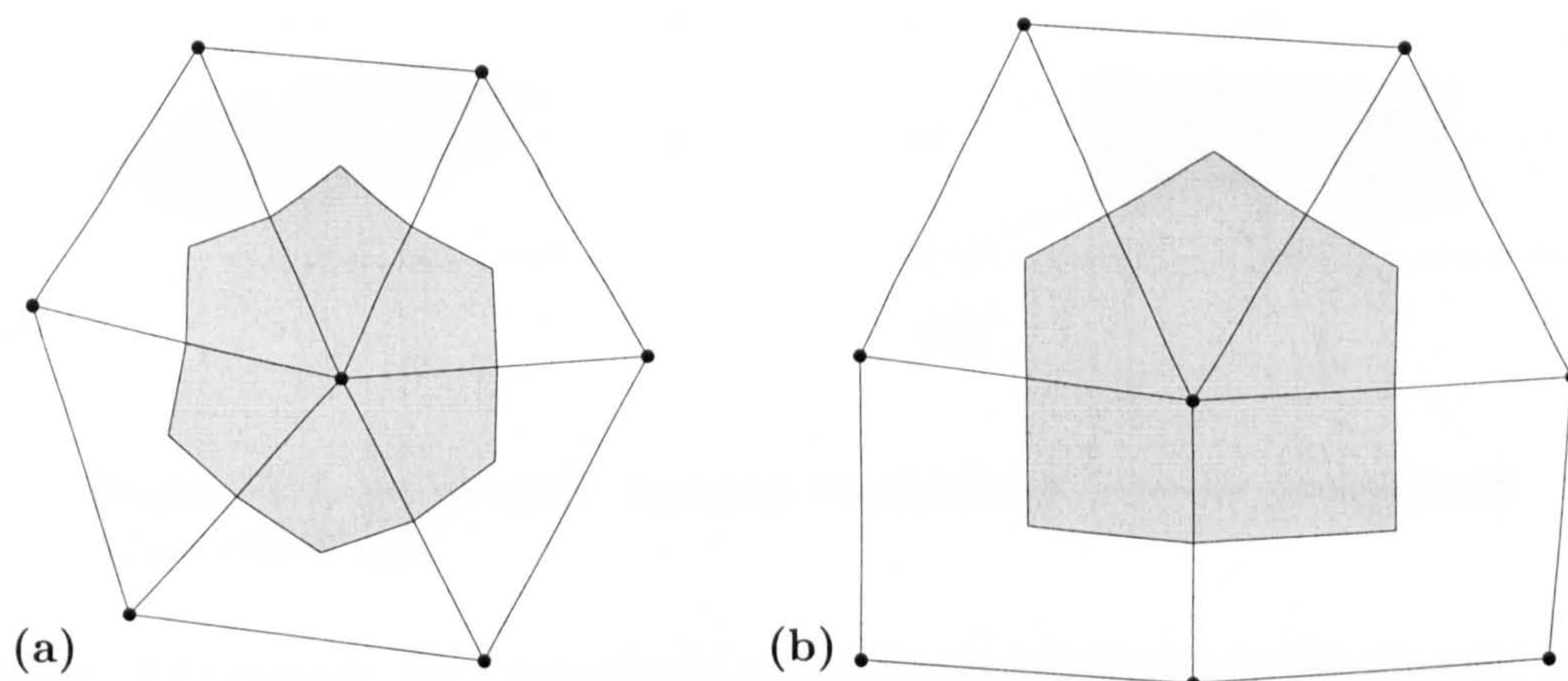


Figure 3.1: Median dual on (a) triangular grid and (b) mixed grid. Control volumes are shown shaded.

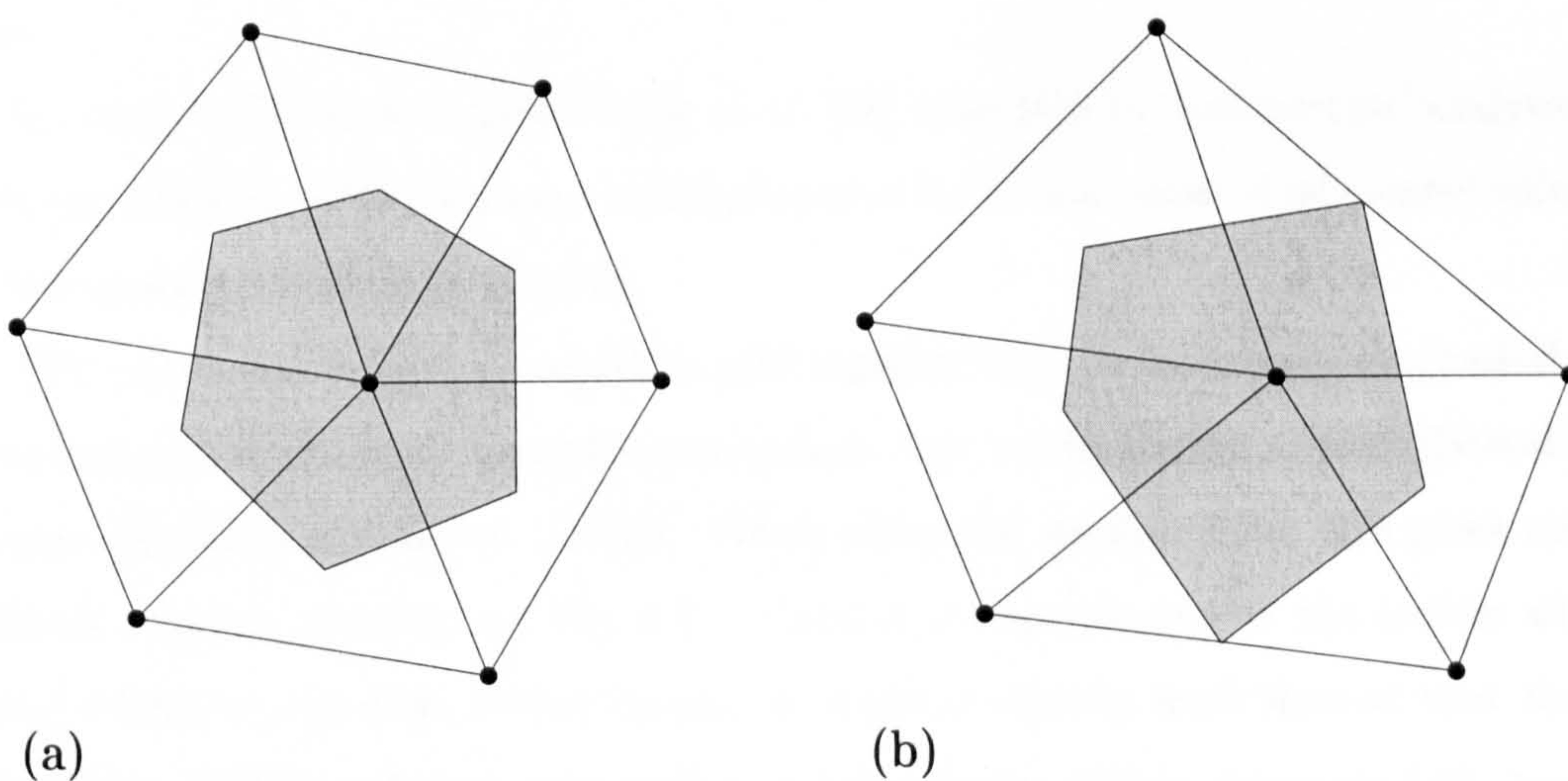


Figure 3.2: Containment dual on (a) acute triangular grid and (b) obtuse triangular grid. Control volumes are shown shaded.

There is no natural extension of the containment dual to quadrilateral or mixed grids.

3.3.3 Comparison

The containment dual is particularly useful on grids generated for high-Reynolds-number flows, which usually consist of highly stretched grids adjacent to solid walls. The median dual on such grids is shown in Fig. 3.3(a), revealing highly distorted control

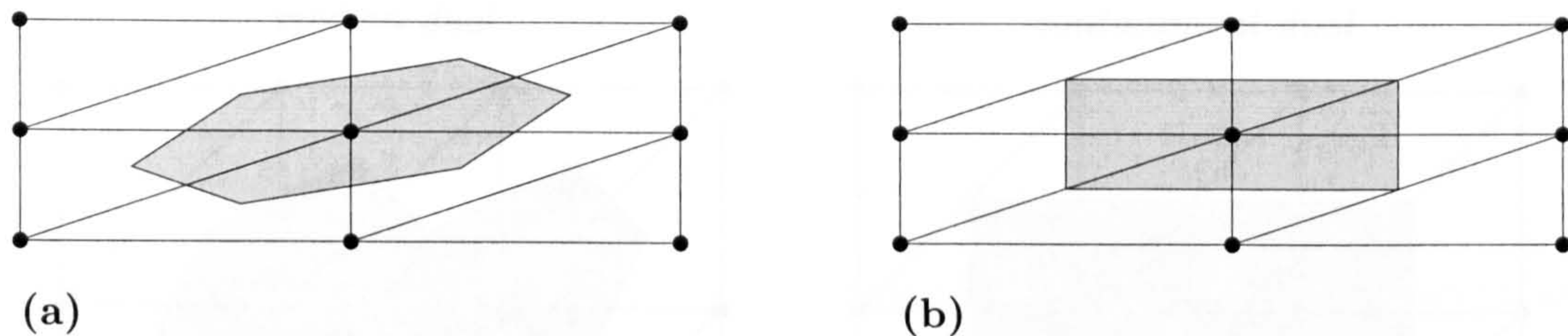


Figure 3.3: (a) Median dual (b) Containment dual on triangulated quadrilateral grid.

volumes. By contrast, the containment dual gives rectangular control volumes, as depicted in Fig. 3.3(b). Barth [5] has shown that containment-dual control volumes greatly reduce numerical diffusion compared to median-dual control volumes by calculating an inviscid flow over a NACA 0012 aerofoil on a grid generated for high-Reynolds-number flows.

It is interesting to note that Viozat et al. [48] were able to demonstrate analytically the advantages of control volumes which reduce to the containment dual control volumes on triangulated quadrilateral grids.

The containment dual is helpful in still another way. A frequently overlooked disadvantage of triangulated quadrilateral grids is that triangulating a quadrilateral grid by inserting diagonals is not unique. When using the median dual, this gives rise to different control volumes, see Fig. 3.4.* Numerical experiments by the author with a scalar transport equation solved subject to a given velocity field showed that the results can be influenced very strongly by the orientation of the diagonals [18]. In fact, the influence of the orientation of the diagonals was found to be more important than that of grid distortion. This form of grid-dependence is rather undesirable in viscous regions. The containment dual avoids this drawback and results in identical control volumes irrespective of the orientation of the diagonals.

Although the containment dual on stretched triangulated quadrilateral grids improves the accuracy, the efficiency of the calculation is reduced. This is because the flux calculation encounters dual edges of very small or zero length, whose contributions

*The triangulated quadrilateral grid shown in Fig. 3.4(a) is sometimes referred to as a Friedrichs-Keller triangulation after Friedrichs and Keller [13], who were among the first to analyse numerical methods on such grids. The triangulated quadrilateral grid shown in Fig. 3.4(b) is sometimes referred to as a Union-Jack triangulation for obvious reasons.

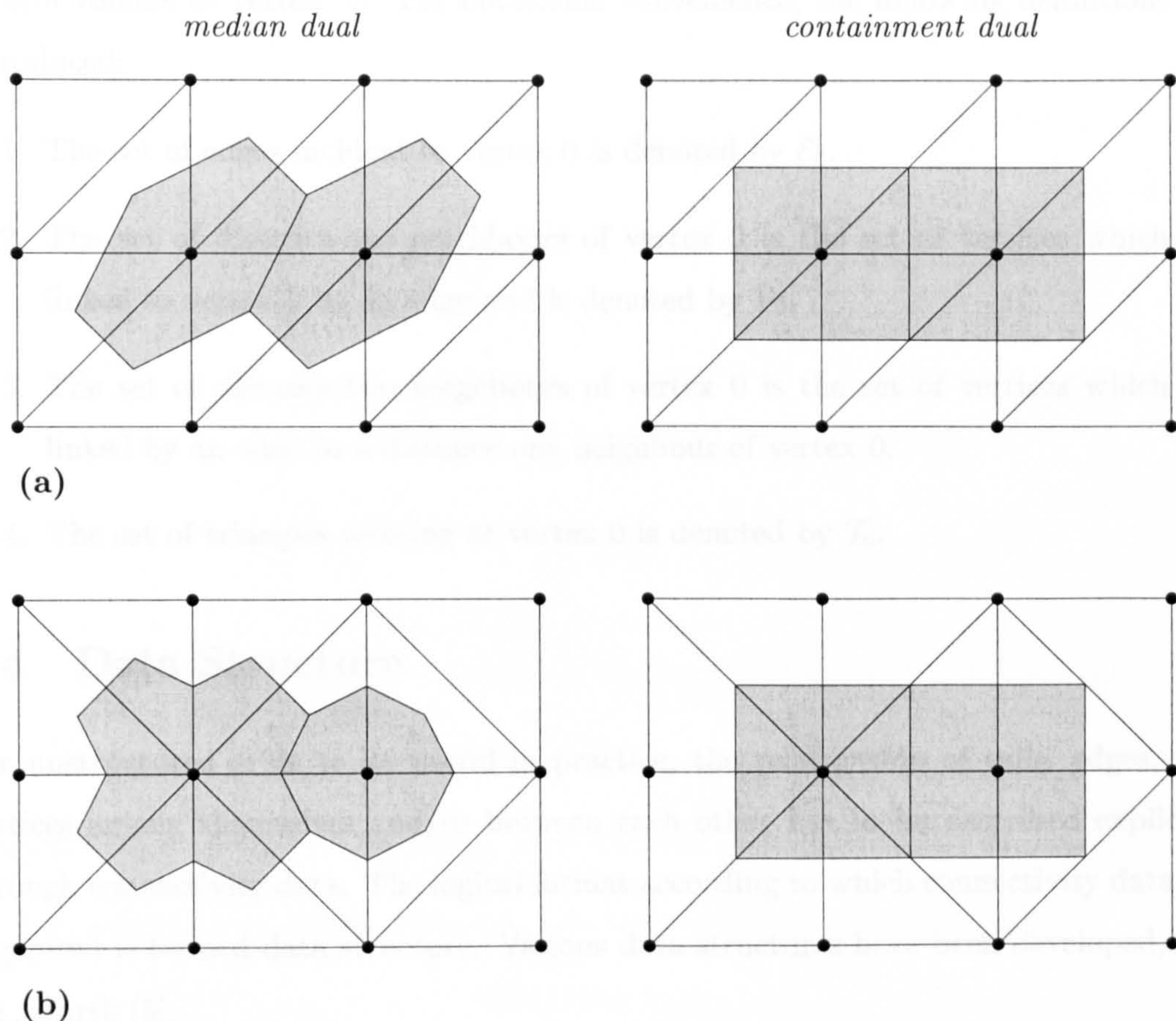


Figure 3.4: Effect of diagonal edges on median dual and containment dual for triangulated quadrilateral grid with (a) diagonal edges of positive slope and (b) diagonal edges of alternating slope.

to the solution update are therefore very small or identically zero. Looping over these edges could be prevented by a conditional statement, but this is also inefficient. The best option is to delete the dual edges with small or zero length altogether, which leads to mixed grids in a natural way. These advantages and disadvantages of the containment dual will be demonstrated in Chapter 6 for an inviscid flow.

Alternative definitions of dual cells for stretched triangular grids were used also by Kasbarian et al. [24], Dervieux et al. [12], Debiez [9], Meister [27], and Viozat et al. [48]. Like the containment dual, these definitions reduce to rectangular control volumes on triangulated quadrilateral grids.

The following sections and Chapter 4 describe the discretisation for an arbitrary dual

control volume at vertex '0.' For notational convenience, the following definitions are introduced:

1. The set of edges incident to vertex 0 is denoted by \mathcal{E}_0 .
2. The set of distance-one neighbours of vertex 0 is the set of vertices which are linked to vertex 0 by an edge and is denoted by \mathcal{V}_0 .
3. The set of distance-two neighbours of vertex 0 is the set of vertices which are linked by an edge to a distance-one neighbour of vertex 0.
4. The set of triangles meeting at vertex 0 is denoted by \mathcal{T}_0 .

3.4 Data Structure

For unstructured grids to be useful in practice, the relationship of cells, edges, and vertices among themselves and/or between each other has to be described explicitly through connectivity data. The logical format according to which connectivity data are organised is termed data structure. Various data structures have been developed, see, e.g., Barth [5].

Since the data structure largely determines which operations can be carried out, the data structure needs to be matched to the solution method. In the present case, the essential operation of the finite-volume method is the computation of fluxes through control-volume faces. As described in the previous section, the control-volume faces are given by the edges of the dual grid. Because of the association between edges of the dual grid and edges of the primal grid, the computation of fluxes can be carried out simply by looping over the edges of the primal grid. Therefore, the present flow-solution method employs an edge-based data structure [5].

The edge-based data structure can be stored in two arrays. For reasons which will become clear in Section 3.5, the current implementation of the edge-based data structure entails the storage of three arrays.

The first array, $\mathbf{e2v}(2, \mathbf{nEdges})$, lists the two vertices defining each edge. Referring to Fig. 3.5(a), for edge ne ,

$$\mathbf{e2v}(1, ne) = v_1$$

$$\mathbf{e2v}(2, ne) = v_2.$$

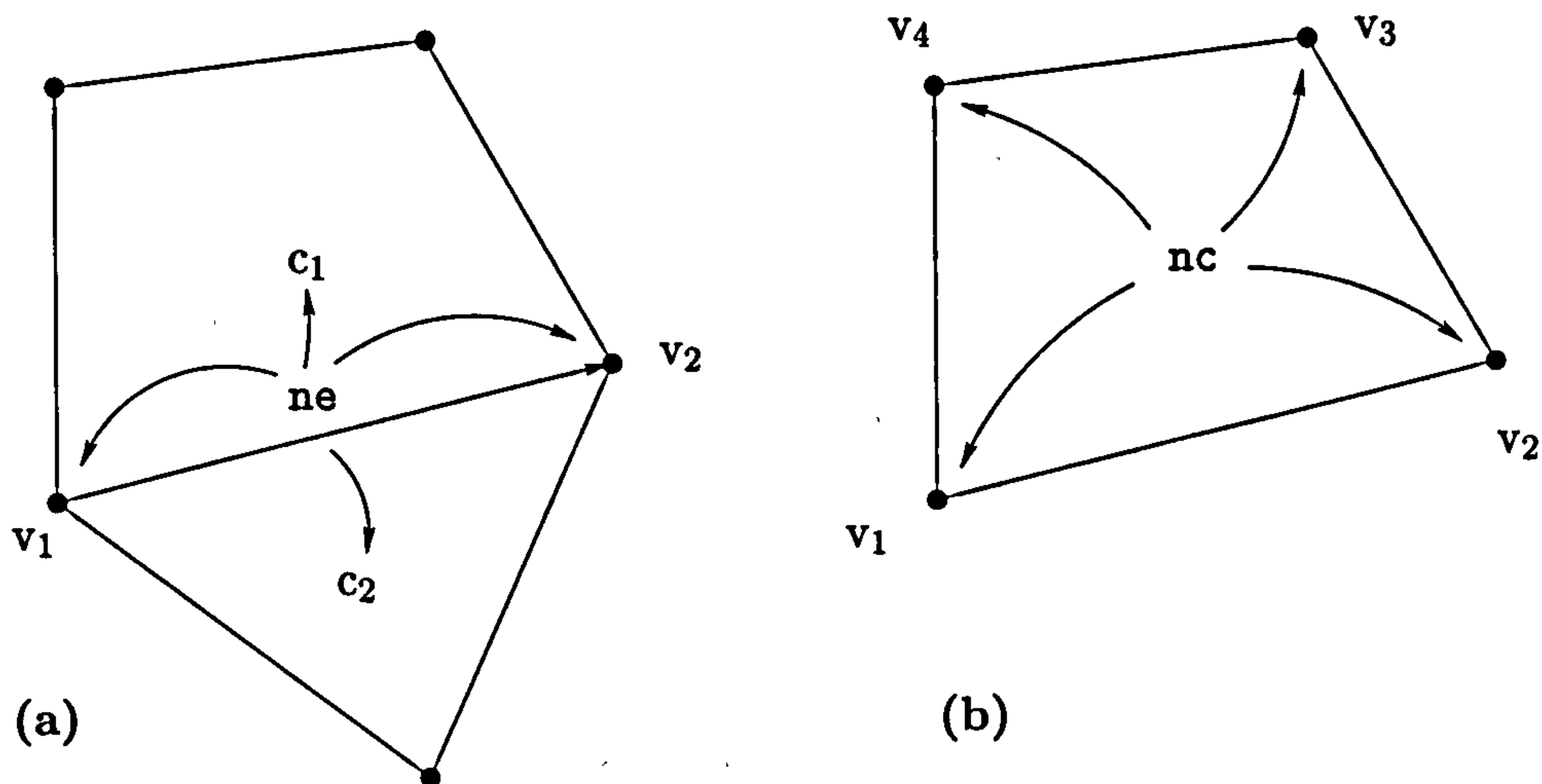


Figure 3.5: Schematic illustration of data structure. (a) $e2v$ and $e2c$ -arrays, and (b) $c2v$ -array.

The convention is adopted that edge ne is directed from vertex v_1 to vertex v_2 .

The second array, $e2c(2, nEdges)$, lists the two cells sharing edge ne ,

$$e2c(1, ne) = c_1$$

$$e2c(2, ne) = c_2,$$

as depicted in Fig. 3.5(a). The entries are ordered such that the cells c_1 and c_2 are to the left and right of edge ne , respectively. For an edge lying on a boundary, the corresponding entry in $e2c$ is set to 0.

The third array, $c2v(4, nCells)$, lists the vertices of each cell in counter-clockwise order. For cell nc , as illustrated in Fig. 3.5(b),

$$c2v(1, nc) = v_1$$

$$c2v(2, nc) = v_2$$

$$c2v(3, nc) = v_3$$

$$c2v(4, nc) = v_4.$$

If cell nc is a triangle, the fourth entry is set equal to the first entry, $v_4 = v_1$.

The above described the data structure for the interior of the solution domain. The boundary edges are stored in Compressed Sparse Row (CSR) format [35] for each boundary region in counter-clockwise order.

3.5 Grid Transparency

The use of mixed grids raises the question of how the existence of different cell types affects the solution method. While it may be unavoidable to treat triangular and quadrilateral cells differently or separately in the pre- and post-processing stages, it is inconvenient to treat them differently or separately during the flow-solution stage. This may require additional data structure arrays, result in conditional statements, lead to untidy computer code, and adversely affect program speed. It is therefore desirable to treat the different cell types identically wherever possible. The ideal is a code which is independent of the cell type and requires a data structure of minimal extent. Such a code is termed 'grid-transparent' in the present work.

The key to formulating a grid-transparent code is to shift attention away from cell types and focus on edges and vertices. This amounts to regarding a grid as being described by geometric entities of lower level, because cells are constructed from edges, and edges are defined by two vertices. As a result, different cell types are handled automatically. In fact, a grid-transparent code does not distinguish between triangular, quadrilateral, and mixed grids for a given set of vertices in that the same operations are carried out in precisely the same manner. The only difference is the different number of edges and different values of control-volume areas and faces.

In order that a code be grid-transparent, it must be ensured that the algorithms used in that code are grid-transparent. In this context, it is instructive to regard grid-transparent algorithms as a subset of edge-based algorithms, since only the first data-structure array described in Section 3.4 is required. This has important implications on the discretisation stencils, because with the remaining data-structure array, only distance-one neighbours can be included *directly* in the stencil at a given vertex. Distance-two neighbours have to be included in the stencil indirectly by a two-step procedure. In the first step, an intermediate quantity is computed and stored at the distance-one neighbours. In the second step, the intermediate quantities are processed and accumulated at the given vertex to give the desired result. Figure 3.6 depicts the vertices which are included directly and indirectly for a quadrilateral and a mixed grid. On a triangular grid, all the vertices of the cells meeting at a vertex are involved in the stencil at that vertex.

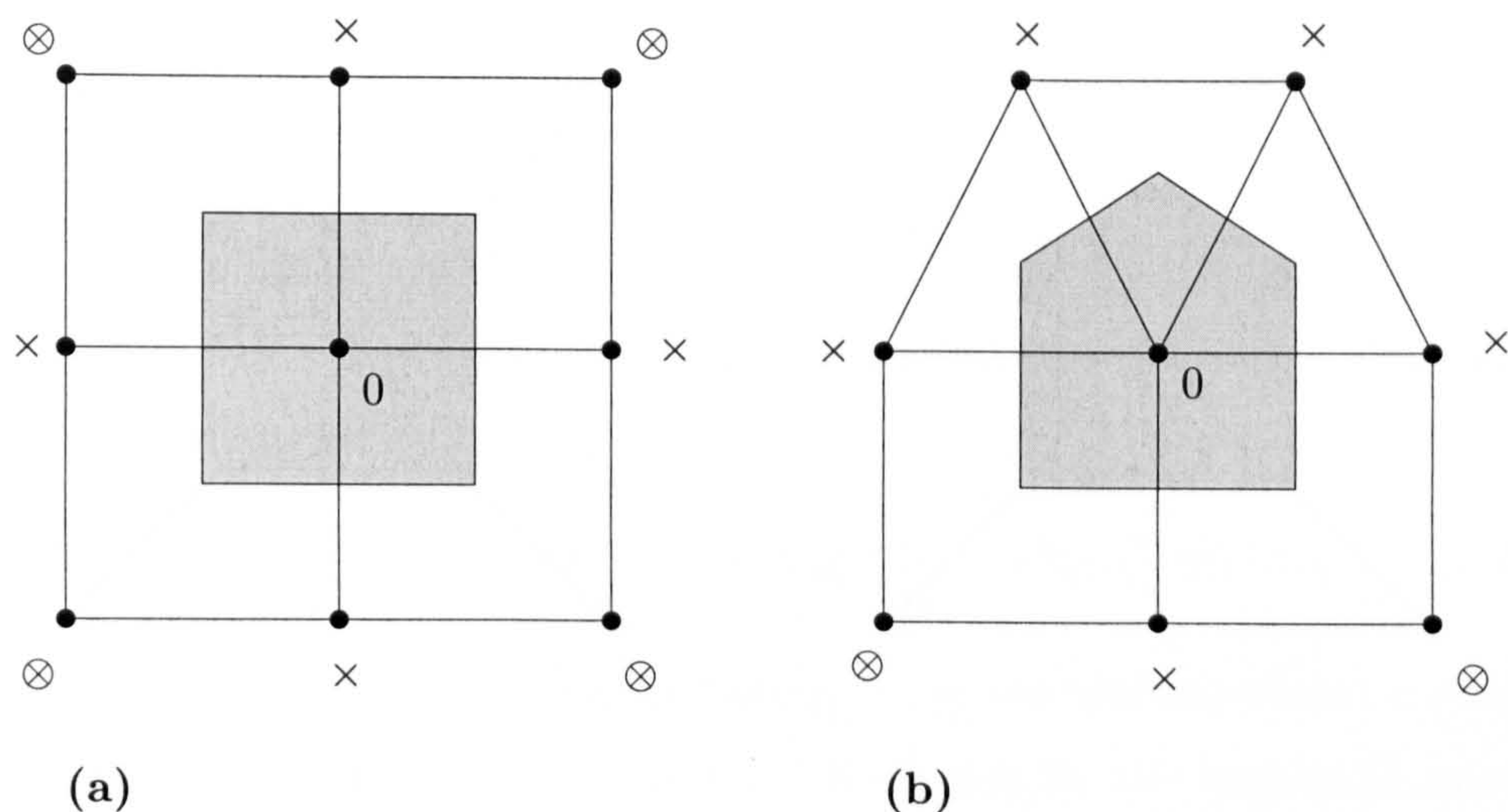


Figure 3.6: Grid-transparent stencil on (a) quadrilateral grid and (b) mixed grid. Vertices included directly in stencil at vertex 0 are denoted by 'x'. Vertices which can only be included in a two-step procedure are denoted by '⊗'.

The preceding discussion focussed on two dimensions where there are only two cell types and two cells meet at each interior edge. The real benefits of grid-transparent algorithms will only emerge on three-dimensional mixed grids where up to four cell types can be used and the number of cells meeting at an interior edge is strongly dependent on the cell types meeting at that edge. For example, the number of cells meeting at an edge is essentially arbitrary for a tetrahedral grid, and may vary considerably on mixed grids. The array `e2c` would then have to be stored in compressed sparse row or linked list format. It is clear that a substantial simplification will be achieved if one does not have to refer to a large (and variable) number of cells at each edge. A further motivation for the development of grid-transparent methods is that it may not be possible to construct at all the second and third data-structure arrays for the complex polygonal cells on the coarse-grid levels generated by the agglomeration multigrid method.

A recent paper by Perroomian et al. [31] also addressed the development of solution methods for different types of grids or mixed grids. Their method is also labelled 'grid-transparent' because it can handle structured, unstructured, and mixed grids. An important difference, however, is that the present solution method is not simply capable of handling triangular, quadrilateral, and mixed grids. As explained above, the present method does not, in fact, differentiate between such grids for a given set of vertices once

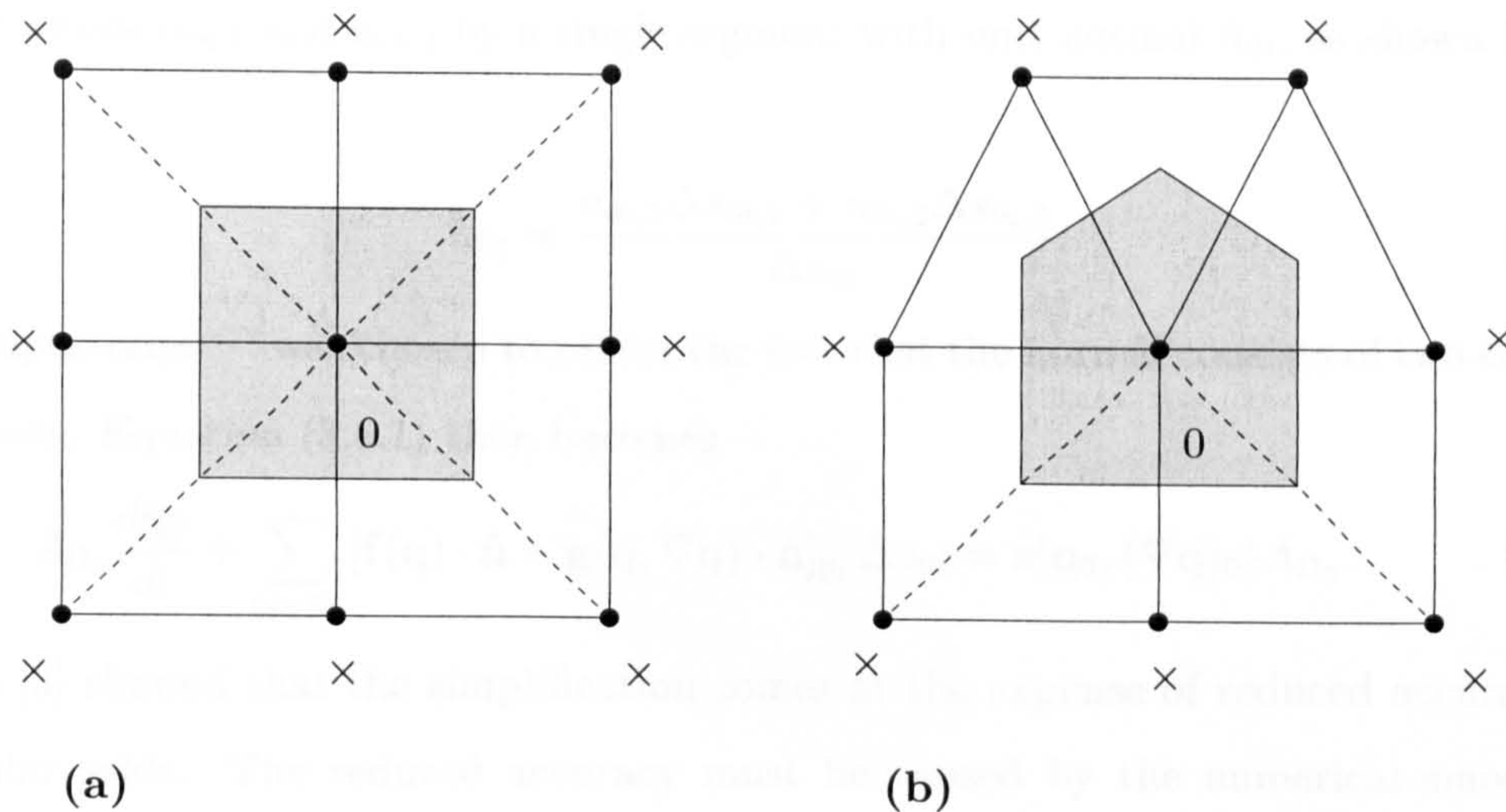


Figure 3.7: Grid-transparent stencil on (a) quadrilateral grid and (b) mixed grid through subdivision of non-simplicial cells with virtual edges. Virtual edges are denoted by dashed lines.

control volumes and face areas have been computed.

Another way of avoiding the treatment of different cell types would be to subdivide the non-simplicial cells into simplicial cells by virtual edges, as depicted schematically in Fig. 3.7. However, this is not regarded as suitable since it would lead to considerable additional memory requirements, thus defeating the original objective of attempting to treat different cell types with a unified data structure of minimal extent.

The issue of grid-transparency will be discussed further as appropriate.

3.6 Flux Quadrature

Using the edge-based data structure, Eq. (3.2.6) can be recast as

$$A_{\Omega_0} \frac{d\mathbf{q}_0}{dt} + \sum_{0i \in \mathcal{E}_0} \sum_{k=1}^2 [\mathbf{f}(\mathbf{q}) \cdot \mathbf{n} - \mathbf{g}(\mathbf{q}, \nabla \mathbf{q}) \cdot \mathbf{n}]_{0i,k} \Delta s_{0i,k} = \mathbf{s}(\mathbf{q}_0, (\nabla \mathbf{q})_0) A_{\Omega_0}, \quad (3.6.1)$$

where the inner summation arises for the median dual because each dual edge consists of two straight segments, as shown in Fig. 3.8 for edge $0i$. In Fig. 3.8, the symbol ‘ \otimes ’ denotes the location of the quadrature points.

Simplification of Flux Quadrature in Interior of Solution Domain. In order to reduce the complexity of the flux quadrature, it is common to replace the two segments with

unit normals $\mathbf{n}_{0i,1}$ and $\mathbf{n}_{0i,2}$ by a single segment with unit normal $\hat{\mathbf{n}}_{0i}$, as shown in Fig. 3.8.[†]

$$\hat{\mathbf{n}}_{0i} = \frac{\mathbf{n}_{0i,1}\Delta s_{0i,1} + \mathbf{n}_{0i,2}\Delta s_{0i,2}}{\Delta s_{0i}}. \quad (3.6.2)$$

The superscript ‘^’ was chosen to reflect the fact that the normal consists of two straight segments. Equation (3.6.1) then becomes

$$A_{\Omega_0} \frac{dq_0}{dt} + \sum_{0i \in \mathcal{E}_0} [\mathbf{f}(\mathbf{q}) \cdot \hat{\mathbf{n}} - \mathbf{g}(\mathbf{q}, \nabla \mathbf{q}) \cdot \hat{\mathbf{n}}]_{0i} \Delta s_{0i} = \mathbf{s}(\mathbf{q}_0, (\nabla \mathbf{q})_0) A_{\Omega_0}. \quad (3.6.3)$$

Barth [3] showed that the simplification comes at the expense of reduced accuracy on irregular grids. The reduced accuracy must be caused by the numerical smoothing terms, as the centred part of the discretisation is treated exactly.

The complexity can be reduced further if the position of flux quadrature is not located at the midpoint of the simplified dual edge, but at the midpoint of the associated primal edge, as shown in Fig. 3.8(c). This simplification will introduce further errors into the flux quadrature. It is tacitly assumed that the reduced complexity offered by the two simplifications outweighs the reduced accuracy on distorted grids.

For the containment dual, each dual edge is a straight segment. The unit normal $\hat{\mathbf{n}}_{0i}$ is therefore simply equal to the normal of the straight segment. Only the second simplification is required.

Simplification of Flux Quadrature at Boundary of Solution Domain. The flux-quadrature points on boundaries are also modified. The theoretical position of the quadrature points for triangular points is as shown in Fig. 3.9(a).[‡] Two modifications of the flux quadrature points on boundaries are carried out.

First, the location of the quadrature points for the fluxes through the primal boundary edge is repositioned as shown in Fig. 3.9(b). The motivation is grid-transparency, since the modified location allows the boundary fluxes to be computed in the same manner irrespective of whether triangular or quadrilateral cells are on the boundary.

[†]On non-uniform triangular grids, this leads to a slight ambiguity. The redefined median-dual cells are identical to the centroid-dual cells (constructed by connecting centroids) but their areas are not identical.

[‡]The derivation is analogous to that of the Green-Gauss reconstruction on triangular grids in Subsection 3.7.2 by simply starting from the divergence theorem instead of the Green-Gauss theorem. No equivalent positions for the flux quadrature points on quadrilateral grids can be derived within the current data structure.

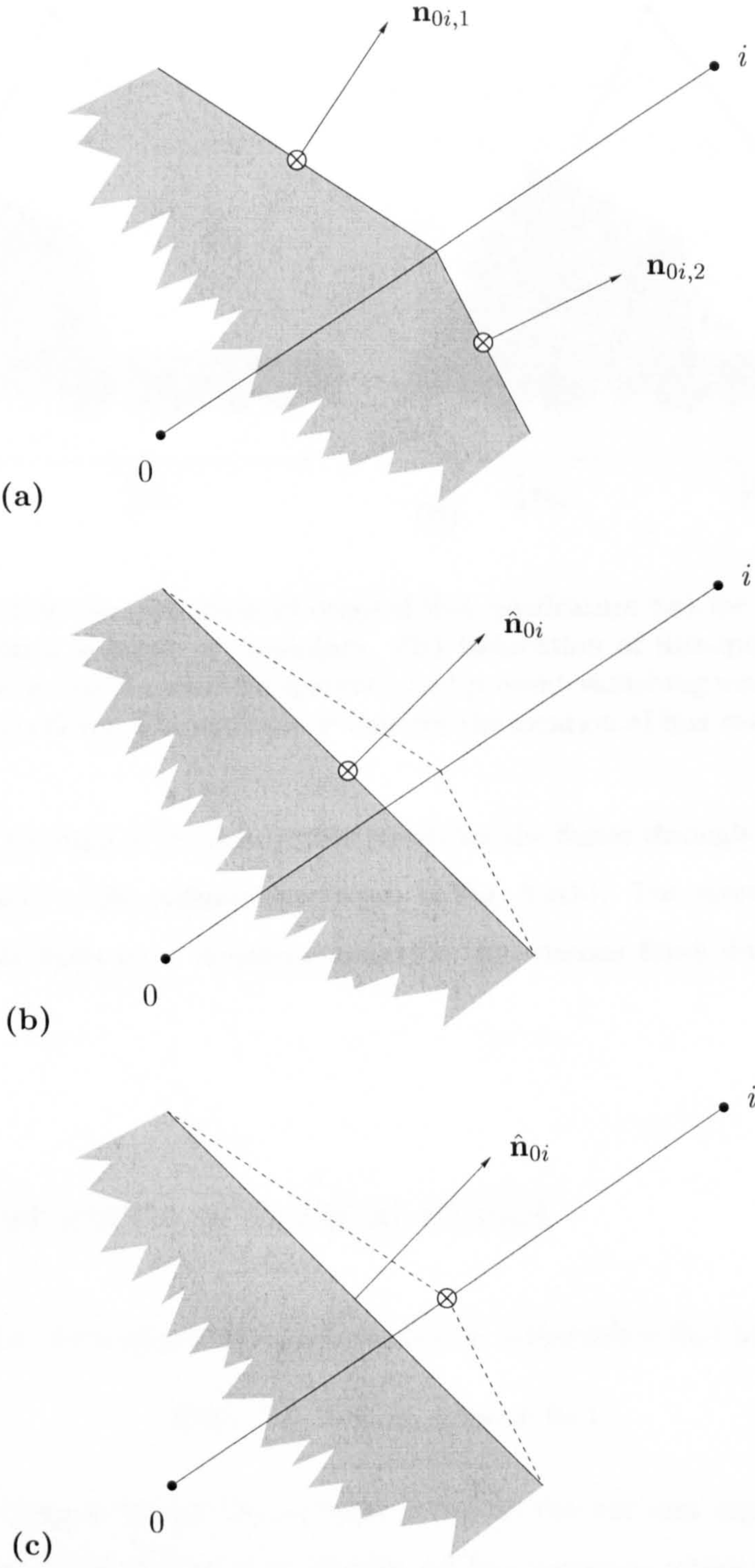


Figure 3.8: Simplification of original flux quadrature (a) for median-dual control volumes. (b) Approximation of dual edge by single straight segment. (c) Relocation of flux-quadrature location to midpoint of primal edge. The symbol ' \otimes ' denotes the location of flux evaluation. Normal vectors are not drawn to scale.

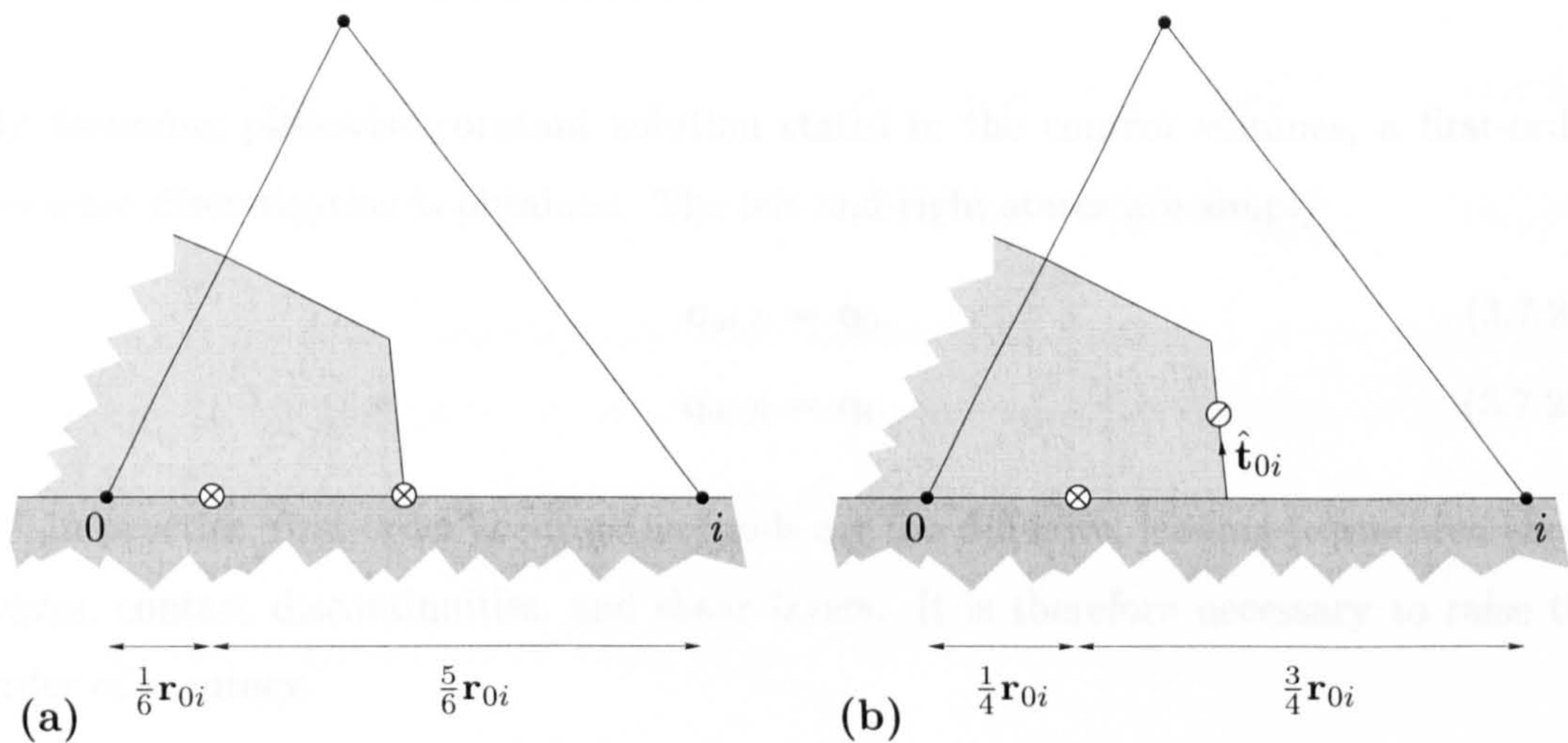


Figure 3.9: Simplification of original flux quadrature (a) for median-dual control volumes at boundary. (b) Relocation of flux-quadrature locations to enable grid-transparency and prevent vanishing mass fluxes for viscous flows. The symbol ‘ \otimes ’ denotes the location of flux evaluation.

Second, the location of the quadrature points for the fluxes through the dual boundary edge is moved to its midpoint as shown in Fig. 3.9(b). The reasoning is that its original position leads to a vanishing mass flux for viscous flows due to the no-slip condition.

3.7 Discretisation of Inviscid Fluxes

The inviscid flux at an edge $0i$ is approximated by a numerical flux function,

$$[\mathbf{f}(\mathbf{q}) \cdot \hat{\mathbf{n}}]_{0i} = \Phi(\mathbf{q}_{0i,L}, \mathbf{q}_{0i,R}; \hat{\mathbf{n}}_{0i}), \quad (3.7.1)$$

where $\mathbf{q}_{0i,L}$ and $\mathbf{q}_{0i,R}$ denote the solution states to the left and right of the control volume face associated with edge $0i$. Numerical flux functions which reconcile the two states at a control volume face to give a unique flux are called Riemann solvers.

The order of accuracy obtained by a particular numerical flux function is only dependent on how the left and right states are determined from surrounding solution states.

3.7.1 First-Order Discretisation

By assuming piecewise constant solution states in the control volumes, a first-order accurate discretisation is obtained. The left and right states are simply

$$\mathbf{q}_{0i,L} = \mathbf{q}_0, \quad (3.7.2a)$$

$$\mathbf{q}_{0i,R} = \mathbf{q}_i. \quad (3.7.2b)$$

In practice, first-order accurate methods are too diffusive, leading to smeared shock waves, contact discontinuities, and shear layers. It is therefore necessary to raise the order of accuracy.

3.7.2 Second-Order Discretisation

Second-order accuracy can be obtained by reconstructing a linear variation of the solution variables in each control volume. Equations (3.7.2a) and (3.7.2b) are replaced by

$$\mathbf{q}_{0i,L} = \mathbf{q}_0 + \frac{1}{2} \left[(1 - \kappa)(\nabla \mathbf{q})_0 \cdot \Delta \mathbf{r}_{0i} + \kappa(\mathbf{q}_i - \mathbf{q}_0) \right], \quad (3.7.3a)$$

$$\mathbf{q}_{0i,R} = \mathbf{q}_i - \frac{1}{2} \left[(1 - \kappa)(\nabla \mathbf{q})_i \cdot \Delta \mathbf{r}_{0i} + \kappa(\mathbf{q}_i - \mathbf{q}_0) \right], \quad (3.7.3b)$$

where $\Delta \mathbf{r}_{0i} = \mathbf{r}_i - \mathbf{r}_0$ and $(\nabla \mathbf{q})_0$ is the gradient at node 0. On uniform quadrilateral grids, these formulae reduce to the MUSCL extrapolation of van Leer [44].

Experience has shown that the use of the primitive state vector $\mathbf{p} = \{\rho, u, v, p\}^t$ in the reconstruction gives better results than the conservative state vector \mathbf{q} [20]. They are linked by a transformation matrix M ,

$$\mathbf{q} = M\mathbf{p}. \quad (3.7.4)$$

The transformation matrix and its inverse are given by

$$M = \begin{bmatrix} 1 & 0 & 0 & 0 \\ 0 & \rho & 0 & 0 \\ 0 & 0 & \rho & 0 \\ 0 & \frac{1}{2}\rho u & \frac{1}{2}\rho v & \frac{1}{\gamma-1} \end{bmatrix}, \quad M^{-1} = \begin{bmatrix} 1 & 0 & 0 & 0 \\ 0 & \frac{1}{\rho} & 0 & 0 \\ 0 & 0 & \frac{1}{\rho} & 0 \\ 0 & -\frac{\gamma-1}{2}u & -\frac{\gamma-1}{2}v & \gamma-1 \end{bmatrix}. \quad (3.7.5)$$

The actual reconstruction is therefore given by

$$\mathbf{q}_{0i,L} = M_{0i,L} \left\{ \mathbf{p}_0 + \frac{1}{2} \left[(1 - \kappa)(\nabla \mathbf{p})_0 \cdot \Delta \mathbf{r}_{0i} + \kappa(\mathbf{p}_i - \mathbf{p}_0) \right] \right\}, \quad (3.7.6a)$$

$$\mathbf{q}_{0i,R} = M_{0i,R} \left\{ \mathbf{p}_i - \frac{1}{2} \left[(1 - \kappa)(\nabla \mathbf{p})_i \cdot \Delta \mathbf{r}_{0i} + \kappa(\mathbf{p}_i - \mathbf{p}_0) \right] \right\}, \quad (3.7.6b)$$

where $M_{0i,L}$ and $M_{0i,R}$ are the transformation matrices evaluated at the states $\mathbf{p}_{0i,L}$ and $\mathbf{p}_{0i,R}$. In the present work, only $\kappa = 0$ was used, giving the scheme of Barth and Jespersen [6] in which only nodal gradients are used. In the framework of the MUSCL-scheme of van Leer [44], the reconstruction method of Barth and Jespersen corresponds to the scheme originally advanced by Fromm [14].

Remark 3.5: The use of nodal gradients corresponds to a centred approximation of gradients. This means that the state at vertex 0 does not influence the gradient at that vertex. Consequently, nodal gradients do not detect oscillations on the scale of the grid spacing on uniform grids. This is a more severe problem on quadrilateral grids since they allow more spurious solution modes than triangular grids. This problem could be circumvented by setting $\kappa \neq 0$, similar to the approaches advanced by the French research groups.

The solution states at the quadrature points for dual boundary edges are obtained from

$$\mathbf{q}_{0i,L} = M_{0i,L} \left[\mathbf{p}_0 + \frac{1}{2} (\nabla \mathbf{p})_0 \cdot (\Delta \mathbf{r}_{0i} + \Delta s_{0i} \hat{\mathbf{t}}_{0i}) \right], \quad (3.7.7)$$

where $\hat{\mathbf{t}}_{0i}$ is the unit tangent vector along the dual edge oriented such that $\hat{\mathbf{n}}_{0i} \times \hat{\mathbf{t}}_{0i} > 0$ as indicated in Fig. 3.9. The right solution state is obtained similarly.

Gradient Reconstruction. The variable to be reconstructed will be denoted by ϕ in order to emphasize that the reconstruction procedures may be used for purposes other than the higher-order inviscid fluxes.

Green-Gauss Reconstruction (Triangular Grids). This reconstruction procedure was suggested by Barth and Jespersen [6].

The Green-Gauss theorem

$$\int_{\Omega_{0'}} \nabla \phi dA = \oint_{\partial\Omega_{0'}} \phi \mathbf{n} ds \quad (3.7.8)$$

is applied to the region $0'$ formed by the union of triangles meeting at vertex 0. Equation (3.7.8) may then be approximated as

$$(\nabla \phi)_0 \approx \frac{1}{A_{\Omega_{0'}}} \oint_{\partial\Omega_{0'}} \phi \mathbf{n} ds. \quad (3.7.9)$$

Equation (3.7.9) is an exact relation if the function ϕ is linear.

At interior vertices, the contour integral is approximated by the trapezoidal rule to give

$$(\nabla \phi)_0 \approx \frac{1}{A_{\Omega_{0'}}} \sum_{i \in \mathcal{V}_0} \frac{1}{2} (\phi_i + \phi_{i+1}) \mathbf{n}_{i+1/2}, \quad (3.7.10)$$

where the notation is explained in Fig. 3.10, and it should be noted that $\mathbf{n}_{i+1/2}$ is a scaled normal vector. Since the sum is cyclic, a shift in the indices may be employed to rewrite the above equation as

$$(\nabla \phi)_0 \approx \frac{1}{A_{\Omega_{0'}}} \sum_{i \in \mathcal{V}_0} \frac{1}{2} \phi_i (\mathbf{n}_{i+1/2} + \mathbf{n}_{i-1/2}). \quad (3.7.11)$$

Since the sum of the normals is equal to zero, a constant value may be added to the summation, giving

$$(\nabla \phi)_0 \approx \frac{1}{A_{\Omega_{0'}}} \sum_{i \in \mathcal{V}_0} \frac{1}{2} (\phi_0 + \phi_i) (\mathbf{n}_{i+1/2} + \mathbf{n}_{i-1/2}). \quad (3.7.12)$$

Equation (3.7.12) may be rewritten using the identities

$$\mathbf{n}_{i+1/2} = 3\mathbf{n}_{0i,1} - \frac{1}{2}\mathbf{n}_{0i}, \quad (3.7.13a)$$

$$\mathbf{n}_{i-1/2} = 3\mathbf{n}_{0i,2} + \frac{1}{2}\mathbf{n}_{0i}, \quad (3.7.13b)$$

which follow directly from the definition of the median dual, to give

$$(\nabla \phi)_0 \approx \frac{1}{A_{\Omega_{0'}}} \sum_{i \in \mathcal{V}_0} \frac{3}{2} (\phi_0 + \phi_i) (\mathbf{n}_{0i,1} + \mathbf{n}_{0i,2}). \quad (3.7.14)$$

In other words, exploiting the compatibility with the edge-based data structure,

$$(\nabla \phi)_0 \approx \frac{3}{A_{\Omega_{0'}}} \sum_{0i \in \mathcal{E}_0} \frac{1}{2} (\phi_0 + \phi_i) \hat{\mathbf{n}}_{0i}. \quad (3.7.15)$$

By noting that $A_{\Omega_{0'}}/3$ is equal to the area A_{Ω_0} of the median-dual control volume at

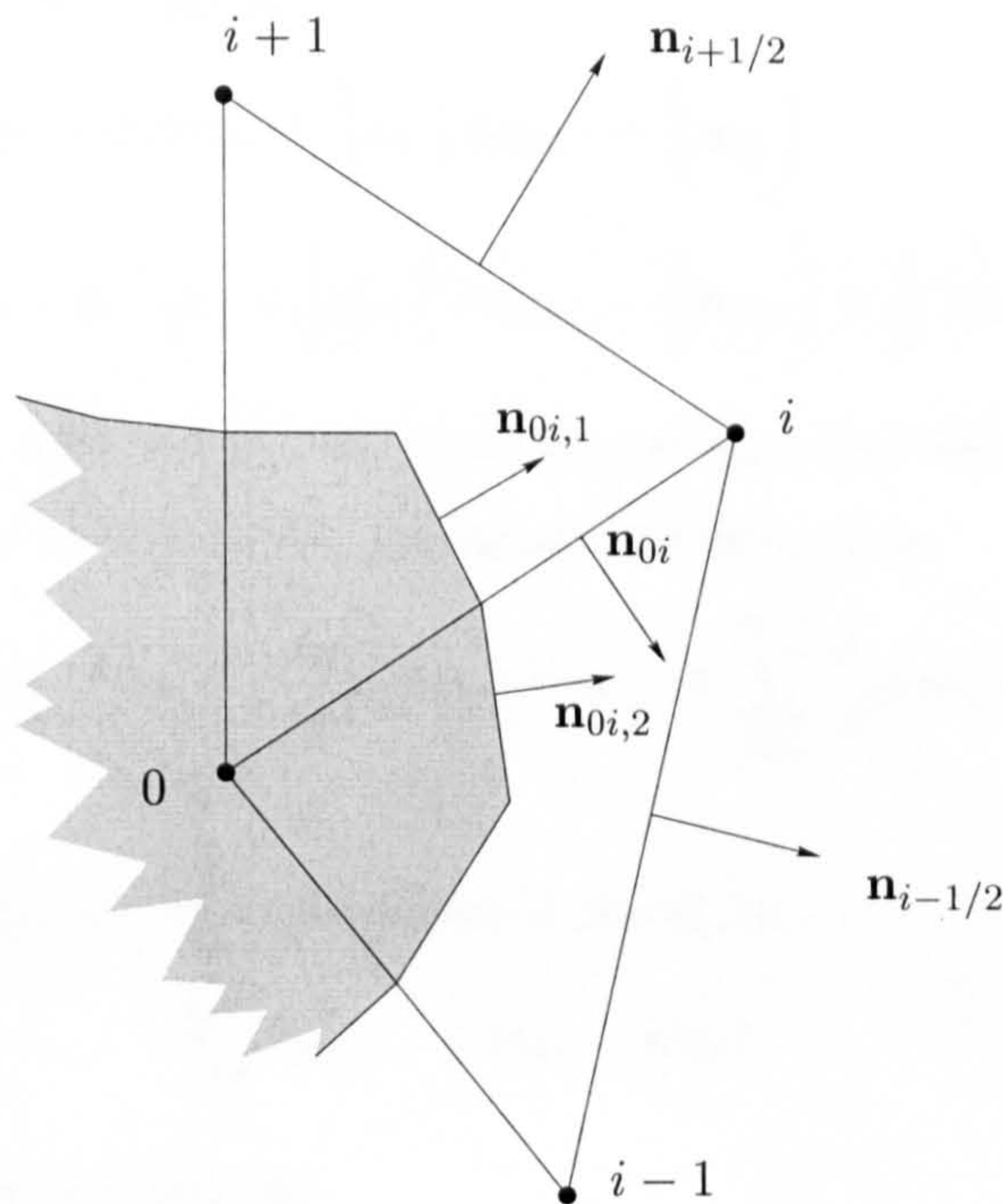


Figure 3.10: Definition of normal vectors used in derivation of Green-Gauss gradient reconstruction. Normal vectors are not drawn to scale.

vertex 0, Eq. (3.7.15) may be expressed as

$$(\nabla\phi)_0 \approx \frac{1}{A_{\Omega_0}} \sum_{0i \in \mathcal{E}_0} \frac{1}{2} (\phi_0 + \phi_i) \hat{\mathbf{n}}_{0i}. \quad (3.7.16)$$

If the vertex 0 lies on a boundary, additional terms arise from the boundary edges. In the derivation of these additional terms, reference is made to Fig. 3.11, in which the degree of vertex 0 is exaggerated for the purpose of illustration. At vertex 0 in Fig. 3.11, the equivalent of Eq. (3.7.10) is given by

$$(\nabla\phi)_0 \approx \frac{1}{A_{\Omega_{0'}}} \left[\frac{1}{2} (\phi_0 + \phi_1) \mathbf{n}_{01} + \sum_{i=1}^{m-1} \frac{1}{2} (\phi_i + \phi_{i+1}) \mathbf{n}_{i+1/2} + \frac{1}{2} (\phi_0 + \phi_m) \mathbf{n}_{0m} \right]. \quad (3.7.17)$$

Employing a shift in the indices, the summation may be rewritten as

$$\begin{aligned} (\nabla\phi)_0 \approx & \frac{1}{A_{\Omega_{0'}}} \left[\frac{1}{2} (\phi_0 + \phi_1) \mathbf{n}_{01} + \frac{1}{2} \phi_1 \mathbf{n}_{3/2} \right. \\ & \left. + \sum_{i=2}^{m-1} \frac{1}{2} \phi_i (\mathbf{n}_{i+1/2} + \mathbf{n}_{i-1/2}) + \frac{1}{2} \phi_m \mathbf{n}_{m-1/2} + \frac{1}{2} (\phi_0 + \phi_m) \mathbf{n}_{0m} \right]. \end{aligned} \quad (3.7.18)$$

Equation (3.7.18) may be recast as

$$(\nabla\phi)_0 \approx \frac{1}{A_{\Omega_0'}} \left[\frac{1}{2} (\phi_0 + \phi_1) \mathbf{n}_{01} + \frac{1}{2} \phi_1 \left(3\mathbf{n}_{01,1} - \frac{1}{2}\mathbf{n}_{01} \right) + \sum_{i=2}^{m-1} \frac{1}{2} \phi_i (\mathbf{n}_{i+1/2} + \mathbf{n}_{i-1/2}) + \frac{1}{2} \phi_m \left(3\mathbf{n}_{0m,2} - \frac{1}{2}\mathbf{n}_{0m} \right) + \frac{1}{2} (\phi_0 + \phi_m) \mathbf{n}_{0m} \right] \quad (3.7.19)$$

For the boundary edges, $\mathbf{n}_{01,1} = \hat{\mathbf{n}}_{01}$ and $\mathbf{n}_{0m,2} = \hat{\mathbf{n}}_{0m}$, and also using the identities given by Eqs. (3.7.13a) and (3.7.13b), the above equation gives

$$(\nabla\phi)_0 \approx \frac{1}{A_{\Omega_0'}} \left[\frac{1}{2} \phi_0 (\mathbf{n}_{01} + \mathbf{n}_{0m}) + \frac{1}{4} \phi_1 (6\hat{\mathbf{n}}_{01} + \mathbf{n}_{01}) + \sum_{i=2}^{m-1} \frac{3}{2} \phi_i \hat{\mathbf{n}}_{0i} + \frac{1}{4} \phi_m (6\hat{\mathbf{n}}_{0m} + \mathbf{n}_{0m}) \right]. \quad (3.7.20)$$

Using the condition that the control volume is closed, i.e.,

$$\sum_{i=1}^m \hat{\mathbf{n}}_{0i} = -\frac{1}{2} (\mathbf{n}_{01} + \mathbf{n}_{0m}), \quad (3.7.21)$$

Eq. (3.7.20) can be reformulated as

$$(\nabla\phi)_0 \approx \frac{1}{A_{\Omega_0'}} \left[\left(\frac{5}{4} \phi_0 + \frac{1}{4} \phi_1 \right) \mathbf{n}_{01} + \frac{3}{2} \sum_{i=1}^m (\phi_0 + \phi_i) \hat{\mathbf{n}}_{0i} + \left(\frac{5}{4} \phi_0 + \frac{1}{4} \phi_m \right) \mathbf{n}_{0m} \right], \quad (3.7.22)$$

which, upon using $A_{\Omega_0} = A_{\Omega_0'}/3$ may finally be expressed as

$$(\nabla\phi)_0 \approx \frac{1}{A_{\Omega_0}} \left[\frac{1}{2} \left(\frac{5}{6} \phi_0 + \frac{1}{6} \phi_1 \right) \mathbf{n}_{01} + \frac{1}{2} \sum_{i=1}^m (\phi_0 + \phi_i) \hat{\mathbf{n}}_{0i} + \frac{1}{2} \left(\frac{5}{6} \phi_0 + \frac{1}{6} \phi_m \right) \mathbf{n}_{0m} \right]. \quad (3.7.23)$$

The second term is easily recognised as that already derived for the interior edges, and the first and third terms represent the boundary contributions.

Remark 3.6: The so-called Hermitian interpolation used by French research groups [11] constructs gradients by an area-weighted summation of the gradients computed in the triangles meeting at a given vertex. This can be shown to be equivalent to the Green-Gauss reconstruction.

Remark 3.7: Equation (3.7.16) suggests a midpoint approximation around the median-dual control volume. As shown by the above derivation, it is actually equivalent to an approximation by the trapezoidal rule on the slightly larger region given by the union of the triangles meeting at vertex 0. However, on triangular grids with containment dual

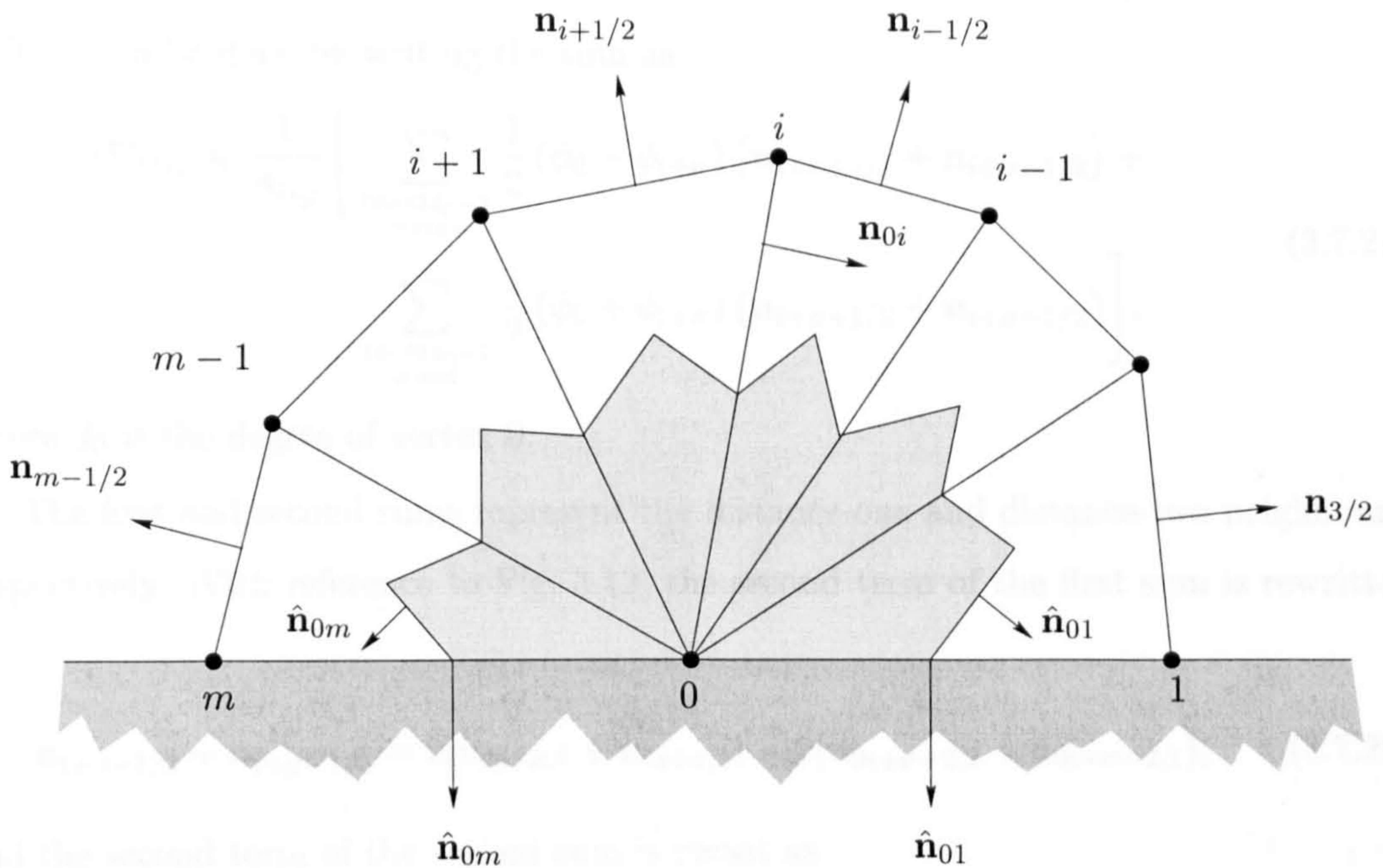


Figure 3.11: Nomenclature for Green-Gauss gradient reconstruction at boundary. Normal vectors are not drawn to scale.

control volumes, mixed and quadrilateral grids, Eq. (3.7.16) is equivalent to a midpoint approximation.

Green-Gauss Reconstruction (Quadrilateral Grids). As stated above, Eq. (3.7.16) can be used as a midpoint approximation around the control volume to the gradient on quadrilateral grids. Equation (3.7.16) is, however, not equivalent to the actual Green-Gauss reconstruction on quadrilateral grids. Therefore, it does not recover exact gradients for linear functions on arbitrary quadrilateral grids. It can be shown that exact gradients are computed on quadrilateral grids consisting of uniform parallelograms and trapeziums with two opposing edges of equal length due to error cancellation. Since neither of these cell shapes lead to quadrilateral grids usable in practice, this fortunate result is of rather academic importance.

It is instructive to derive the Green-Gauss reconstruction formula for quadrilateral grids. The derivation may be started from Eq. (3.7.12), because it does not contain any information on cell geometry. As for triangular grids, the derivation proceeds by reformulating the sum of the two normal vectors. However, in contrast to triangular

grids, the sum needs to be split into distance-one and distance-two neighbours of vertex 0. This can be done by writing the sum as

$$(\nabla\phi)_0 \approx \frac{1}{A_{\Omega_{0'}}} \left[\sum_{\substack{0 \leq \sigma \leq 62d_0-2 \\ \sigma \text{ even}}} \frac{1}{2} (\phi_0 + \phi_{i+\sigma}) (\mathbf{n}_{i+\sigma+1/2} + \mathbf{n}_{i+\sigma-1/2}) + \sum_{\substack{1 \leq \sigma \leq 62d_0-1 \\ \sigma \text{ odd}}} \frac{1}{2} (\phi_0 + \phi_{i+\sigma}) (\mathbf{n}_{i+\sigma+1/2} + \mathbf{n}_{i+\sigma-1/2}) \right], \quad (3.7.24)$$

where d_0 is the degree of vertex 0.

The first and second sums represent the distance-one and distance-two neighbours, respectively. With reference to Fig. 3.12, the second term of the first sum is rewritten as

$$\mathbf{n}_{i+\sigma+1/2} + \mathbf{n}_{i+\sigma-1/2} = 2(\mathbf{n}_{0i+\sigma,1} + \mathbf{n}_{0i+\sigma,2}) - 2(\mathbf{n}_{0i+\sigma+2,2} + \mathbf{n}_{0i+\sigma-2,1}), \quad (3.7.25)$$

and the second term of the second sum is recast as

$$\mathbf{n}_{i+\sigma+1/2} + \mathbf{n}_{i+\sigma-1/2} = 2(\mathbf{n}_{0i+\sigma-1,1} + \mathbf{n}_{0i+\sigma+1,2}). \quad (3.7.26)$$

Substituting Eqs. (3.7.25) and (3.7.26) into Eq. (3.7.24) gives

$$(\nabla\phi)_0 \approx \frac{2}{A_{\Omega_{0'}}} \left\{ \sum_{\substack{0 \leq \sigma \leq 62d_0-2 \\ \sigma \text{ even}}} \frac{1}{2} (\phi_0 + \phi_{i+\sigma}) [\mathbf{n}_{0i+\sigma,1} + \mathbf{n}_{0i+\sigma,2} - (\mathbf{n}_{0i+\sigma+2,2} + \mathbf{n}_{0i+\sigma-2,1})] + \sum_{\substack{1 \leq \sigma \leq 62d_0-1 \\ \sigma \text{ odd}}} \frac{1}{2} (\phi_0 + \phi_{i+\sigma}) (\mathbf{n}_{0i+\sigma-1,1} + \mathbf{n}_{0i+\sigma+1,2}) \right\}. \quad (3.7.27)$$

With the usual definition of the dual edge associated with edge $0i$ and the assumption of a uniform quadrilateral grid, where $\hat{\mathbf{n}}_{0i+\sigma+2,2} + \hat{\mathbf{n}}_{0i+\sigma-2,1} = 0$, the above equation becomes

$$(\nabla\phi)_0 \approx \frac{2}{A_{\Omega_{0'}}} \left[\underbrace{\sum_{\substack{0 \leq \sigma \leq 62d_0-2 \\ \sigma \text{ even}}} \frac{1}{2} (\phi_0 + \phi_{i+\sigma}) \hat{\mathbf{n}}_{0i+\sigma}}_{\text{component of edge } 0i} + \underbrace{\sum_{\substack{1 \leq \sigma \leq 62d_0-1 \\ \sigma \text{ odd}}} \frac{1}{2} (\phi_0 + \phi_{i+\sigma}) (\mathbf{n}_{0i+\sigma-1,1} + \mathbf{n}_{0i+\sigma+1,2})}_{\text{component of virtual edge}} \right]. \quad (3.7.28)$$

The gradient may thus be regarded as being composed of a sum over the dual edges of the grid and a sum over virtual edges, which link the distance-two neighbours to

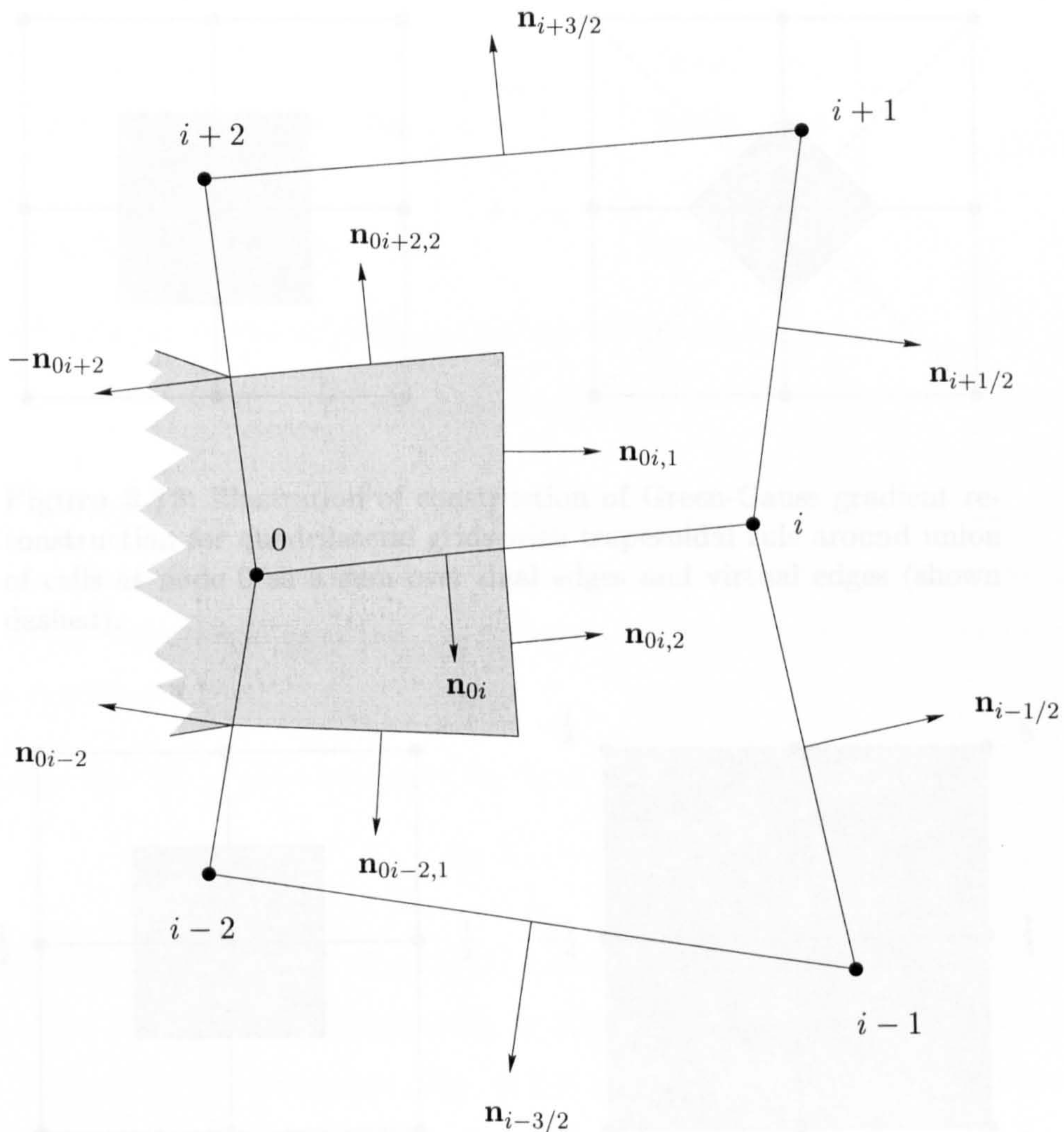


Figure 3.12: Nomenclature for Green-Gauss gradient reconstruction on quadrilateral grid. Normal vectors are not drawn to scale.

vertex 0, as illustrated in Fig. 3.13. In order to implement this scheme on quadrilateral grids, additional data structure arrays would be required. As argued in Section 3.5 on grid-transparency, this can lead to considerable additional memory requirements, thus defeating the original objective of attempting to treat different cell types with a data structure of minimal extent. For this reason, this scheme was not used in the present work, and Eq. (3.7.16) is used irrespective of the cell type.

The differences in the stencil weights between Eqs. (3.7.16) and (3.7.28) for the x -derivative is illustrated in Fig. 3.14. It is interesting to note that Eq. (3.7.28) reduces to Eq. (3.7.16) if the contributions by the virtual edges are assumed to be equal to those

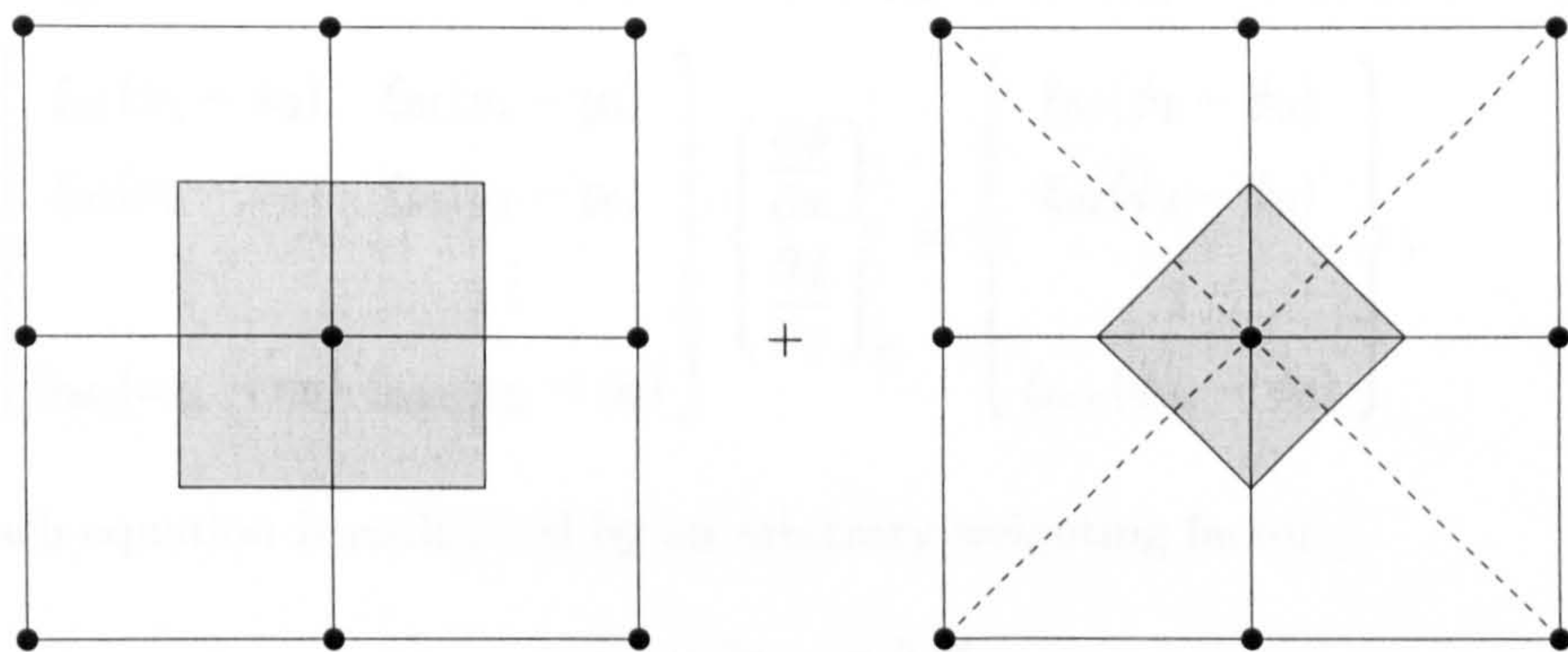


Figure 3.13: Illustration of construction of Green-Gauss gradient reconstruction for quadrilateral grids with trapezoidal rule around union of cells at node 0 as a sum over dual edges and virtual edges (shown dashed).

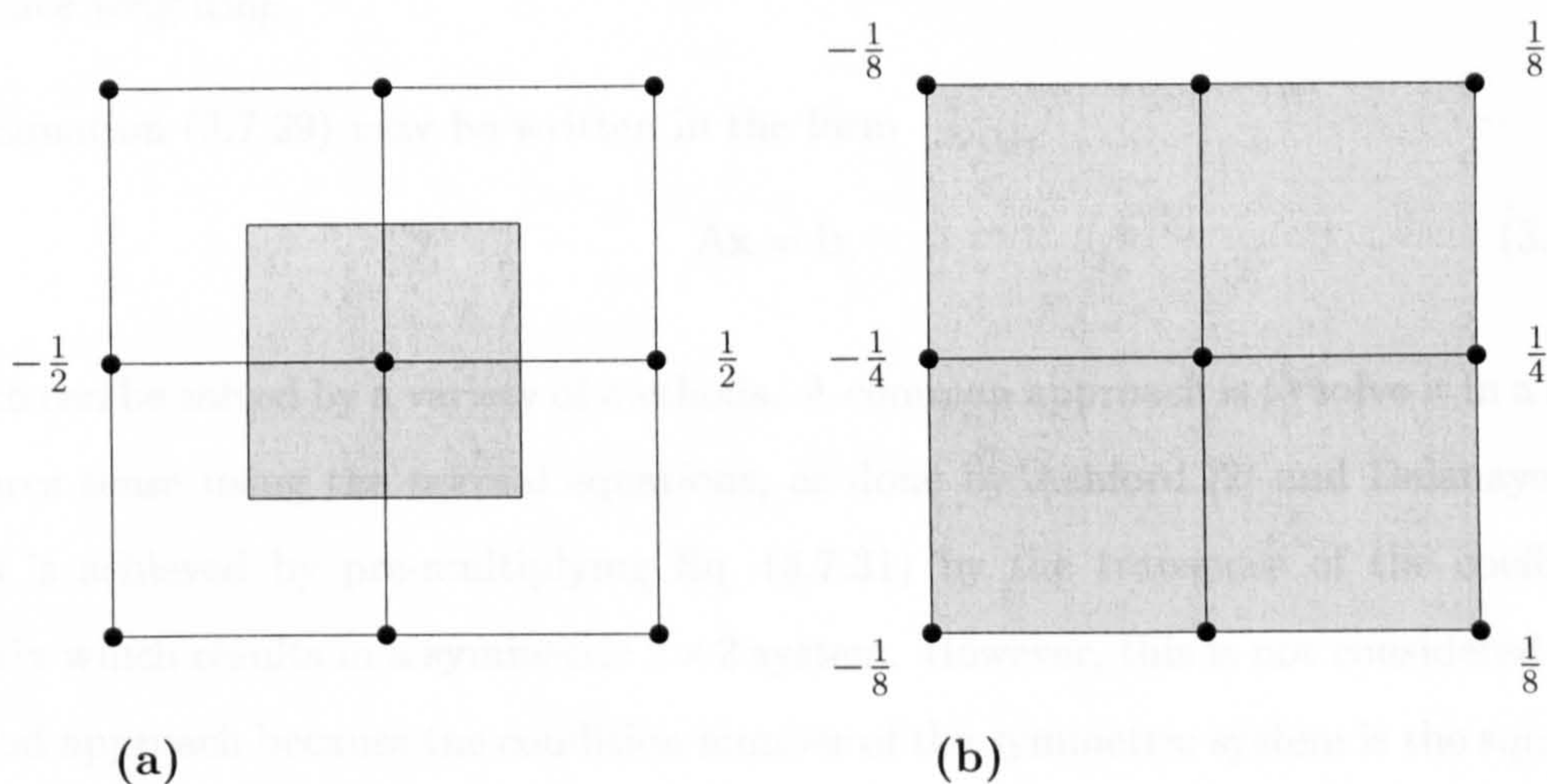


Figure 3.14: Comparison of stencils obtained with Green-Gauss reconstruction of x -derivative for uniform quadrilateral grids with (a) mid-point rule around control volume and (b) trapezoidal rule around union of cells meeting at node 0.

of the actual edges.

Müller and Giles [29] recently used a concept similar to virtual edges to derive a version of the Green-Gauss method which reconstructs gradients of linear functions exactly on quadrilateral grids.

Least-Squares Reconstruction. A truncated Taylor series may be applied to each of the

d_0 edge-neighbours of vertex 0. This results in the following overdetermined system

$$\begin{bmatrix} \xi_{01}(x_1 - x_0) & \xi_{01}(y_1 - y_0) \\ \xi_{02}(x_2 - x_0) & \xi_{02}(y_2 - y_0) \\ \vdots & \vdots \\ \xi_{0d_0}(x_{d_0} - x_0) & \xi_{0d_0}(y_{d_0} - y_0) \end{bmatrix} \begin{Bmatrix} \frac{\partial \phi}{\partial x} \\ \frac{\partial \phi}{\partial y} \end{Bmatrix}_0 = \begin{Bmatrix} \xi_{01}(\phi_1 - \phi_0) \\ \xi_{02}(\phi_2 - \phi_0) \\ \vdots \\ \xi_{0d_0}(\phi_{d_0} - \phi_0) \end{Bmatrix}, \quad (3.7.29)$$

where each equation is multiplied by an arbitrary weighting factor

$$\xi_{0i} = \|\mathbf{r}_i - \mathbf{r}_0\|^{-p}, \quad (3.7.30)$$

with $p \geq 0$. For $p = 0$, the reconstruction is referred to as unweighted linear least-squares, otherwise as weighted linear least-squares. The weighting factors can be used to reduce the influence of more distant vertices. For example, $p = 1$ gives inverse-distance weighting.

Equation (3.7.29) may be written in the form

$$\mathbf{A}\mathbf{x} = \mathbf{b}, \quad (3.7.31)$$

which can be solved by a variety of methods. A common approach is to solve it in a least-squares sense using the normal equations, as done by Ashford [2] and Delanaye [10]. This is achieved by pre-multiplying Eq. (3.7.31) by the transpose of the coefficient matrix which results in a symmetric 2×2 system. However, this is not considered to be a good approach because the condition number of the symmetric system is the square of that of Eq. (3.7.31). This means that the gradient calculation may become inaccurate on highly stretched grids.

An approach which does not suffer from this limitation is to factor the matrix \mathbf{A} using the QR-decomposition

$$\mathbf{A} = \mathbf{Q}\mathbf{R} \quad (3.7.32)$$

into an $d_0 \times 2$ orthogonal matrix \mathbf{Q} and a 2×2 upper triangular matrix \mathbf{R} as suggested by Anderson and Bonhaus [1]. The QR-decomposition is carried out using the classical Gram-Schmidt method described in Golub and van Loan [16].

The decomposition may be derived explicitly. The derivation starts by writing Eq.

(3.7.32) in column form

$$\begin{bmatrix} \mathbf{a}_1 & \mathbf{a}_2 \end{bmatrix} = \begin{bmatrix} \mathbf{q}_1 & \mathbf{q}_2 \end{bmatrix} \begin{bmatrix} r_{11,0} & r_{12,0} \\ 0 & r_{22,0} \end{bmatrix}.$$

In other words,

$$\mathbf{a}_1 = r_{11,0} \mathbf{q}_1 \quad (3.7.33a)$$

$$\mathbf{a}_2 = r_{12,0} \mathbf{q}_1 + r_{22,0} \mathbf{q}_2, \quad (3.7.33b)$$

which can be inverted to give

$$\mathbf{q}_1 = \frac{\mathbf{a}_1}{r_{11,0}} \quad (3.7.34a)$$

$$\mathbf{q}_2 = \frac{\mathbf{a}_2}{r_{22,0}} - \frac{r_{12,0}}{r_{11,0} r_{22,0}} \mathbf{a}_1. \quad (3.7.34b)$$

From Eq. (3.7.34a),

$$\mathbf{q}_1 \equiv \frac{\mathbf{a}_1}{\|\mathbf{a}_1\|} = \frac{\mathbf{a}_1}{r_{11,0}}, \quad (3.7.35)$$

where $r_{11,0}$ follows from Eq. (3.7.29)

$$r_{11,0} \equiv \sqrt{\sum_{0i \in \mathcal{E}_0} \xi_{0i}^2 (x_i - x_0)^2}. \quad (3.7.36)$$

In addition, define

$$\mathbf{a}'_2 \equiv \mathbf{a}_2 - (\mathbf{a}_2 \cdot \mathbf{q}_1) \mathbf{q}_1, \quad (3.7.37)$$

and

$$\mathbf{q}_2 \equiv \frac{\mathbf{a}'_2}{\|\mathbf{a}'_2\|}. \quad (3.7.38)$$

Using Eq. (3.7.35), Eq. (3.7.37) can be rewritten as

$$\mathbf{a}'_2 = \mathbf{a}_2 - \left(\mathbf{a}_2 \cdot \frac{\mathbf{a}_1}{r_{11,0}} \right) \frac{\mathbf{a}_1}{r_{11,0}} \quad (3.7.39a)$$

$$= \mathbf{a}_2 - \frac{1}{r_{11,0}} \sum_{0i \in \mathcal{E}_0} \xi_{0i}^2 (x_i - x_0)(y_i - y_0) \frac{\mathbf{a}_1}{r_{11,0}}. \quad (3.7.39b)$$

Define r_{12} as

$$r_{12} \equiv \frac{1}{r_{11,0}} \sum_{0i \in \mathcal{E}_0} \xi_{0i}^2 (x_i - x_0)(y_i - y_0) \quad (3.7.40)$$

and rewrite Eq. (3.7.39b) as

$$\mathbf{a}'_2 = \mathbf{a}_2 - \frac{r_{12,0}}{r_{11,0}} \mathbf{a}_1. \quad (3.7.41)$$

This gives

$$\|\mathbf{a}'_2\|^2 = \mathbf{a}_2 \cdot \mathbf{a}_2 - 2 \frac{r_{12,0}}{r_{11,0}} \mathbf{a}_1 \cdot \mathbf{a}_2 + \left(\frac{r_{12,0}}{r_{11,0}} \right)^2 \mathbf{a}_1 \cdot \mathbf{a}_1 \quad (3.7.42a)$$

$$= \sum_{0i \in \mathcal{E}_0} \xi_{0i}^2 (y_i - y_0)^2 - r_{12}^2 \quad (3.7.42b)$$

and define $r_{22,0}$ as

$$r_{22,0} \equiv \sqrt{\sum_{0i \in \mathcal{E}_0} \xi_{0i}^2 (y_i - y_0)^2 - r_{12}^2}, \quad (3.7.43)$$

so that both \mathbf{q}_1 and \mathbf{q}_2 are defined.

The solution to $\mathbf{Ax} = \mathbf{b}$ therefore follows from Eq. (3.7.32) as

$$\mathbf{x} = \mathbf{R}^{-1} \mathbf{Q}^t \mathbf{b}. \quad (3.7.44)$$

Using the results derived above, this can be written as

$$\mathbf{x} = \sum_{0i \in \mathcal{E}_0} \left\{ \begin{array}{c} \frac{\xi_{0i}^2}{r_{11,0}^2} (x_i - x_0) - \frac{\xi_{0i}^2 r_{12,0}}{r_{11,0} r_{22,0}^2} \left[(y_i - y_0) - \frac{r_{12,0}}{r_{11,0}} (x_i - x_0) \right] \\ \frac{\xi_{0i}^2}{r_{22,0}^2} (y_i - y_0) - \frac{\xi_{0i}^2 r_{12,0}}{r_{11,0} r_{22,0}^2} (x_i - x_0) \end{array} \right\} (\phi_i - \phi_0) \quad (3.7.45)$$

The gradients at vertex 0 may therefore be computed by a loop over edges

$$(\nabla \phi)_0 \approx \sum_{0i \in \mathcal{E}_0} \omega_{0i} (\phi_i - \phi_0) \quad (3.7.46)$$

where $\omega_{0i} = \{\omega_{x,0i}, \omega_{y,0i}\}^t$ is the vector of edge weights. Its components are given by

$$\omega_{x,0i} = \frac{\xi_{0i}^2}{r_{11,0}^2} (x_i - x_0) - \frac{\xi_{0i}^2 r_{12,0}}{r_{11,0} r_{22,0}^2} \left[(y_i - y_0) - (x_i - x_0) \frac{r_{12,0}}{r_{11,0}} \right] \quad (3.7.47a)$$

$$\omega_{y,0i} = \frac{\xi_{0i}^2}{r_{22,0}^2} \left[(y_i - y_0) - (x_i - x_0) \frac{r_{12,0}}{r_{11,0}} \right]. \quad (3.7.47b)$$

where $r_{11,0}$, $r_{12,0}$, and $r_{22,0}$ are defined by Eqs. (3.7.36), (3.7.40), and (3.7.43), respectively. By pre-computing and storing $r_{11,0}$, $r_{12,0}$, and $r_{22,0}$, the gradient may be computed by a single loop over the edges. The gradient of a linear function is computed exactly by design for arbitrary grids. The least-squares reconstruction has the additional advantage that no special treatment is required at boundaries.

On highly stretched grids, it might be expected that the repeated use of coordi-

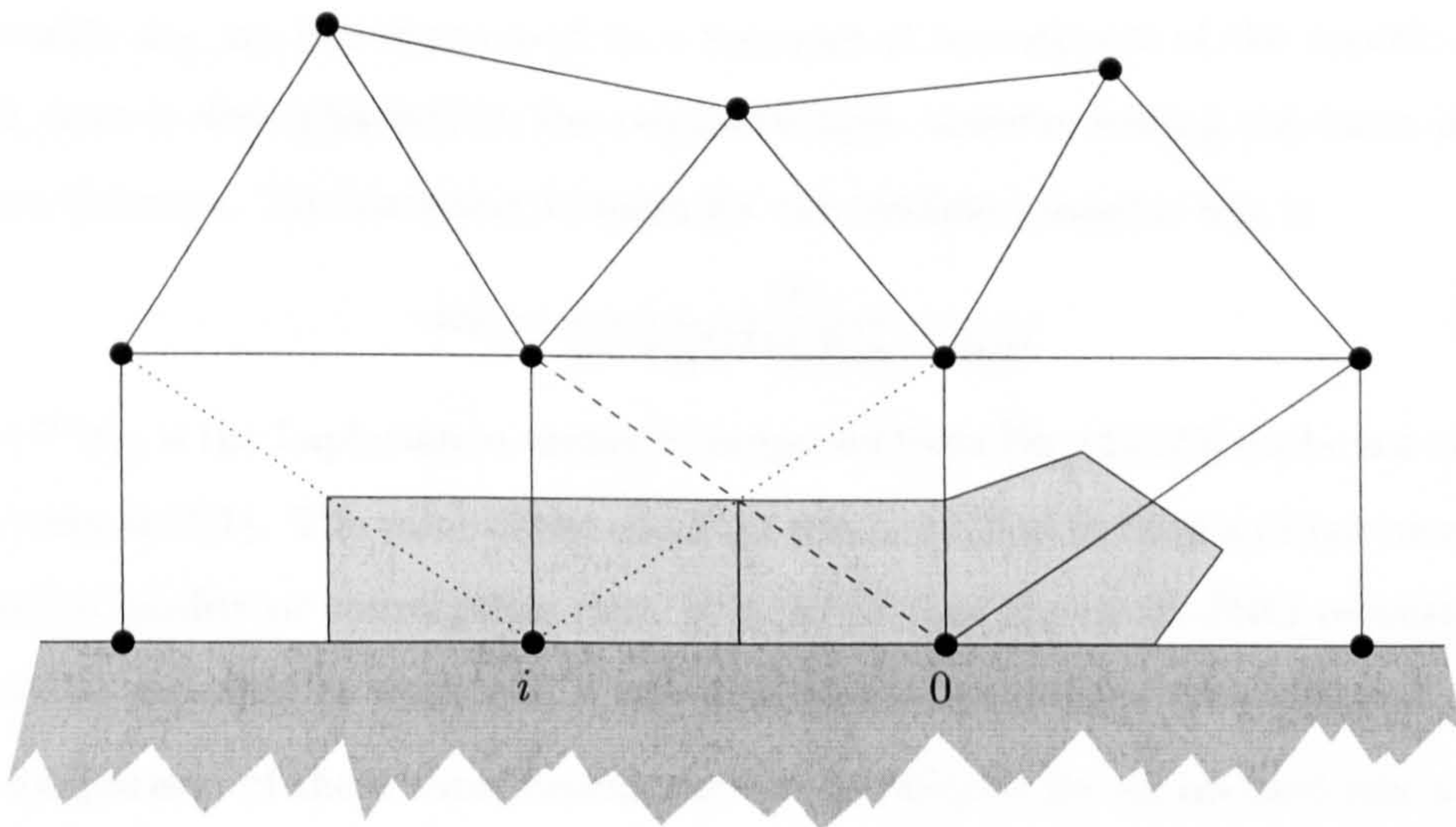


Figure 3.15: Virtual edges are inserted into quadrilateral cells on boundaries to increase the support of least-squares gradient reconstruction. Virtual edges at vertex i are shown dotted, whereas the virtual edge at vertex 0 is shown dashed.

nate differences of widely varying magnitude could lead to inaccurate weights. It has been verified that the differences in the computed weights between single- and double-precision arithmetic are negligible even on highly stretched grids.

The weights for the least-squares reconstruction in three dimensions were derived by Haselbacher and Blažek [19].

Virtual Edges. When using quadrilateral cells near flat boundaries, the gradient normal to the boundary is computed from a single edge. This is in contrast to triangular cells, where at least two edges can be used to compute the gradient. In some cases, this increased support on triangular grids was found to lead to slightly better results than on quadrilateral grids when least-squares reconstruction was used. This observation prompted the construction of virtual edges, which are additional edges inserted into the quadrilateral cells on boundaries, as illustrated in Fig. 3.15. The virtual edges require only one additional integer data structure array. The concept of virtual edges was first used by Haselbacher and Blažek [19].

Quasi-ENO Reconstruction. Ollivier-Gooch [30] suggested a quasi-ENO reconstruction scheme. It is based on the weighted linear least-squares reconstruction described above.

The weights ω_{0i} are modified based on a measure of smoothness of the function. Non-smooth data is deemphasised in the reconstruction, thereby having the same effect as a limiter function. The resulting formula for the modified weights $\bar{\omega}_{0i}$ is

$$\bar{\omega}_{0i} = \frac{\omega_{0i}}{1 + c|(\nabla^2 \phi)_0|(\phi_i - \phi_0)^2} \quad (3.7.48)$$

where $(\nabla^2 \phi)_0$ is the Laplacian at vertex 0 computed from Eq. (4.2.20) and c is a constant whose value is $O(1)$. The value of the constant was not found to have a pronounced effect on solution quality or convergence rate. It is noted that the quasi-ENO reconstruction can only be expected to work well if non-dimensional quantities are employed.

A comparison of these three reconstruction techniques for an inviscid test case can be found in Chapter 6.

Limiter Functions. Unfortunately, second-order accurate schemes show oscillations in regions of high gradients. This is a consequence of Godunov's Theorem which states that no linear higher-order scheme can be monotone [20]. It is therefore necessary to make higher-order schemes non-linear. The non-linearity is introduced by so-called limiter functions. They reduce the order of accuracy to first order in regions of high solution gradients, thus preventing oscillations.

When using higher-order discretisations in conjunction with Green-Gauss or least-squares reconstruction, Eqs. (3.7.6a) and (3.7.6b) are modified to give

$$\mathbf{q}_{0i,L} = M_{0i,L} \left\{ \mathbf{p}_0 + \frac{1}{2} \lambda_0(\mathbf{p}) \left[(1 - \kappa)(\nabla \mathbf{p})_0 \cdot \Delta \mathbf{r}_{0i} + \kappa(\mathbf{p}_i - \mathbf{p}_0) \right] \right\} \quad (3.7.49a)$$

$$\mathbf{q}_{0i,R} = M_{0i,R} \left\{ \mathbf{p}_i - \frac{1}{2} \lambda_i(\mathbf{p}) \left[(1 - \kappa)(\nabla \mathbf{p})_i \cdot \Delta \mathbf{r}_{0i} + \kappa(\mathbf{p}_i - \mathbf{p}_0) \right] \right\}, \quad (3.7.49b)$$

where $0 \leq \lambda_0(\mathbf{p}) \leq 1$ is the limiter function at vertex 0.

Conditions for Monotonic Solutions. Before turning to the definition of the limiter functions, it is instructive to derive the conditions under which the solution of a scalar convection equation will be monotone. The derivation is patterned after Barth [5] and uses the fact that a discretisation of the form

$$\frac{d\phi_0}{dt} = \sum_{0i \in \mathcal{E}_0} \omega_{0i}(\phi_i - \phi_0) \quad (3.7.50)$$

will be monotone if the edge weights $\omega_{0i} \geq 0$. Positive edge weights ensure monotonic-

ity because, if ϕ_0 is a local maximum (minimum) over the extent of the stencil, ϕ_0 will decrease (increase). This is equivalent to the local extremum diminishing (LED) conditions of Jameson [22].

The derivation starts from the semi-discretised form

$$A_{\Omega_0} \frac{d\phi_0}{dt} = - \sum_{0i \in \mathcal{E}_0} \Phi(\phi_{0i,L}, \phi_{0i,R}; \hat{\mathbf{n}}_{0i}) \Delta s_{0i}. \quad (3.7.51)$$

It is assumed that the numerical flux function may be written as

$$\Phi(\phi_{0i,L}, \phi_{0i,R}; \hat{\mathbf{n}}_{0i}) = \frac{1}{2} (f(\phi_{0i,L}) + f(\phi_{0i,R})) \cdot \hat{\mathbf{n}}_{0i} - \frac{1}{2} |d(\phi_{0i,L}, \phi_{0i,R}; \hat{\mathbf{n}}_{0i})| (\phi_{0i,R} - \phi_{0i,L}) \quad (3.7.52)$$

and that it is based on the linearisation (cf. Roe linearisation, Eq. (3.7.70))

$$(f(\phi_{0i,R}) - f(\phi_{0i,L})) \cdot \hat{\mathbf{n}}_{0i} = d(\phi_{0i,L}, \phi_{0i,R}; \hat{\mathbf{n}}_{0i}) (\phi_{0i,R} - \phi_{0i,L}). \quad (3.7.53)$$

If the following definitions

$$d(\phi_{0i,L}, \phi_{0i,R}; \hat{\mathbf{n}}_{0i}) = d^+(\phi_{0i,L}, \phi_{0i,R}; \hat{\mathbf{n}}_{0i}) + d^-(\phi_{0i,L}, \phi_{0i,R}; \hat{\mathbf{n}}_{0i}) \quad (3.7.54a)$$

$$|d(\phi_{0i,L}, \phi_{0i,R}; \hat{\mathbf{n}}_{0i})| = d^+(\phi_{0i,L}, \phi_{0i,R}; \hat{\mathbf{n}}_{0i}) - d^-(\phi_{0i,L}, \phi_{0i,R}; \hat{\mathbf{n}}_{0i}) \quad (3.7.54b)$$

are used, then Eq. (3.7.51) can be written as

$$A_{\Omega_0} \frac{d\phi_0}{dt} = - \sum_{0i \in \mathcal{E}_0} [f(\phi_{0i,L}) \cdot \hat{\mathbf{n}}_{0i} + d^-(\phi_{0i,L}, \phi_{0i,R}; \hat{\mathbf{n}}_{0i}) (\phi_{0i,R} - \phi_{0i,L})] \Delta s_{0i}. \quad (3.7.55)$$

Application of Eq. (3.7.53) to the states ‘0i, L’ and ‘0,’ and the fact that the summation of a constant term is identically equal to zero, gives

$$A_{\Omega_0} \frac{d\phi_0}{dt} = - \sum_{0i \in \mathcal{E}_0} [d_{0,L}^+(\phi_{0i,L} - \phi_0) + d_{0,L}^-(\phi_{0i,L} - \phi_0) + d_{L,R}^-(\phi_{0i,R} - \phi_{0i,L})] \Delta s_{0i}, \quad (3.7.56)$$

where the abbreviations

$$d_{0,L}^+ = d^+(\phi_0, \phi_{0i,L}; \hat{\mathbf{n}}_{0i}) \quad (3.7.57a)$$

$$d_{0,L}^- = d^-(\phi_0, \phi_{0i,L}; \hat{\mathbf{n}}_{0i}) \quad (3.7.57b)$$

$$d_{L,R}^- = d^-(\phi_{0i,R}, \phi_{0i,L}; \hat{\mathbf{n}}_{0i}) \quad (3.7.57c)$$

were introduced. By defining the ratios of solution gradients (which are tacitly assumed

to exist),

$$\Xi_{0ik} = \frac{\phi_{0i,L} - \phi_0}{\phi_0 - \phi_k} \quad (3.7.58a)$$

$$\Psi_{0i} = \frac{\phi_{0i,L} - \phi_0}{\phi_i - \phi_0} \quad (3.7.58b)$$

$$\Theta_{0i} = \frac{\phi_{0i,R} - \phi_{0i,L}}{\phi_i - \phi_0} \quad (3.7.58c)$$

where $k \in \mathcal{V}_0$, Eq. (3.7.56) may be written as

$$A_{\Omega_0} \frac{d\phi_0}{dt} = \sum_{0i \in \mathcal{E}_0} \left[d_{0,L}^+ \Xi_{0ik} (\phi_k - \phi_0) - d_{0,L}^- \Psi_{0i} (\phi_i - \phi_0) - d_{L,R}^- \Theta_{0i} (\phi_i - \phi_0) \right] \Delta s_{0i}. \quad (3.7.59)$$

Because $d^\pm(\phi_0, \phi_{0i,L}; \hat{n}_{0i}) \geq 0$, the solution will be monotone if, $\forall i \in \mathcal{V}_0$,

$$\Xi_{0ik} \geq 0 \quad (3.7.60a)$$

$$\Psi_{0i} \geq 0 \quad (3.7.60b)$$

$$\Theta_{0i} \geq 0. \quad (3.7.60c)$$

It is important to note that the first two conditions are local to each control volume, but the third condition must be satisfied at each control-volume face. Therefore, the third condition is non-local. The inequality given by Eq. (3.7.60a) should be interpreted as: find any $k \in \mathcal{V}_0$ such that the inequality exists.

Remark 3.8: The reason for introducing the difference $(\phi_0 - \phi_k)$ in Eq. (3.7.58a) is to avoid a contradiction. Using the difference $(\phi_0 - \phi_i)$ would lead to

$$\Xi_{0i} \equiv \frac{\phi_{0i,L} - \phi_0}{\phi_0 - \phi_i} = -\Psi_{0i},$$

and it would be impossible for both Ξ_{0i} and Ψ_{0i} to be positive.

The first two conditions may be satisfied by requiring that

$$\min_{0i \in \mathcal{E}_0} (\phi_0, \phi_i) \leq \phi_{0i,L} \leq \max_{0i \in \mathcal{E}_0} (\phi_0, \phi_i), \quad (3.7.61)$$

or, using Eq. (3.7.49a),

$$\min_{0i \in \mathcal{E}_0} (\phi_0, \phi_i) - \phi_0 \leq \frac{1}{2} \lambda_0(\phi) (\nabla \phi)_0 \cdot \Delta \mathbf{r}_{0i} \leq \max_{0i \in \mathcal{E}_0} (\phi_0, \phi_i) - \phi_0. \quad (3.7.62)$$

The third condition is not strictly enforced; see the comments in Barth [4]. This can

lead to small oscillations near strong unsteady shock waves, see, e.g., the comments in Sonar [37].

The aim is to find the largest value of $\lambda_0(\phi)$ which ensures that the value of the reconstructed function inside the control volume at vertex 0 is bounded by the function values at vertex 0 and at the neighbouring vertices i . The current algorithm employs the limiter functions of Barth and Jespersen [6] or Venkatakrishnan [47].

Barth and Jespersen Limiter Function. The limiter function of Barth and Jespersen is computed by considering the edges incident to vertex 0 and the unlimited values of the variable ϕ_{0i} at the face $0i$,

$$\phi_{0i} = \phi_0 + \frac{1}{2}(\nabla\phi)_0 \cdot \Delta\mathbf{r}_{0i}, \quad (3.7.63)$$

where the subscript ' L ' was omitted for convenience. By defining

$$\phi_{\max} = \max_{0i \in \mathcal{E}_0}(\phi_0, \phi_i) \quad (3.7.64a)$$

$$\phi_{\min} = \min_{0i \in \mathcal{E}_0}(\phi_0, \phi_i) \quad (3.7.64b)$$

$$\Delta_{1,\max} = \phi_{\max} - \phi_0 \quad (3.7.64c)$$

$$\Delta_{1,\min} = \phi_{\min} - \phi_0 \quad (3.7.64d)$$

$$\Delta_2 = \phi_{0i} - \phi_0, \quad (3.7.64e)$$

the conditions given by Eq. (3.7.62) with $\lambda_0(\phi)$ can be expressed as

$$\Delta_{1,\min} \leq \lambda_0(\phi) \Delta_2 \leq \Delta_{1,\max}, \quad (3.7.65)$$

where the limiter function associated with vertex 0 is defined as the minimum of the limiter function applied to the edges incident to vertex 0,

$$\lambda_0(\phi) = \min_{0i \in \mathcal{E}_0} \lambda_{0i}(\phi). \quad (3.7.66)$$

The limiter function λ_{0i} associated with edge $0i$ is given by

$$\lambda_{0i}(\phi) = \begin{cases} \min\left(1, \frac{\Delta_{1,\max}}{\Delta_2}\right) & \text{if } \Delta_2 > 0 \\ \min\left(1, \frac{\Delta_{1,\min}}{\Delta_2}\right) & \text{if } \Delta_2 < 0 \\ 1 & \text{if } \Delta_2 = 0. \end{cases} \quad (3.7.67)$$

The limiter function of Barth and Jespersen strictly enforces monotonicity (with the

above proviso) but may deteriorate convergence. Venkatakrishnan [47] showed that the deterioration of convergence is caused by the limiter function reacting to machine-level noise in regions where the solution variables are nearly constant.

Venkatakrishnan Limiter Function. The limiter function of Venkatakrishnan [47] provides improved convergence behaviour at the expense of strict monotonicity. Using the same notation as above, the limiter function is defined by

$$\lambda_{0i}(\phi) = \begin{cases} \frac{1}{\Delta_2} \frac{(\Delta_{1,\max}^2 + \varepsilon^2)\Delta_2 + 2\Delta_2^2\Delta_{1,\max}}{\Delta_{1,\max}^2 + 2\Delta_2^2 + \Delta_{1,\max}\Delta_2 + \varepsilon^2} & \text{if } \Delta_2 > 0 \\ \frac{1}{\Delta_2} \frac{(\Delta_{1,\min}^2 + \varepsilon^2)\Delta_2 + 2\Delta_2^2\Delta_{1,\min}}{\Delta_{1,\min}^2 + 2\Delta_2^2 + \Delta_{1,\min}\Delta_2 + \varepsilon^2} & \text{if } \Delta_2 < 0 \\ 1 & \text{if } \Delta_2 = 0 \end{cases} \quad (3.7.68)$$

where $\varepsilon^2 = (Kh)^3$, K is a constant of $O(1)$, and h is an estimate of the local grid spacing. In the present work, h is taken as the square-root of the control-volume area. Note that the above definition of ε can be expected to work well only if non-dimensional quantities are used. The limiter function at node 0 is again computed from Eq. (3.7.66).

The effect of the variable ε on the limiter function can be illustrated in one dimension by considering an extremum of the reconstructed function to occur at vertex 0. Assume that the magnitude of the gradient along each edge is equal to c , as depicted in Fig. 3.16. Then the Barth-Jespersen limiter function gives $\lambda_0(\phi) = 0$ to ensure a monotonic reconstruction. In contrast, the Venkatakrishnan limiter function gives

$$\lambda_0(\phi) = \frac{K^3}{\frac{c^2}{2h} + K^3},$$

thus allowing an extremum to occur in the reconstructed function unless $K = 0$.

In practice, it was found that while convergence with the limiter function of Barth and Jespersen may stall convergence after a reduction of about one order of magnitude in the residual norms, Venkatakrishnan's limiter function allows reductions of the residual norms of around four orders of magnitude in single-precision arithmetic.

3.7.3 Numerical Flux Function

Various approximate Riemann solvers were implemented in the numerical method described in this chapter. Of these, only the flux-difference splitting of Roe [34] is described, as numerical experiments not reported here indicated that it offered the best

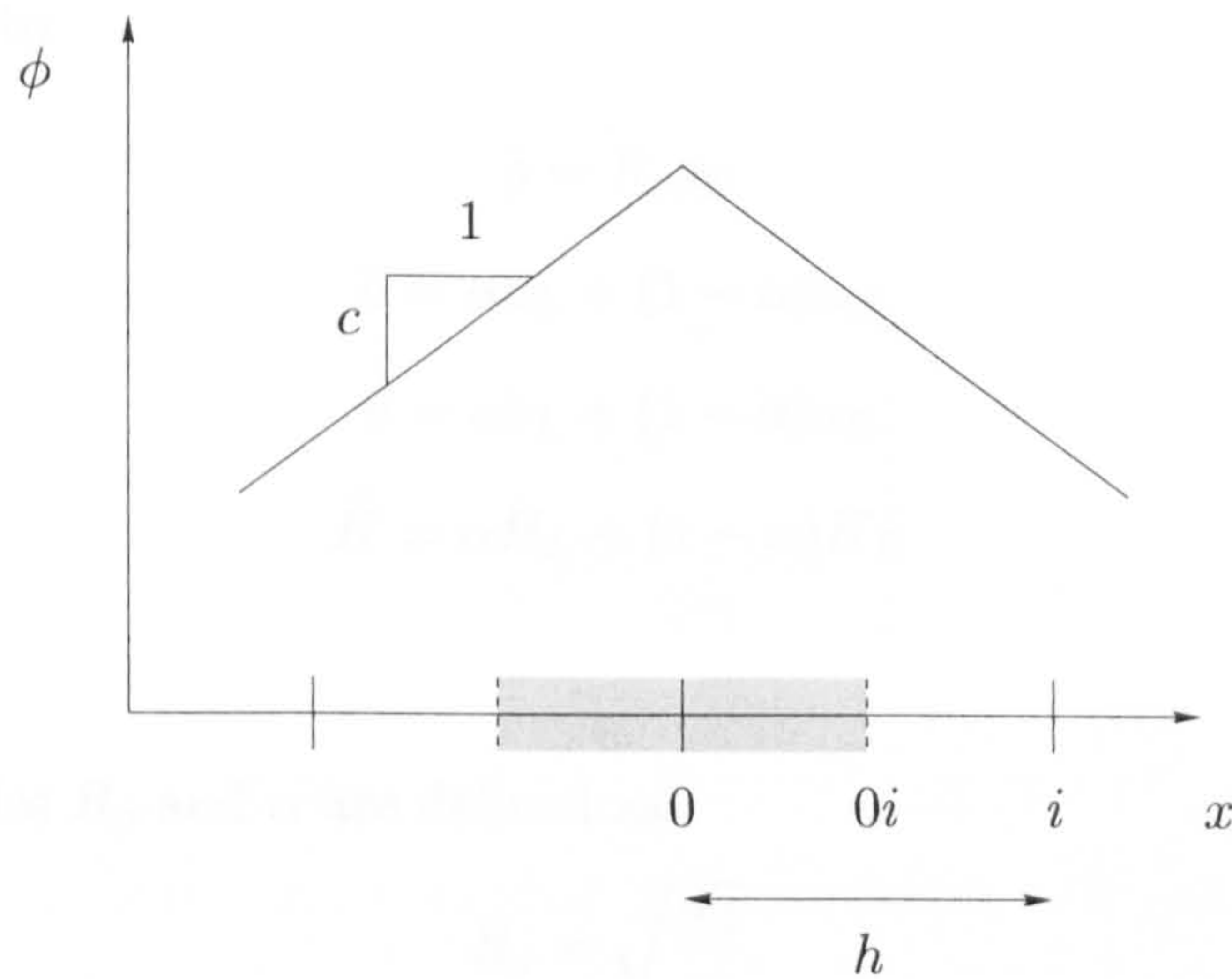


Figure 3.16: Function used to illustrate difference between Barth-Jespersen and Venkatakrishnan limiter functions.

compromise between solution quality and computational cost.

In this subsection, the subscript ‘0i’ is dropped for the sake of simplicity.

Roe Flux-Difference Splitting. The flux-difference splitting of Roe [34] is given by the numerical flux function

$$\Phi(\mathbf{q}_L, \mathbf{q}_R; \mathbf{n}) = \frac{1}{2} [\mathbf{f}(\mathbf{q}_L) + \mathbf{f}(\mathbf{q}_R)] \cdot \mathbf{n} - \frac{1}{2} |\hat{\mathbf{A}}(\mathbf{q}_L, \mathbf{q}_R)| (\mathbf{q}_R - \mathbf{q}_L) \cdot \mathbf{n}, \quad (3.7.69)$$

where the matrix $\hat{\mathbf{A}}(\mathbf{q}_L, \mathbf{q}_R)$ is constructed such that the following conditions are fulfilled.

1. For any pair \mathbf{q}_L and \mathbf{q}_R

$$\mathbf{f}(\mathbf{q}_R) - \mathbf{f}(\mathbf{q}_L) = \hat{\mathbf{A}}(\mathbf{q}_L, \mathbf{q}_R)(\mathbf{q}_R - \mathbf{q}_L), \quad (3.7.70)$$

allowing exact representation of isolated discontinuities.

2. If $\mathbf{q}_L = \mathbf{q}_R = \mathbf{q}$ then $\hat{\mathbf{A}}(\mathbf{q}, \mathbf{q}) = \mathbf{A}(\mathbf{q})$, where \mathbf{A} is the Jacobian of the inviscid flux vector, guaranteeing that the approximate solution is exact if the left and right states are equal.
3. The matrix $\hat{\mathbf{A}}$ has real eigenvalues and linearly independent eigenvectors, ensuring that the linearised system is hyperbolic.

Roe showed that these properties can be achieved if the Jacobian matrix \mathbf{A} is formed

at the state given by

$$\hat{\rho} = R_\rho \rho_L \quad (3.7.71a)$$

$$\hat{u} = \alpha u_L + (1 - \alpha) u_R \quad (3.7.71b)$$

$$\hat{v} = \alpha v_L + (1 - \alpha) v_R \quad (3.7.71c)$$

$$\hat{H} = \alpha H_L + (1 - \alpha) H_R \quad (3.7.71d)$$

where the quantities R_ρ and α are defined as

$$R_\rho = \sqrt{\frac{\rho_R}{\rho_L}}, \quad (3.7.72)$$

and

$$\alpha = \frac{1}{1 + R_\rho}. \quad (3.7.73)$$

In practice, it is common to rewrite the dissipation term in terms of the eigenvalues, the right eigenvector matrix and the wave strengths as

$$\Phi(\mathbf{q}_L, \mathbf{q}_R; \mathbf{n}) = \frac{1}{2} [\mathbf{f}(\mathbf{q}_L) + \mathbf{f}(\mathbf{q}_R)] \cdot \mathbf{n} - \frac{1}{2} \sum_{i=1}^4 |\hat{\lambda}_i| \Delta \hat{\mathbf{V}}_i \hat{\mathbf{R}}_i \quad (3.7.74)$$

where

$$\hat{\lambda} = \begin{pmatrix} \hat{q} - \hat{a} \\ \hat{q} \\ \hat{q} \\ \hat{q} + \hat{a} \end{pmatrix} \quad (3.7.75)$$

and where $\hat{\mathbf{R}}$ is the matrix whose columns are the right eigenvectors

$$\hat{\mathbf{R}} = \begin{bmatrix} 1 & 0 & 1 & 1 \\ \hat{u} - n_x \hat{a} & -n_y \hat{a} & \hat{u} & \hat{u} + n_x \hat{a} \\ \hat{v} - n_y \hat{a} & n_x \hat{a} & \hat{v} & \hat{v} + n_y \hat{a} \\ \hat{H} - \hat{q} \hat{a} & \hat{r} \hat{a} & \frac{1}{2}(\hat{u}^2 + \hat{v}^2) & \hat{H} + \hat{q} \hat{a} \end{bmatrix} \quad (3.7.76)$$

and

$$\Delta \hat{\mathbf{V}} = \begin{Bmatrix} \frac{\Delta p - \hat{\rho} \hat{a} \Delta q}{2 \hat{a}^2} \\ \frac{\hat{\rho} \Delta r}{\hat{a}} \\ \Delta \rho - \frac{\Delta p}{\hat{a}^2} \\ \frac{\Delta p + \hat{\rho} \hat{a} \Delta q}{2 \hat{a}^2} \end{Bmatrix} \quad (3.7.77)$$

where $\Delta(\cdot) = (\cdot)_R - (\cdot)_L$. In Eqs. (3.7.75), (3.7.76), and (3.7.77), q and r denote the components of the velocity vector normal and tangential to a given normal vector \mathbf{n} respectively,

$$q = \mathbf{v} \cdot \mathbf{n} = un_x + vn_y \quad (3.7.78a)$$

$$r = \mathbf{v} \cdot \mathbf{t} = un_y - vn_x. \quad (3.7.78b)$$

Entropy Fix. Roe's flux-difference splitting captures isolated normal shock waves and contact discontinuities exactly by design. Unfortunately, discontinuous expansions are also recognised as valid solutions because Roe's scheme does not satisfy an entropy inequality. This makes a so-called entropy fix necessary, of which several forms have been proposed. In the present work, the entropy fix of van Leer et al. [45] was adopted.

The acoustic eigenvalues are modified according to

$$|\hat{\lambda}| = \begin{cases} |\hat{\lambda}| & \text{if } |\hat{\lambda}| \geq \delta\lambda/2 \\ \frac{\hat{\lambda}^2}{\delta\lambda} + \frac{\delta\lambda}{4} & \text{if } |\hat{\lambda}| < \delta\lambda/2 \end{cases} \quad (3.7.79)$$

where $\delta\lambda$ is a threshold to prevent the acoustic eigenvalues from going to zero and is given by

$$\delta\lambda = \max[4(\lambda_R - \lambda_L), 0]. \quad (3.7.80)$$

Grid Transparency. The discretisation of the inviscid fluxes is grid transparent as the loops are carried out over edges only.

3.8 Discretisation of Viscous Fluxes

The discretisation of viscous fluxes on mixed unstructured grids is discussed in detail in Chapter 4.

3.9 Discretisation of Spalart-Allmaras Turbulence Model

To enhance stability and robustness, the convection term is approximated by a first-order scheme. The diffusion terms are discretised using Scheme 2 described in Subsection 4.2.5. The source terms are assumed to be constant over the control volume. Limiting procedures to ensure the positivity of $\tilde{\nu}$ were not found to be necessary.

3.9.1 Computation of Distance Function

The distance function is defined as the function which gives the shortest distance to a solid wall for each interior vertex. By reference to Fig. 3.17, the value $d_{A,0i}$ of the distance function at vertex A due to the boundary edge $0i$ is given by

$$d_{A,0i} = \begin{cases} \Delta \mathbf{r}_{A0} & \text{if } \omega_{A,0i} < 0 \\ \Delta \mathbf{r}_{AjA} & \text{if } 0 \leq \omega_{A,0i} \leq 1 \\ \Delta \mathbf{r}_{Ai} & \text{if } \omega_{A,0i} > 1 \end{cases} \quad (3.9.1)$$

where

$$\Delta \mathbf{r}_{AjA} = \Delta \mathbf{r}_{A0} - \omega_{A,0i} \Delta \mathbf{r}_{0i}, \quad (3.9.2)$$

and

$$\omega_{A,0i} = \frac{\|\Delta \mathbf{r}_{jA0}\|}{\|\Delta \mathbf{r}_{0i}\|} = \frac{\Delta \mathbf{r}_{A0} \cdot \Delta \mathbf{r}_{0i}}{\|\Delta \mathbf{r}_{0i}\|^2}. \quad (3.9.3)$$

The distance function d_A is then given by the minimum of all $d_{A,0i}$ computed for all boundary edges on solid walls, i.e.,

$$d_A = \min_{0i} d_{A,0i}. \quad (3.9.4)$$

The distance function for vertex B is computed in an analogous fashion.

In the present implementation, the distance function is computed in a preprocessing step by nested loops over all vertices and boundary edges on solid walls. This is a

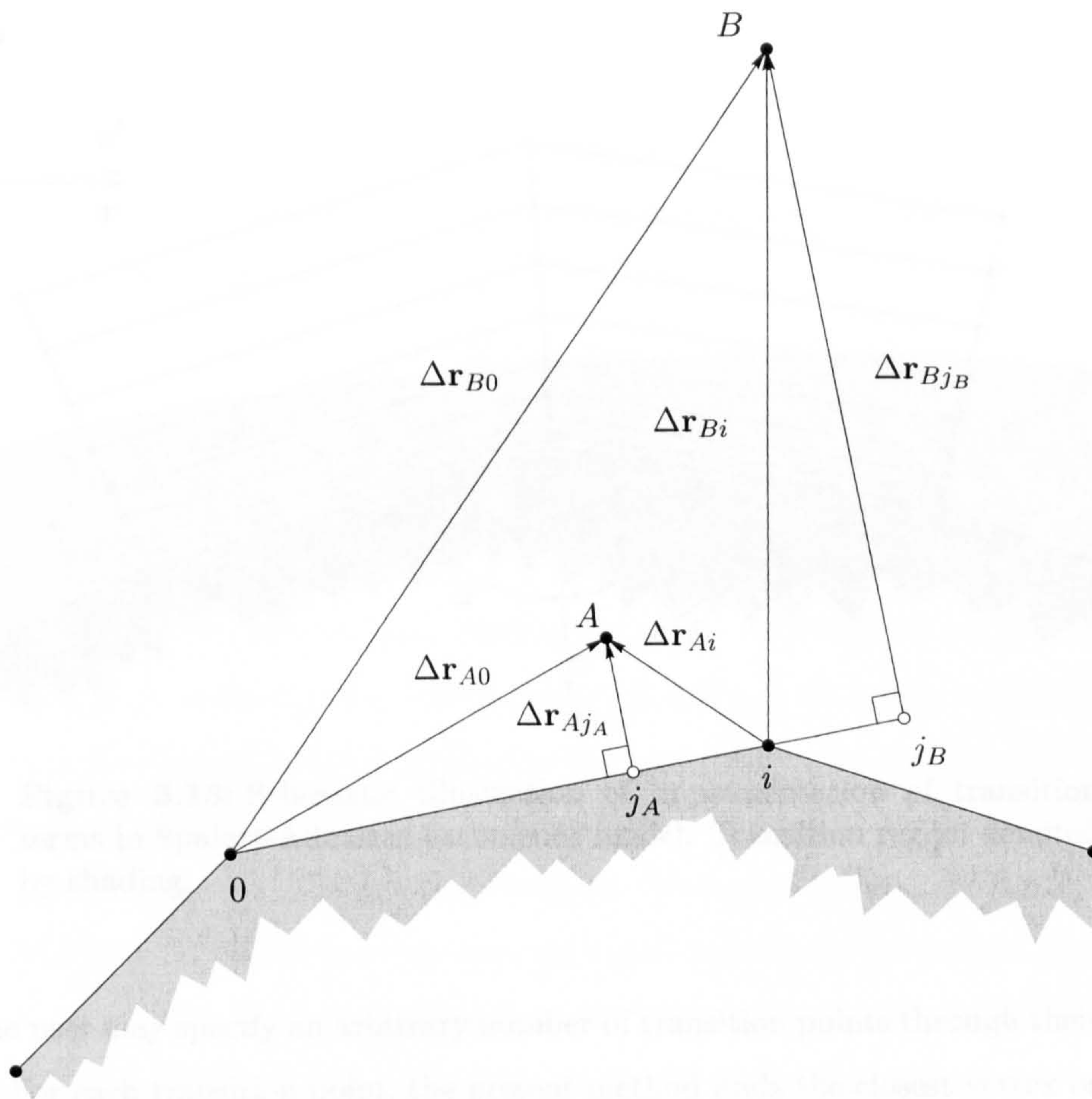


Figure 3.17: Illustration of computation of distance function for Spalart-Allmaras turbulence model.

simplistic implementation since the cost of computing the distance function can become considerable.

Wigton [51] described a fast algorithm for computing the distance function. Menter et al. [28] suggested solving a Poisson equation for the distance function in the vicinity of solid walls.

3.9.2 Treatment of Transition Terms

Transition from laminar to turbulent flow can be simulated in the Spalart-Allmaras turbulence model using the dedicated source terms. These extra terms are only active locally in the immediate vicinity of the transition location. The facility of specifying transition within the Spalart-Allmaras model seems to have been seldom used so far. For this reason, the current implementation is described briefly.

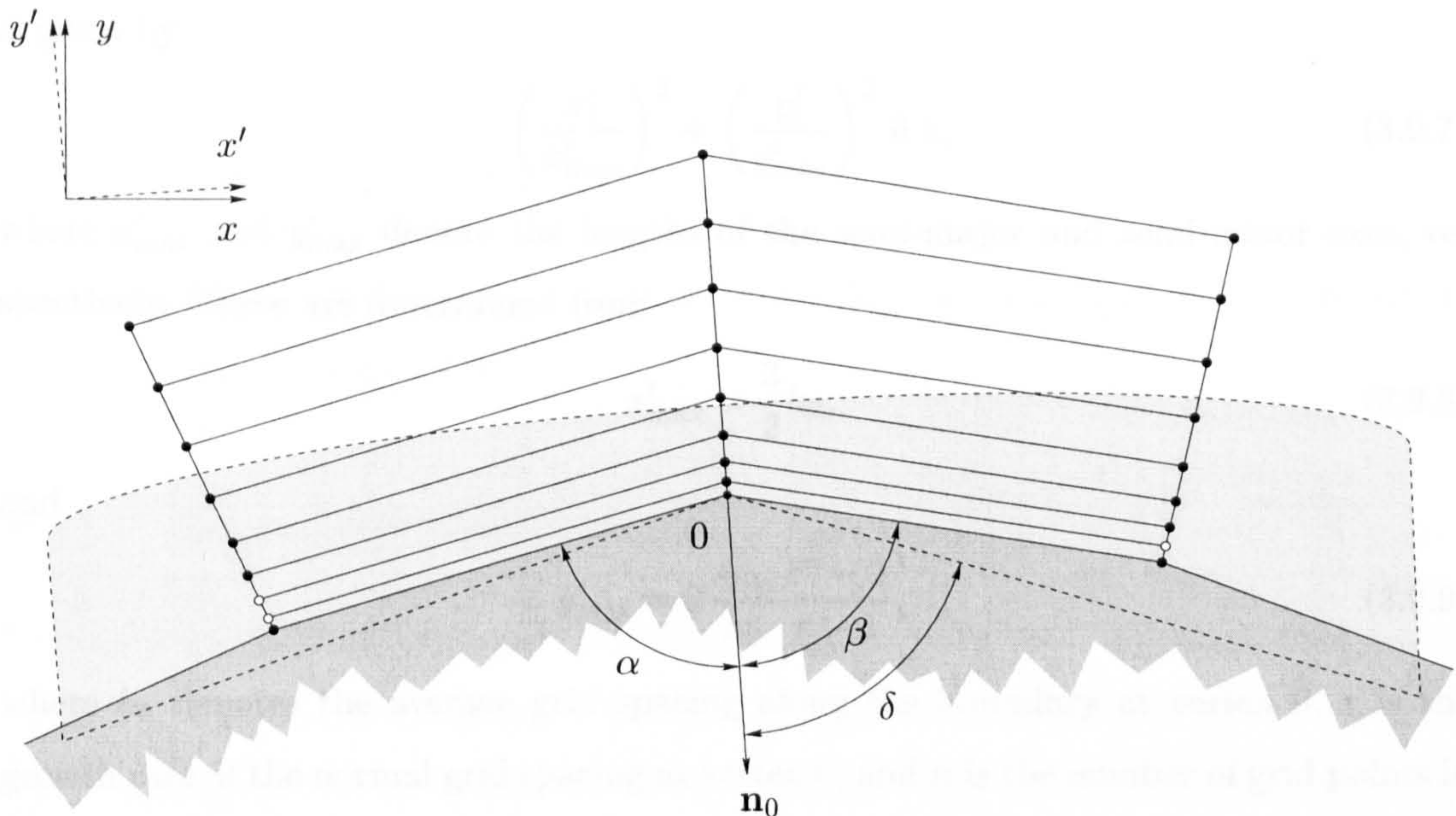


Figure 3.18: Schematic illustration of implementation of transition terms in Spalart-Allmaras turbulence model. Transition region denoted by shading.

The user may specify an arbitrary number of transition points through their coordinates. For each transition point, the present method finds the closest vertex on a solid boundary. In the following, such a vertex is designated as a transition vertex, marked as ‘0’ in Fig. 3.18. To determine the region in which the extra source terms are to be active, a local coordinate system (x', y') is first constructed. This is done by the simple linear coordinate transformation

$$\begin{Bmatrix} x' \\ y' \end{Bmatrix} = \begin{bmatrix} \cos \theta & \sin \theta \\ -\sin \theta & \cos \theta \end{bmatrix} \begin{Bmatrix} x - x_0 \\ y - y_0 \end{Bmatrix}, \quad (3.9.5)$$

where the angle θ is given by

$$\tan \theta = -\frac{n_{x,0}}{n_{y,0}}, \quad (3.9.6)$$

and where $n_{x,0}$ and $n_{y,0}$ are the components of the outward-pointing normal vector \mathbf{n}_0 at the transition vertex. This transformation aligns the y' -axis with the negative direction of the outward-pointing unit normal \mathbf{n}_0 .

The local coordinate system is used to define a so-called transition ellipse, which includes the points which are to be part of the transition region. The transition ellipse

is given by

$$\left(\frac{x'_i}{x'_{\max}}\right)^2 + \left(\frac{y'_i}{y'_{\max}}\right)^2 \leq 1, \quad (3.9.7)$$

where x'_{\max} and y'_{\max} denote the lengths of the semi-major and semi-minor axes, respectively. These are determined from

$$x'_{\max} = \frac{3}{2}h_0, \quad (3.9.8)$$

and

$$y'_{\max} = 2\frac{A_{\Omega_0}}{h_0}\frac{r^n - 1}{r - 1}, \quad (3.9.9)$$

where h_0 denotes the average grid spacing along the boundary at vertex 0, r is the growth rate of the normal grid spacing at vertex 0, and n is the number of grid points in the normal direction at vertex 0 which should be included in the transition ellipse. The reasoning behind Eq. (3.9.9) is that the normal grid spacing grows geometrically with rate r , and that the semi-minor axis should include n grid points. The term $2A_{\Omega_0}/h_0$ in Eq. (3.9.9) is an estimate of the near-wall grid spacing in the normal direction at vertex 0. In practice, the values taken for r and n were 1.2 and 12, respectively.

The problem with the transition ellipse is that it may fail to include vertices if the curvature at vertex 0 is large, or even for small curvature if the grid is highly stretched near solid walls, as is usually the case for viscous flow simulations. In Fig. 3.18, such points are marked by unfilled circles. To prevent this from happening, all points i which satisfy the conditions defined by the conditions,

$$\Delta \mathbf{r}_{i0} \cdot \mathbf{n}_0 \geq 0 \quad (3.9.10a)$$

$$\frac{\Delta \mathbf{r}_{i0} \cdot \mathbf{n}_0}{\|\Delta \mathbf{r}_{i0}\| \|\mathbf{n}_0\|} \geq \cos\left(\frac{\alpha + \beta}{2} - \delta\right) \quad (3.9.10b)$$

$$x'_i \leq x'_{\max}. \quad (3.9.10c)$$

where $\Delta \mathbf{r}_{i0} = \mathbf{r}_i - \mathbf{r}_0$, and the angles are as defined in Fig. 3.18, are also included in the transition region. Equation (3.9.10b) is necessary because of thin bodies, such as leading edges, where the sole use of Eqs. (3.9.10a) and (3.9.10c) will include points on the other side of the body. The angle δ is taken as 75° .

Hence, all vertices i which are not on a solid wall, satisfy Eq. (3.9.7), and Eqs. (3.9.10a)-(3.9.10c) are included in the transition region. These vertices are stored in compressed sparse row format for each transition vertex. With this treatment, the

implementation of the transition terms requires negligible storage and processing time.

3.10 Initial Conditions

The flowfield is initialised by setting it to the freestream state for external flows and to the inlet state for internal flows.

3.11 Boundary Conditions

The previous sections addressed the discretisation of the governing equations in the interior of the solution domain. The present section describes the discretisation of the boundary conditions defined in Section 2.5. The discrete boundary conditions are discussed in some detail since they have a strong influence on solution quality and convergence behaviour.

A consequence of using a vertex-centred scheme is that solution variables are located on the boundaries. At first, this may be expected to simplify the imposition of boundary conditions. However, it is somewhat unnatural in the finite-volume framework and leads to some interesting difficulties which are discussed below. The comments by Roache [33] on the differences between the implementation of boundary conditions in cell-centred and vertex-centred schemes are also interesting in this regard.

Boundary conditions can be imposed in a strong fashion, where the solution variables are directly set to the desired values. Alternatively, the boundary conditions can be imposed in a weak fashion, where the fluxes through the boundary are modified.

It was attempted to keep the weak formulation of the boundary conditions as consistent as possible with the computation of the fluxes in the interior of the solution domain. This is achieved through the definition of left and right solution states on the boundaries as shown schematically in Fig. 3.19. Consistent with the definition that the normal vector to the boundary is pointing outward, the left state is taken as the state of the vertex on the boundary.

For purposes of discussion, the boundary conditions are classified into fluid-solid (non-permeable) and fluid-fluid (permeable) boundaries. It is noted that this classification distinguishes between physical and non-physical boundaries. Non-physical boundaries are those boundaries which are chosen to bound a potentially infinite, or

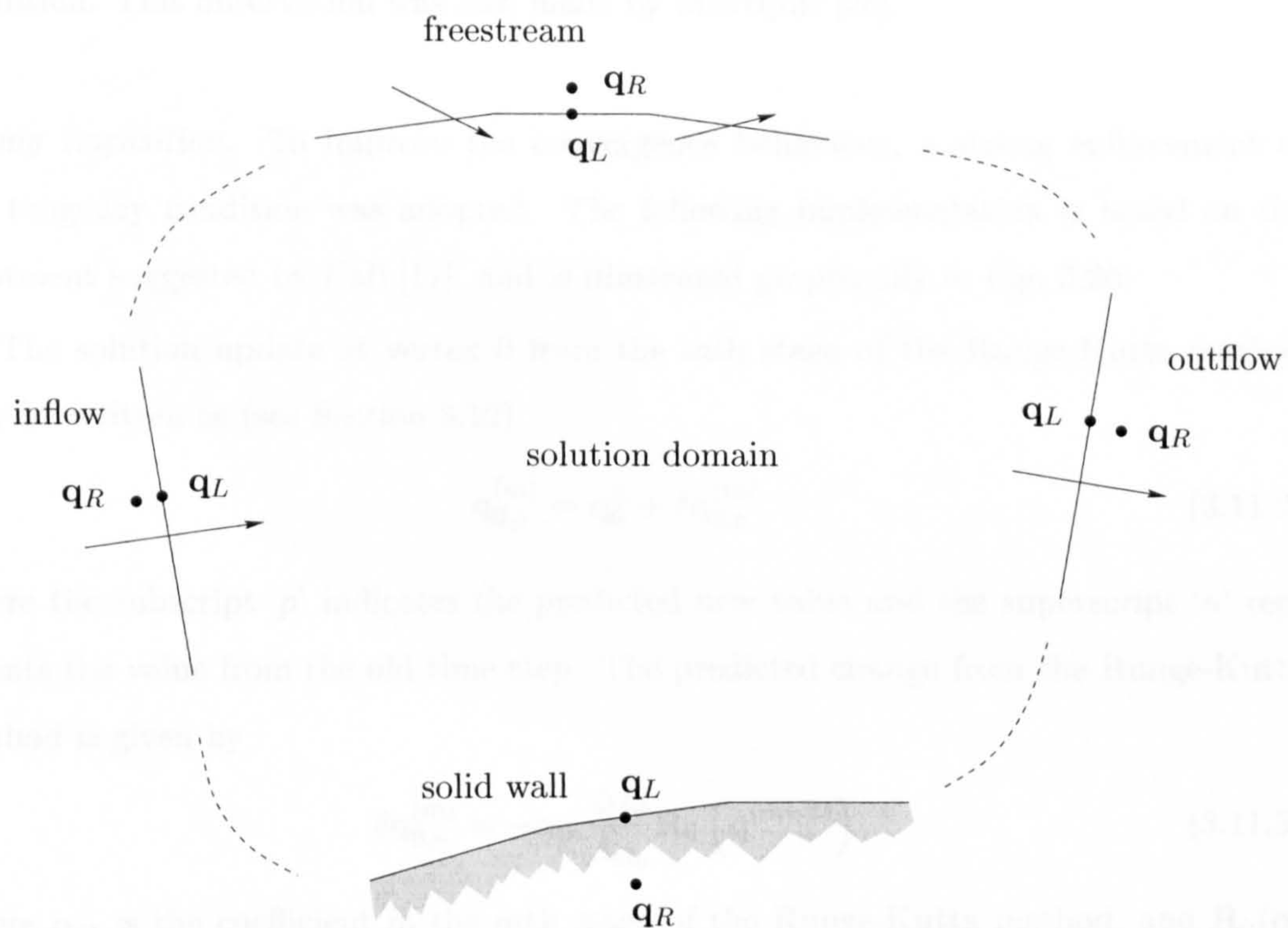


Figure 3.19: Introduction of left and right solution states on boundaries allows calculation of fluxes through boundaries to be consistent with that in interior of solution domain.

impractically large, solution domain.

3.11.1 Fluid-Solid Boundary Conditions

Slip-Wall Boundary. The tangency condition $\mathbf{v} \cdot \mathbf{n} = 0$ reduces the inviscid flux vector to

$$\mathbf{f}(\mathbf{q}) \cdot \mathbf{n} = p \begin{Bmatrix} 0 \\ n_x \\ n_y \\ 0 \end{Bmatrix}. \quad (3.11.1)$$

Weak Imposition. Using Eq. (3.11.1) to enforce the tangency condition in a weak fashion was found to lead to poor convergence behaviour. This was traced to a very lightly-damped limit cycle of the velocity vector on the slip-wall boundaries. The velocity vector was observed to oscillate between two states, whose average satisfied the tangency

condition. This observation was also made by Mavriplis [26].

Strong Imposition. To improve the convergence behaviour, a strong enforcement of the tangency condition was adopted. The following implementation is based on the treatment suggested by Hall [17], and is illustrated graphically in Fig. 3.20.

The solution update at vertex 0 from the m th stage of the Runge-Kutta method may be written as (see Section 3.12)

$$\mathbf{q}_{0,p}^{(m)} = \mathbf{q}_0^n + \delta \mathbf{q}_{0,p}^{(m)}, \quad (3.11.2)$$

where the subscript ' p ' indicates the predicted new value and the superscript ' n ' represents the value from the old time step. The predicted change from the Runge-Kutta method is given by

$$\delta \mathbf{q}_{0,p}^{(m)} = -\alpha_m \frac{\Delta t_0}{A_{\Omega_0}} \mathbf{R}_0(\mathbf{q}^{(m-1)}), \quad (3.11.3)$$

where α_m is the coefficient in the m th stage of the Runge-Kutta method, and $\mathbf{R}_0(\mathbf{q})$ represents the residual at vertex 0. The values of $(\rho u)_{0,p}^{(m)}$ and $(\rho v)_{0,p}^{(m)}$ do not necessarily satisfy the tangency condition.

To ensure that $(\rho u)_0^{(m)}$ and $(\rho v)_0^{(m)}$ satisfy the tangency condition, the predicted velocity vector is projected onto the boundary,

$$(\rho q)_{0,t}^{(m)} = (\rho u)_{0,p}^{(m)} n_y - (\rho v)_{0,p}^{(m)} n_x. \quad (3.11.4)$$

The corrections to the predicted velocity vector follow from

$$\delta(\rho u)_{0,c}^{(m)} = (\rho q)_{0,t}^{(m)} n_y - (\rho u)_{0,p}^{(m)}, \quad (3.11.5a)$$

$$\delta(\rho v)_{0,c}^{(m)} = (\rho q)_{0,t}^{(m)} n_x - (\rho v)_{0,p}^{(m)}. \quad (3.11.5b)$$

The modified residual which leads to a tangential velocity vector is therefore given by

$$\mathbf{R}_0(\mathbf{q}^{(m-1)}) = -\frac{A_{\Omega_0}}{\alpha_m \Delta t_0} \delta \mathbf{q}_{0,c}^{(m)}. \quad (3.11.6)$$

The residuals of the continuity and energy equations are not modified.

A modification of the above approach, in which the corrected values of pressure and density are obtained from the conditions of constant entropy and total enthalpy, did not lead to the expected improvements in solution accuracy and resulted in convergence

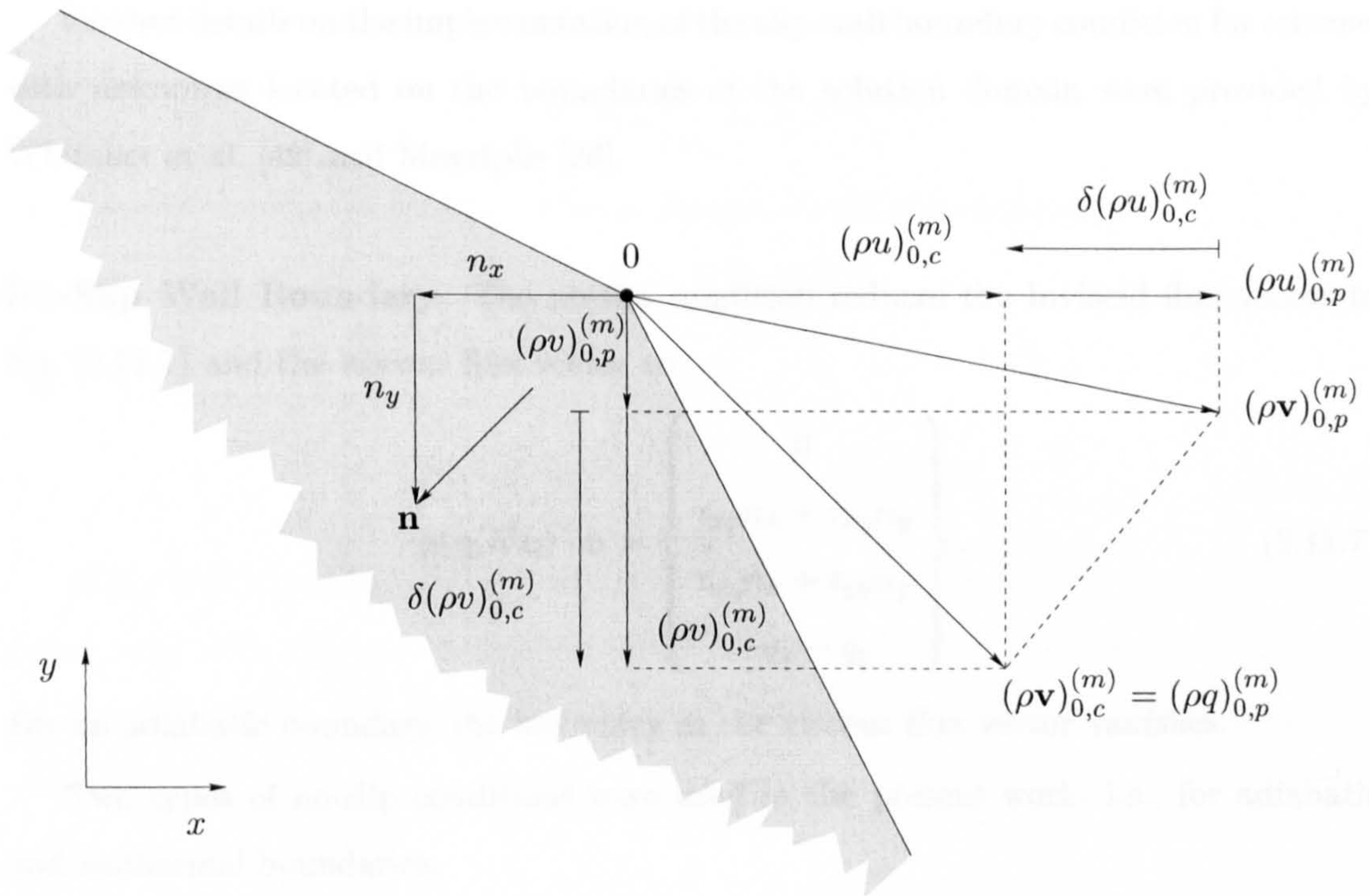


Figure 3.20: Illustration of strong imposition of slip-wall boundary condition.

problems when used in conjunction with the multigrid method described in Chapter 5.

Difficulties with Strong Imposition. The strong imposition of the slip condition as described above requires the definition of a normal vector at a boundary vertex. This is taken to be the normalised average of the normal vectors of the two edges meeting at the vertex. It is clear that this definition becomes questionable if the included angle between the two edges is much less than 180° . One practical example is the flow at a finite-angle trailing edge of an aerofoil. In this case, the Kutta condition requires that the velocity vector vanishes. When implemented numerically, this was found to lead to very large losses in total pressure. Aligning the velocity vector with the bisector of the included angle at the trailing edge gave good convergence rates and satisfactory solution quality near the trailing edge. The disadvantage of this approach is that it is strictly speaking valid only if the total pressures on the upper and lower surfaces are equal. For this reason, the velocity vector at a trailing edge is not corrected. The above-described deficiencies are not regarded as significant because the computation of inviscid flows is not a major goal of the present work.

Further details on the implementation of the slip-wall boundary condition for schemes with unknowns located on the boundaries of the solution domain were provided by Whitaker et al. [49] and Mavriplis [26].

No-Slip Wall Boundary. The no-slip condition reduces the inviscid flux vector to Eq. (3.11.1) and the viscous flux vector to

$$\mathbf{g}(\mathbf{q}, \nabla \mathbf{q}) \cdot \mathbf{n} = \begin{Bmatrix} 0 \\ \tau_{xx}n_x + \tau_{xy}n_y \\ \tau_{yx}n_x + \tau_{yy}n_y \\ -q_x - q_y \end{Bmatrix}. \quad (3.11.7)$$

For an adiabatic boundary, the last entry in the viscous flux vector vanishes.

Two types of no-slip conditions were used in the present work, i.e., for adiabatic and isothermal boundaries.

Adiabatic Boundary. The condition of zero heat flux through the surface is enforced in a weak fashion. Since the update for the momentum equations on solid walls is always zero, it is not necessary to compute any fluxes through an adiabatic boundary.

Problems with Adiabatic Boundary. The solutions obtained by solving for density and total internal energy on the boundary while the residuals for the x - and y -momentum equations are simply set to zero often showed poor convergence. This was traced back to the velocity components in near-wall regions having entered a limit cycle. It is believed that the limit cycle arose because of weak coupling between the flow field immediately near the wall and the wall pressure. In some cases, slight oscillations of the pressure on the wall were also detected.

Isothermal Boundary. Anderson and Bonhaus [1] employed an isothermal boundary condition. Their approach consists of defining a constant wall temperature equal to the adiabatic wall temperature encountered in theoretical studies of compressible boundary layers,

$$\frac{T_{\text{wall}}}{T_{\infty}} = 1 + \sqrt{\text{Pr}} \frac{\gamma - 1}{2} M_{\infty}^2. \quad (3.11.8)$$

Using the change in density computed from the solution update,

$$\delta\rho_0^{(m)} = -\alpha_m \frac{\Delta t_0}{A_{\Omega_0}} \mathbf{R}_0 \left(\rho^{(m-1)} \right), \quad (3.11.9)$$

the equation of state is used to define a change in total internal energy,

$$\delta(\rho E)_0^{(m)} = \frac{RT_{\text{wall}} \delta\rho_0^{(m)}}{\gamma - 1}, \quad (3.11.10)$$

which is converted back into a residual by

$$\mathbf{R}_0((\rho E)^{(m-1)}) = -\frac{A_{\Omega_0}}{\alpha_m \Delta t_0} \delta(\rho E)_0^{(m)}. \quad (3.11.11)$$

Using this approach, convergence to steady-state was found to be more robust and faster than with adiabatic boundary conditions. The slight oscillations of the pressure on the wall, which were sometimes observed with adiabatic boundary conditions, also disappeared.

Problems with Isothermal Boundary. It must be noted that Eq. (3.11.8) is valid only for compressible laminar boundary layers in zero pressure gradient. The factor $\sqrt{\text{Pr}}$ should be replaced by $\sqrt[3]{\text{Pr}}$ for compressible turbulent boundary layers in zero pressure gradient and by Pr for Couette flow [50]. From a theoretical point of view, the above treatment cannot be regarded as entirely satisfactory. However, numerical investigations found negligible differences in practice.

3.11.2 Fluid-Fluid Boundary Conditions

Inflow Boundary. For subsonic inflows, total pressure p_0 , total temperature T_0 , and the angle α between the flow direction and the boundary normal are specified.

The treatment of Chima [8] is used, in which the definition of the backward-propagating Riemann invariant

$$R_- = \mathbf{v} \cdot \mathbf{n} - \frac{2a}{\gamma - 1} = V \cos \alpha - \frac{2a}{\gamma - 1} \quad (3.11.12)$$

and the definition of the total speed of sound

$$a_0^2 = \gamma R T_0 = a^2 + \frac{\gamma - 1}{2} V^2 \quad (3.11.13)$$

are used to formulate a quadratic for the velocity magnitude of the right state, which

gives

$$V_R = \frac{(\gamma - 1)R_- \cos \alpha + \sqrt{4a_0^2 \left(\frac{2}{\gamma - 1} + \cos^2 \alpha \right) - 2(\gamma - 1)R_-^2}}{2 + (\gamma - 1) \cos^2 \alpha}, \quad (3.11.14)$$

The remaining variables can then be determined from the definitions of total temperature and total pressure, the equation of state, and the definition of the total internal energy. It is noted that the assumption of a constant total temperature amounts to isenthalpic flow.

Remark 3.9: While the above procedure was found to work well in general, problems were encountered if $V_R \rightarrow 0$, i.e., if the inflow boundary specified a reservoir condition. It is readily shown that the evaluation of V_R from Eq. (3.11.14) becomes dominated by round-off errors for vanishing V_R . This problem was circumvented by combining Eqs. (3.11.12) and (3.11.13) to give a quadratic equation for the speed of sound, which leads to

$$a_R = -R_- \frac{\gamma - 1}{(\gamma - 1) \cos^2 \alpha + 2} \left[1 + \cos \alpha \sqrt{\frac{(\gamma - 1) \cos^2 \alpha + 2}{\gamma - 1} \frac{a_0^2}{R_-^2} - \frac{\gamma - 1}{2}} \right]. \quad (3.11.15)$$

Using the above equation, a more robust procedure resulted.

For supersonic flows, the above interpolation is not used. Instead, the value of inflow Mach number is specified.

Outflow Boundary. For subsonic outflows, the static pressure is prescribed. Following Spekrijse [39] and Richter [32], the right state is defined using the three Riemann invariants

$$R_t = \mathbf{v} \cdot \mathbf{t} \quad (3.11.16a)$$

$$R_s = \frac{p}{\rho^\gamma} \quad (3.11.16b)$$

$$R_+ = \mathbf{v} \cdot \mathbf{n} + \frac{2a}{\gamma - 1}. \quad (3.11.16c)$$

The pressure for the right state is taken as the prescribed static pressure. The

density then follows from Eq. (3.11.16b) as

$$\rho_R = \rho_L \left(\frac{p_R}{p_L} \right)^{\frac{1}{\gamma}}. \quad (3.11.17)$$

Equations (3.11.16a) and (3.11.16c) can be used to solve for the components of the velocity vector at the right state

$$u_R = u_L + \frac{2n_x}{\gamma - 1}(a_L - a_R) \quad (3.11.18a)$$

$$v_R = v_L + \frac{2n_y}{\gamma - 1}(a_L - a_R), \quad (3.11.18b)$$

where $a_R = \sqrt{\gamma p_R / \rho_R}$ and the total internal energy follows from

$$(\rho E)_R = \frac{p_R}{\gamma - 1} + \frac{1}{2} \rho_R (u_R^2 + v_R^2). \quad (3.11.19)$$

For supersonic outflows, the right state is set equal to the left state. Since there is no discontinuity at the interface, no Riemann solver is required.

Freestream Boundary. The treatment of the freestream boundary depends on whether the flow about the aerofoil enclosed by the freestream boundary produces lift. The freestream boundary is assumed to be inviscid.

At a freestream boundary, the density ρ_∞ , pressure p_∞ , Mach number M_∞ , and angle of attack α are assumed to be specified.

Non-Lifting Flow. The right state-vector is computed by

$$u_R = M_\infty \sqrt{\frac{\gamma p_\infty}{\rho_\infty}} \cos \alpha \quad (3.11.20a)$$

$$v_R = M_\infty \sqrt{\frac{\gamma p_\infty}{\rho_\infty}} \sin \alpha \quad (3.11.20b)$$

and

$$(\rho E)_R = p_\infty \left(\frac{1}{\gamma - 1} + \frac{\gamma}{2} M_\infty^2 \right). \quad (3.11.21)$$

Lifting Flow. For lifting flows, the freestream boundary treatment described above can give poor results for force coefficients if the outer boundary is located too close to the aerofoil. This is due to the farfield being influenced by the lift generated by the aerofoil. Thomas and Salas [43] suggested that this influence be modelled by a point

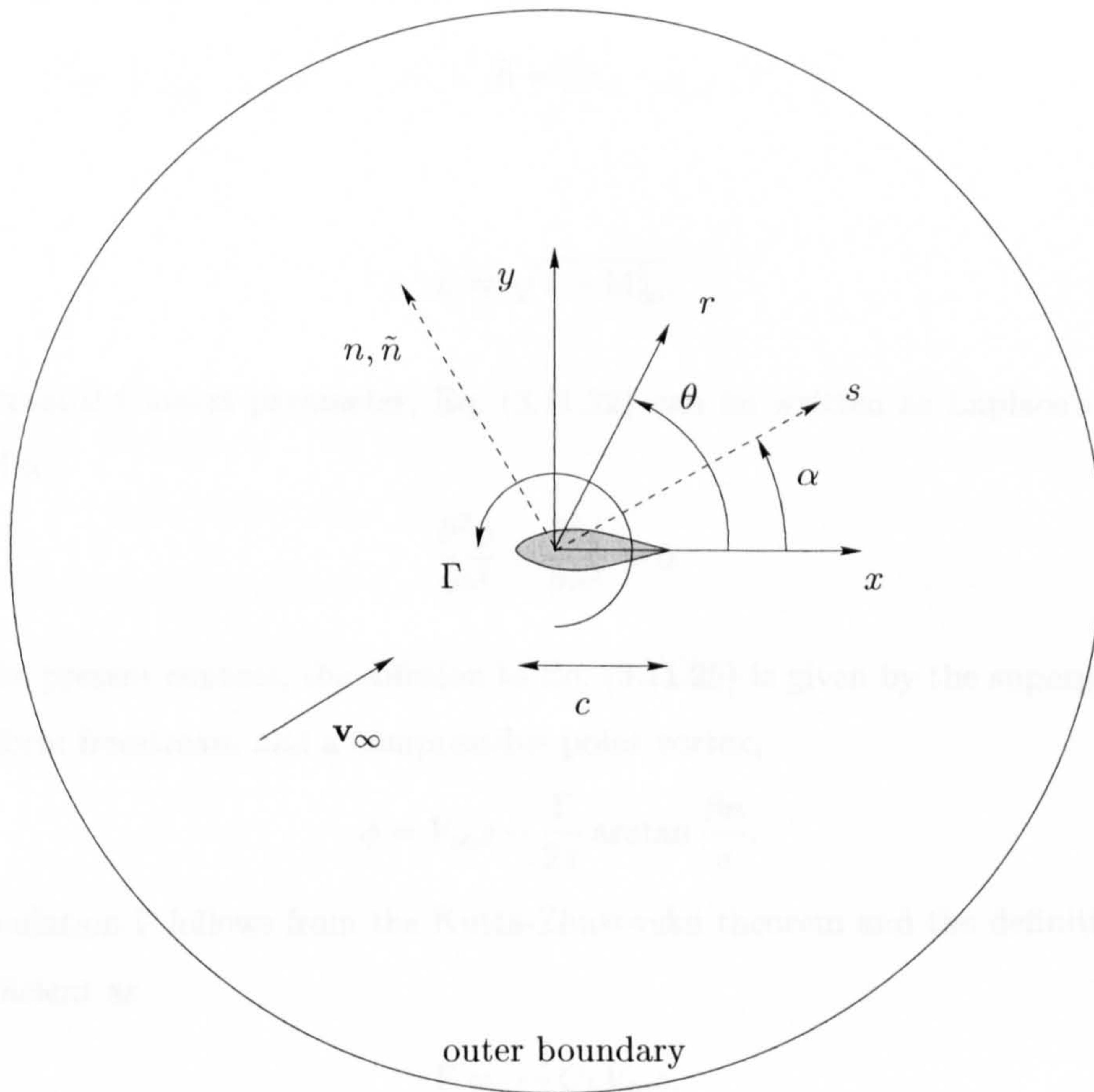


Figure 3.21: Nomenclature used in derivation of freestream boundary condition for lifting flows. Outer boundary need not be circular.

vortex located at the quarter-chord point of the aerofoil. The strength (circulation) of the point vortex is equivalent to the lift generated by the aerofoil. The boundary treatment for lifting flows is formulated as a correction to the treatment described above for non-lifting flows.

The correction is derived by assuming the flow in the farfield to be modelled by the Prandtl-Glauert equation,

$$(1 - M_\infty^2) \frac{\partial^2 \phi}{\partial s^2} + \frac{\partial^2 \phi}{\partial n^2} = 0, \quad (3.11.22)$$

where ϕ is the velocity potential, s and n are the coordinate directions aligned with and normal to the freestream direction, whose origin is at the quarter-chord point of the aerofoil. The relevant nomenclature is shown in Fig. 3.21.

Through the coordinate transformation

$$\tilde{n} = \beta n, \quad (3.11.23)$$

where

$$\beta = \sqrt{1 - M_\infty^2}, \quad (3.11.24)$$

is the Prandtl-Glauert parameter, Eq. (3.11.22) can be written as Laplace's equation in s and \tilde{n} ,

$$\frac{\partial^2 \phi}{\partial s^2} + \frac{\partial^2 \phi}{\partial \tilde{n}^2} = 0. \quad (3.11.25)$$

In the present context, the solution to Eq. (3.11.25) is given by the superposition of the uniform freestream and a compressible point vortex,

$$\phi = V_\infty s - \frac{\Gamma}{2\pi} \arctan \frac{\beta n}{s}. \quad (3.11.26)$$

The circulation Γ follows from the Kutta-Zhukovskii theorem and the definition of the lift coefficient as

$$\Gamma = -\frac{1}{2} C_L V_\infty c, \quad (3.11.27)$$

where c is the chord of the aerofoil and it is noted that the circulation is negative for positive lift.

The velocity components in the s - and n -directions are given by

$$u_s = \frac{\partial \phi}{\partial s} = V_\infty \left(1 + \frac{C_L c}{4\pi} \frac{\beta n}{s^2 + \beta^2 n^2} \right) \quad (3.11.28a)$$

$$u_n = \frac{\partial \phi}{\partial n} = \frac{C_L V_\infty c}{4\pi} \frac{\beta s}{s^2 + \beta^2 n^2}. \quad (3.11.28b)$$

Rotating the velocity components into the original coordinate system gives

$$u_R = \bar{u}_\infty = V_\infty \left(\cos \alpha + \frac{C_L c}{4\pi r} \frac{\beta \sin \theta}{1 - M_\infty^2 \sin^2(\theta - \alpha)} \right) \quad (3.11.29a)$$

$$v_R = \bar{v}_\infty = V_\infty \left(\sin \alpha - \frac{C_L c}{4\pi r} \frac{\beta \cos \theta}{1 - M_\infty^2 \sin^2(\theta - \alpha)} \right). \quad (3.11.29b)$$

where $\bar{(\cdot)}$ denotes freestream variables modified due to the effect of the lift of the aerofoil. With the condition that the entropy and the stagnation enthalpy of the modified and original freestream variables be identical, the modified freestream pressure and density

are

$$p_R = \bar{p}_\infty = \left[p_\infty^{\frac{\gamma-1}{\gamma}} + \frac{\gamma-1}{2\gamma} \left(\frac{\rho_\infty^\gamma}{p_\infty} \right)^{\frac{1}{\gamma}} (V_\infty^2 - \bar{V}_\infty^2) \right]^{\frac{\gamma}{\gamma-1}}, \quad (3.11.30)$$

and

$$\rho_R = \bar{\rho}_\infty = \rho_\infty \left(\frac{\bar{p}_\infty}{p_\infty} \right)^{\frac{1}{\gamma}}. \quad (3.11.31)$$

Symmetry Boundary. For ease of implementation, symmetry boundaries are assumed to be aligned with either the x - or the y -coordinate direction.

Assuming, for the purpose of discussion, the symmetry boundary to be aligned with the x -coordinate direction, the conditions to be enforced are

$$v = 0 \quad (3.11.32a)$$

$$\frac{\partial \rho}{\partial y} = 0 \quad (3.11.32b)$$

$$\frac{\partial u}{\partial y} = 0 \quad (3.11.32c)$$

$$\frac{\partial T}{\partial y} = 0. \quad (3.11.32d)$$

These conditions are enforced in a weak fashion.

The corresponding conditions for a symmetry boundary aligned with the y -coordinate direction follow in a straightforward fashion.

3.12 Solution Algorithm

3.12.1 Euler and Navier-Stokes Equations

The semi-discrete approximation given by Eq. (3.6.3) is first re-written

$$\frac{d\mathbf{q}_0}{dt} = -\frac{1}{A_{\Omega_0}} \mathbf{R}_0(\mathbf{q}), \quad (3.12.1)$$

where

$$\mathbf{R}_0(\mathbf{q}) = - \sum_{0i \in \mathcal{E}_0} [\Phi(\mathbf{q}_{0i,L}, \mathbf{q}_{0i,R}; \hat{\mathbf{n}}_{0i}) - \Gamma(\mathbf{p}_{0i}, (\nabla \mathbf{p})_{0i}; \hat{\mathbf{n}}_{0i})] \Delta s_{0i} \quad (3.12.2)$$

represents the residual for the control volume at vertex 0. In the present work, Eq.

Table 3.1: Stage coefficients of Runge-Kutta scheme for first- and second-order schemes. Table taken from [42].

stage	order	
	first	second
1	0.0834	0.1400
2	0.2071	0.2939
3	0.4267	0.5252
4	1.0000	1.0000

(3.12.1) is solved using a four-stage Runge-Kutta method,

$$\begin{aligned}
 \mathbf{q}_0^{(0)} &= \mathbf{q}_0^n \\
 \mathbf{q}_0^{(1)} &= \mathbf{q}_0^{(0)} - \alpha_1 \frac{\Delta t_0}{A_{\Omega_0}} \mathbf{R}_0 \left(\mathbf{q}^{(0)} \right) \\
 \mathbf{q}_0^{(2)} &= \mathbf{q}_0^{(0)} - \alpha_2 \frac{\Delta t_0}{A_{\Omega_0}} \mathbf{R}_0 \left(\mathbf{q}^{(1)} \right) \\
 \mathbf{q}_0^{(3)} &= \mathbf{q}_0^{(0)} - \alpha_3 \frac{\Delta t_0}{A_{\Omega_0}} \mathbf{R}_0 \left(\mathbf{q}^{(2)} \right) \\
 \mathbf{q}_0^{(4)} &= \mathbf{q}_0^{(0)} - \alpha_4 \frac{\Delta t_0}{A_{\Omega_0}} \mathbf{R}_0 \left(\mathbf{q}^{(3)} \right) \\
 \mathbf{q}_0^{n+1} &= \mathbf{q}_0^{(4)}
 \end{aligned}$$

where Δt_0 is the time step for vertex 0, and the superscripts in parentheses denote sub-iteration indices.

The computation of the time step is detailed in Subsection 3.13.1.

Detailed information on Runge-Kutta schemes can be found in Swanson and Turkel [41].

Choice of Stage Coefficients. The stage coefficients are those determined by van Leer et al. [46] to give optimal smoothing of the high-frequency error components. Strong smoothing of the high-frequency error components is imperative when using a multigrid method. The coefficients are listed in Table 3.1 for the first-order scheme and the second-order scheme with $\kappa = 0$.

3.12.2 Spalart-Allmaras Turbulence Model Equation

Point-Implicit Treatment of Source Term. The production and destruction terms in the source term of the Spalart-Allmaras turbulence model are treated implicitly. This may be explained by reference to Eq. (2.4.19)

$$\frac{\partial}{\partial t} \int_{\Omega} \rho \tilde{\nu} dA + \oint_{\partial\Omega} \rho \tilde{\nu} \mathbf{v} \cdot \mathbf{n} ds = \frac{1}{\sigma} \oint_{\partial\Omega} \rho (\nu + \tilde{\nu}) \nabla \tilde{\nu} \cdot \mathbf{n} ds + \int_{\Omega} \mathcal{S}(\rho \tilde{\nu}) dA. \quad (3.12.3)$$

The time-derivative is approximated by the forward Euler scheme,

$$\int_{\Omega_0} \frac{\partial \rho \tilde{\nu}}{\partial t} dA \approx \frac{A_{\Omega_0}}{\Delta t_0} ((\rho \tilde{\nu})_0^{n+1} - (\rho \tilde{\nu})_0^n),$$

and the residual is defined as

$$\mathbf{R}_0(\rho \tilde{\nu}) = - \sum_{0i \in \mathcal{E}_0} (\Phi - \Gamma)_{0i}^n \Delta s_{0i} + \mathcal{S}_0^{n+1} A_{\Omega_0} \quad (3.12.4)$$

where it is indicated that the convection and diffusion terms are evaluated at time level n , whereas the source term is evaluated at time level $n+1$. This gives

$$\frac{A_{\Omega_0}}{\Delta t_0} ((\rho \tilde{\nu})_0^{n+1} - (\rho \tilde{\nu})_0^n) = - \sum_{0i \in \mathcal{E}_0} (\Phi - \Gamma)_{0i}^n \Delta s_{0i} + \mathcal{S}_0^{n+1} A_{\Omega_0} \quad (3.12.5)$$

The source term is linearised about time level n by introducing the scalar Jacobian $\partial \mathcal{S} / \partial \rho \tilde{\nu}$, abbreviated as \mathcal{S}_{∂} , to give

$$A_{\Omega_0} \left(\frac{1}{\Delta t_0} - (\mathcal{S}_{\partial})_0^n \right) ((\rho \tilde{\nu})_0^{n+1} - (\rho \tilde{\nu})_0^n) = - \sum_{0i \in \mathcal{E}_0} (\Phi - \Gamma)_{0i}^n \Delta s_{0i} + \mathcal{S}_0^n A_{\Omega_0}, \quad (3.12.6)$$

which may be written in the form

$$(\rho \tilde{\nu})_0^{n+1} = (\rho \tilde{\nu})_0^n - \left[A_{\Omega_0} \left(\frac{1}{\Delta t_0} - (\mathcal{S}_{\partial})_0^n \right) \right]^{-1} \left(\sum_{0i \in \mathcal{E}_0} (\Phi - \Gamma)_{0i}^n \Delta s_{0i} - \mathcal{S}_0^n A_{\Omega_0} \right), \quad (3.12.7)$$

or,

$$(\rho \tilde{\nu})_0^{n+1} = (\rho \tilde{\nu})_0^n - \frac{\Delta t_0^*}{A_{\Omega_0}} \left(\sum_{0i \in \mathcal{E}_0} (\Phi - \Gamma)_{0i}^n \Delta s_{0i} - \mathcal{S}_0^n A_{\Omega_0} \right). \quad (3.12.8)$$

where the modified time-step Δt_0^* is given by

$$\Delta t_0^* = \frac{\Delta t_0}{1 - \mathcal{S}_{\partial} \Delta t_0}. \quad (3.12.9)$$

Thus, it may be seen that the update is of the same form as for the Euler and Navier-Stokes equations, but with a modified time-step. The Spalart-Allmaras model

is integrated using the same Runge-Kutta time-stepping scheme, where the update in the m -th subiteration is

$$(\rho\tilde{\nu})_0^{(m)} = (\rho\tilde{\nu})_0^n - \alpha_m \frac{\Delta t_0^*}{A_{\Omega_0}} \left(\sum_{0i \in \mathcal{E}_0} (\Phi - \Gamma)_{0i}^n \Delta s_{0i} - \mathcal{S}_0^n A_{\Omega_0} \right), \quad (3.12.10)$$

where the modified time-step is now given by

$$\Delta t_0^* = \frac{\Delta t_0}{1 - \mathcal{S}_\partial \alpha_m \Delta t_0}. \quad (3.12.11)$$

Determination of the Jacobian. As suggested by Spalart and Allmaras [38], the Jacobian of the source term includes the production and destruction terms, and is defined as

$$\frac{\partial \mathcal{S}}{\partial \rho\tilde{\nu}} = \text{neg} \left(\frac{\partial \mathcal{P}}{\partial \rho\tilde{\nu}} - \frac{\partial \mathcal{D}}{\partial \rho\tilde{\nu}} \right) \quad (3.12.12)$$

where

$$\text{neg}(x) = \begin{cases} x & \text{if } x < 0 \\ 0 & \text{if } x \geq 0. \end{cases} \quad (3.12.13)$$

The Jacobian is determined analytically. This gives for the production term,

$$\frac{\partial \mathcal{P}}{\partial \rho\tilde{\nu}} = c_{b1} \left\{ \tilde{\Omega} + \frac{\tilde{\nu}}{\rho} \left[\Omega \frac{\partial f_{v3}}{\partial \tilde{\nu}} + \frac{1}{\kappa^2 d^2} \left(f_{v2} + \tilde{\nu} \frac{\partial f_{v2}}{\partial \tilde{\nu}} \right) \right] \right\} \quad (3.12.14)$$

where

$$\frac{\partial f_{v2}}{\partial \tilde{\nu}} = -\frac{3}{c_{v2}\nu} \left(1 + \frac{\chi}{c_{v2}} \right)^{-4} \quad (3.12.15)$$

$$\frac{\partial f_{v3}}{\partial \tilde{\nu}} = \frac{1}{\chi} \left[(1 - f_{v2}) \left(\frac{f_{v1}}{\nu} + \chi \frac{\partial f_{v1}}{\partial \tilde{\nu}} \right) - (1 + \chi f_{v1}) \frac{\partial f_{v2}}{\partial \tilde{\nu}} - \frac{f_{v3}}{\nu} \right] \quad (3.12.16)$$

$$\frac{\partial f_{v1}}{\partial \tilde{\nu}} = \frac{1}{\nu} \frac{3\chi^2 c_{v1}^3}{(\chi^3 + c_{v1}^3)^2}. \quad (3.12.17)$$

For the destruction term,

$$\frac{\partial \mathcal{D}}{\partial \rho\tilde{\nu}} = -\frac{c_w}{\rho} \frac{\tilde{\nu}}{\rho d} \left(2 \frac{f_w}{d} - \frac{\tilde{\nu}}{d} \frac{\partial f_w}{\partial g} \frac{\partial g}{\partial r} \frac{\partial r}{\partial \tilde{\nu}} \right) \quad (3.12.18)$$

where

$$\frac{\partial f_w}{\partial g} = \frac{f_w}{g} - \frac{g^{11}}{f_w^5} \frac{1 + c_{w3}^6}{(g^6 + c_{w3}^6)^2} \quad (3.12.19)$$

$$\frac{\partial g}{\partial r} = 1 + c_{w2}(6r^5 - 1) \quad (3.12.20)$$

$$\frac{\partial r}{\partial \tilde{\nu}} = \frac{1}{\tilde{\Omega} \kappa^2 d^2} \left\{ 1 - \frac{\tilde{\nu}}{\tilde{\Omega}} \left[\Omega \frac{\partial f_{v3}}{\partial \tilde{\nu}} + \frac{1}{\kappa^2 d^2} \left(f_{v2} + \tilde{\nu} \frac{\partial f_{v2}}{\partial \tilde{\nu}} \right) \right] \right\} \quad (3.12.21)$$

3.13 Implementation Details

3.13.1 Time-Step Calculation

Various methods of calculating the time step were assessed. The method described below was found to work best in the sense that the maximum CFL number did not have to be adjusted much for a wide range of test cases.

The time step is calculated by discretising the generic convection-diffusion equation

$$\int_{\Omega_0} \frac{\partial \rho \phi}{\partial t} dA + \oint_{\partial \Omega_0} \rho \phi \mathbf{v} \cdot \mathbf{n} ds = \oint_{\partial \Omega_0} \mu \nabla \phi \cdot \mathbf{n} ds \quad (3.13.1)$$

The convection term is approximated by a simple upwind scheme as

$$\oint_{\partial \Omega_0} \rho \phi \mathbf{v} \cdot \mathbf{n} ds \approx \sum_{0i \in \mathcal{E}_0} (q_{0i}^+ (\rho \phi)_0^n + q_{0i}^- (\rho \phi)_i^n) \Delta s_{0i} \quad (3.13.2)$$

where $q_{0i}^\pm = (q_{0i} \pm |q_{0i}|)/2$, $q_{0i} = \mathbf{v}_{0i} \cdot \hat{\mathbf{n}}_{0i}$ and $\mathbf{v}_{0i} = (\mathbf{v}_0 + \mathbf{v}_i)/2$.

The diffusive fluxes are approximated by Scheme 1 described in Section 4.2.5, given by Eq. (4.2.20),

$$\oint_{\partial \Omega_0} \mu \nabla \phi \cdot \mathbf{n} ds \approx \sum_{0i \in \mathcal{E}_0} \mu \frac{\Delta s_{0i}}{\Delta n_{0i}} (\phi_i^n - \phi_0^n). \quad (3.13.3)$$

The time derivative is approximated by the forward Euler scheme,

$$\int_{\Omega_0} \frac{\partial \rho \phi}{\partial t} dA \approx \frac{A_{\Omega_0}}{\Delta t_0} ((\rho \phi)_0^{n+1} - (\rho \phi)_0^n).$$

Collecting terms gives

$$\begin{aligned} (\rho \phi)_0^{n+1} = (\rho \phi)_0^n & \left[1 - \frac{\Delta t_0}{A_{\Omega_0}} \sum_{0i \in \mathcal{E}_0} \left(q_{0i}^+ \Delta s_{0i} + \frac{\mu}{\rho} \frac{\Delta s_{0i}}{\Delta n_{0i}} \right) \right] \\ & - \frac{\Delta t_0}{A_{\Omega_0}} \sum_{0i \in \mathcal{E}_0} \left(q_{0i}^- \Delta s_{0i} - \frac{\mu}{\rho} \frac{\Delta s_{0i}}{\Delta n_{0i}} \right) (\rho \phi)_i^n. \end{aligned} \quad (3.13.4)$$

By requiring $(\rho \phi)_0^{n+1}$ to be a convex combination of $(\rho \phi)_0^n$ and $(\rho \phi)_i^n$, the following

restriction on the time step Δt_0 emerges

$$\Delta t_0 \leq \frac{\text{CFL } A_{\Omega_0}}{\sum_{0i \in \mathcal{E}_0} \left(q_{0i}^+ \Delta s_{0i} + \frac{\mu}{\rho} \frac{\Delta s_{0i}}{\Delta n_{0i}} \right)}. \quad (3.13.5)$$

The above analysis is strictly applicable to scalar equations only. In order to extend the time-step calculation to systems of equations, the positive projection is replaced by the spectral radius of the inviscid flux Jacobian,

$$q_{0i}^+ \leftarrow q_{0i}^+ + a_{0i}, \quad (3.13.6)$$

where $a_{0i} = (a_0 + a_i)/2$. Furthermore, the viscous contribution to the time step is multiplied by a factor of four to provide a safety margin and to account for contributions not included in the Laplacian.

In order to accelerate convergence to the steady state, local time-stepping is used, i.e., each control volume is advanced at its computed time step, as described above.

3.13.2 Convergence Monitoring

In order to monitor the iterative process, a convergence measure is defined by

$$\text{CM}(\mathbf{q}) = \frac{1}{N} \sqrt{\sum_{i=1}^N \frac{(\mathbf{q}_i^{n+1} - \mathbf{q}_i^n)^2}{(\mathbf{q}_i^n)^2 + \varepsilon}}, \quad (3.13.7)$$

where N is the number of vertices in the grid and ε is a small number used to prevent division by zero.

The iterative process is declared converged when the convergence tolerance drops below an user-specified tolerance, usually taken as $1 \cdot 10^{-8}$. Experience showed that it is usually more appropriate to monitor global parameters of physical significance, such as lift, drag, and moment coefficients and the net outflow of mass. The iterative process was stopped when some specified absolute or relative tolerance of the changes in the global parameters was reached.

3.14 Closure

The present chapter described the numerical solution method for single-grid calculations in detail, with the exception of the discretisation of the viscous fluxes. The treatment of triangular, quadrilateral, and mixed grids was studied in detail. The concept of

grid-transparency was developed. This allows the solution method to operate on grids composed of arbitrary grids without distinguishing between the various cell types.

The description of the numerical method is continued in Chapter 4, which investigates the discretisation of the viscous fluxes on unstructured grids, and in Chapter 5, which describes the implementation of the agglomeration multigrid method.

References

- [1] Anderson W.K. and Bonhaus D.L., *An Implicit Upwind Algorithm for the Computation of Turbulent Flows on Unstructured Grids*, Comp. Fl., Vol. 23, No. 1, pp. 1-21, 1994
- [2] Ashford G.A., *An Unstructured Grid Generation and Adaptive Solution Technique for High-Reynolds Number Compressible Flows*, Ph.D. Thesis, University of Michigan, Ann Arbor, MI, 1996
- [3] Barth T.J., *On Unstructured Grids and Solvers*, in: *Computational Fluid Dynamics Lecture Series 1990-03*, von Kármán Institute for Fluid Dynamics, March 1990
- [4] ———, *Aspects of Unstructured Grids and Finite-Volume Solvers for the Euler and Navier-Stokes Equations*, in: *Special Course on Unstructured Grid Methods for Advection Dominated Flows*, AGARD Report 787, pp. 6-1 to 6-61, May 1992
- [5] ———, *Aspects of Unstructured Grids and Finite-Volume Solvers for the Euler and Navier-Stokes Equations*, in: *Computational Fluid Dynamics Lecture Series 1994-05*, von Kármán Institute for Fluid Dynamics, March 1994
- [6] Barth T.J. and Jespersen D.C., *The Design and Application of Upwind Schemes on Unstructured Meshes*, AIAA Paper 89-0366, 27th Aerospace Sciences Meeting, Reno, NV, January 1989
- [7] Carey G.F. and Oden J.T., *Finite Elements: Computational Aspects*, The Texas Finite Element Series, Vol. III, Prentice-Hall, Eaglewood Cliffs, 1984
- [8] Chima R.V., *Inviscid and Viscous Flows in Cascades with an Explicit Multigrid Algorithm*, AIAA J., Vol. 23, No. 19, pp. 1556-1563, 1985
- [9] Debiez C., *Contribution à l'étude des schémas aux volumes finis décentrées à faible dissipation transverse*, INRIA Technical Report No. 2985, September 1996
- [10] Delanaye M., *Polynomial Reconstruction Finite Volume Schemes for the Compressible Euler and Navier-Stokes Equations on Unstructured Adaptive Grids*, Ph.D. Thesis, Université de Liège, September 1996
- [11] Dervieux A., *Steady Euler Simulations Using Unstructured Meshes*, in: *Computational Fluid Dynamics Lecture Series 1985-04*, von Kármán Institute of Fluid Dynamics, March 1985
- [12] Dervieux A., Fézoui L., Leclercq M.-P., and Stoufflet B., *A General Upwind Formulation for Compressible Flows on Multielement Meshes*, in: *Numerical Methods for Fluid Dynamics IV*, Proc. Int. Conf. on Numerical Methods in Fluid Dynamics, Baines M.J. and Morton K.W. (Eds.), Clarendon Press, Oxford, pp. 257-264, 1992

- [13] Friedrichs K.O. and Keller H.B., *A Finite-Difference Scheme for Generalised Neumann Problems*, in: *Numerical Solution of Partial Differential Equations*, Bramble J.H. (Ed.), Academic Press, pp. 1-19, 1966
- [14] Fromm J.E., *A Method for Reducing Dispersion in Convective Difference Schemes*, J. Comp. Phys., Vol. 3, pp. 176-189, 1968
- [15] Godunov S.K., *A Finite-Difference Method for the Numerical Computation of Discontinuous Solutions of the Equations of Fluid Dynamics*, Math. Sbornik, Vol. 47, pp. 271-306, 1959
- [16] Golub G.H. and Van Loan C.F., *Matrix Computation*, 2nd. Ed. The John Hopkins University Press, Baltimore, MD, 1989
- [17] Hall M.G., *Cell-Vertex Multigrid Schemes for Solution of the Euler Equations*, in: *Numerical Methods for Fluid Dynamics II*, K.W. Morton and M.J. Baines (Eds.), Oxford University Press, pp. 303-345, 1986
- [18] Haselbacher A., *The Computation of Compressible Turbulent Flows on Unstructured Grids*, Qualifying Dissertation for Ph.D. Status, Loughborough University, October 1995
- [19] Haselbacher A. and Blažek J., *On the Accurate and Efficient Discretisation of the Navier-Stokes Equations on Mixed Grids*, AIAA Paper 99-3363, 14th Computational Fluid Dynamics Conference, Norfolk, VA, June/July 1999
- [20] Hirsch C., *Numerical Computation of Internal and External Flows*, Vol. 2, Computational Methods for Inviscid and Viscous Flows, Wiley, 1990
- [21] Idelsohn S.R. and Oñate E., *Finite Volumes and Finite Elements: Two Good Friends*, Int. J. Num. Meth. Eng., Vol. 37, pp. 3323-3341, 1994
- [22] Jameson A., *Artificial Diffusion, Upwind Biasing, Limiters and their Effect on Accuracy and Convergence in Transonic and Hypersonic Flows*, AIAA Paper 93-3359, 11th Computational Fluid Dynamics Conference, Orlando, FL, July 1993
- [23] Jameson A., Schmidt W., and Turkel E., *Numerical Solution of the Euler Equations by Finite-Volume Methods using Runge-Kutta Time-Stepping Schemes*, AIAA Paper 81-1259, 14th Fluid and Plasma Dynamics Conference, Palo Alto, CA, June 1981
- [24] Kasbarian C., Leclercq M.-P., Ravachol M., and Stoufflet B., *Improvements of Upwind Formulations on Unstructured Meshes*, in: *Nonlinear Hyperbolic Problems: Theoretical, Applied, and Computational Aspects*, Proc. 4th Int. Conf. on Hyperbolic Problems, Donato A. and Oliveri F. (Eds.), Notes on Numerical Fluid Mechanics, Vol. 43, Vieweg, Braunschweig, pp. 363-368, 1992
- [25] Leonard B.P., *Comparison of Truncation Error of Finite-Difference and Finite-Volume Formulations of the Convection Terms*, NASA TM-105861, September 1992
- [26] Mavriplis D.J., *Accurate Multigrid Solution of the Euler Equations on Unstructured and Adaptive Meshes*, AIAA J., Vol. 28, No. 2, pp. 213-221, February 1990
- [27] Meister A., *Zur zeitgenauen numerischen Simulation reibungsbehafteter, kompressibler, turbulenter Strömungsfelder mit einer impliziten Finite-Volumen-Methode vom Box-Typ*, DLR-Forschungsbericht 96-08, DLR Göttingen, May 1996

- [28] Menter F.R, Grotjans H., and Unger F., *Numerical Aspects of Turbulence Modelling for the Reynolds Averaged Navier-Stokes Equations*, in: *Computational Fluid Dynamics Lecture Series 1997-02*, von Kármán Institute for Fluid Dynamics, March 1997
- [29] Müller J.-D. and Giles M.B., *Edge-Based Multigrid Schemes for Hybrid Grids*, in: *Numerical Methods for Fluid Dynamics VI*, M.J. Baines (Ed.), Institute of Computational Fluid Dynamics, Oxford University Computing Laboratory, pp. 425-432, 1998
- [30] Ollivier-Gooch C.F., *A New Class of ENO Schemes Based on Unlimited Data-Dependent Least-Squares Construction*, AIAA Paper 96-0887, 34th Aerospace Sciences Meeting and Exhibit, Reno, NV, January 1996
- [31] Perroomian O., Chakravarthy S., and Goldberg U.C., *A "Grid-Transparent" Methodology for CFD*, AIAA Paper 97-0724, 35th Aerospace Sciences Meeting and Exhibit, Reno, NV, January 1997
- [32] Richter R., *Schémas de capture de discontinuité en maillage non-structuré avec adaptation dynamique. Applications aux écoulements de l'aérodynamique*, Ph.D. Thesis No. 1164, Ecole Polytechnique Fédérale de Lausanne, 1993
- [33] Roache P.J., *Fundamentals of Computational Fluid Dynamics*, Hermosa Publishers, Albuquerque, NM, 1998
- [34] Roe P.L., *Approximate Riemann Solvers, Parameter Vectors, and Difference Schemes*, J. Comp. Phys., Vol. 43, pp. 357-372, 1981
- [35] Saad Y., *Iterative Methods for Sparse Linear Systems*, PWS Publishing Company, Boston, 1996
- [36] Selmin V., *The Node-Centred Finite-Volume Approach: Bridge Between Finite Differences and Finite Elements*, Comp. Meth. Appl. Mech. Eng., Vol. 102, pp. 107-138, 1993
- [37] Sonar T., *Mehrdimensionale ENO-Verfahren*, Teubner, Stuttgart, 1997
- [38] Spalart P.R. and Allmaras S.R., *A One-Equation Turbulence Model for Aerodynamic Flows*, AIAA Paper 92-0349, 30th Aerospace Sciences Meeting, Reno, NV, January 1992
- [39] Spekreijse S.P., *Multigrid Solution of the Steady Euler Equations*, Ph.D. Thesis, Technical University Delft, November 1987
- [40] Stoer J. and Bulirsch R., *Introduction to Numerical Analysis*, 2nd Ed., Springer, 1992
- [41] Swanson R.C. and Turkel E., *Multistage Schemes with Multigrid for Euler and Navier-Stokes Equations*, NASA TP-3631, August 1997
- [42] Tai C.-H., Sheu J.-H., and van Leer B., *Optimal Multistage Schemes for Euler Equations with Residual Smoothing*, AIAA J., Vol. 33, No. 6, pp. 1008-1016, June 1995
- [43] Thomas J.L. and Salas M.D., *Far-Field Boundary Conditions for Transonic Lifting Solutions to the Euler Equations*, AIAA J., Vol. 24, No. 7, pp. 1074-1080, 1986
- [44] van Leer B., *Towards the Ultimate Conservative Difference Scheme, V. A Second-Order Sequel to Godunov's Method*, J. Comp. Phys., Vol. 32, pp. 101-136, 1979

- [45] van Leer B., Lee W.-T., and Powell K.G., *Sonic-Point Capturing*, AIAA Paper 89-1945, 9th Computational Fluid Dynamics Conference, Buffalo, NY, June 1989
- [46] van Leer B., Tai C.-H., and Powell K.G., *Design of Optimally Smoothing Multi-Stage Schemes for the Euler Equations*, AIAA Paper 89-1933, 9th Computational Fluid Dynamics Conference, Buffalo, NY, June 1989
- [47] Venkatakrishnan V., *Convergence to Steady-State Solutions of the Euler Equations on Unstructured Grids with Limiters*, J. Comp. Phys., Vol. 118, pp. 120-130, 1995
- [48] Viozat C., Held C., Mer K., and Dervieux A., *On Vertex-Centered Unstructured Finite-Volume Methods for Stretched Anisotropic Triangulations*, INRIA Research Report No. 3464, July 1998
- [49] Whitaker D.L., Grossman B., and Löhner R., *Two-Dimensional Euler Computations on a Triangular Mesh Using an Upwind, Finite-Volume Scheme*, AIAA Paper 89-0470, 27th Aerospace Sciences Meeting, Reno, NV, January 1989
- [50] White F.M., *Viscous Fluid Flow*, McGraw-Hill, 1991
- [51] Wigton L.B., *Optimizing CFD Codes and Algorithms for Use on Cray Computers*, in: *Frontiers of Computational Fluid Dynamics 1998*, Caughey D.A. and Hafez M.M. (Eds.), World Scientific, pp. 277-292, 1998

Chapter 4

The Discretisation of Viscous Fluxes on Unstructured Grids

The discretisation of the viscous fluxes on arbitrary unstructured grids is investigated. Laplace's equation is studied as a model equation, for which criteria are developed to judge the merits of different discretisations. Particular attention is given to positivity of the coefficients and grid-transparency. It is shown that currently used discretisations perform poorly even on regular triangular and quadrilateral grids. Alternative discretisations are developed and extended to the Navier-Stokes equations.

4.1 Introduction

The discretisation of the viscous fluxes by a finite-volume method requires the approximation of gradients of the dependent variables at the control-volume faces. The quality of the discretisation hinges crucially on the approximation of these gradients.

On structured grids, the gradients can be approximated easily by divided differences in the corresponding coordinate directions of the curvilinear coordinate system. For this reason, and because the physical characteristics of the inviscid fluxes are more difficult to simulate, the discretisation of the viscous fluxes is usually regarded as straightforward.

On unstructured grids, where identifiable coordinate directions usually do not exist, the approximation of gradients is considerably more complicated. It is relatively simple to generate discretisation stencils of poor quality. Coirier [13] observed that such stencils can lead to diverging calculations for low Reynolds-number flows. For high-Reynolds number flows, it might be argued that the influence of viscous stencils of poor quality

is small and does not deserve much attention. However, there are good reasons why attention should be paid to the discretisation of the viscous fluxes.

The computation of high-Reynolds-number flows invariably requires the use of turbulence models. These models often involve transport equations for quantities, such as the turbulence kinetic energy, which are positive by definition. It is therefore natural to demand that the discretised transport equations mirror this property. If the discretisation does not prevent negative values from occurring, these can lead to counter-gradient diffusion and explosion-like numerical instability. A heuristic and crude approach to resolving this problem is to resort to some form of limiting procedure, whereby positive values are prevented from dropping below a user-specified threshold, or by simply replacing negative values by their absolute values. Not surprisingly, convergence often suffers if such practices are used, see, e.g., Jongen and Marx [27]. A fundamentally sounder approach is to construct the discretisation such that negative values cannot occur a priori.

Positivity of a solution variable can be achieved in general by requiring the coefficients in the discretisation stencil to be positive. Since it is well-known how the discretisation of convective and source terms can be made positive, what remains to be done is to find a discretisation of the diffusive terms which gives positive coefficients. In fact, this is particularly important, since the steep gradients exhibited by most turbulence quantities mean that diffusive transport is significant. As will be shown in this chapter, it is quite simple to construct discretisations of the diffusive terms which do not lead to positive coefficients.

The preceding argument is based upon, but not restricted to, transport equations for turbulence variables. Indeed, the argument applies also to transport equations for other variables which are guaranteed to be positive, such as mass fractions in the simulation of chemically reacting flows. On a more general note, it seems inappropriate from a fundamental modelling viewpoint to have numerous and sophisticated inviscid numerical fluxes in comparison to the little-researched viscous numerical fluxes.

For these reasons, it is important to study the discretisation of the viscous fluxes on unstructured grids. Studies of the discretisation of the viscous fluxes are rare and widely dispersed in the literature. This chapter aims to collect and review previous results and attempts to study further the discretisation of the viscous fluxes on unstructured grids.

Particular attention is focussed on mixed grids.

4.2 Laplace's Equation

For incompressible flows and constant viscosity, the viscous terms given by Eqs. (2.3.4) and (2.3.3) reduce to Laplace's operator. It is therefore convenient to study the discretisation of the viscous terms by investigating the discretisation of Laplace's equation

$$\nabla^2 \phi = 0.$$

The idea is to develop a suitable discretisation of Laplace's equation and to extend it to the viscous terms in the Navier-Stokes equations. The suitability of a given discretisation of Laplace's equation is assessed by various conditions, which are formulated in the following subsection.

4.2.1 Conditions on Discretisation

Any discretisation of Laplace's equation can be written as

$$(\nabla^2 \phi)_0 \approx \sum_{i=0}^n \omega_i \phi_i = 0, \quad (4.2.1)$$

where the coefficients ω_i depend on the coordinates of the grid vertices, ϕ_i is the value of ϕ at (x_i, y_i) , and the summation is carried out over the n points involved in the stencil at the central vertex 0, as depicted schematically in Fig. 4.1.

The following paragraphs describe the conditions which the discretisation given by Eq. (4.2.1) ought to fulfill in order to be physically and numerically accurate. Although the present study is based on dual cells as control volumes, the results described in the following paragraphs are also relevant to discretisations with control volumes based on primal cells.

Positivity. Laplace's equation has a number of interesting properties. An important property in the present context is that solutions of Laplace's equation cannot exhibit a maximum or minimum inside the solution domain. For this reason, solutions to Laplace's equation are said to exhibit a maximum principle. The maximum principle may be regarded as the mathematical expression of the smoothing of extrema through diffusion.

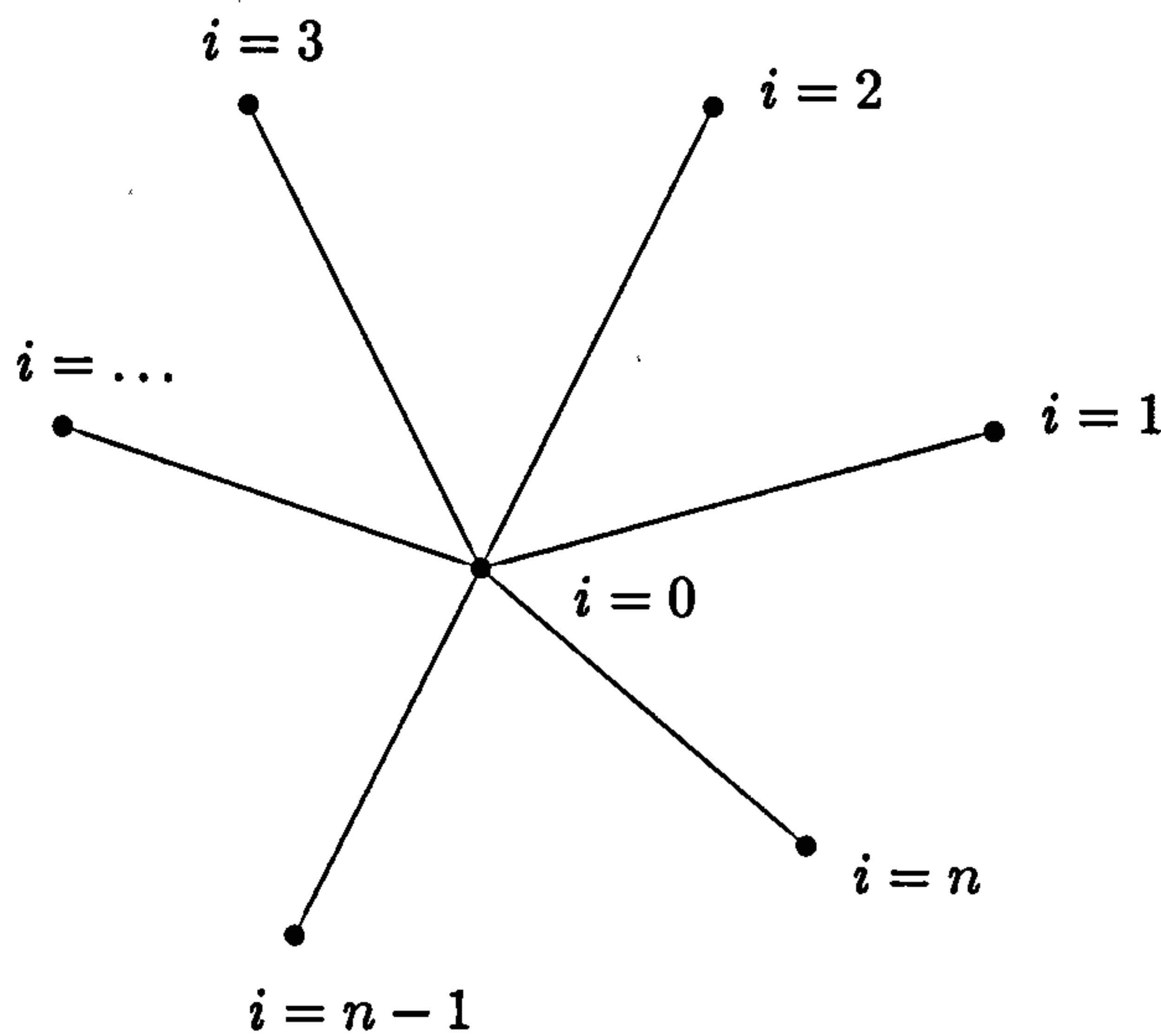


Figure 4.1: Definition of nomenclature used in Eq. (4.2.1).

It is desired that the discretisation obey the maximum principle. To find the conditions under which the discretisation satisfies the maximum principle, Eq. (4.2.1) is solved for ϕ_0 ,

$$\phi_0 = - \sum_{i=1}^n \frac{\omega_i}{\omega_0} \phi_i. \quad (4.2.2)$$

For the maximum principle to hold for the discrete set of equations, it is required that

$$\min_{1 \leq i \leq n} \phi_i \leq \phi_0 \leq \max_{1 \leq i \leq n} \phi_i. \quad (4.2.3)$$

This condition is satisfied by Eq. (4.2.2) only if the ratios of the coefficients ω_i/ω_0 are negative. Therefore, it is necessary that the central coefficient ω_0 is negative while the coefficients ω_i of the neighbours are positive. The discretisation is then said to satisfy a discrete maximum principle.

If the discretisation obeys the maximum principle, the coefficient matrix is an M -matrix [55]. This is a desirable property since classical iterative methods are stable for M -matrices, see, e.g., Wesseling [57].

Accuracy. In order to investigate the local accuracy of the discretisation, ϕ_i is ex-

panded by a Taylor series to fourth order,

$$\phi_i = \phi_0 + \sum_{k=1}^4 \sum_{m=0}^k \frac{1}{(k-m)!m!} \Delta x_{0i}^{k-m} \Delta y_{0i}^m \left(\frac{\partial^k \phi}{\partial x^{k-m} \partial y^m} \right)_0, \quad (4.2.4)$$

where $\Delta x_{0i} = x_i - x_0$ and $\Delta y_{0i} = y_i - y_0$. By multiplying the above equation by ω_i and summing over i , the conditions for a second-order accurate discrete Laplacian are derived,*

First-Order Accuracy (Consistency):

$$\sum_{i=0}^n \omega_i = 0 \quad (4.2.5a)$$

$$\sum_{i=1}^n \omega_i (x_i - x_0) = 0 \quad (4.2.5b)$$

$$\sum_{i=1}^n \omega_i (y_i - y_0) = 0 \quad (4.2.5c)$$

$$\sum_{i=1}^n \omega_i (x_i - x_0)^2 = 2 \quad (4.2.5d)$$

$$\sum_{i=1}^n \omega_i (x_i - x_0)(y_i - y_0) = 0 \quad (4.2.5e)$$

$$\sum_{i=1}^n \omega_i (y_i - y_0)^2 = 2 \quad (4.2.5f)$$

Second-Order Accuracy: Eqs. (4.2.5a) – (4.2.5f), and

$$\sum_{i=1}^n \omega_i (x_i - x_0)^3 = 0 \quad (4.2.6a)$$

$$\sum_{i=1}^n \omega_i (x_i - x_0)^2 (y_i - y_0) = 0 \quad (4.2.6b)$$

$$\sum_{i=1}^n \omega_i (x_i - x_0)(y_i - y_0)^2 = 0 \quad (4.2.6c)$$

$$\sum_{i=1}^n \omega_i (y_i - y_0)^3 = 0 \quad (4.2.6d)$$

In general, $\frac{1}{d!} \prod_{k=2}^{d+1} (p+k)$ equations arise for a discretisation of order p in d dimensions.

*For completeness, it is noted that Eqs. (4.2.5d)-(4.2.5f) are related through the Cauchy-Schwartz inequality.

By recognising that Eq. (4.2.5a) gives

$$\omega_0 = - \sum_{i=1}^n \omega_i, \quad (4.2.7)$$

Eq. (4.2.1) can be rewritten as

$$(\nabla^2 \phi)_0 \approx \sum_{i=1}^n \omega_{0i} (\phi_i - \phi_0) = 0, \quad (4.2.8)$$

where the weights ω_i were replaced by ω_{0i} to emphasize that the weights are associated with edges. Equation (4.2.8) will be used for the remainder of this chapter because it automatically satisfies the condition expressed by Eq. (4.2.5a).

Linearity Preservation. If applied to a linear function, the Laplacian will be identically zero and hence preserve it.

For the discretisation given by Eq. (4.2.8) to be linearity preserving, it is required that $(\nabla^2 \phi)_0 = 0$ if $\phi_i = \phi_0 + (\nabla \phi)_0 \cdot \Delta \mathbf{r}_{0i}$ where $(\nabla \phi)_0 = (a, b)^t$ with $a, b = \text{constant}$. This leads to the conditions given by Eqs. (4.2.5b) and (4.2.5c).

Conservation. For the discretisation given by Eq. (4.2.8) to be conservative, it is required that $\omega_{0i} = \omega_{i0}$ where it is noted that the edge-weight does *not* include the control-volume area. The reasoning is that the contributions of edge $0i$ to the vertices 0 and i must cancel for conservation to hold, i.e.,

$$\omega_{0i} (\phi_i - \phi_0) + \omega_{i0} (\phi_0 - \phi_i) = 0,$$

which gives $\omega_{0i} = \omega_{i0}$.

For the more general case where the coefficient multiplying the difference is a matrix W_{0i} , it is required that $W_{0i} = W_{i0}$.

Coupling. A further requirement is that the discretisation should not exhibit spurious solution modes. A solution mode is referred to as spurious if it satisfies the discrete equations, but not the differential equations. The following will analyse stencils on rectangular grids only, because the likelihood of spurious modes is usually greater on quadrilateral grids and the analysis is less involved.

There are three possible spurious modes, as shown schematically in Fig. 4.2. A

A low smoothing factor gives good high-frequency smoothing properties and is indicative of strong coupling. The smoothing factor depends on the discretisation and the iterative scheme. In the following, it is assumed that the iterative scheme is the Gauss-Seidel method with lexicographical ordering of the unknowns, but the conclusions do not depend on this assumption.

Accuracy. Strong coupling also leads to lower truncation error for a given order of accuracy. This may be seen from the two formulae for the second derivative on a uniform grid in one dimension,

$$\begin{aligned}\frac{\phi_{i+1} - 2\phi_i + \phi_{i-1}}{\Delta x^2} &= \left(\frac{\partial^2 \phi}{\partial x^2}\right)_i + \frac{\Delta x^2}{12} \left(\frac{\partial^4 \phi}{\partial x^4}\right)_i + \text{HOT} \\ \frac{\phi_{i+2} - 2\phi_i + \phi_{i-2}}{4\Delta x^2} &= \left(\frac{\partial^2 \phi}{\partial x^2}\right)_i + \frac{\Delta x^2}{3} \left(\frac{\partial^4 \phi}{\partial x^4}\right)_i + \text{HOT},\end{aligned}$$

where the second formula, which employs only every other grid point, allows a spurious solution mode and is therefore less accurate. The results of Wood and Kleb [61], who compared methods with strong and weak coupling on triangular grids, corroborate the benefit of strongly-coupled methods in terms of accuracy.

Grid-Transparency. The motivation for grid-transparent solution methods was already discussed in Section 3.5. The aim is to develop a grid-transparent discretisation for the Laplacian with a view to extending it to the viscous terms in the Navier-Stokes equations.

In terms of the discretisation of the Laplacian, a consequence of grid-transparency is that on uniform triangular and quadrilateral grids, the classical stencils shown in Fig. 4.3 are recovered. It should be noted that these stencils are the simplest which can be obtained. For more complicated stencils on quadrilateral grids, see Thom and Appelt [54]. Collatz [15] tabulated various stencils on quadrilateral, triangular, and hexahedral grids.

Discretisations of the diffusion equation which are not grid-transparent were developed by Roberts [50] and Wieners [59].

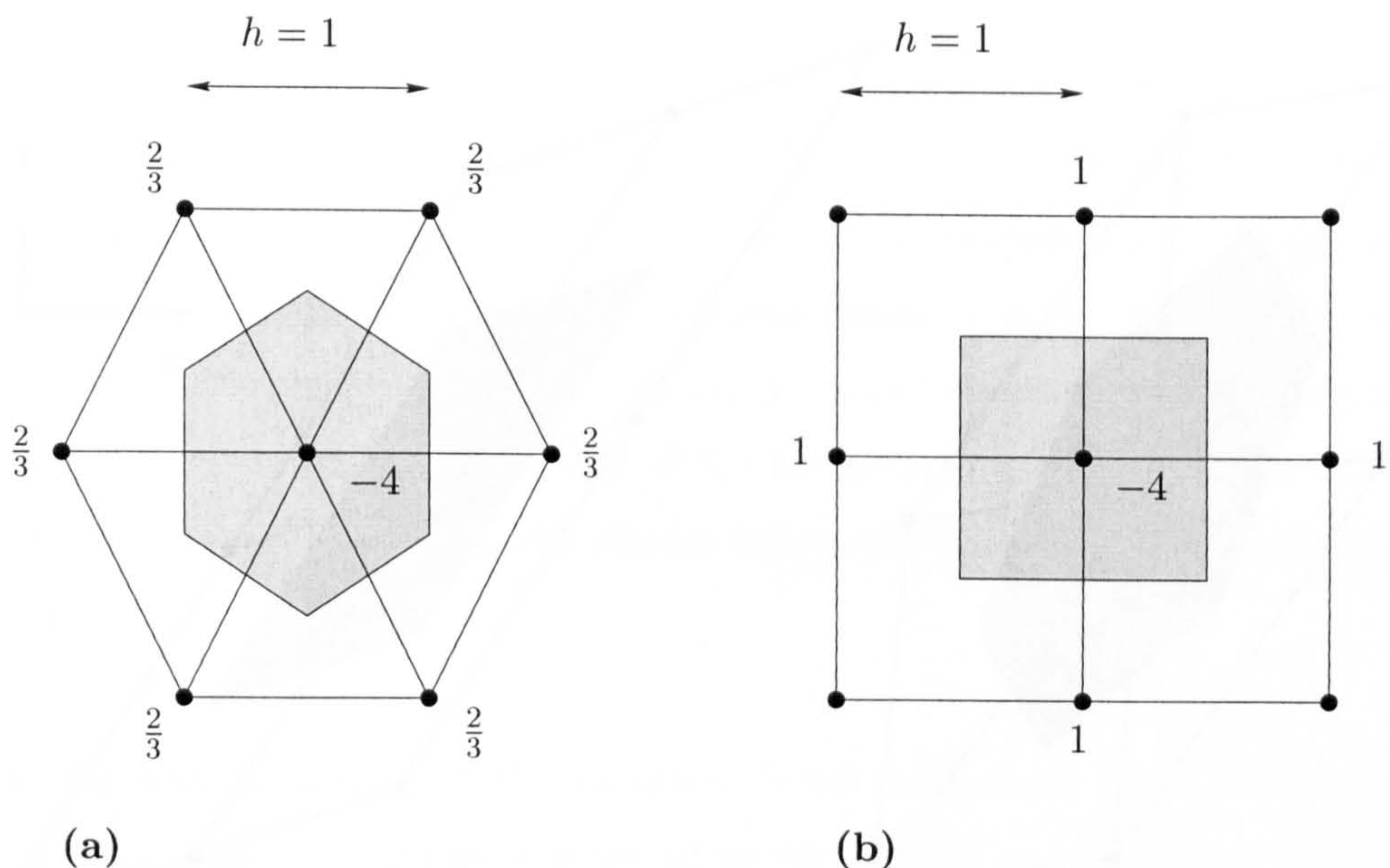


Figure 4.3: Grid-transparent stencils for Laplacian on uniform (a) triangular and (b) quadrilateral grids.

4.2.2 Discussion of Conditions

It is instructive to consider how the various conditions on the discretisations discussed above influence each other.

Positivity versus Accuracy. It may be asked if it is possible to achieve accuracy and positivity simultaneously. Unfortunately, this is not possible on arbitrary grids, as shown by Kershaw [30]. This is easily seen by writing the conditions given by Eqs. (4.2.5b)-(4.2.6d) in the form $C\omega = \mathbf{r}$,

$$\begin{bmatrix} \Delta x_{01} & \Delta x_{02} & \cdots & \Delta x_{0n} \\ \Delta y_{01} & \Delta y_{02} & \cdots & \Delta y_{0n} \\ \vdots & \vdots & \ddots & \vdots \\ \Delta y_{01}^3 & \Delta y_{02}^3 & \cdots & \Delta y_{0n}^3 \end{bmatrix} \begin{bmatrix} \omega_1 \\ \omega_2 \\ \vdots \\ \omega_n \end{bmatrix} = \begin{bmatrix} 0 \\ 0 \\ \vdots \\ 0 \end{bmatrix} \quad (4.2.11)$$

where C is a $9 \times n$ matrix, and ω and \mathbf{r} are n -vectors.

The conditions under which positivity and accuracy are in conflict can be obtained by inspecting the row-entries in C and the corresponding entry in \mathbf{r} . Any row in C whose entries are either all positive or all negative and whose corresponding entry in \mathbf{r}

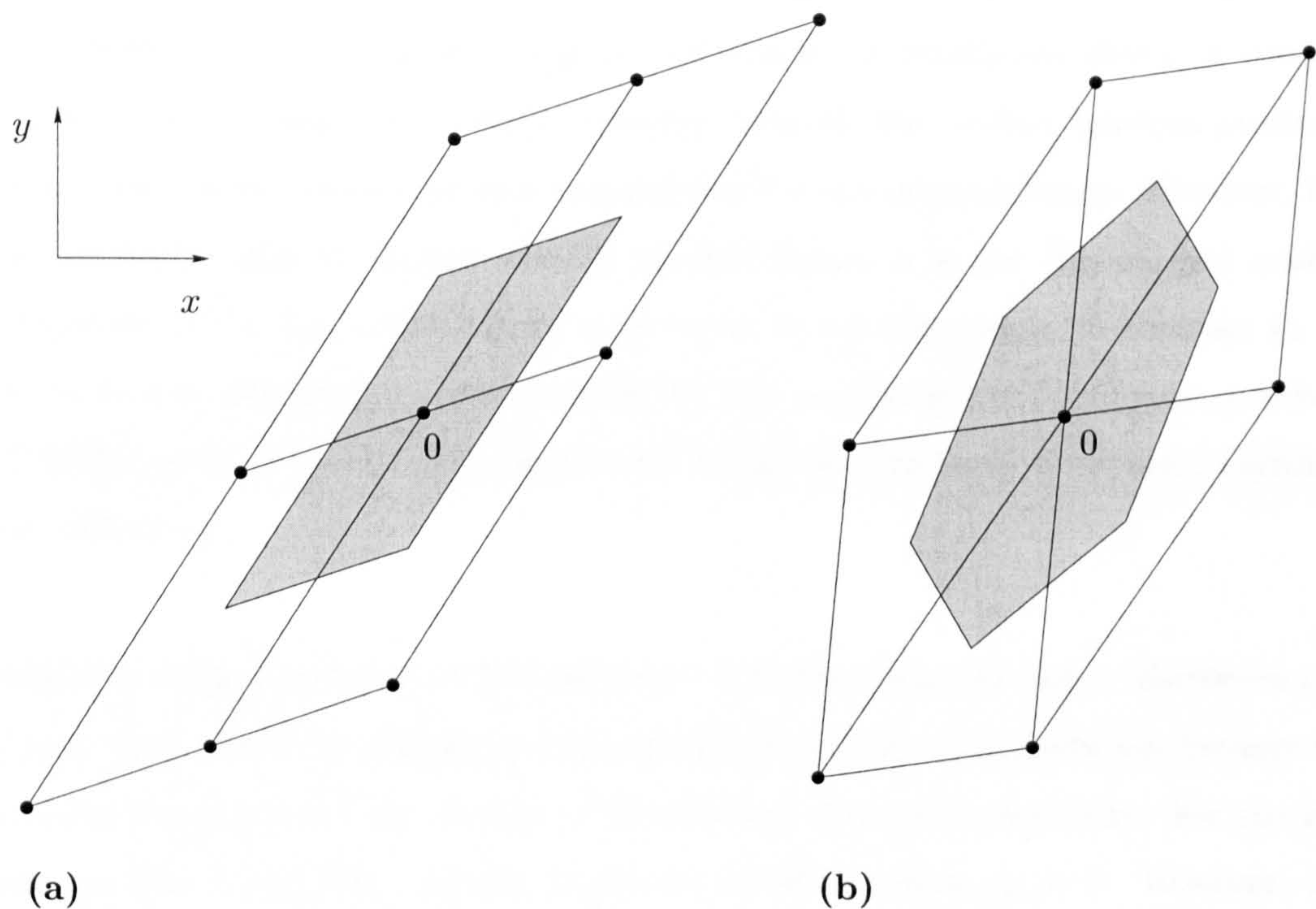


Figure 4.4: Examples of **(a)** quadrilateral grid and **(b)** triangular grid for which $\Delta x_{0i}\Delta y_{0i} > 0$. Positivity and consistency cannot be achieved simultaneously for these stencils.

is zero cannot be satisfied if the entries of ω are either positive or negative. There are seven rows for which this is possible, corresponding to Eqs. (4.2.5b), (4.2.5c), (4.2.5e), and (4.2.6a)-(4.2.6d).

At interior grid points, the row consisting of $\Delta x_{0i}\Delta y_{0i}$ is the most restrictive. The problem thus arises if $\Delta x_{0i}\Delta y_{0i} \neq 0$. Unfortunately, this inequality corresponds to a constraint on consistency. A stencil which satisfies the inequality may be visualised as a stencil whose points i all lie in the first and third or the second and fourth quadrants of a local coordinate system centred at vertex 0. An example of triangular and quadrilateral grids where $\Delta x_{0i}\Delta y_{0i} > 0$ is shown in Fig. 4.4. If positivity of the coefficients is enforced, the discretisation at that point is inconsistent. On the other hand, a second-order accurate discretisation will be non-positive. This example illustrates that positivity and accuracy cannot be achieved simultaneously on an arbitrary grid. The practical implications of this result will be discussed further in Section 4.3.

Two comments are in order. First, it is noted that non-positivity of the coeffi-

cients arises because of shearing or skewing of the grid. Simply stretching a grid does not necessarily lead to negative weights. Of course, as mentioned above, a triangular grid cannot be stretched without skewing. Second, the conflict between positivity and accuracy seems similar to that encountered for the inviscid fluxes. However, it is fundamentally different because for the inviscid fluxes, it is not due to grid quality. Non-positivity for the inviscid fluxes may occur in one dimension, in contrast to the viscous fluxes. Furthermore, the trade-off for the inviscid fluxes is between positivity and higher-order accuracy. For the viscous fluxes, the trade-off is between positivity and consistency.

Positivity and Accuracy at Boundaries. It follows from the above discussion that accuracy and positivity cannot be achieved simultaneously at boundaries, because the stencil is biased toward the interior of the solution domain by necessity. For the grid shown in Fig. 4.5(a), Eq. (4.2.5c) cannot be satisfied unless $\omega_p = 0$. However, this means that Eq. (4.2.5f) cannot be fulfilled. Similarly, for the triangular grid shown in Fig. 4.5(b), Eq. (4.2.5c) cannot be satisfied if ω_p and ω_q are of the same sign, which means that positivity must be violated. Again, Eq. (4.2.5f) cannot be fulfilled as a result.

At corners, as shown in Fig. 4.6(a), Eqs. (4.2.5b) and (4.2.5c) cannot be satisfied unless $\omega_p < 0$. Finally, on the grid shown in Fig. 4.6(b), a consistent discretisation is altogether impossible.

The problem of accuracy at boundaries can only be resolved if more distant points are included in the stencil. The inclusion of more distant points in the stencil does not allow positivity to be achieved, however. Furthermore, it is easy to show that the use of virtual edges does not lead to a resolution of the problem of obtaining accuracy and positivity simultaneously at boundaries.

Conservation and Accuracy. The approach of Holmes and Connell [24], which guarantees a linearly transparent pseudo-Laplacian on arbitrary grids (see Subsection 4.2.3), gives rise to two weights for each edge. Since the two edge weights are not identical except on uniform grids, the approach is not conservative. Thus there seems to be a contradiction between conservation and accuracy on arbitrary grids.

4.2.3 Review of Previous Work

From the fundamental properties of Laplace’s equation it is known that the solution is harmonic in the interior of the domain. The solution is also unique if the boundary values are specified. The problem is to find a numerical approximation to the solution.

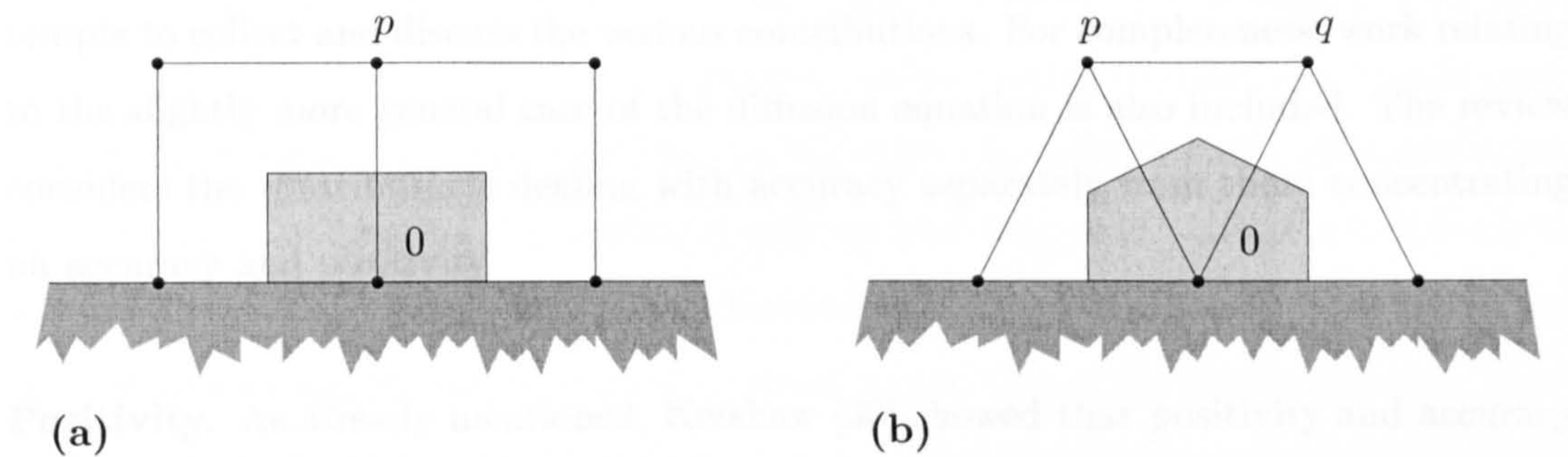


Figure 4.5: Examples of (a) quadrilateral grid (b) triangular grid near boundaries where positivity and accuracy cannot be achieved simultaneously.

For the purpose of this paper, we consider the problem of finding a numerical approximation to the solution of Laplace’s equation in a domain D with boundary ∂D .

Let u be the solution of Laplace’s equation in D with boundary values f on ∂D . We assume that f is continuous on ∂D and that u is continuous on \bar{D} .

Let \mathcal{T}_h be a triangulation of D with maximum element size h . Let u_h be the piecewise linear function on \mathcal{T}_h that interpolates u at the vertices of \mathcal{T}_h .

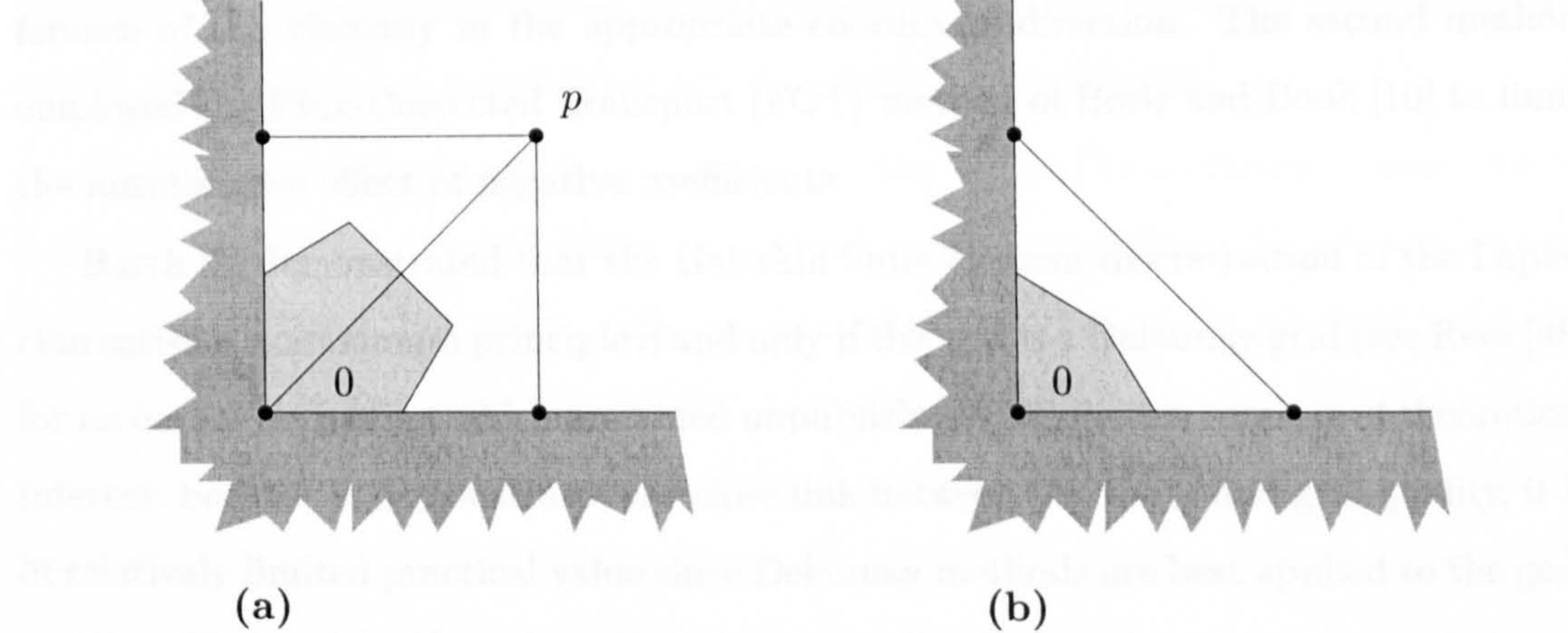


Figure 4.6: Examples of grids near boundaries where (a) positivity and accuracy cannot be achieved simultaneously and (b) consistency is impossible to achieve.

Let \mathcal{T}_h be a triangulation of D with maximum element size h . Let u_h be the piecewise linear function on \mathcal{T}_h that interpolates u at the vertices of \mathcal{T}_h . Let \mathcal{E}_h be the set of edges of \mathcal{T}_h that are on the boundary ∂D .

4.2.3 Review of Previous Work

Given the fundamental difficulties described above, it is surprising that little work has been carried out on the discretisation of Laplace's equation. The following review attempts to collect and discuss the various contributions. For completeness, work relating to the slightly more general case of the diffusion equation is also included. The review considers the contributions dealing with accuracy separately from those concentrating on accuracy and positivity.

Positivity. As already mentioned, Kershaw [30] showed that positivity and accuracy cannot be achieved simultaneously on arbitrary grids. He relied on the stability of the implicit solution procedure to ensure that negative solution values existed only in the transient and disappeared at the steady-state. While this may have been a satisfactory practice for the simple linear diffusion problems considered by Kershaw, it cannot be regarded as an acceptable practice for more general problems.

Pert [45] examined two methods for obtaining a positive discretisation of the diffusion equation with a tensorial viscosity coefficient. It was noticed that the antisymmetric terms did not necessarily satisfy the maximum principle. The first method examined by Pert employed upwind differences for the fluxes based on the sign of the first difference of the viscosity in the appropriate coordinate direction. The second method employed the Flux-Corrected Transport (FCT) method of Boris and Book [10] to limit the antidiffusive effect of negative coefficients.

Barth [3] demonstrated that the Galerkin finite-element discretisation of the Laplacian satisfies a maximum principle if and only if the grid is a Delaunay grid (see Rees [48] for an earlier derivation which remained unpublished). While this result is of theoretical interest, because it demonstrates the close link between positivity and grid quality, it is of relatively limited practical value since Delaunay methods are best applied to the generation of isotropic grids and are therefore not well suited to the computation of viscous flows. It should also be noted that in three dimensions, Delaunay grids do not ensure that the Galerkin finite-element discretisation satisfies a maximum principle [3, 32].

Maman [37] studied the problem of obtaining positive coefficients on adaptive triangular grids in the context of the computation of chemically reacting flows. The condition given by Eq. (4.2.5e) under which there exists a basic contradiction between accuracy

and consistency was derived. However, it was stated incorrectly that there is no linear scheme which ensured positivity. As will be shown below, it is in fact very simple to derive a scheme which ensures positivity. Several attempts were made by Maman to construct schemes which guarantee accuracy and positivity. These attempts involved extended stencils and modified test functions. An interesting idea examined by Maman was the development of nonlinear schemes based on the definition of a diffusion velocity. Through dimensional arguments, it may be said that $\rho \mathbf{v} \phi = \mu \nabla \phi$, which leads to $\mathbf{v} = \nu \nabla \ln \phi$, where \mathbf{v} may now be interpreted as a diffusion velocity. Positivity may then be guaranteed by simple upwinding based on the sign of the normal velocity. However, this scheme clearly has difficulties as $\phi \rightarrow 0$, for which a truncation error analysis reveals inconsistency, and the scheme is not defined for $\phi < 0$. These difficulties prevent an application to viscous flows. The method adopted by Maman to guarantee positive coefficients for the Galerkin linear finite-element discretisation was to employ Delaunay triangulations.

The most relevant piece of work in the present context is that of Coirier [13]. He analysed the accuracy and positivity of six schemes on adaptively refined Cartesian grids. The analysis was motivated by the observation that non-positive schemes lead to non-monotone solutions and even divergence for low-Reynolds-number flows. Adaptively refined Cartesian grids constitute a particularly severe test cases, as they invariably exhibit large variations in cell areas across refinement boundaries.

Four schemes based on the application of the Green-Gauss theorem were shown to be inconsistent and non-positive on refined or stretched grids. Of these schemes, two lead to decoupled stencils. Two further schemes obtained the gradient from the reconstruction of a linear or quadratic polynomial. This leads to a 3×3 or 6×6 linear system at each control volume face. A careful choice of stencils at each face is required to ensure that the linear systems are invertible. Neither linear nor quadratic reconstruction guaranteed positive stencils on arbitrary grids.

Calculations of low-Reynolds number flows over a backward-facing step showed that the chosen Green-Gauss scheme lead to a larger number of non-positive stencils than the quadratic polynomial reconstruction scheme, but the magnitude of non-positivity was less severe.

In a separate study, Coirier solved Eqs. (4.2.5a)-(4.2.6d) subject to the condition

of positivity. This leads to a quadratic programming problem. Since the system is solved for each control volume, conservation is not ensured. The size of the stencils was reduced until a positive scheme was found, but the resulting procedure was not found to be robust and required an appreciable amount of memory [14]. Furthermore, the computation of the weights may require a significant amount of processing time. For large grids, however, this may be negligible compared to the time required for the complete calculation. In addition, the additional robustness afforded by positivity may also lead to faster convergence.

Accuracy. Erlebacher [19] investigated the accuracy of two discretisations of Laplace's equation on a variety of generic distorted triangular grids. The first discretisation is essentially equivalent to the Galerkin linear finite-element method and the second is identical to that described in Subsection 4.2.4 which averages gradients in the cells adjacent to each edge. Both discretisations were shown to be inconsistent on distorted grids in general, although the second was more accurate.

Baumeister [7] compared Galerkin linear finite-element and finite-difference discretisations of the Laplacian on various generic triangular grids. It was found that the two methods gave identical results provided that the area of the triangles meeting at a given vertex is equal to three times the area of the Voronoi region around that vertex. This implies that at least one of the two methods is inconsistent on arbitrary grids.

In subsequent work, Baumeister [8] suggested the use of linear combinations of Laplacians computed on three stencils. The first stencil is that originally considered, whereas the other two are given by a subset of neighbouring vertices which are suitably retriangulated. The required weights for the linear combinations are obtained by solving a 3×3 system of linear equations corresponding to Eqs. (4.2.5d)-(4.2.5f). For certain geometric configurations, the linear system can become linearly dependent, however.

Renard and Essers [49] investigated the errors incurred by the discretisations of the convection-diffusion equation on randomly distorted quadrilateral grids. Theoretical and numerical results for the classical finite-element method showed that the discretised diffusion terms were inconsistent on irregular grids and that consistency was obtained only on nearly uniform grids.

Montgomery and Fleeter [43] analytically investigated the truncation errors resulting

from the discretisation of Laplace's equation by a finite-difference method on nine-point stencils on quadrilateral grids. A symbolic mathematics package was used to reduce the substantial amount of algebra involved in deriving the leading terms of the truncation error. The sensitivity of grid skewness and aspect ratio was studied. For distorted grids, the discretisation was shown to be highly inconsistent. The effects of skewness were found to be more severe than those of stretching.

Pseudo-Laplacians. Discretisations based on centred differences require artificial diffusion terms to damp oscillations and provide stability. The artificial diffusion terms typically include a so-called pseudo-Laplacian operator. The expression 'pseudo' is used to indicate that the Laplacian is based on undivided differences in its discrete form. This is in contrast to the (proper) Laplacian operator, which is based on divided differences in its discrete form.

There are two important differences between the two forms. First, the weights $\tilde{\omega}_i$ for the pseudo-Laplacian are dimensionless whereas the weights ω_i for the Laplacian are of dimension $(\text{length})^{-2}$. Second, the consistency conditions for the Laplacian given by Eqs. (4.2.5a)-(4.2.5c) actually lead to a second-order accurate pseudo-Laplacian. It is noted again that the conditions expressed by Eqs. (4.2.5b) and (4.2.5c) express the property that the (pseudo-) Laplacian of a linear function is identically zero.

The construction of a second-order accurate pseudo-Laplacian is particularly important since the artificial diffusion terms should not degrade the second-order accuracy of the centred discretisation. Since this requires satisfaction of Eqs. (4.2.5a)-(4.2.5c), the construction of linearly-transparent pseudo-Laplacians is also of interest to the present discussion.

Lindquist [33] investigated the construction of second-order accurate artificial diffusion terms on triangular and quadrilateral grids. The second differences were formed by integrating over cells and summing the contributions of the cells meeting at a node. To prevent the appearance of the chequerboard spurious solution mode, the integration on quadrilateral grids is carried out by subdividing the cells into two triangles and integrating over the triangle which includes the node at which the second difference is formed. A grid-refinement study confirmed that the second differences were indeed of second-order accuracy on uniform grids, with only small reductions in accuracy for

randomly distorted grids.

Holmes and Connell [24] used the method of Lagrange multipliers to derive a linearly-transparent pseudo-Laplacian in two dimensions. By specifying that the deviation of the edge-weights from unity be minimised subject to the constraints expressed by Eqs. (4.2.5b) and (4.2.5c), explicit formulae for the edge-weights were derived. The edge-weights guarantee a linearly-transparent pseudo-Laplacian in the interior and at boundaries regardless of cell types. As noted by Holmes and Connell, the edge-weights can differ significantly from unity on distorted grids and are not guaranteed to be positive. They elected to clip the weights to the range $0 \leq \tilde{\omega}_{0i} \leq 2$. It should be noted that by clipping the weights, the pseudo-Laplacian loses its properties of consistency and transparency to linear functions. A disadvantage of the edge-weights of Holmes and Connell is that they are not uniquely assigned to an edge, and are therefore not conservative.

Crumpton [16] suggested the construction of a linearly-transparent pseudo-Laplacian by subtracting the leading term in the truncation error expression of a pseudo-Laplacian which is not linearly transparent. This requires the storage of the left-hand sides of Eqs. (4.2.5b) and (4.2.5c) and a method which computes the gradients of a linear function exactly.

Comments. Although previous work indicated some ways in which the fundamental problems of discretising the Laplacian operator in an accurate and positive fashion can be attacked, it failed to find an equally fundamental approach which resolves the problems completely.

4.2.4 Non-Canonical Discretisations

The following sections illustrate two schemes which lead to non-positive discretisations on arbitrary grids. They are obtained not by reconstructing gradients at the control-volume faces, but rather by averaging gradients obtained at vertices or at cell centres. This is equivalent to averaging across or along a control-volume face, as depicted in Fig. 4.7.

The discretisations are termed non-canonical because they reconstruct the gradients

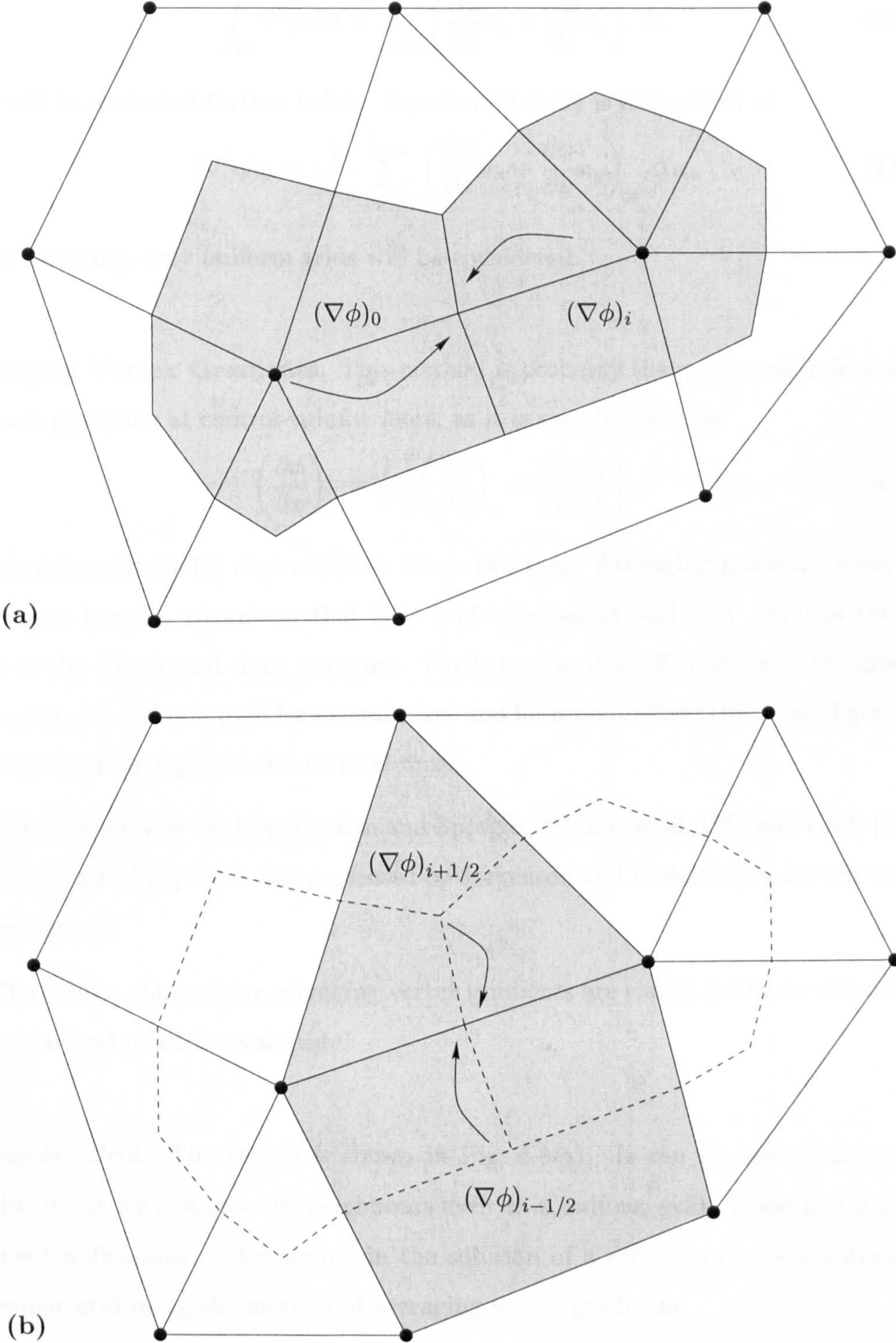


Figure 4.7: Obtaining gradients as control-volume faces by (a) averaging vertex-gradients across control-volume face or (b) averaging cell-gradients along control-volume face.

in the x - and y -directions separately,

$$\int_{\Omega} \nabla^2 \phi dA = \oint_{\partial\Omega} \left(\frac{\partial \phi}{\partial x} n_x + \frac{\partial \phi}{\partial y} n_y \right) ds. \quad (4.2.12)$$

This will be discussed further below. Equation (4.2.12) is discretised as

$$(\nabla^2 \phi)_0 \approx \frac{1}{A_{\Omega_0}} \sum_{0i \in \mathcal{E}_0} \left(\frac{\partial \phi}{\partial x} n_x + \frac{\partial \phi}{\partial y} n_y \right)_{0i} \Delta s_{0i} \quad (4.2.13)$$

In the following, only uniform grids will be considered.

Averaging Vertex Gradients. This method is probably the most straightforward to compute gradients at control-volume faces, as it is simply given by,

$$\left(\frac{\partial \phi}{\partial x} \right)_{0i} = \frac{1}{2} \left[\left(\frac{\partial \phi}{\partial x} \right)_0 + \left(\frac{\partial \phi}{\partial x} \right)_i \right], \quad (4.2.14)$$

and correspondingly for derivatives in the y -direction. Averaging gradients computed at vertices has the advantage that it is grid-transparent and only requires the first array of the edge-based data structure. Furthermore, it is efficient since the gradient computed at a vertex is used for several edges and because it allows the reuse of gradients reconstructed for higher-order inviscid fluxes.

This method was used by Karman and Spragle [29], Luo et al. [36], and Galle [20]. A slightly modified approach was presented by Jorgenson and Pletcher [28] for cell-centred discretisations.

The results obtained by averaging vertex gradients are shown below for the uniform triangular and quadrilateral grid.

Triangular Grid. The stencil is shown in Fig. 4.8(a). It can be seen that negative weights occur for distance-one neighbours even on a uniform grid. Wood and Kleb [61] observed indications of decoupling in the solution of a diffusion problem solved on a triangular grid using the method of averaging vertex gradients.

Quadrilateral Grid. For the uniform quadrilateral grid, the coefficients are positive, but only distance-two neighbours are involved in the stencil, as can be seen from Fig. 4.8(b). This allows the appearance of spurious modes. When substituting Eq. (4.2.9)

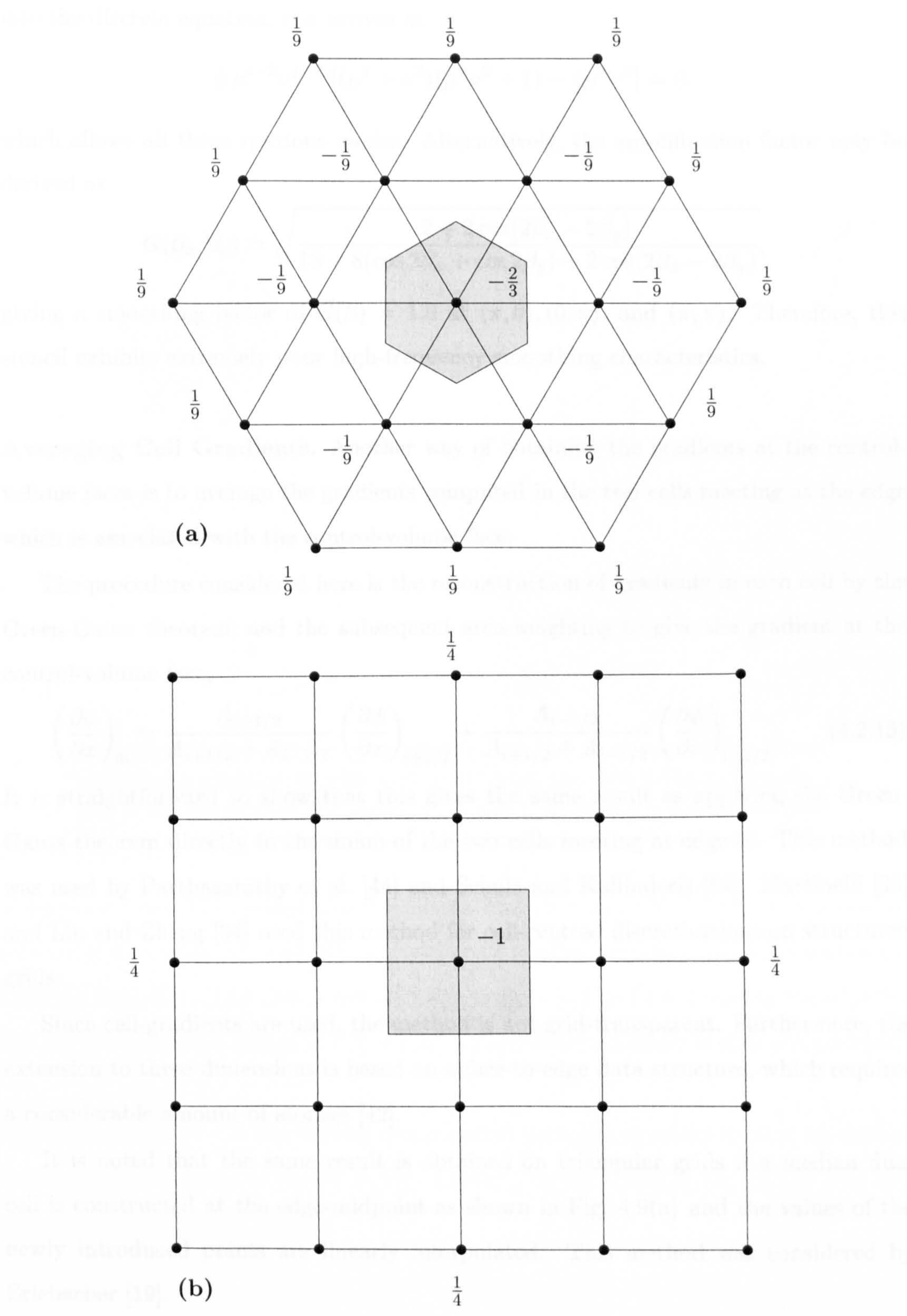


Figure 4.8: Stencils obtained when averaging node-gradients across control-volume faces for (a) equilateral triangular grid and (b) uniform quadrilateral grid.

into the discrete equation, one arrives at

$$\hat{\phi} \mu^{i-2} \nu^{j-2} [(\mu^2 + \nu^2)(\mu^2 \nu^2 + 1) - 4\mu^2 \nu^2] = 0,$$

which allows all three spurious modes. Alternatively, the amplification factor may be derived as

$$G(\beta_x, \beta_y) = \sqrt{\frac{2 + 2 \cos(2\beta_x - 2\beta_y)}{18 - 8(\cos 2\beta_x + \cos 2\beta_y) + 2 \cos(2\beta_x - 2\beta_y)}},$$

giving a smoothing factor of $\bar{G}(\beta) = 1.0$ at $(\pi, 0)$, $(0, \pi)$, and (π, π) . Therefore, this stencil exhibits extremely poor high-frequency smoothing characteristics.

Averaging Cell Gradients. Another way of obtaining the gradients at the control-volume faces is to average the gradients computed in the two cells meeting at the edge which is associated with the control-volume face.

The procedure considered here is the reconstruction of gradients in each cell by the Green-Gauss theorem, and the subsequent area-weighting to give the gradient at the control-volume face,

$$\left(\frac{\partial \phi}{\partial x}\right)_{0i} = \frac{A_{i+1/2}}{A_{i+1/2} + A_{i-1/2}} \left(\frac{\partial \phi}{\partial x}\right)_{i+1/2} + \frac{A_{i-1/2}}{A_{i+1/2} + A_{i-1/2}} \left(\frac{\partial \phi}{\partial x}\right)_{i-1/2}. \quad (4.2.15)$$

It is straightforward to show that this gives the same result as applying the Green-Gauss theorem directly to the union of the two cells meeting at edge $0i$. This method was used by Parthasarathy et al. [44] and Schulz and Kallinderis [51]. Martinelli [38] and Liu and Zheng [34] used this method for cell-centred discretisations on structured grids.

Since cell-gradients are used, the method is not grid-transparent. Furthermore, the extension to three dimensions is based on a face-to-edge data structure, which requires a considerable amount of storage [42].

It is noted that the same result is obtained on triangular grids if a median dual cell is constructed at the edge-midpoint as shown in Fig. 4.9(a) and the values of the newly introduced points are linearly interpolated. This method was considered by Erlebacher [19].

On a uniform grid, Eq. (4.2.15) of course simplifies to

$$\left(\frac{\partial \phi}{\partial x}\right)_{0i} = \frac{1}{2} \left[\left(\frac{\partial \phi}{\partial x}\right)_{i+1/2} + \left(\frac{\partial \phi}{\partial x}\right)_{i-1/2} \right].$$

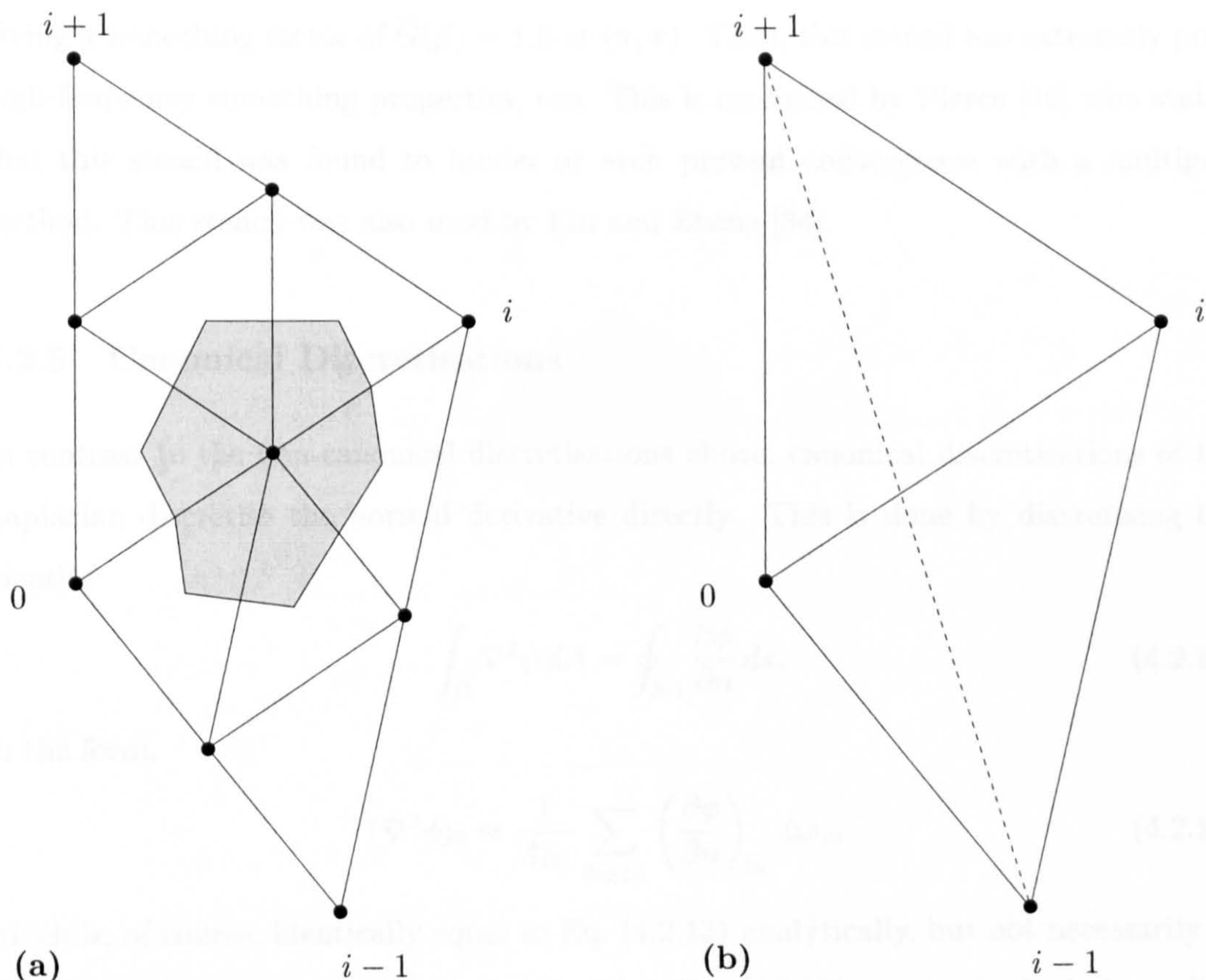


Figure 4.9: (a) Averaging gradients at edges is equivalent to reconstructing a gradient at edge mid-point using the Green-Gauss theorem. (b) If the diagonal of the points $i-1$ and $i+1$ does not bisect the edge $0i$ (as shown), the averaged gradient is not second-order accurate.

Triangular Grid. The desired stencil is obtained, as shown in Fig. 4.10(a). It is straightforward if somewhat tedious to show that the gradient at a cell face will be second-order accurate only if the line drawn between the points $i-1$ and $i+1$ bisects the edge $0i$. For the grid fragment shown in Fig. 4.9(b), second-order accuracy is thus not achieved.

Quadrilateral Grid. On the regular quadrilateral grid, the so-called rotated or skewed Laplacian is obtained, as shown in Fig. 4.10(b). By substituting Eq. (4.2.9) into the difference equation, one derives

$$\hat{\phi} \mu^{i-1} \nu^{j-1} [(\mu^2 + 1)(\nu^2 + 1) - 4\mu\nu] = 0,$$

which allows the checkerboard mode only. The amplification factor is given by

$$G(\beta_x, \beta_y) = \sqrt{\frac{4 \cos^2 \beta_x}{4 \cos^2 \beta_x + 16(1 - \cos \beta_x \cos \beta_y)}},$$

giving a smoothing factor of $\overline{G}(\beta) = 1.0$ at (π, π) . Thus, this stencil has extremely poor high-frequency smoothing properties, too. This is confirmed by Pierce [46] who stated that this stencil was found to hinder or even prevent convergence with a multigrid method. This stencil was also used by Liu and Zheng [34].

4.2.5 Canonical Discretisations

In contrast to the non-canonical discretisations above, canonical discretisations of the Laplacian discretise the normal derivative directly. This is done by discretising the identity

$$\int_{\Omega} \nabla^2 \phi \, dA = \oint_{\partial\Omega} \frac{\partial \phi}{\partial n} \, ds, \quad (4.2.16)$$

in the form,

$$(\nabla^2 \phi)_0 \approx \frac{1}{A_{\Omega_0}} \sum_{0i \in \mathcal{E}_0} \left(\frac{\partial \phi}{\partial n} \right)_{0i} \Delta s_{0i}, \quad (4.2.17)$$

which is, of course, identically equal to Eq. (4.2.13) analytically, but not necessarily at the discrete level. A variety of schemes based on Eq. (4.2.17) may be devised, depending on the way in which the normal derivative is approximated.

Scheme 1. Equation (4.2.17) is discretised as

$$(\nabla^2 \phi)_0 \approx \frac{1}{A_{\Omega_0}} \sum_{0i \in \mathcal{E}_0} \left(\frac{\Delta \phi}{\Delta n} \right)_{0i} \Delta s_{0i}. \quad (4.2.18)$$

At each face, the normal derivative is approximated by

$$\left(\frac{\Delta \phi}{\Delta n} \right)_{0i} \approx \frac{\phi_i - \phi_0}{\Delta n_{0i}} \quad (4.2.19)$$

where $\Delta n_{0i} = \|\mathbf{r}_i - \mathbf{r}_0\|$ to give

$$(\nabla^2 \phi)_0 \approx \frac{1}{A_{\Omega_0}} \sum_{0i \in \mathcal{E}_0} \frac{\Delta s_{0i}}{\Delta n_{0i}} (\phi_i - \phi_0). \quad (4.2.20)$$

It is noted that this discretisation guarantees positive weights regardless of grid distortion. Consequently, it will be inaccurate on distorted grids, as discussed previously.

Triangular and Quadrilateral Grids. Equation (4.2.20) gives the desired stencils shown in Fig. 4.3 on both triangular and quadrilateral grids. Spurious solution modes

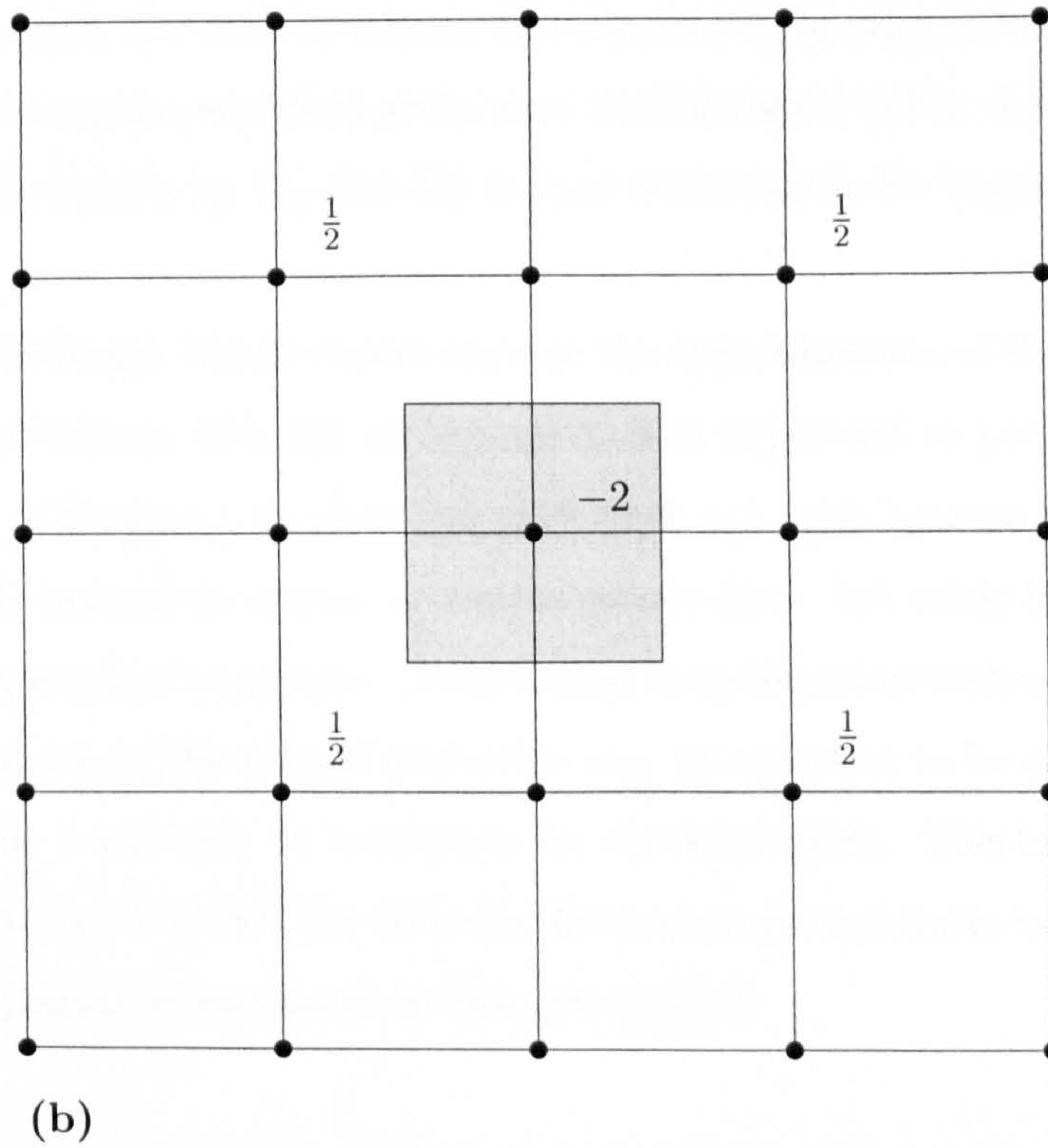
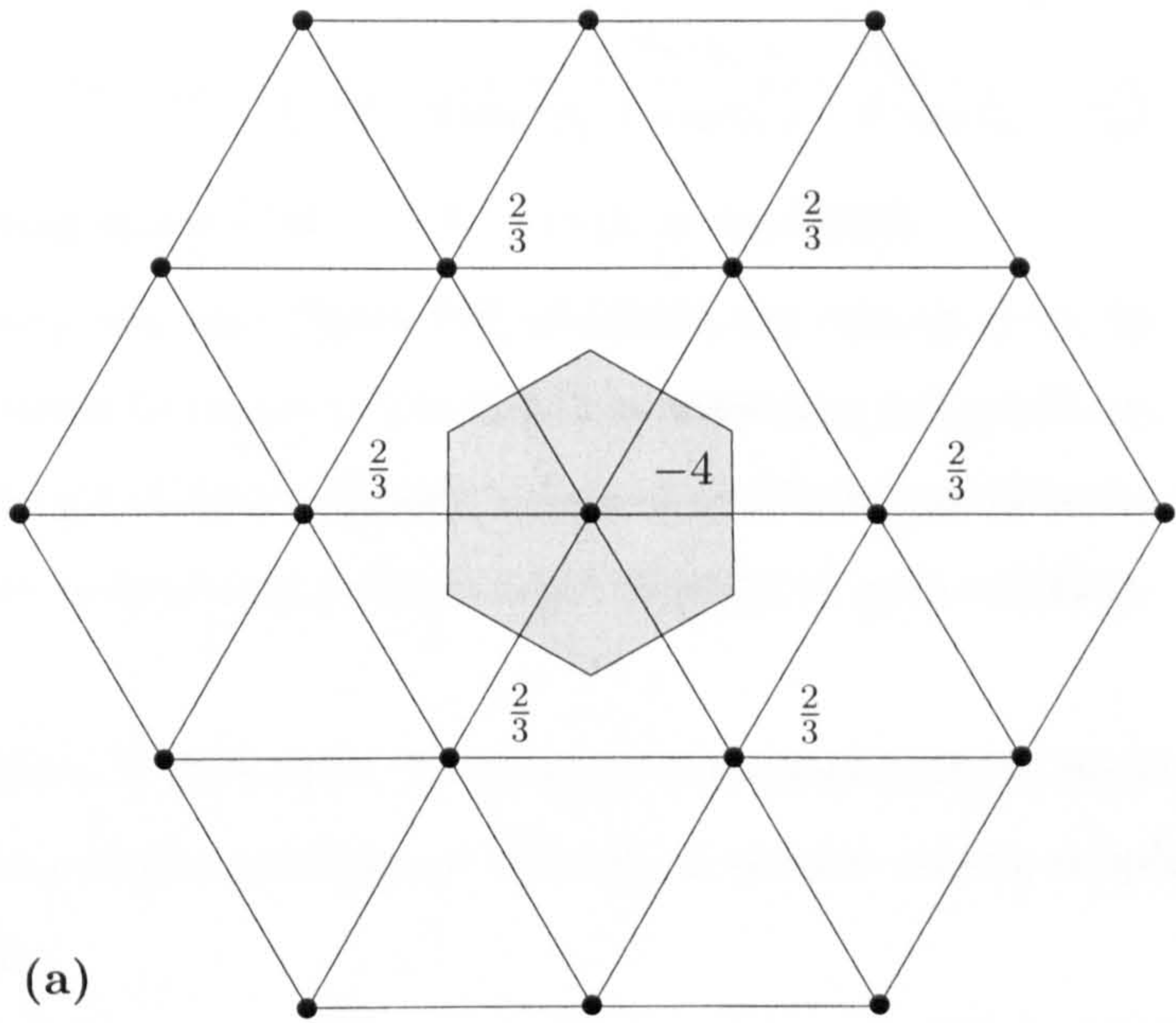


Figure 4.10: Stencils obtained when averaging cell-gradients along control-volume faces for (a) equilateral triangular grid and (b) uniform quadrilateral grid.

do not occur. For the quadrilateral grid, the amplification factor may be derived as

$$G(\beta_x, \beta_y) = \sqrt{\frac{2 + 2 \cos(\beta_x - \beta_y)}{18 - 8(\cos \beta_x + \cos \beta_y) + 2 \cos(\beta_x - \beta_y)}},$$

giving a smoothing factor $\bar{G}(\beta) = 0.5$ at $(\pi/2, \arccos(4/5))$.

Liu and Zheng [35] and Pierce [46] obtained the stencil given by Eq. (4.2.20) by applying a correction to the stencil obtained by averaging cell gradients. This procedure is justified on the grounds of economy since cell gradients can be reused for several cell faces, in contrast to gradients reconstructed directly at each cell face.

Advantages of Normal Derivative. The normal derivative leads to three key advantages: First, it leads to positive coefficients. Second, it ensures strong coupling. Third, it is grid-transparent.

It is clear that Eq. (4.2.19) is a good approximation only if the control-volume face is roughly normal to its associated edge. For the containment dual, this is always the case. For the median dual, the control-volume face can be nearly aligned with its associated edge on highly triangular stretched grids, such as that shown in Fig. 3.3(a). As a result, the approximation given by Eq. (4.2.19) is poor and needs to be improved.

Comment on Positivity. Before describing how the approximation of the normal derivative at a control-volume face can be improved, it is important to point out that the inaccuracy of Scheme 1 on distorted grids does *not* arise because of an inaccurate estimation of the normal derivative at control-volume faces, but solely because its coefficients are guaranteed to be positive. Even if used in conjunction with containment-dual control volumes, where the normal derivative may be expected to be approximated accurately, Scheme 1 will still be inaccurate on distorted grids. This issue will become clearer when the link between the Galerkin finite-element and finite-volume discretisations of the Laplacian is uncovered in Subsection 4.4.2.

Scheme 2. In order to avoid the problems due to non-alignment of edges with control-volume faces, the normal derivative may be approximated at each control-volume face by introducing coordinates $\xi = \xi(x, y)$ along the edge $0i$ and $\eta = \eta(x, y)$ along the control-volume face, as shown in Fig. 4.11.

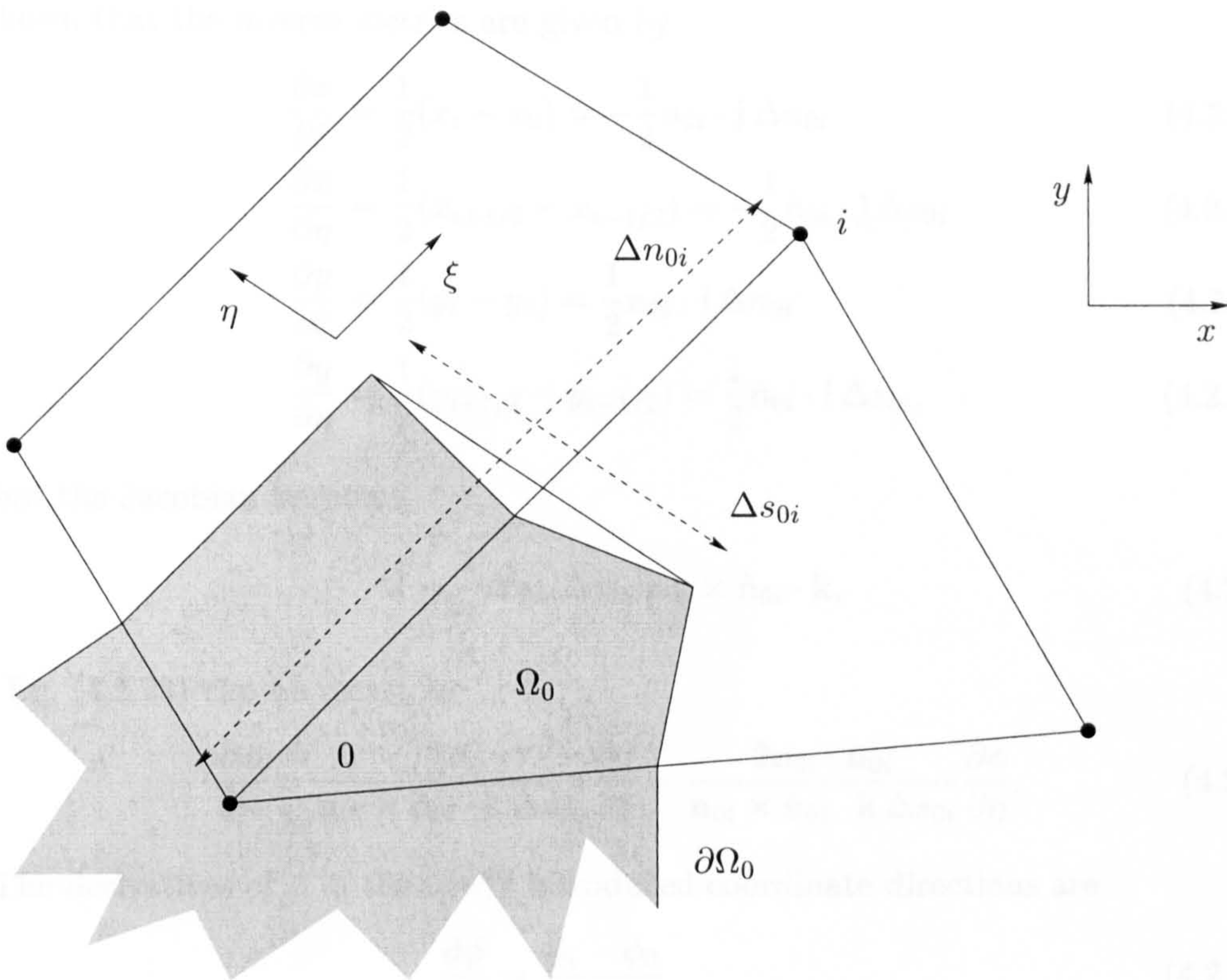


Figure 4.11: Definition of geometric terms for canonical discretisation with Scheme 2.

Using the chain rule of calculus, the normal derivative at the control-volume face may be written as

$$\frac{\partial \phi}{\partial n} = \frac{\partial \phi}{\partial \xi} \left(\frac{\partial \xi}{\partial x} \hat{n}_{0i,x} + \frac{\partial \xi}{\partial y} \hat{n}_{0i,y} \right) + \frac{\partial \phi}{\partial \eta} \left(\frac{\partial \eta}{\partial x} \hat{n}_{0i,x} + \frac{\partial \eta}{\partial y} \hat{n}_{0i,y} \right), \quad (4.2.21)$$

where $\partial \phi / \partial \xi$ and $\partial \phi / \partial \eta$ denote the derivatives along edge $0i$ and tangential to the control-volume face, respectively.

By introducing the Jacobian J , defined as

$$J = \frac{\partial x}{\partial \xi} \frac{\partial y}{\partial \eta} - \frac{\partial x}{\partial \eta} \frac{\partial y}{\partial \xi} \quad (4.2.22)$$

Eq. (4.2.21) can also be written in terms of the inverse metrics as

$$\frac{\partial \phi}{\partial n} = \frac{1}{J} \frac{\partial \phi}{\partial \xi} \left(\frac{\partial y}{\partial \eta} \hat{n}_{0i,x} - \frac{\partial x}{\partial \eta} \hat{n}_{0i,y} \right) - \frac{1}{J} \frac{\partial \phi}{\partial \eta} \left(\frac{\partial y}{\partial \xi} \hat{n}_{0i,x} - \frac{\partial x}{\partial \xi} \hat{n}_{0i,y} \right). \quad (4.2.23)$$

By parameterising the edge $0i$ in $\xi \in [-1, 1]$ and the dual edge in $\eta \in [-1, 1]$, it can

be shown that the inverse metrics are given by

$$\frac{\partial x}{\partial \xi} = \frac{1}{2}(x_i - x_0) = -\frac{1}{2}\mathbf{n}_{0i} \cdot \mathbf{j} \Delta n_{0i} \quad (4.2.24a)$$

$$\frac{\partial x}{\partial \eta} = \frac{1}{2}(x_{i+1/2} - x_{i-1/2}) = -\frac{1}{2}\hat{\mathbf{n}}_{0i} \cdot \mathbf{j} \Delta s_{0i} \quad (4.2.24b)$$

$$\frac{\partial y}{\partial \xi} = \frac{1}{2}(y_i - y_0) = \frac{1}{2}\mathbf{n}_{0i} \cdot \mathbf{i} \Delta n_{0i} \quad (4.2.24c)$$

$$\frac{\partial y}{\partial \eta} = \frac{1}{2}(y_{i+1/2} - y_{i-1/2}) = \frac{1}{2}\hat{\mathbf{n}}_{0i} \cdot \mathbf{i} \Delta s_{0i}, \quad (4.2.24d)$$

so that the Jacobian becomes

$$J = \frac{1}{4} \Delta s_{0i} \Delta n_{0i} \mathbf{n}_{0i} \times \hat{\mathbf{n}}_{0i} \cdot \mathbf{k}, \quad (4.2.25)$$

and Eq. (4.2.23) can be recast as

$$\frac{\partial \phi}{\partial n} = \frac{2}{\mathbf{n}_{0i} \times \hat{\mathbf{n}}_{0i} \cdot \mathbf{k} \Delta n_{0i}} \frac{\partial \phi}{\partial \xi} - \frac{2\mathbf{n}_{0i} \cdot \hat{\mathbf{n}}_{0i}}{\mathbf{n}_{0i} \times \hat{\mathbf{n}}_{0i} \cdot \mathbf{k} \Delta s_{0i}} \frac{\partial \phi}{\partial \eta}. \quad (4.2.26)$$

The derivatives of ϕ in the newly introduced coordinate directions are

$$\frac{\partial \phi}{\partial \xi} = \frac{\phi_i - \phi_0}{2} \quad (4.2.27a)$$

$$\frac{\partial \phi}{\partial \eta} = \frac{\phi_{i+1/2} - \phi_{i-1/2}}{2}, \quad (4.2.27b)$$

where $\phi_{i+1/2}$ and $\phi_{i-1/2}$ are the values at the centroids of the cells $i + 1/2$ and $i - 1/2$.

Equation (4.2.17) can then be written as

$$(\nabla^2 \phi)_0 \approx \frac{1}{A_{\Omega_0}} \sum_{0i \in \mathcal{E}_0} \left[\frac{1}{\mathbf{n}_{0i} \times \hat{\mathbf{n}}_{0i} \cdot \mathbf{k} \Delta n_{0i}} (\phi_i - \phi_0) - \frac{\mathbf{n}_{0i} \cdot \hat{\mathbf{n}}_{0i}}{\mathbf{n}_{0i} \times \hat{\mathbf{n}}_{0i} \cdot \mathbf{k}} (\phi_{i+1/2} - \phi_{i-1/2}) \right]. \quad (4.2.28)$$

By introducing the angle θ_{0i} as defined in Fig. 4.12, it can be shown that

$$\mathbf{n}_{0i} \times \hat{\mathbf{n}}_{0i} \cdot \mathbf{k} = \cos \theta_{0i} \quad (4.2.29a)$$

$$\mathbf{n}_{0i} \cdot \hat{\mathbf{n}}_{0i} = -\sin \theta_{0i}, \quad (4.2.29b)$$

which allows Eq. (4.2.28) to be recast as

$$(\nabla^2 \phi)_0 \approx \frac{1}{A_{\Omega_0}} \sum_{0i \in \mathcal{E}_0} \left[\frac{1}{\cos \theta_{0i} \Delta n_{0i}} (\phi_i - \phi_0) + \tan \theta_{0i} (\phi_{i+1/2} - \phi_{i-1/2}) \right]. \quad (4.2.30)$$

This method was also used by Jiang and Przekwas [25], Jiang et al. [26], and Mathur and Murthy [39] for the computation of incompressible flows in two dimensions. A similar method was derived by Davidson [18].

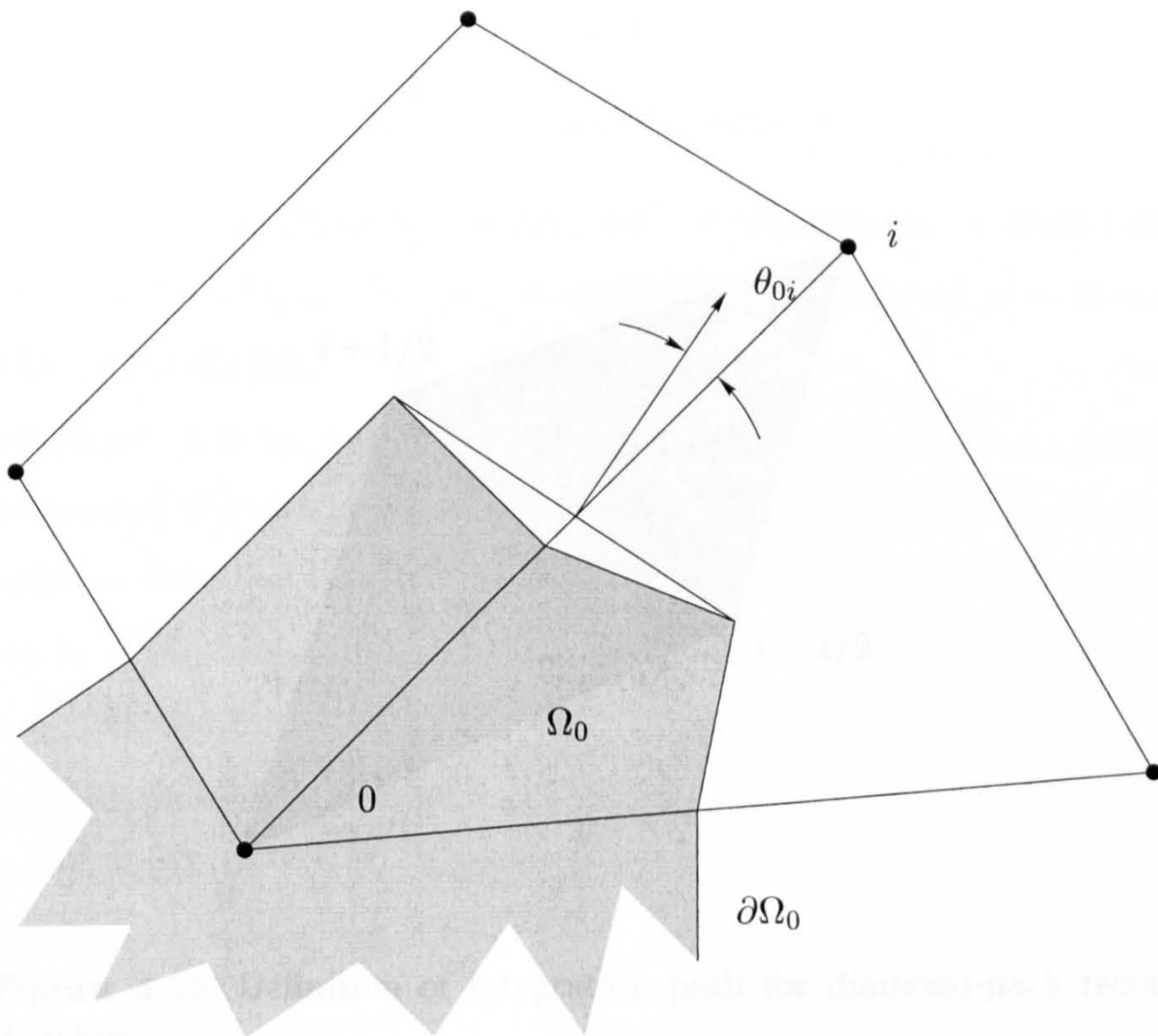


Figure 4.12: Definition of angle θ_{0i} .

For triangular grids, Eq. (4.2.30) can also be rewritten as

$$(\nabla^2 \phi)_0 \approx \frac{1}{A_{\Omega_0}} \sum_{0i \in \mathcal{E}_0} \left[\frac{1}{\cos \theta_{0i}} \frac{\Delta s_{0i}}{\Delta n_{0i}} - \frac{1}{3} (\tan \theta_{0i+1} - \tan \theta_{0i-1}) \right] (\phi_i - \phi_0). \quad (4.2.31)$$

Triangular and Quadrilateral Grids. If the control-volume face is normal to its associated edge, Eq. (4.2.30) reduces to Eq. (4.2.20). As a result, the same stencils and properties are obtained.

Equivalence to Diamond-Path Reconstruction. The discretisation given by Eq. (4.2.30) is equivalent to the discretisation labelled ‘diamond-path reconstruction’ by Coirier [13] and used by Knight [31] and Stolcis and Johnston [52] for cell-centred discretisations on triangular grids. The integration path for the diamond reconstruction scheme is shown schematically in Fig. 4.13.

The Green-Gauss theorem is applied to the path given by connecting the edge

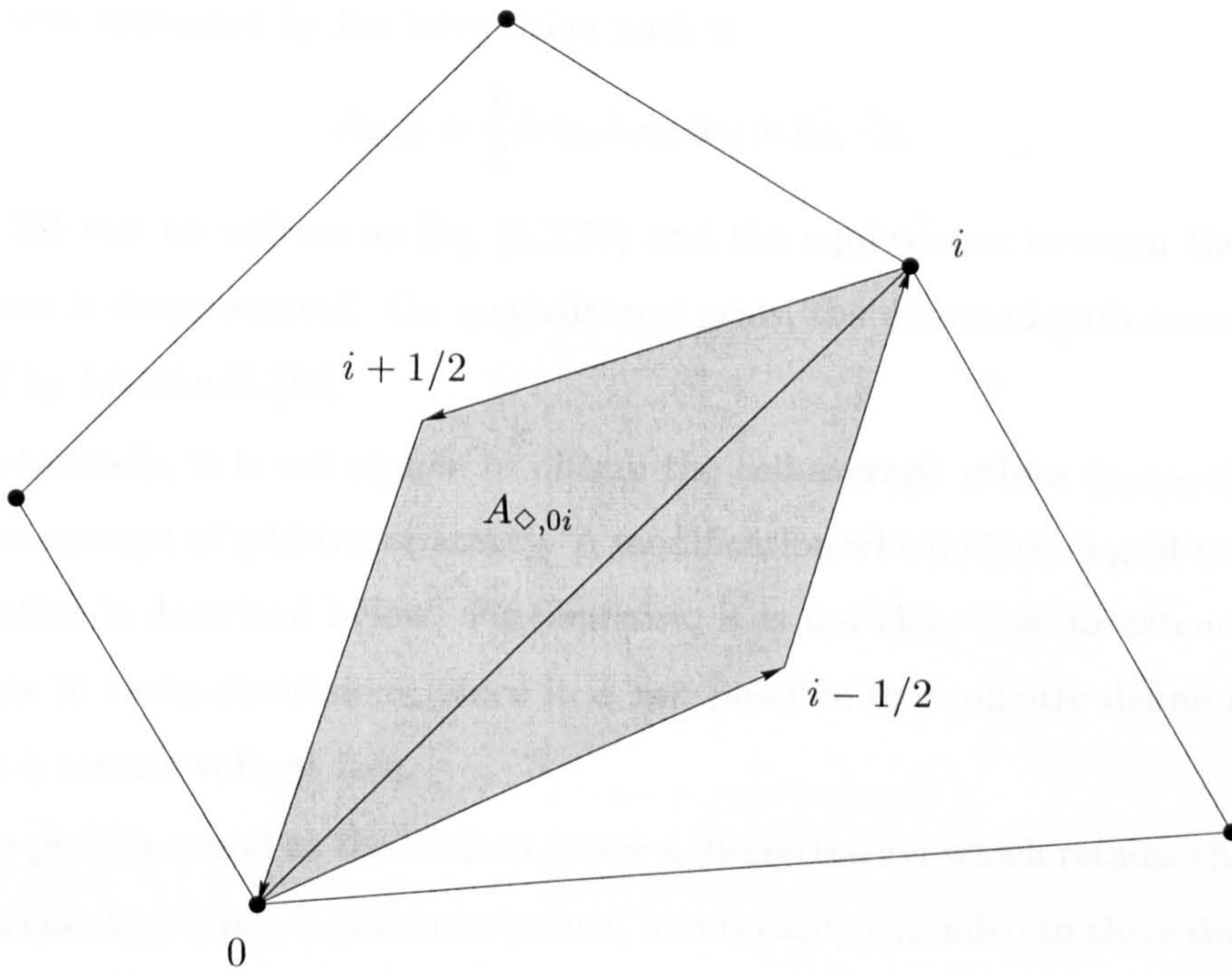


Figure 4.13: Definition of integration path for diamond-path reconstruction.

endpoints to the centroids of the cells sharing that edge. This gives

$$\left(\frac{\partial \phi}{\partial x}\right)_{0i} \approx \frac{1}{2A_{\diamond,0i}} [(\phi_i - \phi_0)(y_{i+1/2} - y_{i-1/2}) - (\phi_{i+1/2} - \phi_{i-1/2})(y_i - y_0)] \quad (4.2.32a)$$

$$\left(\frac{\partial \phi}{\partial y}\right)_{0i} \approx -\frac{1}{2A_{\diamond,0i}} [(\phi_i - \phi_0)(x_{i+1/2} - x_{i-1/2}) - (\phi_{i+1/2} - \phi_{i-1/2})(x_i - x_0)] \quad (4.2.32b)$$

where $A_{\diamond,0i}$ is the area enclosed by the path. The Laplacian at vertex 0 is then formed from Eq. (4.2.13) to give

$$\begin{aligned} (\nabla^2 \phi)_0 \approx \frac{1}{A_{\Omega_0}} \sum_{0i \in \mathcal{E}_0} \frac{1}{2A_{\diamond,0i}} \Big\{ & [(y_{i+1/2} - y_{i-1/2})\hat{n}_{0i,x} - (x_{i+1/2} - x_{i-1/2})\hat{n}_{0i,y}](\phi_i - \phi_0) \\ & - [(y_i - y_0)\hat{n}_{0i,x} - (x_i - x_0)\hat{n}_{0i,y}](\phi_{i+1/2} - \phi_{i-1/2}) \Big\} \Delta s_{0i}. \end{aligned} \quad (4.2.33)$$

Since the normal vectors are given by

$$\hat{\mathbf{n}}_{0i} = \frac{y_{i+1/2} - y_{i-1/2}}{\Delta s_{0i}} \mathbf{i} - \frac{x_{i+1/2} - x_{i-1/2}}{\Delta s_{0i}} \mathbf{j} \quad (4.2.34a)$$

$$\mathbf{n}_{0i} = \frac{y_i - y_0}{\Delta n_{0i}} \mathbf{i} - \frac{x_i - x_0}{\Delta n_{0i}} \mathbf{j} \quad (4.2.34b)$$

and the area contained by the integration path is

$$A_{\diamond,0i} = \frac{1}{2} \Delta n_{0i} \Delta s_{0i} \mathbf{n}_{0i} \times \hat{\mathbf{n}}_{0i} \cdot \mathbf{k}, \quad (4.2.35)$$

Eq. (4.2.33) can be written as Eq. (4.2.30) and the equivalence between the two discretisations is demonstrated. On quadrilateral grids, the diamond-path reconstruction was used by Martinelli [38].

Unfortunately, it is not simple to obtain the cell-average values $\phi_{i+1/2}$ and $\phi_{i-1/2}$ within the concept of grid-transparency. A modification which allows a grid-transparent discretisation is described below. Furthermore, it is not clear how to extend this discretisation to three dimensions, since it is not possible to explicitly define a tangent vector at a control-volume face.

These problems lead to the wish to derive a discretisation which retains the benefits of the normal derivative, is grid-transparent, and is easily extended to three dimensions. One possibility is described below.

Scheme 3. Concepts of non-canonical and canonical discretisations can be combined. For example, it was shown above that the averaging of vertex gradients is grid-transparent but exhibits poor coupling. To remedy these problems, the component of the averaged vertex gradients along the edge is substituted with the divided difference along the edge,

$$(\nabla \phi)_{0i} = (\overline{\nabla \phi})_{0i} - \left[(\overline{\nabla \phi})_{0i} \cdot \frac{\Delta \mathbf{r}_{0i}}{\Delta n_{0i}} - \frac{\phi_i - \phi_0}{\Delta n_{0i}} \right] \frac{\Delta \mathbf{r}_{0i}}{\Delta n_{0i}}, \quad (4.2.36)$$

where $(\overline{\nabla \phi})_{0i}$ denotes the averaged vertex gradient. This approach increases the coupling, guarantees positive weights on uniform grids, and is grid-transparent. It leads to the same stencils as Scheme 1 on uniform grids.

This scheme was used by Vilsmeier [56], Mathur and Murthy [39], Crumpton et al. [17], Weiss et al. [58], Blažek et al. [9], and Haselbacher and Blažek [23]. A similar scheme was used by Liu and Zheng [35] and Pierce [46] as described before.

It is interesting to note that the scalar product of Eq. (4.2.36) with the normal at a control-volume face can be written as

$$(\nabla \phi)_{0i} \cdot \hat{\mathbf{n}}_{0i} = \frac{\phi_i - \phi_0}{\Delta n_{0i}} \hat{\mathbf{n}}_{0i} \cdot \frac{\Delta \mathbf{r}_{0i}}{\Delta n_{0i}} + (\overline{\nabla \phi})_{0i} \times \Delta \mathbf{r}_{0i} \cdot \hat{\mathbf{n}}_{0i} \times \Delta \mathbf{r}_{0i}. \quad (4.2.37)$$

The second term vanishes if the control-volume face is orthogonal to its associated edge.

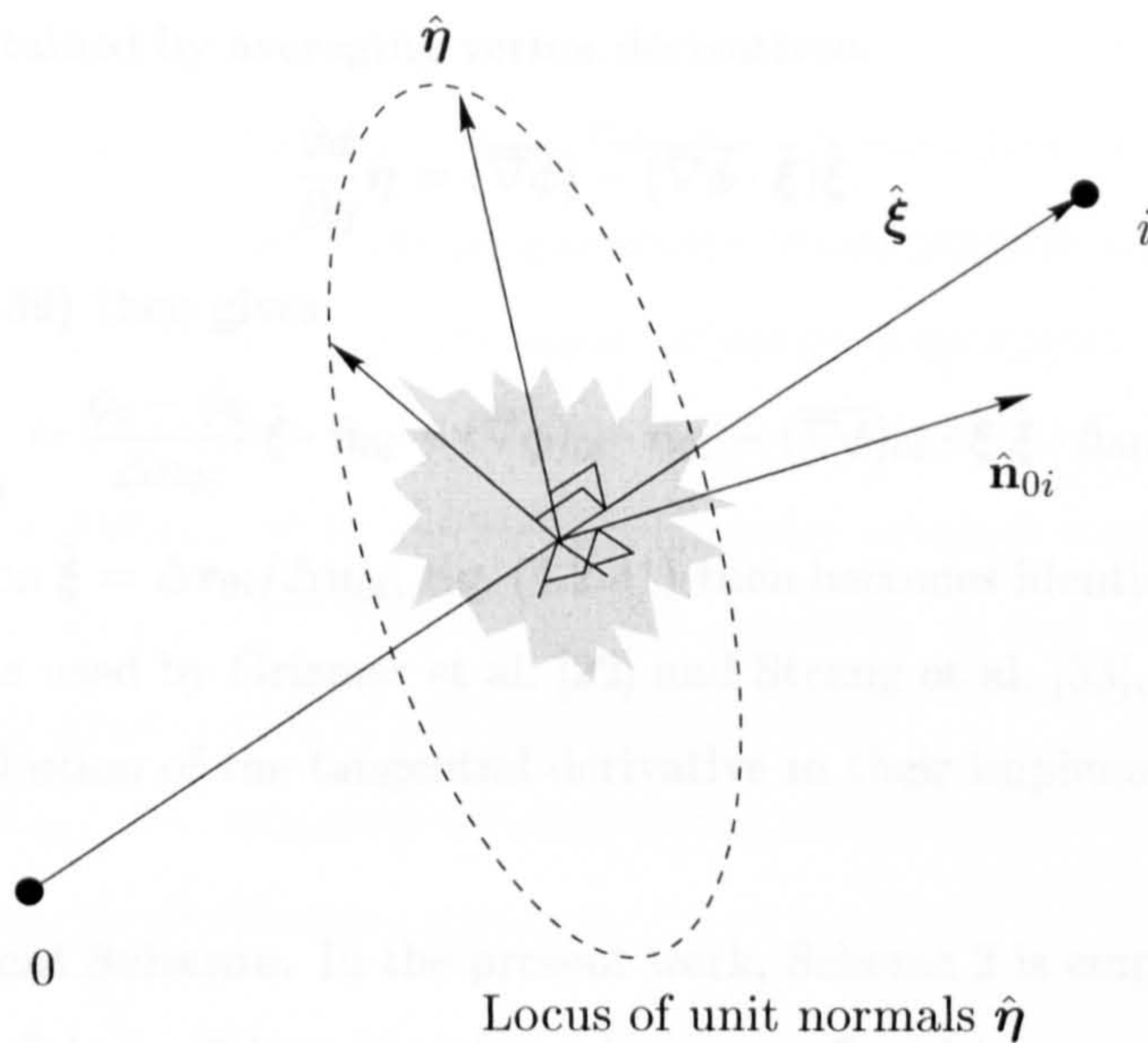


Figure 4.14: Explanation of nomenclature for alternative interpretation of canonical Scheme 3.

For this reason, it may be regarded as a tangential component of the normal projection of the gradient vector at the control-volume face. The main advantage of this scheme therefore lies in the property that the tangential component does not have to be defined explicitly. The main disadvantages are that the scheme requires vertex gradients to be available and that it leads to large stencils on non-uniform grids.

Alternative Interpretation. An alternative interpretation of Scheme 3 may be derived by defining a tangential component ϕ_t of a vector Φ in three dimensions through

$$\phi_t \mathbf{t} = \Phi - \phi_n \mathbf{n}. \quad (4.2.38)$$

By defining the direction ξ along the edge $0i$ (as for Scheme 2), and the direction η to be normal to the edge $0i$ (and hence non-unique), the normal gradient at the control-volume face may be written as

$$\left(\frac{\partial \phi}{\partial n} \right)_{0i} = \left(\frac{\partial \phi}{\partial \xi} \hat{\xi} + \frac{\partial \phi}{\partial \eta} \hat{\eta} \right) \cdot \hat{n}_{0i}, \quad (4.2.39)$$

where the nomenclature is defined in Fig. 4.14. The derivative in the ξ -direction is easily approximated using the divided difference along edge $0i$. Forming the derivative in the (non-unique) η -direction may be circumvented by using Eq. (4.2.38), where the

derivatives are obtained by averaging vertex derivatives,

$$\frac{\partial \phi}{\partial \eta} \hat{\eta} = (\overline{\nabla \phi}) - (\overline{\nabla \phi} \cdot \hat{\xi}) \hat{\xi}. \quad (4.2.40)$$

Equation (4.2.39) then gives

$$\left(\frac{\partial \phi}{\partial n} \right)_{0i} = \frac{\phi_i - \phi_0}{\Delta n_{0i}} \hat{\xi} \cdot \hat{n}_{0i} + (\overline{\nabla \phi})_{0i} \cdot \hat{n}_{0i} - (\overline{\nabla \phi})_{0i} \cdot \hat{\xi} \hat{\xi} \cdot \hat{n}_{0i}. \quad (4.2.41)$$

Using the definition $\hat{\xi} = \Delta \mathbf{r}_{0i} / \Delta n_{0i}$, Eq. (4.2.41) then becomes identical to Eq. (4.2.36). This approach was used by Grismer et al. [22] and Strang et al. [53], but they chose to neglect the contribution of the tangential derivative in their implementation.

Chosen Canonical Scheme. In the present work, Scheme 2 is employed, although it is recognised that Scheme 3 has advantages in terms of grid-transparency, particularly in three dimensions. The reason for employing Scheme 2 is that it was already being used in computations by the time the author became aware of Scheme 3.

4.3 The Case for Canonical Discretisations

At this point, two questions need to be addressed.

First, the above discussion has shown that there exists a fundamental contradiction between accuracy and positivity on an arbitrary grid. Both properties can be achieved on regular grids only. In practice, grids for complex geometries usually exhibit regions of local irregularities. It is unlikely that high-quality solutions will be obtained in these regions, if the irregularities allow a numerical solution to be obtained at all. A robust code is required in such situations, and a canonical scheme contributes toward a robust code.

Second, it was shown above that the maximum principle for Laplace's equation leads to the requirement of positive coefficients. The author is not aware of the existence of a maximum principle for the Navier-Stokes equations, neither in general nor in specific cases. In many instances, solutions to the Navier-Stokes equations do not obey a maximum principle. One might therefore raise the legitimate question as to whether positivity of the coefficients is required from a physical point of view. However, regardless of the answer to that question, it is still desirable to require positive coefficients from a numerical point of view. As argued in the introduction of this chapter, a posi-

tive discretisation ensures the positivity of quantities which are positive by definition, such as, e.g., the turbulence kinetic energy. Positive discretisations of the viscous terms therefore provide an important contribution to an overall positive discretisation.

As pointed out by Coirier [13], the issue of positive operators for high-Reynolds number flows is not as evident as for low-Reynolds number flows since the positivity of the inviscid stencil obtained by limited higher-order schemes might compensate for a non-positive viscous stencil.[†] Relying on the positivity of one stencil to mask the non-positivity of another stencil is not regarded as ideal.

For these reasons, the canonical discretisations are chosen to be extended to the viscous terms in the Navier-Stokes equations.

4.4 Navier-Stokes Equations

The following sections describe the extension of the canonical discretisation to the discretisation of the viscous terms in the Navier-Stokes equations. The widely-used Finite-Element discretisation of Barth [3] is also described.

The discretisation of the viscous terms may be formalised by introducing a viscous numerical flux function,

$$[g(\mathbf{q}, \nabla \mathbf{q}; \hat{\mathbf{n}})]_{0i} = \Gamma(\mathbf{q}_{0i}, (\nabla \mathbf{q})_{0i}; \hat{\mathbf{n}}_{0i}) \quad (4.4.1)$$

by analogy to the inviscid numerical flux function.

4.4.1 Canonical Discretisation

The canonical Schemes 1 and 2 cannot be directly extended to the Navier-Stokes equations because the viscous terms cannot be written in the form of a normal derivative,

$$\oint_{\partial\Omega} \mu \nabla \mathbf{v} \cdot \mathbf{n} \, ds. \quad (4.4.2)$$

In contrast, discretising the viscous terms with the canonical Scheme 3 would not present any difficulty since it gives an expression for the gradient rather than the normal derivative. To gain further insight into the discretisation of the viscous fluxes on unstructured

[†]However, see the work by Barth [4], in which the positivity of the viscous stencil is used to compensate for a non-positive inviscid stencil on a regular triangular grid.

grids, it proves helpful to cast the viscous terms in the Navier-Stokes equations into a form which shows their character more clearly.

For example, using Eqs. (2.3.4) and (2.3.3), the viscous terms in the momentum equations can be written as

$$\oint_{\partial\Omega} \left\{ \mu \nabla \mathbf{v} \cdot \mathbf{n} + \frac{1}{3} \mu \nabla \cdot \mathbf{v} \mathbf{n} + \mu [(\nabla \mathbf{v})^t \cdot \mathbf{n} - \nabla \cdot \mathbf{v} \mathbf{n}] \right\} ds, \quad (4.4.3)$$

or, in component form,

$$\oint_{\partial\Omega} \mu \nabla u \cdot \mathbf{n} ds + \frac{1}{3} \oint_{\partial\Omega} \mu \nabla \cdot \mathbf{v} n_x ds - \oint_{\partial\Omega} \mu \nabla v \cdot \mathbf{t} ds, \quad (4.4.4a)$$

$$\oint_{\partial\Omega} \mu \nabla v \cdot \mathbf{n} ds + \frac{1}{3} \oint_{\partial\Omega} \mu \nabla \cdot \mathbf{v} n_y ds + \oint_{\partial\Omega} \mu \nabla u \cdot \mathbf{t} ds. \quad (4.4.4b)$$

In Expressions (4.4.4a) and (4.4.4b), the first terms represent the Laplacian operator for which a discretisation was developed above. The third terms vanish for constant viscosity due to Stokes' theorem while the second terms vanish for incompressible flow. Even for flows where the second and third terms do not vanish, it may be assumed that they are negligible compared to the first term. Some evidence which substantiates this assumption for laminar flows will be presented in Chapter 7.

However, it should be noted that the third term in Expression (4.4.4a) and, in particular, Expression (4.4.4b), may not be negligible when eddy-viscosity turbulence models are employed. This is because the essentially constant dynamic viscosity is replaced by the sum of the dynamic viscosity and the strongly varying eddy viscosity. The validity of neglecting the third term in Expression (4.4.4b) for turbulent flows will be investigated in Chapter 8.

The viscous fluxes in the energy equation may be written as,

$$\oint_{\partial\Omega} \left\{ \mu \nabla \frac{\|\mathbf{v}\|^2}{2} \cdot \mathbf{n} + \frac{1}{3} \mu \nabla \cdot \mathbf{v} \mathbf{v} \cdot \mathbf{n} + \mu [(\nabla \mathbf{v})^t \cdot \mathbf{v} \cdot \mathbf{n} - \nabla \cdot \mathbf{v} \mathbf{v} \cdot \mathbf{n}] \right. \\ \left. + \mu (\nabla \times \mathbf{v} \times \mathbf{v} \cdot \mathbf{n}) + \kappa \nabla T \cdot \mathbf{n} \right\} ds, \quad (4.4.5)$$

where the terms were grouped to show their counterparts in the terms of the momentum equations. Only the first and last terms are in a form which is easily discretised.

Two approaches for the discretisation of the viscous terms were explored.

Full Viscous Fluxes. The first approach includes all the terms in Expressions (4.4.4a) and (4.4.4b). Because of the second and third terms in these expressions, it is necessary

to reconstruct the x - and y -derivatives separately.

Two Dimensions. In two dimensions, the x - and y -derivatives may be linked to the normal and tangential derivatives by

$$\frac{\partial \phi}{\partial x} = \frac{\partial \phi}{\partial n} n_x - \frac{\partial \phi}{\partial s} n_y \quad (4.4.6a)$$

$$\frac{\partial \phi}{\partial y} = \frac{\partial \phi}{\partial n} n_y + \frac{\partial \phi}{\partial s} n_x, \quad (4.4.6b)$$

where n_x and n_y are the components of the outward unit normal at a particular dual edge and $\partial \phi / \partial s = \nabla \phi \cdot \mathbf{t}$ is the tangential derivative. The first approach therefore employs the above-described method of computing the normal derivative, while the Green-Gauss theorem is used to calculate the tangential derivative. The two are combined according to Eqs. (4.4.6a) and (4.4.6b) to give the gradients in the x - and y -coordinate directions which are then used to compute the viscous fluxes.

The use of normal and tangential derivative components has been described previously by Holmes and Connell [24]. The present derivation highlights how this decomposition naturally arises from studying Laplace's equation and the viscous terms in the Navier-Stokes equations.

Three Dimensions. In three dimensions, the tangential derivative cannot be defined directly, as discussed above. To circumvent the explicit definition of the tangential derivative, canonical Scheme 3 may be employed.

Approximate Viscous Fluxes. The second approach resorts to an approximate treatment. Neglecting the third terms in Expressions (4.4.4a) and (4.4.4b), and approximating the second terms using Eqs. (4.4.6a) and (4.4.6b), where the product of the tangential derivative and the normal vector components is assumed to be small, gives

$$\oint_{\partial \Omega} \mu \nabla u \cdot \mathbf{n} ds + \frac{1}{3} \oint_{\partial \Omega} \mu (\nabla u \cdot \mathbf{n} n_x^2 + \nabla v \cdot \mathbf{n} n_x n_y) ds \quad (4.4.7a)$$

$$\oint_{\partial \Omega} \mu \nabla v \cdot \mathbf{n} ds + \frac{1}{3} \oint_{\partial \Omega} \mu (\nabla u \cdot \mathbf{n} n_x n_y + \nabla v \cdot \mathbf{n} n_y^2) ds. \quad (4.4.7b)$$

Similarity to Thin-Shear-Layer (TSL) Approximation. An examination of the neglected

terms reveals that the approximate viscous fluxes can be interpreted as a kind of thin-shear-layer approximation in all coordinate directions. This may be shown by comparison with the systematic derivation of the formulation of the viscous terms in three-dimensional curvilinear coordinates by Gnoffo [21]: Retaining Gnoffo's nomenclature, a thin-layer approximation in the χ -coordinate direction was derived as

$$\tau_{ns} = \mu \left(\frac{\partial \nu}{\partial \chi} + \frac{1}{3} \frac{\partial U}{\partial \chi} n_s \right) \nabla \chi \cdot \mathbf{n}, \quad (4.4.8)$$

where τ_{ns} represents the shear stress acting in the s -coordinate direction on a control-volume face with outward unit normal vector \mathbf{n} , ν is a dummy variable for u or v corresponding to the coordinate direction s , and U is the control volume face normal velocity. Putting $\chi = y$ and $s = x$ gives

$$\tau_{nx} = \mu \left[\frac{\partial u}{\partial y} + \frac{1}{3} \left(\frac{\partial u}{\partial y} n_x + \frac{\partial v}{\partial y} n_y \right) n_x \right] n_y, \quad (4.4.9)$$

to which the integrand in Expression (4.4.7a) effectively reduces for control-volume faces which are approximately aligned with the x -coordinate direction.

For the viscous fluxes in the energy equation, the stresses are approximated using velocity gradients from Eqs. (4.4.6a) and (4.4.6b) where the product of the tangential derivative component with the normal vector components is once more neglected. The heat flux is easily approximated, because it is of the form given by Expression (4.4.2).

It must be emphasized that the present approximate discretisation of the viscous fluxes does not require knowledge of normal and tangential directions at a solid wall, in contrast to the traditional thin-shear-layer approximation.

Extension to Three Dimensions. The extension to three dimensions is straightforward. Boschitsch [11] obtained good agreement with the complete viscous fluxes for laminar flows in three dimensions.

Other Approximate Discretisations. In an attempt to derive a simplified discretisation of the viscous fluxes on mixed grids, Mavriplis and Venkatakrishnan [41] chose to discretise the full viscous terms on tetrahedral cells only and discretised the Laplacian on hexahedral, prismatic, and pyramidal cells. Although this reduces the computational work required, the approximation cannot be regarded as entirely satisfactory. Assum-

ing that hexahedral and prismatic elements are employed near boundaries, their scheme simplifies the viscous terms in viscous regions while the full viscous terms are retained in regions which are likely to be completely or nearly inviscid. In contrast to the method of Mavriplis and Venkatakrishnan, the present approximation does not depend on the cell type. Instead, it relies more on approximations justified from flow conditions; this is believed to be a better approach.

Evaluation of Wall Shear Stress. It is of some interest to describe the evaluation of wall shear stress. In the present work, the wall shear stress is computed from

$$\tau_{\text{wall}} = -\mathbf{T} \cdot \mathbf{n} \cdot \mathbf{t}, \quad (4.4.10)$$

where \mathbf{n} is the unit normal pointing outward of the solution domain and \mathbf{t} is a suitably defined tangential vector defined below. The negative sign in Eq. (4.4.10) arises because the unit normal points out of the solution domain.

To evaluate the wall shear stress from Eq. (4.4.10), the form of the viscous fluxes given by Expressions (4.4.4a) and (4.4.4b) is particularly useful. It is helpful to analyze Expressions (4.4.4a) and (4.4.4b) at a solid wall for a steady flow field.

For a steady flow, the continuity equation becomes

$$\nabla \cdot (\rho \mathbf{v}) = 0, \quad (4.4.11)$$

which, on expanding and using the no-slip condition, becomes

$$\nabla \cdot \mathbf{v} = 0. \quad (4.4.12)$$

Thus the second terms in Expressions (4.4.4a) and (4.4.4b) vanish.

The third terms in Eqs. (4.4.4a) and (4.4.4b) vanish also on account of the no-slip condition on solid walls. The only terms which remain on solid walls for a steady flow field are the Laplacian terms.

Hence the wall shear stress becomes

$$\tau_{\text{wall}} = -\mu \nabla \mathbf{v} \cdot \mathbf{n} \cdot \mathbf{t}. \quad (4.4.13)$$

On expanding, this may be written as

$$\tau_{\text{wall}} = -\mu \left[\left(\frac{\partial u}{\partial x} t_x + \frac{\partial v}{\partial x} t_y \right) n_x + \left(\frac{\partial u}{\partial y} t_x + \frac{\partial v}{\partial y} t_y \right) n_y \right]. \quad (4.4.14)$$

It is this expression which was used in this work to evaluate the wall shear stress. It

is noted that the gradients appearing in Eq. (4.4.14) are evaluated at the midpoints of the edges lying on solid boundaries.

Alternative Interpretation. It is interesting to note that Eq. (4.4.14) may be simplified further using the no-slip conditions to become

$$\tau_{\text{wall}} = -\mu \left[\frac{\partial}{\partial x} (u t_x + v t_y) n_x + \frac{\partial}{\partial y} (u t_x + v t_y) n_y \right] \quad (4.4.15)$$

where the velocity tangential to the solid boundary is defined as

$$q = u t_x + v t_y \quad (4.4.16)$$

which allows Eq. (4.4.15) to be written as the more familiar expression

$$\tau_{\text{wall}} = -\mu \frac{\partial q}{\partial n}. \quad (4.4.17)$$

Definition of Tangential Vector. The vector \mathbf{t} is defined to be a tangent vector to the solid wall in the same direction as the main flow. Using FORTRAN functions, \mathbf{t} is defined as

$$\mathbf{t} = (\text{ABS}(n_y), -n_x \text{ SIGN}(1.0, n_y))^t \quad (4.4.18)$$

for flow in the positive x -direction.

4.4.2 Galerkin Finite-Element Discretisation

The Galerkin finite-element discretisation presented by Barth [3] was used by Anderson and Bonhaus [1], Barth and Linton [6], and Ashford [2]. The method is discussed here in some detail for the sake of completeness and because it helps to illustrate some of the issues discussed above. Furthermore, it will be used to validate the discretisations of the viscous fluxes developed in the present work in Chapter 7.

Since the viscous fluxes are essentially linear combinations of the viscosity and derivatives of the dependent variables, it is convenient to derive the Galerkin finite-element discretisation of the Hessian-like matrix

$$\nabla(\mu (\nabla \phi)^t) = \begin{bmatrix} \frac{\partial}{\partial x} \left(\mu \frac{\partial \phi}{\partial x} \right) & \frac{\partial}{\partial x} \left(\mu \frac{\partial \phi}{\partial y} \right) \\ \frac{\partial}{\partial y} \left(\mu \frac{\partial \phi}{\partial x} \right) & \frac{\partial}{\partial y} \left(\mu \frac{\partial \phi}{\partial y} \right) \end{bmatrix}. \quad (4.4.19)$$

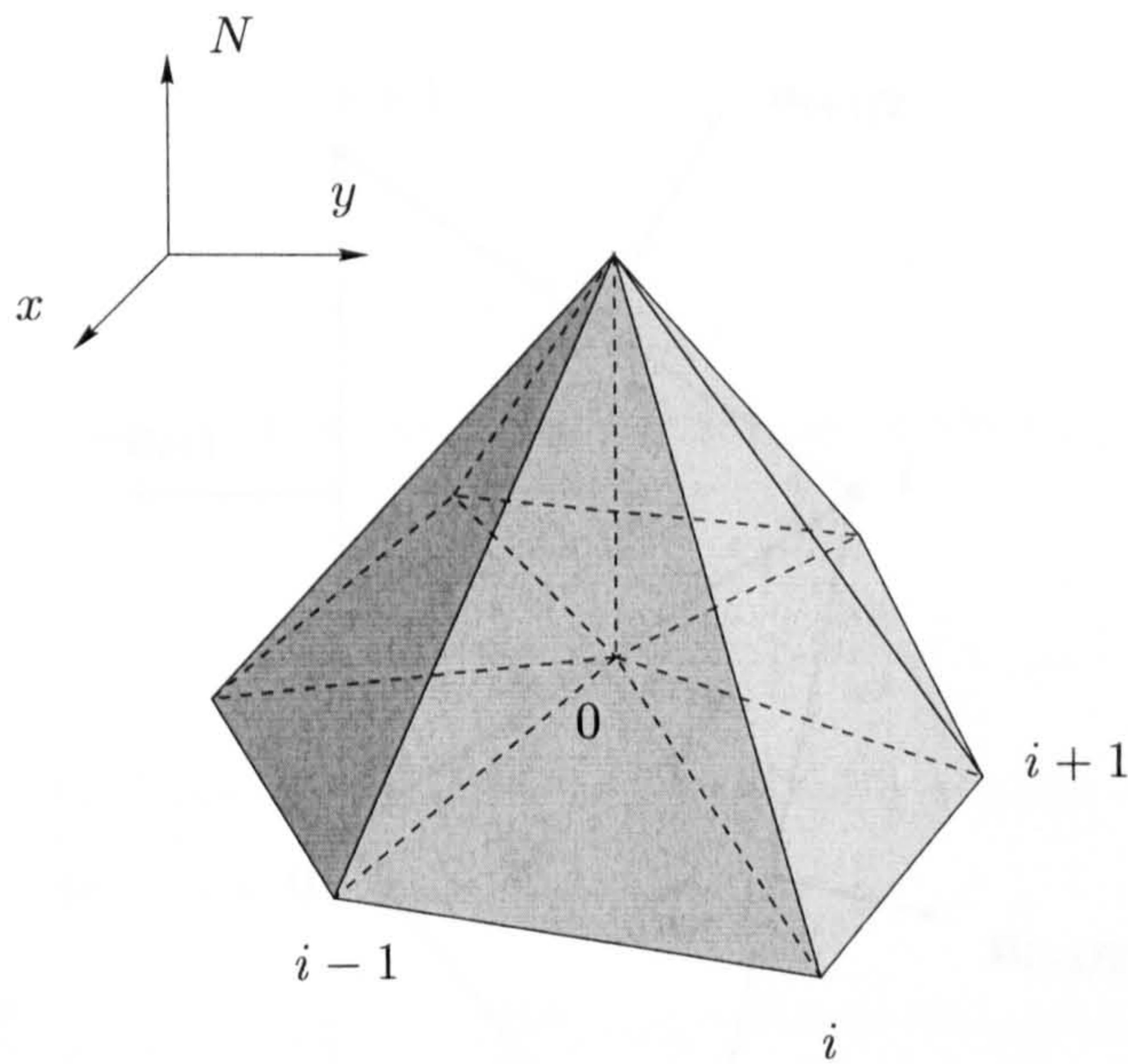


Figure 4.15: Piecewise linear shape function at node 0.

Cell-Based Formulation. Multiplying by the piecewise linear shape function N as depicted in Fig. 4.15 and integrating by parts over the domain $\Omega_{0'}$ given by the union of the triangles meeting at vertex 0 results in

$$\int_{\Omega_{0'}} N \nabla \mu (\nabla \phi)^t dA = \int_{\Omega_{0'}} \nabla N \mu (\nabla \phi)^t dA - \int_{\Omega_{0'}} \mu (\nabla N) (\nabla \phi)^t dA. \quad (4.4.20)$$

Using the divergence theorem, this may be rewritten as

$$\int_{\Omega_{0'}} N \nabla \mu (\nabla \phi)^t dA = \oint_{\partial \Omega_{0'}} N \mu d\mathbf{n} (\nabla \phi)^t - \int_{\Omega_{0'}} \mu \nabla N (\nabla \phi)^t dA. \quad (4.4.21)$$

For the moment, it is assumed that the vertex 0 is not part of a boundary; hence the contour integral in the above equation is identically zero. This leaves

$$\int_{\Omega_{0'}} N \nabla \mu (\nabla \phi)^t dA = - \int_{\Omega_{0'}} \mu \nabla N (\nabla \phi)^t dA, \quad (4.4.22)$$

which may be rewritten as a sum over triangles meeting at vertex 0,

$$\int_{\Omega_{0'}} N \nabla \mu (\nabla \phi)^t dA = - \sum_{i \in \mathcal{T}_0} \int_{\mathcal{T}_{i+1/2}} \mu \nabla N (\nabla \phi)^t_{\mathcal{T}_{i+1/2}} dA, \quad (4.4.23)$$

where $\mathcal{T}_{i+1/2}$ is the triangle defined by the vertex triplet $(0, i, i+1)$. The gradient of the shape function in triangle $\mathcal{T}_{i+1/2}$ follows from the application of the Green-Gauss theorem as

$$(\nabla N)_{\mathcal{T}_{i+1/2}} = - \frac{\mathbf{n}_{i+1/2}}{2A_{i+1/2}} \quad (4.4.24)$$

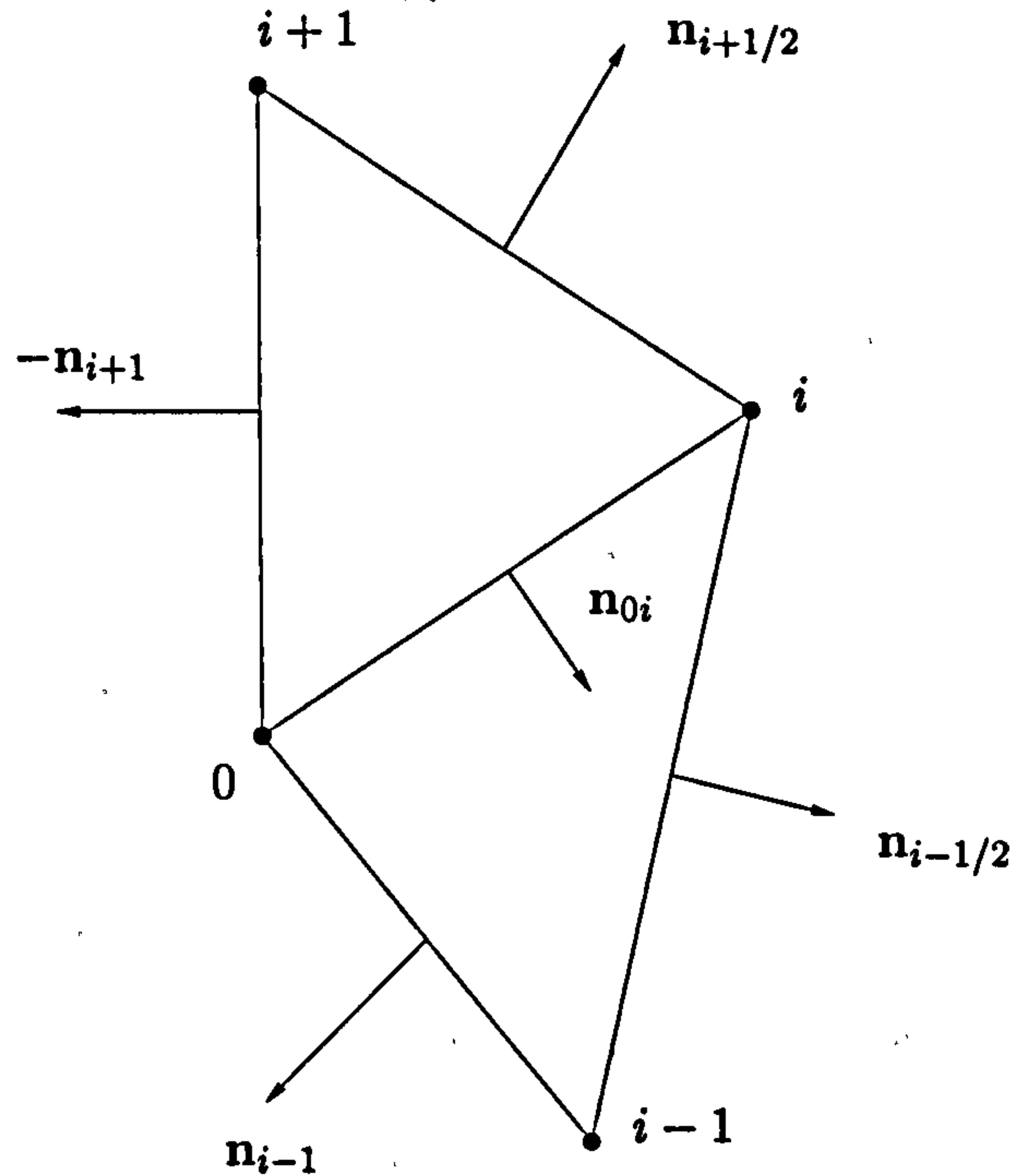


Figure 4.16: Definition of nomenclature used in derivation of Galerkin finite-element discretisation. Normal vectors are not drawn to scale.

where $A_{i+1/2}$ is the area of triangle $\mathcal{T}_{i+1/2}$ and $\mathbf{n}_{i+1/2}$ is the scaled normal to the edge from vertex i to vertex $i+1$. The relevant nomenclature is explained in Fig. 4.16.

Using Eq. (4.4.24) and the assumption of linear variations of the dependent variables, Eq. (4.4.23) can be rewritten as

$$\int_{\Omega_0'} N \nabla \mu (\nabla \phi)^t dA = \sum_{i \in \mathcal{T}_0} \frac{\mathbf{n}_{i+1/2}}{2A_{i+1/2}} (\nabla \phi)_{\mathcal{T}_{i+1/2}}^t \int_{\mathcal{T}_{i+1/2}} \mu dA. \quad (4.4.25)$$

By defining

$$\bar{\mu}_{i+1/2} = \frac{1}{A_{i+1/2}} \int_{\mathcal{T}_{i+1/2}} \mu dA \quad (4.4.26)$$

as the average value of viscosity, Eq. (4.4.25) gives

$$\int_{\Omega_0'} N \nabla \mu (\nabla \phi)^t dA = \frac{1}{2} \sum_{i \in \mathcal{T}_0} \bar{\mu}_{i+1/2} \mathbf{n}_{i+1/2} (\nabla \phi)_{\mathcal{T}_{i+1/2}}^t. \quad (4.4.27)$$

For an assumed linear variation of viscosity, the average value is given by

$$\bar{\mu}_{i+1/2} = \frac{1}{3} (\mu_0 + \mu_i + \mu_{i+1}).$$

In the energy equation, the dissipation terms involve products of the viscosity and the

velocity components. An analogous derivation therefore requires the approximation of terms such as

$$(\overline{\mu\psi})_{i+1/2} = \frac{1}{A_{i+1/2}} \int_{\tau_{i+1/2}} \mu\psi dA. \quad (4.4.28)$$

The corresponding approximation for linear variations of viscosity and the velocity components is derived to be

$$(\overline{\mu\psi})_{i+1/2} = \frac{1}{12} [(\mu_0 + \mu_i)(\psi_0 + \psi_i) + (\mu_0 + \mu_{i+1})(\psi_0 + \psi_{i+1}) + (\mu_i + \mu_{i+1})(\psi_i + \psi_{i+1})].$$

The gradient of the dependent variable in Eq. (4.4.27) is given by the application of the Green-Gauss theorem as

$$(\nabla\phi)_{\tau_{i+1/2}} = -\frac{1}{2A_{i+1/2}} (\phi_0 \mathbf{n}_{i+1/2} - \phi_i \mathbf{n}_{i+1} + \phi_{i+1} \mathbf{n}_{0i}), \quad (4.4.29)$$

which is exact if the function ϕ is linear, and Eq. (4.4.27) becomes

$$\int_{\Omega_0'} N \nabla \mu (\nabla \phi)^t dA = -\frac{1}{4} \sum_{i \in \mathcal{T}_0} \frac{\bar{\mu}_{i+1/2}}{A_{i+1/2}} \mathbf{n}_{i+1/2} (\phi_0 \mathbf{n}_{i+1/2}^t - \phi_i \mathbf{n}_{i+1}^t + \phi_{i+1} \mathbf{n}_{0i}^t). \quad (4.4.30)$$

Since $\mathbf{n}_{i+1/2} = -\mathbf{n}_{0i} + \mathbf{n}_{i+1}$, Eq. (4.4.30) can be expressed as

$$\int_{\Omega_0'} N \nabla \mu (\nabla \phi)^t dA = \frac{1}{4} \sum_{i \in \mathcal{T}_0} \frac{\bar{\mu}_{i+1/2}}{A_{i+1/2}} \mathbf{n}_{i+1/2} [(\phi_i - \phi_0) \mathbf{n}_{i+1}^t - (\phi_{i+1} - \phi_0) \mathbf{n}_{0i}^t] \quad (4.4.31)$$

which, due to the sum being cyclic, can be recast by shifting the indices in the second term in the summation to give

$$\int_{\Omega_0'} N \nabla \mu (\nabla \phi)^t dA = \frac{1}{4} \sum_{i \in \mathcal{T}_0} \left(\frac{\bar{\mu}_{i+1/2}}{A_{i+1/2}} \mathbf{n}_{i+1/2} \mathbf{n}_{i+1}^t - \frac{\bar{\mu}_{i-1/2}}{A_{i-1/2}} \mathbf{n}_{i-1/2} \mathbf{n}_{i-1}^t \right) (\phi_i - \phi_0). \quad (4.4.32)$$

The summation in Eq. (4.4.32) may be interpreted as a loop over edges where an edge-weight, given by the matrix

$$W_{0i} = \frac{1}{4} \left(\frac{\bar{\mu}_{i+1/2}}{A_{i+1/2}} \mathbf{n}_{i+1/2} \mathbf{n}_{i+1}^t - \frac{\bar{\mu}_{i-1/2}}{A_{i-1/2}} \mathbf{n}_{i-1/2} \mathbf{n}_{i-1}^t \right), \quad (4.4.33)$$

is multiplied by the difference of the dependent variable along the edge. Unfortunately, this formula is not compatible with the edge-based data structure. Before considering how Eq. (4.4.32) can be reformulated to be compatible with the edge-based data structure, the formulae which result if vertex 0 lies on a boundary are stated.

Approximation of Contour Integral. If vertex 0 lies on a boundary, the contour integral

in Eq. (4.4.21) has to be taken into account. Introducing the parameterised coordinate $0 \leq \xi \leq 1$ along the edge $0i$, this gives for the momentum equations,

$$\oint_{\partial\Omega_0} N_0 \mu \mathbf{n}_{0i} (\nabla\phi)_{i+1/2}^t d\xi = \mathbf{n}_{0i} (\nabla\phi)_{\mathcal{T}_{i+1/2}}^t \int_0^1 N_0 (\mu_0 N_0 + \mu_i N_i) d\xi \quad (4.4.34a)$$

$$= \frac{1}{2} \left(\frac{2}{3} \mu_0 + \frac{1}{3} \mu_i \right) \mathbf{n}_{0i} (\nabla\phi)_{\mathcal{T}_{i+1/2}}^t, \quad (4.4.34b)$$

and for the energy equation,

$$\begin{aligned} & \oint_{\partial\Omega_0} N_0 \mu \psi \mathbf{n}_{0i} (\nabla\phi)_{\mathcal{T}_{i+1/2}}^t d\xi \\ &= \mathbf{n}_{0i} (\nabla\phi)_{\mathcal{T}_{i+1/2}}^t \int_0^1 N_0 (\mu_0 N_0 + \mu_i N_i) (\psi_0 N_0 + \psi_i N_i) d\xi \end{aligned} \quad (4.4.35a)$$

$$= \frac{1}{2} \left[\frac{1}{2} \mu_0 \psi_0 + \frac{1}{6} (\mu_0 \psi_i + \mu_i \psi_0 + \mu_i \psi_i) \right] \mathbf{n}_{0i} (\nabla\phi)_{\mathcal{T}_{i+1/2}}^t. \quad (4.4.35b)$$

Edge-Based Formulation. Identities between the scaled normal vectors are employed to recast the edge-weights in a form which is compatible with the edge-based data structure. Referring to Fig. 4.16, it can be shown that for median-dual control volumes,

$$\mathbf{n}_{i+1/2} = 3\mathbf{n}_{0i,1} - \frac{1}{2}\mathbf{n}_{0i} \quad (4.4.36a)$$

$$\mathbf{n}_{i+1} = 3\mathbf{n}_{0i,1} + \frac{1}{2}\mathbf{n}_{0i}, \quad (4.4.36b)$$

and

$$\mathbf{n}_{i-1/2} = 3\mathbf{n}_{0i,2} + \frac{1}{2}\mathbf{n}_{0i} \quad (4.4.37a)$$

$$\mathbf{n}_{i-1} = -3\mathbf{n}_{0i,2} + \frac{1}{2}\mathbf{n}_{0i}. \quad (4.4.37b)$$

Using these identities, the tensor product of the scaled normal vectors in Eq. (4.4.32) can be conveniently decomposed into symmetric and anti-symmetric parts to give

$$\mathbf{n}_{i+1/2} \mathbf{n}_{i+1}^t = - \left(\frac{1}{4} \mathbf{n}_{0i} \mathbf{n}_{0i}^t - 9 \mathbf{n}_{0i,1} \mathbf{n}_{0i,1}^t \right) + \frac{3}{2} (\mathbf{n}_{0i,1} \mathbf{n}_{0i}^t - \mathbf{n}_{0i} \mathbf{n}_{0i,1}^t) \quad (4.4.38)$$

and

$$\mathbf{n}_{i-1/2} \mathbf{n}_{i-1}^t = \left(\frac{1}{4} \mathbf{n}_{0i} \mathbf{n}_{0i}^t - 9 \mathbf{n}_{0i,2} \mathbf{n}_{0i,2}^t \right) + \frac{3}{2} (\mathbf{n}_{0i,2} \mathbf{n}_{0i}^t - \mathbf{n}_{0i} \mathbf{n}_{0i,2}^t). \quad (4.4.39)$$

The anti-symmetric parts can be shown to be given by

$$\frac{3}{2} (\mathbf{n}_{0i,1} \mathbf{n}_{0i}^t - \mathbf{n}_{0i} \mathbf{n}_{0i,1}^t) = \frac{1}{2} \|\mathbf{n}_{i+1/2} \times \mathbf{n}_{i+1}\| \begin{bmatrix} 0 & 1 \\ -1 & 0 \end{bmatrix} = A_{i+1/2} \begin{bmatrix} 0 & 1 \\ -1 & 0 \end{bmatrix}, \quad (4.4.40)$$

and

$$\frac{3}{2} (\mathbf{n}_{0i,2} \mathbf{n}_{0i}^t - \mathbf{n}_{0i} \mathbf{n}_{0i,2}^t) = \frac{1}{2} \|\mathbf{n}_{i-1/2} \times \mathbf{n}_{i-1}\| \begin{bmatrix} 0 & -1 \\ 1 & 0 \end{bmatrix} = A_{i-1/2} \begin{bmatrix} 0 & -1 \\ 1 & 0 \end{bmatrix}. \quad (4.4.41)$$

Substituting Eqs. (4.4.36a)-(4.4.37b) into Eq. (4.4.33) and using Eqs. (4.4.38)-(4.4.41) results in

$$\int_{\Omega_0} N \nabla \mu (\nabla \phi)^t dA = \sum_{0i \in \mathcal{E}_0} W_{0i} (\phi_i - \phi_0), \quad (4.4.42)$$

which is compatible with the edge-based data structure.

The matrix W_{0i} can be split into symmetric and anti-symmetric parts

$$W_{0i} = W_{0i}^s + W_{0i}^a \quad (4.4.43)$$

where the symmetric and antisymmetric terms are given by[†]

$$W_{0i}^s = -\frac{1}{4} \left(\bar{\mu}_{i+1/2} \frac{\frac{1}{4} \mathbf{n}_{0i} \mathbf{n}_{0i}^t - 9 \mathbf{n}_{0i,1} \mathbf{n}_{0i,1}^t}{A_{i+1/2}} + \bar{\mu}_{i-1/2} \frac{\frac{1}{4} \mathbf{n}_{0i} \mathbf{n}_{0i}^t - 9 \mathbf{n}_{0i,2} \mathbf{n}_{0i,2}^t}{A_{i-1/2}} \right) \quad (4.4.44)$$

and

$$W_{0i}^a = \frac{1}{4} (\bar{\mu}_{i+1/2} - \bar{\mu}_{i-1/2}) \begin{bmatrix} 0 & 1 \\ -1 & 0 \end{bmatrix}. \quad (4.4.45)$$

The two terms in W_{0i}^s involving geometric quantities only may be pre-computed and stored as weights for each edge.

Comments. Several comments may be made about these edge-weights.

Cross-Derivatives and Conservation. The cross-derivatives lead to the anti-symmetric term given by Eq. (4.4.45) in the edge-based formulation. The anti-symmetric term involves the difference in the average values of the viscosity in the cells meeting at the edge $0i$. Because this term is anti-symmetric, it is non-conservative. Therefore, the edge-based formulation of the Galerkin finite-element discretisation is only conservative

[†]It is interesting to note that Winslow [60] derived the equivalent of Eq. (4.4.44) as early as 1967 for the discretisation of the diffusion equation.

for constant viscosity, in contrast to the cell-based formulation and finite-volume discretisations. This has also been pointed out by Ashford [2]. The anti-symmetric term arises if the second and third terms in Expressions (4.4.4a) and (4.4.4b) are discretised.

Positivity. As already stated, Barth [3] demonstrated that the Galerkin finite-element discretisation of Laplace's equation, i.e., where the edge-weights are given by $\text{tr}(W_{0i})$ with constant viscosity, leads to a positive discretisation only if the triangular grid obeys the Delaunay criterion. As demonstrated by Letniowski [32], this property does not hold in three dimensions, where more restrictive conditions apply.

It can also be seen that for the viscous terms in the Navier-Stokes equations, the anti-symmetric terms may lead to negative coefficients if large gradients of the viscosity exist. This may be of importance when eddy-viscosity models are employed.

Simplified Discretisations. In order to simplify the corresponding discretisation in three dimensions (for a derivation, see Barth [3]), Mavriplis [40] suggested replacing the cell-averaged values of the viscosity by an edge average,

$$\bar{\mu}_{i+1/2} = \bar{\mu}_{i-1/2} = \frac{1}{2}(\mu_0 + \mu_i).$$

Consequently, the anti-symmetric term vanishes.

Equivalence to Finite-Volume Discretisation for Diffusion Equation. If the diffusion equation is discretised by a finite-volume method and the flux through the face associated with edge $0i$ is approximated by

$$\mu_{0i} (\nabla \phi)_{0i} \cdot \hat{n}_{0i} = \bar{\mu}_{i+1/2} (\nabla \phi)_{i+1/2} \cdot \hat{n}_{0i,1} + \bar{\mu}_{i-1/2} (\nabla \phi)_{i-1/2} \cdot \hat{n}_{0i,2}, \quad (4.4.46)$$

it can be shown that the resulting expression is identical to that obtained from the Galerkin finite-element method, where the edge-weight is given by $W_{0i} = \text{tr}(W_{0i})$.

It is instructive to reformulate the finite-volume discretisation for control-volumes based on Dirichlet regions. Using the definitions of the normal vectors shown in Figs.

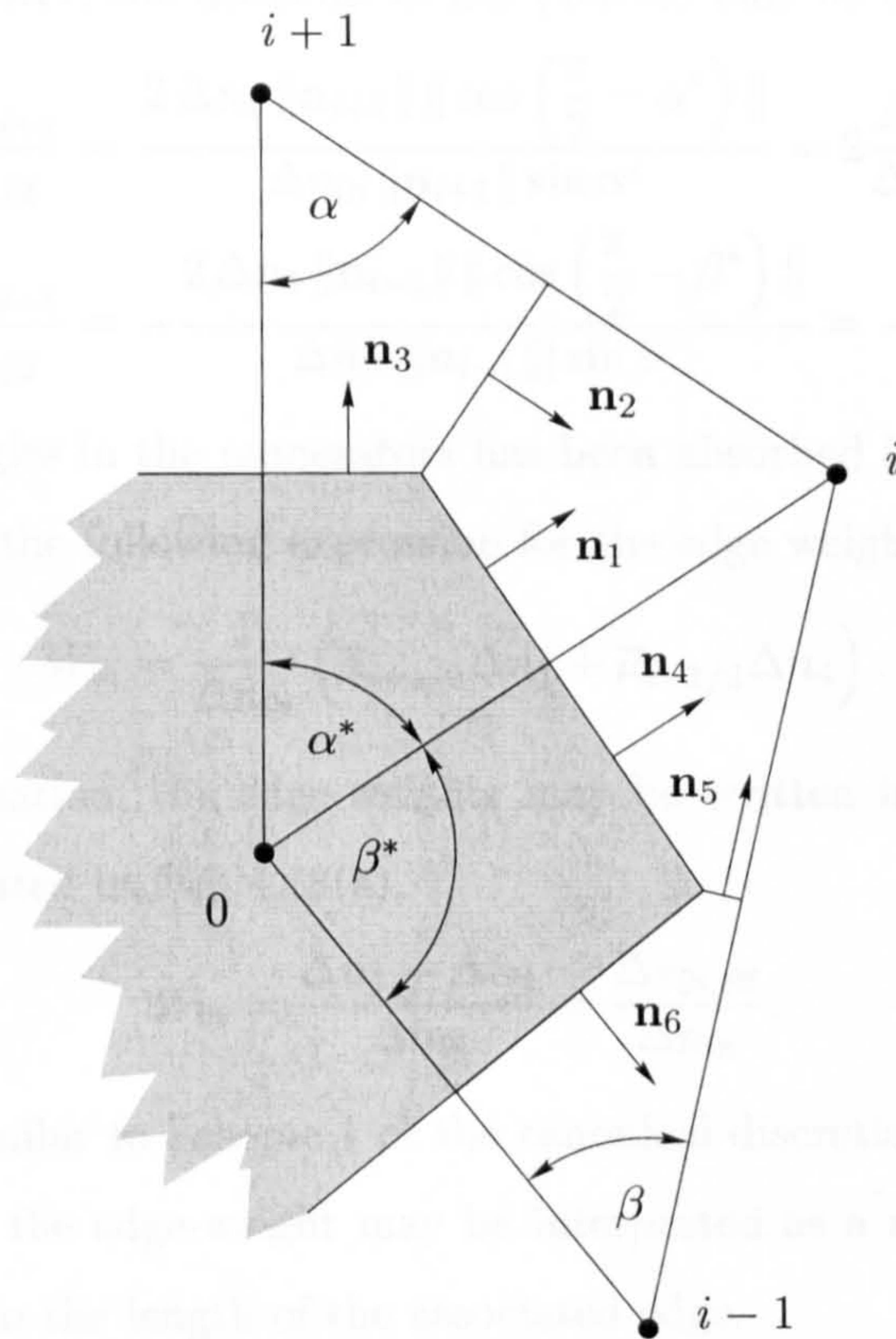


Figure 4.17: Definition of normal vectors for Dirichlet region. Normal vectors are not drawn to scale.

4.16 and 4.17, it can be shown that

$$\mathbf{n}_{i+1} = 2(\mathbf{n}_1 + \mathbf{n}_2) \quad (4.4.47a)$$

$$\mathbf{n}_{i+1/2} = 2(\mathbf{n}_1 + \mathbf{n}_3) \quad (4.4.47b)$$

$$\mathbf{n}_{i-1/2} = 2(\mathbf{n}_4 + \mathbf{n}_6) \quad (4.4.47c)$$

$$\mathbf{n}_{i-1} = -2(\mathbf{n}_4 + \mathbf{n}_5). \quad (4.4.47d)$$

Substituting these relations into the diagonal elements of Eq. (4.4.33) leads to

$$W_{0i} = \frac{1}{2} \left(\bar{\mu}_{i+1/2} \frac{\mathbf{n}_1 \cdot \mathbf{n}_{i+1}}{A_{i+1/2}} - \bar{\mu}_{i-1/2} \frac{\mathbf{n}_4 \cdot \mathbf{n}_{i-1}}{A_{i-1/2}} \right). \quad (4.4.48)$$

Referring to Fig. 4.17, the fractions in Eq. (4.4.48) may be expressed as

$$\frac{\mathbf{n}_1 \cdot \mathbf{n}_{i+1}}{A_{i+1/2}} = \frac{2 \Delta n_1 \|\mathbf{n}_{i+1}\| \left\| \cos \left(\frac{\pi}{2} - \alpha^* \right) \right\|}{\Delta n_{0i} \|\mathbf{n}_{i+1}\| \sin \alpha^*} = 2 \frac{\Delta n_1}{\Delta n_{0i}} \quad (4.4.49a)$$

$$\frac{\mathbf{n}_4 \cdot \mathbf{n}_{i-1}}{A_{i-1/2}} = -\frac{2 \Delta n_4 \|\mathbf{n}_{i-1}\| \left\| \cos \left(\frac{\pi}{2} - \beta^* \right) \right\|}{\Delta n_{0i} \|\mathbf{n}_{i-1}\| |\sin \beta^*|} = -2 \frac{\Delta n_4}{\Delta n_{0i}} \quad (4.4.49b)$$

where the sign of angles in the numerators has been absorbed into the quantities Δn_1 and Δn_4 . This gives the following expression for the edge weight

$$W_{0i} = \frac{1}{\Delta n_{0i}} \left(\bar{\mu}_{i+1/2} \Delta n_1 + \bar{\mu}_{i-1/2} \Delta n_4 \right). \quad (4.4.50)$$

For Laplace's equation, the edge-weights may be written in terms of an *effective* edge length, as indicated in Fig. 4.18(a),

$$W_{0i} = \frac{\Delta n_1 + \Delta n_4}{\Delta n_{0i}} = \frac{\Delta s_{0i, \text{eff}}}{\Delta n_{0i}}. \quad (4.4.51)$$

This expression is similar to Scheme 1 of the canonical discretisations described above (cf. (4.2.20)) in that the edge-weight may be interpreted as a ratio of the length of a control-volume face to the length of the associated edge.

The main difference between the two schemes is that, in contrast to Scheme 1, the Galerkin finite-element discretisation is not guaranteed to be positive. This is because the effective length of the control-volume face for the Galerkin finite-element discretisation can become negative for triangular grids which do not satisfy the Delaunay criterion, as demonstrated by Barth [3]. This situation is illustrated in Fig. 4.18(b). The effective control-volume face length becomes negative because the scalar products in Eq. (4.4.49a) and (4.4.49b) become negative and positive, respectively, so that the edge-weight given by Eq. (4.4.51) becomes negative.

Using the basic trigonometric results that

$$r_{i+1/2} = \frac{\Delta n_{0i}}{2 \sin \alpha}, \quad (4.4.52)$$

where $r_{i+1/2}$ is the radius of the circumcircle, as indicated in Fig. 4.18(a), and

$$\cos \alpha = \frac{\Delta n_1}{r_{i+1/2}}, \quad (4.4.53)$$

the edge weight may be written as

$$W_{0i} = \frac{1}{2} \left(\frac{1}{\tan \alpha} + \frac{1}{\tan \beta} \right) = \frac{\sin(\alpha + \beta)}{2 \sin \alpha \sin \beta}. \quad (4.4.54)$$

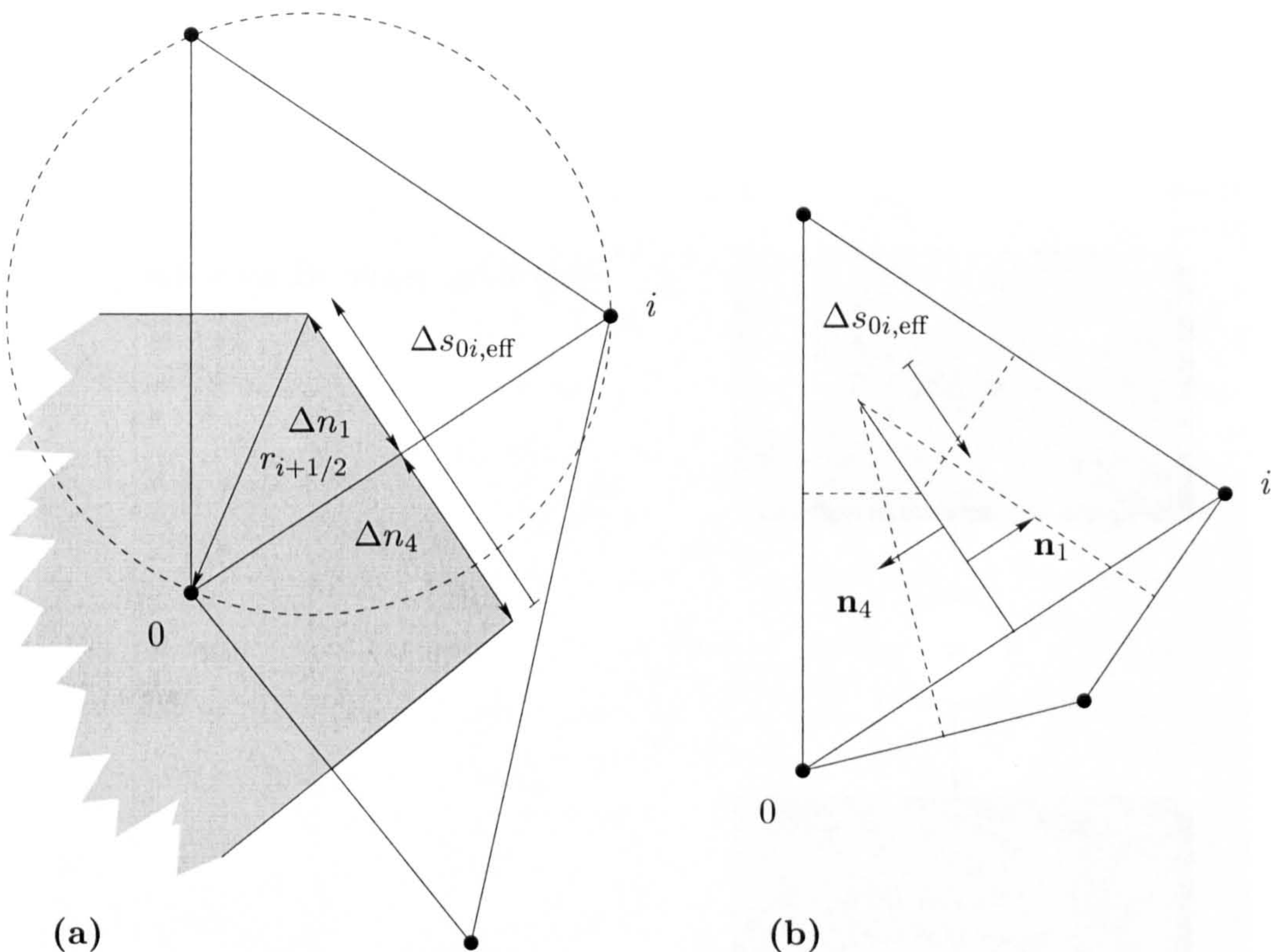


Figure 4.18: Definition of equivalent control-volume face for discretisation of diffusion equation by Galerkin finite-element method. Normal vectors are not drawn to scale.

Equation (4.4.54) is equal to that previously derived by Barth for the discretisation of the diffusion equation by the Galerkin finite-element method. The condition for positivity follows as

$$\alpha + \beta \leq \pi. \quad (4.4.55)$$

As shown by Putti and Cordes [47], the Galerkin finite-element discretisation of the diffusion equation in three dimensions cannot be cast into an equivalent finite-volume discretisation with Dirichlet regions as control volumes.

4.5 Conclusions and Outlook

The discretisation of the viscous fluxes on mixed unstructured grids was studied using the Laplacian as a model. It was shown that a positive and accurate discretisation of Laplace's equation cannot be achieved on arbitrary grids. Using a number of cri-

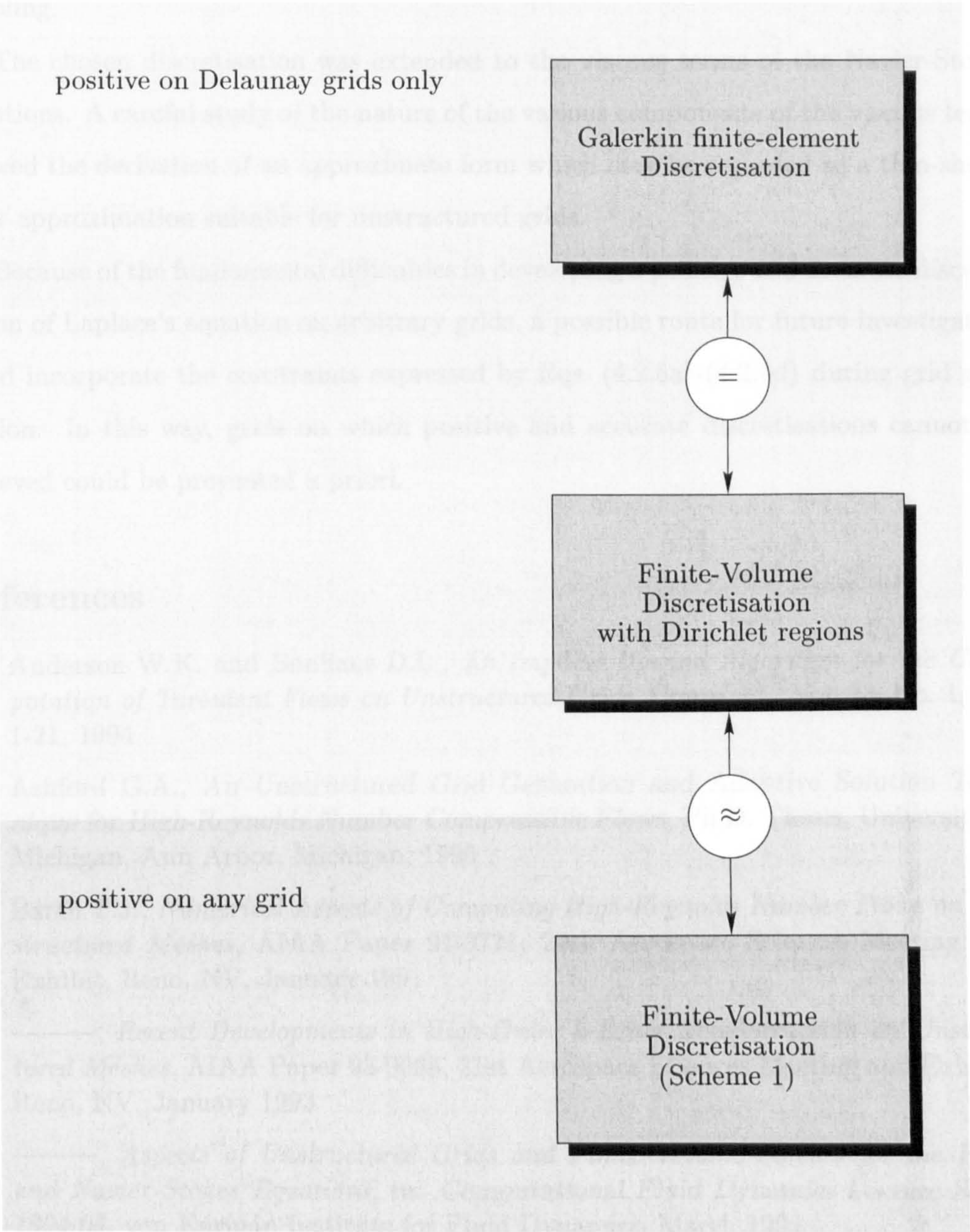


Figure 4.19: Illustration of correspondence between Galerkin finite-element discretisation, finite-volume discretisation with Dirichlet regions, and Scheme 1.

teria, various discretisations of Laplace's equation were compared. It was shown that canonical discretisations, which approximate directly the normal derivative at a control-volume face, lead to more compact stencils with lower truncation error and stronger coupling.

The chosen discretisation was extended to the viscous terms of the Navier-Stokes equations. A careful study of the nature of the various components of the viscous terms allowed the derivation of an approximate form which may be regarded as a thin-shear-layer approximation suitable for unstructured grids.

Because of the fundamental difficulties in developing a positive and accurate discretisation of Laplace's equation on arbitrary grids, a possible route for future investigation could incorporate the constraints expressed by Eqs. (4.2.5a)-(4.2.6d) during grid generation. In this way, grids on which positive and accurate discretisations cannot be achieved could be prevented a priori.

References

- [1] Anderson W.K. and Bonhaus D.L., *An Implicit Upwind Algorithm for the Computation of Turbulent Flows on Unstructured Grids*, Comp. Fl., Vol. 23, No. 1, pp. 1-21, 1994
- [2] Ashford G.A., *An Unstructured Grid Generation and Adaptive Solution Technique for High-Reynolds Number Compressible Flows*, Ph.D. Thesis, University of Michigan, Ann Arbor, Michigan, 1996
- [3] Barth T.J., *Numerical Aspects of Computing High-Reynolds Number Flows on Unstructured Meshes*, AIAA Paper 91-0721, 29th Aerospace Sciences Meeting and Exhibit, Reno, NV, January 1991
- [4] ———, *Recent Developments in High-Order k -Exact Reconstruction on Unstructured Meshes*, AIAA Paper 93-0668, 31st Aerospace Sciences Meeting and Exhibit, Reno, NV, January 1993
- [5] ———, *Aspects of Unstructured Grids and Finite-Volume Solvers for the Euler and Navier-Stokes Equations*, in: *Computational Fluid Dynamics Lecture Series 1994-05*, von Kármán Institute for Fluid Dynamics, March 1994
- [6] Barth T.J. and Linton S.W., *An Unstructured-Mesh Newton Solver for Compressible Fluid Flow and Its Parallel Implementation*, AIAA Paper 95-0221, 33rd Aerospace Sciences Meeting and Exhibit, Reno, NV, January 1995
- [7] Baumeister K.J., *Discretisation Formulas for Unstructured Grids*, in: *Numerical Grid Generation in Computational Fluid Mechanics '88*, Proc. 2nd Int. Conf. on Grid Generation in Computational Fluid Mechanics, Sengupta S. et al. (Eds.), Miami Beach, FL, Pineridge Press, Swansea, pp. 665-674, December 1988

- [8] ———, *Galerkin Finite Difference Laplacian Operators on Isolated Unstructured Triangular Meshes by Linear Combinations*, in: *Recent Advances and Applications in Computational Fluid Dynamics*, Proc. Winter Annual Meeting of the ASME, Dallas, TX, Baysal O. (Ed.), FED Vol. 103, pp. 137-144, November 1990
- [9] Blažek J., Irmisch S., and Haselbacher A., *Unstructured Mixed-Grid Navier-Stokes Solver for Turbomachinery Applications*, AIAA Paper 99-0664, 37th Aerospace Sciences Meeting and Exhibit, Reno, NV, January 1999
- [10] Boris J.P. and Book D.L., *Flux-Corrected Transport: I. SHASTA, A Fluid Transport Algorithm that works*, J. Comp. Phys., Vol. 11, pp. 38-69, 1973
- [11] Boschitsch A., private communication, February 19, 1998
- [12] Brandt A., *Multigrid Techniques: 1984 Guide with Applications to Fluid Dynamics*, GMD-Studien No. 85, Gesellschaft für Mathematik und Datenverarbeitung MBH, Bonn, Germany, May 1984
- [13] Coirier W.J., *An Adaptively-Refined, Cartesian, Cell-Based Scheme for the Euler and Navier-Stokes Equations*, NASA TM 106754, October 1994
- [14] ———, private communication, March 11, 1996
- [15] Collatz L., *The Numerical Treatment of Differential Equations*, 3rd Ed., Springer, 1960
- [16] Crumpton P.I., *An Efficient Cell-Vertex Method for Unstructured Tetrahedral Grids*, Report No. 95/19, Oxford University Computing Laboratory, Numerical Analysis Group, Oxford University, October 1995
- [17] Crumpton P.I., Moinier P., and Giles M.B., *An Unstructured Algorithm for High-Reynolds-Number Flows on Highly-Stretched Grids*, in: *Numerical Methods for Laminar and Turbulent Flows*, Taylor C. and Cross J.T. (Eds.), Pineridge Press, Wales, pp. 561-572, 1997
- [18] Davidson L., *A Pressure-Correction Method for Unstructured Meshes with Arbitrary Control Volumes*, Int. J. Num. Meth. Fl., Vol. 22, pp. 265-281, 1996
- [19] Erlebacher G., *Finite Difference Operators on Unstructured Triangular Meshes*, in: *The Free-Lagrange Method*, Proc. 1st Int. Conf. on Free-Lagrange Methods, Hilton Head Island, South Carolina, Araki H. et al. (Eds.), Lecture Notes in Physics, Vol. 238, Springer Verlag, Berlin, 1985
- [20] Galle M., *Ein Verfahren zur numerischen Simulation kompressibler, reibungsbehafteter Strömungen auf hybriden Netzen*, DLR Forschungsbericht 99-04, DLR Braunschweig, Januar 1999
- [21] Gnoffo P.A., *An Upwind-Biased, Point-Implicit Relaxation Algorithm for Viscous, Compressible Perfect-Gas Flows*, NASA TP-2953, February 1990
- [22] Grismer M.J., Strang W.Z., Tomaro R.F., and Witzeman F.C., *Cobalt: A Parallel, Implicit, Unstructured Euler/Navier-Stokes Solver*, Adv. Eng. Software, Vol. 29, No. 3-6, pp. 365-373, 1998
- [23] Haselbacher A. and Blažek J., *On the Accurate and Efficient Discretisation of the Navier-Stokes Equations on Mixed Grids*, AIAA Paper 99-3363, 14th Computational Fluid Dynamics Conference, Norfolk, VA, June/July 1999

- [24] Holmes D.G. and Connell S.D., *Solution of the Two-Dimensional Navier-Stokes Equations on Unstructured Adaptive Grids*, AIAA Paper 89-1932, 9th Computational Fluid Dynamics Conference, Buffalo, NY, June 1989
- [25] Jiang Y. and Przekwas A.J., *Implicit, Pressure-Based Incompressible Navier-Stokes Equations Solver for Unstructured Meshes*, AIAA Paper 94-0305, 32nd Aerospace Sciences Meeting and Exhibit, Reno, NV, January 1994
- [26] Jiang Y., Wang Z.J., and Przekwas A.J., *Pressure-Based High-Order Accuracy Flow Solver on Adaptive, Mixed-Type Unstructured Grids*, AIAA Paper 96-0417, 34th Aerospace Sciences Meeting and Exhibit, Reno, NV, January 1996
- [27] Jongen T. and Marx Y.P., *Design of an Unconditionally Stable, Positive Scheme for the $k - \epsilon$ and Two-Layer Turbulence Models*, Comp. Fl., Vol. 26, No. 5, pp. 469-487, 1997
- [28] Jorgenson P.C.E. and Pletcher R.H., *An Implicit Numerical Method for the Simulation of Internal Viscous Flow On Unstructured Grids*, Comp. Fl., Vol. 25, No. 5, pp. 447-466, 1996
- [29] Karman Jr. S.L. and Spragle S.J., *Development of an Unstructured CFD Method*, AIAA Paper 91-0019, 29th Aerospace Sciences Meeting and Exhibit, Reno, NV, January 1991
- [30] Kershaw D.S., *Differencing of the Diffusion Equation in Lagrangian Hydrodynamic Codes*, J. Comp. Phys., Vol. 39, pp. 375-395, 1981
- [31] Knight D.D., *A Fully Implicit Navier-Stokes Algorithm Using an Unstructured Grid and Flux-Difference Splitting*, Appl. Num. Math., Vol. 16, pp. 101-128, 1994
- [32] Letniowski F.W., *Three-Dimensional Triangulations for Finite-Element Approximations to a Second-Order Diffusion Operator*, SIAM J. Sci. Stat. Comput. Vol. 13, No. 3, pp. 765-770, 1992
- [33] Lindquist D.R., *A Comparison of Numerical Schemes on Triangular and Quadrilateral Meshes*, M.Sc. Thesis, Massachusetts Institute of Technology, May 1988
- [34] Liu F. and Zheng X., *Staggered Finite-Volume Scheme for Solving Cascade Flow with a $k - \omega$ Turbulence Model*, AIAA J., Vol. 32, No. 8, pp. 1589-1597, August 1994
- [35] Liu F. and Zheng X., *A Strongly Coupled Time-Marching Method for Solving the Navier-Stokes and $k - \omega$ Turbulence Model Equations with Multigrid*, J. Comp. Phys., Vol. 128, pp. 289-300, 1996
- [36] Luo H., Baum J.D., Löhner R., and Cabello J., *Adaptive Edge-Based Finite Element Schemes for the Euler and Navier-Stokes Equations on Unstructured Grids*, AIAA Paper 93-0336, 31st Aerospace Sciences Meeting and Exhibit, Reno, NV, January 1993
- [37] Maman N., *Algorithmes d'adaptation dynamique de maillages en éléments finis. Application à des écoulements réactifs instationnaires*, Ph.D. Thesis, University Paul Sabatier, Toulouse, May 1992
- [38] Martinelli L., *Calculations of Viscous Flows with a Multigrid Method*, Ph.D. Thesis, Princeton University, October 1987
- [39] Mathur S.R. and Murthy J.Y., *A Pressure-Based Method for Unstructured Meshes*, Num. Heat Transfer, Part B, Vol. 31, pp. 195-215, 1997

- [40] Mavriplis D.J., *A Three-Dimensional Multigrid Reynolds-Averaged Navier-Stokes Solver for Unstructured Meshes*, ICASE Report No. 94-29, May 1994
- [41] Mavriplis D.J. and Venkatakrishnan V., *A Unified Multigrid Solver for the Navier-Stokes Equations on Mixed Element Meshes*, ICASE Report No. 95-53, July 1995
- [42] Minyard T., private communication, November 1, 1998
- [43] Montgomery M. and Fleeter S., *The Effect of Grid Irregularity on Truncation Error for Discretisations of Laplace's Equation*, Int. J. Num. Meth. Eng., Vol. 38, pp. 3243-3257, 1995
- [44] Parthasarathy V., Kallinderis Y., and Nakajima K., *Hybrid Adaptation Method and Directional Viscous Multigrid with Prismatic-Tetrahedral Meshes*, AIAA Paper 95-0670, 33rd Aerospace Sciences Meeting and Exhibit, Reno, NV, January 1995
- [45] Pert G.J., *Physical Constraints in Numerical Calculations of Diffusion*, J. Comp. Phys., Vol. 42, pp. 20-52, 1981
- [46] Pierce N., *Preconditioned Multigrid Methods for Compressible Flow Calculations on Stretched Meshes*, Ph.D. Thesis, Oxford University, August 1997
- [47] Putti M. and Cordes C., *Finite-Element Approximation of the Diffusion Operator on Tetrahedra*, SIAM J. Sci. Comput., Vol. 19, No. 4, pp. 1154-1168, July 1998
- [48] Rees M.D., *Numerical Solution of the Heat Equation on Triangular Grids*, Report No. 88/2, Oxford University Computing Laboratory, Numerical Analysis Group, Oxford University, United Kingdom, January 1988
- [49] Renard E. and Essers J.A., *An Analysis of Severe Grid Distortion Effects on the Accuracy of Some Discretisation Schemes for Convection-Diffusion Equations*, in: *Numerical Grid Generation in Computational Fluid Mechanics '88*, Proc. 2nd Int. Conf. on Grid Generation in Computational Fluid Mechanics, Sengupta S. et al. (Eds.), Miami Beach, FL, Pineridge Press, Swansea, pp. 845-853, December 1988
- [50] Roberts R.M., *Hexahedra, Wedge, Tetrahedron and Pyramid Diffusion Operator Discretisation*, Los Alamos National Laboratories, Report No. LA-UR-96-3501, August 1996
- [51] Schulz K. and Kallinderis Y., *Unsteady Flow Structure Interaction for Incompressible Flows Using Deformable Hybrid Grids*, J. Comp. Phys., Vol. 143, No. 2, pp. 569-597, July 1998
- [52] Stolcis L. and Johnston L.J., *Compressible-Flow Calculation Using a Two-Equation Turbulence Model and Unstructured Grids*, in: *Proc. 7th Int. Conf. on Numerical Methods for Laminar and Turbulent Flow*, Taylor C. et al. (Eds.), Pineridge Press, pp. 852-862, 1991
- [53] Strang W.Z., Tomaro R.F., and Grismer M.J., *The Defining Methods of Cobalt₆₀: A Parallel, Implicit, Unstructured Euler/Navier-Stokes Flow Solver*, AIAA Paper 99-0786, 37th Aerospace Sciences Meeting and Exhibit, Reno, NV, January 1999
- [54] Thom A. and Appelt C.J., *Field Computations in Engineering and Physics*, Van Nostrand, London, 1961
- [55] Varga R.S., *Matrix Iterative Analysis*, Prentice-Hall, Eaglewood Cliffs, NJ, 1962
- [56] Vilsmeier R., *Lösung der Erhaltungsgleichungen auf unstrukturierten Gittern*, Ph.D. Thesis, Mercator Universität, Duisburg, December 1996

- [57] Wesseling P., *Introduction to Multigrid Methods*, Wiley, 1993
- [58] Weiss J., Maruszewski J.P., and Smith W.A., *Implicit Solution of Preconditioned Navier-Stokes Equations Using Algebraic Multigrid*, AIAA J., Vol. 37, No. 1, pp. 29-36, 1999
- [59] Wieners C., *Conformal Discretisations on Tetrahedrons, Pyramids, Prisms and Hexahedrons*, preprint available at: <http://dom.ica3.uni-stuttgart.de/~wieners/paper.html>
- [60] Winslow A.M., *Numerical Solution of the Quasilinear Poisson Equation in a Nonuniform Triangle Mesh*, J. Comp. Phys., Vol. 2, pp. 149-172, 1967
- [61] Wood W.A. and Kleb W., *Comments on the Diffusive Behaviour of Two Upwind Schemes*, NASA/TM-1998-208378, October 1998
- [62] Zheng X. and Liu F., *Staggered Upwind Method for Solving the Navier-Stokes and $k - \omega$ Turbulence Model Equations*, AIAA J., Vol. 33, No. 6, pp. 991-998, 1995

Chapter 5

Multigrid Numerical Method

The implementation of the agglomeration multigrid method on mixed unstructured grids is described. The generation of coarse grid levels through agglomeration of control volumes is explained. Intergrid transfer operators and the cycling strategy are defined.

5.1 Introduction

The solution method presented in Chapter 3 generally shows slow asymptotic convergence after a rapid reduction of residuals during the first few iterations. Nearly all iterative methods exhibit slow asymptotic convergence to some degree. This problem is particularly severe for the computation of three-dimensional turbulent flows since it is exacerbated with an increasing number of grid points and grid stretching.

Analysis shows that iterative methods typically damp high-frequency error components well, but exhibit poor damping of low-frequency error components. Thus, the rapid reduction of residuals during the first few iterations corresponds to the annihilation of the high-frequency error components while the slow asymptotic convergence is caused by the remaining low-frequency error components. Multigrid methods accelerate convergence by capitalizing on the high-frequency damping properties of a given iterative method. This is accomplished by using a sequence of successively coarser grids, on which low-frequency error components reappear as high-frequency error components.

Multigrid methods were first developed by Fedorenko [6] and Bakhvalov [1] for elliptic equations in the late 1960's, and further refined by Brandt [2] and Hackbusch [11] in the 1970's. Rigorous mathematical analyses for elliptic equations show that multigrid methods can exhibit convergence rates which are independent of grid size. This gives rise to an optimal complexity since the cost of obtaining the solution of a set of equations is directly proportional to the number of unknowns. Typically, $O(10)$ residual evaluations

are required. Because of the progressively coarser grids, storage requirements are only modestly increased.

The application of multigrid methods to the Euler equations was pioneered by Ni [22], Jameson [7], and Jespersen [8] in the early 1980's. Convergence rates are improved because low-frequency error components are propagated more rapidly out of the solution domain.* This was shown analytically by Lötstedt [17], who proved that for first-order partial differential equations with constant coefficients, the propagation of low-frequency error components is accelerated by a factor proportional to $(2^L - 1)$, where L is the number of grid levels. Although considerable improvements in convergence rates are observed when applying multigrid methods to the Euler equations, the resulting convergence rates are not as low as those for elliptic equations. The main reasons are discontinuities and the need for very low numerical dissipation.

For the Reynolds-averaged Navier-Stokes (RANS) equations, the situation is similar to that for the Euler equations. The application of multigrid leads to an improvement in convergence rates, but they are also far removed from those obtained for elliptic equations. The reasons for this discrepancy are, in addition to those already mentioned above, the stiffness caused by the highly stretched grids, and the stiffness and highly non-linear behaviour of turbulence models. The most promising approach of dealing with these difficulties appears to be a combination of anisotropic coarsening and preconditioning, see, e.g., Pierce [23]. Brandt [4] provided a complete list of the barriers which need to be overcome for multigrid to achieve convergence rates for the Euler and RANS equations similar to those for elliptic equations.

Detailed information on multigrid methods can be found in the monographs by Brandt [3] and Briggs [5] and the textbooks by Hackbusch [12] and Wesseling [30]. Wesseling [29] reviewed the use of multigrid methods in CFD.

As explained in Chapter 1, the application of multigrid methods to unstructured grids required the development of new methods for the generation of coarse grid levels. In the present work, the agglomeration method originally devised by Lallemand [15] is used. The present implementation differs from previous ones mainly in two points, both of which attempt to address recognised shortcomings of the agglomeration multigrid

*This does not explain why convergence is accelerated for problems with periodic boundaries, as error components propagated out of the domain through one periodic boundary re-enter through the other.

method. First, the viscous fluxes on the coarse grid levels are discretised in the same way as on the finest grid level. Second, a linear prolongation operator is constructed. A further difference compared to previous implementations is a modified agglomeration algorithm.

Since the agglomeration multigrid method can be applied to triangular, quadrilateral, and mixed grids with relative ease, the present work provides an opportunity to study the performance of the multigrid method on these grid types.

5.2 Full Approximation Storage (FAS) Scheme

At the steady-state, the solution \mathbf{q} to Eq. (3.12.1) will be given by

$$\mathbf{R}_0(\mathbf{q}) = 0. \quad (5.2.1)$$

Approximate solutions $\tilde{\mathbf{q}}$ do not satisfy the above equation and lead to a defect \mathbf{d}_0

$$\mathbf{R}_0(\tilde{\mathbf{q}}) = \mathbf{d}_0. \quad (5.2.2)$$

The approximate and exact solutions at vertex 0 are related through

$$\mathbf{q}_0 = \tilde{\mathbf{q}}_0 + (\delta\mathbf{q})_0. \quad (5.2.3)$$

Various algorithms to solve Eq. (5.2.2) have been constructed within the multigrid framework. In the present work, the Full Approximation Storage (FAS) scheme of Brandt [3] was used. The FAS scheme is particularly well-suited to the solution of nonlinear problems, because it does not require the linearisation of the equation to be solved.

In the following, the FAS scheme is described assuming two grid levels. The generalisation to an arbitrary number of grid levels is straightforward. The two grid levels are denoted by the superscripts h and H , the capitalization indicating that the grid spacing on grid H is larger than that on grid h . Equations (5.2.1) and (5.2.2) may then be expressed on the fine-grid level as

$$\mathbf{R}_0^h(\mathbf{q}^h) = 0 \quad (5.2.4)$$

and

$$\mathbf{R}_0^h(\tilde{\mathbf{q}}^h) = \mathbf{d}_0^h. \quad (5.2.5)$$

Subtracting Eq. (5.2.5) from Eq. (5.2.4) gives

$$\mathbf{R}_0^h(\mathbf{q}^h) - \mathbf{R}_0^h(\tilde{\mathbf{q}}^h) = -\mathbf{d}_0^h. \quad (5.2.6)$$

Using Eq. (5.2.3), Eq. (5.2.6) is rewritten as

$$\mathbf{R}_0^h(\tilde{\mathbf{q}}^h + (\delta\mathbf{q})^h) - \mathbf{R}_0^h(\tilde{\mathbf{q}}^h) = -\mathbf{d}_0^h. \quad (5.2.7)$$

Expressing Eq. (5.2.7) on grid level H leads to

$$\mathbf{R}_{0'}^H(\mathcal{I}_h^H \tilde{\mathbf{q}}^h + (\delta\mathbf{q})^H) - \mathbf{R}_{0'}^H(\mathcal{I}_h^H \tilde{\mathbf{q}}^h) = -\bar{\mathcal{I}}_h^H \mathbf{d}_0^h, \quad (5.2.8)$$

where the subscript '0' denotes the control volume on level H which contains the control volume associated with vertex 0 on level h , and \mathcal{I}_h^H and $\bar{\mathcal{I}}_h^H$ are restriction and interpolation operators, respectively. They are defined in Subsections 5.6.1 and 5.6.3, respectively.

Using Eq. (5.2.5) on grid level H , Eq. (5.2.8) is written as

$$\mathbf{R}_{0'}^H \hat{\mathbf{q}}^H = \mathbf{R}_{0'}^H(\mathcal{I}_h^H \tilde{\mathbf{q}}^h) - \bar{\mathcal{I}}_h^H(\mathbf{R}_0^h(\tilde{\mathbf{q}}^h)), \quad (5.2.9)$$

where the coarse-grid solution vector, denoted by the superscript $\widehat{(\cdot)}$, is defined as

$$\hat{\mathbf{q}}_{0'}^H = \mathcal{I}_h^H \tilde{\mathbf{q}}_0^h + (\delta\mathbf{q})_{0'}^H. \quad (5.2.10)$$

The right-hand side of Eq. (5.2.9) is the forcing function

$$\mathbf{F}_{0'}^H = \mathbf{R}_{0'}^H(\mathcal{I}_h^H \tilde{\mathbf{q}}^h) - \bar{\mathcal{I}}_h^H(\mathbf{R}_0^h(\tilde{\mathbf{q}}^h)), \quad (5.2.11)$$

which represents the difference between the residual of the restricted fine-grid state vector and interpolated fine-grid residual. The coarse-grid solution vector defined by Eq. (5.2.10) and the forcing function defined in Eq. (5.2.11) are the two key constructs in the FAS scheme. The forcing function ensures that the coarse-grid levels do not generate corrections if the fine-grid equations are satisfied.

Having obtained an approximate coarse-grid solution $\hat{\mathbf{q}}_{0'}^H$ to Eq. (5.2.9), the correction is interpolated to the fine grid in order to compute a new approximate solution from

$$\tilde{\mathbf{q}}_0^h \leftarrow \tilde{\mathbf{q}}_0^h + \mathcal{I}_H^h(\hat{\mathbf{q}}_{0'}^H - \mathcal{I}_h^H \tilde{\mathbf{q}}_0^h), \quad (5.2.12)$$

where \mathcal{I}_H^h is a prolongation operator as defined in Subsection 5.6.2.

It is important to note that the restricted approximate fine-grid state vector $\mathcal{I}_h^H \tilde{\mathbf{q}}_0^h$

in Eqs. (5.2.9), (5.2.10), and (5.2.12) must be identical.

5.3 Coarsening Algorithm

Having specified how the coarse-grid levels are used to accelerate the convergence of the single-grid solution method, the next step requires the construction of the coarse grid levels. As already stated, the coarse-grid levels are generated by agglomerating control volumes.

The coarsening algorithm used in the present work consists of three main steps:

1. Selection of seed vertices,
2. Agglomeration of control volumes,
3. Movement of seed vertices.

Each of the above steps is described in the following subsections. The description assumes that level 1 denotes the finest grid level, and level n denotes the grid level obtained by applying the coarsening algorithm $n - 1$ times to level 1.

In describing the coarsening algorithm, it is useful to retain the designations ‘vertex’ and ‘edge,’ although, strictly speaking, neither exist on coarse grid levels. The reason for keeping these terms is that a vertex may still be thought of as a storage location for the dependent variables, and that an edge may still be regarded as being associated with a control-volume face.

For notational convenience, the set of control volumes on grid h contained within control volume $0'$ on grid H is denoted by $C_{0'}^H$.

5.3.1 Selection of Seed Vertices

The agglomeration of control volumes is preceded by the selection of so-called seed vertices from the vertices in a given grid and by storing the seed vertices in a list. Seed vertices are those vertices whose control volumes agglomerate the unagglomerated control volumes of neighbouring vertices.

In the present work, the list of seed vertices consists of all vertices for the sake of simplicity. This is less sophisticated than choosing the seed vertices to form an approximate maximal independent set as done by Mavriplis and Venkatakrishnan [20].

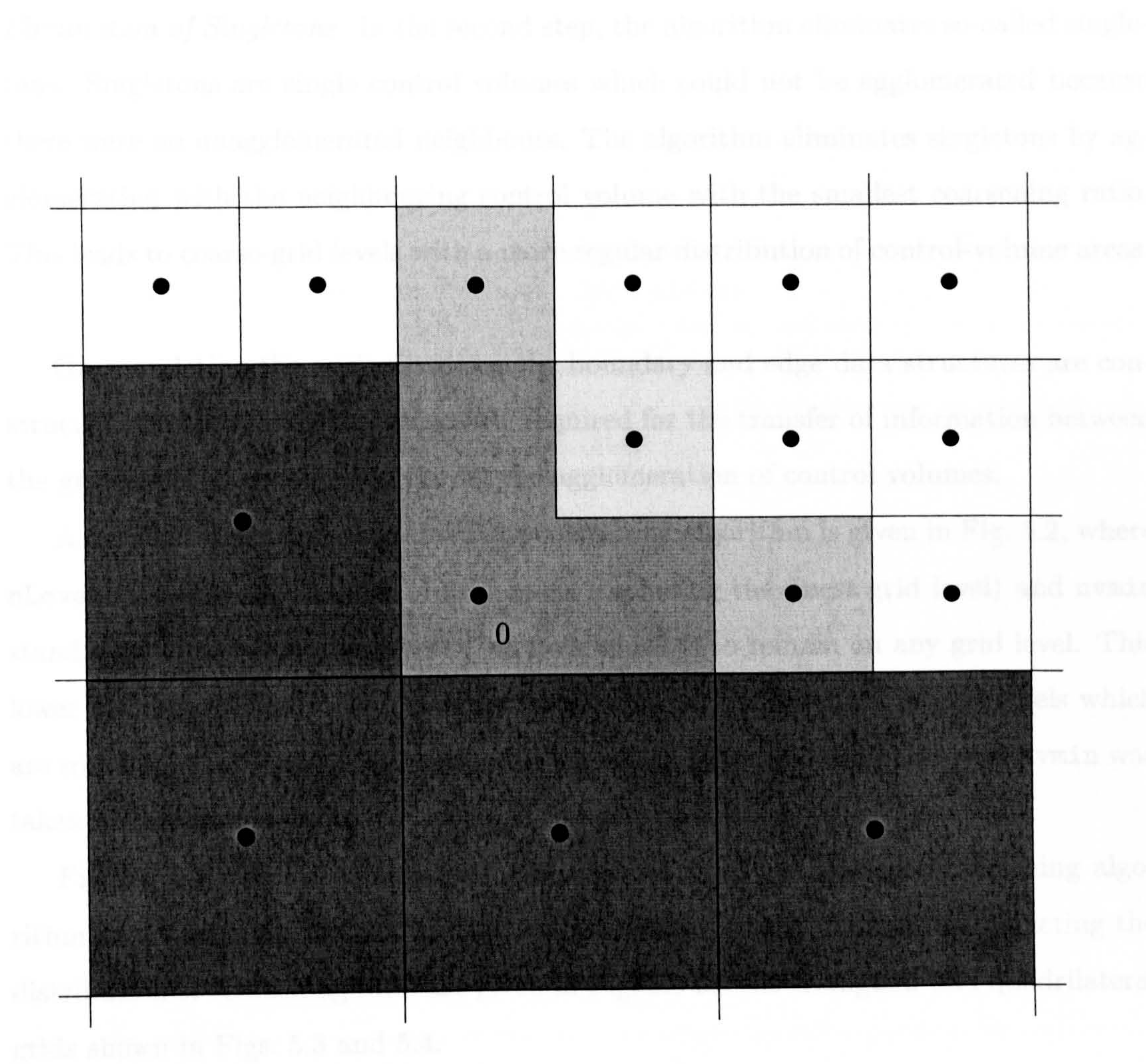
The simpler method used in the present work is not believed to have a negative impact on the performance of the multigrid method.

In the present implementation of the agglomeration multigrid method, boundary conditions are enforced on the coarse grid levels in the same manner as on the finest grid level. For this reason, it is necessary that there are vertices on the boundaries of the coarse grid levels. This is ensured by listing all boundary vertices at the beginning of the list of seed vertices.

5.3.2 Agglomeration of Control Volumes

Isotropic Coarsening. The isotropic coarsening algorithm used in the present work consists of two nested loops. The outer loop visits each seed vertex. The inner loop runs over all edges and agglomerates all unagglomerated neighbours of a seed vertex. Once all unagglomerated neighbours at a seed vertex are agglomerated, two further steps are carried out.

Check of Coarsening Ratio. First, the coarsening ratio of each control volume is checked. The coarsening ratio of a coarse-grid control volume is defined as the number of fine-grid control volumes contained within it. This check is necessary to ensure a bounded complexity of the multigrid method with W-cycles, for which the coarsening ratio must be at least a factor of four, see, e.g., Wesseling [30]. If the coarsening ratio is less than four, the algorithm attempts to agglomerate as many unagglomerated control volumes as necessary to reach a coarsening ratio of four. Since the nearest neighbours were already agglomerated, unagglomerated neighbours of the nearest neighbours have to be considered. In general, several unagglomerated distance-two neighbours exist. The coarsening algorithm agglomerates the first distance-two vertex which is a distance-one neighbour of at least two distance-one neighbours, as illustrated in Fig. 5.1. This choice has two advantages. First, it leads to coarse-grid control volumes of better quality. Second, it allows the coarse-grid control volumes to be of quadrilateral shape if the finest level is a quadrilateral grid. This procedure was previously used by Mavriplis and Venkatakrishnan [21].





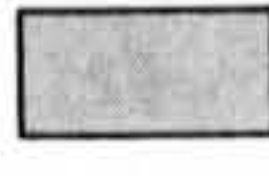


-  previously agglomerated control volumes
-  control volume 0 and agglomerated distance-one neighbours
-  distance-two neighbours of control volume 0, candidates for agglomeration
-  distance-two neighbour of control volume 0, chosen for agglomeration
-  unagglomerated control volumes

Figure 5.1: Illustration of step in agglomeration algorithm to ensure coarsening ratio of four on quadrilateral grid.

Elimination of Singletons. In the second step, the algorithm eliminates so-called singletons. Singletons are single control volumes which could not be agglomerated because there were no unagglomerated neighbours. The algorithm eliminates singletons by agglomerating with the neighbouring control volume with the smallest coarsening ratio. This leads to coarse-grid levels with a more regular distribution of control-volume areas.

On completing the agglomeration, the boundary and edge data structures are constructed. The intergrid data structure, required for the transfer of information between the grid levels, is constructed during the agglomeration of control volumes.

A detailed structural diagram of the coarsening algorithm is given in Fig. 5.2, where `nLevels` denotes the number of grid levels (including the finest grid level) and `nvmin` stands for the minimum number of vertices which is to remain on any grid level. This lower limit was found to be necessary to prevent the construction of grid levels which are so coarse that the solution method is unstable. Typically, the parameter `nvmin` was taken to be equal to eight.

Figures 5.3 and 5.4 demonstrate the application of the isotropic coarsening algorithm to a triangular and a quadrilateral grid, respectively. Histograms depicting the distribution of coarsening ratio are given in Fig. 5.5 for the triangular and quadrilateral grids shown in Figs. 5.3 and 5.4.

Anisotropic Coarsening. The above algorithm could be extended easily to produce anisotropic coarsening. Anisotropic agglomeration methods were presented by Mavriplis [18] and Lassaline and Zingg [16].

5.3.3 Movement of Seed Vertices

Once the agglomeration of control volumes on a given grid level is complete, the seed vertices are moved according to

$$\mathbf{r}_0^H = \frac{\sum_{i \in \mathcal{C}_{0'}^H} A_{\Omega_i} \mathbf{r}_i^h}{\sum_{i \in \mathcal{C}_{0'}^H} A_{\Omega_i}}, \quad (5.3.1)$$

where \mathbf{r}_i^h is the position vector to vertex i contained in $\mathcal{C}_{0'}^H$. The effect is illustrated in Fig. 5.6. On a uniform grid, the repositioned seed vertices coincide with the centre of gravity of the coarse-grid control volumes. The movement of seed vertices in the

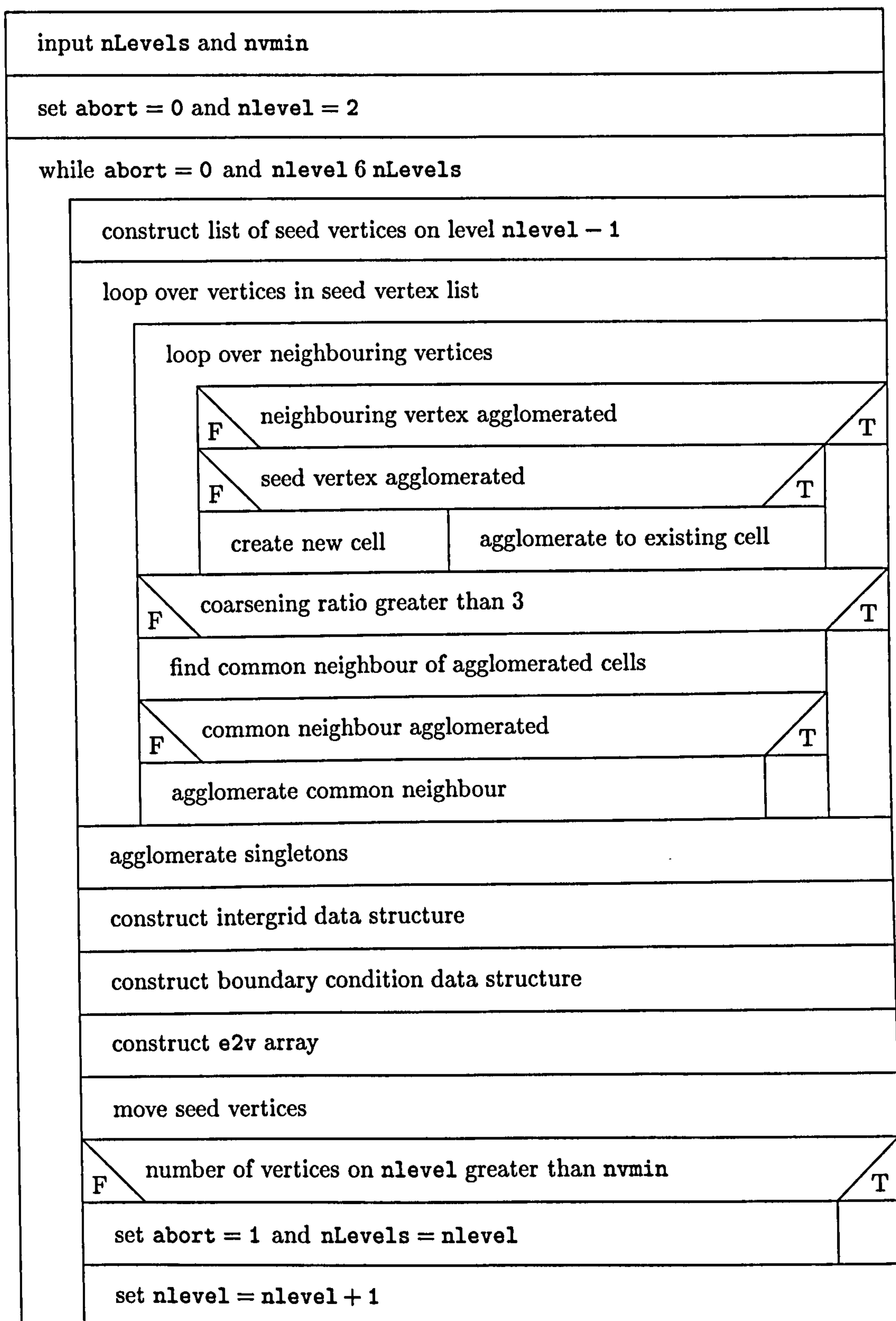
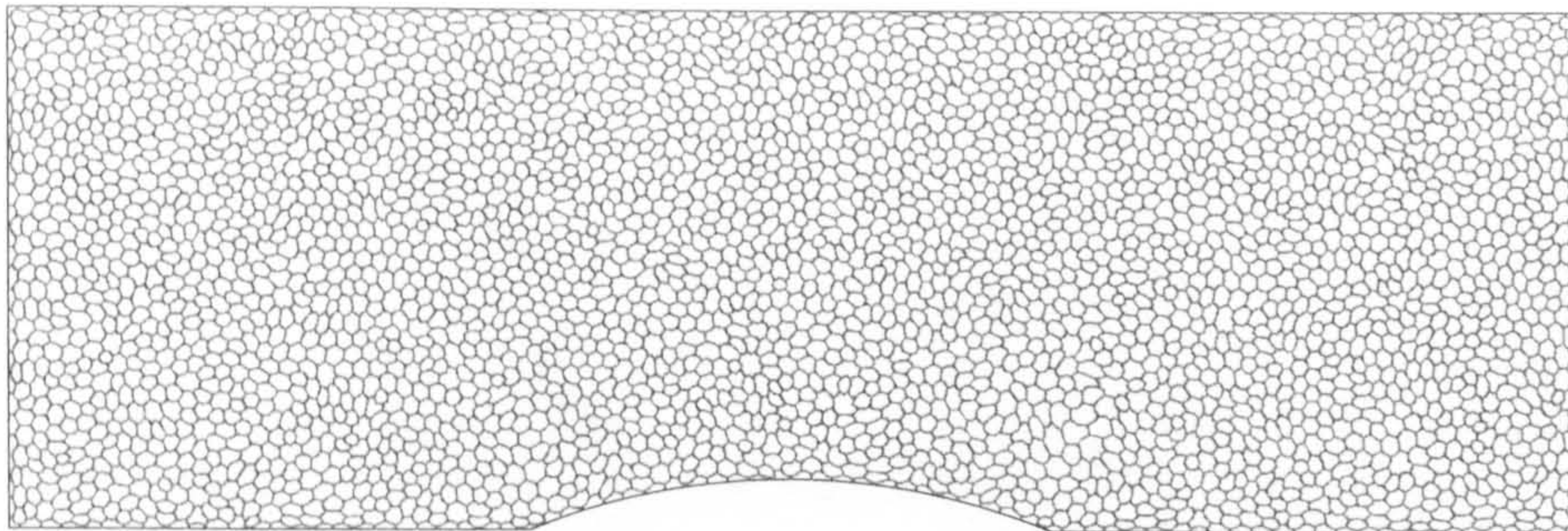
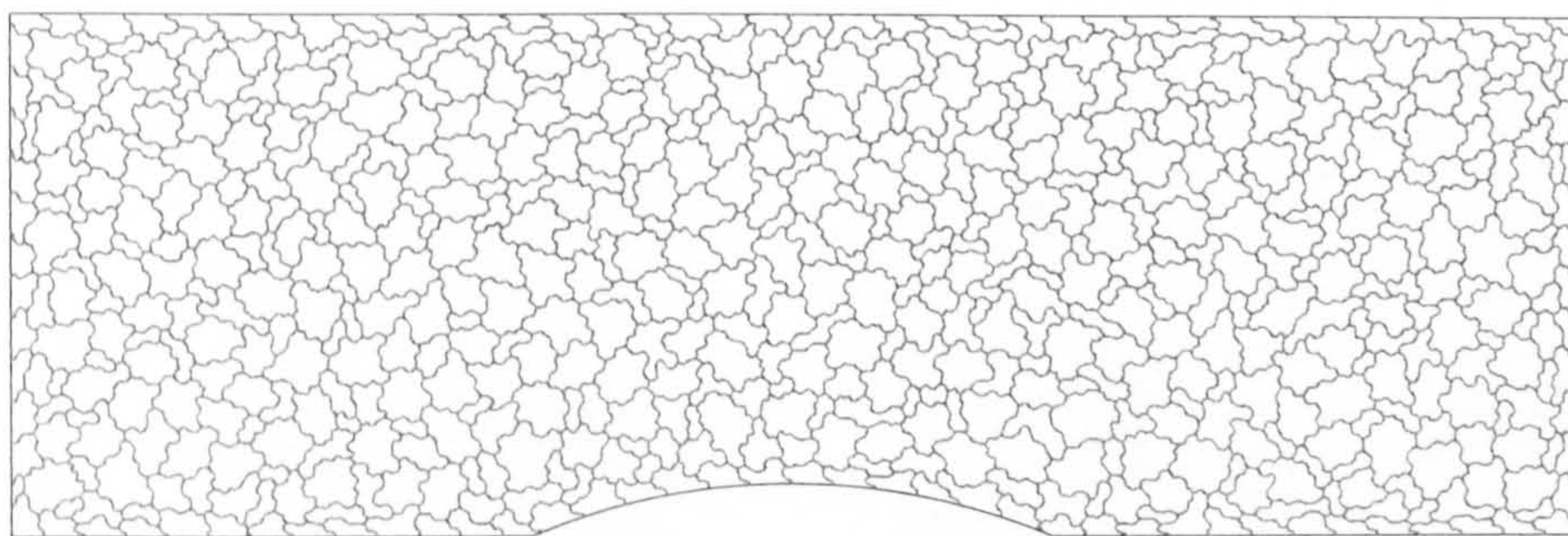


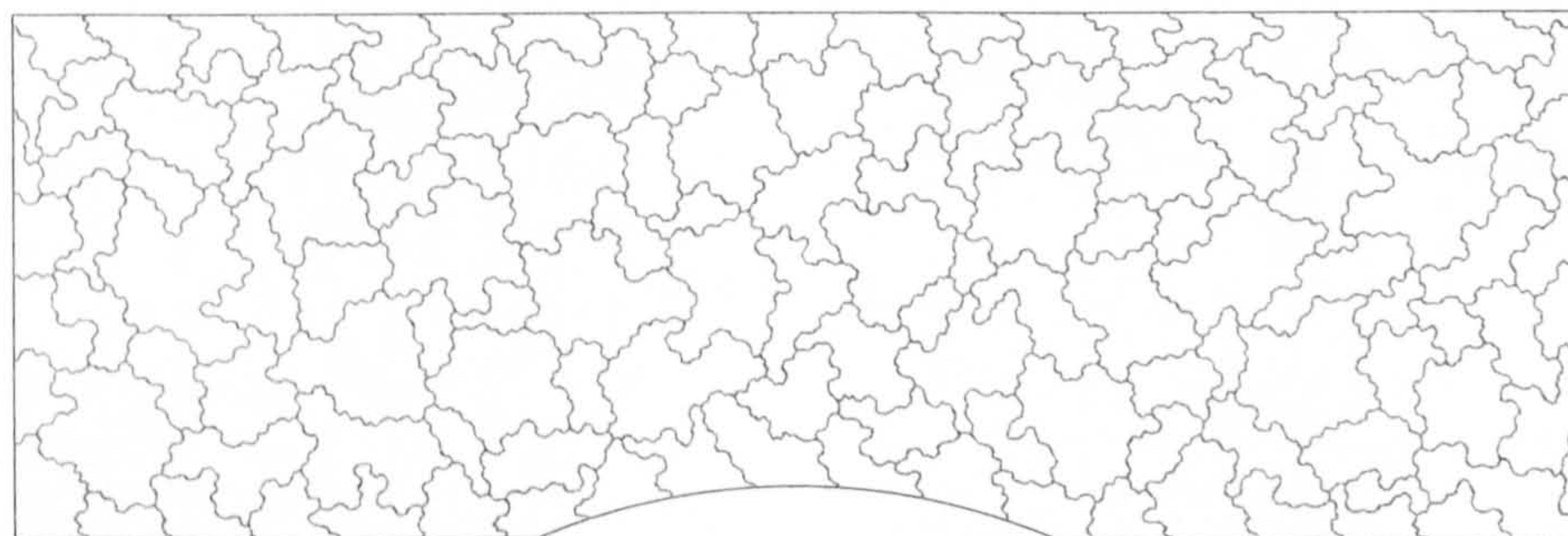
Figure 5.2: Structural diagram of coarsening algorithm. 'F' is a shorthand for 'false' and 'T' is a shorthand for 'true.'



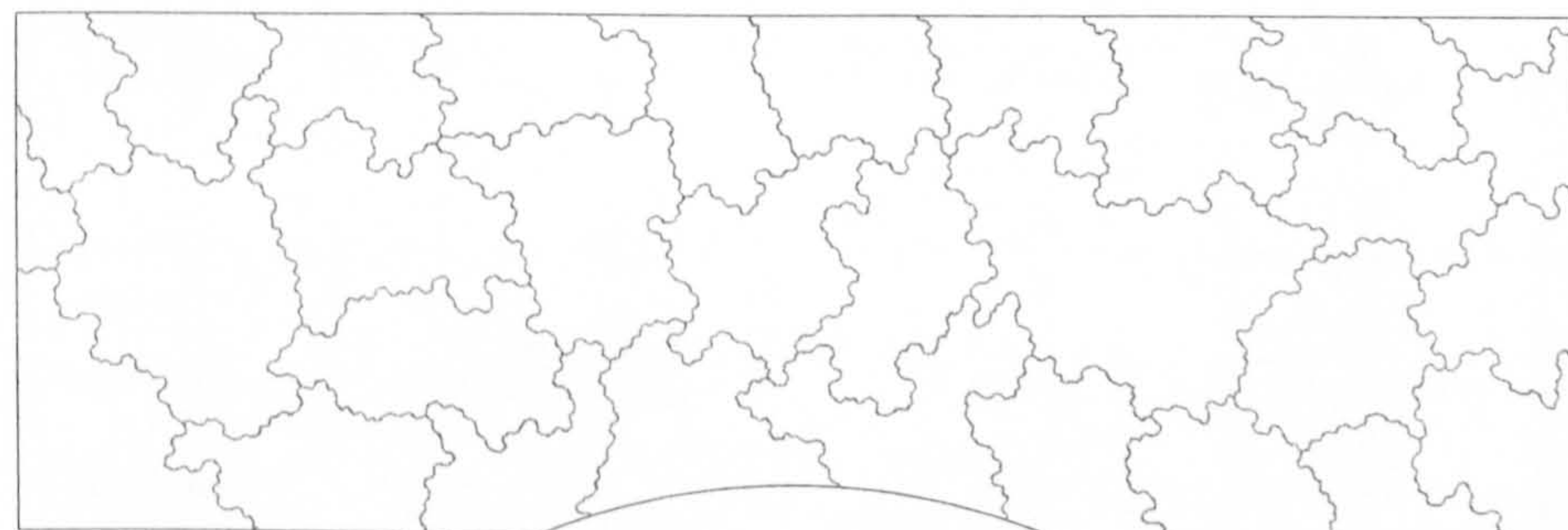
level 1, 3276 vertices and 9625 edges (control-volume faces)



level 2, 637 vertices and 1808 control-volume faces

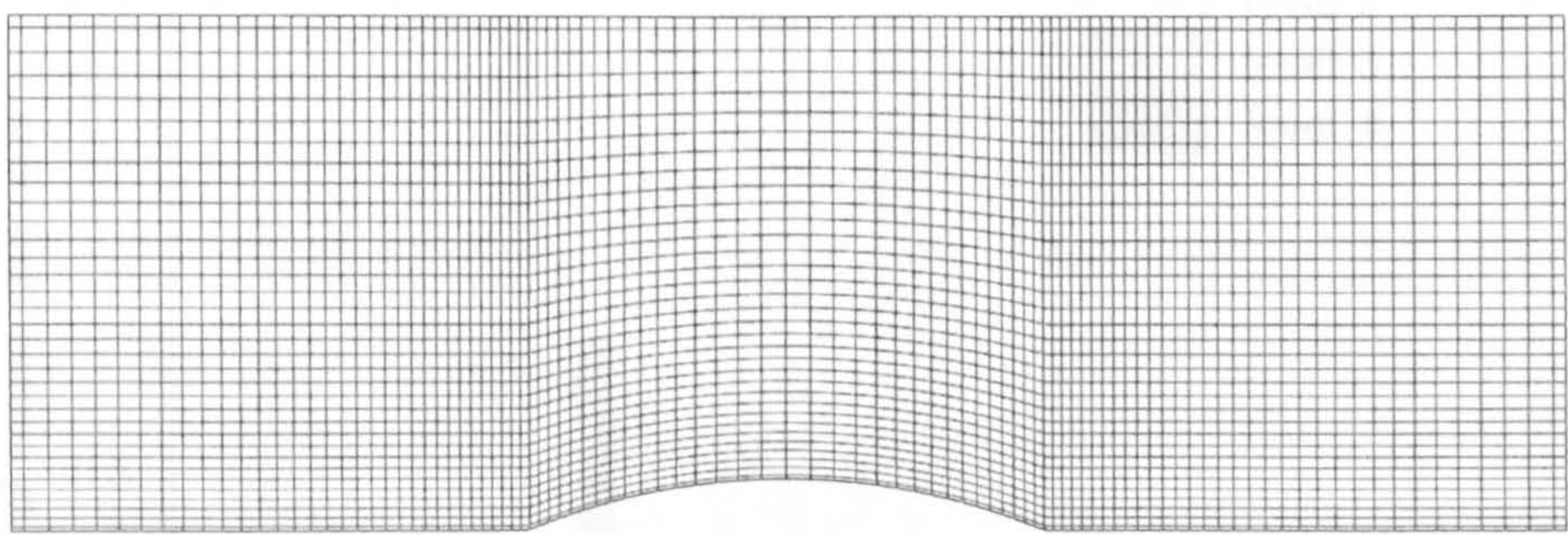


level 3, 135 vertices and 353 control-volume faces

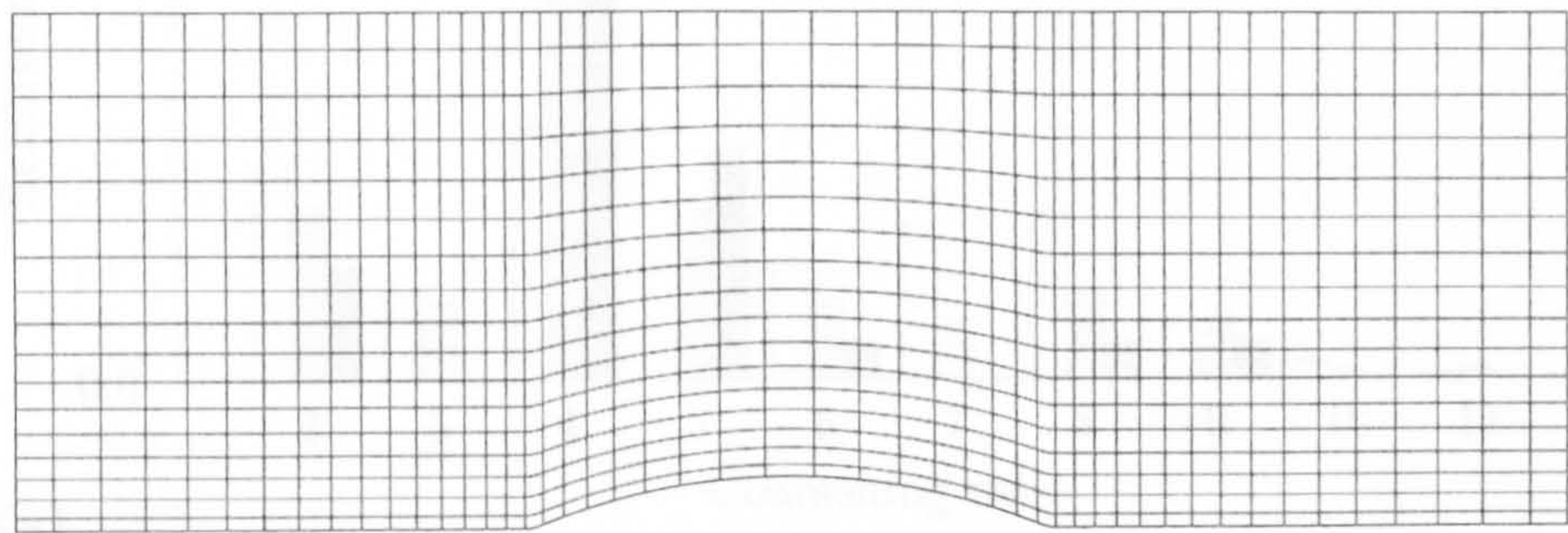


level 4, 31 vertices and 68 control-volume faces

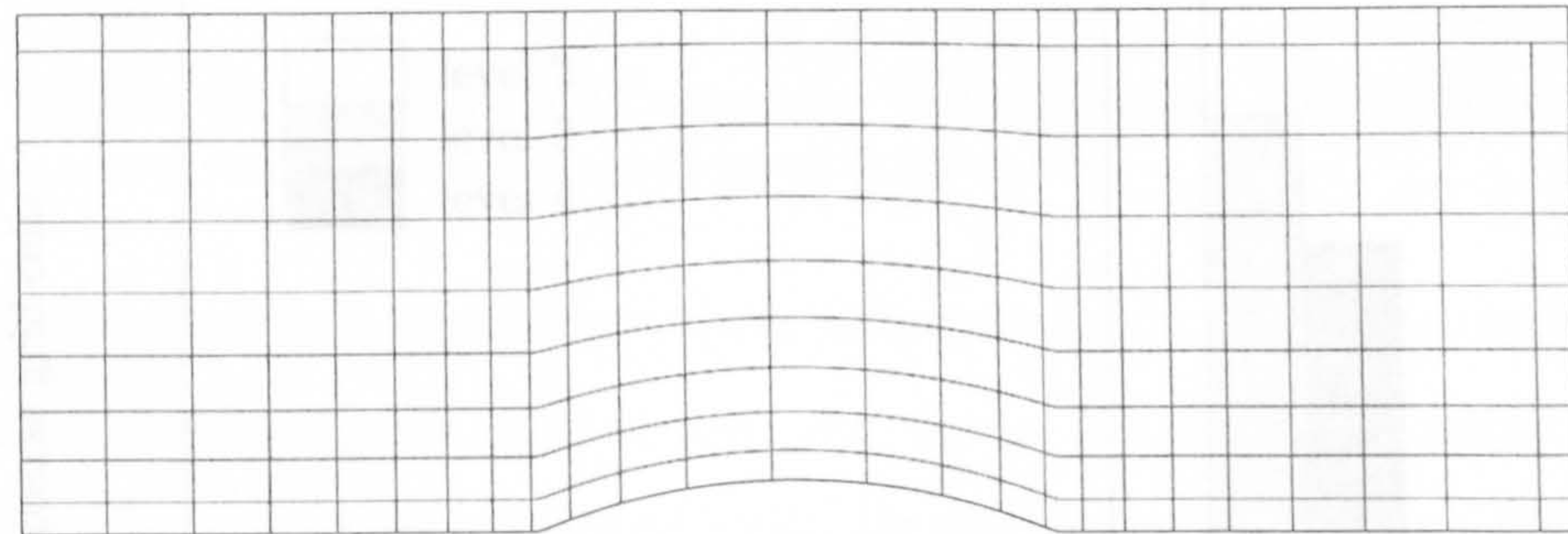
Figure 5.3: Illustration of isotropic agglomeration algorithm on triangular grid.



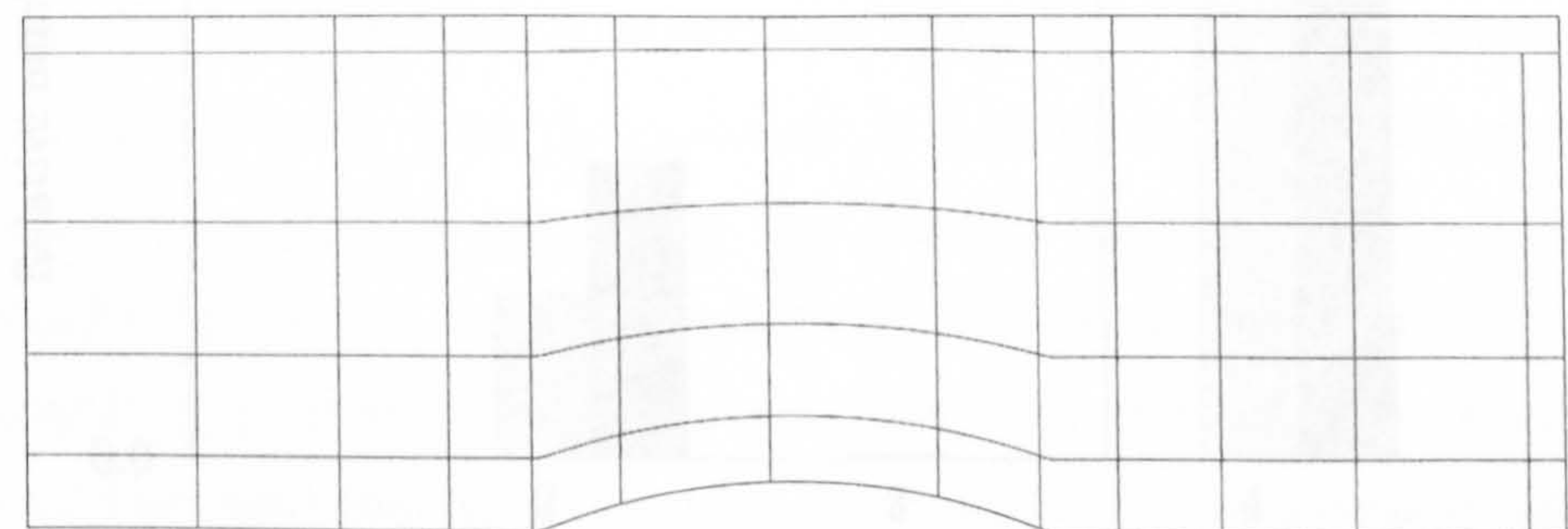
level 1, 3201 vertices and 6532 edges (control-volume faces)



level 2, 833 vertices and 1600 control-volume faces



level 3, 224 vertices and 415 control-volume faces



level 4, 64 vertices and 111 control-volume faces

Figure 5.4: Illustration of isotropic agglomeration for quadrilateral grid.

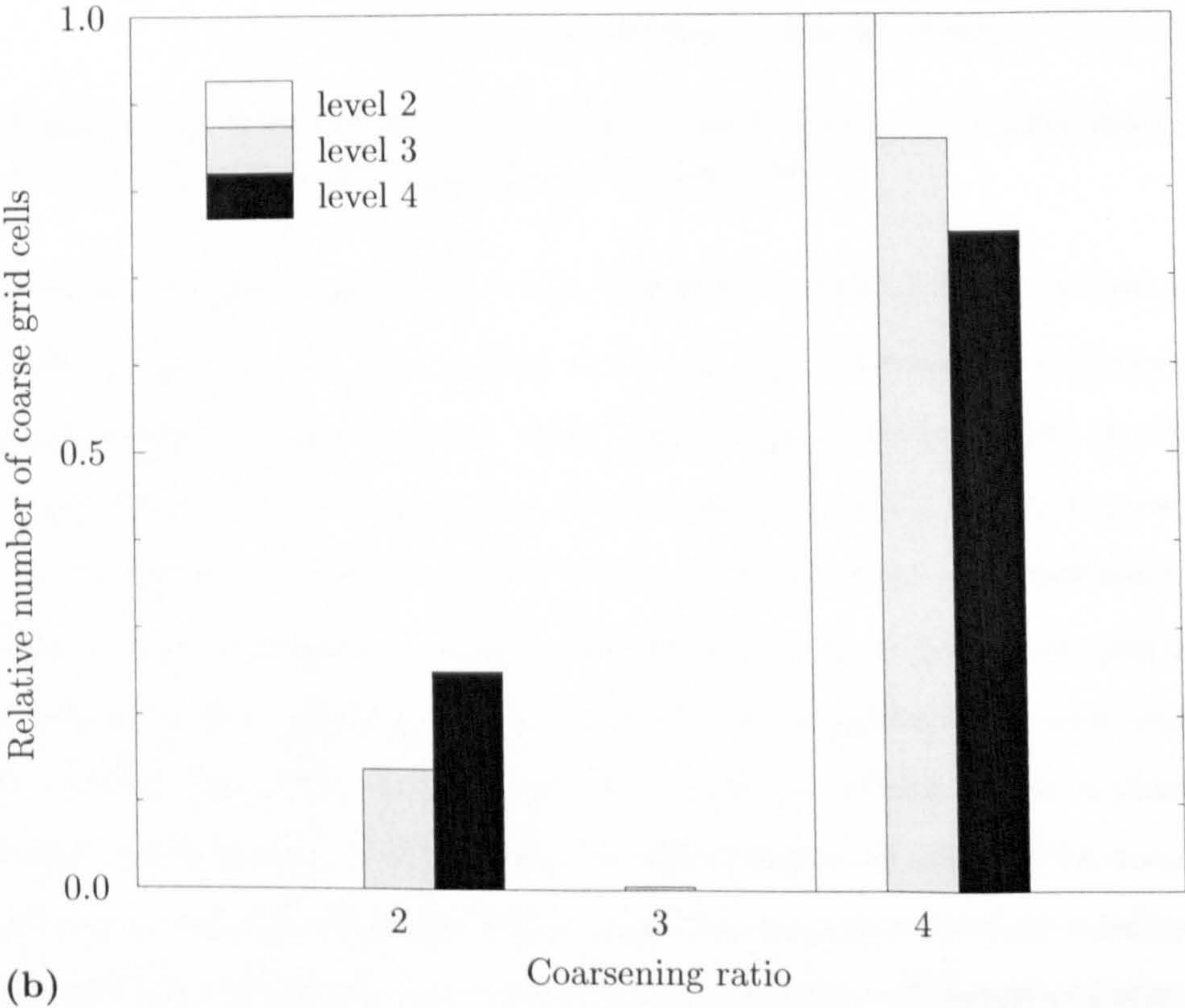
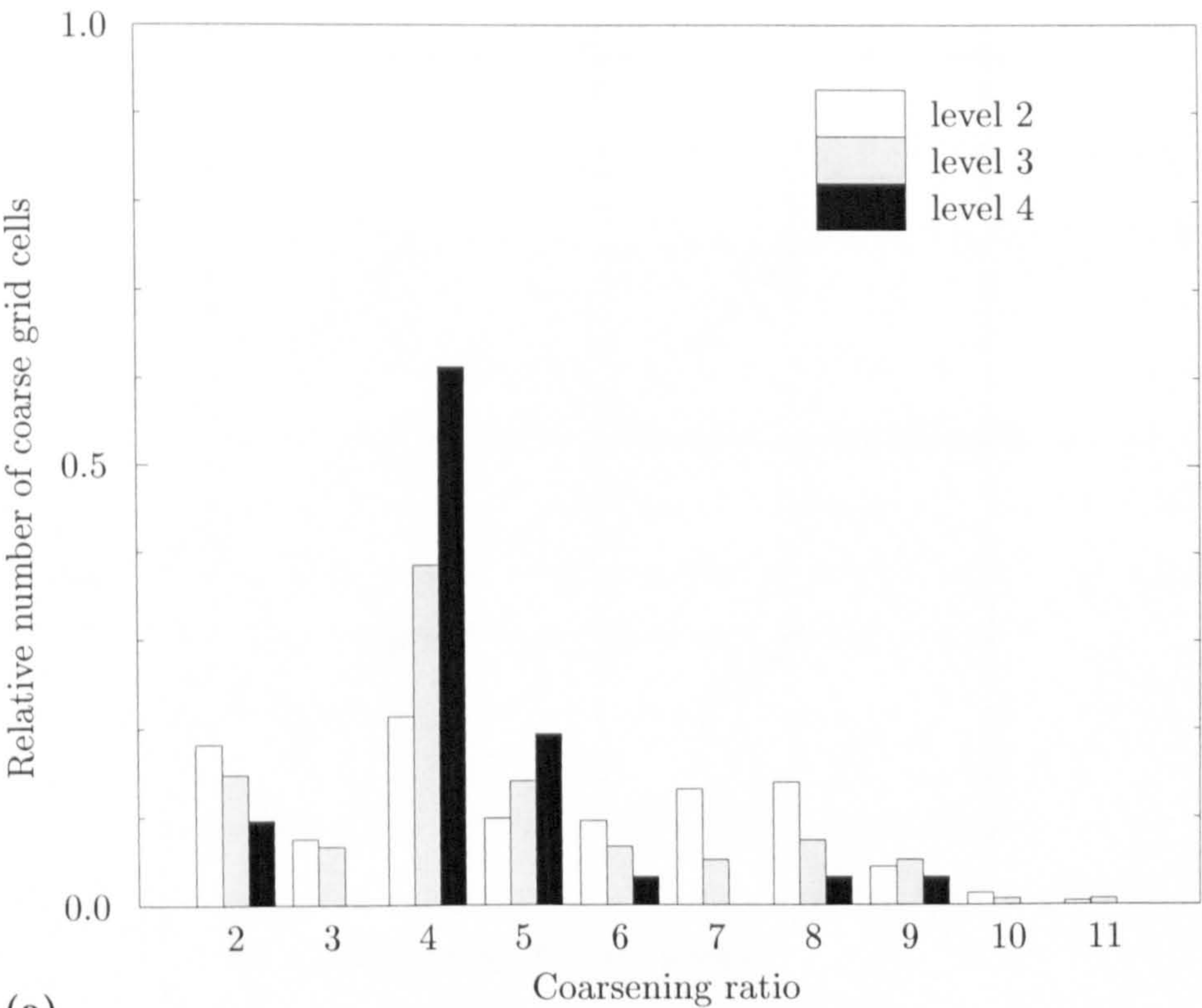


Figure 5.5: Histograms of coarsening ratio for (a) sequence of triangular grids shown in Fig. 5.3 and (b) sequence of quadrilateral grids shown in Fig. 5.4.

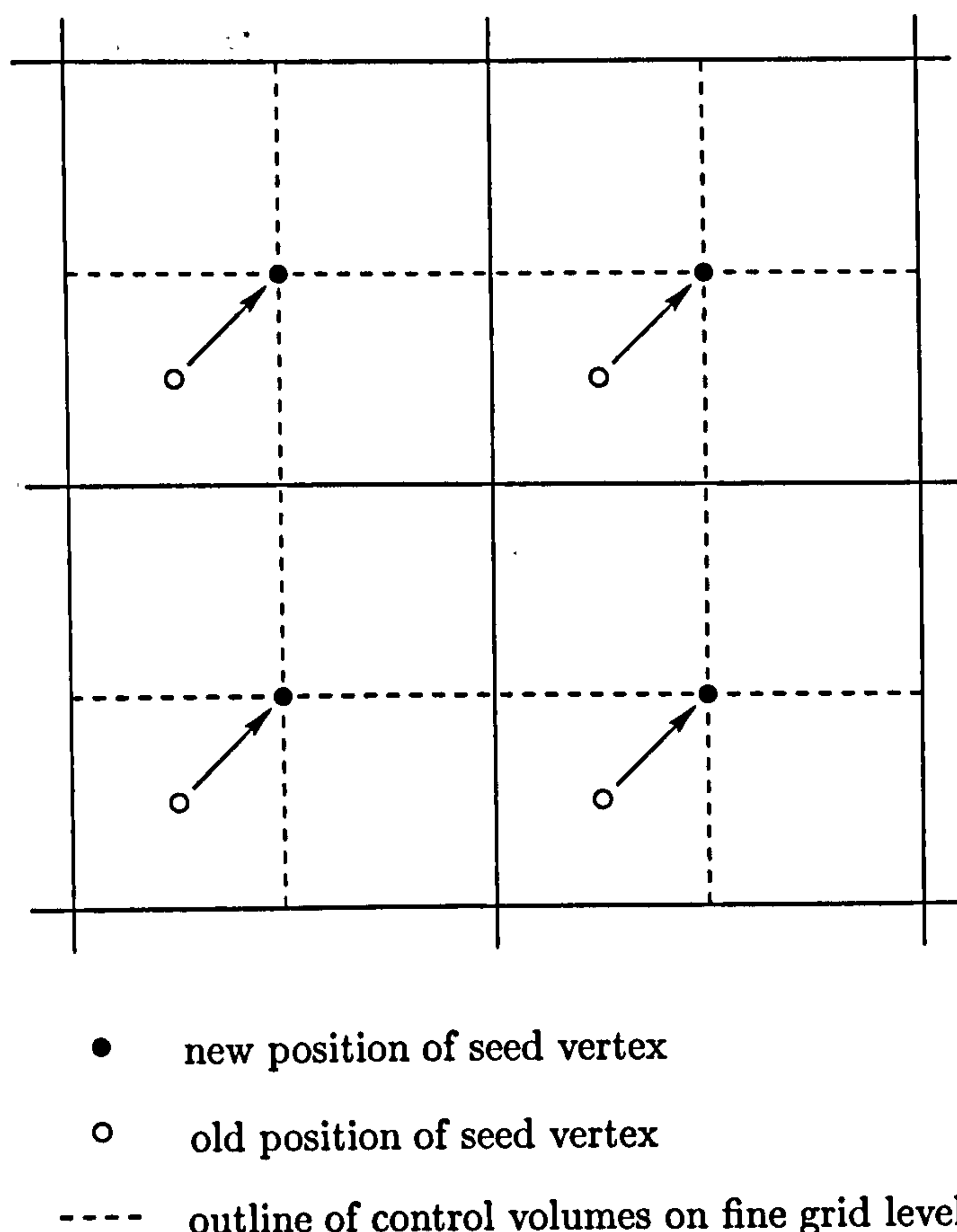


Figure 5.6: Illustration of movement of seed vertices on coarse grid levels for fine grid consisting of quadrilateral cells.

agglomeration multigrid algorithm is a new technique developed in the present work.

The idea of moving the seed vertices arose out of the decision to rediscrétise the governing equations on the coarse grid levels. By moving the seed vertices, the discretisation on the coarse grid levels is carried out on a dual grid which is more regular. This should improve both the stability and accuracy of the coarse-grid discretisation.

Problems may occur with the movement of seed vertices for coarse-grid control volumes which are strongly non-convex, since the new position of the seed vertex, as determined from Eq. (5.3.1), may lie outside the control volume. More sophisticated algorithms could be developed which move the seed vertex more carefully for non-convex control volumes, and place it at the centre of gravity for convex control volumes. The agglomeration algorithm could also be modified to prevent the formation of non-convex control volumes on coarse grid levels.

Seed vertices on boundaries are not moved.

5.4 Coarse-Grid Discretisation

The discretisation of the governing equations on the coarse grid levels proceeds in the same manner as on the finest grid. This is in contrast to previous work on the agglomeration multigrid method, where the residuals due to the viscous fluxes on the coarse grid were not obtained through rediscretisation, but through the Galerkin approach, see, e.g., Mavriplis and Venkatakrishnan [20]. Thus, the present implementation of the agglomeration multigrid approach is based on a geometric, rather than algebraic, interpretation. The motivation for investigating the rediscretisation is that it may lead to further improvements in convergence rates.

On the coarse grid levels, Eq. (3.12.1) is written as

$$\frac{dq_{0'}^H}{dt} = -\frac{1}{A_{\Omega_{0'}}} (\mathbf{R}_{0'}^H(\mathbf{q}) + \mathbf{F}_{0'}^H), \quad (5.4.1)$$

where $A_{\Omega_{0'}}$ is the area of the coarse-grid control volume and $\mathbf{F}_{0'}^H$ was defined in Eq. (5.2.11).

The computation of the residual on the coarse grid levels is carried out in much the same way as on the fine grid. In order to avoid distinguishing between the grid levels in the computer program, loops over edges are written as

```
DO ne = nedges(edge_beg(nlevel)), nedges(edge_end(nlevel))
...
ENDDO ! ne
```

where

```
edge_beg(1) = 1
edge_beg(2) = edge_end(1) + 1
...
edge_beg(N) = edge_end(N-1) + 1.
```

and

```
edge_end(1) = NO_EDGES_LEVEL_1
edge_end(2) = edge_beg(2) + NO_EDGES_LEVEL_2 - 1
...
edge_end(N) = edge_beg(N) + NO_EDGES_LEVEL_N - 1.
```

Loops over vertices are written in a similar fashion. As a result, the routines which compute the residual and update the solution are used in the same way on all grid levels.

The control-volume faces on the coarse grid levels are simplified in a manner similar to that described in Section 3.6.

5.4.1 Inviscid Fluxes

The discretisation of the inviscid fluxes is carried out in precisely the same manner as on the finest grid level.

5.4.2 Viscous Fluxes

On coarse grid levels, the viscous fluxes are approximated by the thin-shear-layer approximation given by Expressions (4.4.7a) and (4.4.7b). The first term in Eq. (4.2.30) is used to approximate the normal derivative at a control-volume face. The inclusion of the factor $1/\cos\theta_{0i}$ was found to be crucial in obtaining a stable discretisation on the coarse grids.

5.4.3 Boundary Conditions

On coarse grid levels, boundary conditions are enforced in the same manner as on the fine grid. This is in contrast to the work of Mavriplis [19] in which the boundary conditions are inferred from the fine-grid equations and the solution variables on the boundaries are not updated on the coarse-grid levels.

5.5 Cycling Strategy

The sequence in which the grid levels are visited is termed a cycling strategy. In the present work, V-, W-, and F-cycles were investigated. These cycles are illustrated in Fig. 5.7 for four grid levels.

The structural diagram of an algorithm which allows an arbitrary number of grid levels to be used with a given cycle type is shown in Fig. 5.8. The algorithm parameters which determine the cycle type are listed in Table 5.1.

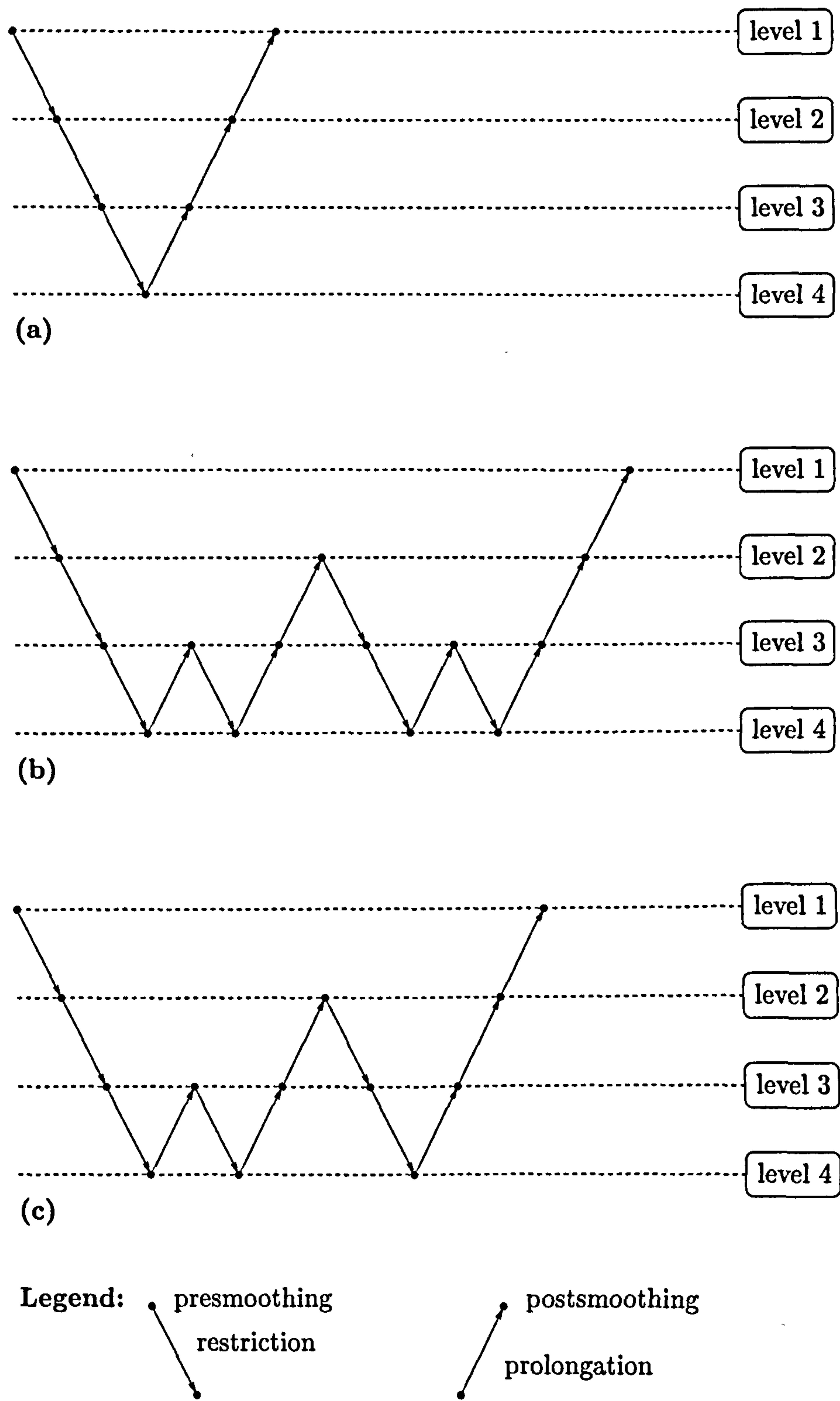


Figure 5.7: Illustration of (a) V-cycle, (b) W-cycle, and (c) F-cycle for 4 grid levels.

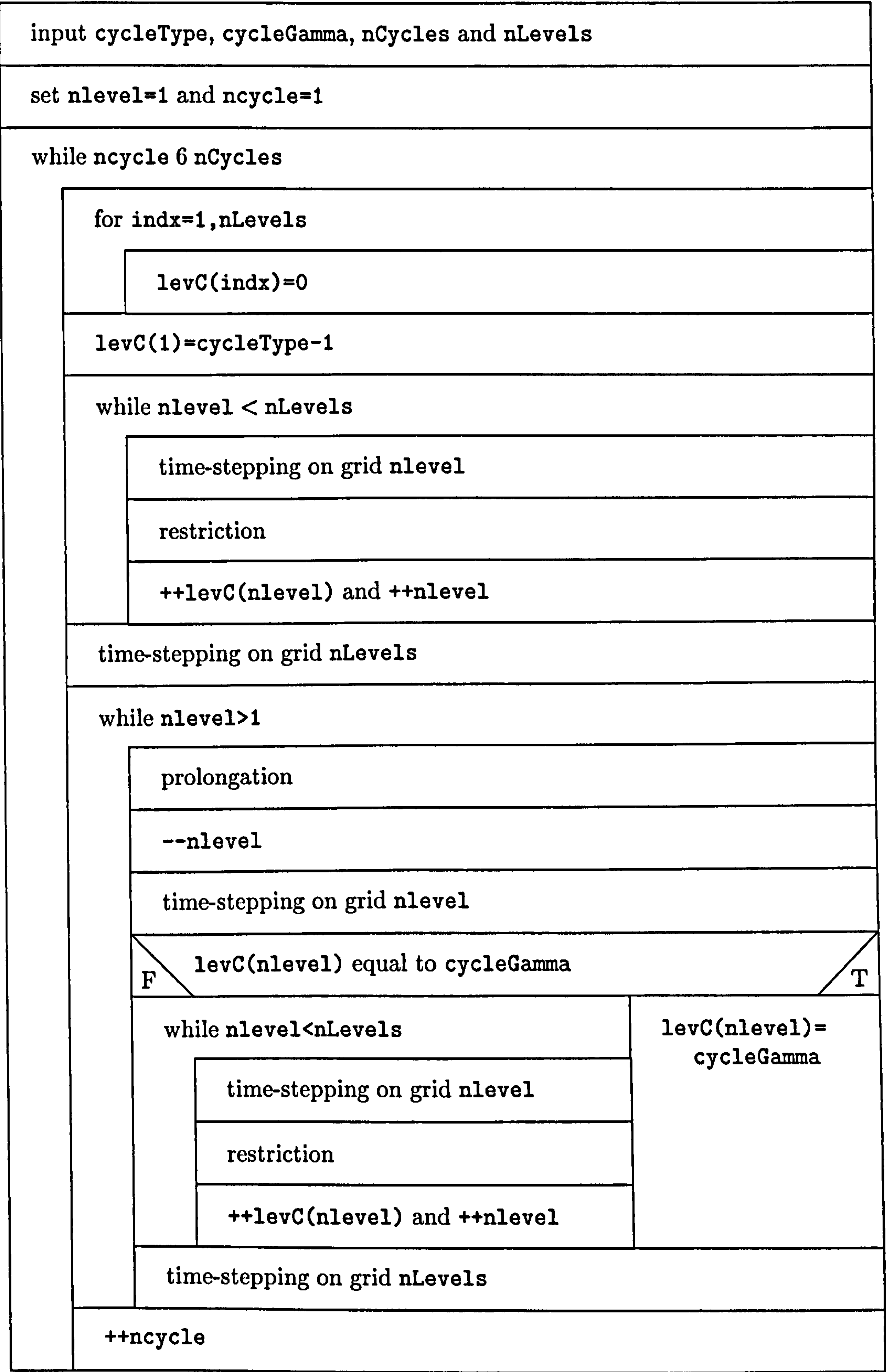


Figure 5.8: Structural diagram of cycling algorithm. See also Table 5.1. The notations ++(·) and --(·) are abbreviations for (·) ← (·) + 1 and (·) ← (·) − 1, respectively.

Table 5.1: Parameters determining the type of cycle in cycling algorithm depicted in Fig. 5.8.

Cycle	cycleType	cycleGamma
V	1	0
W	2	0
F	2	1

5.6 Intergrid-Transfer Operators

Intergrid-transfer operators interpolate information between the fine- and coarse-grid levels and vice versa. Transfer operators are usually characterised by the degree of the polynomial which is transferred exactly by the application of the transfer operator. The order of a transfer operator is defined as $m + 1$ if m is the degree of the polynomial which is transferred exactly.

In general, transfer operators cannot be chosen arbitrarily. This is because the proofs of grid-independent convergence rates for elliptic problems require that

$$m_{\mathcal{I}_h^H} + m_{\mathcal{I}_H^h} > m \quad (5.6.1)$$

where $m_{\mathcal{I}_h^H}$ and $m_{\mathcal{I}_H^h}$ represent the orders of the restriction and prolongation operators, respectively, and m is the order of the differential equation being solved, see, e.g. Hackbusch [12] and Hemker [13].

The inequality implies that intergrid-transfer operators used for the Euler equations ($m = 1$) are not suitable for the Navier-Stokes equations ($m = 2$). Numerical experiments which confirm this implication were carried out by Wesseling [28].

5.6.1 Restriction Operator

The restriction operator is defined as a simple volume-weighted average,

$$\mathcal{I}_h^H \phi_0^h = \frac{\sum_{i \in \mathcal{C}_{0'}^H} A_{\Omega_i} \phi_i^h}{\sum_{i \in \mathcal{C}_{0'}^H} A_{\Omega_i}} = \frac{1}{A_{\Omega_{0'}}} \sum_{i \in \mathcal{C}_{0'}^H} A_{\Omega_i} \phi_i^h. \quad (5.6.2)$$

The order of the restriction operator is $0 \leq m_{\mathcal{I}_h^H} \leq 1$.

5.6.2 Prolongation Operator

Two different prolongation operators were used in the present work. They correspond to piecewise-constant interpolation (injection) and piecewise-linear interpolation.

Piecewise-Constant Interpolation (Injection). The injection operator is defined by

$$\mathcal{I}_H^h \phi_{0'}^H = \phi_i^h, \quad i \in \mathcal{C}_{0'}^H, \quad (5.6.3)$$

giving an order of $m_{\mathcal{I}_H^h} = 1$. Used in conjunction with the restriction operator given by Eq. (5.6.2), this results in a multigrid method which does not satisfy Eq. (5.6.1) for the Navier-Stokes equations. This deficiency manifests itself in an inconsistency between fine- and coarse-grid equations for the diffusion terms and leads to slower convergence. An ad hoc cure for the deficiency was suggested by Mavriplis and Venkatakrishnan [20], who scaled the viscous contributions by a factor of 2^{-n} on grid level n . The scaling was originally derived by Koobus et al. [14] for the Poisson equation on the unit square.

Piecewise-Linear Interpolation. A piecewise-linear prolongation may be defined by

$$\mathcal{I}_H^h \phi_{0'}^H \equiv \phi_i^h = \phi_{0'}^H + \lambda_{0'} (\nabla \phi)_{0'}^H \cdot \Delta \mathbf{r}_{0'i}, \quad i \in \mathcal{C}_{0'}^H, \quad (5.6.4)$$

where the gradient $(\nabla \phi)_{0'}^H$ is computed from the linear least-squares reconstruction described in Subsection 3.7.2, and the values of the limiter function $\lambda_{0'}$ are computed from the Barth-Jespersen limiter function also described in Subsection 3.7.2.

The order of the piecewise-linear prolongation operator is $1 \leq m_{\mathcal{I}_H^h} \leq 2$, depending on the severity of the limiting.

Comment. Venkatakrishnan et al. [27] discussed the possibility of reconstructing a linear variation of the corrections. They argued that the use of a reconstruction would imply a triangulation, the avoidance of which is the main motivation of the agglomeration method. Their argument is correct if the reconstruction is based on an integral-based approach such as the Green-Gauss method described in Subsection 3.7.2, as used by Galle [9]. However, it should be noted that the reconstruction of gradients with the least-squares method described in Subsection 3.7.2 is not coupled in any way to the existence

of a grid. It simply requires connections between the point at which the gradients are to be reconstructed and the points which are part of the stencil. These connections can correspond to actual edges in the grid or to virtual edges. With this interpretation, the use of least-squares reconstruction becomes uncoupled from the existence of a grid and may be applied to the reconstruction of linear variations of the corrections.

Other Approaches. Guillard and Marco [10] suggested the use of a linear reconstruction operator based on a heuristic weighting with control-volume areas. Although results were given which demonstrated grid-independent convergence rates for Laplace's equation, their method was not found to perform well for the cases considered in the present work.

5.6.3 Interpolation Operator

The interpolation operator transfers residuals from fine grid levels to coarse grid levels. To ensure conservation, it is defined as a simple summation,

$$\bar{\mathcal{I}}_h^H \phi_0^h = \sum_{\mathbf{i} \in \mathcal{C}_0^H} \phi_{\mathbf{i}}^h. \quad (5.6.5)$$

5.7 Closure

The present chapter described the implementation of the agglomeration multigrid method in detail. Particular attention was given to the coarsening algorithm and the definition of intergrid transfer operators. A novel feature of the present agglomeration multigrid algorithm is that is based on rediscritisation. A new method developed in the present work is the movement of seed vertices.

References

- [1] Bakhvalov N.S., *On the Convergence of a Relaxation Method with Natural Constraints on the Elliptic Operator*, USSR Comp. Math. Math. Phys., Vol. 6, pp. 101-135, 1966
- [2] Brandt A., *Multi-Level Adaptive Solutions to Boundary-Value Problems*, Math. Comp., Vol. 31, No. 138, pp. 333-390, 1977
- [3] ———, *Multigrid Techniques: 1984 Guide with Applications to Fluid Dynamics*, GMD-Studien No. 85, Gesellschaft für Mathematik und Datenverarbeitung MBH, Bonn, Germany, May 1984

- [4] ———, *Barriers to Achieving Textbook Multigrid Efficiency (TME) in CFD*, NASA CR-1998-207647, April 1998
- [5] Briggs W.L., *A Multigrid Tutorial*, SIAM, Philadelphia, 1987
- [6] Fedorenko R.P., *The Speed of Convergence of One Iterative Process*, USSR Comp. Math. Math. Phys., Vol. 4, pp. 227-235, 1964
- [7] Jameson A., *Solution of the Euler Equations for Two-Dimensional Flow by a Multigrid Method*, Appl. Math. Comp., Vol. 13, No. 3 & 4, pp. 327-355, November 1983
- [8] Jespersen D.C., *Design and Implementation of a Multigrid Code for the Euler Equations*, Appl. Math. Comp., Vol. 13, No. 3 & 4, pp. 357-374, November 1983
- [9] Galle M., *Ein Verfahren zur numerischen Simulation kompressibler, reibungsbehafteter Strömungen auf hybriden Netzen*, DLR Forschungsbericht 99-04, DLR Braunschweig, Januar 1999
- [10] Guillard H. and Marco N., *Some Aspects of Multigrid on Non-Structured Meshes*, in: *Seventh Copper Mountain Conference on Multigrid Methods*, Melson N.D. et al. (Eds.), NASA CP 3339, pp. 347-362, September 1996
- [11] Hackbusch W., *On the Multi-Grid Method Applied to Difference Equations*, Computing, Vol. 20, pp. 291-306, 1978
- [12] ———, *Multi-Grid Methods and Applications*, Series in Computational Mathematics, Vol. 4, Springer, 1985
- [13] Hemker P.W., *On the Orders of Prolongations and Restrictions in Multigrid Procedures*, J. Comp. Appl. Math., Vol. 32, pp. 423-429, 1990
- [14] Koobus B., Lallemand M.-H., and Dervieux A., *Unstructured Volume-Agglomeration Multigrid: Solution of the Poisson Equation*, Comp. Fl., Vol. 18, pp. 27-42, 1994
- [15] Lallemand M.-H., *Schémas décentrées multigrilles pour la résolution des équations d'Euler en éléments finis*, Ph.D. Thesis, L'université de Provence, March 1988
- [16] Lassaline J.V. and Zingg D.W., *Development of an Agglomeration Multigrid Method with Directional Coarsening*, AIAA Paper 99-3338, 14th Computational Fluid Dynamics Conference, Norfolk, VA, June/July 1999
- [17] Lötstedt P., *Grid-Independent Convergence of the Multigrid Method for First-Order Equations*, SIAM J. Numer. Anal., Vol. 29, No. 5, pp. 1370-1394, October 1992
- [18] Mavriplis D.J., *Directional Agglomeration Multigrid Techniques for High Reynolds Number Viscous Flow Solvers*, AIAA Paper 98-0612, 36th Aerospace Sciences Meeting and Exhibit, Reno, NV, January 1998
- [19] ———, private communication, February 23, 1998
- [20] Mavriplis D.J. and Venkatakrishnan V., *Agglomeration Multigrid for Viscous Turbulent Flows*, ICASE Report 94-62, July 1994
- [21] ———, *A Unified Multigrid Solver for the Navier-Stokes Equations on Mixed Element Meshes*, ICASE Report No. 95-53, July 1995. Also: Int. J. Comp. Fl. Dyn., Vol. 8, No. 4, pp. 247-263, August 1997
- [22] Ni R.-H., *A Multiple-Grid Scheme for Solving the Euler Equations*, AIAA J., Vol. 20, No. 11, pp. 1565-1571, 1982

- [23] Pierce N.A., *Preconditioned Multigrid Methods for Compressible Flow Calculations on Stretched Meshes*, Ph.D. Thesis, Oxford University, August 1997
- [24] Roache P.J., *Need for Control of Numerical Accuracy*, J. Spacecraft, Vol. 27, No. 2, pp. 98-102, March/April 1990
- [25] ———, *Perspective: A Method for Uniform Reporting of Grid Refinement Studies*, J. Fluids Eng., Vol. 116, pp. 405-413, September 1994
- [26] ———, *Quantification of Uncertainty in Computational Fluid Dynamics*, Ann. Rev. Fl. Mech., Vol. 29, pp. 123-160, 1997
- [27] Venkatakrishnan V., Mavriplis D.J., and Berger M.J., *Unstructured Multigrid through Agglomeration*, in: *Sixth Copper Mountain Conference on Multigrid Methods*, Melson N.D. et al. (Eds.), NASA CP 3224, pp. 649-662, November 1993
- [28] Wesseling P., *Linear Multigrid Methods*, in: *Multigrid Methods*, McCormick S.F. (Ed.), SIAM, pp. 31-55, 1987
- [29] ———, *Multigrid Methods in Computational Fluid Dynamics*, Z. Angew. Math. Mech., Vol. 70, No. 5, pp. T337-T347, 1990
- [30] ———, *Introduction to Multigrid Methods*, Wiley, 1993

PART III

VALIDATION AND

APPLICATION OF METHOD

Chapter 6

Validation of Method for Inviscid Flows

The numerical method is validated for inviscid flows on both triangular and quadrilateral grids by applying it to three test cases. The first test case involves the flow generated by a supersonic free vortex. A grid refinement study is used to infer the order of accuracy of the solution method. The second test case deals with subsonic, transonic, and supersonic flows over a circular-arc bump in a straight-walled channel. The third test case considers the subsonic and transonic flows over the NACA 0012 aerofoil.

6.1 Introduction

The accurate simulation of inviscid flows is an essential requirement for any solution method aimed at viscous flows. It is important to ensure that the numerical dissipation introduced in the discretisation of the inviscid fluxes is in some sense low such that shear layers can be computed accurately. Since the discretisations of the inviscid and viscous fluxes are carried out separately, it is convenient to validate the discretisation of the inviscid fluxes before the solution method is extended to include the viscous fluxes. The validation typically involves an assessment of the shock-capturing capabilities of the solution method.

These issues are investigated in general terms by applying the solution method described in Chapter 3 to three test cases. The test cases include the supersonic flow generated by a free vortex, the flow over a circular-arc bump in a straight-walled channel and the flow over a NACA 0012 aerofoil. Specific issues are investigated for each test case also.

It is noted that contour lines are not directly labelled in the figures; instead, the

values of the initial and final levels and the number of levels are listed in the figure caption.

6.2 Supersonic Free Vortex

The flow generated by a free vortex models the isentropic flow of a compressible fluid between two concentric circles where the velocity magnitude varies inversely with the radius. The supersonic free vortex was previously used as a test case by Aftosmis et al. [1], Luo et al. [4], Coirier and Jorgenson [2], and Ollivier-Gooch [7]. Aftosmis et al., Luo et al., and Ollivier-Gooch used cells of the dual grid as control volumes whereas Coirier and Jorgenson employed cells of the primal grid as control volumes.

The supersonic free vortex flow is particularly useful because the existence of an analytical solution allows an assessment of the numerical errors. Since the flow is shock-free, the results are not affected by limiter functions and may be expected to indicate the accuracy of the solution method in regions of smooth flow.

6.2.1 Analytical Solution

The analytical solution may be derived from the condition that the velocity magnitude V varies inversely with the radius r ,

$$Vr = \text{constant}, \quad (6.2.1)$$

from the momentum equation in the radial direction,

$$\frac{\partial p}{\partial r} = \frac{\rho V^2}{r}, \quad (6.2.2)$$

and from the condition of isentropic flow,

$$\left(\frac{p}{\rho_t}\right) = \left(\frac{\rho}{\rho_t}\right)^\gamma = \text{constant}. \quad (6.2.3)$$

Using Eqs. (6.2.1) and (6.2.3), Eq. (6.2.2) can be integrated to give an expression for the density,

$$\frac{\rho}{\rho_i} = \left\{ 1 + \frac{\gamma-1}{2} M_i^2 \left[1 - \left(\frac{r_i}{r}\right)^2 \right] \right\}^{\frac{1}{\gamma-1}}, \quad (6.2.4)$$

where the subscript 'i' denotes values at the inner radius. The solution domain and boundary conditions are shown in Fig. 6.1.

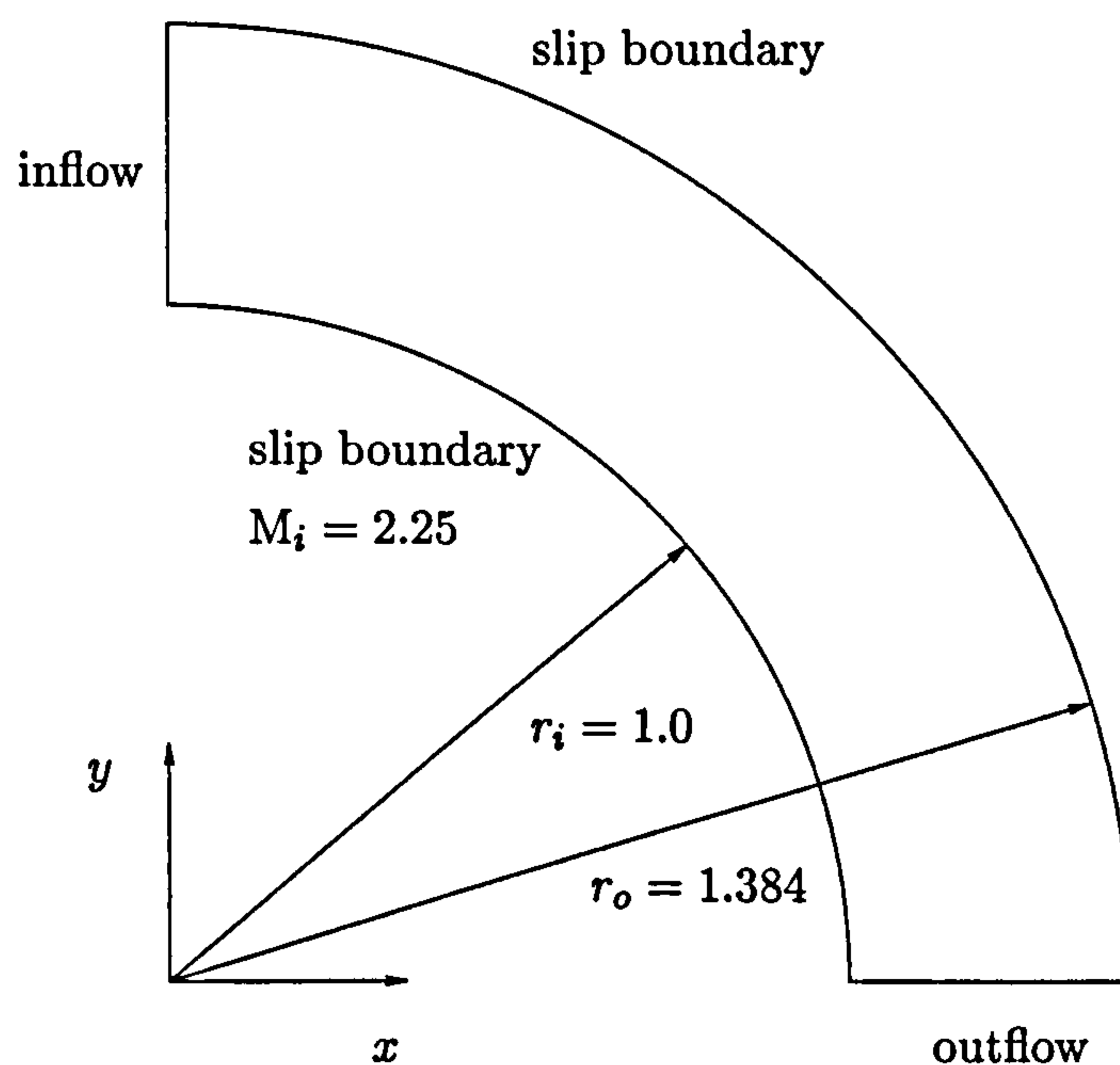


Figure 6.1: Solution domain and boundary conditions for supersonic free vortex flow.

6.2.2 Grid-Refinement Study

Since numerical errors can be calculated, the order of accuracy of the solution method can be inferred from a grid-refinement study. The procedure is as follows.

On a given grid, the distribution of density errors is calculated from Eq. (6.2.4). The norm of the density errors is computed from

$$E_p = \left(\frac{1}{N} \sum_{k=1}^N \left| \frac{\rho - \rho_k}{\rho_k} \right|^p \right)^{\frac{1}{p}} \quad \text{for } p = 1, 2, \infty \quad (6.2.5)$$

where N is the number of vertices in a given grid. The order of the solution method is then inferred in the following way: The logarithms of the norms of the density errors are plotted against the logarithms of a measure of the grid spacings. The order of the solution method is then given by the slope of the linear least-squares curve fit through the data points in the plot.

Five different grid types are used in the grid-refinement study. They consist of one quadrilateral grid and four triangular grids. Since the triangular grids were generated by subdivision of the quadrilateral grid, they contain the same number of vertices and hence unknowns. The four triangular grids differ from each other in the way in which the quadrilateral grid was subdivided. The motivation for using these grids is to investigate

the influence of the orientation of the additional edges.

For each grid type, three telescoping grid levels of 41×11 , 81×21 , and 161×41 vertices are constructed. The point distributions differ slightly from the grids used by Aftosmis et al., Luo et al., and Ollivier-Gooch. In the present work, the grids were generated such that the grid spacings in the radial and circumferential directions are approximately equal at the point $(x, y) = (r_i, 0)$.

The coarsest level of each grid type is shown in Fig. 6.2. The associated dual grids are also shown in order to illustrate how the shape of the median dual is influenced by the orientation of the edges.

The goals of the grid-refinement study are

1. to assess the relative accuracy of the solution method on triangular and quadrilateral grids, and
2. to compare the Green-Gauss and least-squares reconstruction methods.

Results for First-Order Scheme. The behaviour of the norms of the density error with grid refinement and the resulting orders of accuracy are shown in Fig. 6.3. In all norms, the error level is highest for the quadrilateral grids. The error levels for the triangular grids are lower than for the quadrilateral grids. The computed values of the order of accuracy are in the range of $0.94 - 1.15$. The lowest values for the order of accuracy are obtained on the triangular grid with irregular orientation of the diagonals. Aftosmis et al. noted a drop in accuracy for grid type 3 compared to the quadrilateral grid, which is not observed in the present results. A possible explanation for this difference is that the present grids contain a larger number of grid points in the radial direction compared to the circumferential direction than the grids employed by Aftosmis et al., leading to less highly stretched triangular grid cells. Increased stretching leads to a larger angle between the edges and their associated dual edges, a feature which was identified by Aftosmis et al. as a key source of errors.

Results for Second-Order Schemes. The results for Green-Gauss reconstruction are shown in Fig. 6.4. In contrast to the first-order accurate results discussed above, the error levels on the quadrilateral grids are not higher than those obtained on triangular

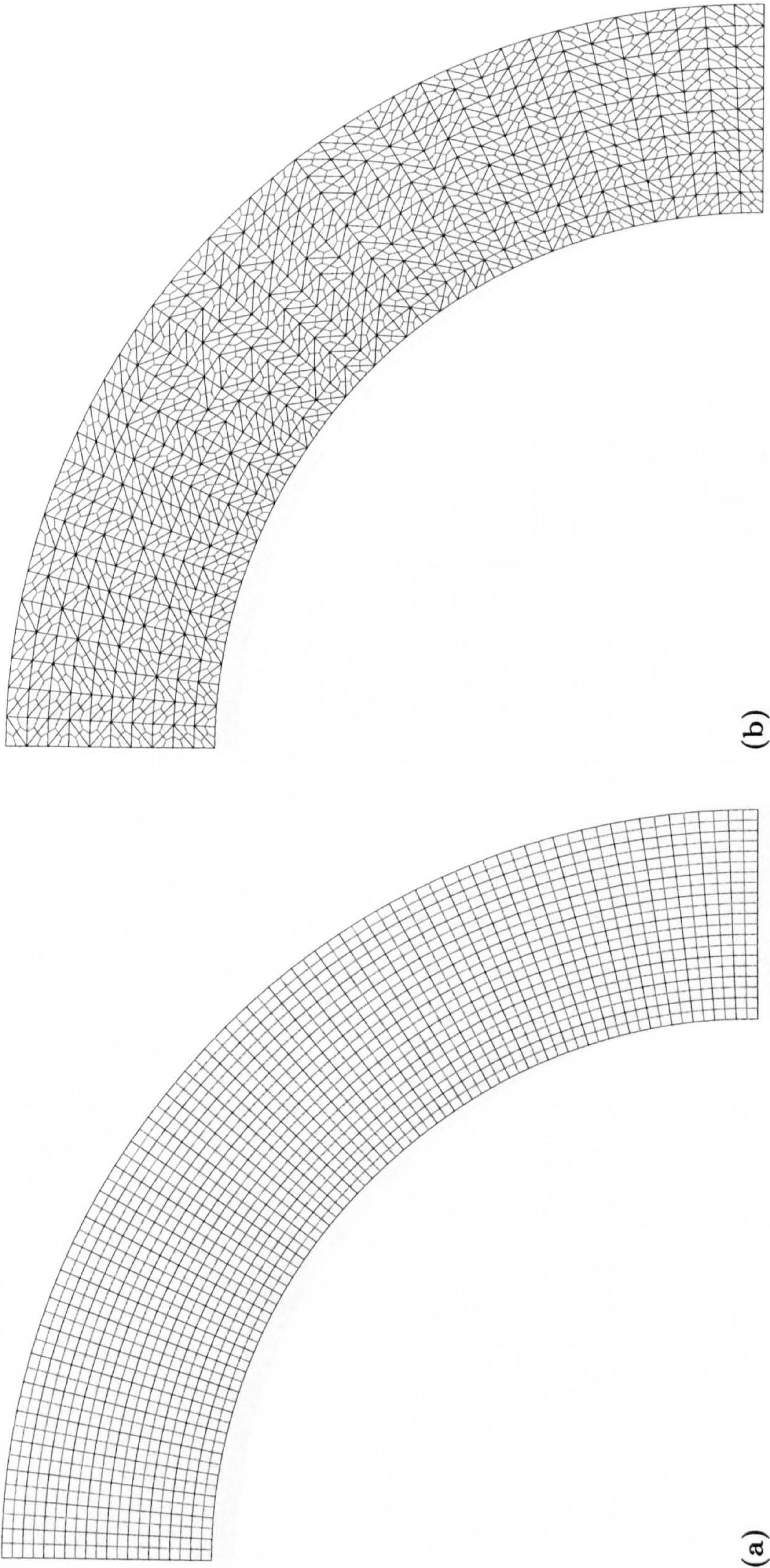


Figure 6.2: 41×11 grids and associated dual grids for (a) quadrilateral grid (symbol \square) in Figs. 6.3-6.5) (b) ‘type 1’ triangular grid (symbol \triangle).

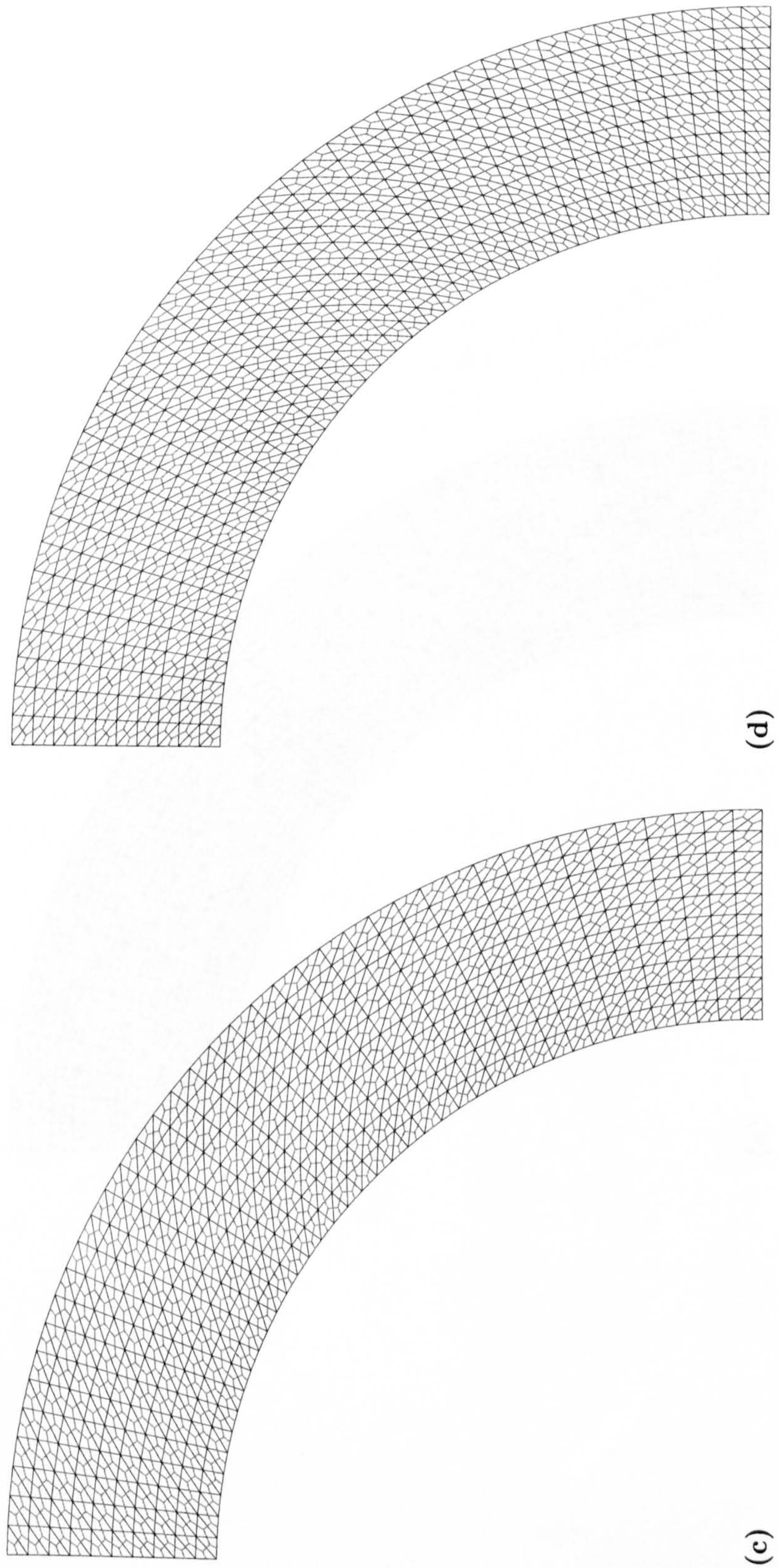


Figure 6.2 (continued): (c) ‘type 2’ triangular grid (symbol C) (d) ‘type 3’ triangular grid (symbol ∇).

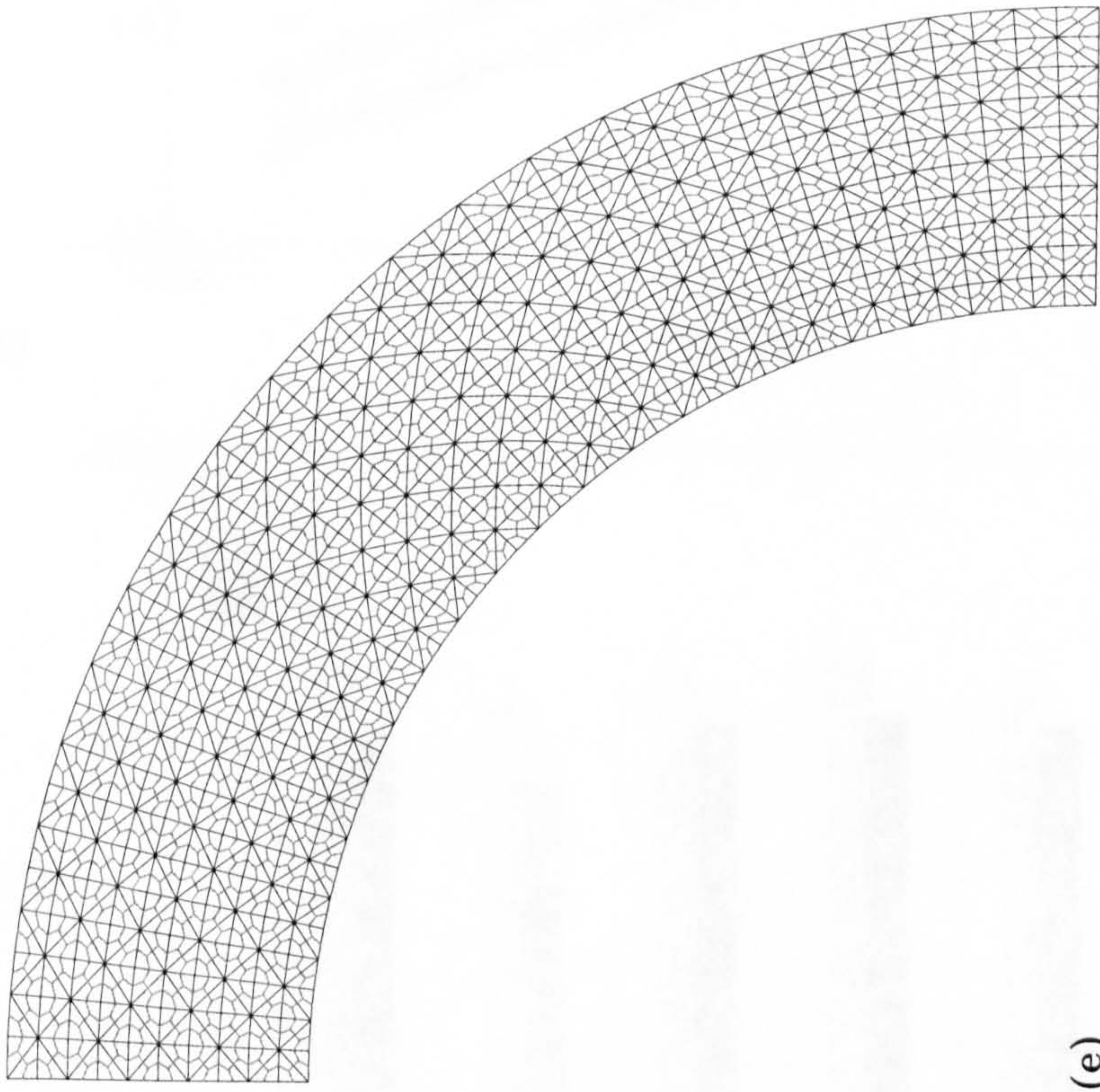


Figure 6.2 (continued): (e) ‘type 4’ triangular grid (symbol B).

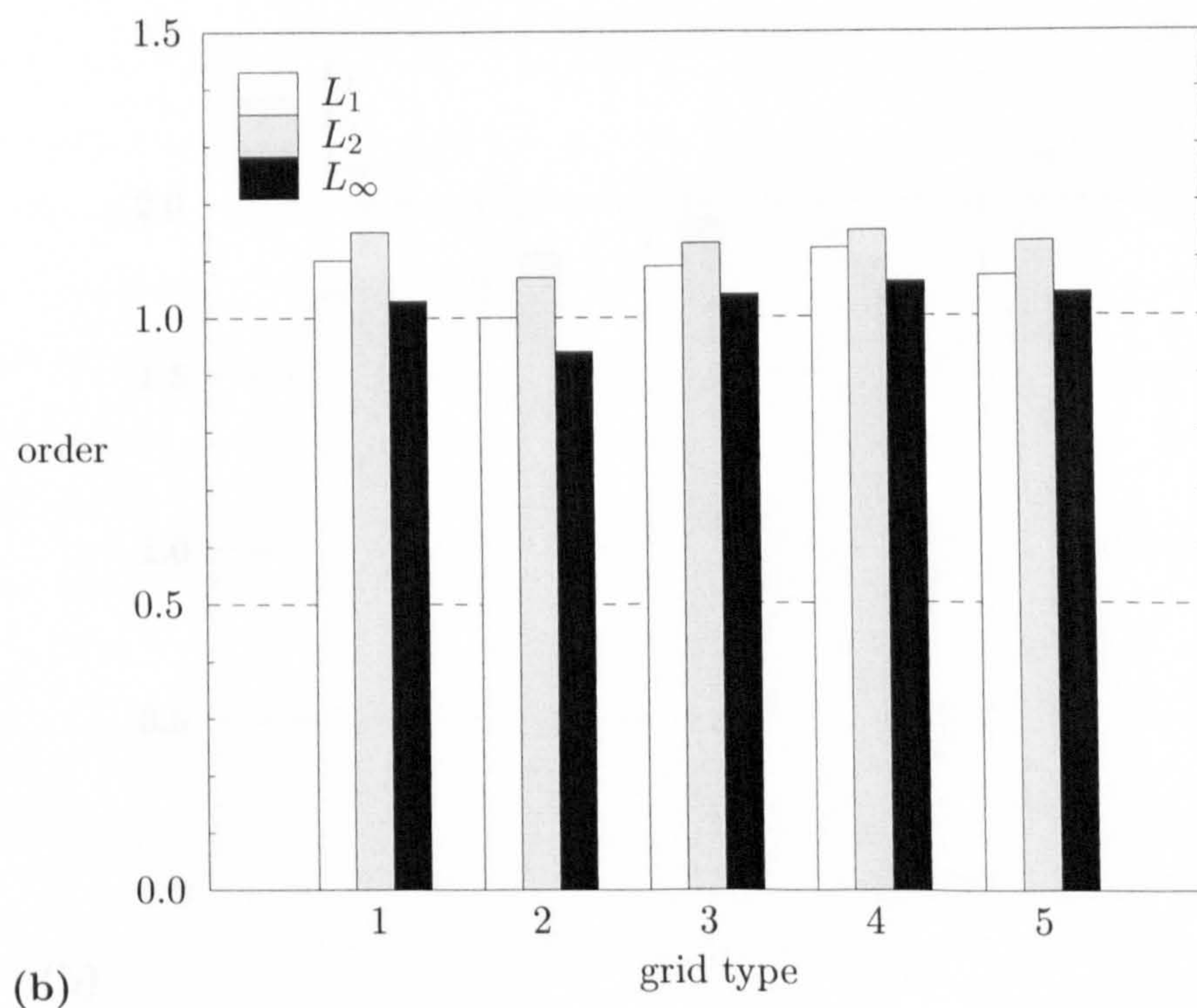
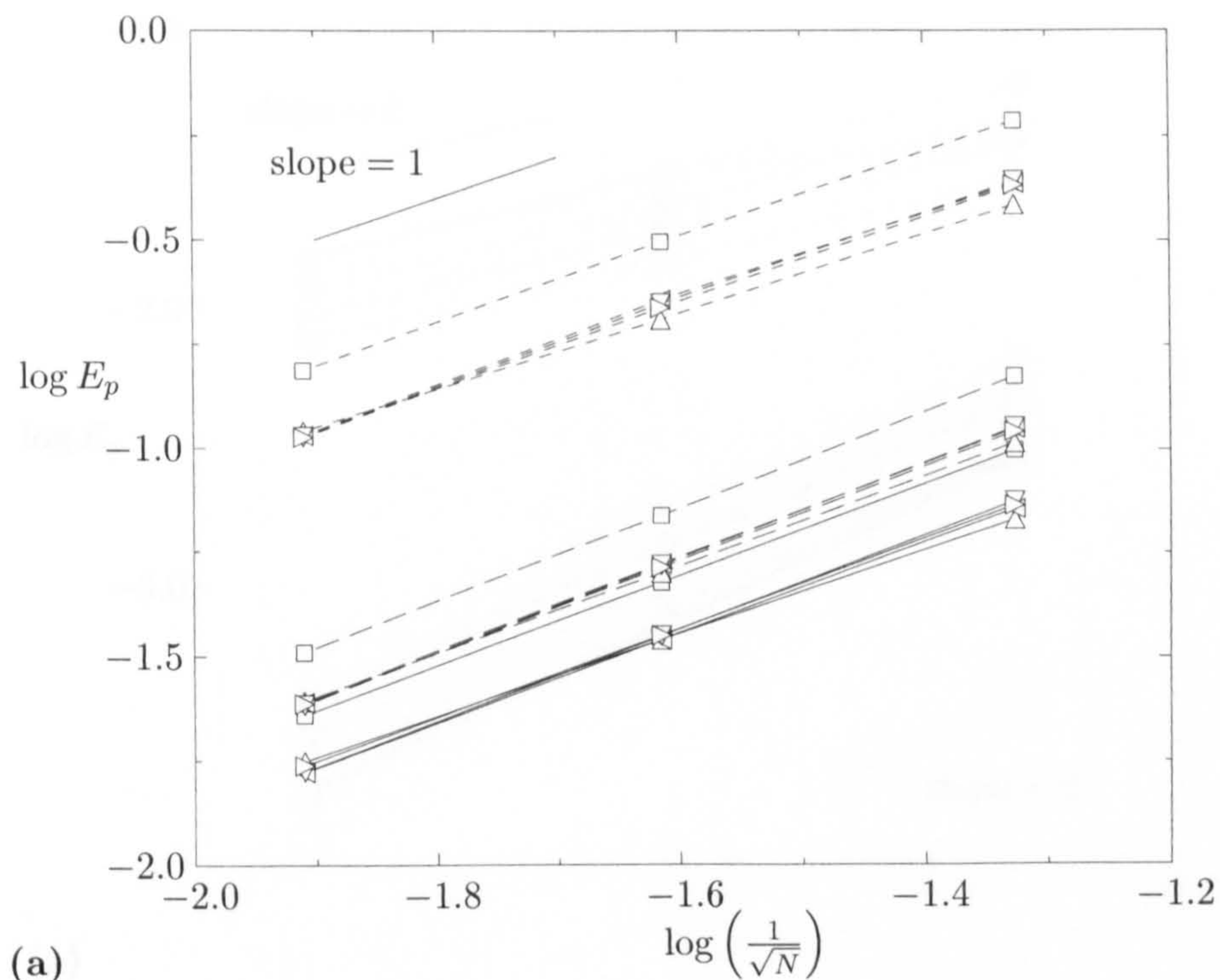


Figure 6.3: Results for first-order scheme for free-vortex flow. (a) Behaviour of norms of density error with grid refinement and (b) computed orders of accuracy. — L_1 -norm, — — — L_2 -norm, - - - - L_∞ -norm; \square quadrilateral grid, \triangle triangular grid type 1, C grid type 2, ∇ grid type 3, B grid type 4.

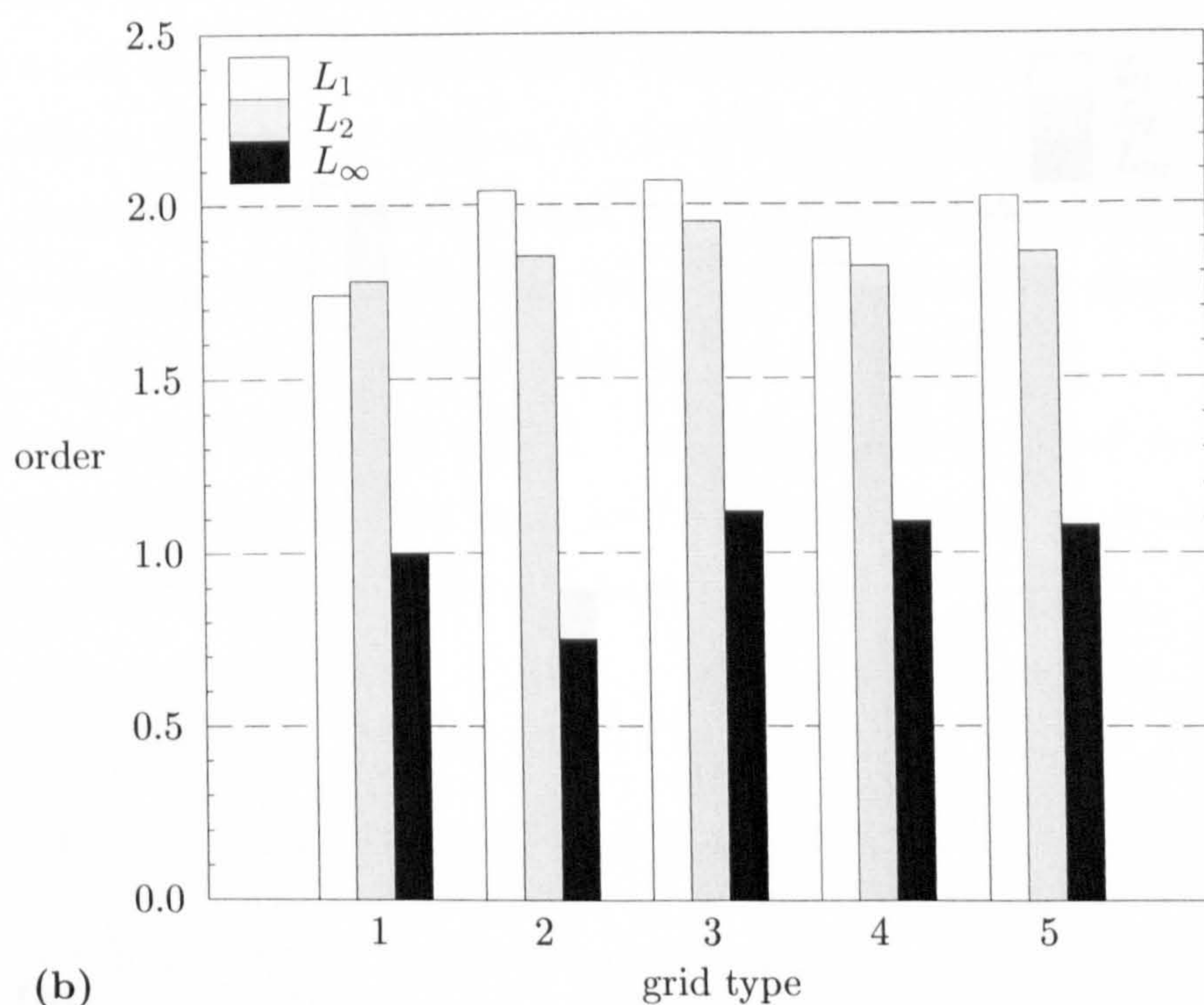
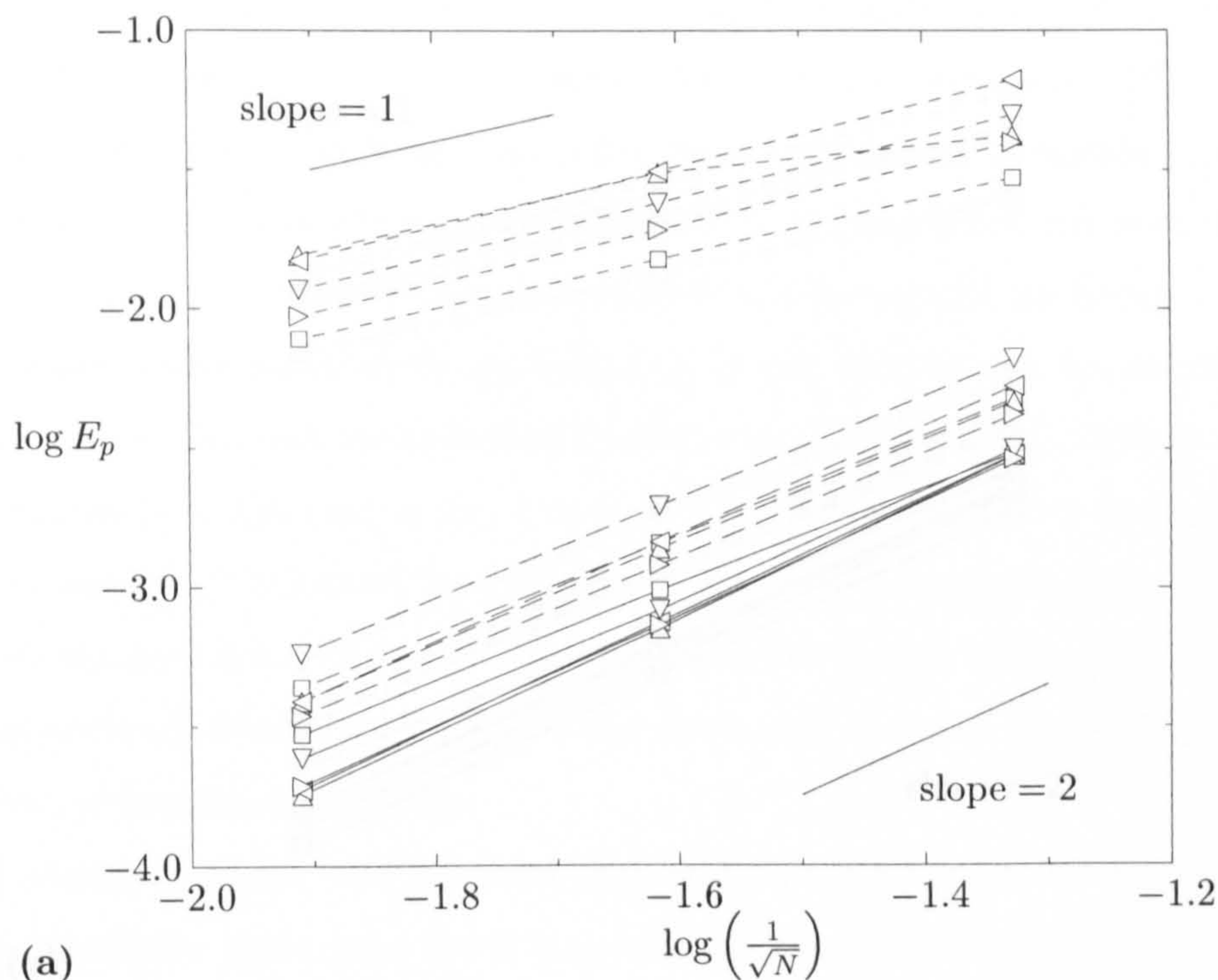
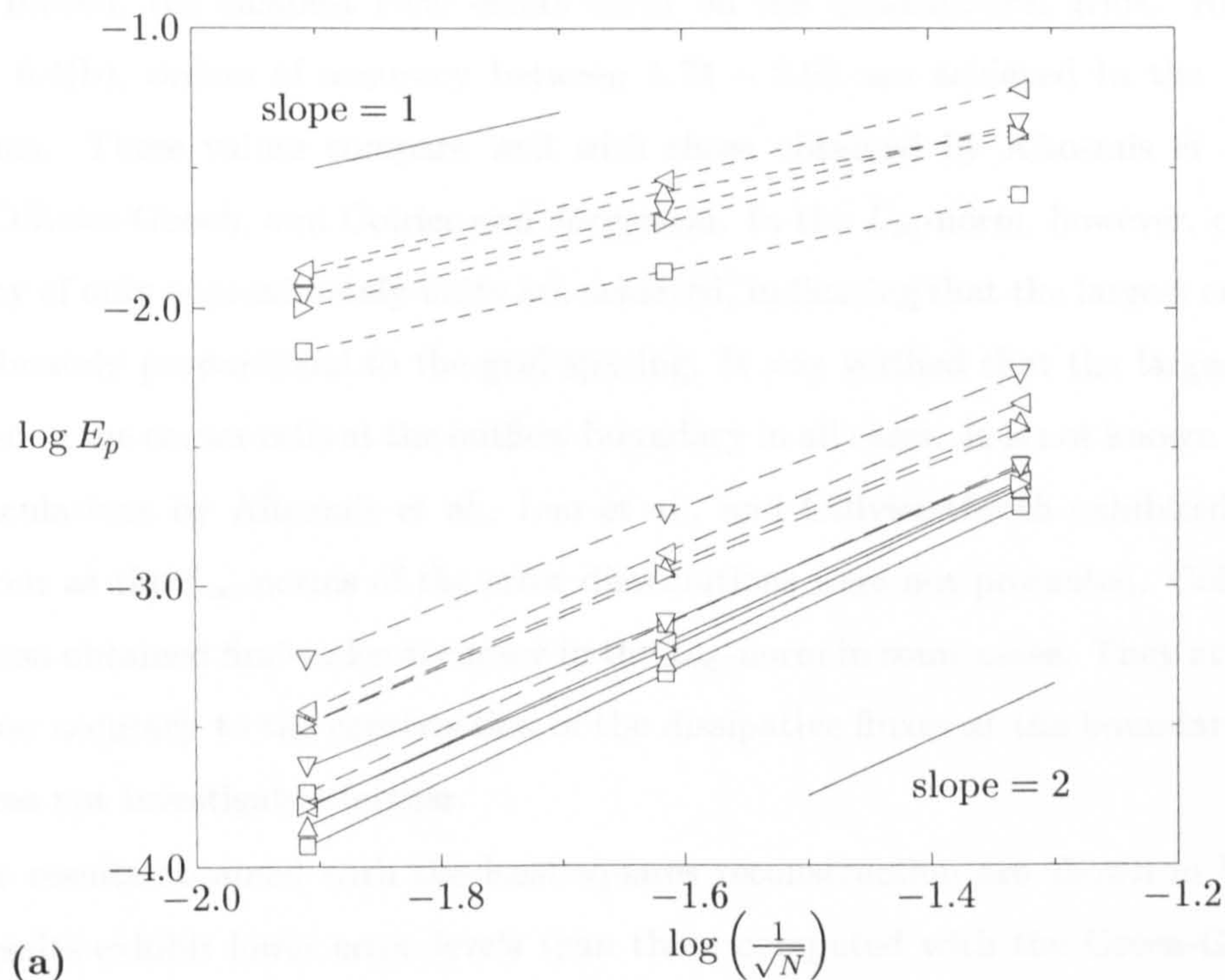
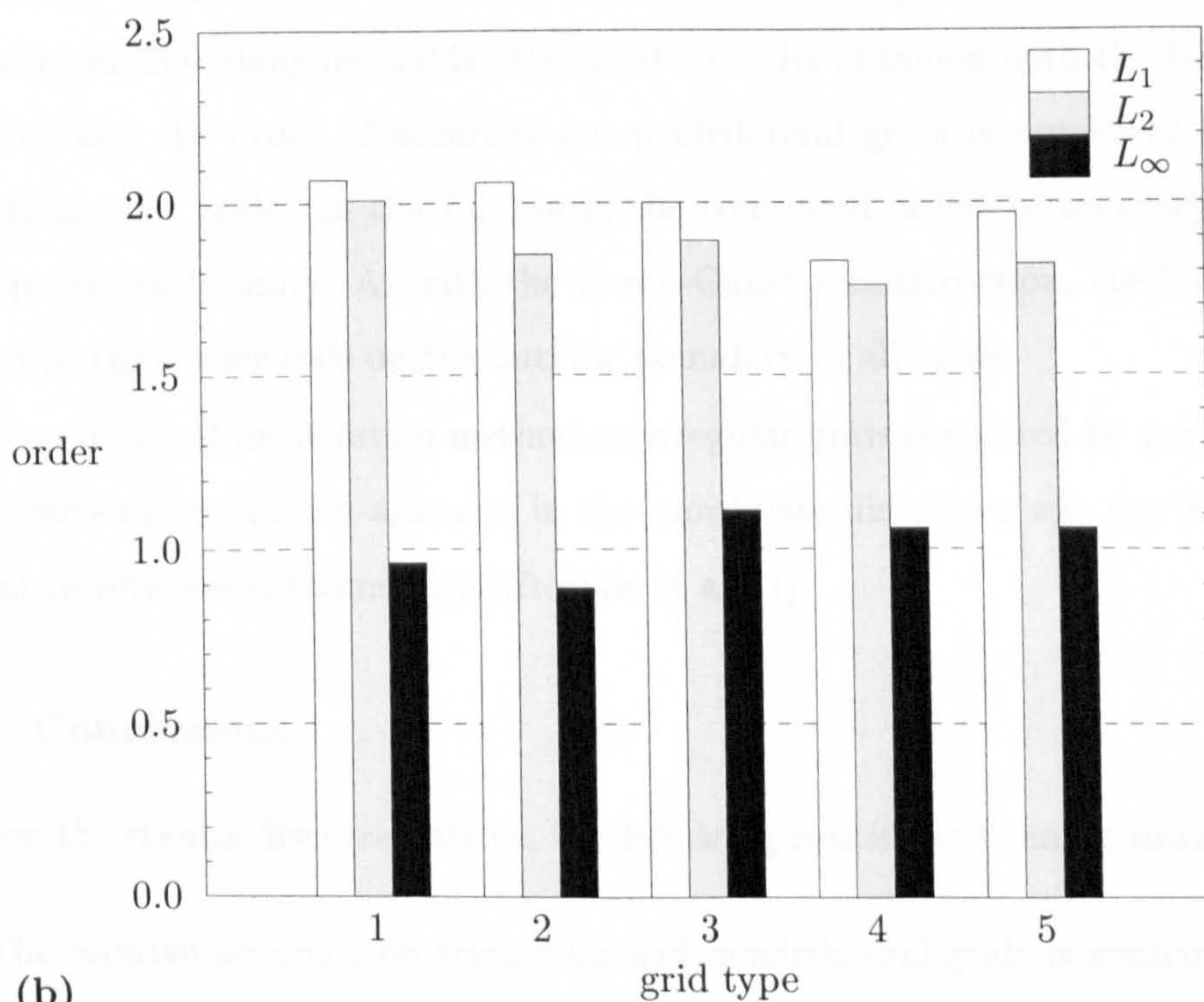


Figure 6.4: Results for second-order scheme with Green-Gauss reconstruction for free-vortex flow. (a) Behaviour of norms of density error with grid refinement and (b) computed orders of accuracy. — L_1 -norm, — — — L_2 -norm, - - - - L_∞ -norm; \square quadrilateral grid, \triangle triangular grid type 1, C grid type 2, ∇ grid type 3, B grid type 4.



(a)



(b)

Figure 6.5: Results for second-order scheme with least-squares reconstruction for free-vortex flow. (a) Behaviour of norms of density error with grid refinement and (b) computed orders of accuracy. — L_1 -norm, — — — L_2 -norm, - - - - L_∞ -norm; \square quadrilateral grid, \triangle triangular grid type 1, C grid type 2, ∇ grid type 3, B grid type 4.

grids. Indeed, the smallest local errors occur on the quadrilateral grids. As shown in Fig. 6.4(b), orders of accuracy between 1.74 – 2.07 are achieved in the L_1 - and L_2 -norms. These values compare well with those obtained by Aftosmis et al., Luo et al., Ollivier-Gooch, and Coirier and Jorgenson. In the L_∞ -norm, however, orders of accuracy of only approximately unity are achieved, indicating that the largest errors are approximately proportional to the grid spacing. It was verified that the largest errors occurred in the corner cells at the outflow boundary in all cases. It is not known whether the calculations by Aftosmis et al., Luo et al., and Ollivier-Gooch exhibited similar behaviour as the L_∞ -norms of the error distributions were not presented. Coirier and Jorgenson obtained first-order accuracy in the L_∞ -norm in some cases. They attributed the lower accuracy to the construction of the dissipative fluxes at the boundaries. The issue was not investigated further.

The results obtained with the least-squares reconstruction are shown in Fig. 6.5. The results exhibit lower error levels than those computed with the Green-Gauss reconstruction. The errors obtained on the quadrilateral grids are lower in all norms than those on the triangular grids. Unlike the results obtained with the Green-Gauss reconstruction, the order of accuracy on quadrilateral grids is not lower than those on the triangular grids. In the L_∞ -norm, the computed orders of accuracy are again only approximately unity. As with the Green-Gauss reconstruction, the largest errors occurred in the corner cells on the outflow boundary in all cases.

The accuracy of the solution method on irregular grids generated by perturbing the interior vertices by random amounts in the coordinate directions was not investigated. Relevant results were obtained by Aftosmis et al. [1].

6.2.3 Conclusions

Based on the results discussed above, the following conclusions can be drawn:

1. The relative accuracy on triangular and quadrilateral grids is similar. As previously shown by Aftosmis et al. [1], the larger number of edges in the triangular grids does not result in higher accuracy.
2. The Green-Gauss reconstruction resulted in larger errors on all grids and lower orders of accuracy for quadrilateral grids than least-squares reconstruction.

Based on Conclusion 2, the Green-Gauss method is not considered further for the reconstruction of gradients used in the second-order accurate inviscid fluxes.

6.3 Bump in Channel

The test case involving the inviscid flow over a circular-arc bump in a straight-walled channel was first suggested by Ni [5]. The geometry and boundary conditions are depicted in Fig. 6.6, where h represents the height of the bump as a fraction of its chord. Depending on the boundary conditions, subsonic, transonic, and supersonic flows may be generated, allowing the investigation of several aspects of the solution method.

Calculations were carried out in order

1. to compare the solution quality on triangular and quadrilateral grids,
2. to compare the solution quality on quadrilateral grids with that on triangular grids obtained by inserting diagonal edges into the quadrilateral grids, and
3. to assess the performance of the multigrid scheme for inviscid flows on the triangular and quadrilateral grids considered under 1.

Solutions are compared using contour plots of pressure and line plots of the pressure coefficients on the lower and upper walls of the channel. The pressure coefficient is

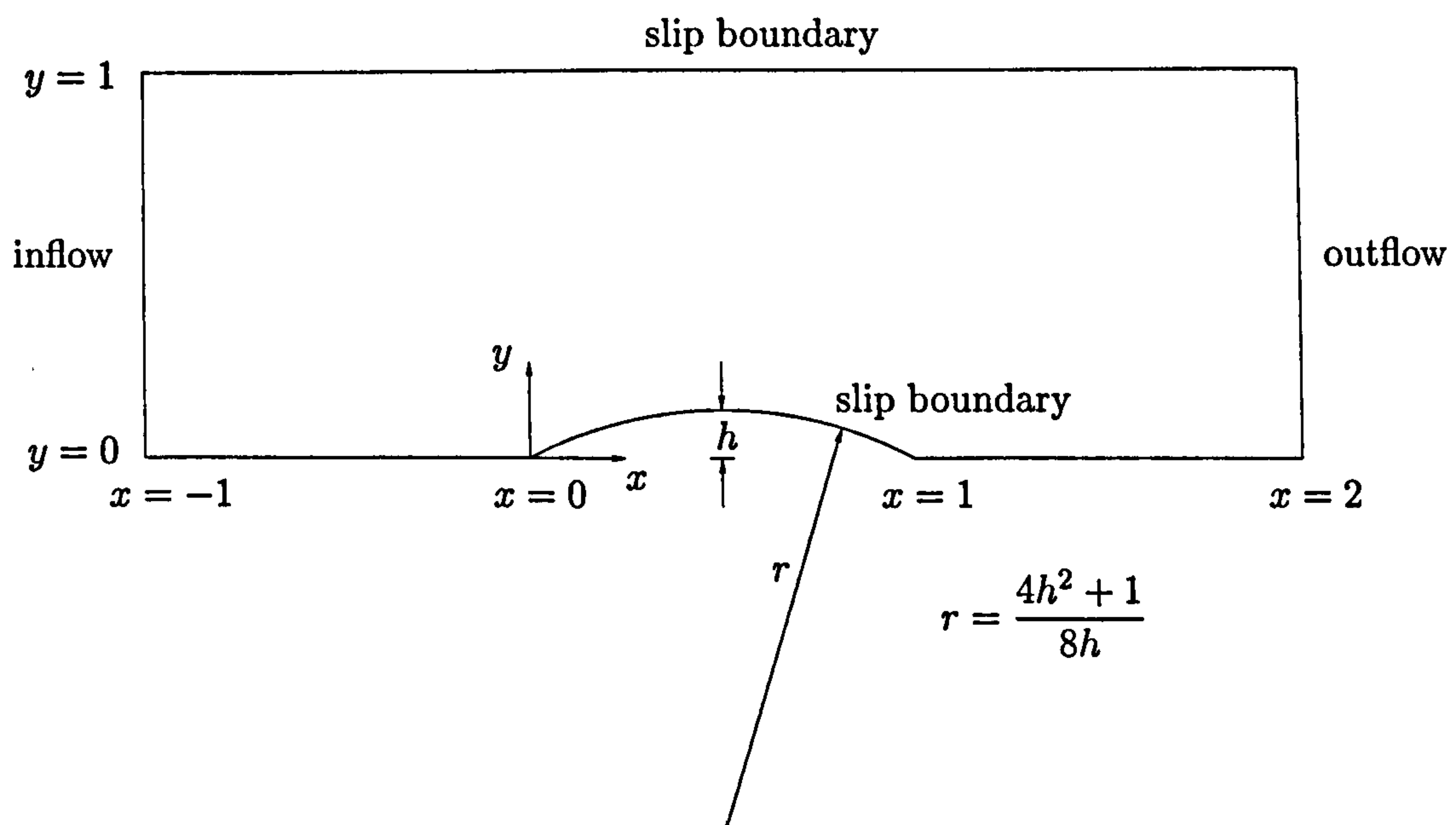


Figure 6.6: Solution domain and boundary conditions for flow over bump in channel.

defined as

$$C_p = \frac{2}{\gamma M_0^2} \left(\frac{p}{p_0} - 1 \right) \quad (6.3.1)$$

where the subscript '0' denotes quantities at the inlet boundary. The solution quality is assessed using the entropy parameter Σ defined as

$$\Sigma = \frac{p}{p_0} \left(\frac{\rho_0}{\rho} \right)^\gamma - 1 \quad (6.3.2)$$

which is identically zero for isentropic flow. The entropy parameter is positive for an increase in entropy. The only physical mechanism for the production of entropy in an inviscid flow is a shock wave. Deviations from $\Sigma = 0$ away from a shock wave are entirely numerical and have no physical counterpart.

The performance of the multigrid scheme is assessed through the number of iterations required to reach a convergence measure of the continuity residual of 10^{-8} . Since the convergence measure of the residuals of the continuity equation was usually $O(10^{-3} - 10^{-4})$, this corresponds to a reduction of roughly 4 – 5 orders of magnitude. An average convergence rate (ACR) is then computed from

$$\text{ACR} = \left(\frac{\text{CM}_1(\rho)}{\text{CM}_n(\rho)} \right)^{\frac{1}{n-1}}, \quad (6.3.3)$$

where n denotes the number of iterations for single-grid calculations and the number of cycles for multigrid calculations. It is important to note that fast convergence is associated with low values of the convergence rate.

Convergence histories will be shown in terms of work units (WU). Following Weseling [14], a work unit is defined as the time required to carry out one time step on the finest grid. A further comparison will be made through the scaled CPU time (SCT) for a given calculation which is the CPU time for a given calculation normalised by the shortest CPU time achieved for that calculation with a given sequence of grids. This may be regarded as a direct measure of the convergence acceleration afforded by employing the agglomeration multigrid method.

6.3.1 Subsonic Case

The subsonic case is defined by an inflow Mach number of $M_0 = 0.5$ and a bump height of $h = 0.1$. As the flow remains subsonic over the bump, there is no physical mechanism of generating an increase in entropy and the flow pattern should be completely symmetric

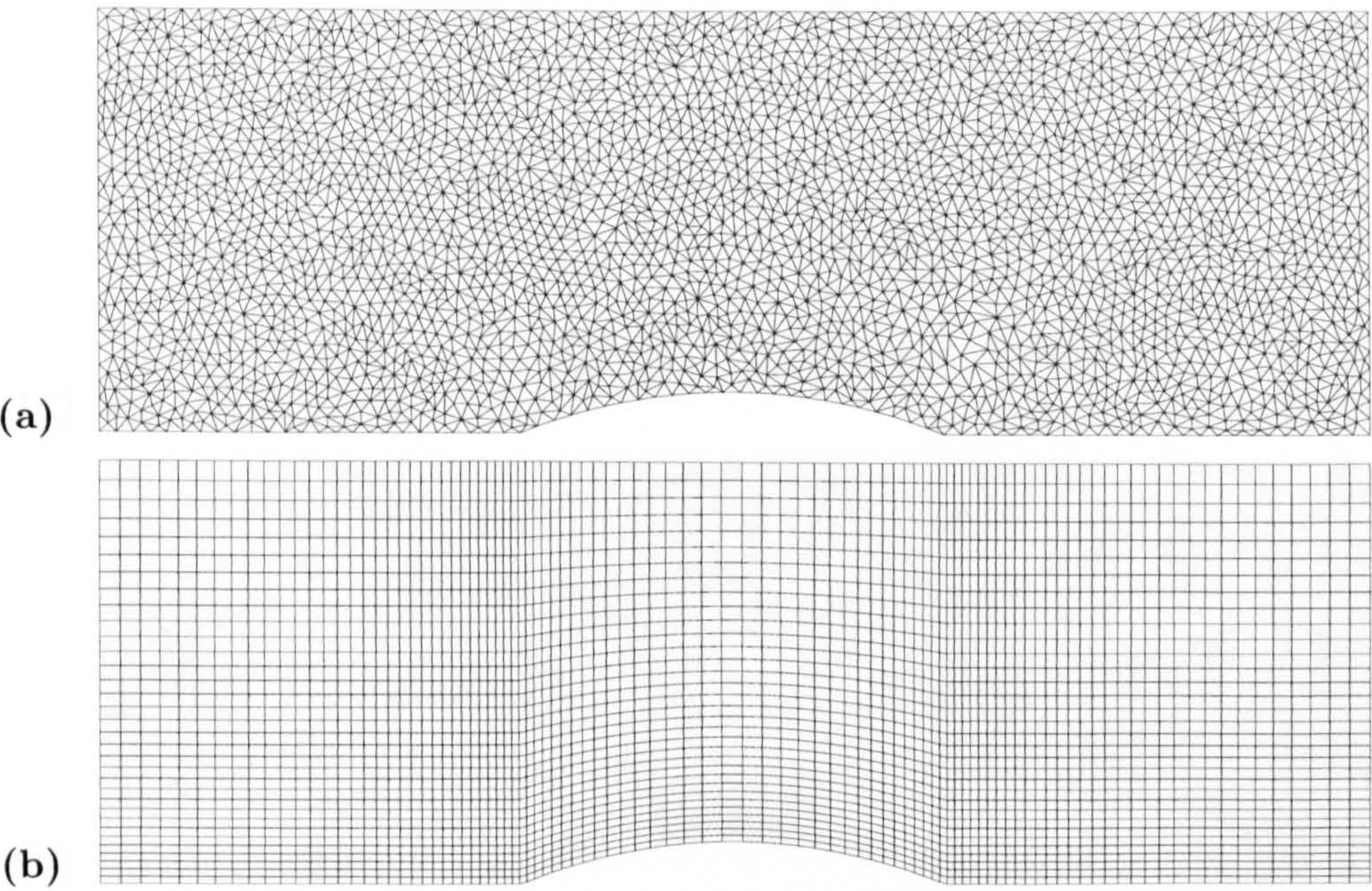


Figure 6.7: (a) triangular grid and (b) quadrilateral grid used for subsonic and transonic bump flow calculations.

Table 6.1: Summary of grid characteristics used in computational study for subsonic and transonic bump flow calculations.

grid	vertices	edges	triangles	quadrilaterals
triangular	3276	9625	6350	–
quadrilateral	3332	6532	–	3201

with respect to $x = 0.5$. The second-order accurate solutions were obtained without a limiter function.

Comparison of Triangular and Quadrilateral Grids. The calculations were carried out on the triangular and quadrilateral grids shown in Fig. 6.7. Their characteristics are listed in Table 6.1. Note that the two grids contain roughly the same number of vertices, and hence unknowns.

The contours of pressure for the first-order accurate solutions are shown in Fig. 6.8. The jaggedness of the contour lines in the solution on the triangular grid is due to the irregularities of the triangular grid and the plotting package. Overall, the solutions are quite similar. The corresponding second-order accurate solutions are shown in Fig. 6.9.

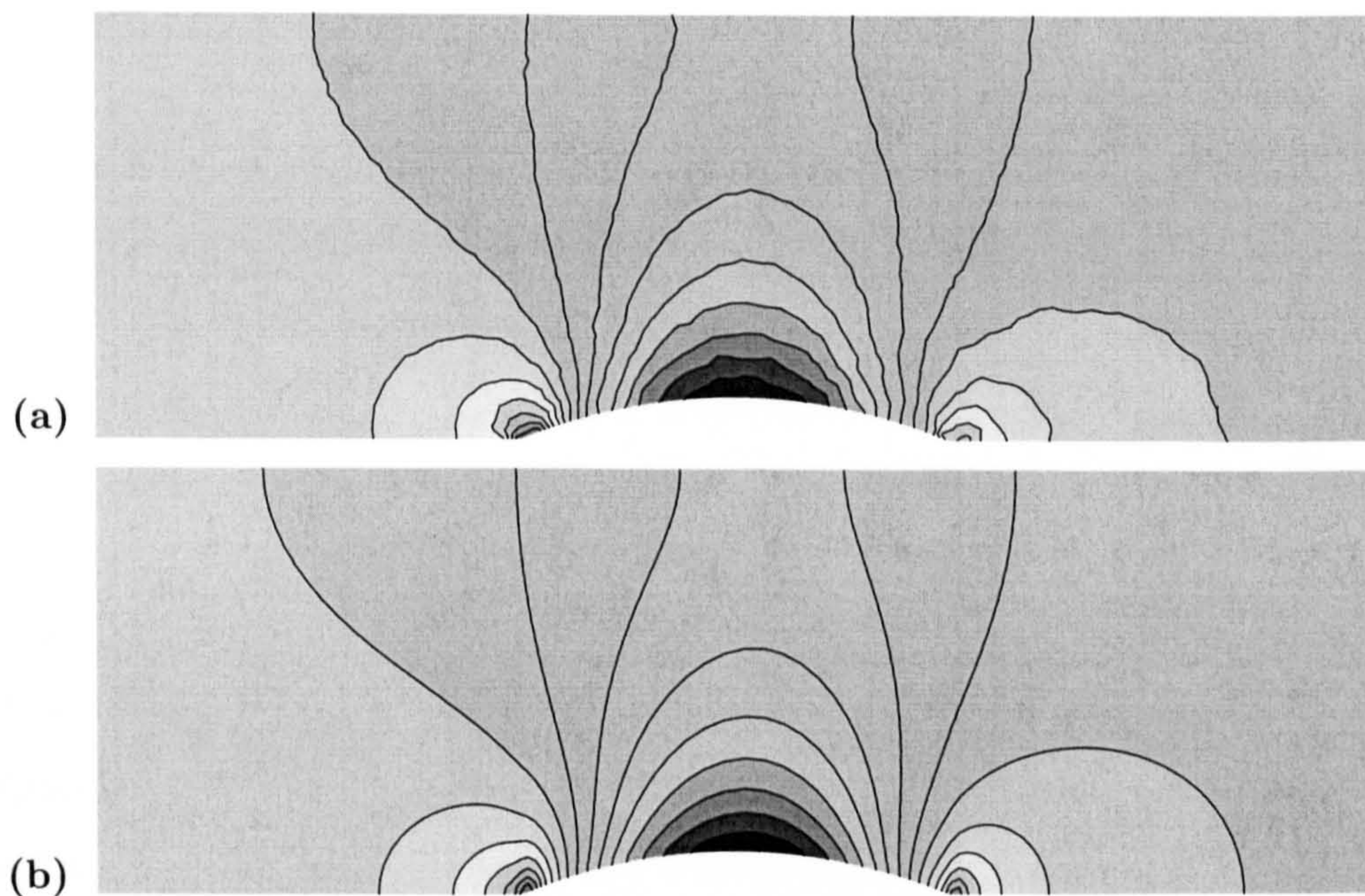


Figure 6.8: Contours of pressure for first-order solutions on (a) triangular grid (0.635, 0.777; 15) and (b) quadrilateral grid (0.631, 0.780; 15) for subsonic bump flow.

It is noted that the jaggedness of the contours is reduced substantially. Once again, the solutions on the triangular and quadrilateral grid are quite similar.

The variations of the pressure coefficient on the lower and upper walls are plotted in Fig. 6.10 for both first- and second-order accurate solutions. Differences between the first-order accurate solutions on the triangular and quadrilateral grids exist mainly at the leading and trailing edges as well as at the crest of the bump. For the second-order accurate solutions, the irregularities disappear almost completely with the exception of the leading edge.

Perhaps the most interesting comparison is made through the entropy parameter as shown in Fig. 6.11. For the first-order accurate solutions, the two most notable features are the spikes at the leading and trailing edges for the triangular grid and that the variation of the entropy parameter exhibits a (local) peak at the crest of the bump for the quadrilateral grid. This might be related to the grid stretching in the x -direction, which increases from the leading edge of the bump to the crest, and decreases from the crest to the trailing edge. Another explanation might be that the entropy is diffusing away from the solid wall. Beyond the trailing edge, the entropy parameter remains

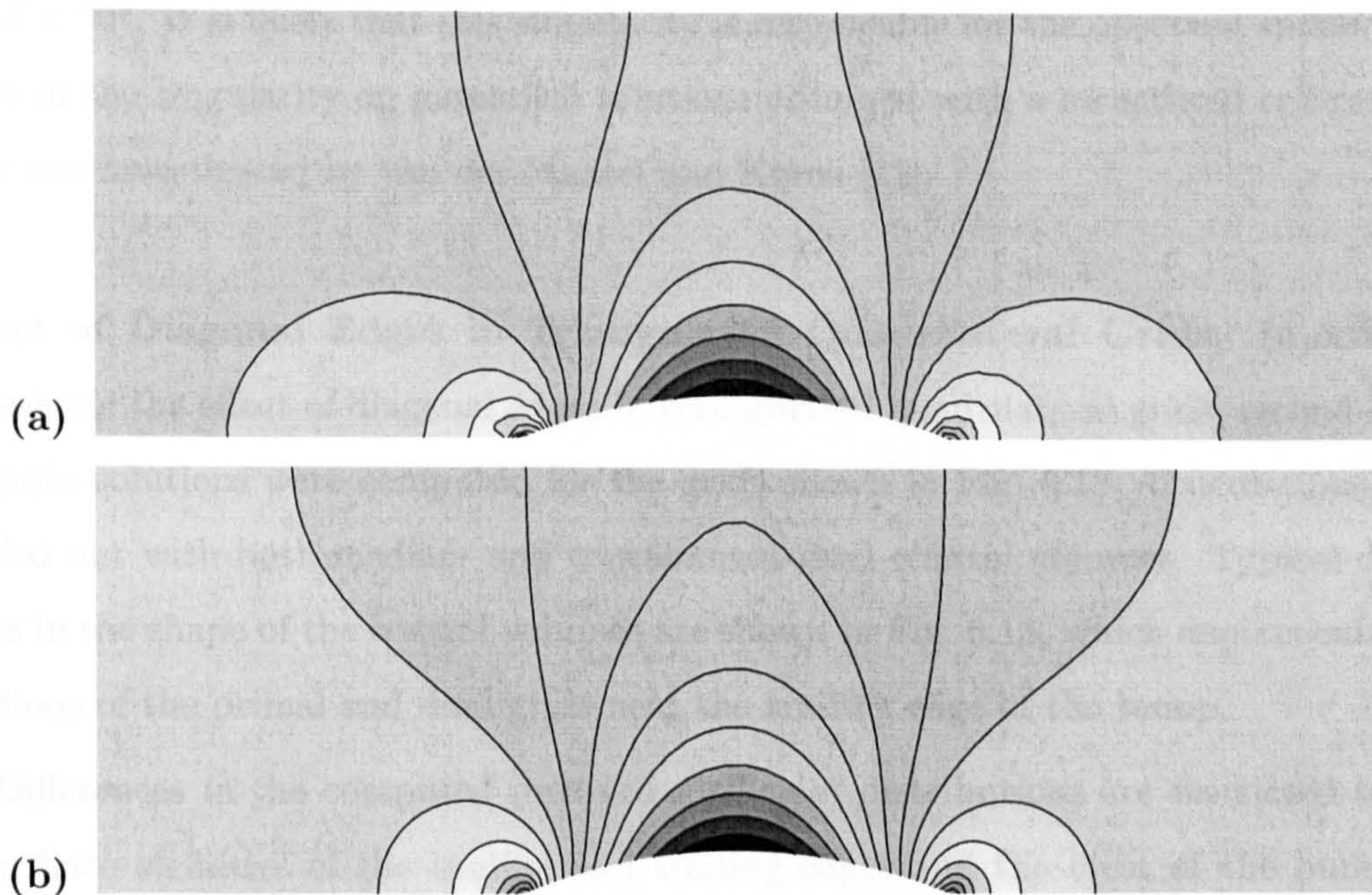


Figure 6.9: Contours of pressure for second-order solutions on (a) triangular grid (0.623,0.787;15) and (b) quadrilateral grid (0.622,0.778;15) for subsonic bump flow.

constant on the quadrilateral grid, whereas it decreases on the triangular grid. It is also interesting to note that the spikes at the leading and trailing edges are in opposite directions for the second-order accurate solutions.

It is worth noting that potential flow analysis of the radial and circumferential velocity components near a corner gives

$$u_r \propto r^{\frac{\delta}{\pi-\delta}} \cos\left(\frac{\pi-\theta}{\pi-\delta}\delta\right),$$

and

$$u_\theta \propto r^{\frac{\delta}{\pi-\delta}} \sin\left(\frac{\pi-\theta}{\pi-\delta}\delta\right),$$

where (r, θ) are the polar coordinates with origin at the corner and δ is the angle at the corner. Both angles are positive measured in the counterclockwise direction with respect to the positive x -axis. For the bump,

$$\delta = \arcsin\left(\frac{4h}{4h^2 + 1}\right) = 22.62^\circ.$$

It can be seen that for $\delta > 0$, a stagnation point exists at the corner as expected. More interestingly, there is a singularity in the velocity derivatives at the corner if

$0 < \delta < 90^\circ$. It is likely that this singularity is responsible for the observed spikes. The effect of the singularity on numerical solutions obtained with a structured cell-centred code was investigated by van der Maarel and Koren [12].

Effect of Diagonal Edges in Triangulated Quadrilateral Grids. In order to investigate the effect of diagonal edges in triangulated quadrilateral grids, second-order accurate solutions were computed for the grids shown in Fig. 6.12. Calculations were carried out with both median- and containment-dual control volumes. Typical differences in the shape of the control volumes are shown in Fig. 6.13, which depicts enlarged fractions of the primal and dual grids near the trailing edge of the bump.

Differences in the computed pressure coefficient distributions are restricted to the immediate vicinities of the leading and trailing edges and the crest of the bump, as shown in Fig. 6.14. The distributions of the entropy parameter are shown in Fig. 6.15. It is interesting to see that the triangulated quadrilateral grids also show a maximum of the entropy parameter at the crest of the bump like the quadrilateral grids. This suggests that the cause is the distribution of grid points, as surmised above, and not the cell type.

Assessment of Multigrid Acceleration. Up to 5 grid levels have been used for both triangular and quadrilateral grids. The first four grid levels are shown in Figs. 5.3 and 5.4. The grid characteristics are listed in Table 6.2. It is noted that the coarsening is more aggressive on the triangular grid. The average coarsening ratios are 4.5 on the triangular and 3.6 on the quadrilateral grids.

To restrict the number of calculations, only V-cycles were used. It is expected that the behaviour of multigrid acceleration on triangular and quadrilateral grids with W-cycles will be similar to that observed with V-cycles. For all the calculations reported in this chapter, 2 pre- and postsmoothing iterations were carried out with 4 iterations on the coarsest grid level. Separate calculations showed that this combination is a good compromise between fast convergence and additional required processing time. Injection is used as a prolongation operator. The use of unlimited and limited linear prolongation was not found to lead to faster convergence, and in some cases actually led to stalled convergence.

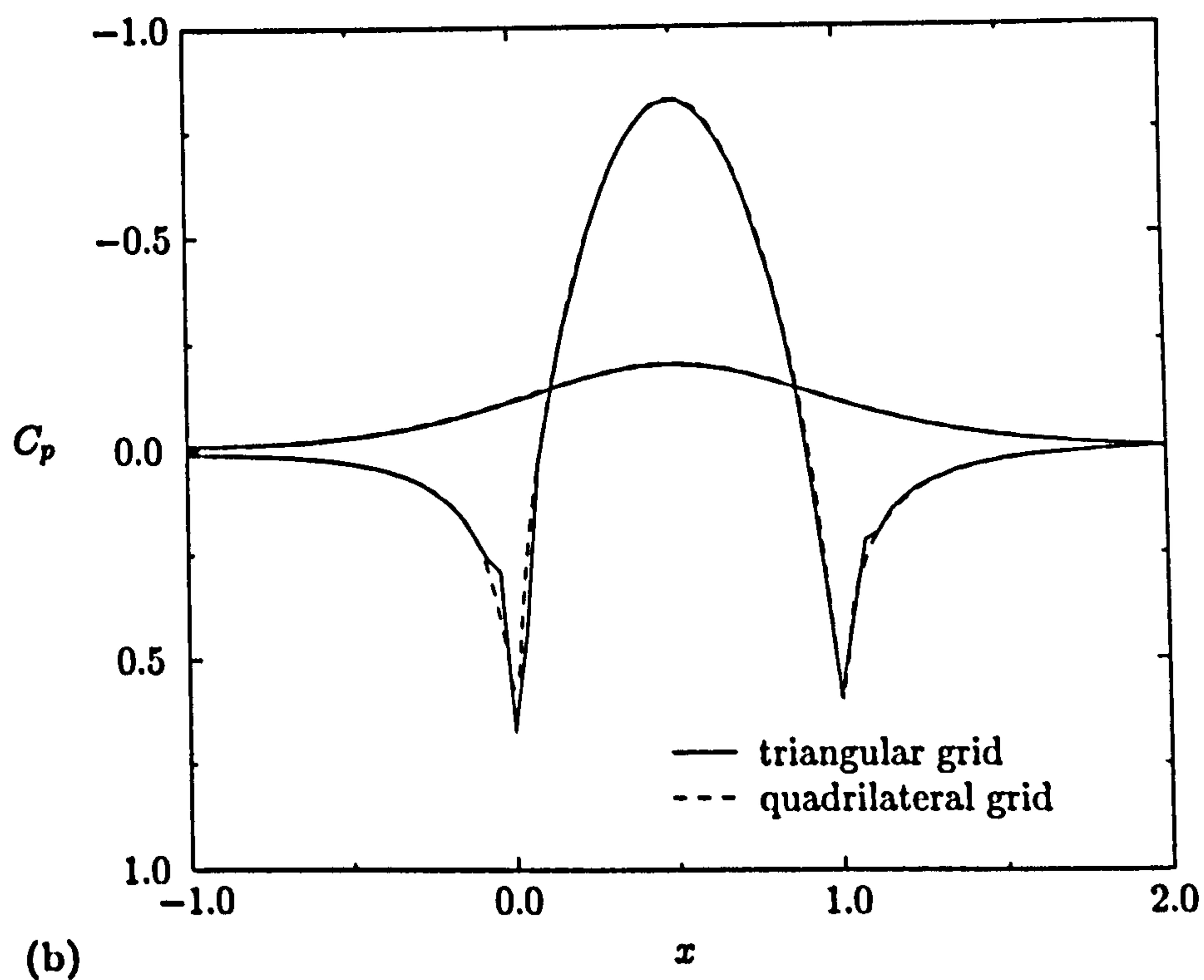
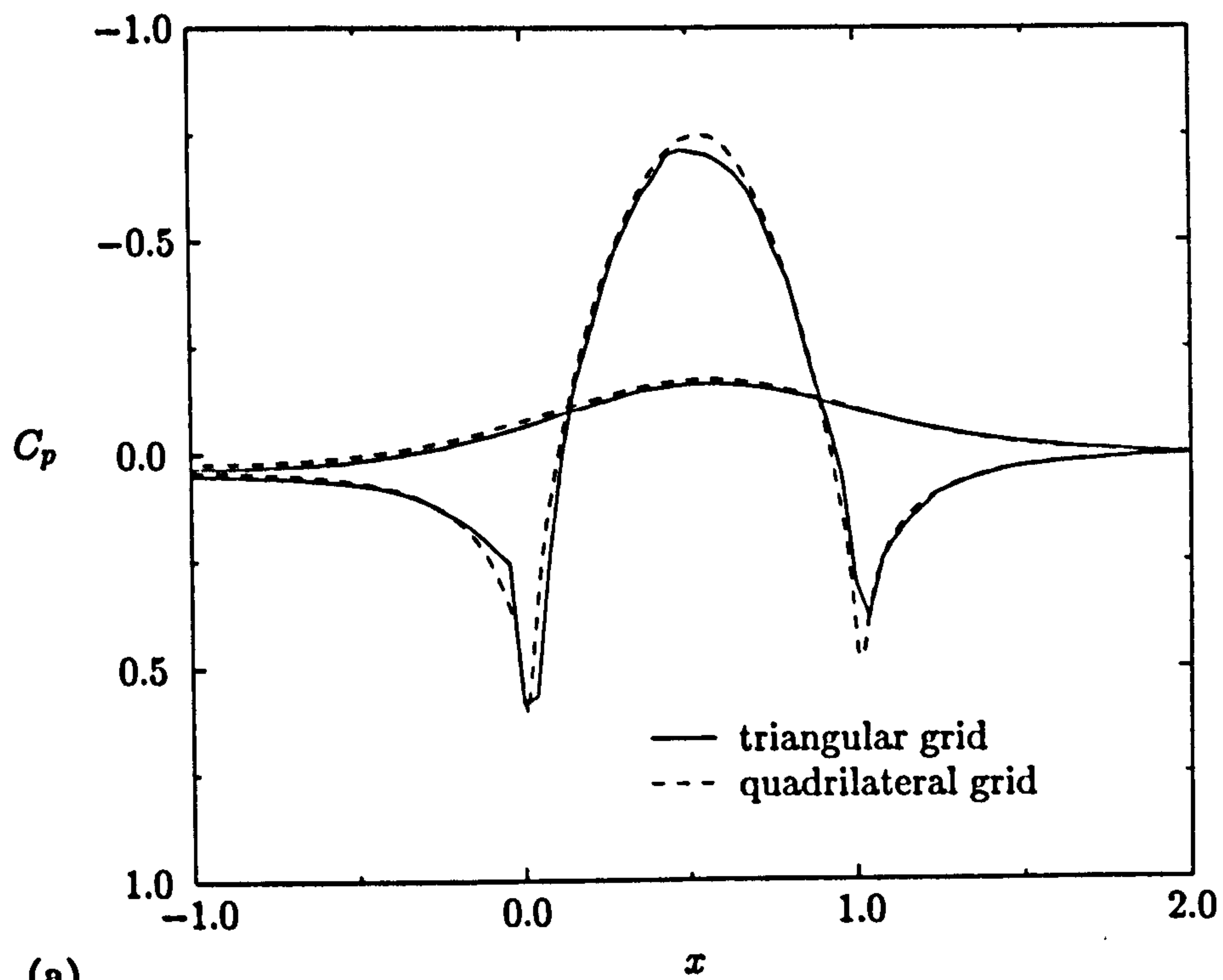


Figure 6.10: Comparison of pressure coefficient for (a) first-order solutions and (b) second-order solutions on triangular and quadrilateral grids for subsonic bump flow.

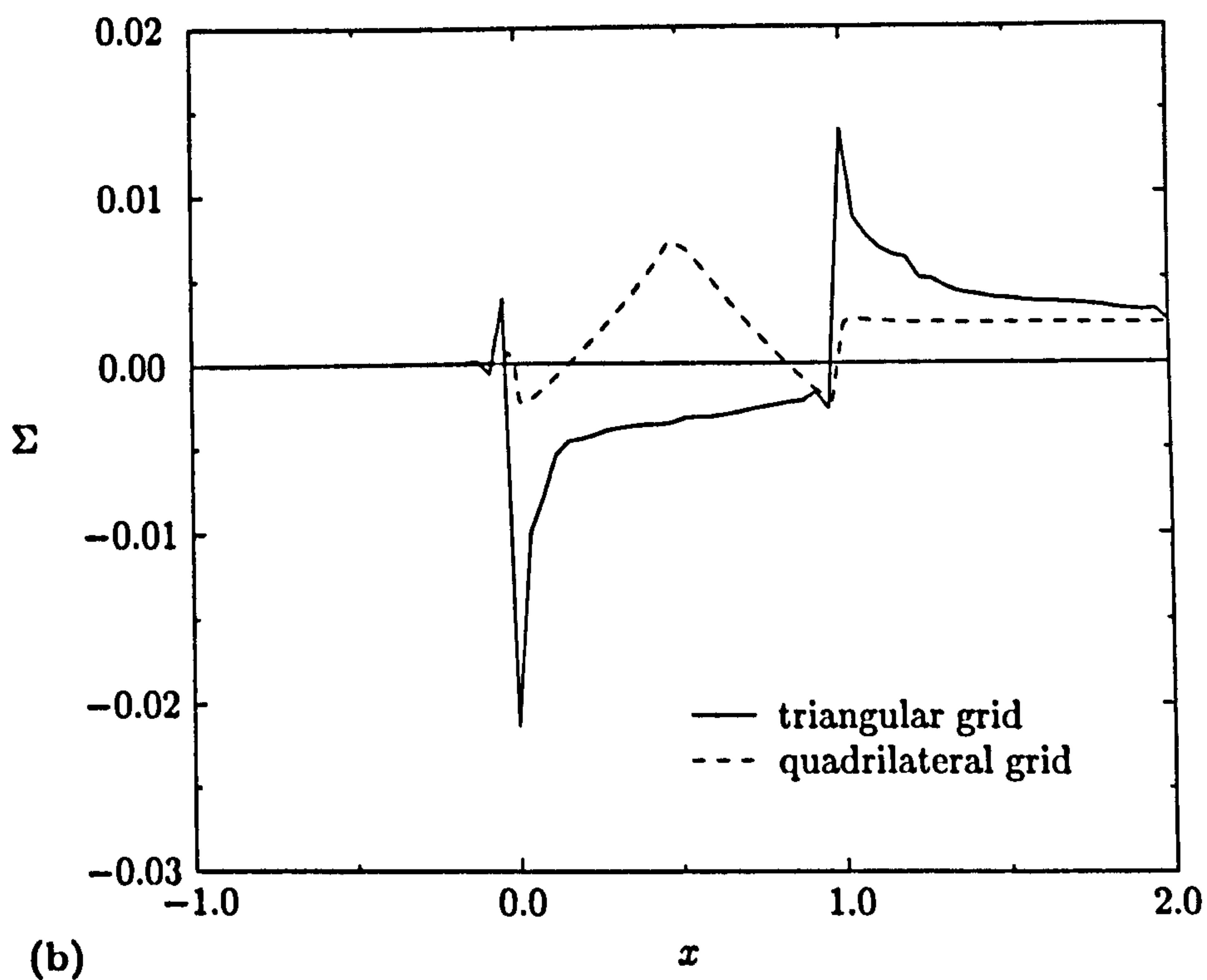
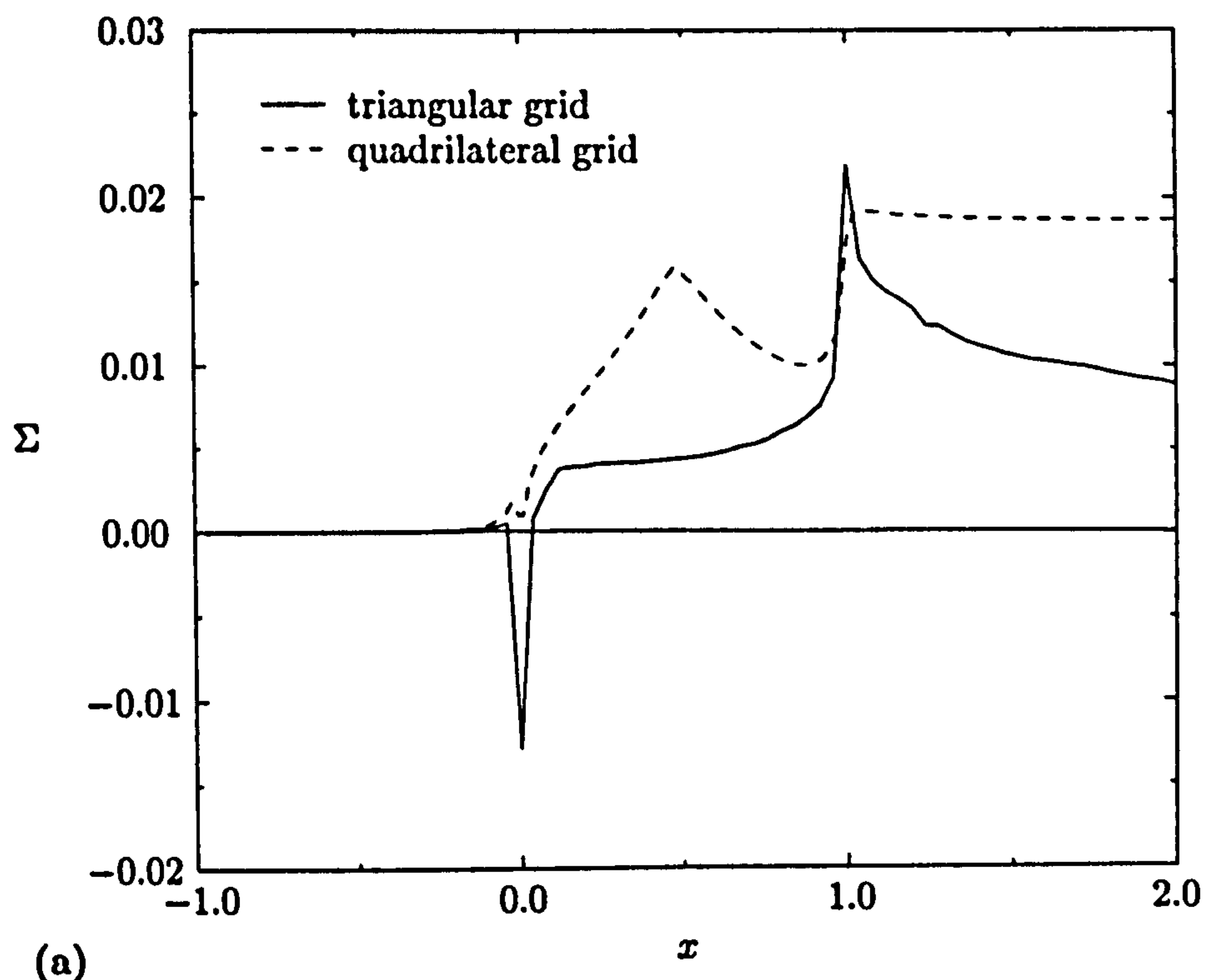


Figure 6.11: Comparison of entropy parameter for (a) first-order solutions and (b) second-order solutions on triangular and quadrilateral grids for subsonic bump flow.

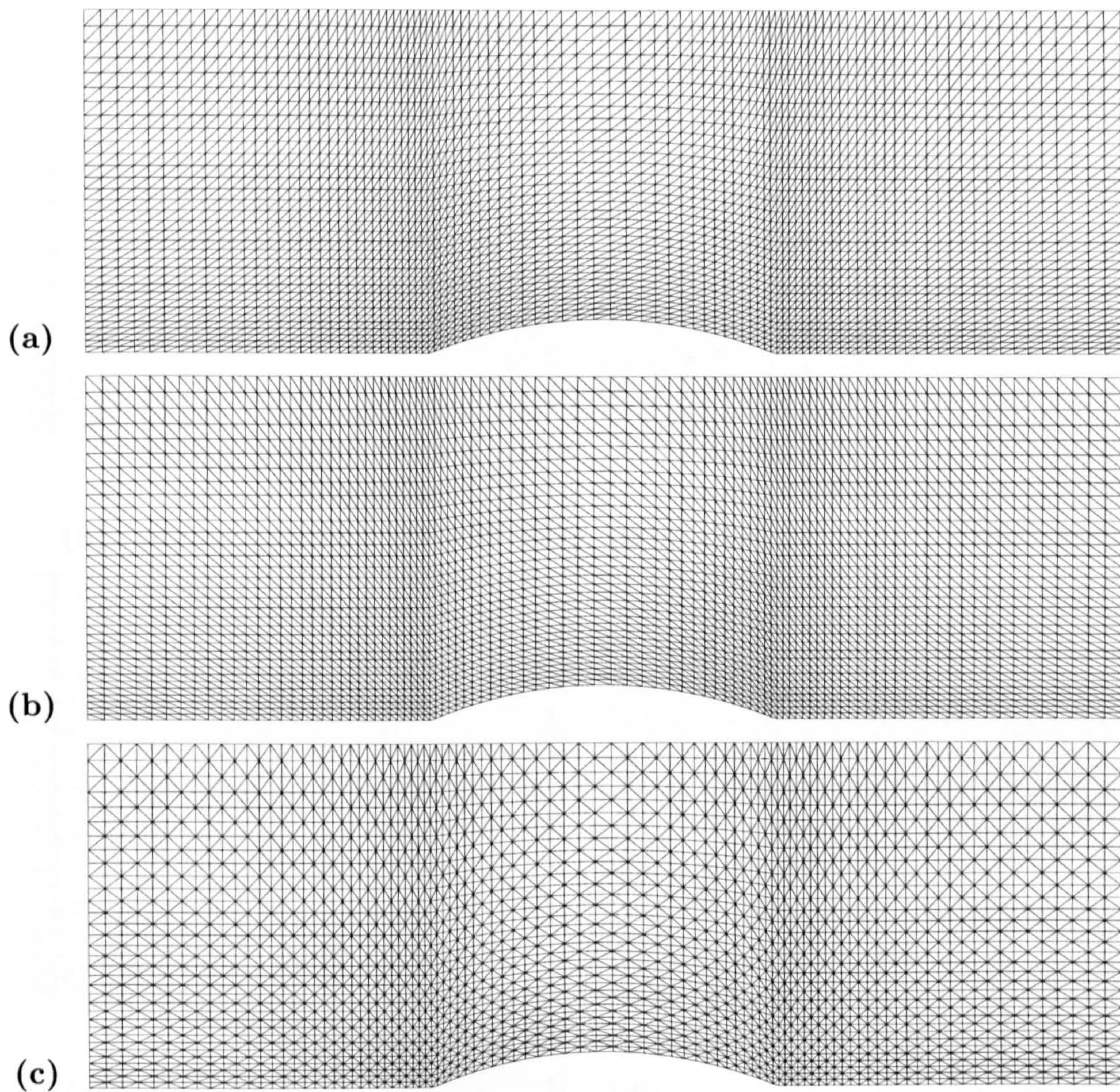


Figure 6.12: Triangulated quadrilateral grids with 3332 vertices, 9733 edges and 6402 cells obtained from grid shown in Fig. 6.7(b). (a) Grid type 1 and (b) grid type 2 and (c) grid type 3.

The results obtained with first-order accurate discretisations on the triangular and quadrilateral grids are summarised in Table 6.3. It is noted that for single-grid calculations, the number of cycles is equivalent to the number of iterations. For multigrid calculations, each cycle consists of several iterations. The corresponding convergence histories are shown in Fig. 6.16. The convergence histories for 5 grid levels are not plotted for the sake of clarity. The same procedure will be followed for all other calculations in this thesis if the clarity of the figures illustrating convergence histories suffers.

Several observations can be made from Table 6.3. Both the triangular and quadrilateral grids require about the same number of iterations to converge with a single grid level. The multigrid scheme performs better on the triangular grid, where the use of 5

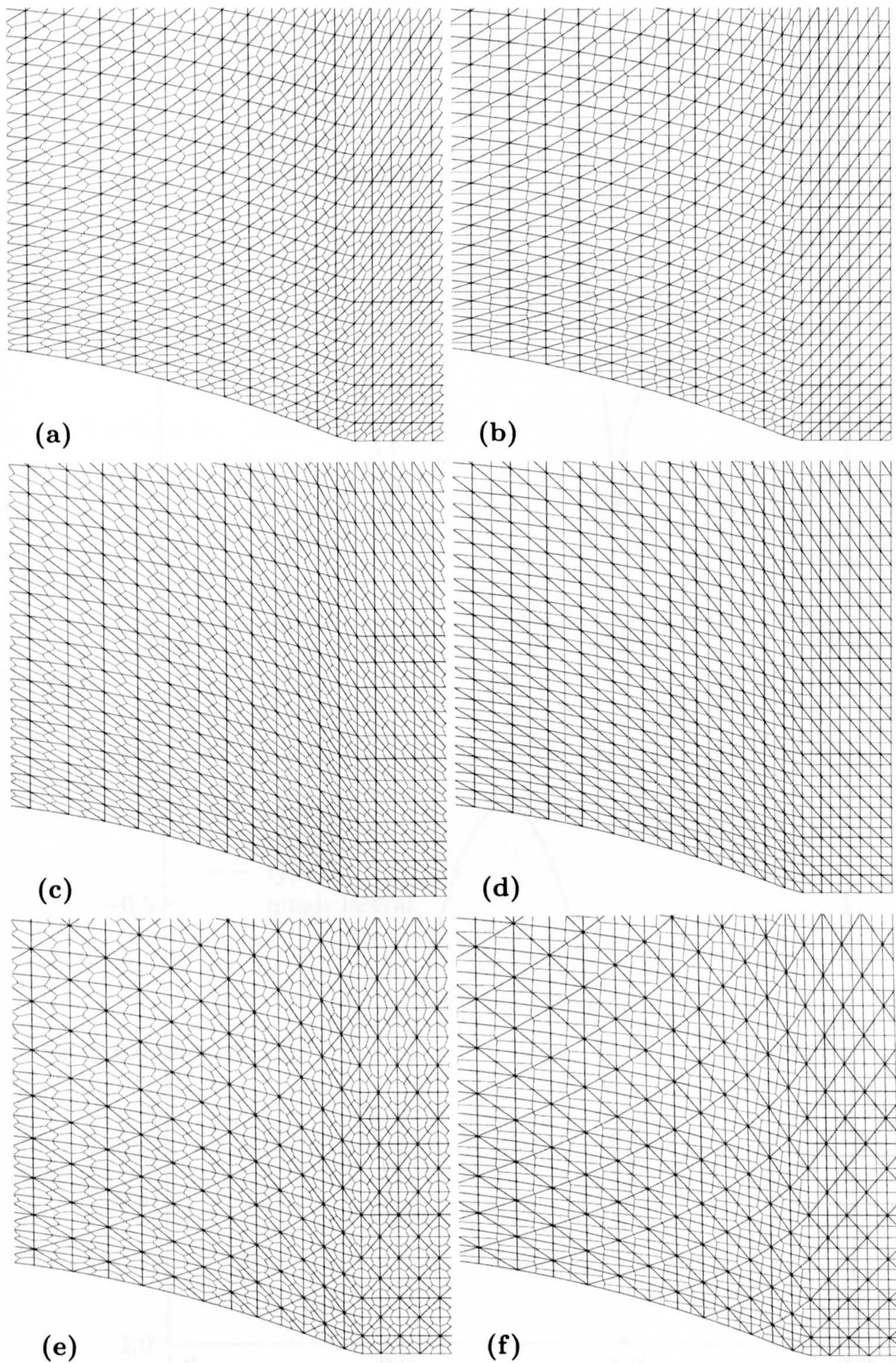


Figure 6.13: Detail view of effect of diagonal edges on control-volume shape near trailing edge of bump. (a) Grid type 1 with median dual, (b) grid type 1 with containment dual, (c) grid type 2 with median dual, (d) grid type 2 with containment dual, (e) grid type 3 with median dual, (f) grid type 3 with containment dual.

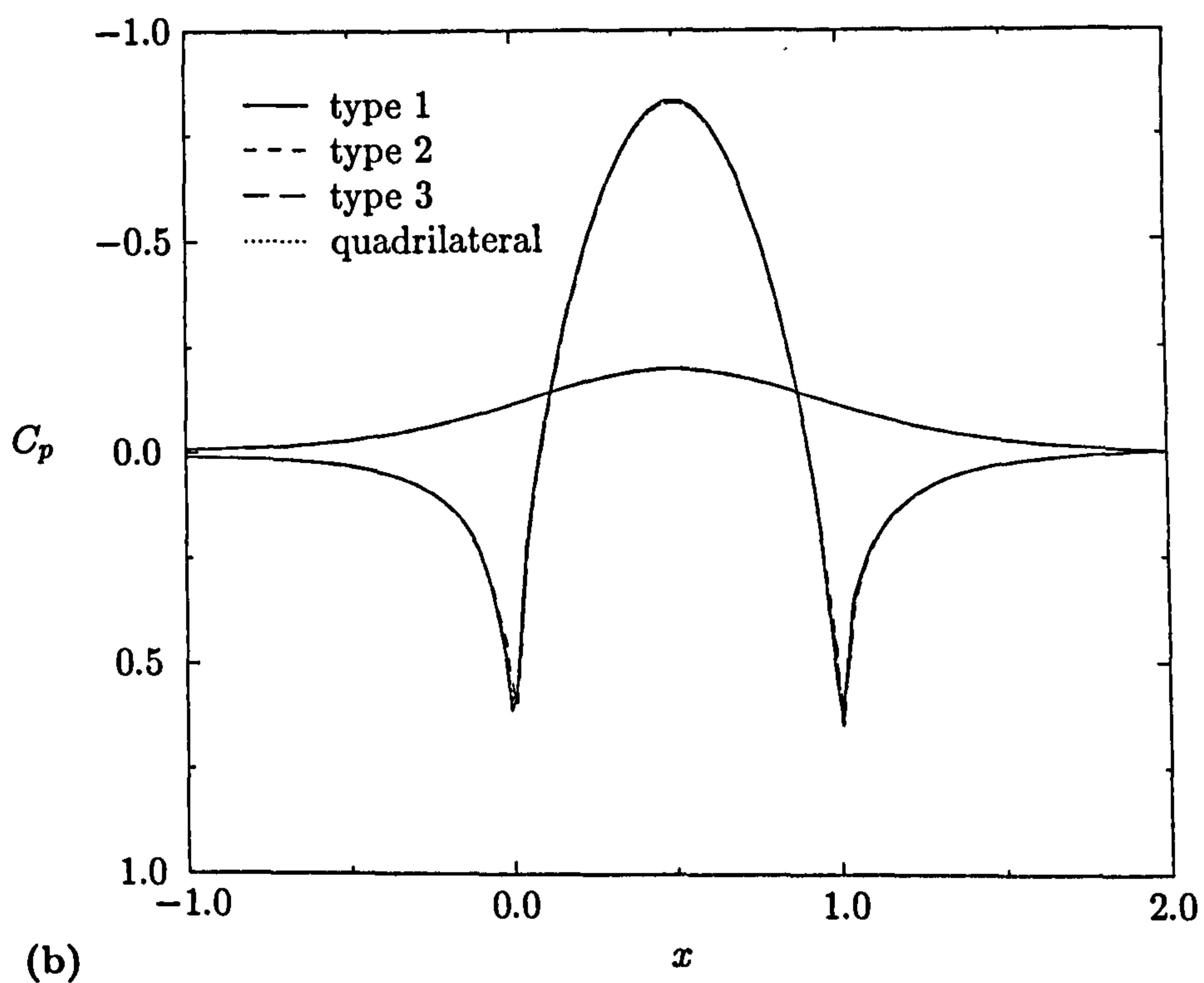
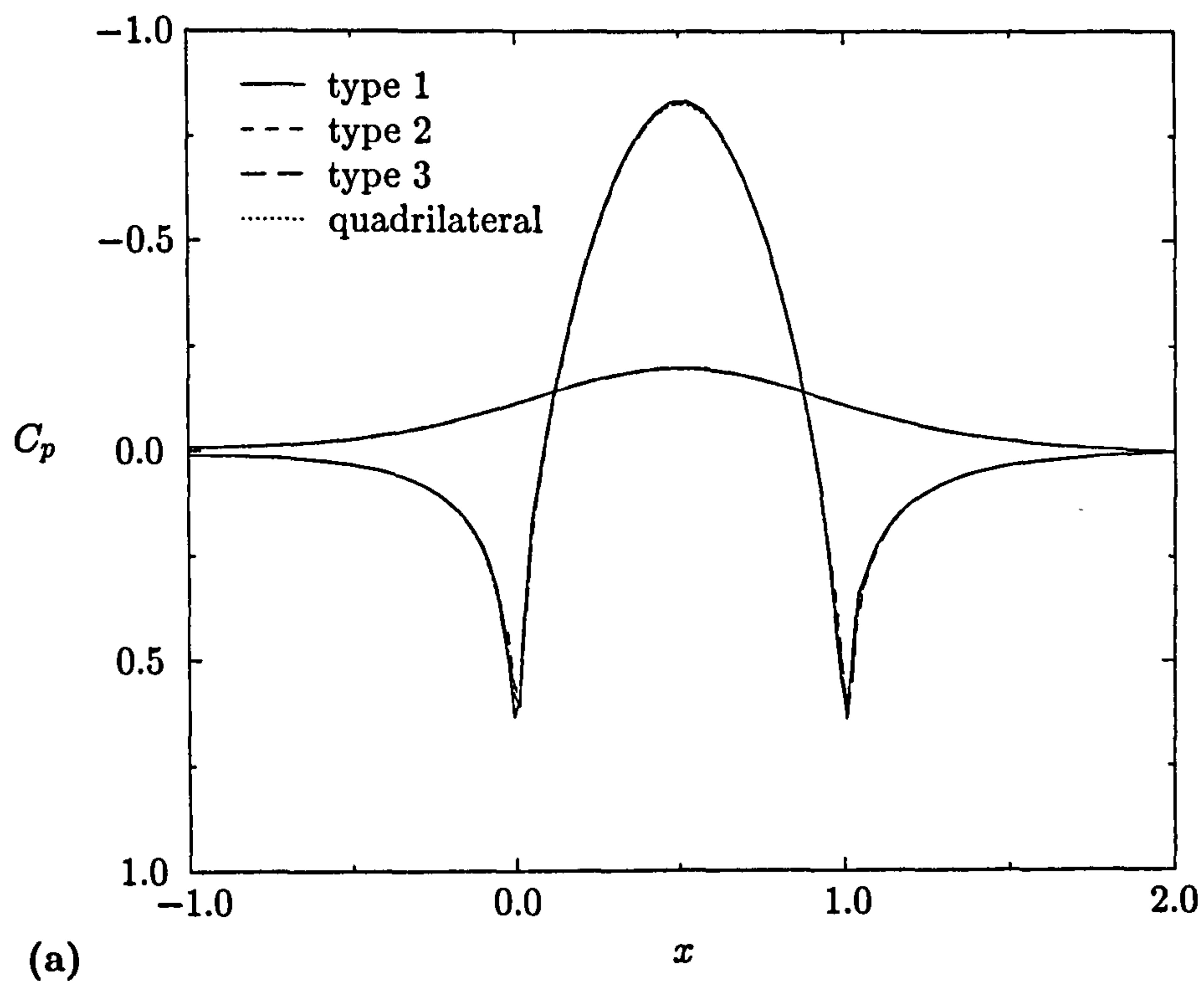


Figure 6.14: Comparison of pressure coefficient for (a) median dual and (b) containment dual for second-order solutions on triangulated quadrilateral grids for subsonic bump flow.

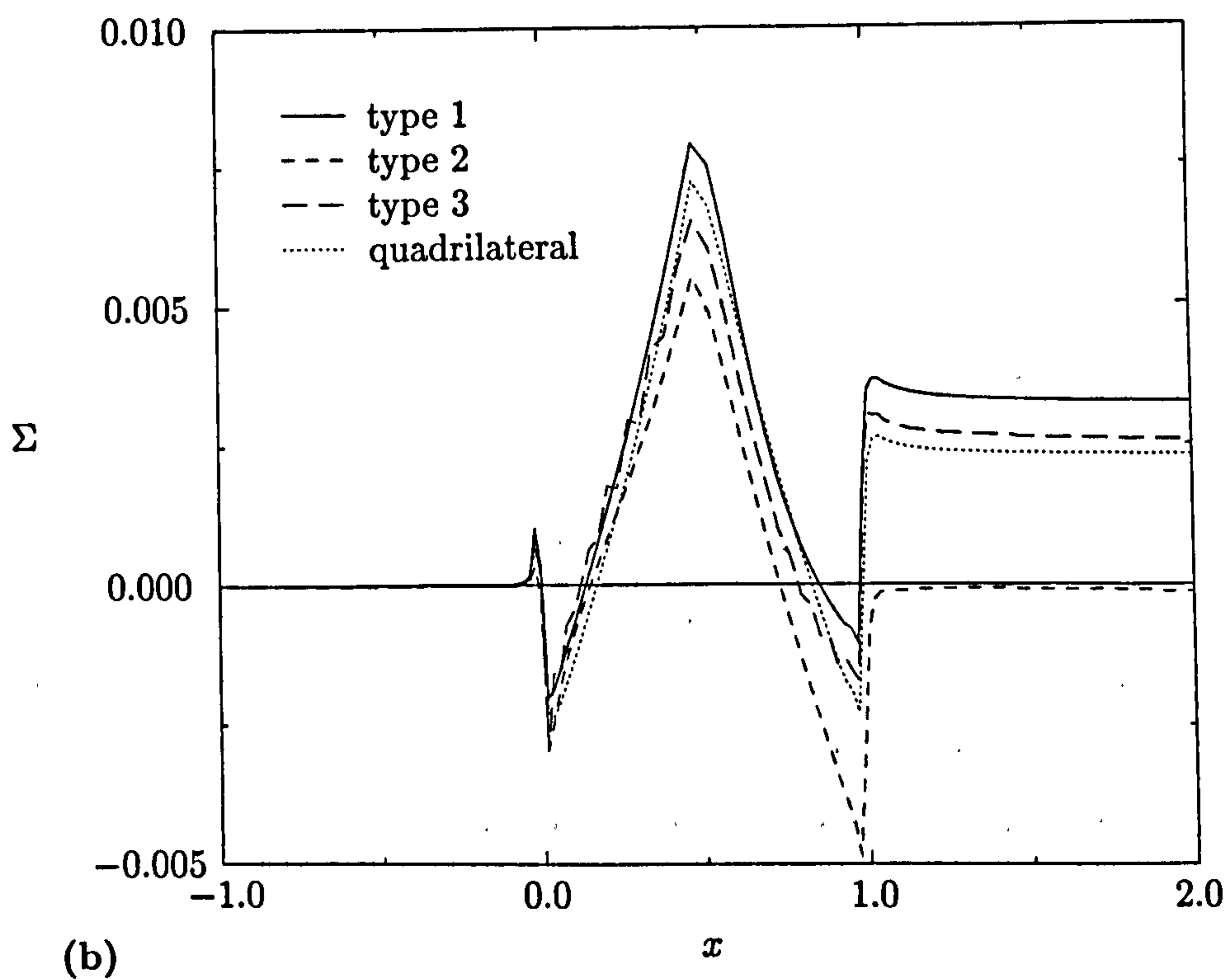
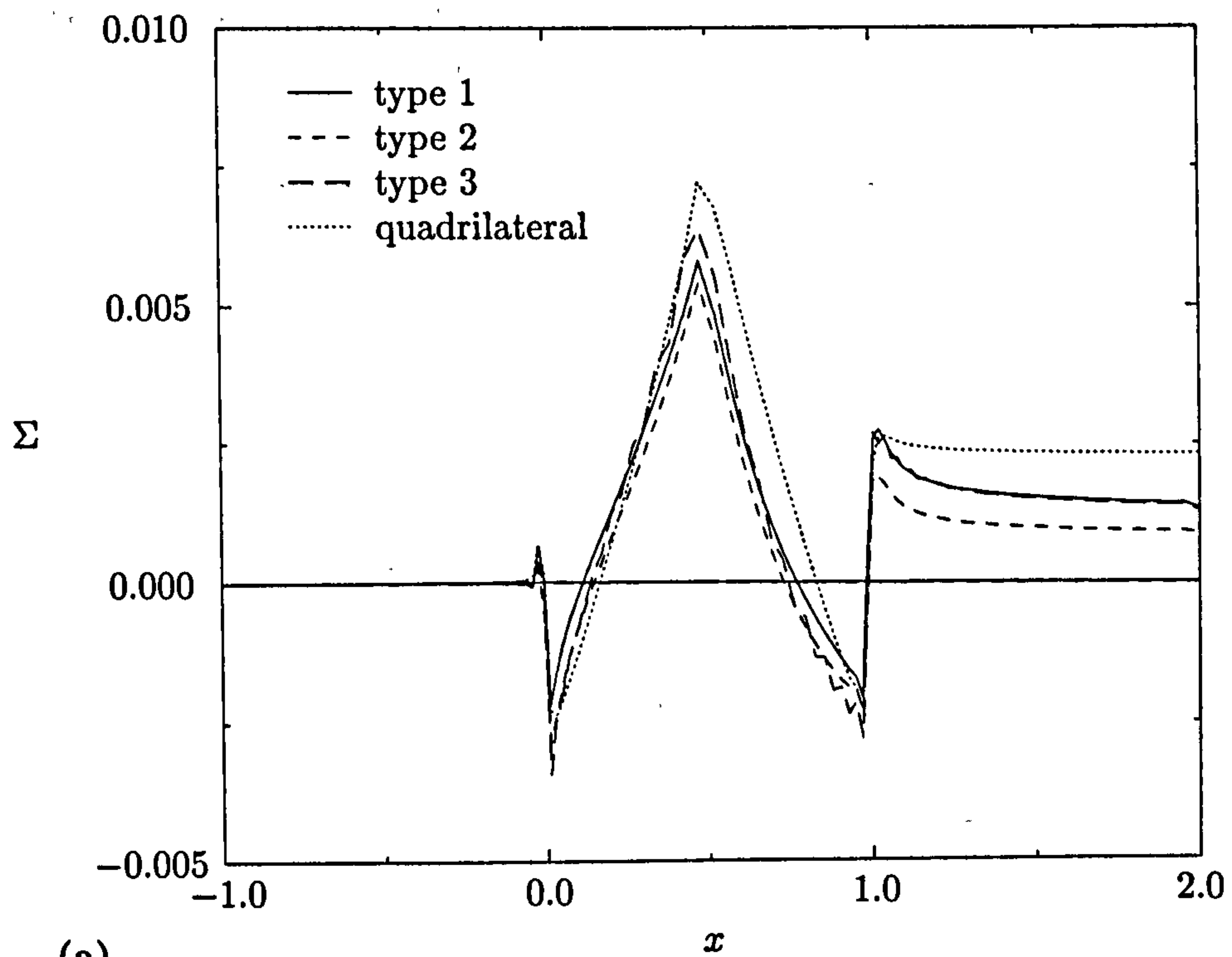


Figure 6.15: Comparison of entropy parameter for (a) median dual and (b) containment dual for second-order solutions on triangulated quadrilateral grids for subsonic bump flow.

Table 6.2: Summary of characteristics of the 5 grid levels used in assessment of agglomeration multigrid scheme for subsonic and transonic bump flow.

level	triangular grids		quadrilateral grids	
	vertices	edges	vertices	edges
1	3276	9625	3332	6532
2	637	1808	833	1600
3	135	353	224	415
4	31	68	64	111
5	8	13	20	31

Table 6.3: Summary of first-order results for agglomeration multigrid scheme applied to subsonic bump flow.

level	triangular grid			quadrilateral grid		
	ACR	cycles	SCT	ACR	cycles	SCT
1	0.993	1432	19.10	0.993	1421	5.23
2	0.917	112	7.70	0.917	114	2.19
3	0.810	46	3.20	0.831	54	1.12
4	0.685	26	2.60	0.808	47	1.00
5	0.501	14	1.00	0.808	47	1.00

grid levels leads to a speed-up of nearly 20. On the quadrilateral grid, the use of 5 grid levels does not improve convergence over 4 grid levels. A maximum speed-up of just over 5 is obtained.

When applying the multigrid scheme to the second-order discretisation, gradients are reconstructed on the finest grid level only. Thus convergence will be accelerated partly through reduced operation count. The results for the second-order scheme are listed in Table 6.4. The convergence histories are shown in Fig. 6.17 in terms of work units (WU). As with the results for the first-order scheme, the triangular grid requires more iterations than the quadrilateral grid on a single grid level. The multigrid scheme again performs better on the triangular grid, leading to a speed-up of just over 100 with 5 grid levels. On the quadrilateral grid, the use of 5 grid levels leads to a slight worsening in convergence over 4 levels. The speed-up on the quadrilateral grid with 4 grid levels is roughly 50.

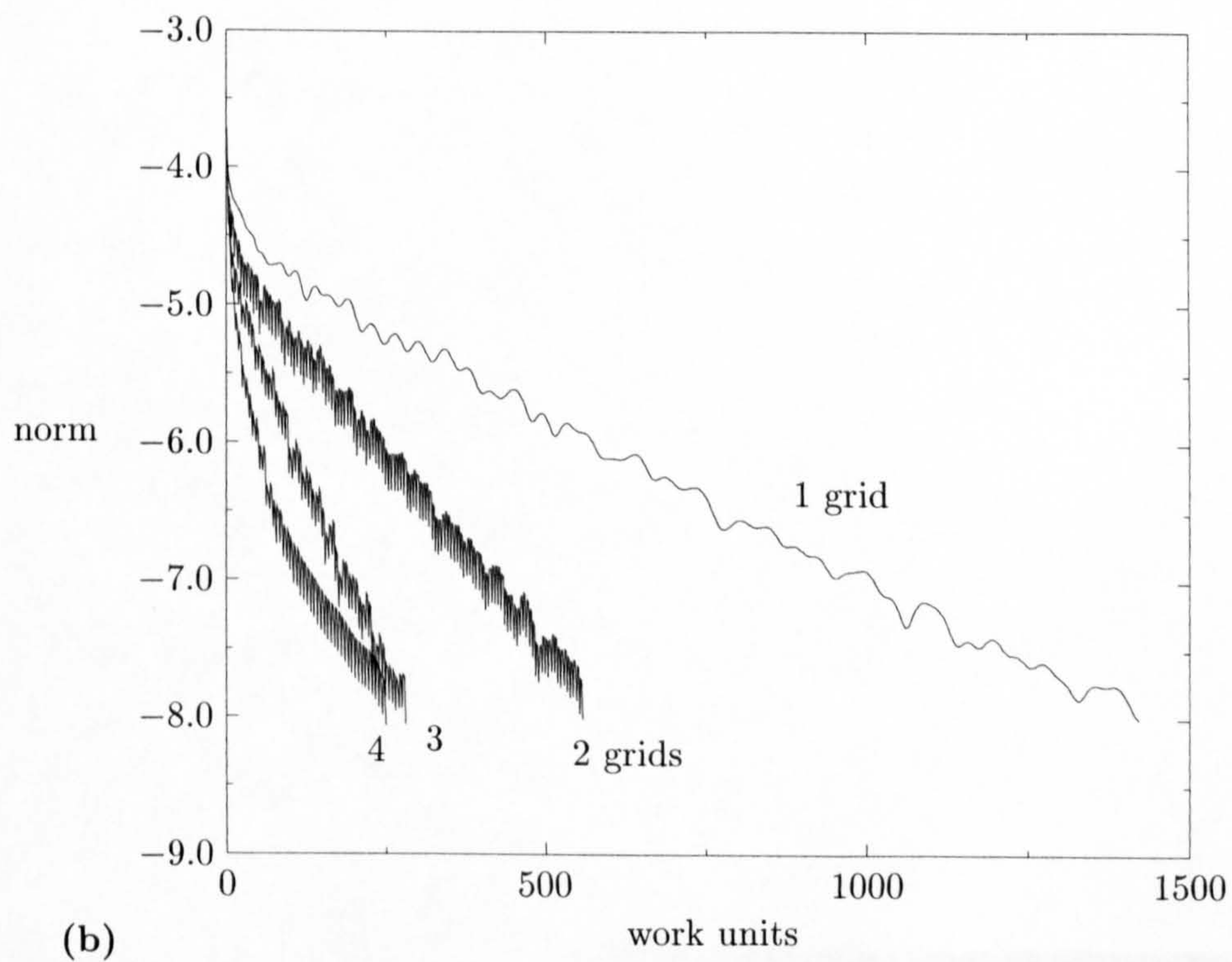
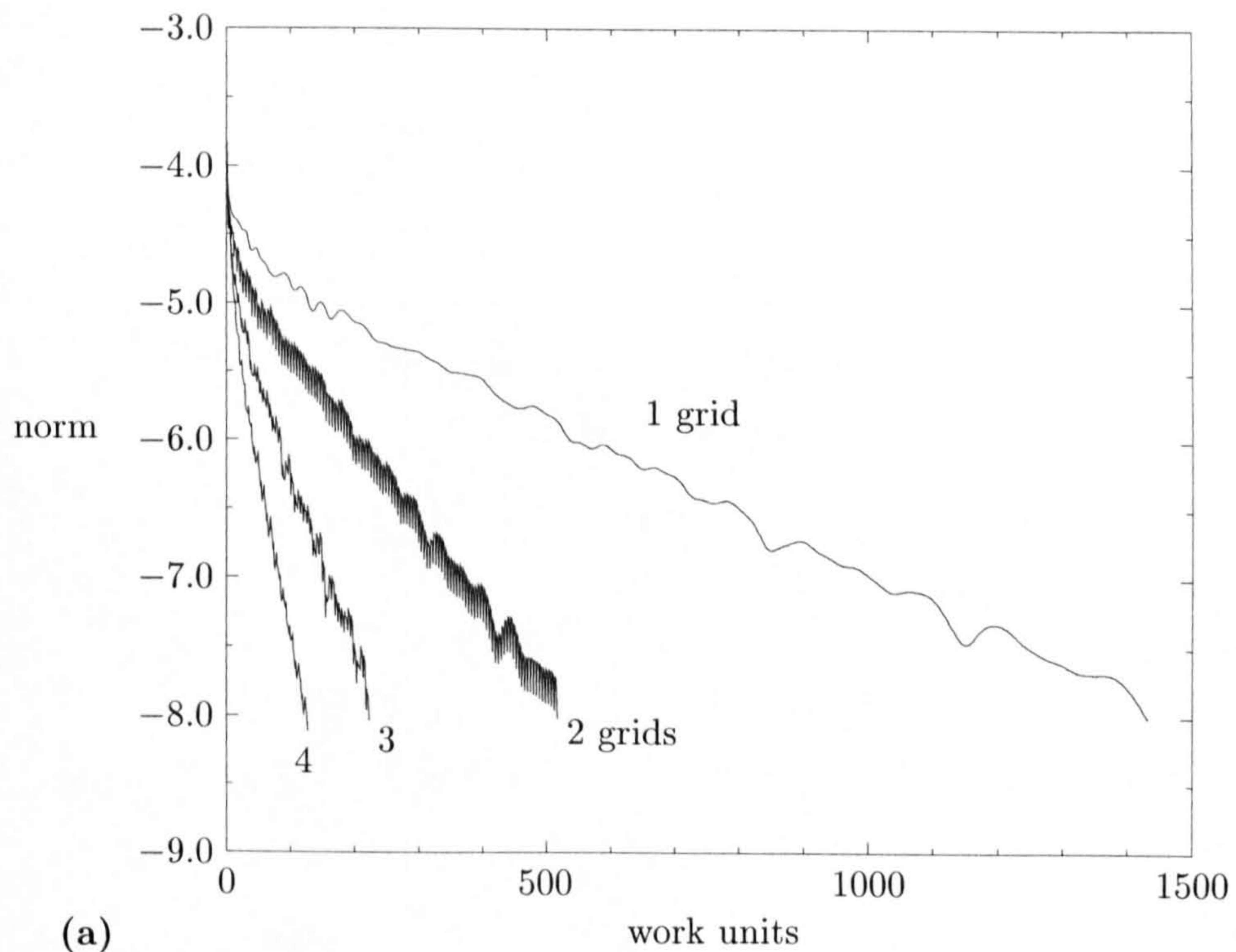


Figure 6.16: Comparison of multigrid convergence for first-order schemes on (a) triangular grid and (b) quadrilateral grid for subsonic bump flow.

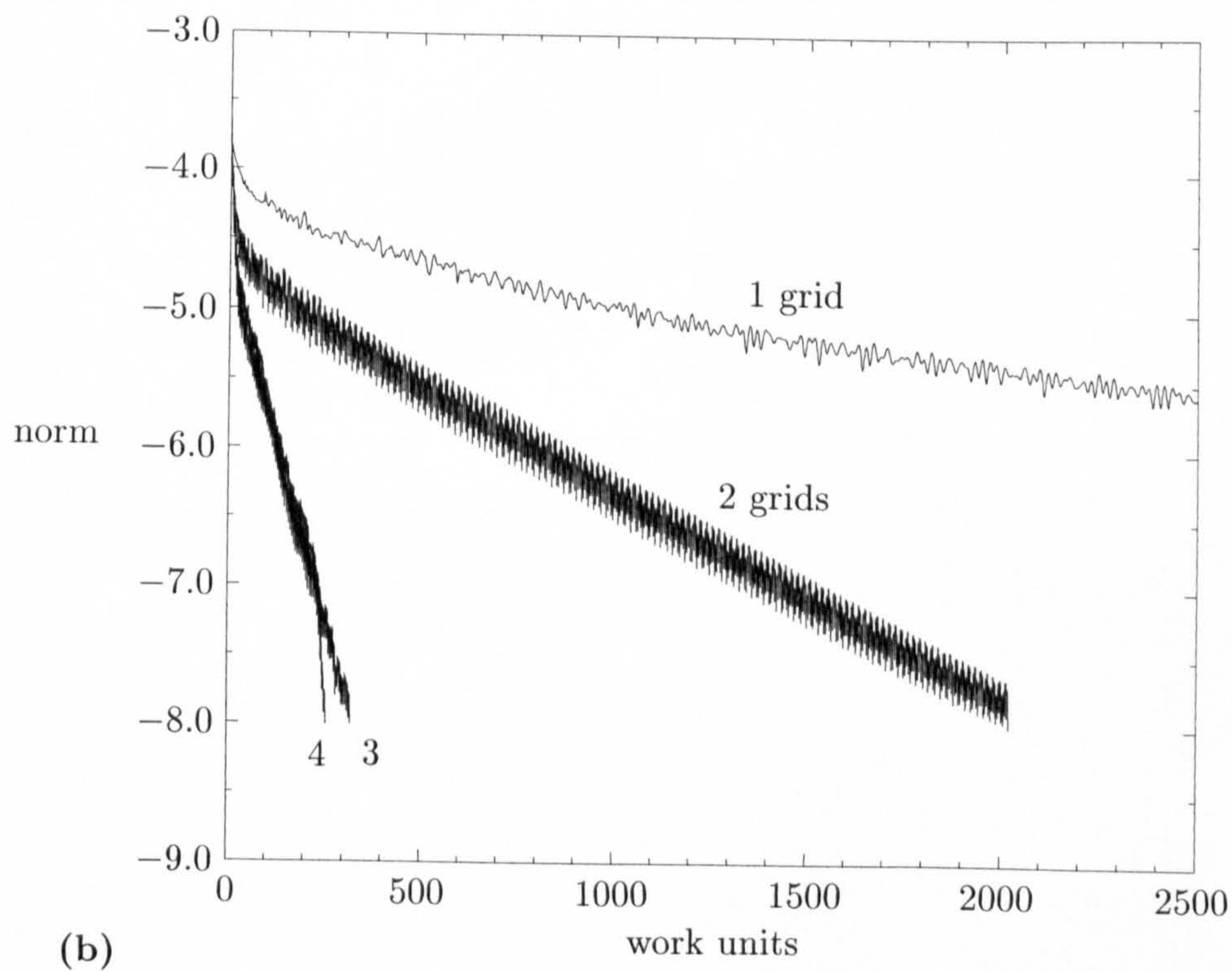
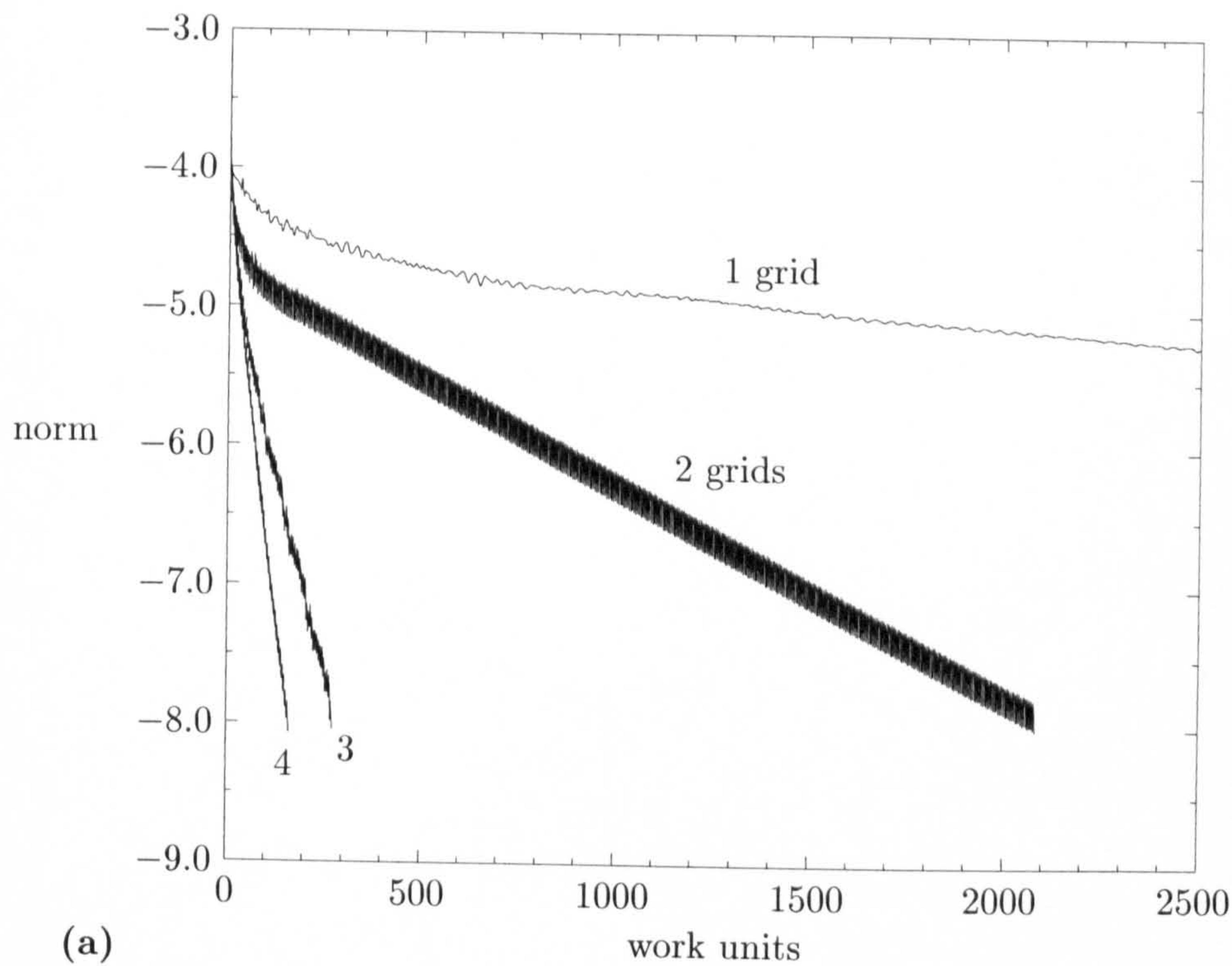


Figure 6.17: Comparison of multigrid convergence for second-order schemes on (a) triangular grid and (b) quadrilateral grid for subsonic bump flow.

Table 6.4: Summary of second-order results for agglomeration multi-grid scheme applied to subsonic bump flow.

level	triangular grid			quadrilateral grid		
	ACR	cycles	SCT	ACR	cycles	SCT
1	0.999	17001	102.82	0.999	13553	48.95
2	0.979	473	13.53	0.977	443	7.80
3	0.849	61	1.76	0.861	68	1.25
4	0.756	36	1.05	0.828	54	1.00
5	0.746	34	1.00	0.831	55	1.02

6.3.2 Transonic Case

The transonic case is specified by an inlet Mach number of $M_0 = 0.675$ and a bump height of $h = 0.1$. As will be seen below, this leads to a relatively weak shock wave on the leeward side of the bump. This allows the assessment of the Barth-Jespersen and Venkatakrishnan limiter functions as well as the quasi-ENO reconstruction of Ollivier-Gooch.

Comparison of Triangular and Quadrilateral Grids. The grids depicted in Fig. 6.7 are employed.

The pressure contours for the first-order calculations on the triangular grid are shown in Fig. 6.18. As expected, the shock wave is strongly smeared on both the triangular and quadrilateral grids, although slightly less so on the latter.

The second-order accurate results for the triangular grid are shown in Fig. 6.19. The results obtained with the Barth-Jespersen limiter function show kinks in the contour lines near the boundaries, whereas both the Venkatakrishnan limiter function and the quasi-ENO reconstruction do not exhibit kinks. The corresponding results obtained on the quadrilateral grid are shown in Fig. 6.20. It can be seen that the results for the Barth-Jespersen limiter function show much reduced kinks in the contour lines compared to those on the triangular grid. The shock wave is resolved better than on the triangular grid, probably due to the fact that one family of grid lines is approximately aligned with the shock wave.

The considerable improvement obtained by using second-order accurate schemes compared to first-order schemes can also be judged from the line plots of pressure

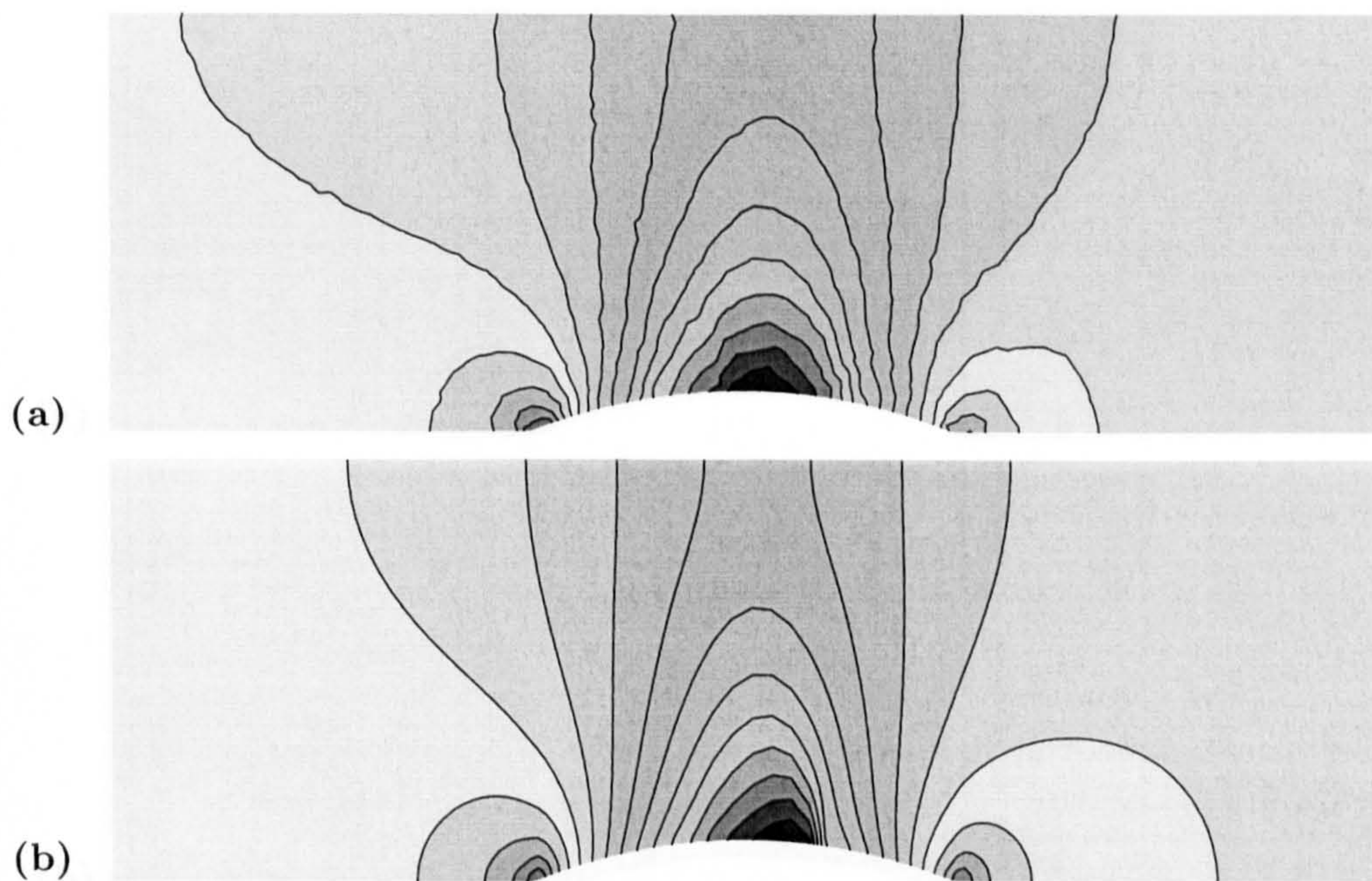


Figure 6.18: Contours of pressure for first-order solutions on (a) triangular grid (0.477,0.829;15) and (b) quadrilateral grid (0.429,0.834;15) for transonic bump flow.

coefficient shown in Fig. 6.21. On the triangular grid, some differences exist between the second-order schemes just before the leading edge and behind the trailing edge of the bump. The shock wave is located at about 70% of the chord of the bump. On the quadrilateral grid, the second-order schemes give virtually the same variation of the pressure coefficient. For the Venkatakrishnan limiter function and the quasi-ENO reconstruction, the expansion immediately behind the foot of the shock wave [16] is also resolved. The shock wave is located at about 71% of the chord of the bump.

The distribution of the entropy parameter depicted in Fig. 6.22 shows the features already described in the section on the subsonic test case. The oscillations apparent in the solution obtained with the Barth-Jespersen limiter function on the quadrilateral grid are probably due to the incomplete convergence. For both triangular and quadrilateral grids, the variation of the entropy parameter reveals that the numerical errors are quite large since the non-physical increases in entropy are approximately of the same magnitude as the physical increase through the shock wave.

Finally, the convergence history for the Barth-Jespersen and Venkatakrishnan limiter functions on the quadrilateral grid is depicted in Fig. 6.23. The convergence history

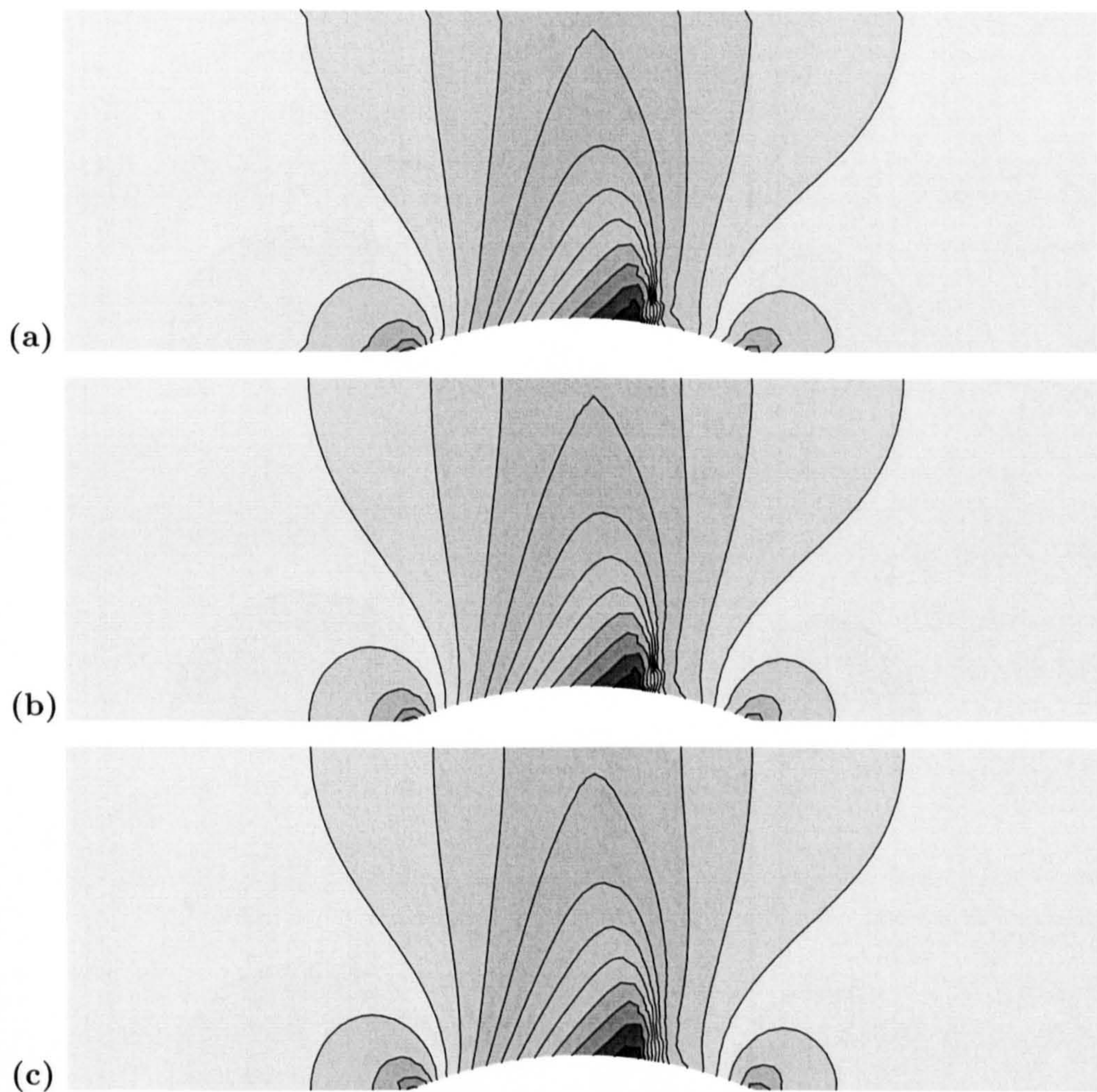


Figure 6.19: Contours of pressure for second-order solutions with (a) Barth-Jespersen limiter function (0.355,0.850;15), (b) Venkatakrishnan limiter function (0.355,0.850;15), and (c) Ollivier-Gooch reconstruction (0.355,0.850;15) on triangular grid for transonic bump flow.

of the quasi-ENO reconstruction is virtually indistinguishable to that obtained with the Venkatakrishnan limiter function and therefore not shown for the sake of clarity. The Barth-Jespersen limiter function leads to stalled convergence. For this reason, the Barth-Jespersen limiter function is not considered further in the present work.

The use of the Venkatakrishnan limiter function was typically about 2% more expensive in terms of CPU time per iteration than the use of the Barth-Jespersen limiter function and the quasi-ENO reconstruction was typically roughly 12% cheaper than the Barth-Jespersen limiter function. Despite this advantage of the quasi-ENO reconstruction, it is not further considered in the present work because of the difficulties in

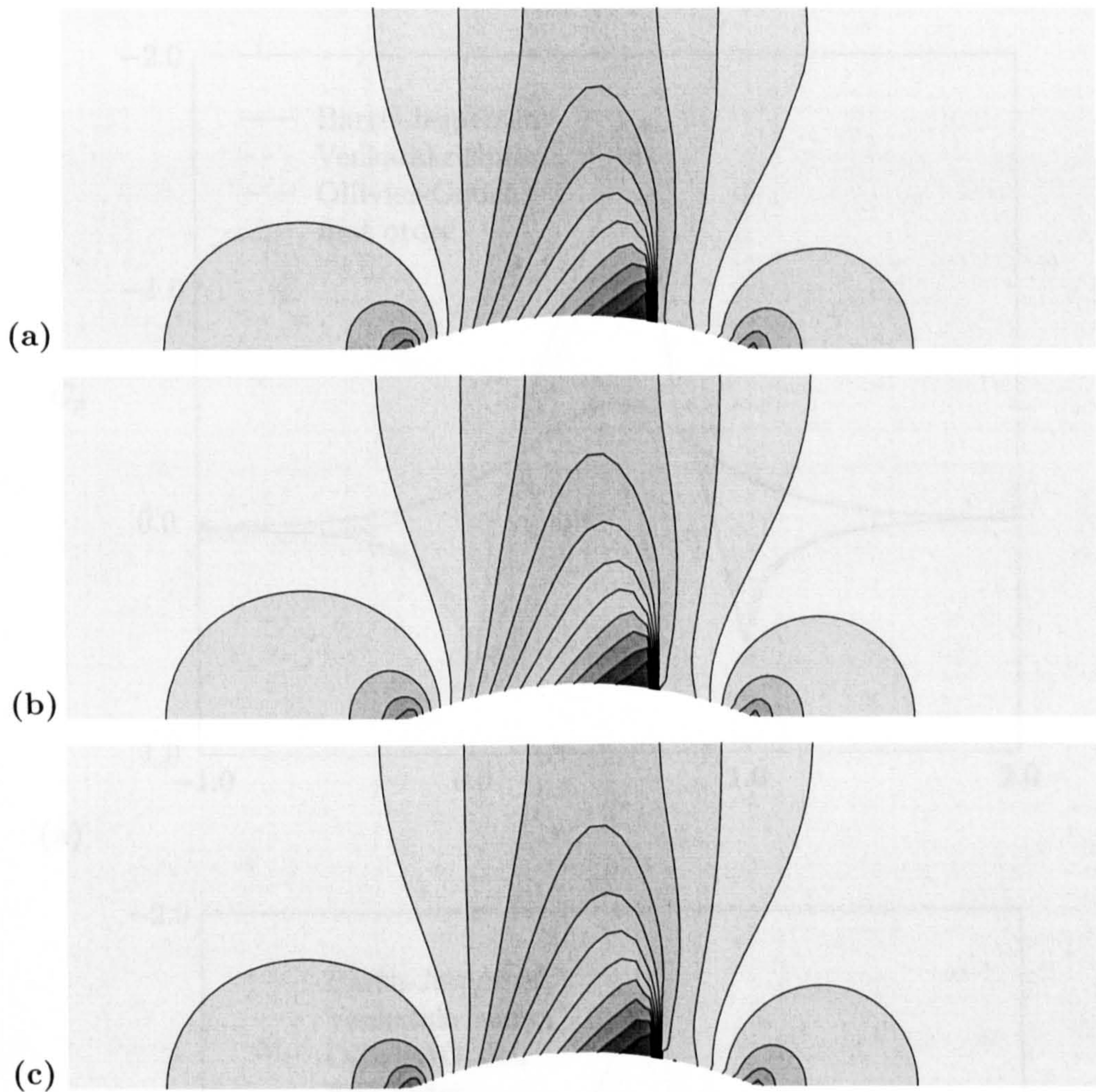


Figure 6.20: Contours of pressure for second-order solutions with (a) Barth-Jespersen limiter function (0.340,0.825;15), and (b) Venkatakrishnan limiter function (0.340,0.825;15), (c) Ollivier-Gooch reconstruction (0.340,0.825;15) on quadrilateral grid for transonic bump flow.

constructing an accurate Laplacian at boundaries. More accurate discretisations of second derivatives near boundaries are possible to achieve, but will destroy the advantage of less computational time per iteration.

Effect of Diagonal Edges in Triangulated Quadrilateral Grids. The effect of the diagonal edges introduced into a quadrilateral grid is investigated by computing the transonic flow over the circular arc bump using the Venkatakrishnan limiter. The grids are identical to those used for the equivalent comparison for subsonic flow and are shown in Fig. 6.8. Again, both median and containment dual control-volumes are used.

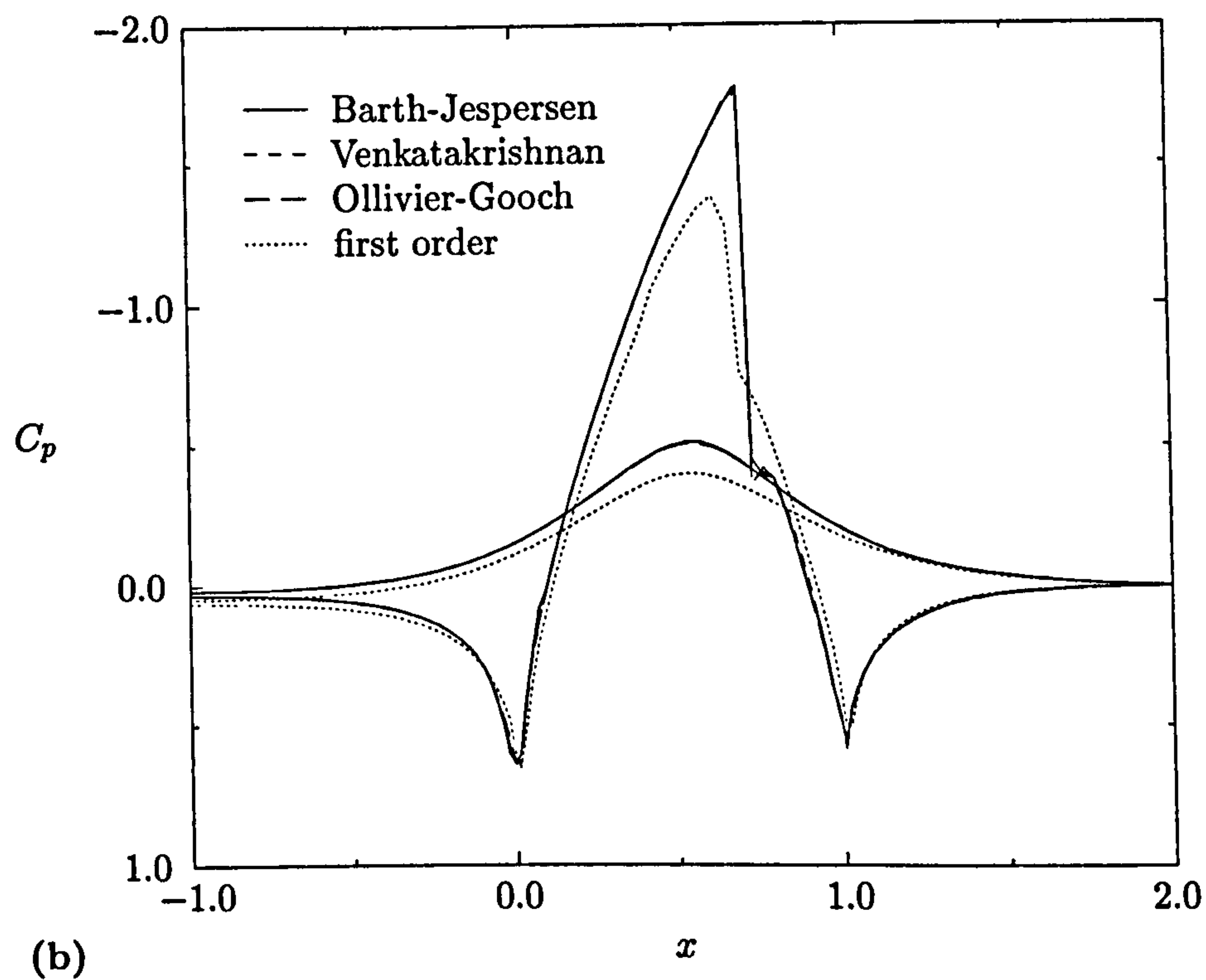
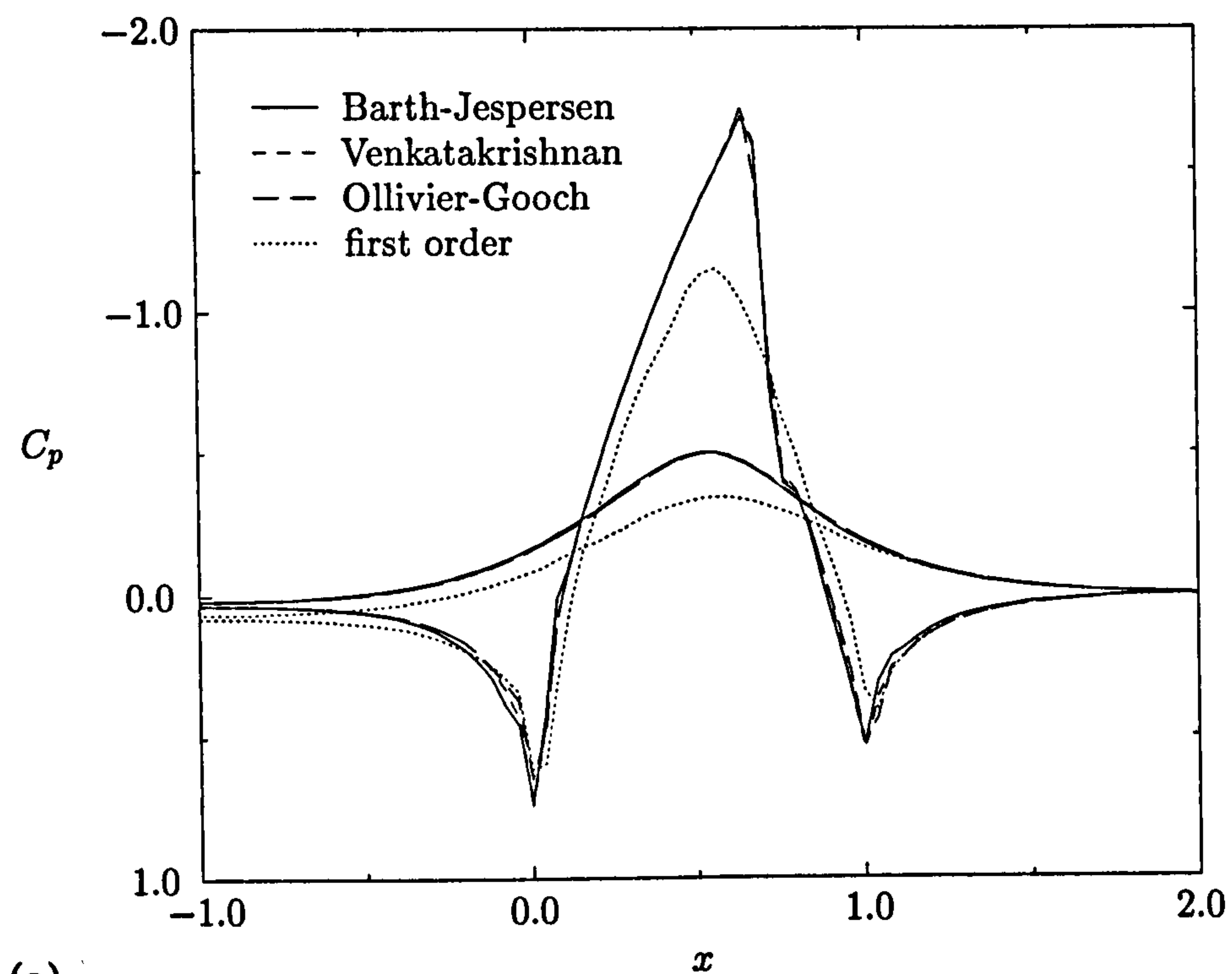


Figure 6.21: Comparison of pressure coefficient for second-order solutions on (a) triangular grid and (b) quadrilateral grid for transonic bump flow.

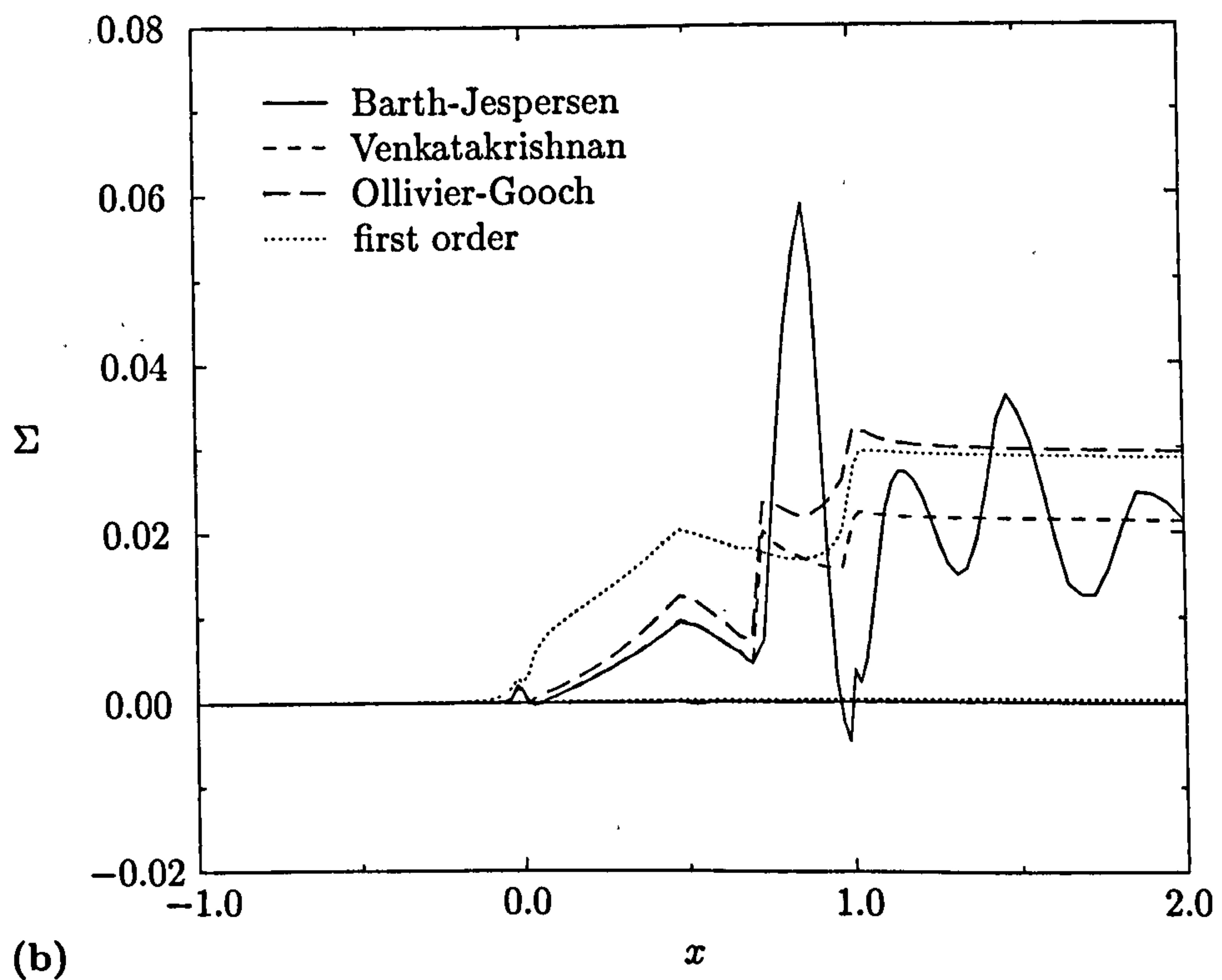
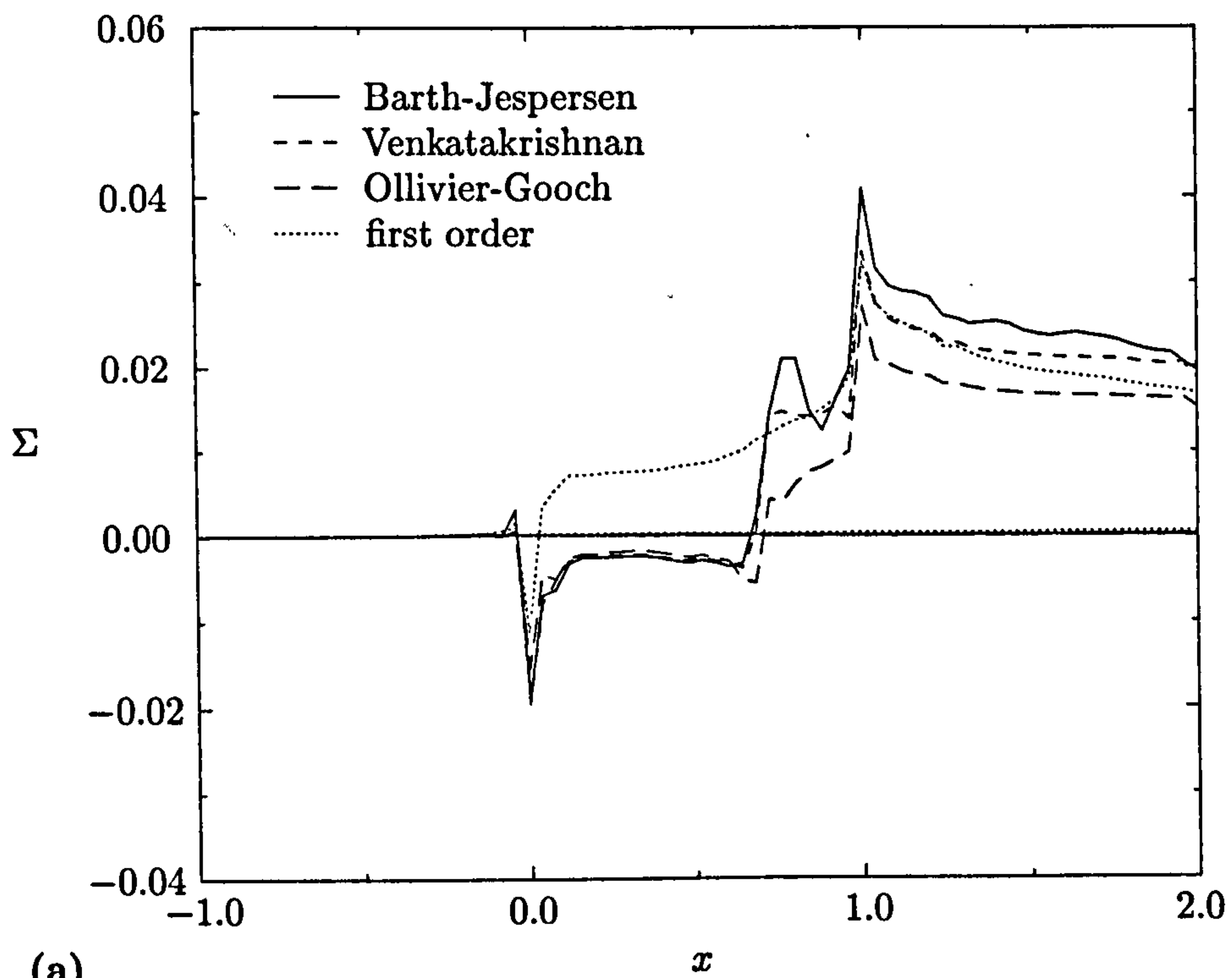


Figure 6.22: Comparison of entropy parameter for second-order solutions on (a) triangular grid and (b) quadrilateral grid for transonic bump flow.

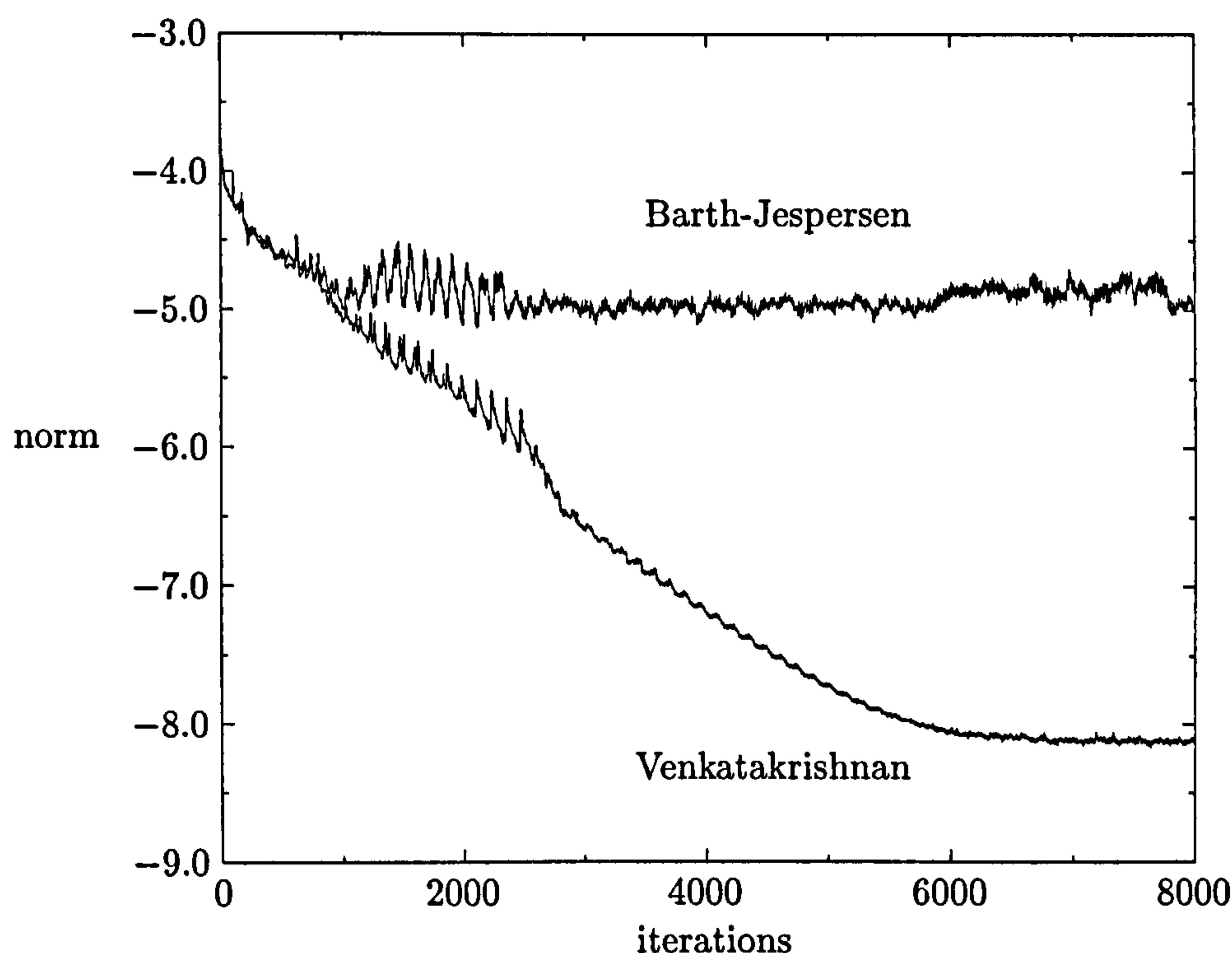


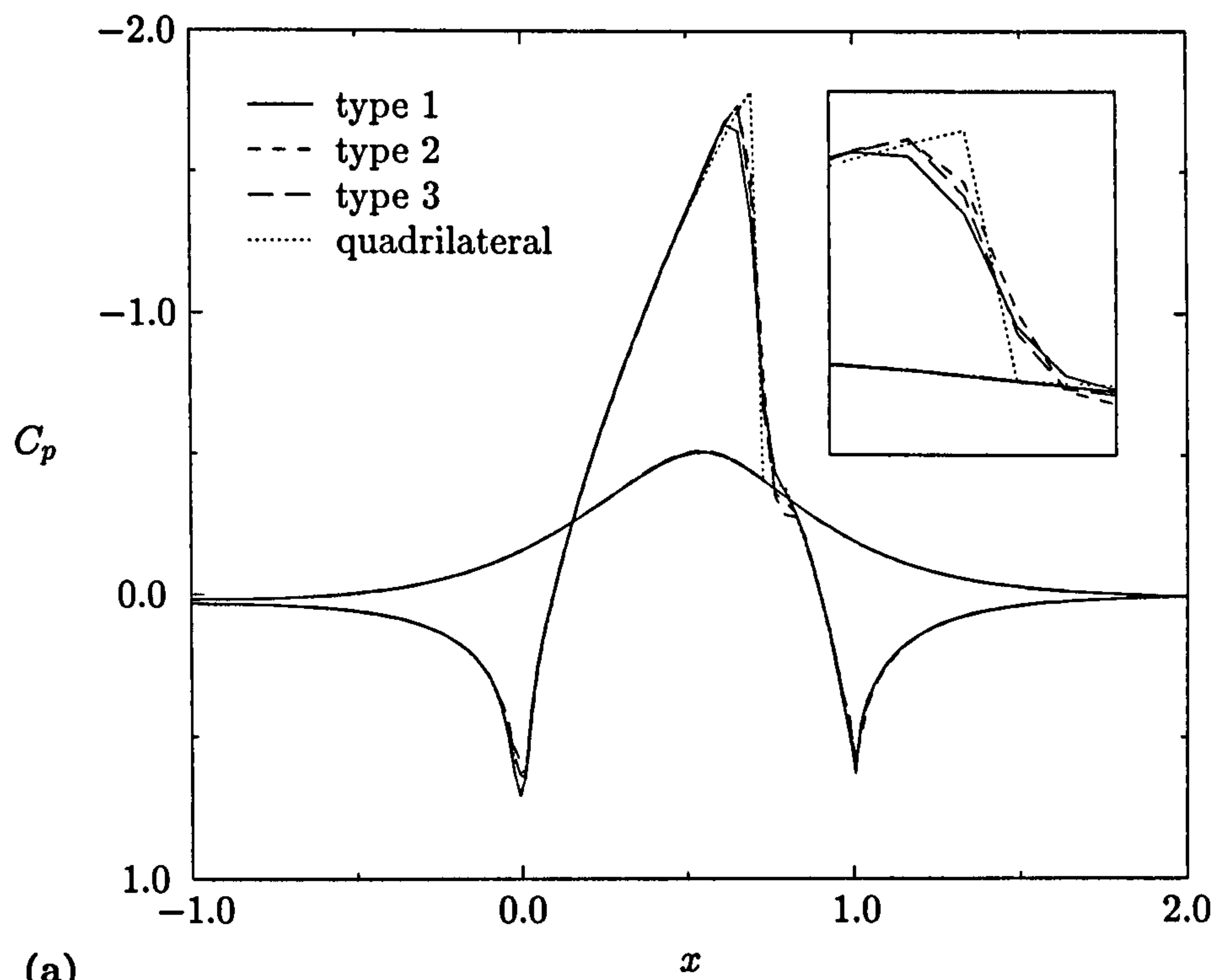
Figure 6.23: Convergence history for second-order schemes with Barth-Jespersen and Venkatakrishnan limiter functions on quadrilateral grid for transonic bump flow.

The pressure coefficients are shown in Fig. 6.24. The insets display the variation of the pressure coefficient in the immediate vicinity of the shock wave in more detail. For comparison, the results for the quadrilateral grid are also shown. For the median dual control-volumes, the shock wave is more heavily smeared. For the containment dual control-volumes, the differences are virtually negligible.

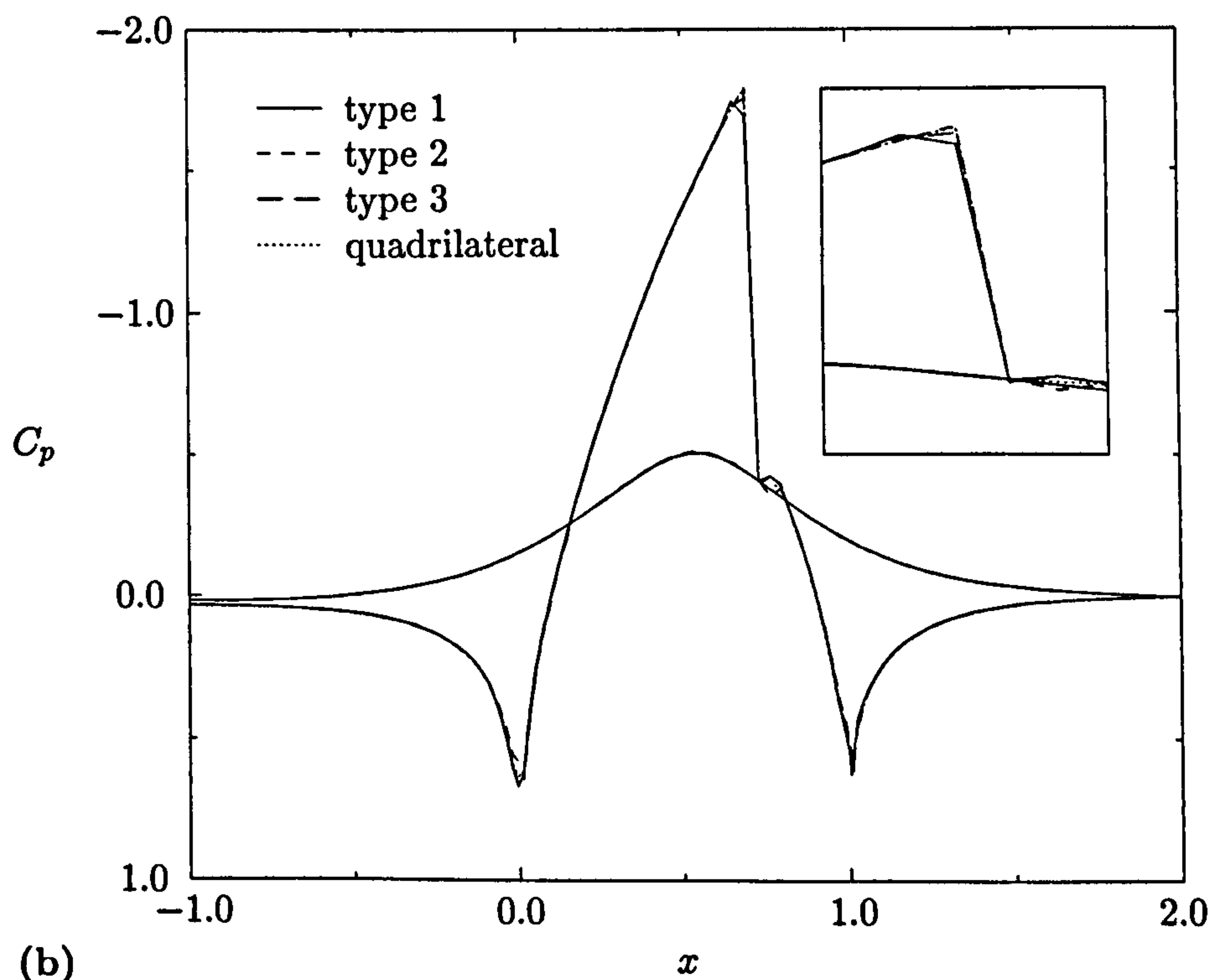
The variation of the entropy parameter shown in Fig. 6.25 indicates that no clear conclusions can be drawn about which triangular grid leads to the largest numerical errors. It is interesting to note the spikes in the entropy parameter at the position of the shock wave which were not visible in the previously shown second-order accurate results. Pike [8] and Salas and Iollo [10] demonstrated that these spikes have a physical counterpart.

Assessment of Multigrid Acceleration. The same sequence of grids is used as for the subsonic case.

The results obtained with the first-order scheme are summarised in Table 6.5. As



(a)



(b)

Figure 6.24: Comparison of pressure coefficient for (a) median dual and (b) containment dual for second-order solutions with Venkatakrishnan limiter function on triangulated quadrilateral grids for transonic bump flow.

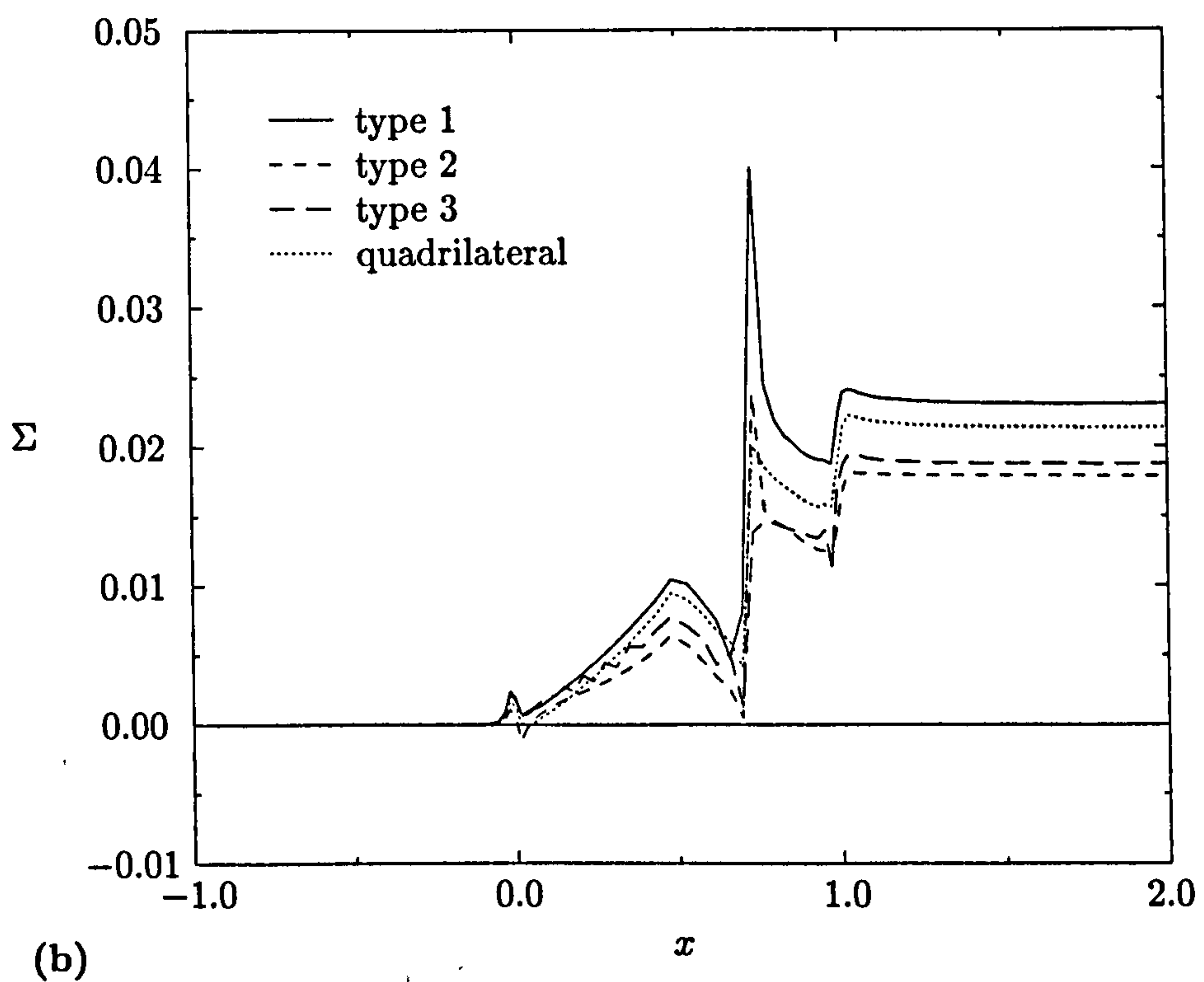
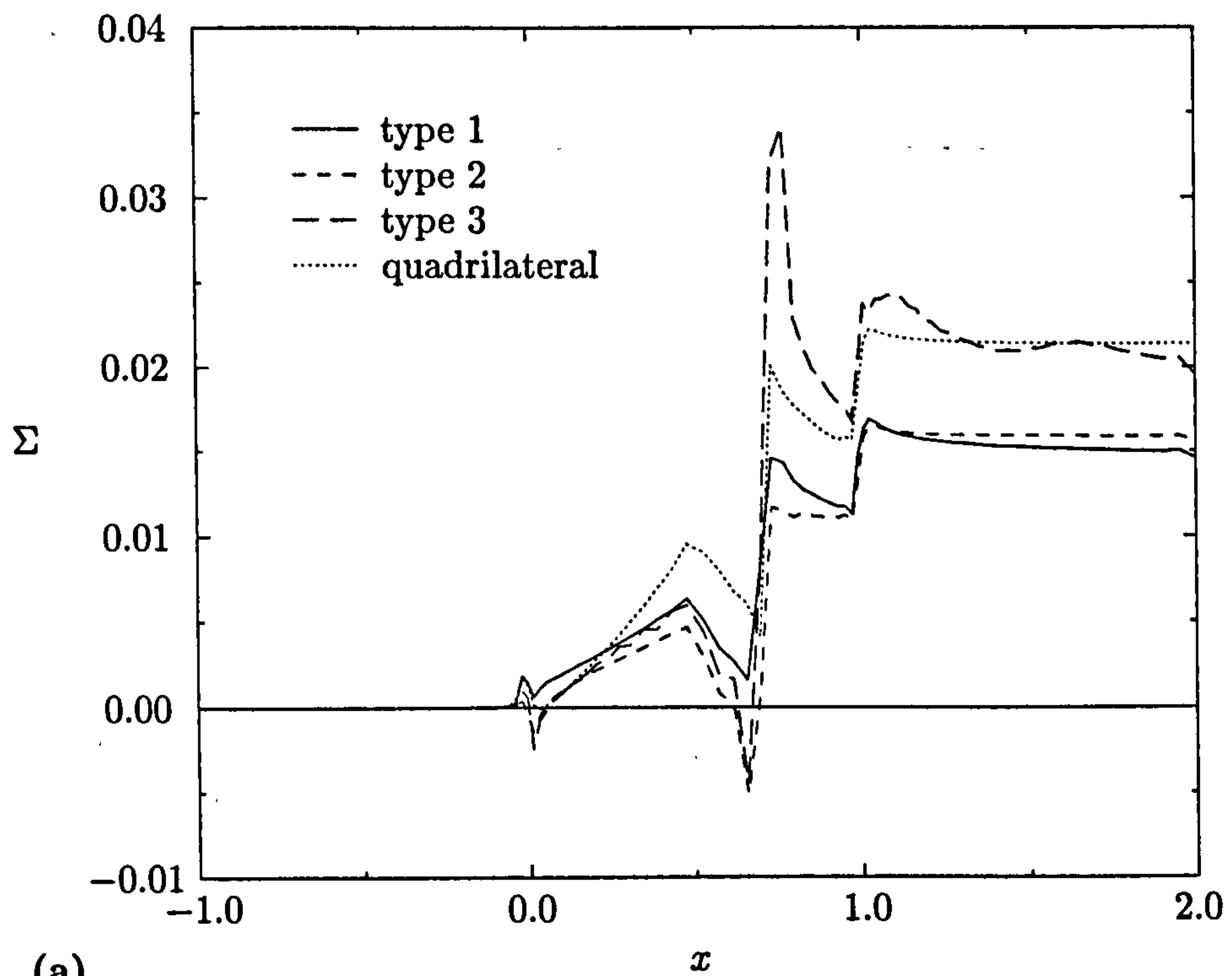


Figure 6.25: Comparison of entropy parameter for (a) median dual and (b) containment dual for second-order solutions with Venkatakrishnan limiter function on triangulated quadrilateral grids for transonic bump flow.

Table 6.5: Summary of first-order results for multigrid scheme applied to transonic bump flow.

level	triangular grid			quadrilateral grid		
	ACR	cycles	SCT	ACR	cycles	SCT
1	0.994	1687	15.00	0.994	1613	6.95
2	0.926	129	11.25	0.929	139	3.18
3	0.836	56	2.60	0.875	76	1.86
4	0.696	28	1.33	0.796	45	1.09
5	0.631	22	1.00	0.780	41	1.00

Table 6.6: Summary of second-order results for multigrid scheme applied to transonic bump flow.

level	triangular grids			quadrilateral grids		
	ACR	cycles	SCT	ACR	cycles	SCT
1	0.996	2662	11.87	0.998	5707	19.52
2	0.942	169	3.41	0.960	257	4.04
3	0.871	73	1.51	0.904	103	1.65
4	0.810	48	1.00	0.855	67	1.22
5	0.817	50	1.02	0.844	61	1.00

with the subsonic case, the number of iterations required to converge is roughly identical for single-grid calculations. The speed-up obtained by the multigrid scheme on triangular grids is again larger than that on quadrilateral grids. The corresponding convergence history is shown in Fig. 6.26.

The results obtained with the multigrid scheme applied to the second-order discretisation are listed in Table 6.6. In contrast to the subsonic case, the quadrilateral grid requires more iterations to converge on a single grid. As a result, a larger speed-up is obtained on the quadrilateral grid than on the triangular grid, despite the fact that the ACRs on the triangular grids are lower than on the quadrilateral grids. For the triangular grid, the use of 5 grid levels did not result in a further improvement over 4 grid levels.

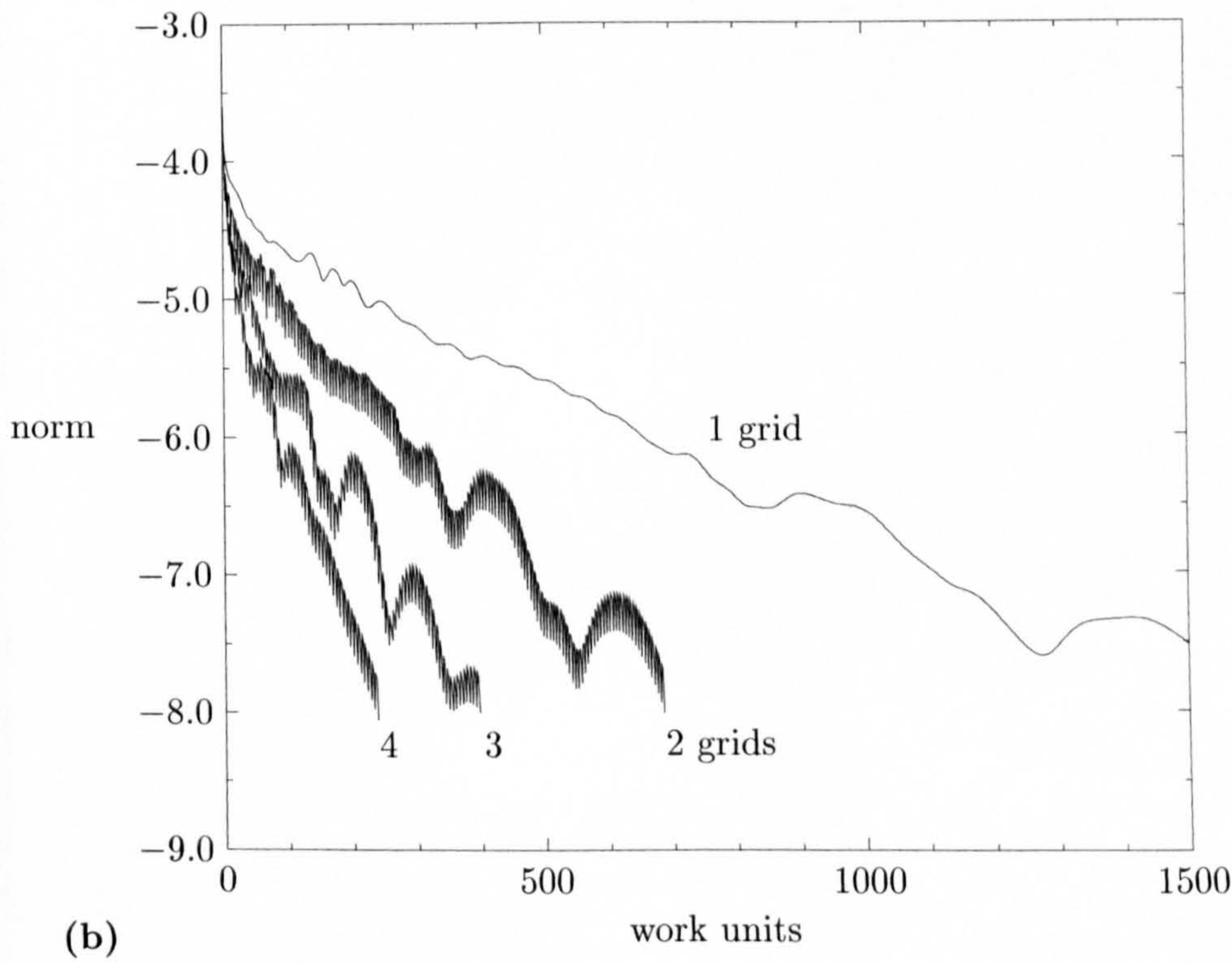
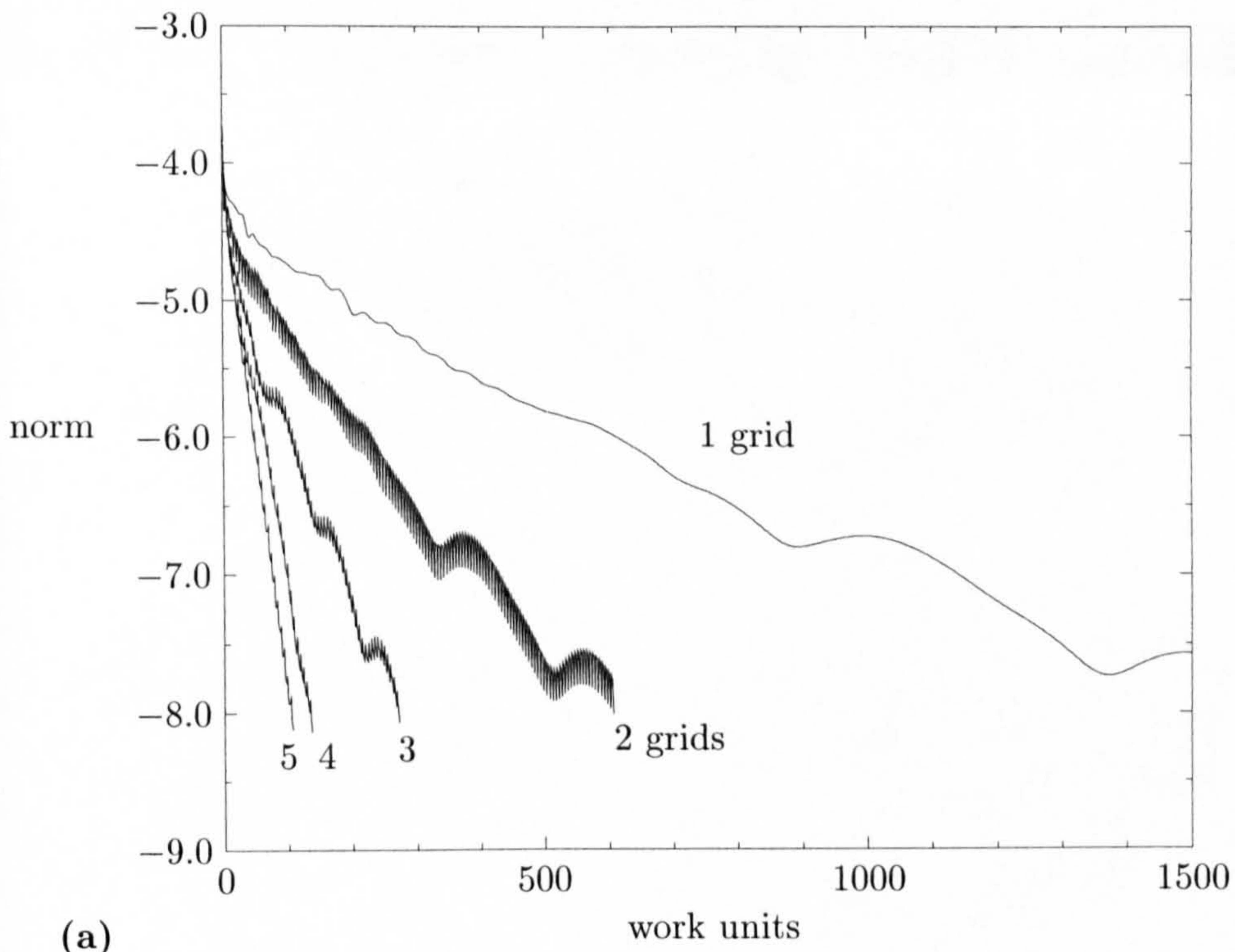


Figure 6.26: Comparison of multigrid convergence for first-order schemes on (a) triangular grid and (b) quadrilateral grid for transonic bump flow.

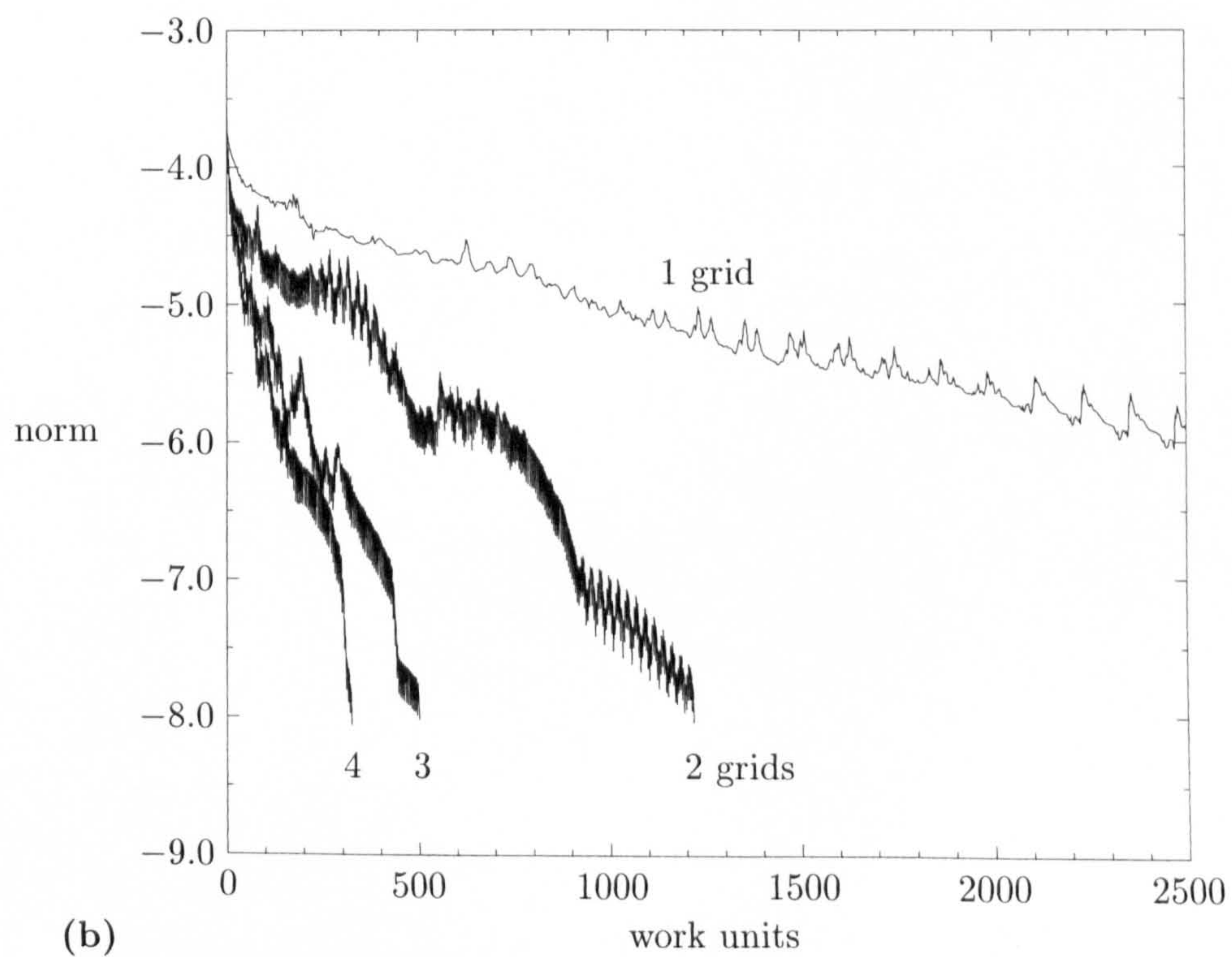
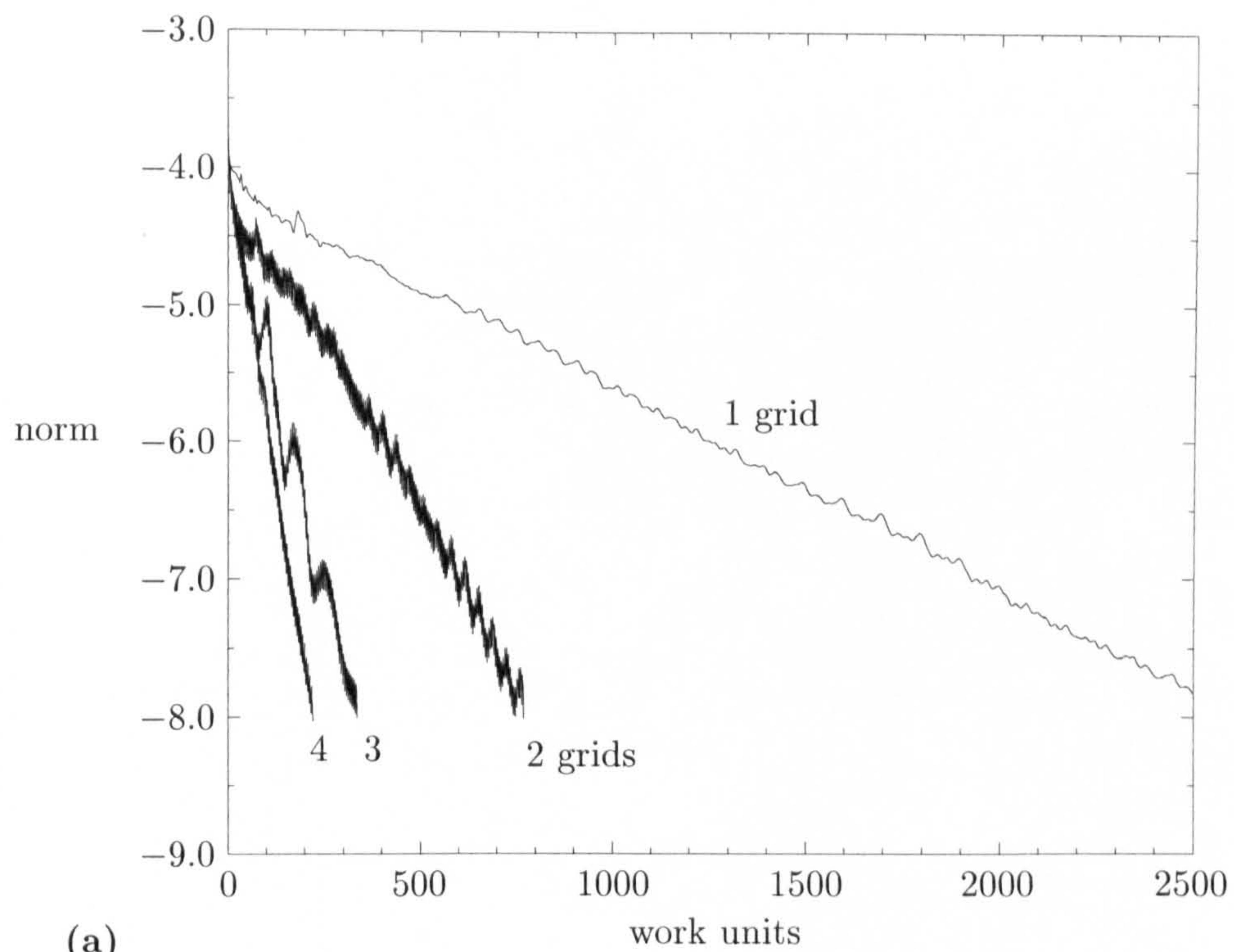


Figure 6.27: Comparison of multigrid convergence for second-order schemes on (a) triangular grid and (b) quadrilateral grid for transonic bump flow.

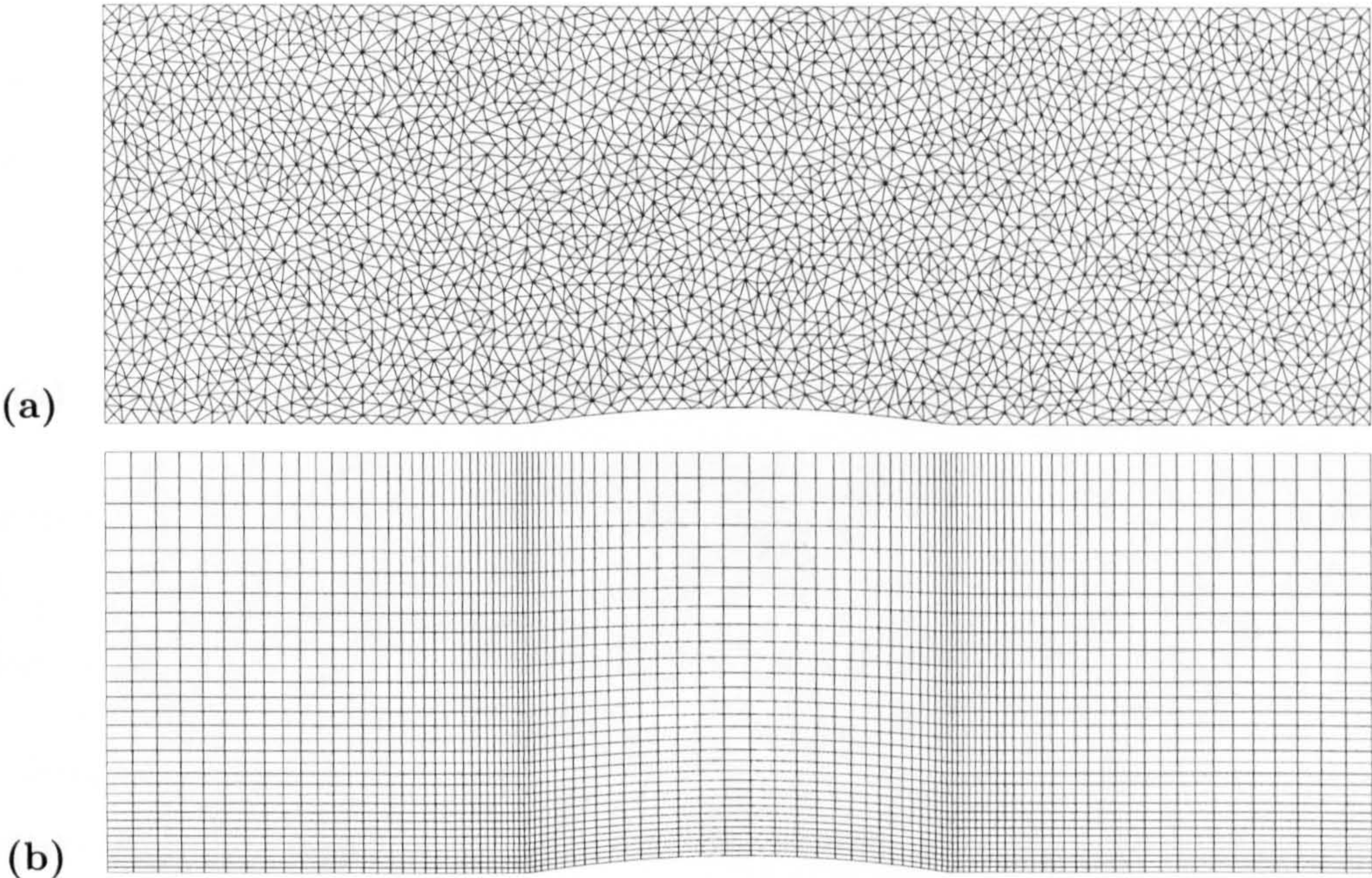


Figure 6.28: (a) triangular grid and (b) quadrilateral grid used for supersonic bump flow calculations.

Table 6.7: Summary of grid characteristics used in computational study for supersonic bump flow calculations.

grid	vertices	edges	triangles	quadrilaterals
triangular	3003	8818	5816	–
quadrilateral	3072	6016	–	2945

6.3.3 Supersonic Case

The supersonic case is specified by an inlet Mach number of $M_0 = 1.4$ and a bump height of $h = 0.04$. These conditions give rise to two oblique shock waves at the leading and trailing edges of the bump. The shock wave from the leading edge is reflected from the top wall and intersects the shock wave from the trailing edge, with a further reflection at the bottom wall and interaction.

The grids depicted in Fig. 6.28 are employed. The corresponding grid characteristics are listed in Table 6.7. Once again, they have approximately the same number of vertices and hence unknowns.

Comparison of Triangular and Quadrilateral Grids. The pressure contours for

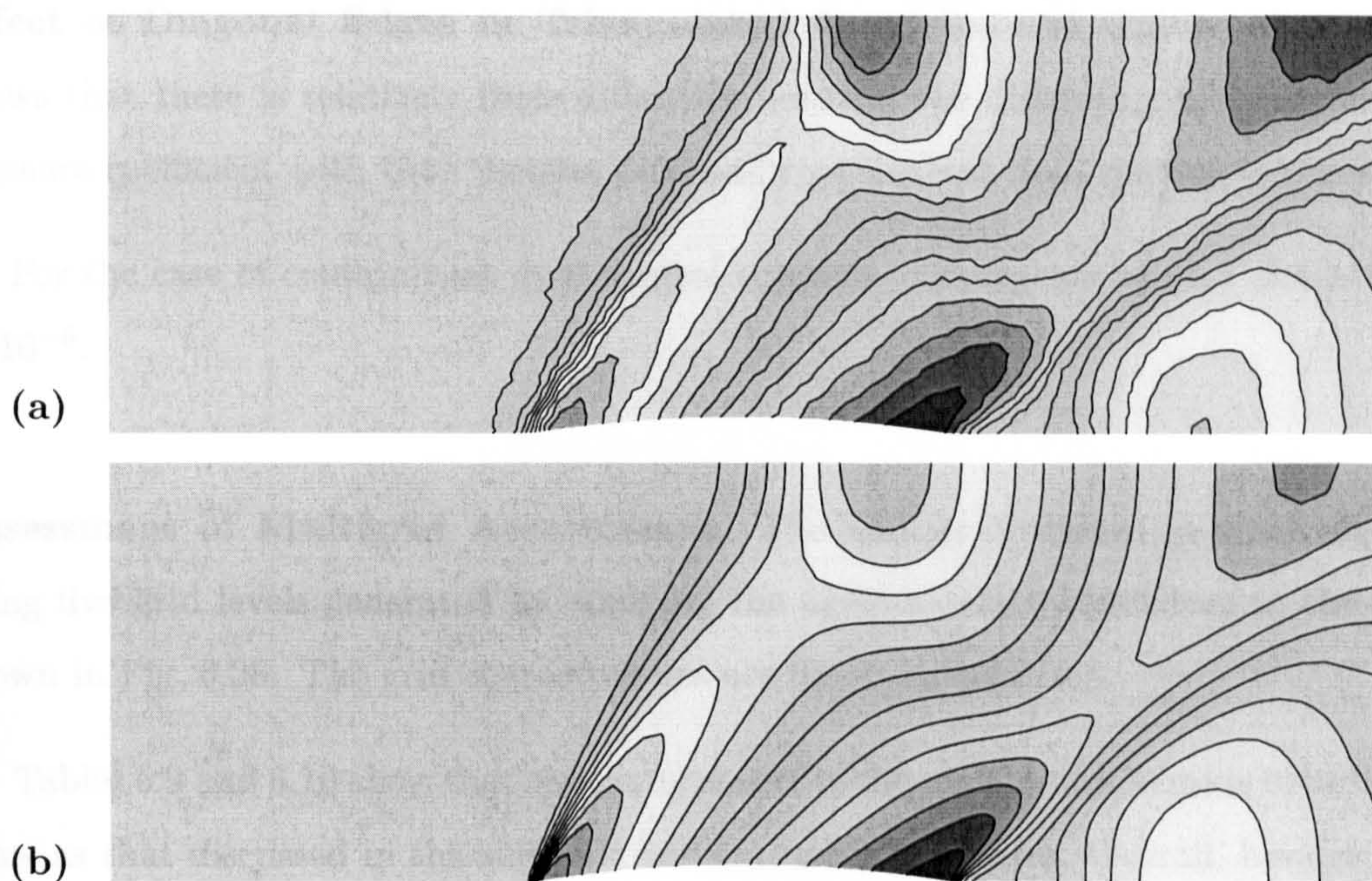


Figure 6.29: Contours of pressure for first-order solutions on (a) triangular grid (0.529,1.059;15) and (b) quadrilateral grid (0.514,1.060;15) for supersonic bump flow.

the first-order accurate scheme are shown in Fig. 6.29, which reveals that the shock waves are heavily smeared. For the quadrilateral grid, the shocks exhibit high spreading rates due to misalignment with the grid lines. Although the shock waves are captured less sharply on the triangular grid, the spreading rates are lower.

The use of a second-order accurate scheme leads to a large improvement in the capturing of the shock waves, particularly of the reflections, as may be seen in Fig. 6.30.

These observations are confirmed by the line plots of the pressure coefficients in Fig. 6.31. For the first-order accurate calculation, the shock reflection at the upper wall is clearly better resolved on the triangular grid. For the second-order accurate results, the quadrilateral grid leads to sharper shock waves and reflections.

The variation of the entropy parameter depicted in Fig. 6.32(a) again demonstrates that the shock wave at the upper wall is poorly captured for the first-order accurate results. The second-order accurate results, shown in Fig. 6.32(b), exhibit a large spike at the leading edge and the already discussed peak at the crest of the bump on the quadrilateral grids. The entropy increase due to the shock reflection on the lower wall is clearly visible on the quadrilateral grid only.

Effect of Diagonal Edges in Triangulated Quadrilateral Grids. Figure 6.33 shows that there is relatively little difference between the different grid types for the pressure coefficient with both median dual and containment dual control volumes.

For the case of containment dual control volumes, convergence stalled at $CM(\rho) = 1 \cdot 10^{-6}$.

Assessment of Multigrid Acceleration. The multigrid scheme is again assessed using five grid levels generated by applying the agglomeration procedure to the grids shown in Fig. 6.28. The grid characteristics are listed in Table 6.8.

Tables 6.9 and 6.10 show that the performance of the multigrid scheme is broadly the same as that discussed in the subsonic and transonic test cases. Overall, however, the speed-ups are much lower and the calculations on more than three grid levels diverged. For the second-order scheme on the quadrilateral grid, the use of three grid levels lead to a slight worsening of the convergence rate compared to that for two grid levels. The convergence histories are shown in Figs. 6.35 and 6.36.

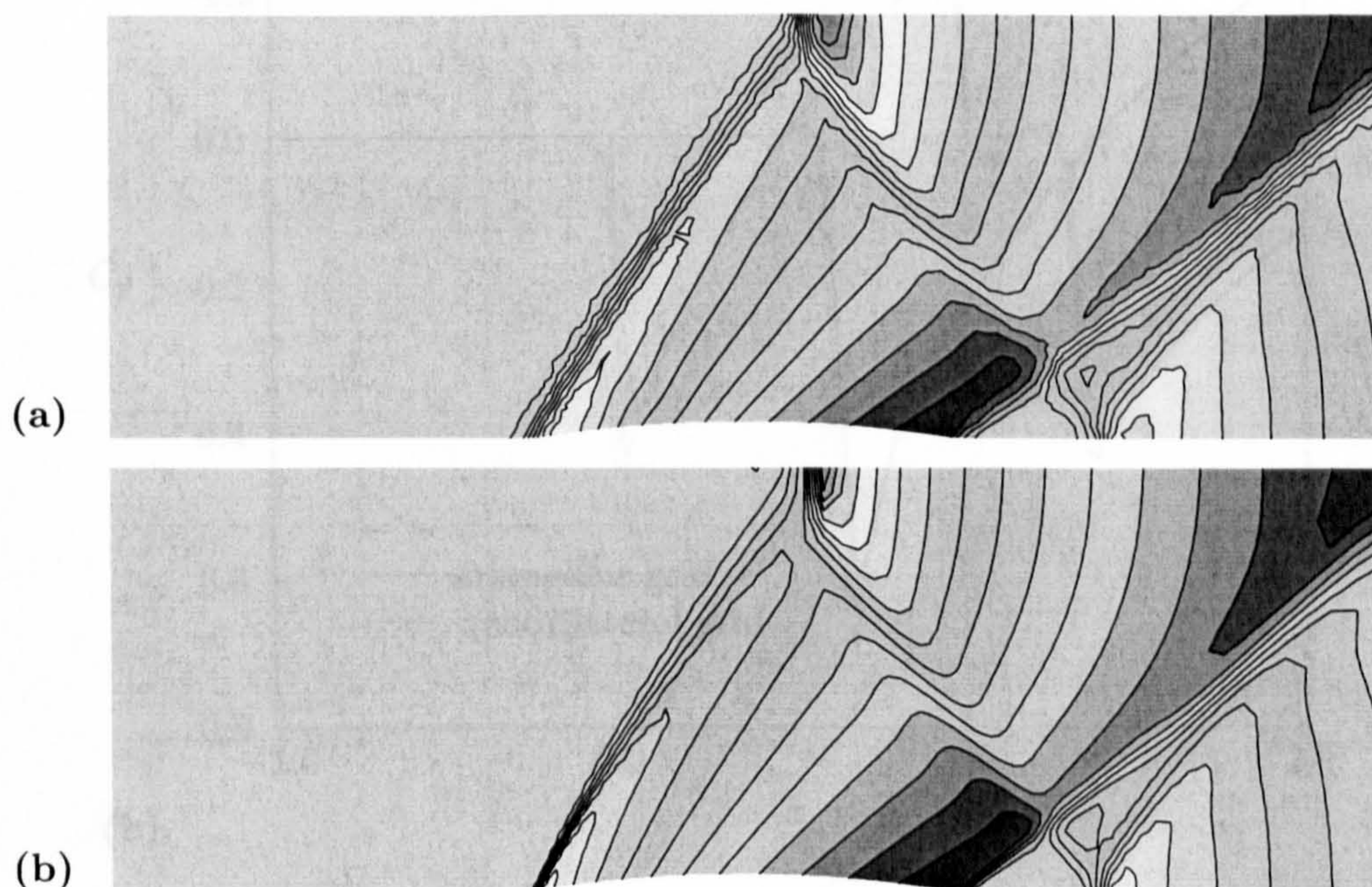


Figure 6.30: Contours of pressure for second-order solutions on (a) triangular grid (0.520,1.275;15) and (b) quadrilateral grid (0.519,1.350;15) for supersonic bump flow.

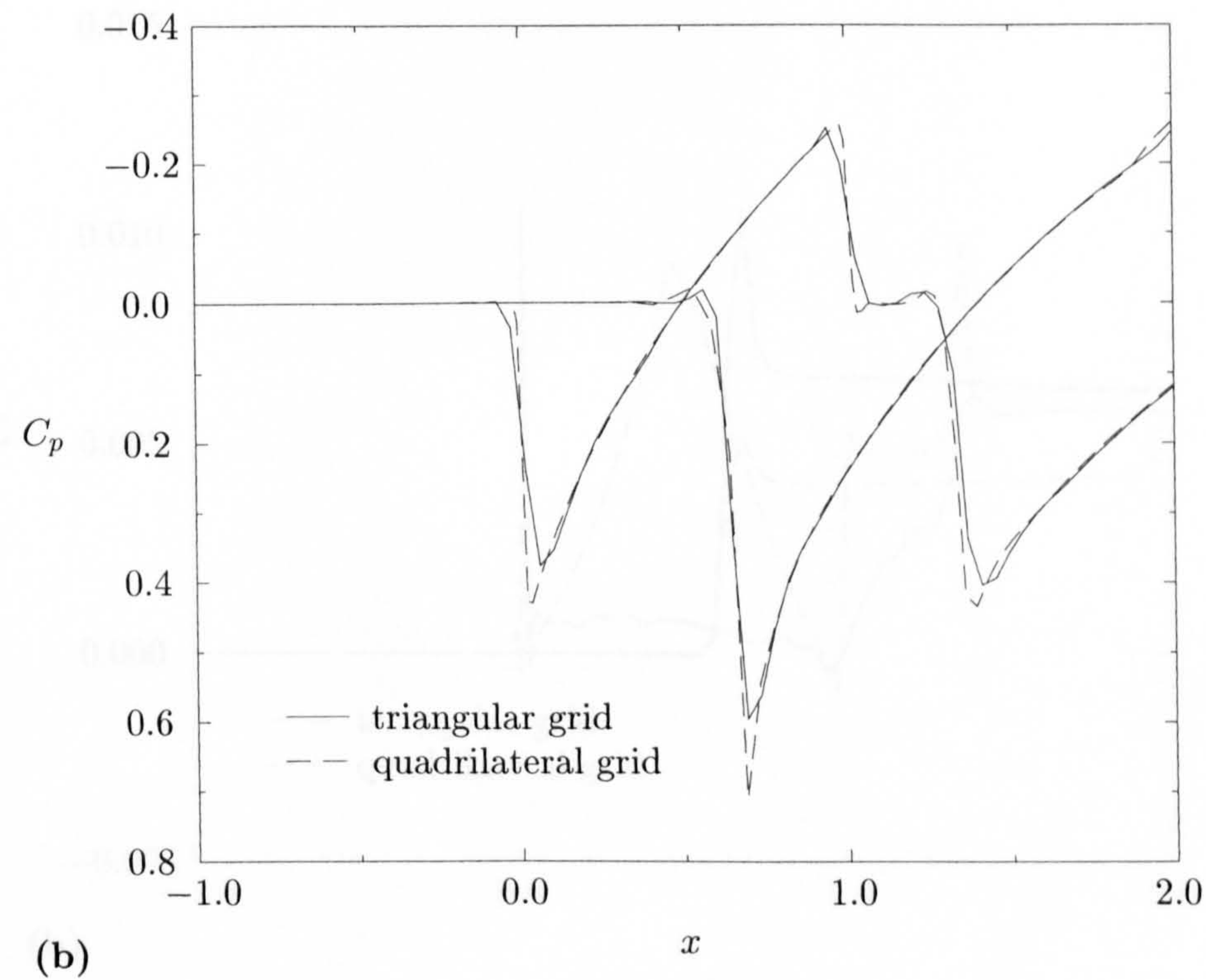
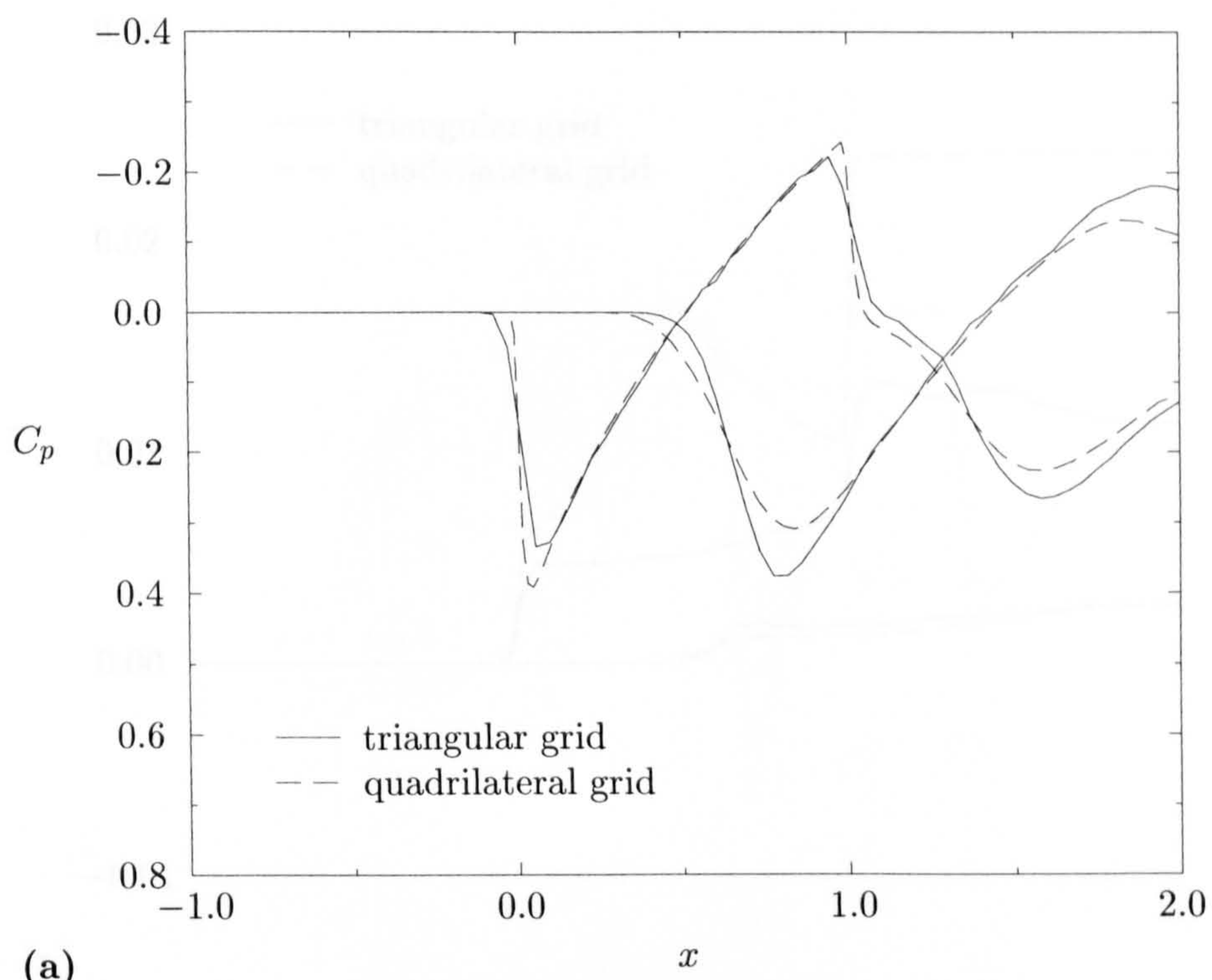


Figure 6.31: Comparison of pressure coefficient for (a) first-order solutions and (b) second-order solutions on triangular and quadrilateral grids for supersonic bump flow.

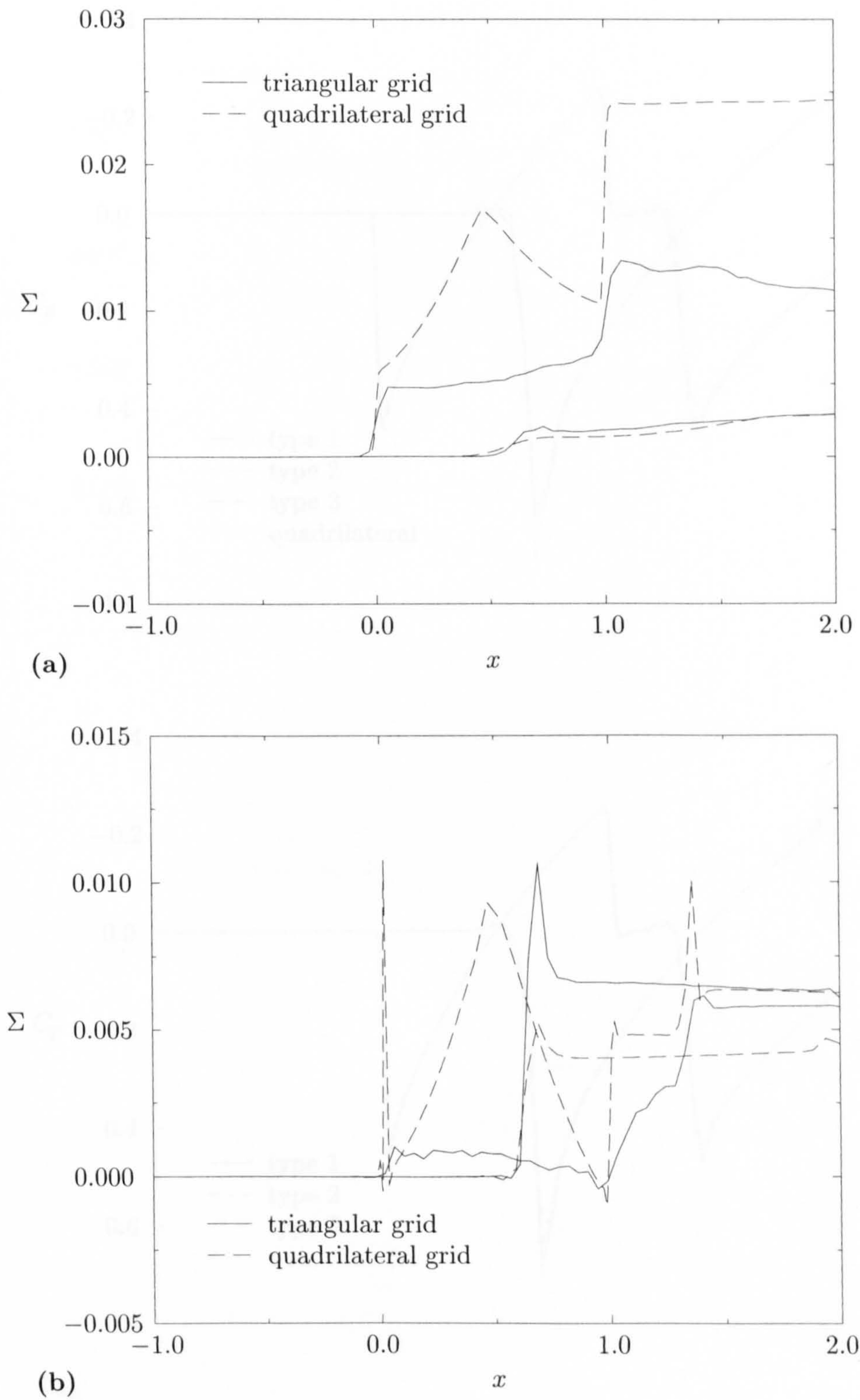


Figure 6.32: Comparison of entropy parameter for (a) first-order solutions and (b) second-order solutions on triangular and quadrilateral grids for supersonic bump flow.

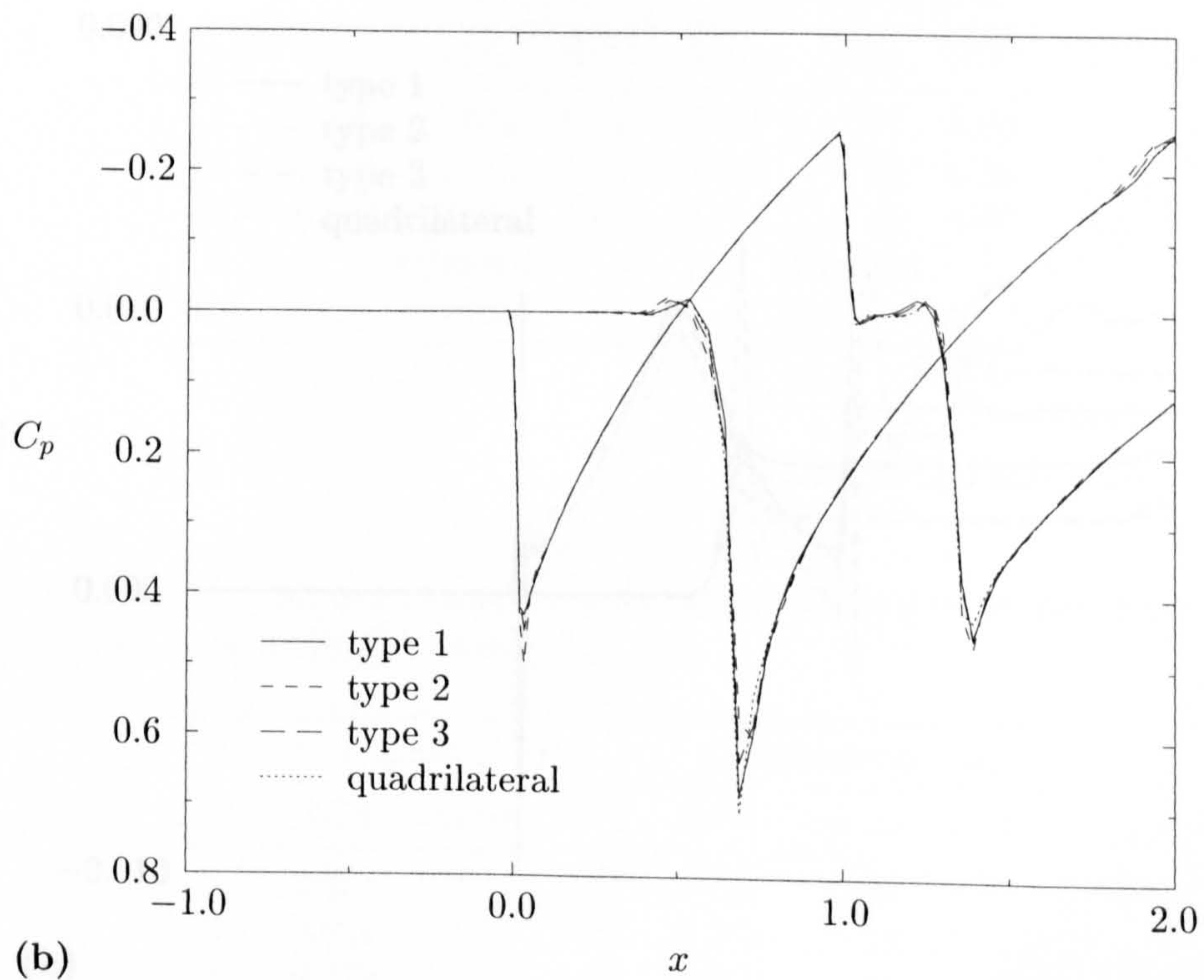
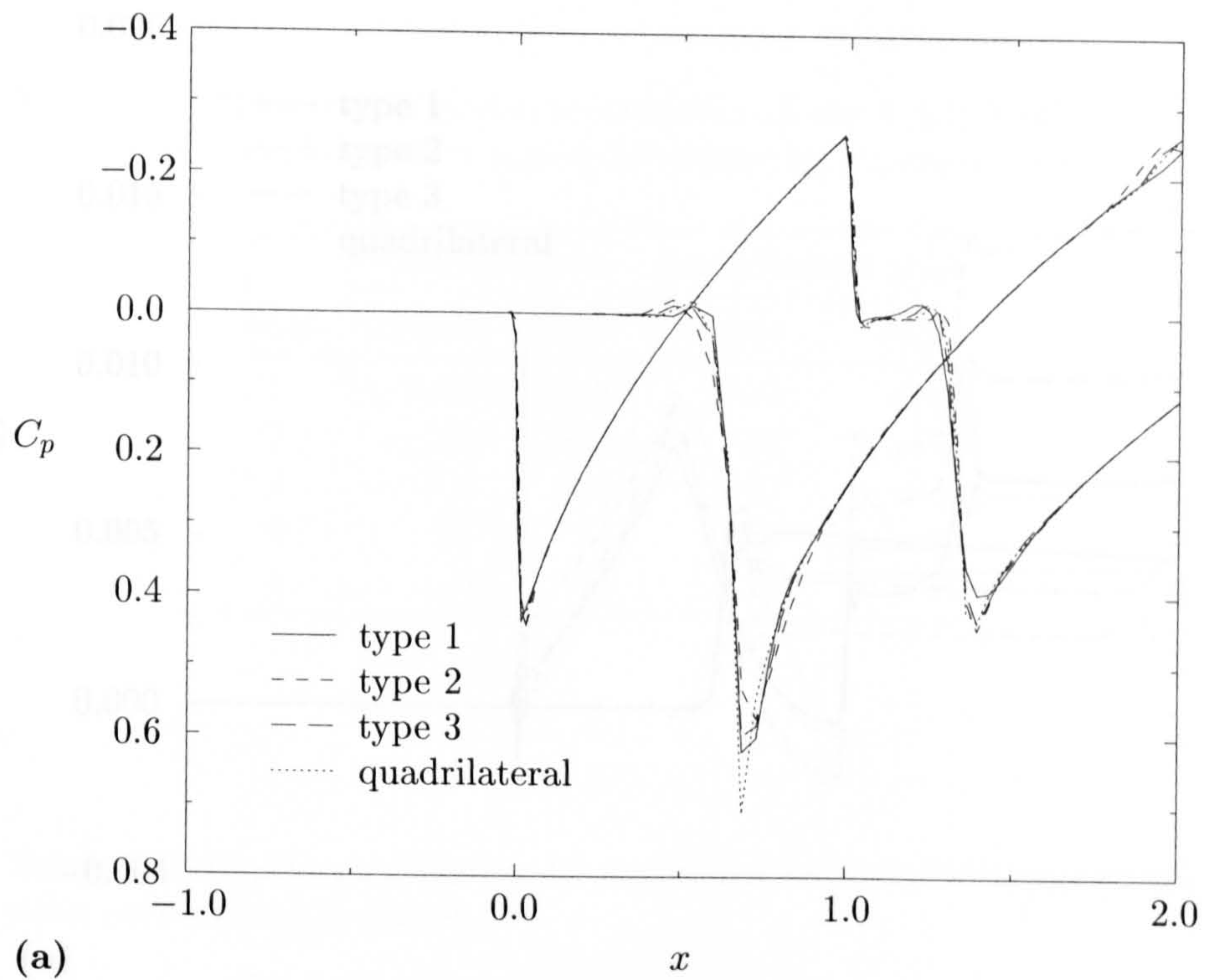


Figure 6.33: Comparison of pressure coefficient for (a) median dual and (b) containment dual for second-order solutions on triangulated quadrilateral grids for supersonic bump flow.

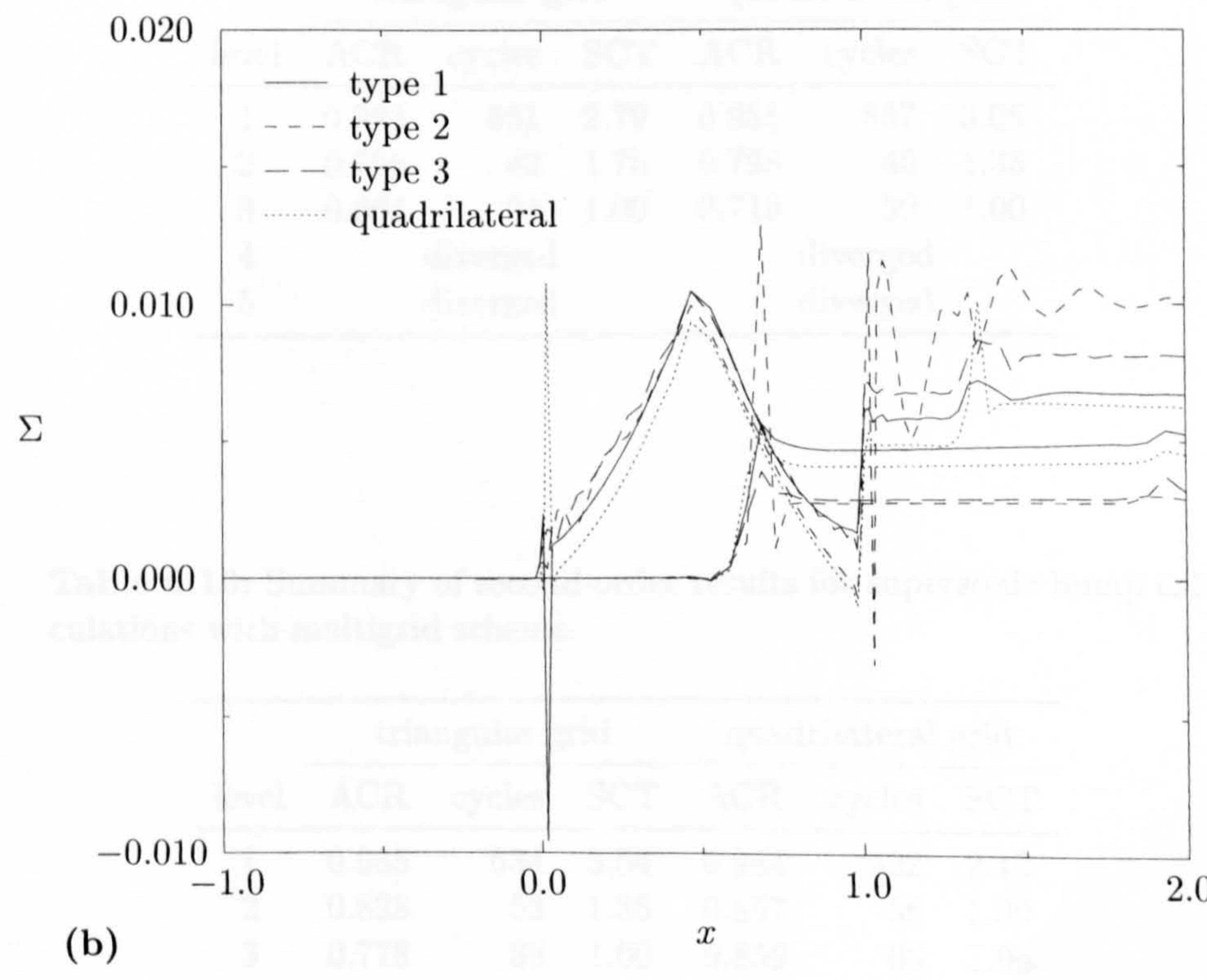
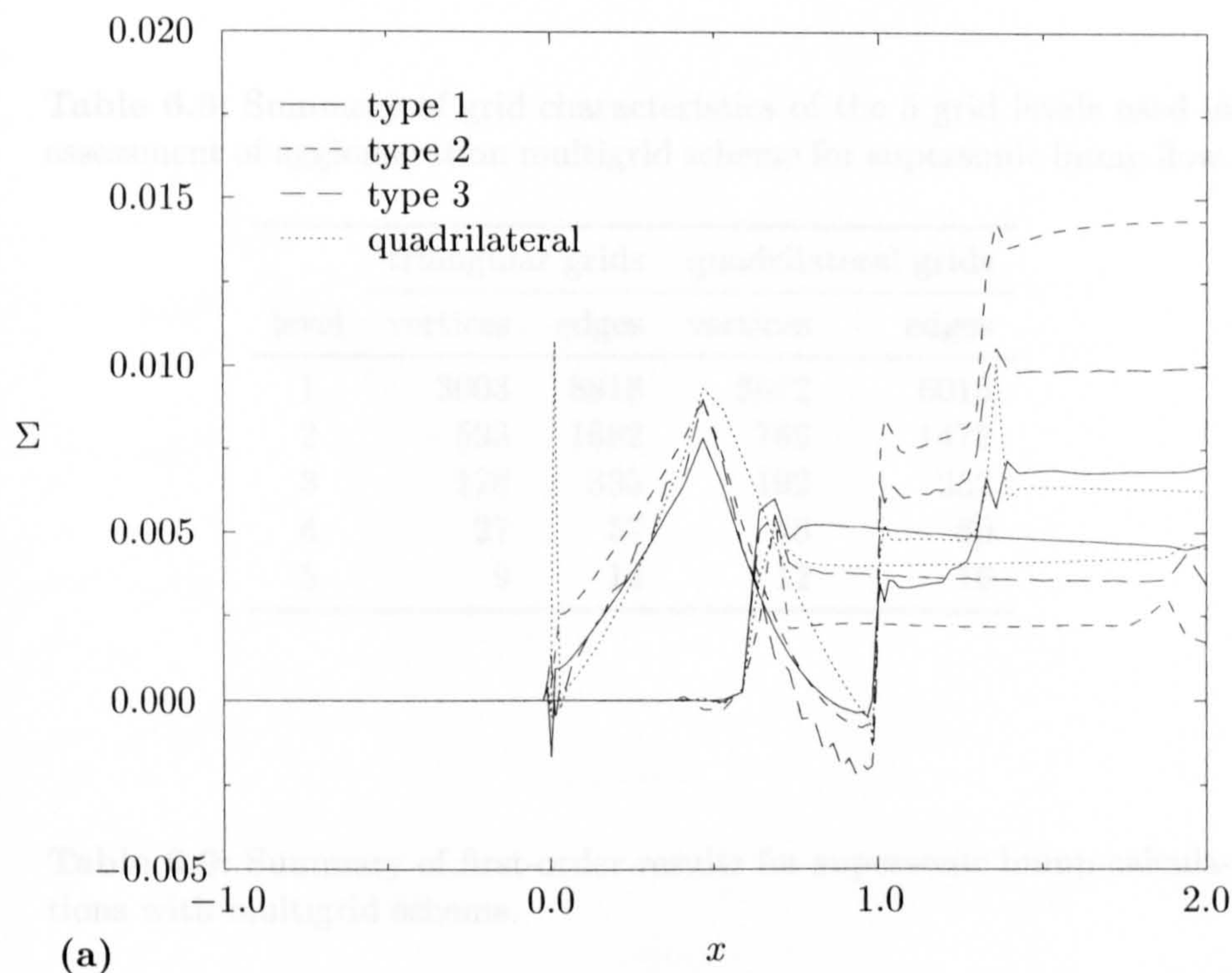


Figure 6.34: Comparison of entropy parameter for (a) median dual and (b) containment dual for second-order solutions on triangulated quadrilateral grids for supersonic bump flow.

Table 6.8: Summary of grid characteristics of the 5 grid levels used in assessment of agglomeration multigrid scheme for supersonic bump flow.

level	triangular grids		quadrilateral grids	
	vertices	edges	vertices	edges
1	3003	8818	3072	6016
2	593	1682	768	1472
3	128	335	192	352
4	27	57	48	80
5	9	14	12	16

Table 6.9: Summary of first-order results for supersonic bump calculations with multigrid scheme.

level	triangular grid			quadrilateral grid		
	ACR	cycles	SCT	ACR	cycles	SCT
1	0.983	551	2.79	0.981	537	3.06
2	0.796	42	1.75	0.798	45	1.33
3	0.664	24	1.00	0.718	30	1.00
4	diverged			diverged		
5	diverged			diverged		

Table 6.10: Summary of second-order results for supersonic bump calculations with multigrid scheme.

level	triangular grid			quadrilateral grid		
	ACR	cycles	SCT	ACR	cycles	SCT
1	0.985	634	3.54	0.984	622	2.12
2	0.828	53	1.35	0.857	66	1.00
3	0.778	39	1.00	0.859	68	1.06
4	diverged			diverged		
5	diverged			diverged		

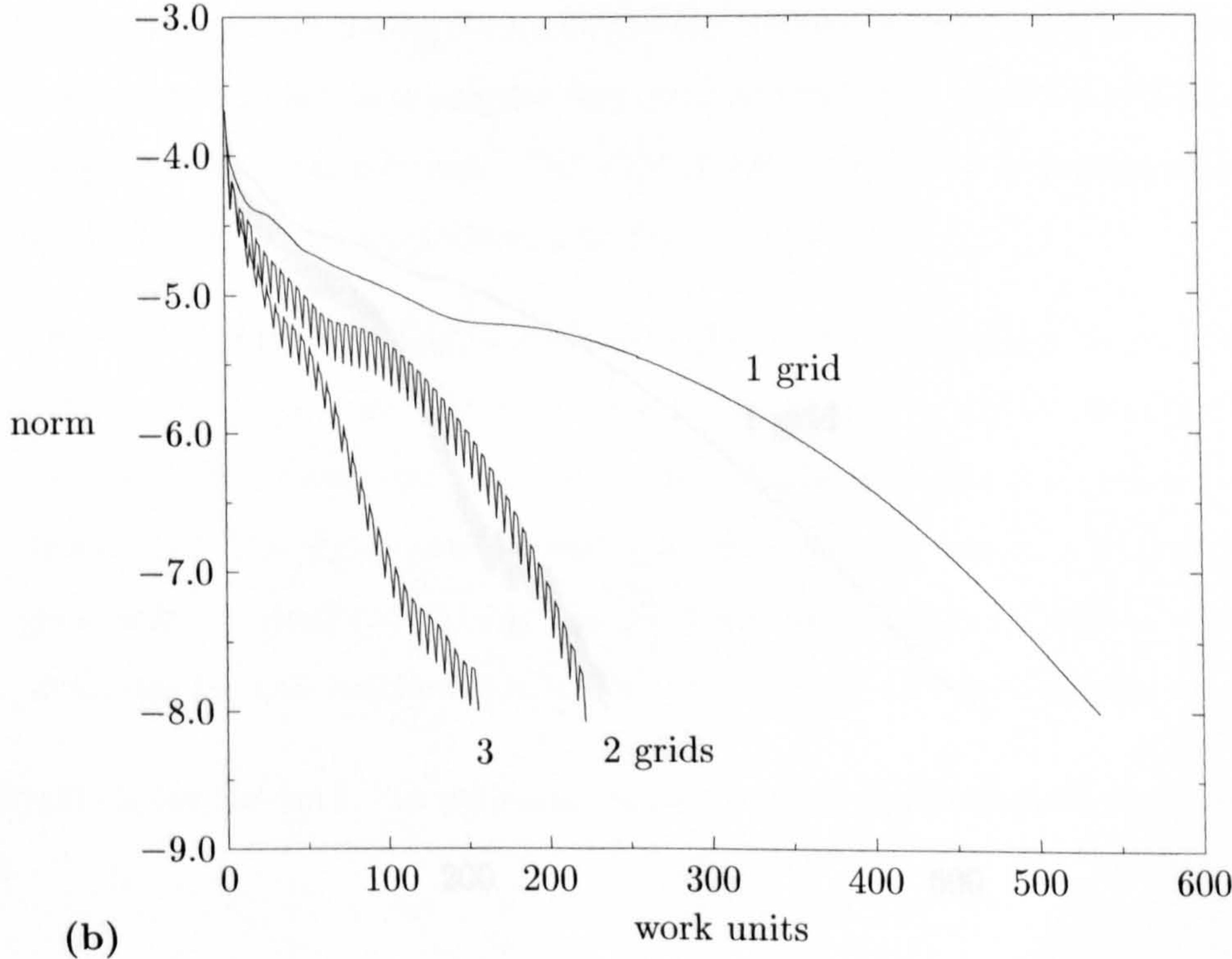
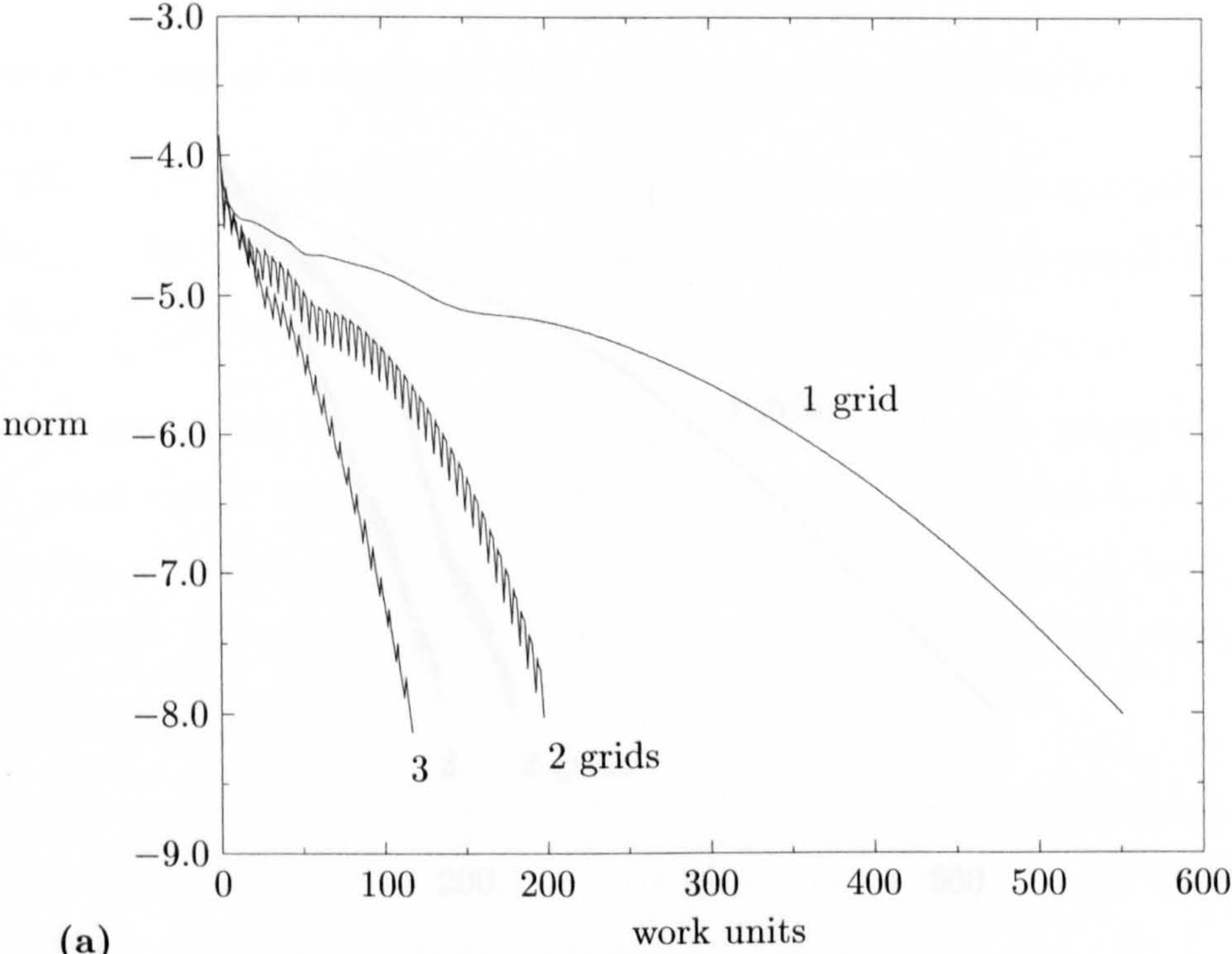


Figure 6.35: Comparison of multigrid convergence for first-order schemes on (a) triangular grid and (b) quadrilateral grid for supersonic bump flow.

6.3.4 Conclusions

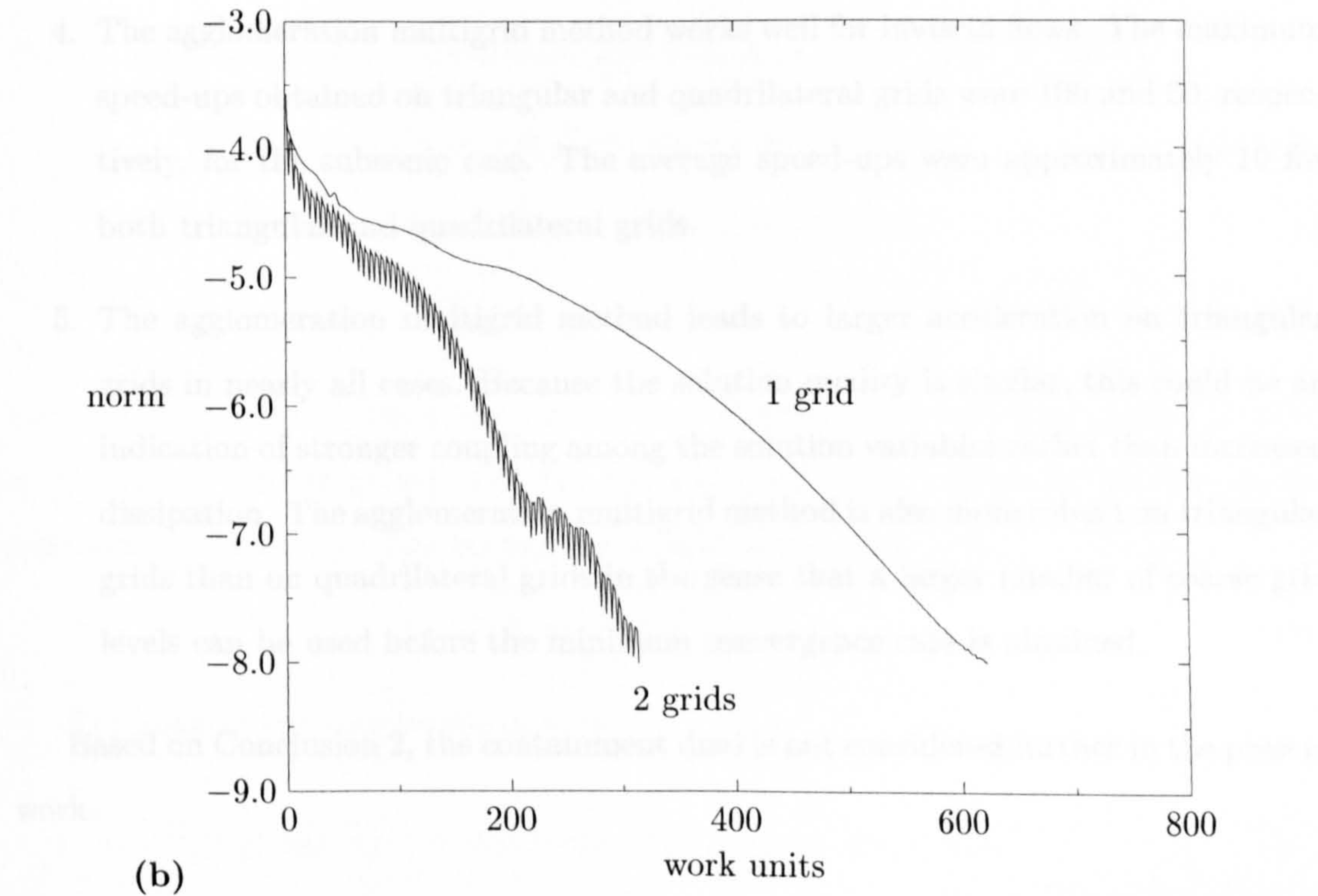
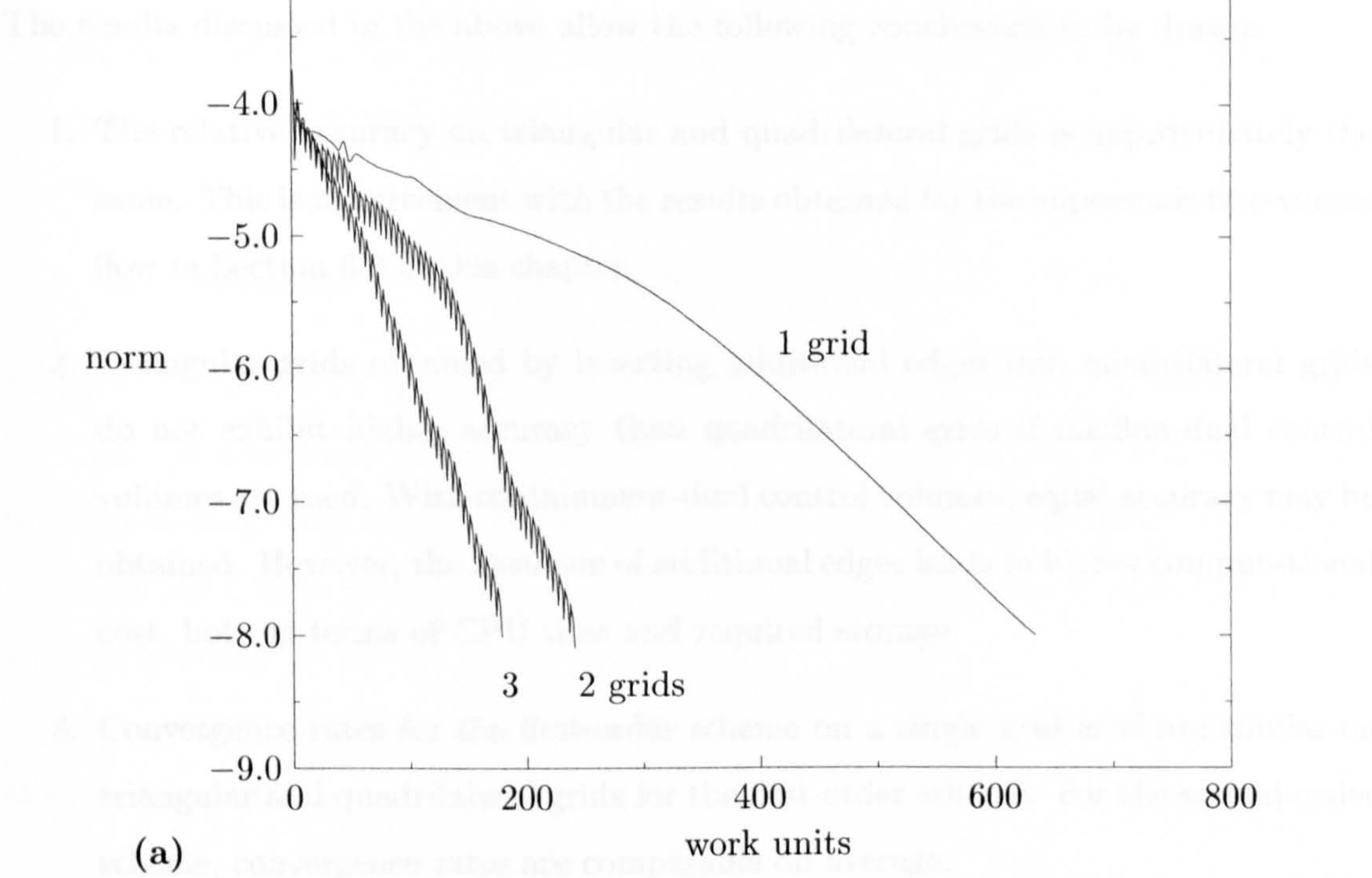


Figure 6.36: Comparison of multigrid convergence for second-order schemes on (a) triangular grid and (b) quadrilateral grid for supersonic bump flow.

6.3.4 Conclusions

The results discussed in the above allow the following conclusions to be drawn:

1. The relative accuracy on triangular and quadrilateral grids is approximately the same. This is in agreement with the results obtained for the supersonic free-vortex flow in Section 6.2 of this chapter.
2. Triangular grids obtained by inserting additional edges into quadrilateral grids do not exhibit higher accuracy than quadrilateral grids if median-dual control volumes are used. With containment-dual control volumes, equal accuracy may be obtained. However, the insertion of additional edges leads to higher computational cost, both in terms of CPU time and required storage.
3. Convergence rates for the first-order scheme on a single grid level are similar on triangular and quadrilateral grids for the first-order scheme. For the second-order scheme, convergence rates are comparable on average.
4. The agglomeration multigrid method works well for inviscid flows. The maximum speed-ups obtained on triangular and quadrilateral grids were 100 and 50, respectively, for the subsonic case. The average speed-ups were approximately 10 for both triangular and quadrilateral grids.
5. The agglomeration multigrid method leads to larger acceleration on triangular grids in nearly all cases. Because the solution quality is similar, this could be an indication of stronger coupling among the solution variables rather than increased dissipation. The agglomeration multigrid method is also more robust on triangular grids than on quadrilateral grids in the sense that a larger number of coarse grid levels can be used before the minimum convergence rate is obtained.

Based on Conclusion 2, the containment dual is not considered further in the present work.

6.4 NACA 0012 Aerofoil

To demonstrate that the solution method can also be used for external flows, it is applied to the NACA 0012 aerofoil.

The geometry of the aerofoil is given by

$$y = -0.06090x^4 + 0.17058x^3 - 0.21096x^2 - 0.07560x + 0.17814\sqrt{x} \quad (6.4.1)$$

where the leading edge of the aerofoil is located at $x = 0$, and $0 \leq x \leq 1.008930411365$.

Two flow conditions will be considered. The same triangular grid will be used for both conditions. The grid is depicted in Fig. 6.38 contains 3014 vertices, 8744 edges, and 5730 cells. 256 vertices are located on the aerofoil. The outer boundary is located at approximately 12 chords.

The solutions will be assessed with the lift, drag, and moment coefficients. Using the pressure coefficient,

$$C_p = \frac{2}{\gamma M_\infty^2} \left(\frac{p}{p_\infty} - 1 \right), \quad (6.4.2)$$

the lift, drag, and moment coefficients are defined as (for a chord of unity),

$$C_L = - \oint C_p (n_x \sin \alpha - n_y \cos \alpha) ds, \quad (6.4.3a)$$

$$C_D = \oint C_p (n_x \cos \alpha + n_y \sin \alpha) ds, \quad (6.4.3b)$$

$$C_M = \oint C_p [-(y - y_{ac})n_x + (x - x_{ac})n_y] ds, \quad (6.4.3c)$$

where α is the angle of attack, the subscript 'ac' denotes the aerodynamic centre (located at the quarter-chord point), and the moment coefficient is taken as positive in the anticlockwise direction. The entropy parameter is given by

$$\Sigma = \frac{p}{p_\infty} \left(\frac{\rho_\infty}{\rho} \right)^\gamma - 1. \quad (6.4.4)$$

The goals of the computations were

1. to demonstrate the solution method for external flows, and
2. to further validate the agglomeration multigrid method.

Only second-order accurate results will be presented.

Table 6.11: Summary of grid characteristics of the 5 grid levels used in assessment of agglomeration multigrid scheme for inviscid flow around NACA 0012 aerofoil.

level	vertices	edges
1	3014	8744
2	777	2189
3	203	544
4	52	127
5	13	27

6.4.1 Subsonic Case

The subsonic case is specified by $M_\infty = 0.5$ and $\alpha = 0^\circ$. Since the flow is non-lifting and sub-critical, the lift, drag, and moment coefficients should be identically zero.

The pressure contours computed with the unlimited second-order scheme are shown in Fig. 6.39. The computed values for the lift, drag, and moment coefficients are -0.001988 , -0.002004 , and 0.000874 . As may be seen from Fig. 6.40(a), the non-zero value of the lift coefficient is mainly due to a slight discrepancy near the trailing edge, see the inset. Close inspection of the variation of the pressure coefficient shows a slight asymmetry along the entire aerofoil surface, however. This is because the grid is not symmetric. The behaviour of the entropy parameter shown in Fig. 6.40(b) shows relatively large errors near the leading edge, although the absolute values are comparable to other results found in the literature.

Assessment of Multigrid Acceleration. The assessment of the agglomeration multigrid scheme is carried out using the five grid levels depicted in Fig. 6.41. Their characteristics are listed in Table 6.11.

The convergence histories for V- and W-cycles in terms of work units are shown in Fig. 6.42. The average convergence rates and scaled CPU-times are listed in Table 6.12.

The maximum acceleration attained by V- and W-cycles is approximately the same at a factor of over 20. With three grid levels, the use of a W-cycle leads to convergence in less than half the time required by using a V-cycle. With four grid levels, the time required to reach convergence is roughly the same. This indicates that the lower convergence rates attained by the W-cycle are balanced by the extra work required.

Table 6.12: Summary of second-order results for calculations with multigrid scheme of subsonic flow around NACA 0012 aerofoil.

level	V cycle			W cycle		
	ACR	cycles	SCT	ACR	cycles	SCT
1	0.998	6269	22.33	0.998	6269	23.20
2	0.977	443	7.59	0.977	443	7.88
3	0.941	166	2.93	0.840	58	1.23
4	0.845	60	1.04	0.797	45	1.00
5	0.838	57	1.00	0.795	44	1.00

The reason for this behaviour may be that the grid level 4 is close to being too coarse, so that the extra time spent by the W-cycle on this level is not useful. This is confirmed by the data compiled in Table 6.12, which indicates that using an additional fifth grid level does not lead to a further acceleration for the W-cycle, and only a very small improvement for the V-cycle.

It is interesting to note that the convergence of the single-grid scheme is considerably faster than that obtained for the subsonic bump flow. This comparison is justified since the two cases are specified by the same inflow and freestream conditions, respectively, and because the two grids contain approximately the same number of unknowns. The main reason for the faster convergence is almost certainly the imposed static pressure at the outflow for the bump calculations, which leads to outgoing waves being reflected.

6.4.2 Transonic Case

The transonic case is specified by $M_\infty = 0.8$ and $\alpha = 1.25^\circ$. The point-vortex correction as described in Section 3.11 is applied at the outer boundary.

The contours of pressure are shown in Fig. 6.43. The strong shock on the upper surface and the weak shock on the lower surface are well captured. The variation of the pressure coefficient and entropy parameter are depicted in Fig. 6.44.

The computed values of lift, drag, and moment coefficients are 0.3512, 0.02112, and -0.04181 . These values agree quite well with other results published in the literature. A comparison with other published results [3, 6, 9, 11, 13, 15] for lift and drag coefficients is shown in Fig. 6.45. It can be seen that while the present value for the lift coefficient lies well within the range of other results, the value for the drag coefficient is somewhat

Table 6.13: Summary of second-order results for calculations with multigrid scheme of transonic flow around NACA 0012 aerofoil.

level	V cycle			W cycle		
	ACR	cycles	SCT	ACR	cycles	SCT
1	0.995	2022	5.98	0.995	2022	8.54
2	0.944	191	4.30	0.944	191	3.65
3	0.896	100	1.38	0.844	65	1.40
4	0.867	77	1.06	0.771	43	1.00
5	0.859	72	1.00	0.779	44	1.09

lower.

The convergence of the agglomeration multigrid method for the transonic case is shown in Fig. 6.46. The corresponding average convergence rates and scaled CPU times are listed in Table 6.13.

The speed-up afforded by the use of 5 multigrid levels is about a factor of 6 for V-cycles and about 8.5 for W-cycles. The lowest convergence rate achieved is about 0.77.

6.4.3 Conclusions

Relative to the goals specified for this test case, the conclusions are:

1. The solution method gives accurate results for external flows.
2. The use of W-cycles in the agglomeration multigrid method leads to substantially higher speed-up for the transonic case than the use of V-cycles, whereas there is little difference for the subsonic case.

6.5 Closure

The main conclusions drawn from the results presented in this chapter can be summarised as follows:

1. For inviscid flows, the solution quality on triangular and quadrilateral grids is similar.

2. Triangular grids obtained by inserting additional edges into a quadrilateral grid entail higher computational cost and do not lead to increased accuracy.
3. The convergence rates without multigrid are similar for first-order accurate solutions on triangular and quadrilateral grids. For second-order accurate solutions, the convergence rates without multigrid on triangular grids are comparable to those on quadrilateral grids on average.
4. The agglomeration multigrid scheme works well for inviscid flows. The lowest convergence rates obtained for first- and second-order accurate solutions are approximately 0.5 and 0.75, respectively.
5. The agglomeration multigrid scheme performs better on the triangular grids for most cases. This seems to be a consequence of stronger coupling among the solution variables rather than higher dissipation.

Having validated the solution method and demonstrated that accurate results are achieved for inviscid flows, attention is turned to laminar flows in the next chapter.

References

- [1] Aftosmis M.J., Gaitonde D., and Tavares T.S., *Behaviour of Linear Reconstruction Techniques on Unstructured Meshes*, AIAA J., Vol. 33, No. 1, pp. 2038-2049, 1995
- [2] Coirier W.J. and Jorgenson P.C.E., *A Mixed Volume Grid Approach for the Euler and Navier-Stokes Equations*, NASA TM 107135, January 1996
- [3] Jameson A. and Mavriplis D.J., *Finite Volume Solutions of the Two-Dimensional Euler Equations on a Regular Triangular Mesh*, AIAA J., Vol. 24, No. 4, pp. 611-618, April 1986
- [4] Luo H., Baum J.D., and Löhrner R., *An Improved Finite-Volume Scheme for Compressible Flows on Unstructured Grids*, AIAA Paper 95-0348, 1995
- [5] Ni R.-H., *A Multiple-Grid Scheme for Solving the Euler Equations*, AIAA J., Vol. 20, No. 11, pp. 1565-1571, 1982
- [6] Ollivier-Gooch C.F., *Multigrid Acceleration of an Upwind Euler Solver on Unstructured Meshes*, AIAA J., Vol. 33, No. 10, pp. 1822-1827, October 1995
- [7] ———, *High-Order ENO Schemes for Unstructured Meshes Based on Least-Squares Reconstruction*, AIAA Paper 97-0540, 1997
- [8] Pike J., *Notes on the Structure of Viscous and Numerically-Captured Shocks*, Aeron. J., pp. 335-338, November 1985

- [9] Pulliam T.H. and Barton J.T., *Euler Computations of AGARD Working Group 07 Airfoil Test Cases*, AIAA Paper 85-0018, 23rd Aerospace Sciences Meeting, Reno, NV, January 1985
- [10] Salas M.D. and Iollo A., *Entropy Jump Across an Inviscid Shock Wave*, ICASE Report 95-12, February 1995
- [11] Stolcis L. and Johnston L.J., *Solution of the Euler Equations on Unstructured Grids for Two-Dimensional Compressible Flow*, Aeron. J., pp. 181-195, June/July 1990
- [12] van der Maarel E. and Koren B., *Spurious, Zeroth-Order Entropy Generation Along a Kinked Wall*, Int. J. Num. Meth. Fl., Vol. 13, pp. 1113-1129, 1991
- [13] Venkatakrishnan V. and Barth T.J., *Application of Direct Solvers to Unstructured Meshes for the Euler and Navier-Stokes Equations Using Upwind Schemes*, AIAA Paper 89-0364, 27th Aerospace Sciences Meeting, Reno, NV, January 1989
- [14] Wesseling P., *Introduction to Multigrid Methods*, Wiley, 1993
- [15] Whitaker D.L., Grossman B., and Löhner R., *Two-Dimensional Euler Computations on a Triangular Mesh Using an Upwind, Finite-Volume Scheme*, AIAA Paper 89-0470, 27th Aerospace Sciences Meeting, Reno, NV, January 1989
- [16] Zierep J., *Theoretische Gasdynamik*, 4th Edition, G. Braun, Karlsruhe, Germany, 1991

freestream boundary

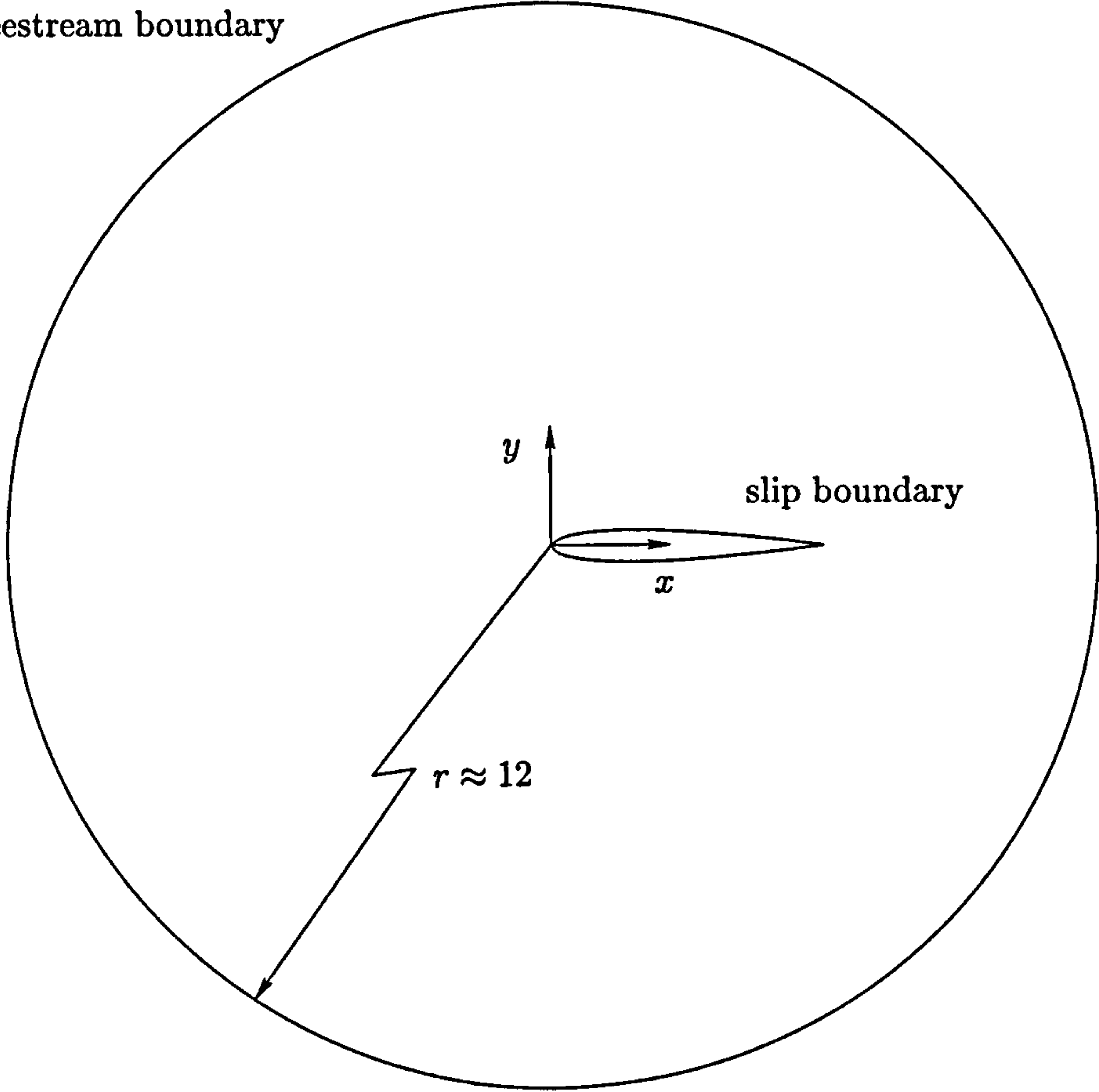


Figure 6.37: Solution domain and boundary conditions for inviscid flow over NACA 0012 aerofoil.

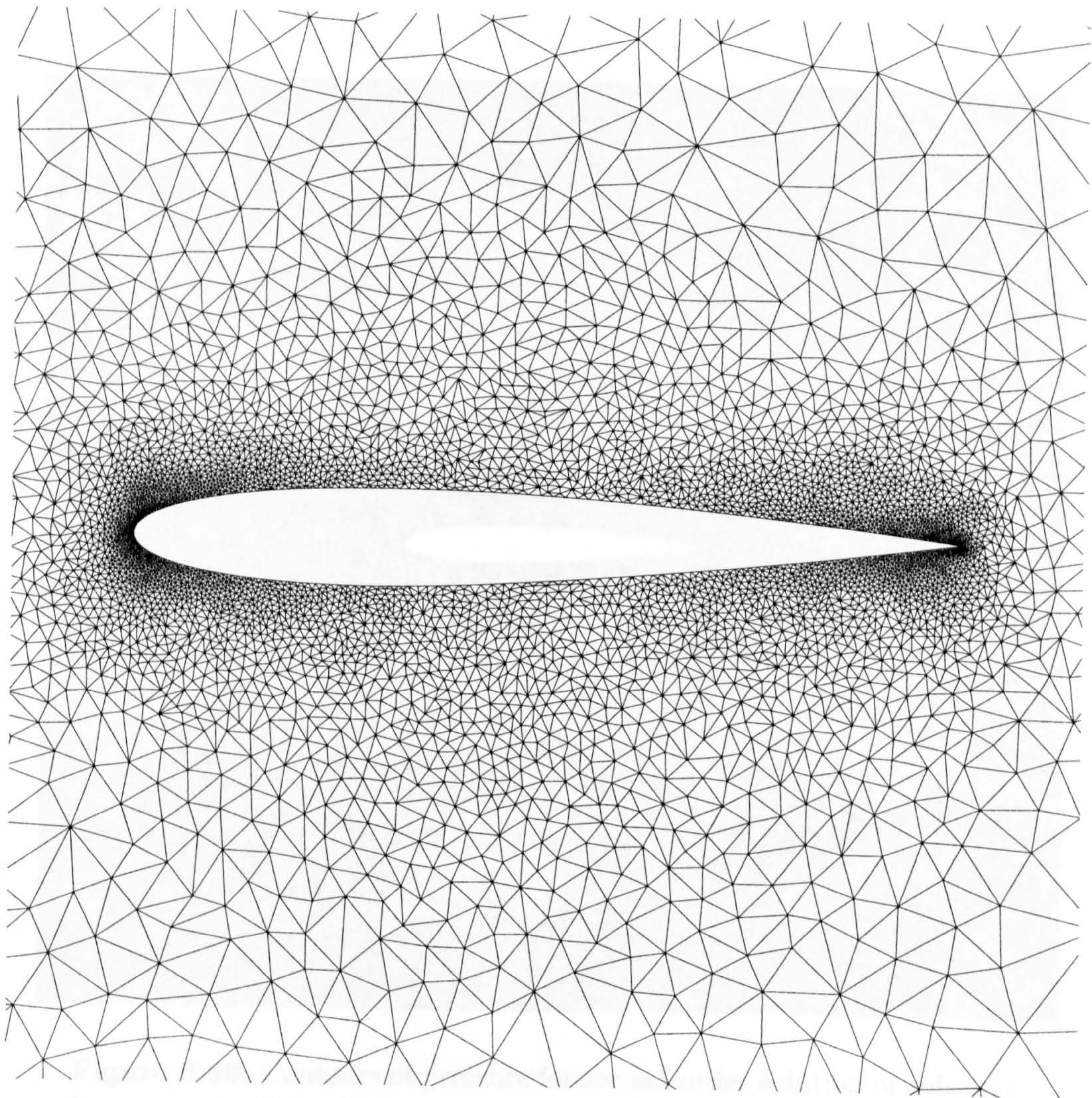


Figure 6.38: Triangular grid used for inviscid flow over NACA 0012 aerofoil.

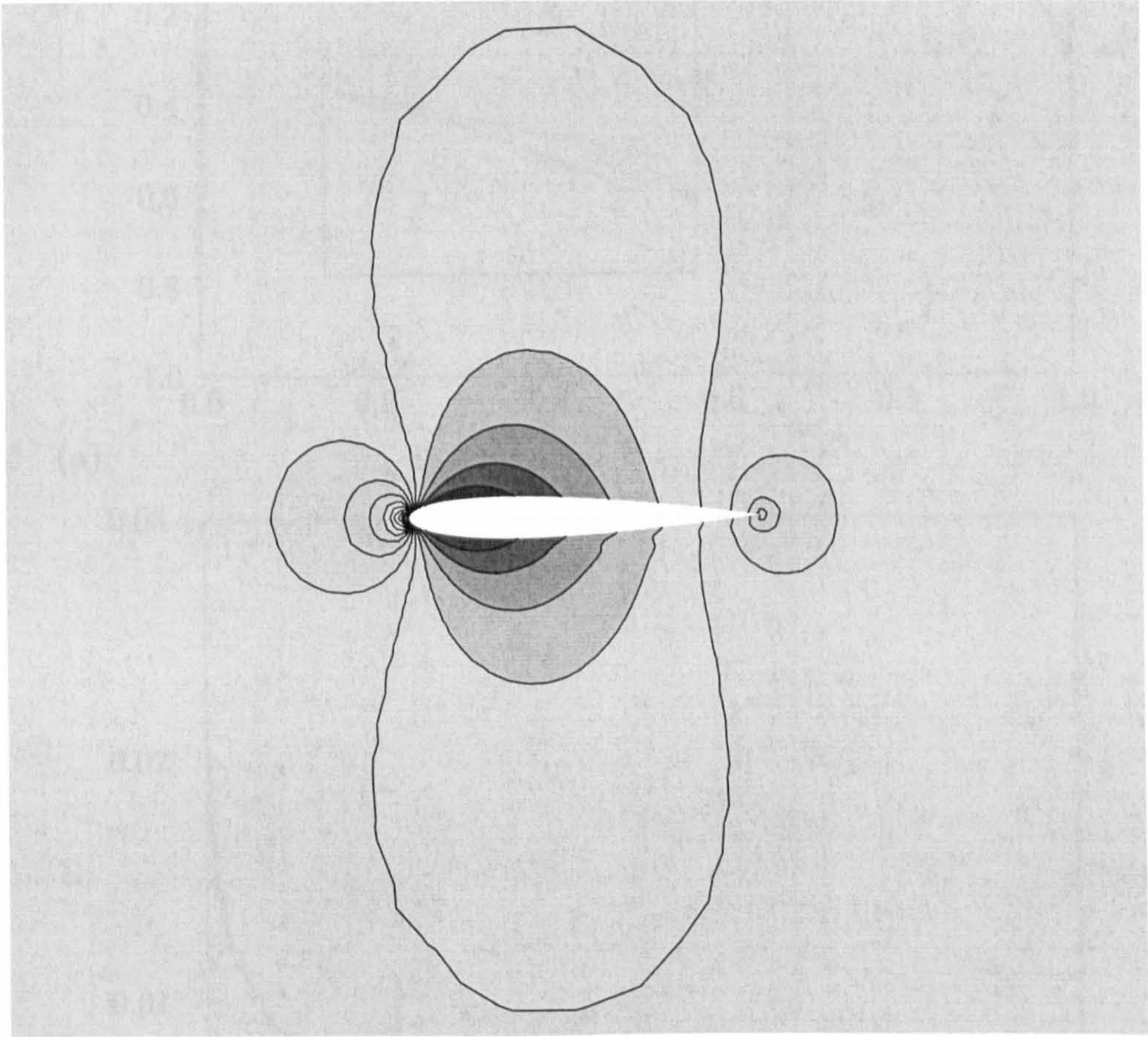
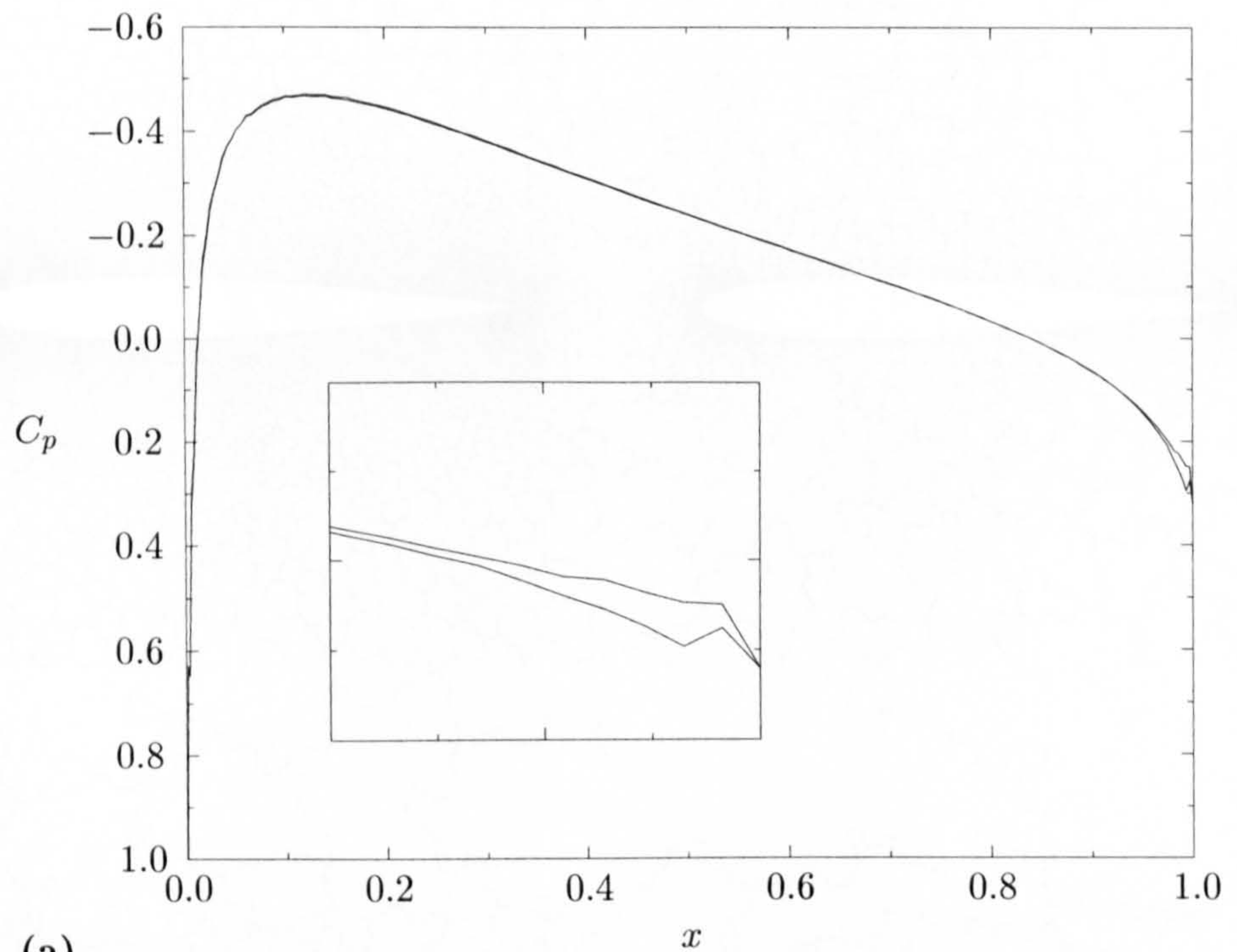
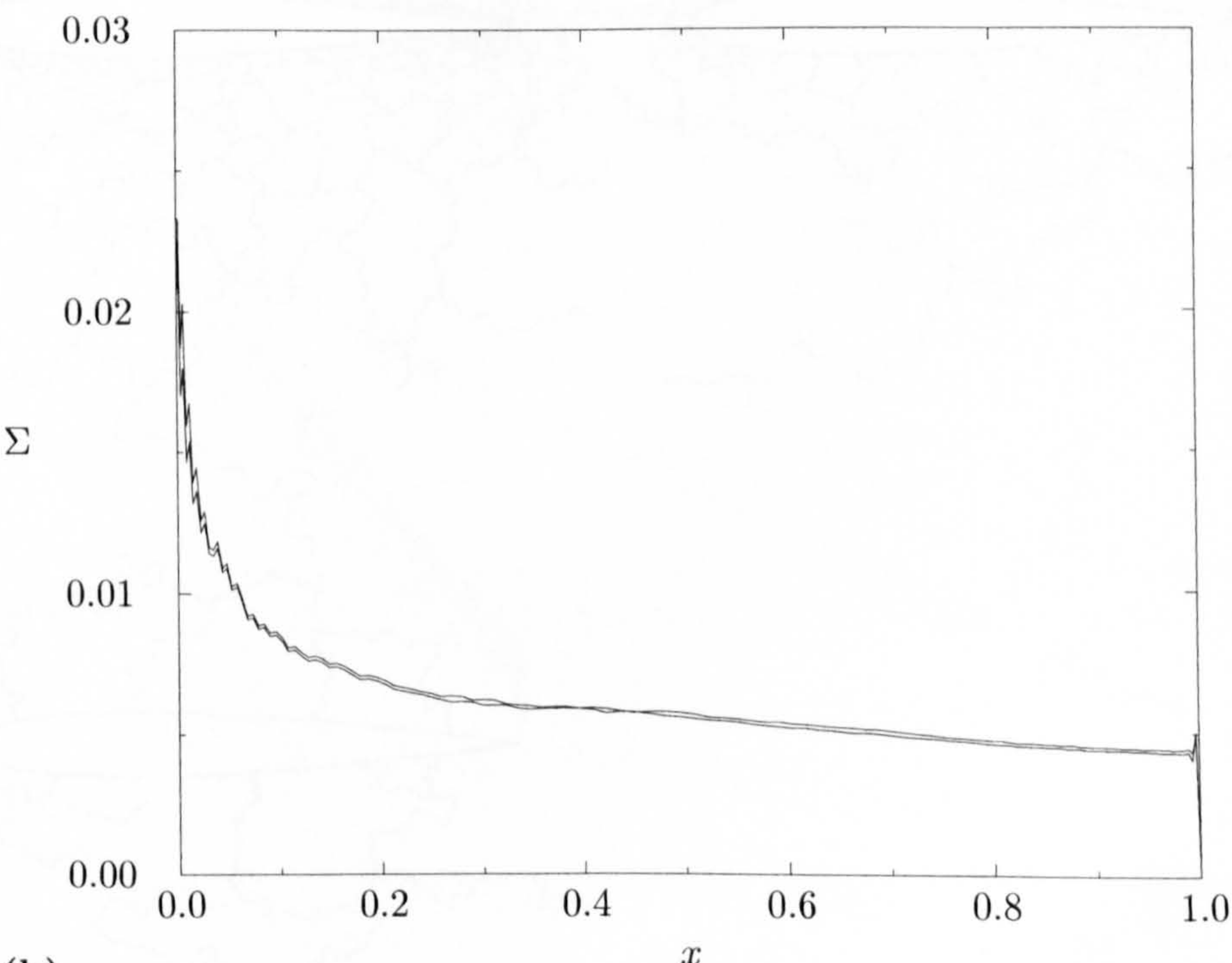


Figure 6.39: Contours of pressure for second-order solution of subsonic flow around NACA 0012 aerofoil (0.667,0.830;15).



(a)



(b)

Figure 6.40: (a) Pressure coefficient and (b) entropy parameter for second-order solution of subsonic flow around NACA 0012 aerofoil. Inset in (a) shows slight asymmetry in solution near vicinity of trailing edge.

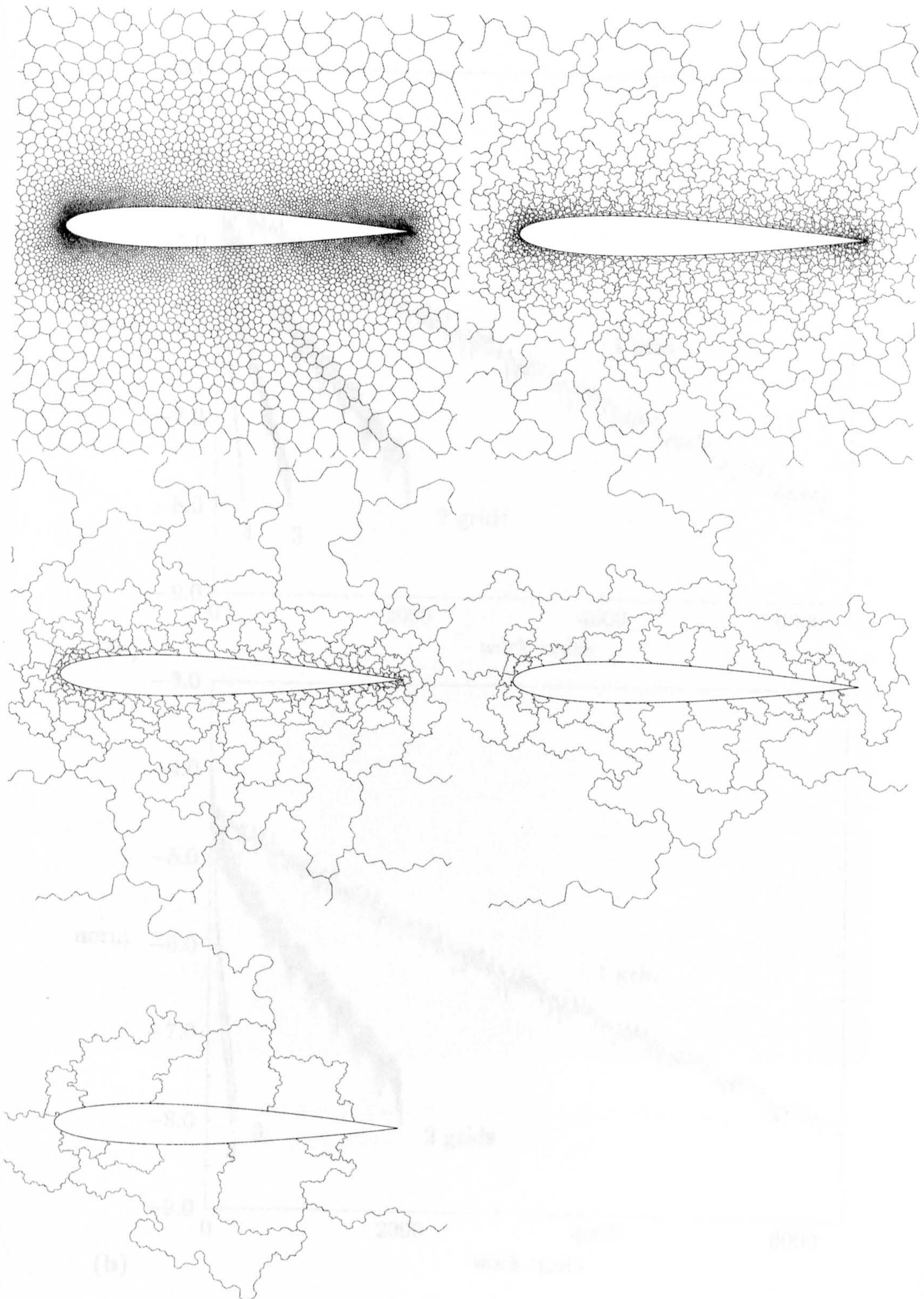


Figure 6.41: The five grid levels used in assessment of agglomeration multigrid scheme for flow around NACA 0012 aerofoil.

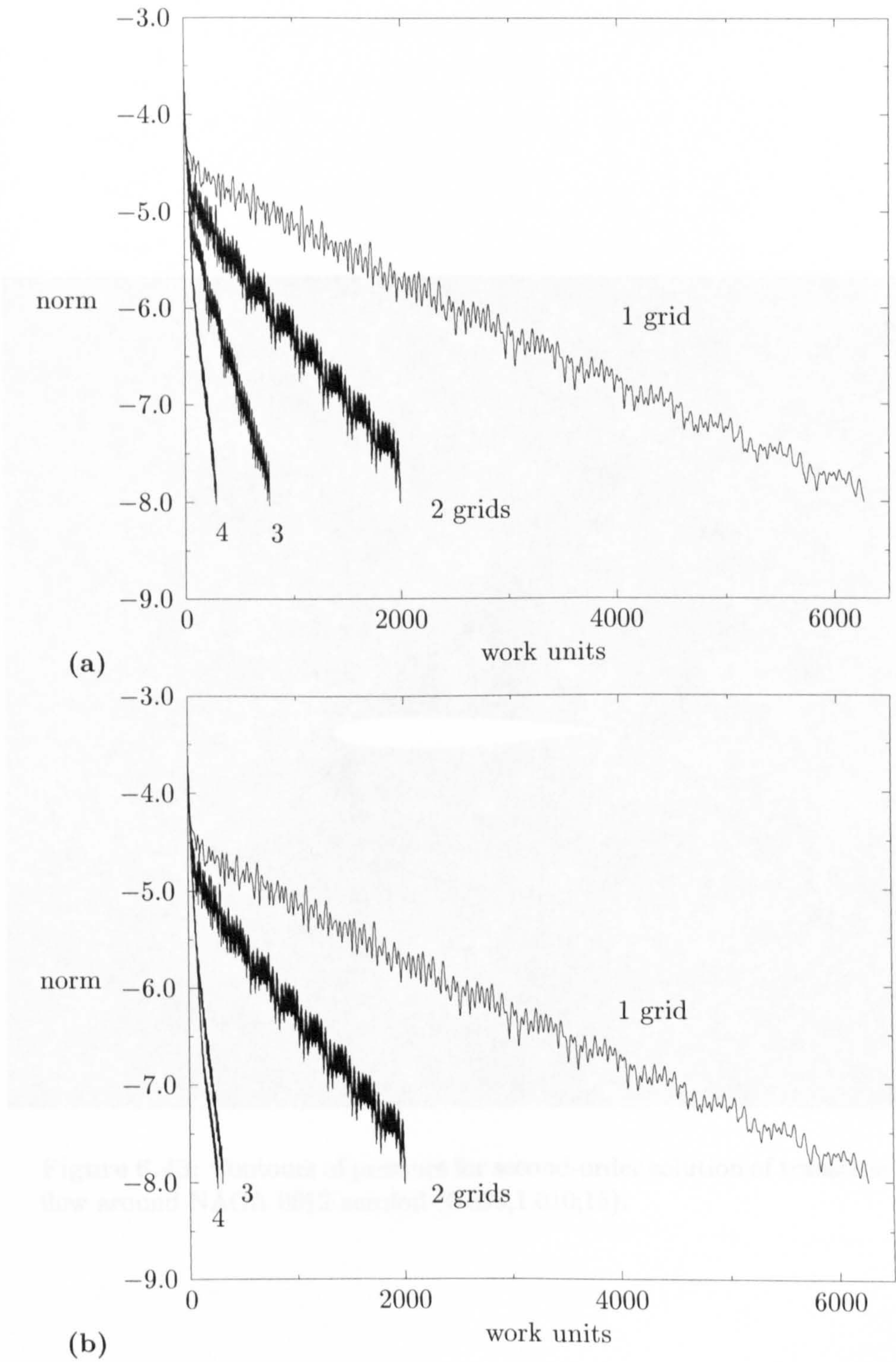


Figure 6.42: Comparison of multigrid convergence for second-order scheme with (a) V cycles and (b) W cycles for subsonic flow around NACA 0012 aerofoil.

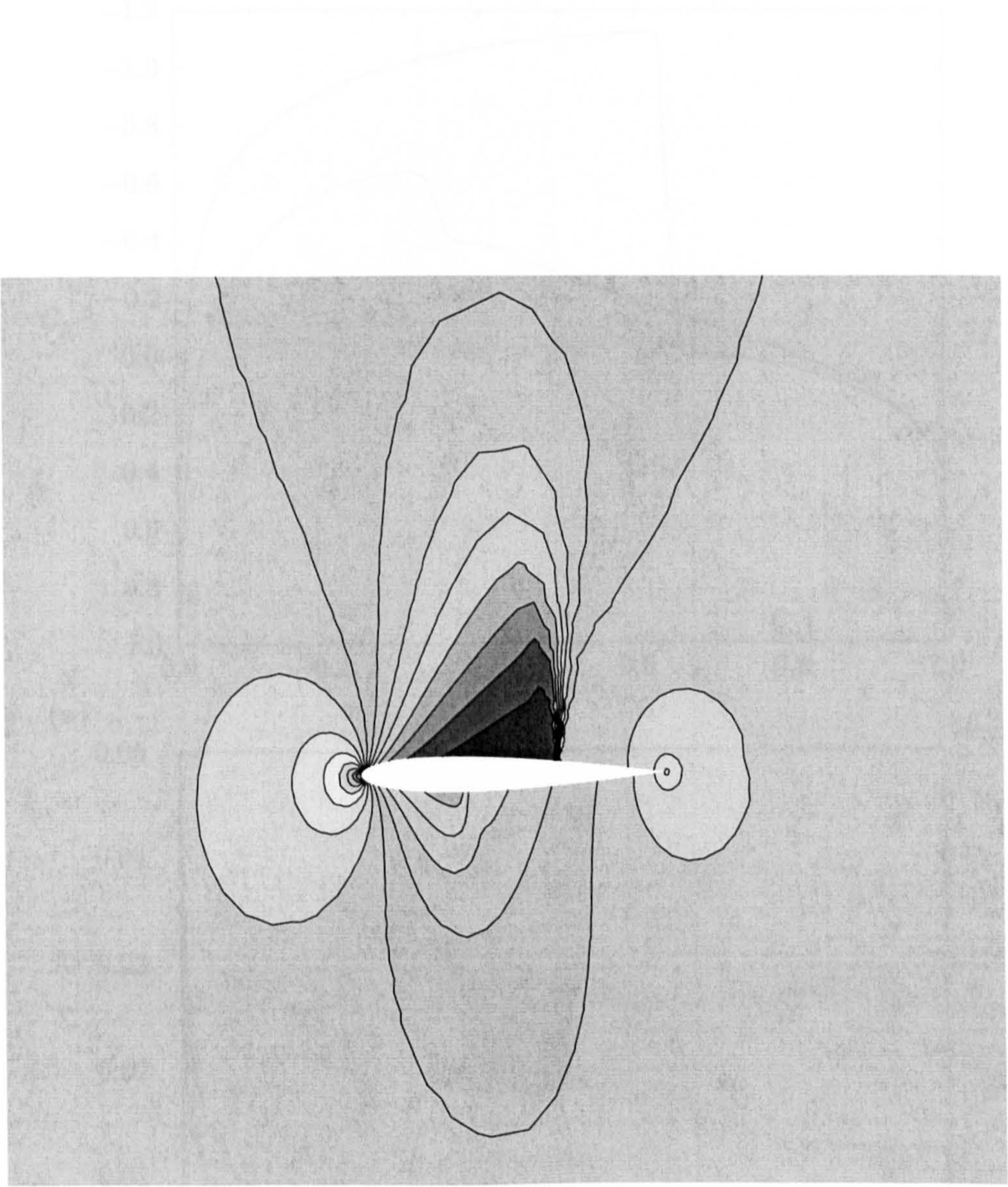


Figure 6.43: Contours of pressure for second-order solution of transonic flow around NACA 0012 aerofoil (0.398,1.010;15).

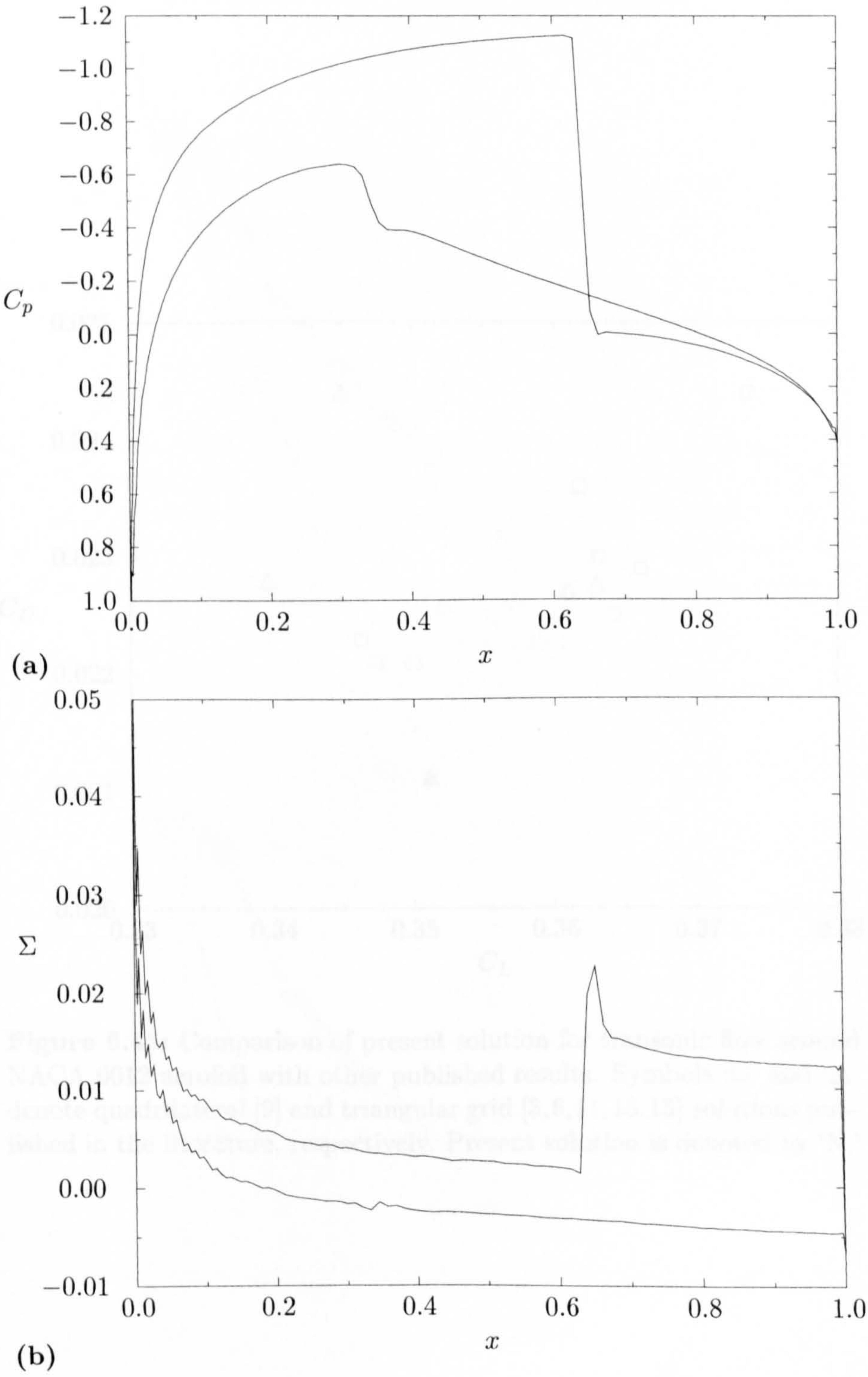


Figure 6.44: (a) Pressure coefficient and (b) entropy parameter for second-order solution of transonic flow around NACA 0012 aerofoil.

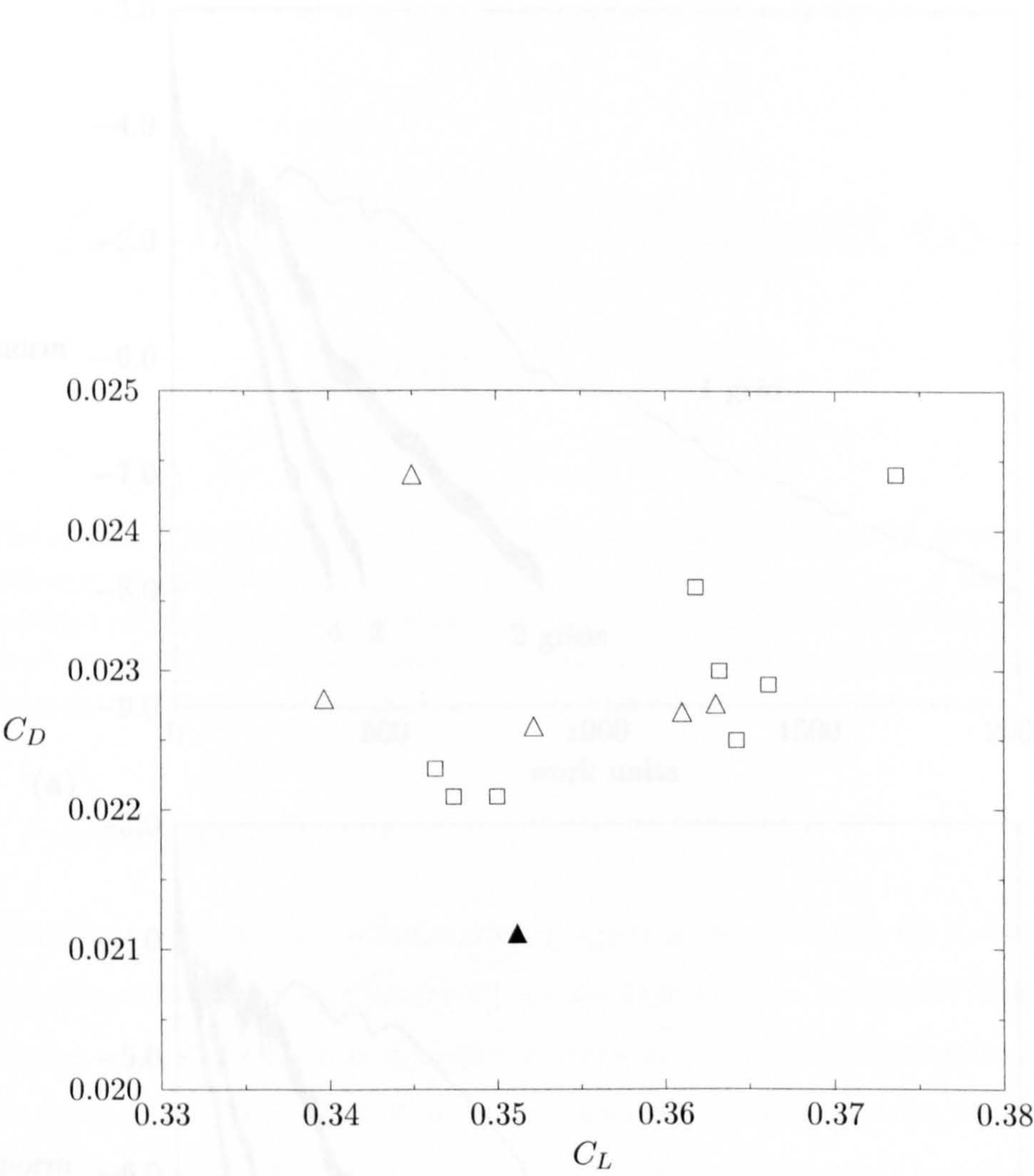


Figure 6.45: Comparison of present solution for transonic flow around NACA 0012 aerofoil with other published results. Symbols ‘ \square ’ and ‘ \triangle ’ denote quadrilateral [9] and triangular grid [3,6,11,13,15] solutions published in the literature, respectively. Present solution is denoted by ‘N.’

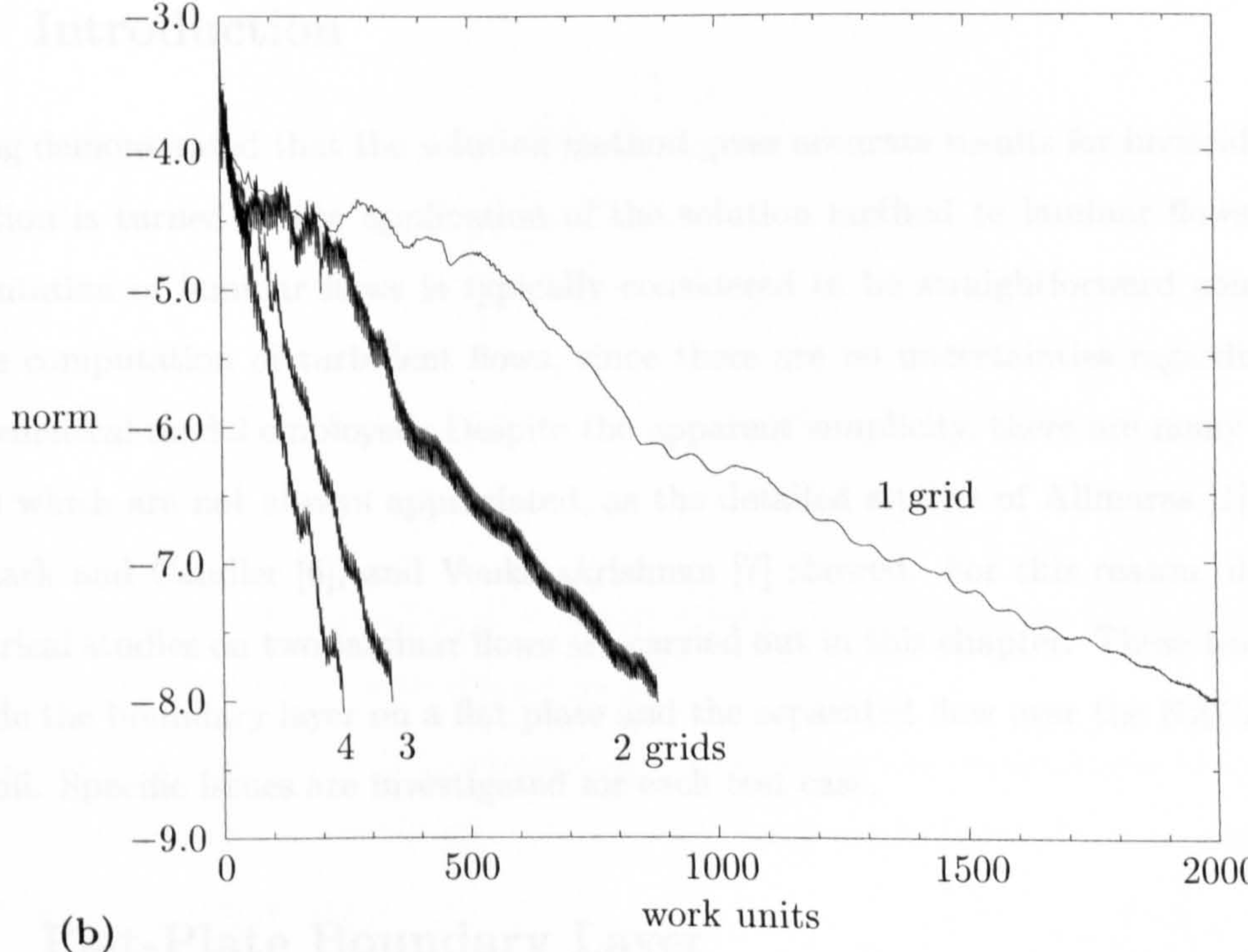
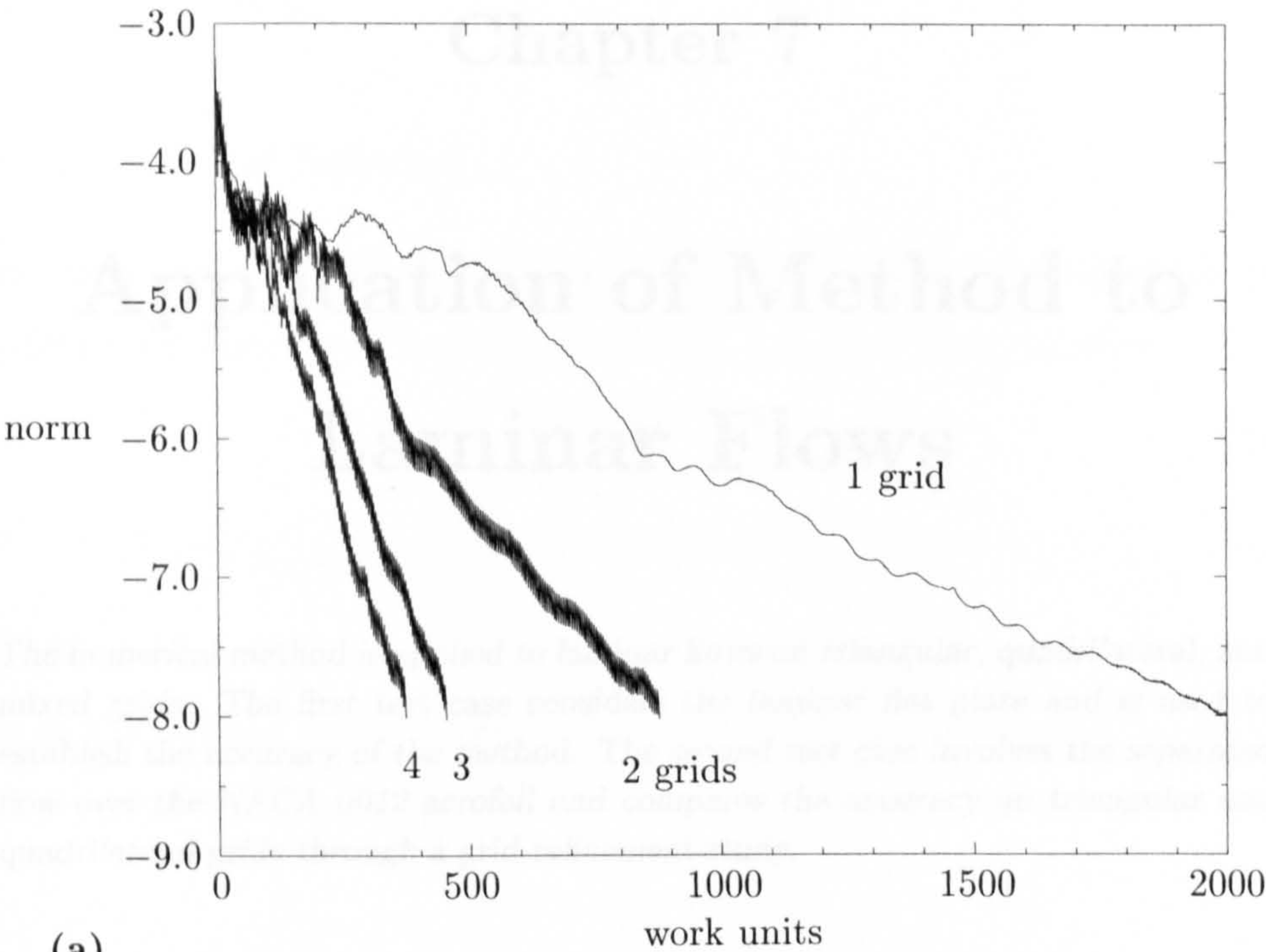


Figure 6.46: Comparison of multigrid convergence for second-order scheme with (a) V-cycles and (b) W-cycles for transonic flow around NACA 0012 aerofoil.

Chapter 7

Application of Method to Laminar Flows

The numerical method is applied to laminar flows on triangular, quadrilateral, and mixed grids. The first test case considers the laminar flat plate and is used to establish the accuracy of the method. The second test case involves the separated flow over the NACA 0012 aerofoil and compares the accuracy on triangular and quadrilateral grids through a grid-refinement study.

7.1 Introduction

Having demonstrated that the solution method gives accurate results for inviscid flows, attention is turned to the application of the solution method to laminar flows. The computation of laminar flows is typically considered to be straightforward compared to the computation of turbulent flows, since there are no uncertainties regarding the mathematical model employed. Despite the apparent simplicity, there are many subtle issues which are not always appreciated, as the detailed studies of Allmaras [1], McCormack and Candler [6], and Venkatakrishnan [7] showed. For this reason, detailed numerical studies on two laminar flows are carried out in this chapter. These test cases include the boundary layer on a flat plate and the separated flow over the NACA 0012 aerofoil. Specific issues are investigated for each test case.

7.2 Flat-Plate Boundary Layer

The most useful test case which may be used as a first test of the discretisation of the viscous fluxes is the incompressible flow of a uniform freestream over a semi-infinite flat plate at zero incidence. The usefulness of the test case stems from the fact that a

theoretical solution may be derived, which allows the accuracy of the numerical method to be analysed rigorously.

7.2.1 Theoretical Solution

For incompressible flow and by invoking the thin-shear layer approximation [8], the Navier-Stokes equations may be simplified to the boundary-layer equations

$$\frac{\partial u}{\partial x} + \frac{\partial v}{\partial y} = 0 \quad (7.2.1a)$$

$$\frac{\partial u}{\partial t} + u \frac{\partial u}{\partial x} + v \frac{\partial u}{\partial y} = \nu \frac{\partial^2 u}{\partial y^2} \quad (7.2.1b)$$

with the boundary conditions $u = v = 0$ at $y = 0$ and $u = V_\infty$ at $y = \infty$.

The lack of a characteristic length scale means that the solution must be self-similar. By introducing the similarity coordinate

$$\eta = \frac{y}{2x} \sqrt{\text{Re}_x} \quad (7.2.2)$$

where

$$\text{Re}_x = \frac{V_\infty x}{\nu} \quad (7.2.3)$$

and the stream function

$$\psi = \sqrt{V_\infty x \nu} f(\eta), \quad (7.2.4)$$

Eq. (7.2.1a) is satisfied identically and Eq. (7.2.1b) may be written as

$$f f'' + f' = 0, \quad (7.2.5)$$

with the boundary conditions $f = f' = 0$ at $\eta = 0$ and $f' = 2$ at $\eta = \infty$. The superscript $(\cdot)'$ denotes differentiation with respect to η .

Blasius [3] solved Eq. (7.2.5) numerically using asymptotic expansions. Values of f and f' were tabulated by White [8]. The velocity components follow from the definition of the stream function as

$$\frac{u}{V_\infty} = f'(\eta) \quad (7.2.6a)$$

$$\frac{v}{V_\infty} = \frac{1}{2\sqrt{\text{Re}_x}} (\eta f'(\eta) - f(\eta)) \quad (7.2.6b)$$

and the thickness δ —defined to be the vertical distance at which $u = 0.99V_\infty$ —and

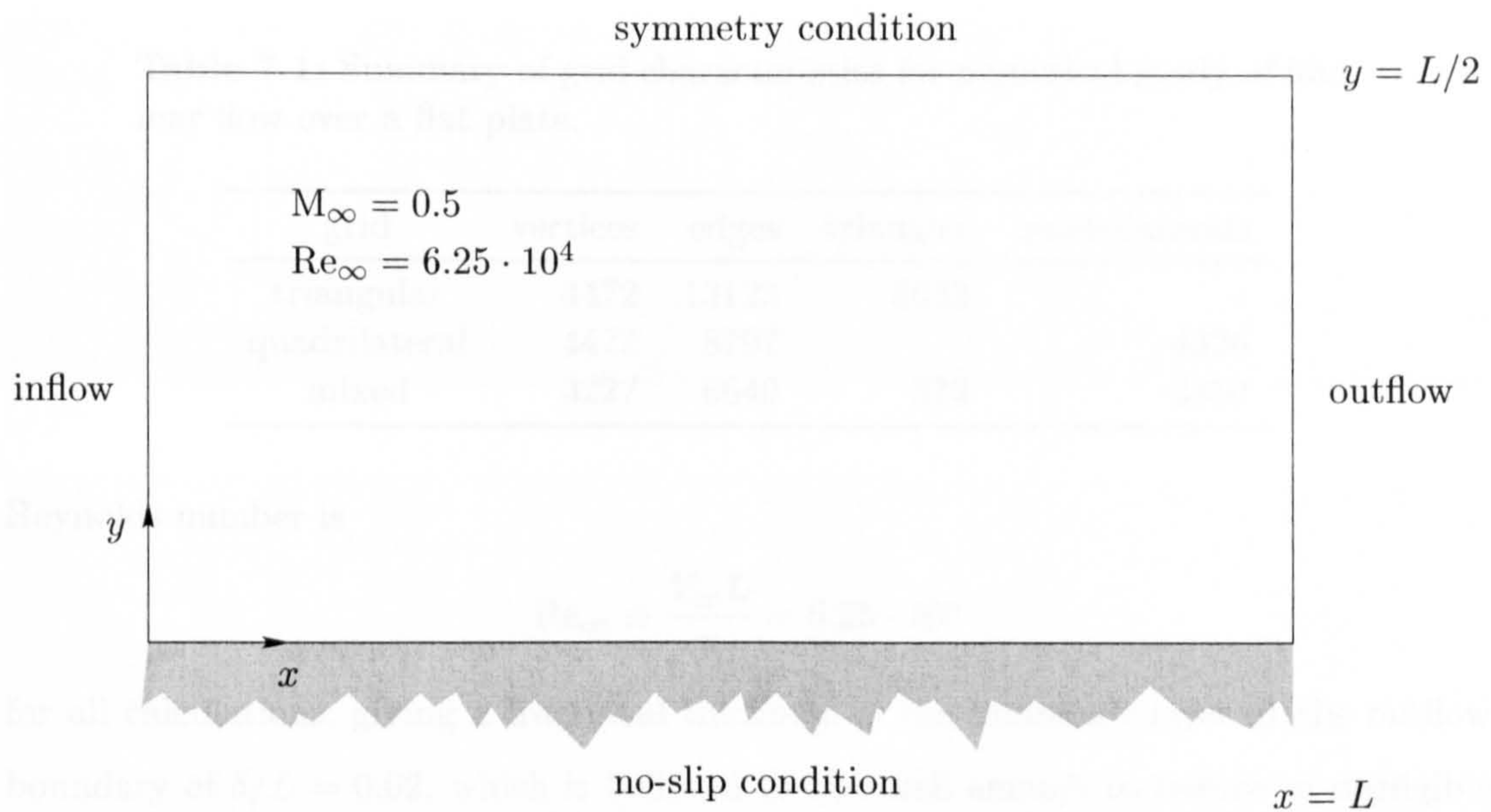


Figure 7.1: Solution domain and boundary conditions for laminar flow over a flat plate at zero incidence.

friction coefficient are given by

$$\frac{\delta}{x} = \frac{5.0}{\sqrt{\text{Re}_x}} \quad (7.2.7)$$

and

$$C_f = \frac{0.664}{\sqrt{\text{Re}_x}}, \quad (7.2.8)$$

respectively.

It is important to note that Eq. (7.2.8) is usually regarded as a theoretical solution to the Navier-Stokes equations, despite it being a numerical solution of the boundary-layer equations. This point of view is justified since experiments have been shown to agree very well with the velocity distributions given by Eqs. (7.2.6a) and (7.2.6b), see, e.g., White [8].

7.2.2 Numerical Solutions

The solution domain is depicted in Fig. 7.1. As indicated, the plate is of length L and the upper boundary is located at $L/2$. The upper boundary is modelled as a symmetry boundary. The freestream Mach number is $M_\infty = 0.5$. This value should be high enough to prevent convergence and accuracy problems with the solution method while being sufficiently low to avoid a marked influence of compressibility on the results. The

Table 7.1: Summary of grid characteristics for numerical study of laminar flow over a flat plate.

grid	vertices	edges	triangles	quadrilaterals
triangular	4472	13123	8652	–
quadrilateral	4472	8797	–	4326
mixed	3227	6649	573	2850

Reynolds number is

$$\text{Re}_\infty \equiv \frac{V_\infty L}{\nu} = 6.25 \cdot 10^4$$

for all calculations, giving a fractional thickness of the boundary layer at the outflow boundary of $\delta/L = 0.02$, which is believed to be small enough to reduce to negligible levels the effect of the symmetry boundary on the boundary-layer development. It is noted that the specification of uniform flow conditions at the inflow boundary leads to a singularity at the leading edge of the plate.

The triangular, quadrilateral, and mixed grids shown in Fig. 7.2 were used in the computational study. Their characteristics are listed in Table 7.1. At the inflow boundary, the grid spacing of the mixed grid in the y -direction is less than for the triangular and quadrilateral grid. Towards the outflow boundary, the grid spacing in the y -direction is approximately the same for all grids. At the outflow boundary, there are roughly 14 grid points in the boundary layer. It is noted that the use of triangles of rapidly increasing size away from the plate in the mixed grid leads to a substantial reduction of the number of vertices and edges. The mixed grid was generated using the CENTAUR package [5].

The objectives of the calculations were:

1. to compare the accuracy of the numerical solutions on the triangular, quadrilateral, and mixed grids,
2. to assess the thin-shear-layer approximation given by Expressions (4.4.7a) and (4.4.7b).

Influence of Grid Type. The variation of the skin-friction coefficient along the plate for the three grid types is compared with the theoretical solution in Fig. 7.3.

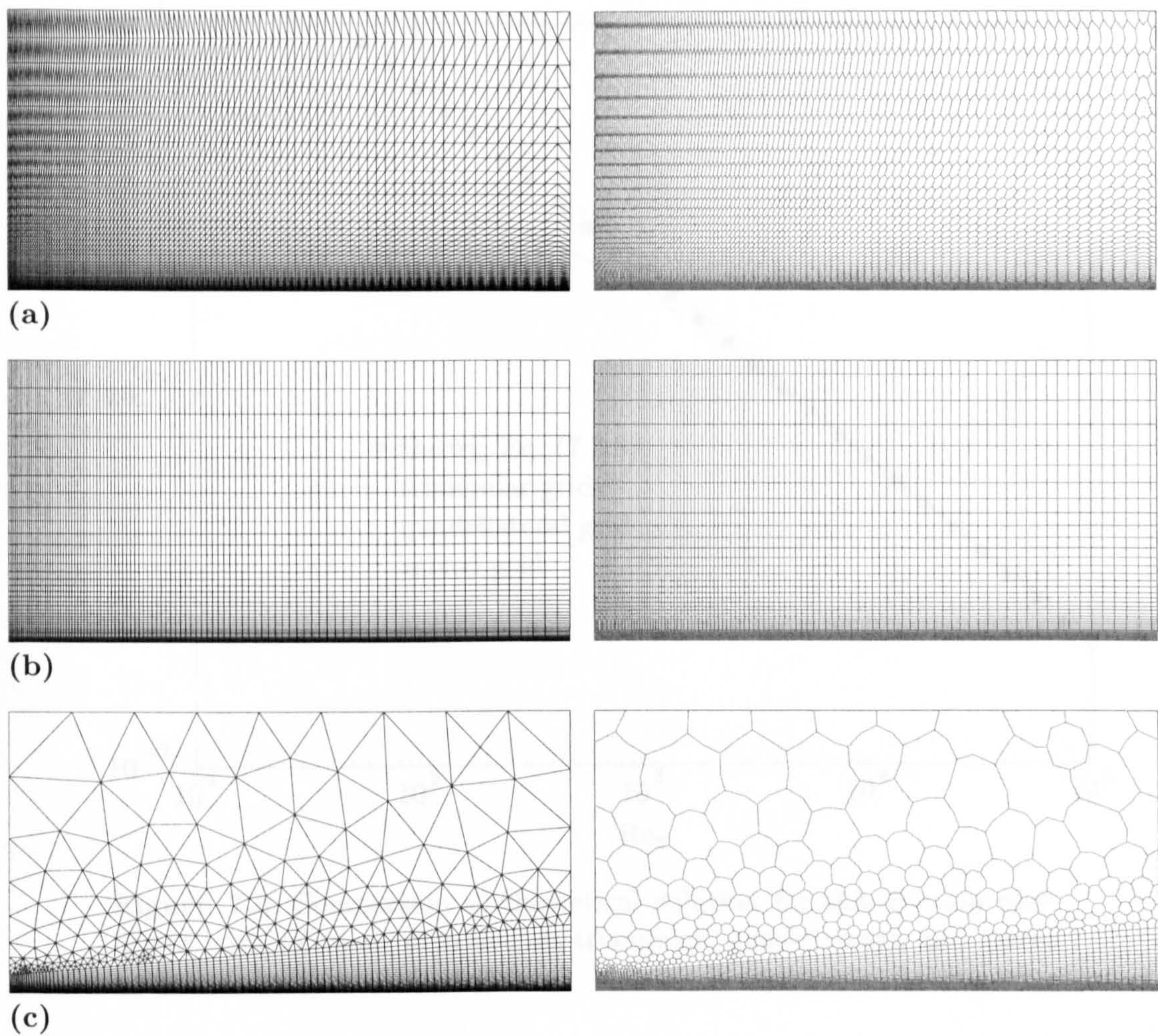


Figure 7.2: Grids used for laminar flow over flat plate. (a) Triangular grid, (b) quadrilateral grid, and (c) mixed grid.

The discrepancies near the leading edge are due to the aforementioned singularity; the somewhat finer grid spacing in the y -direction on the mixed grid reduces the effect of the singularity. Beyond the leading edge, the agreement between the theoretical solution and the results on the quadrilateral and the mixed grids is very good. Close inspection of Fig. 7.3 reveals that the level of skin friction is slightly too high, but the slope of the numerical results is very close to that given by the theory, indicating that the rate of growth of the boundary layer is predicted correctly. It is noted that the use of logarithmic scaling magnifies the very slight discrepancies. With linear scaling, as commonly employed by other authors, the differences would be virtually indiscernible. On the triangular grid, the skin-friction coefficient requires a longer distance to approach

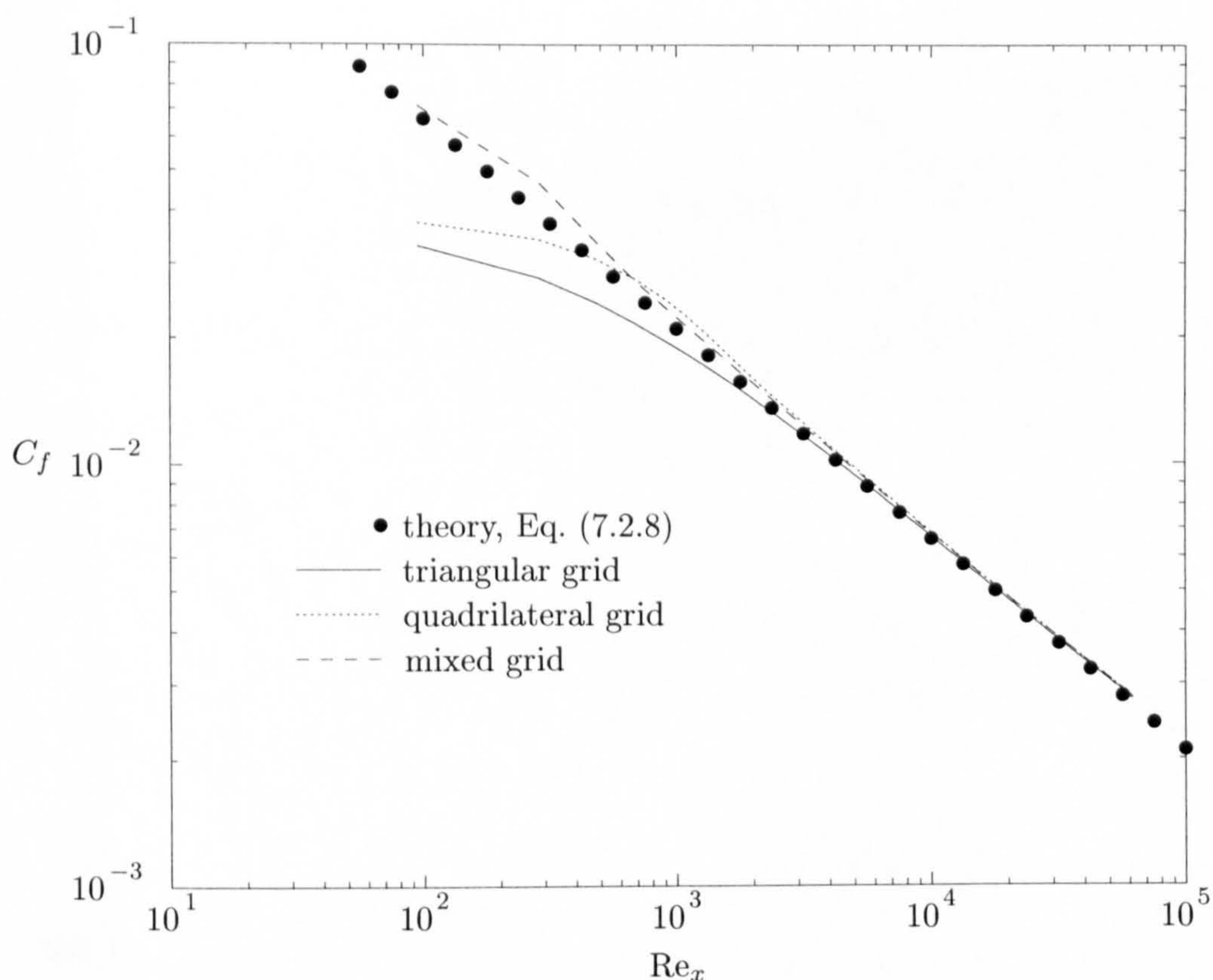


Figure 7.3: Comparison of theoretical solution for skin-friction coefficient with solutions obtained on triangular, quadrilateral, and mixed grids.

the theoretical curve.

The comparison of the velocity profiles in similarity coordinates on the triangular, quadrilateral, and mixed grids is shown in Figs. 7.4–7.6. It may be seen that agreement with the theoretical solution is very close on the quadrilateral and mixed grids, whereas the solution on the triangular grids exhibit relatively large errors. Close inspection of the profiles of normalised u -velocity reveals slight overshoots—readily visible in the normalised v -velocity profiles—which are indicating excessive numerical smoothing. The comparison of the velocity profiles on the quadrilateral and mixed grids shows very close agreement. This demonstrates that mixed grids can attain the same accuracy as quadrilateral grids while taking advantage of triangles of rapidly increasing size away from solid walls to reduce the numbers of vertices and edges. It is clear from Fig. 7.2 that fewer layers of quadrilateral cells could have been generated, leading to an even greater saving of vertices and edges.

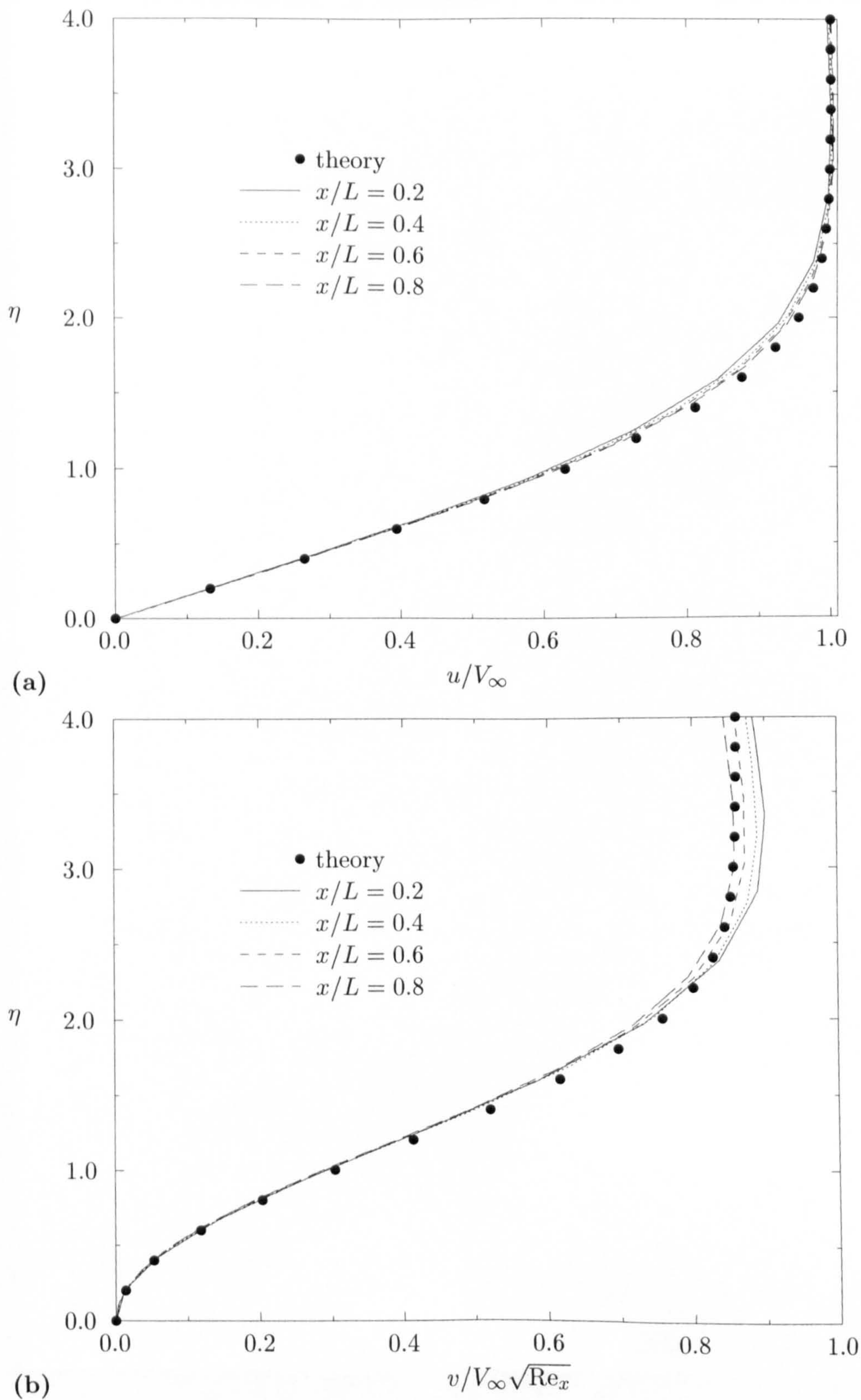


Figure 7.4: Comparison of numerical solution on triangular grid for (a) u -velocity and (b) v -velocity with theoretical solution at four locations along flat plate.

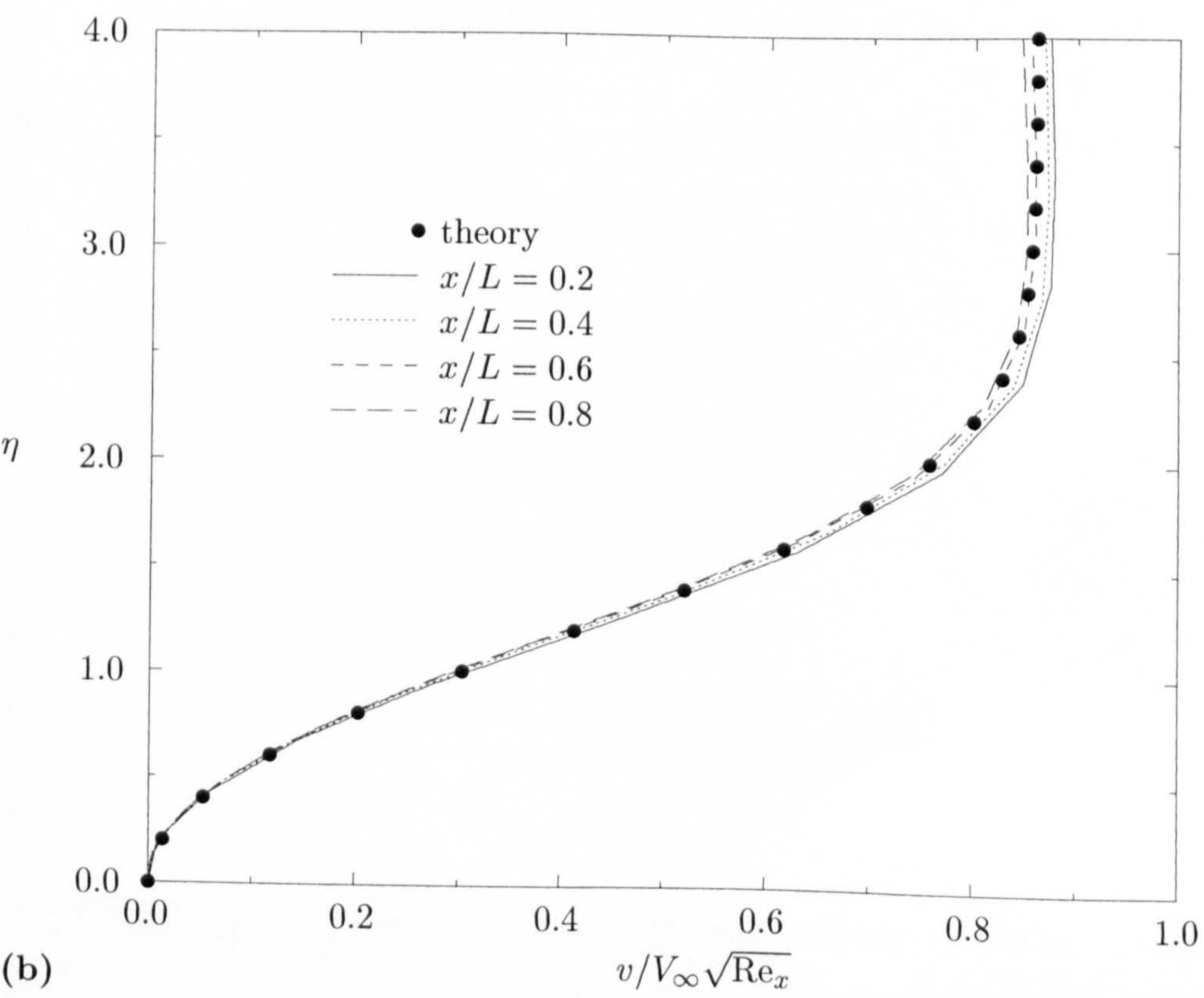
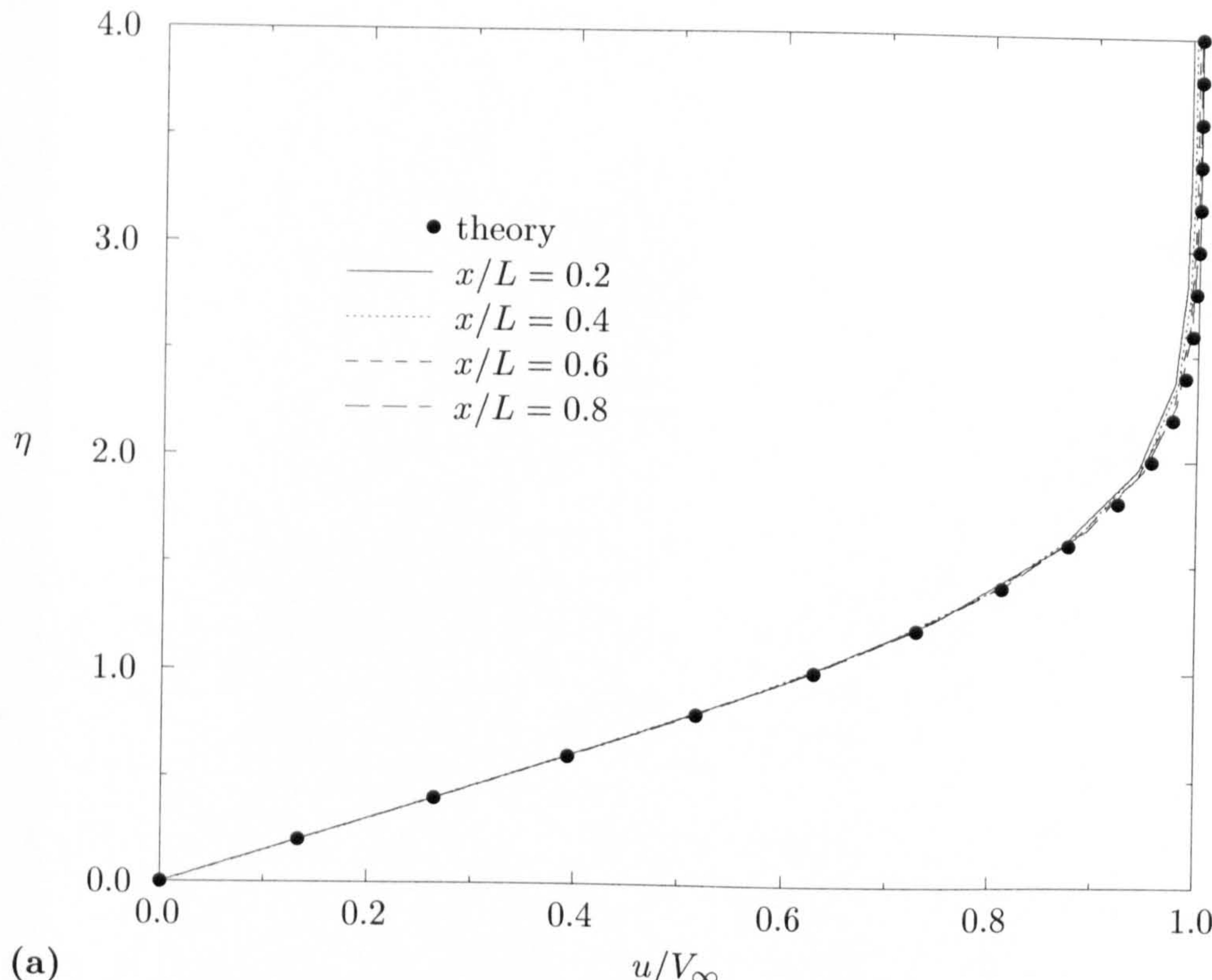


Figure 7.5: Comparison of numerical solution on quadrilateral grid for (a) u -velocity and (b) v -velocity with theoretical solution at four locations along flat plate.

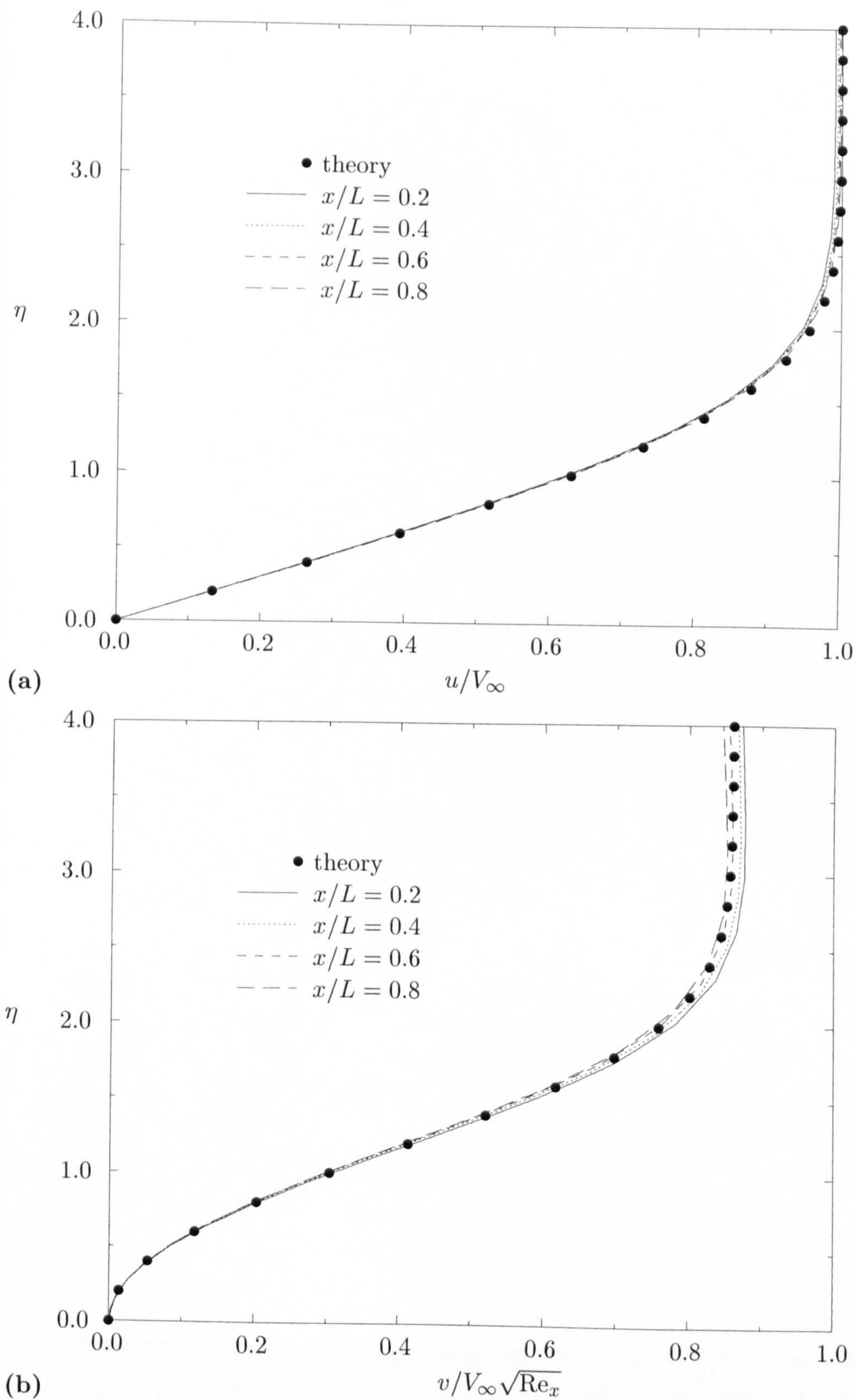


Figure 7.6: Comparison of numerical solution on mixed grid for (a) u -velocity and (b) v -velocity with theoretical solution at four locations along flat plate.

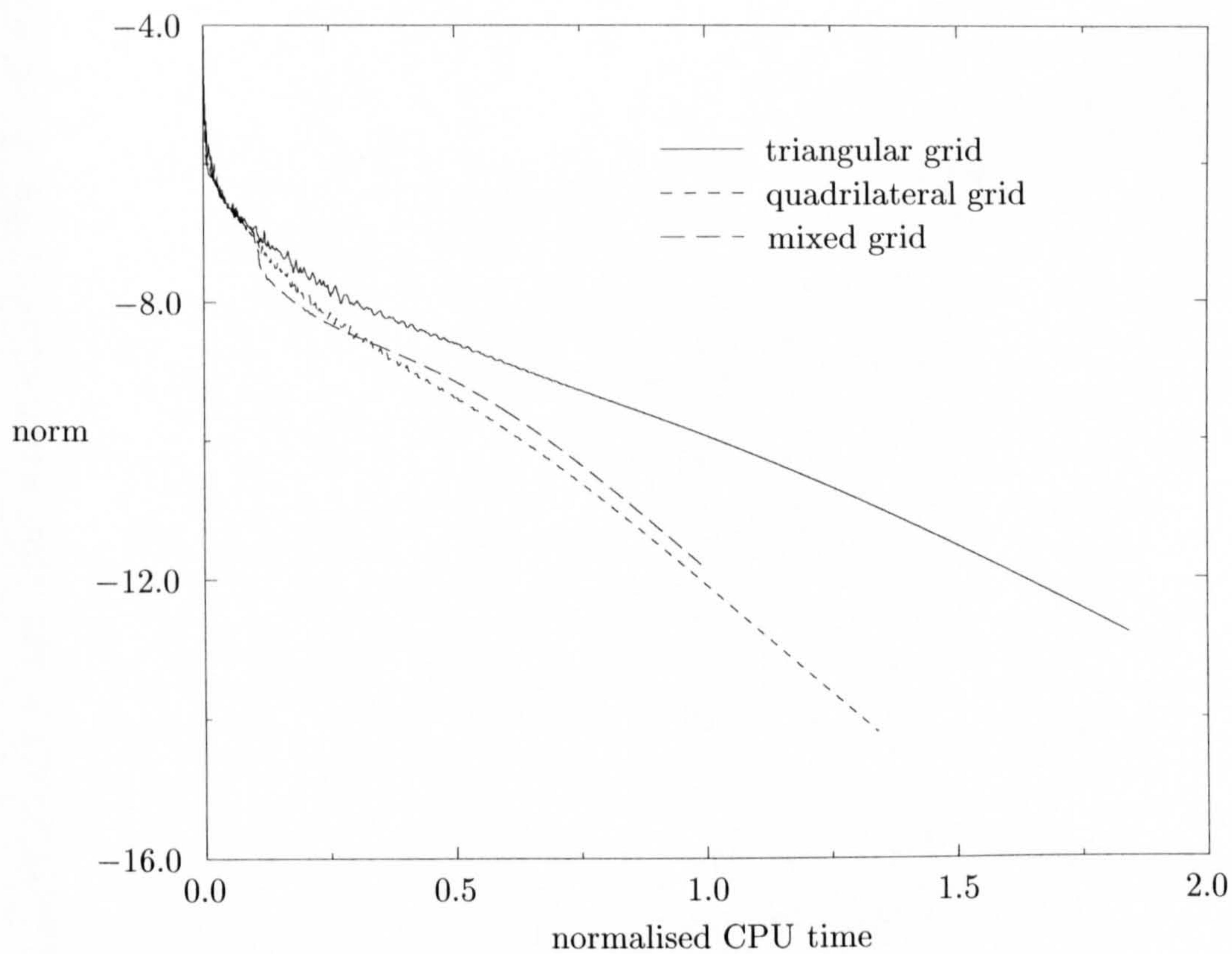


Figure 7.7: Comparison of convergence on triangular, quadrilateral, and mixed grids in terms of normalised CPU time for laminar flow over flat plate.

It is of some interest to compare convergence histories obtained on the triangular, quadrilateral, and mixed grids in relation to the CPU time. This is done in Fig. 7.7, where the abscissa represents the CPU time on a given grid type for a fixed number of iterations divided by the CPU time on the mixed grid. It can be seen that the cost of the solutions on the triangular and quadrilateral grids are approximately 1.8 and 1.3 times larger than that on the mixed grid, respectively. As may be inferred from Table 7.1, these numbers approximate the ratios of edges in the triangular and quadrilateral grids with respect to the edges in the mixed grid. Interestingly, the convergence on the mixed grid is not as good as that on the quadrilateral grid. The most likely explanation for this difference is the higher grid resolution at the leading edge. Other, less likely causes, are the interface between the quadrilateral and triangular cells and the very large cells towards the symmetry boundary.

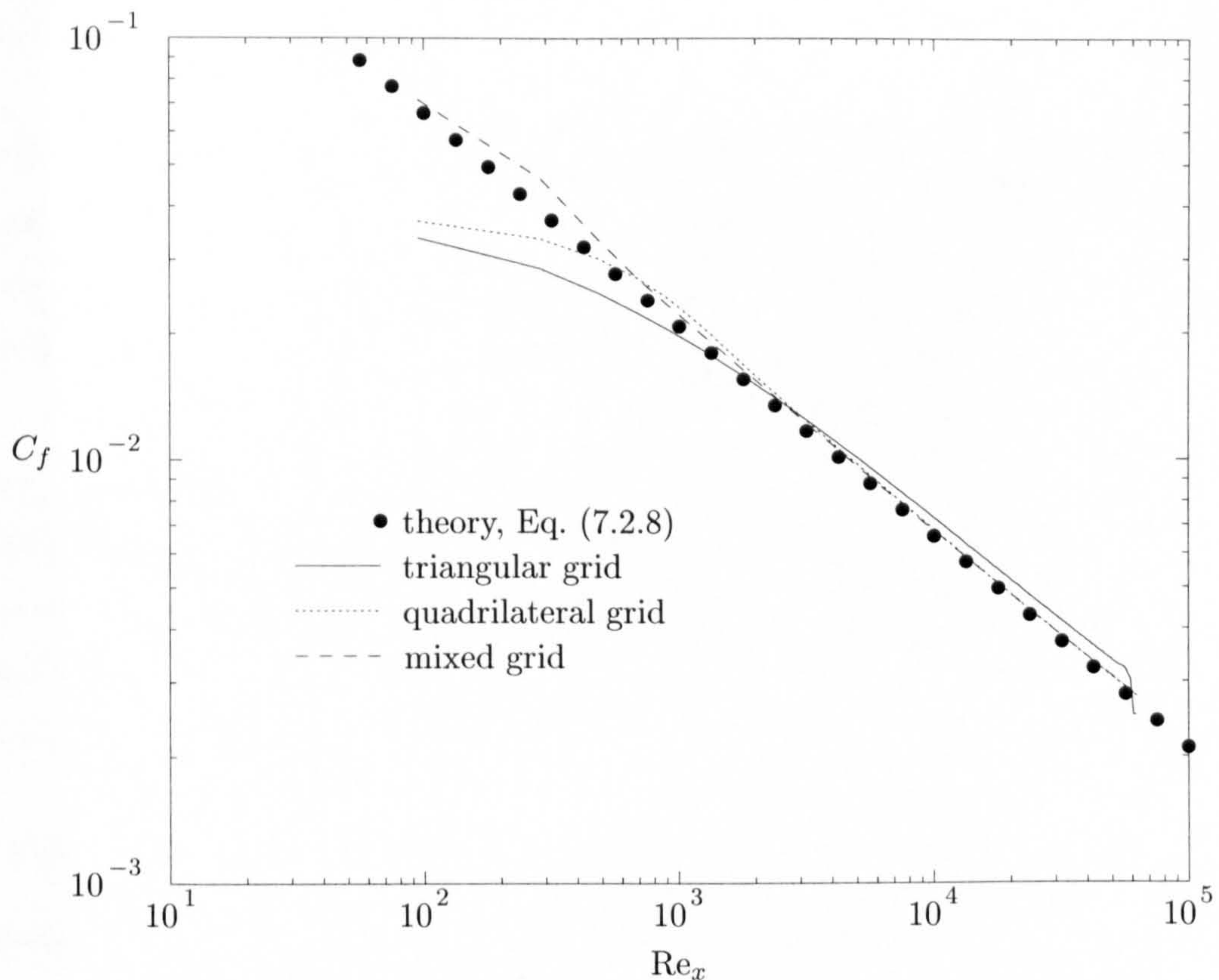


Figure 7.8: Comparison of theoretical solution for skin-friction coefficient with solutions obtained with thin-shear-layer approximation on triangular, quadrilateral, and mixed grids.

Assessment of Thin-Shear-Layer Approximation. The skin-friction coefficients obtained with the thin-shear-layer approximation on the triangular, quadrilateral, and mixed grids are compared with the theoretical variation in Fig. 7.8. The variations on the quadrilateral and mixed grids closely match those obtained with the full viscous fluxes shown in Fig. 7.3. The variation on the triangular grid shows increased discrepancies compared to that obtained with the full viscous fluxes and agreement with the theoretical variation is only fair.

These observations are reflected in the agreement between the computed and theoretical velocity profiles depicted in Figs. 7.9–7.11. On the triangular grid, the trends are opposite to those exhibited by the full viscous fluxes in that the normalised u -velocity is over-predicted and the normalised v -velocity is under-predicted. The discrepancies in the normalised v -velocity are particularly pronounced, reflecting the wrongly predicted level of growth and hence incorrect slope of the skin-friction coefficient in Fig. 7.8. On

the quadrilateral and mixed grids, the agreement with theory is very good.

The reason for the relatively poor results on the triangular grid is due to the approximation of the normal derivative using only the divided difference along the edge. On highly stretched triangular grids, it is impossible to approximate the normal derivative accurately without employing an approximation of the tangential derivative along with the divided difference along the edge.

The agreement obtained with the thin-shear-layer approximation on the quadrilateral and mixed grids indicates that it may be regarded as the extension of the traditionally used approximation to unstructured grids. As already stated in Section 4.4.1, the form of the thin-shear-layer approximation developed in the present work has the advantage that it does not require knowledge of the coordinate directions normal and tangential to a solid boundary.

7.2.3 Conclusions

Based on the results presented above, the following conclusions may be drawn:

1. The accuracy of the results obtained on quadrilateral and mixed grids is approximately the same and very close to the theoretical solution. The solution on the mixed grid is obtained at a lower computational cost.
2. The accuracy of the results obtained on the triangular grid is lower than that on the quadrilateral and mixed grids.
3. The results provide justification for the assertion that mixed grids combine the established accuracy of structured (quadrilateral) grids with the geometric flexibility of unstructured (triangular) grids.
4. The thin-shear-layer approximation delivered results which are very close to those of the full viscous fluxes on quadrilateral and mixed grids.
5. On the triangular grid, the thin-shear-layer approximation lead to relatively poor agreement with the theoretical solution. The disagreement is attributed to the discretisation on highly stretched triangular grids.

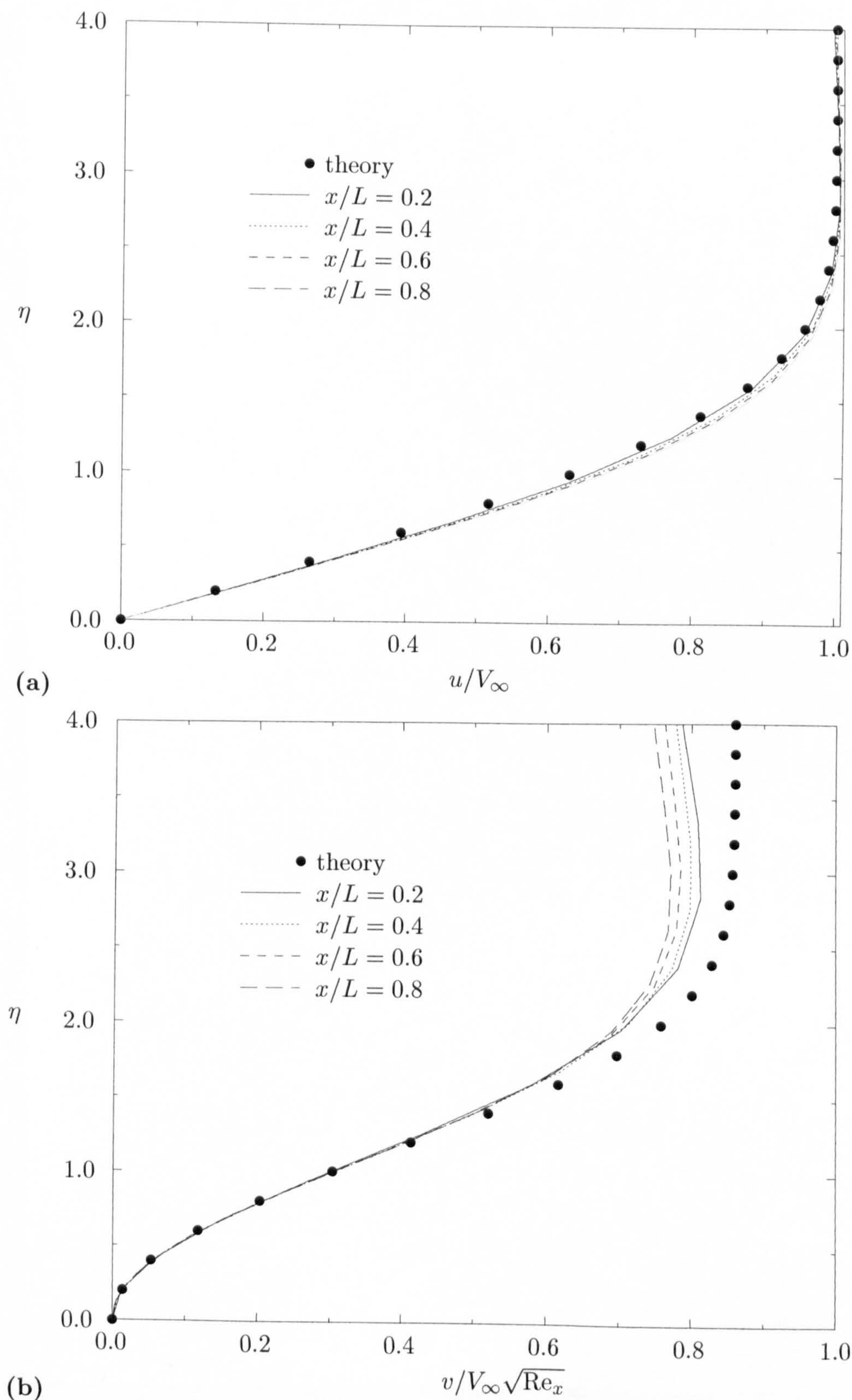


Figure 7.9: Comparison of numerical solution with thin-shear-layer approximation on triangular grid for (a) u -velocity and (b) v -velocity with theoretical solution at four locations along flat plate.

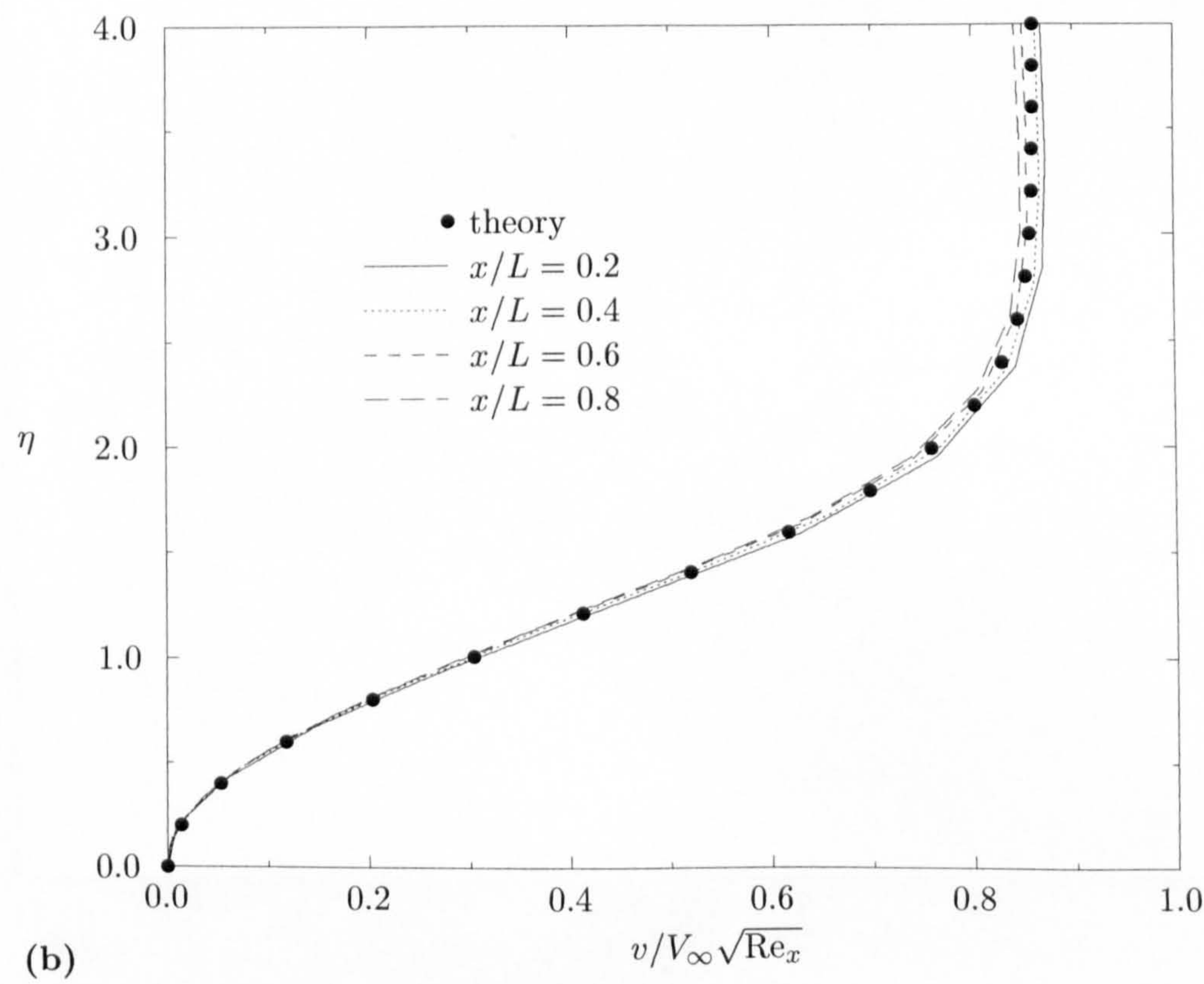
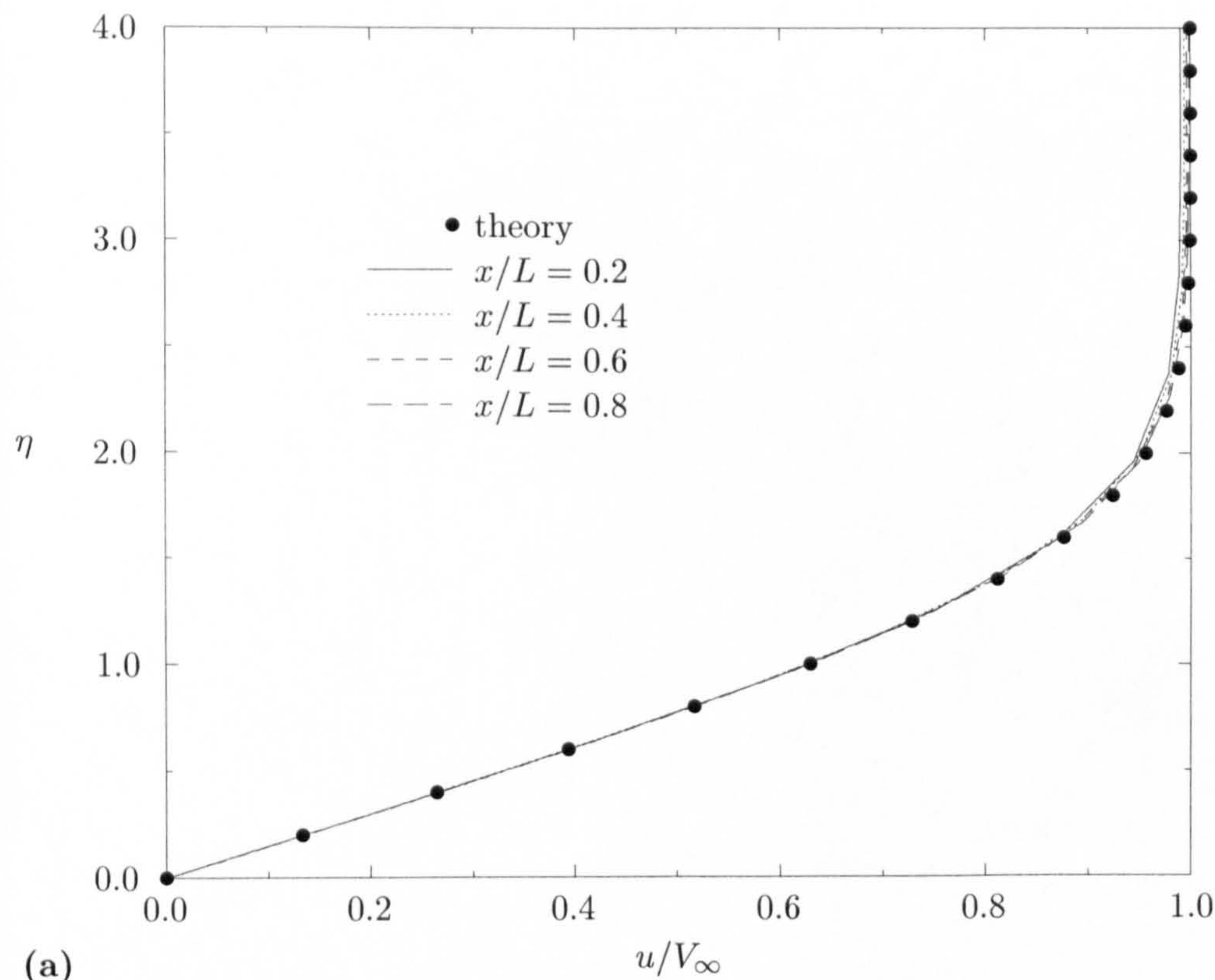


Figure 7.10: Comparison of numerical solution with thin-shear-layer approximation on quadrilateral grid for (a) u -velocity and (b) v -velocity with theoretical solution at four locations along flat plate.

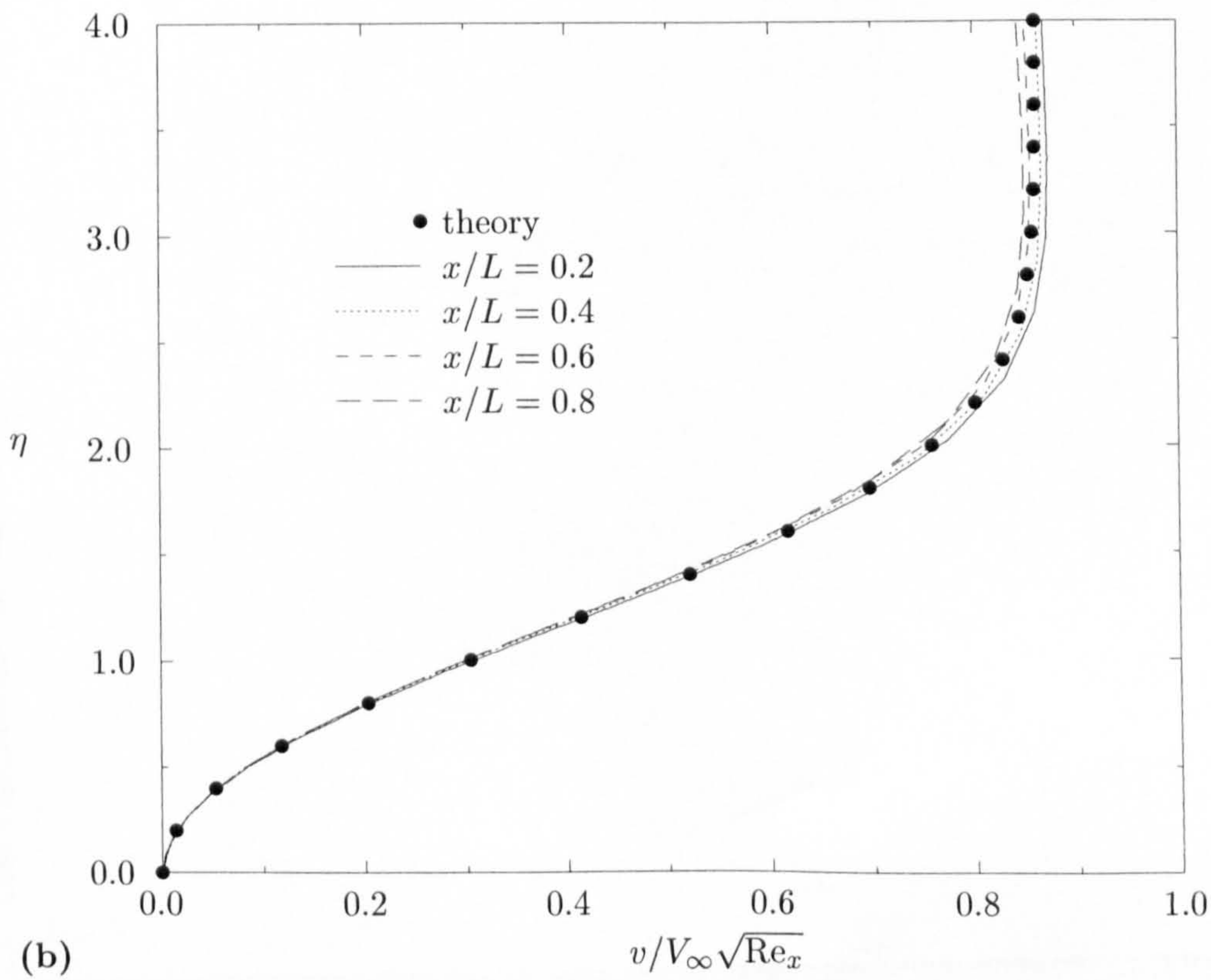
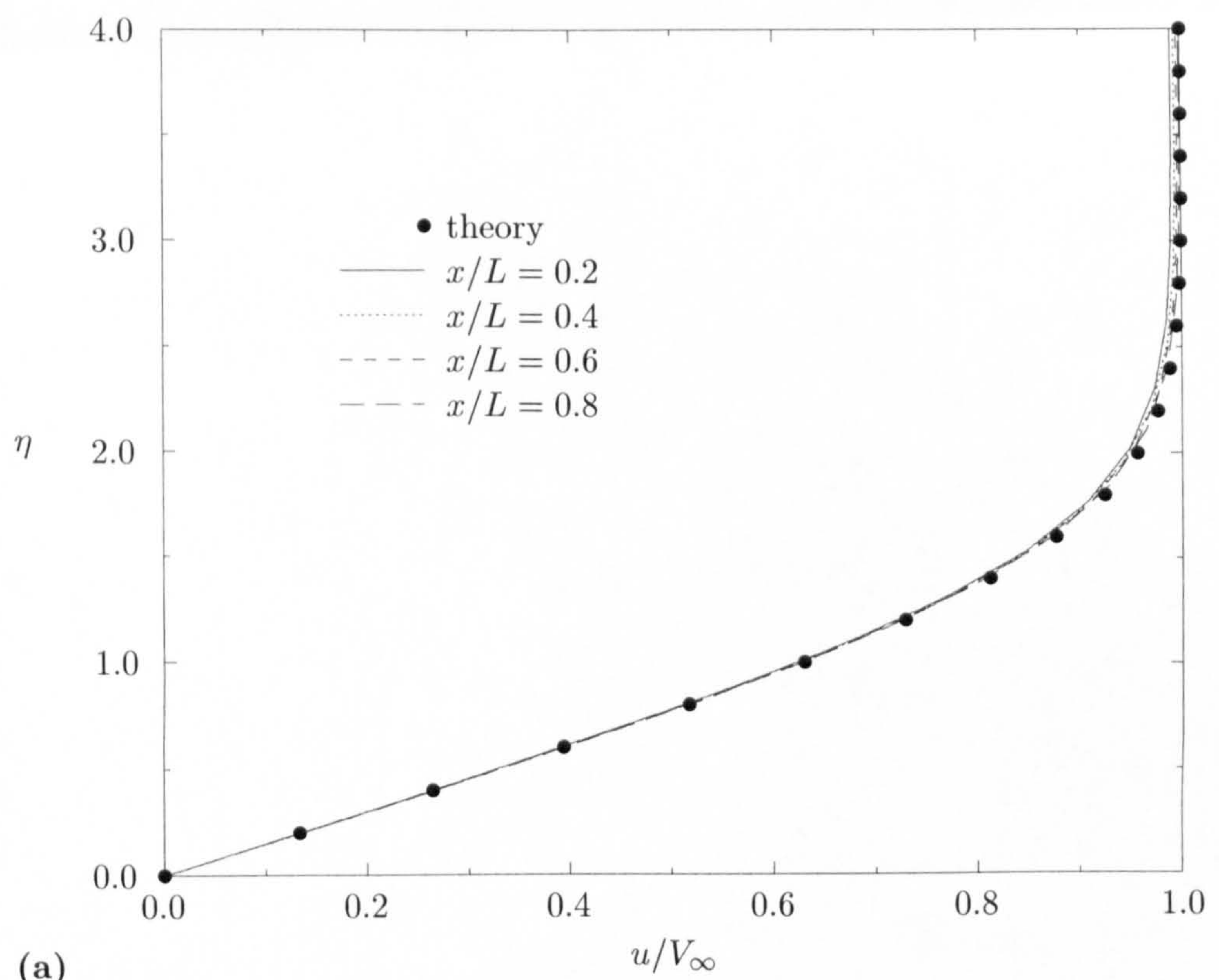


Figure 7.11: Comparison of numerical solution with thin-shear-layer approximation on mixed grid for (a) u -velocity and (b) v -velocity with theoretical solution at four locations along flat plate.

7.3 NACA 0012 Aerofoil

The second test case is the laminar flow about the NACA 0012 aerofoil at a Mach number of $M_\infty = 0.8$, an angle of attack of $\alpha = 10^\circ$, and a Reynolds number of $Re_\infty = 500$. This flow was part of a GAMM workshop [4] as test case A2.

At the conditions stated above, a large separation bubble exists on the upper surface. The challenge posed by this test case is that separation occurs on a curved surface rather than being fixed by a sharp corner. To capture the separation point accurately, the deceleration of the boundary layer approaching the separation point must be captured precisely.

The solution domain is depicted in Fig. 7.12. The outer boundary is located at approximately 10 chords. The far-field point vortex correction described in Subsection 3.11.2 is applied.

The goal of this test case is two-fold:

1. To further study the numerical accuracy obtained on triangular and quadrilateral grids for viscous flows. The large separation bubble makes this test case more challenging than the flow over the flat plate considered in the previous section.
2. To assess the thin-shear-layer approximation under more severe conditions.

Because there exists no analytical solution for this test case, the accuracy of the numerical solutions is assessed by a grid-refinement study. The triangular grids are created by inserting additional edges into the quadrilateral grids. The characteristics of the four telescoping grid levels are listed in Table 7.2. The primal and dual medium triangular and quadrilateral grids are shown in Figs. 7.13 and 7.14, respectively. Note that the additional edges in the triangular grids are inserted such that the approximate symmetry of the grids is preserved.

The solutions are compared using the lift and drag coefficients. The coefficients are considered to consist of inviscid and viscous contributions, and are given by

$$C_L = - \oint [C_p(n_x \sin \alpha - n_y \cos \alpha) + C_f(t_x \sin \alpha - t_y \cos \alpha)] ds \quad (7.3.1a)$$

$$C_D = \oint \underbrace{[C_p(n_x \cos \alpha + n_y \sin \alpha)]}_{C_{Dp}} + \underbrace{[C_f(t_x \cos \alpha + t_y \sin \alpha)]}_{C_{Df}} ds \quad (7.3.1b)$$

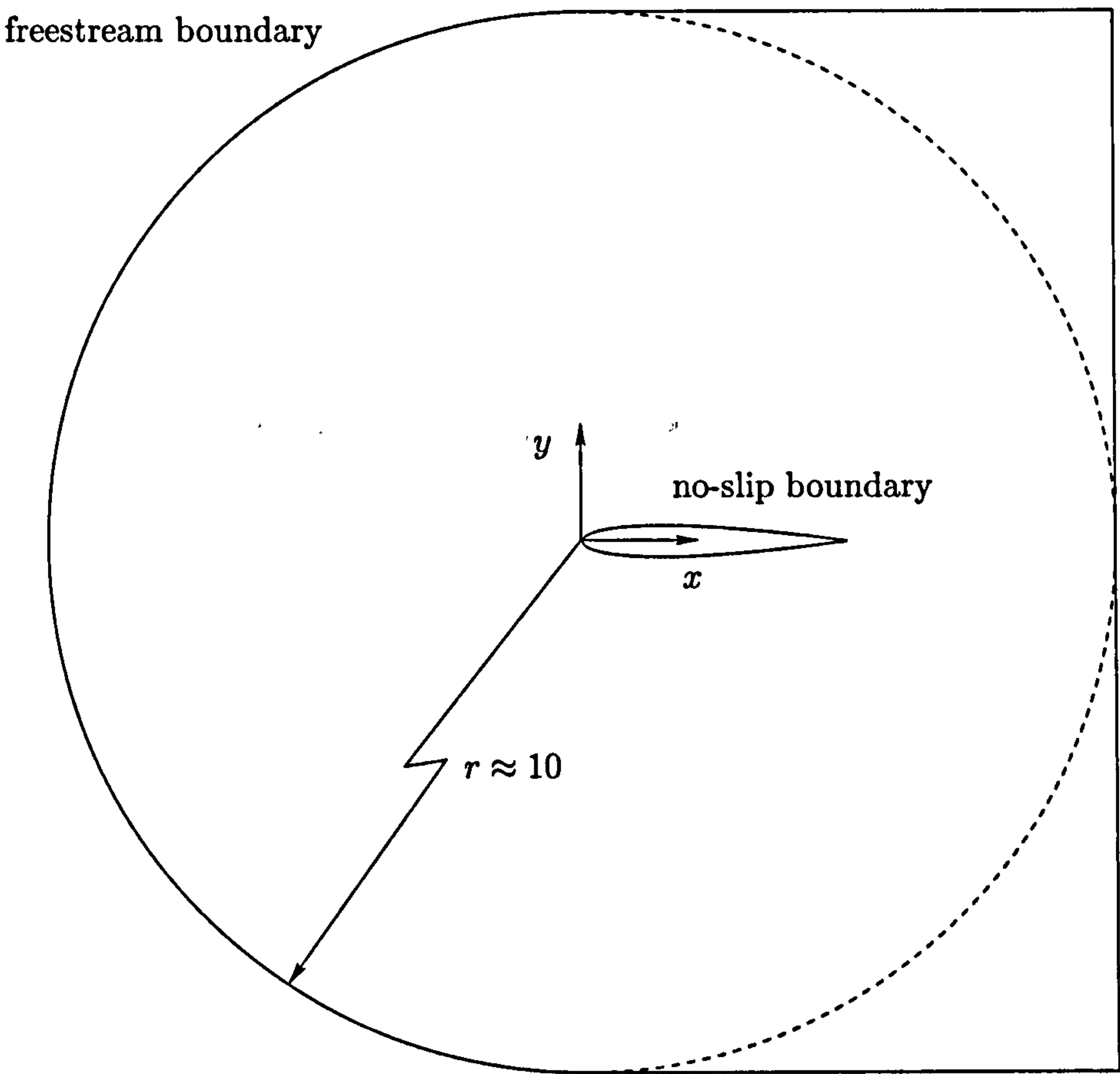


Figure 7.12: Solution domain and boundary conditions for laminar flow about NACA 0012 aerofoil.

Table 7.2: Summary of grid characteristics used in grid-refinement study for subsonic laminar flow about NACA 0012 aerofoil.

level	vertices	triangular grid		quadrilateral grid	
		edges	cells	edges	cells
base	291	803	512	547	256
coarse	1094	3142	2048	2118	1024
medium	4236	12428	8192	8332	4096
fine	16664	49432	32768	33048	16384

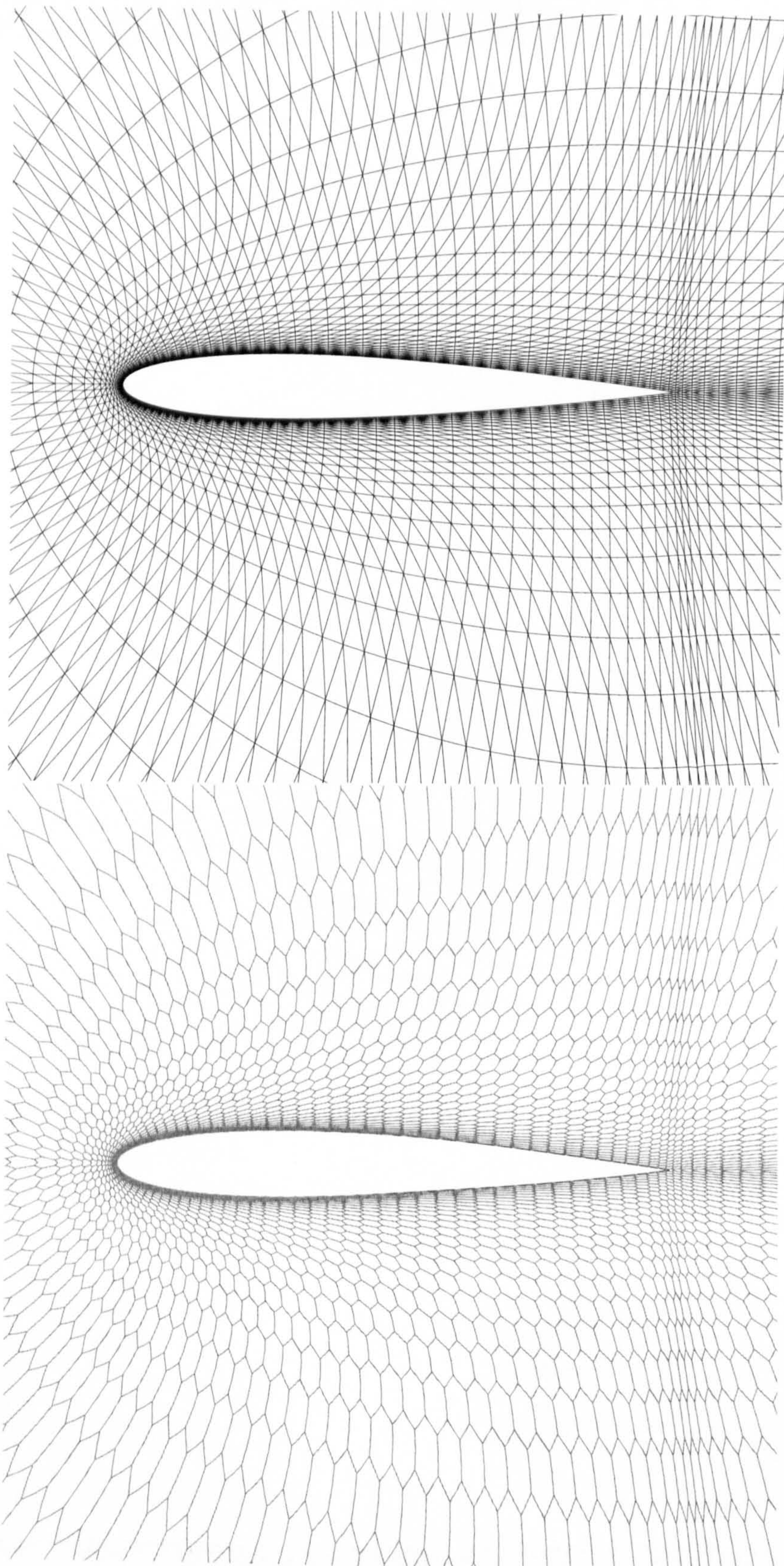


Figure 7.13: Primal and dual medium triangular grids used in grid-refinement study for laminar subsonic flow about NACA 0012 aerofoil.

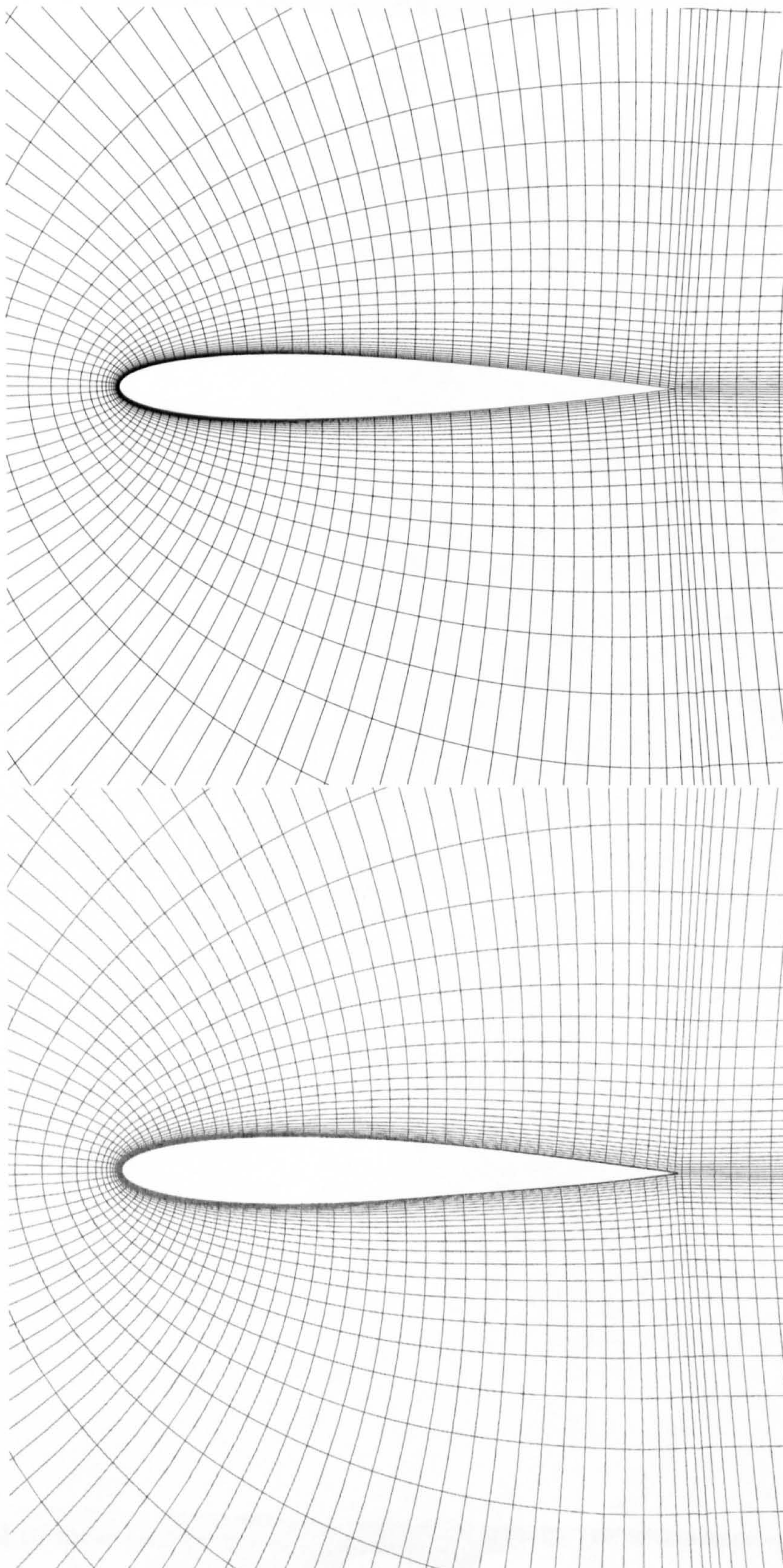


Figure 7.14: Primal and dual medium quadrilateral grids used in grid-refinement study for laminar subsonic flow about NACA 0012 aerofoil.

where the pressure coefficient is defined in Eq. (6.4.2) and the skin-friction coefficient C_f is defined as

$$C_f = \frac{\tau_{\text{wall}}}{\frac{1}{2}\rho_{\infty}V_{\infty}^2}, \quad (7.3.2)$$

where the wall shear stress τ_{wall} is evaluated from Eq. (4.4.14). Since the flow features a large separation bubble, it is of interest to compare the positions of the separation and re-attachment points computed on the various grids.

7.3.1 Grid-Refinement Study

The influence of the grid type is investigated by carrying out a grid-refinement study as stated above. On the triangular grids, the discretisation of the viscous fluxes developed in Chapter 4 is compared to the well-established Galerkin finite-element discretisation of the viscous fluxes on triangular grids.

Influence of Grid Type. The Mach-number contours, plots of the streamlines on the fine grid level, and the behaviour of the pressure and friction coefficients are depicted in Figs. 7.16–7.20 for the quadrilateral and the triangular grids with the finite-volume and finite-element discretisation of the viscous fluxes. For the quadrilateral grids, the variations on the coarse level are already quite close to that on the fine level. For the triangular grids, only the variations on the medium level are approximately as close.

The lift and drag coefficients on the quadrilateral and triangular grids are plotted against the inverse of the square root of the number of vertices on the grid levels in Fig. 7.21. A number of interesting points can be made from this figure:

1. There is virtually no difference between the finite-volume and finite-element discretisations of the viscous fluxes on the triangular grids, thus confirming the validity of the finite-volume discretisation and its implementation.
2. The values of lift and drag coefficients on the finest levels are very close on the quadrilateral and triangular grids. Since the values on the finest levels are not equal to those on the medium levels, the former cannot be claimed to be strictly grid-independent. However, since the differences between the finest and medium levels are much smaller than those between the medium and coarse levels, it is

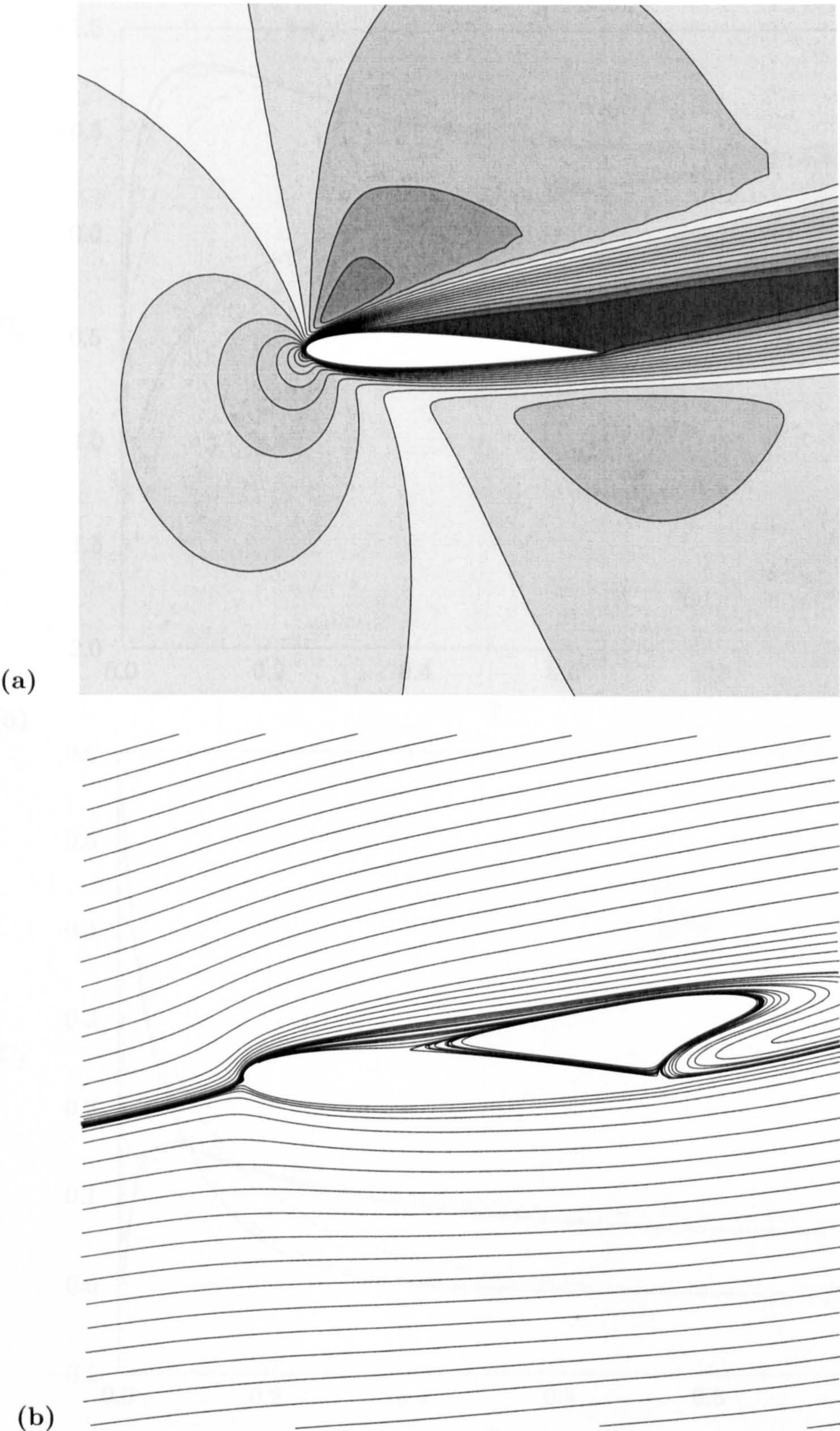


Figure 7.15: (a) Mach contours (0.0,1.110;15) and (b) streamlines with finite-volume discretisation of viscous fluxes on fine level quadrilateral grid.

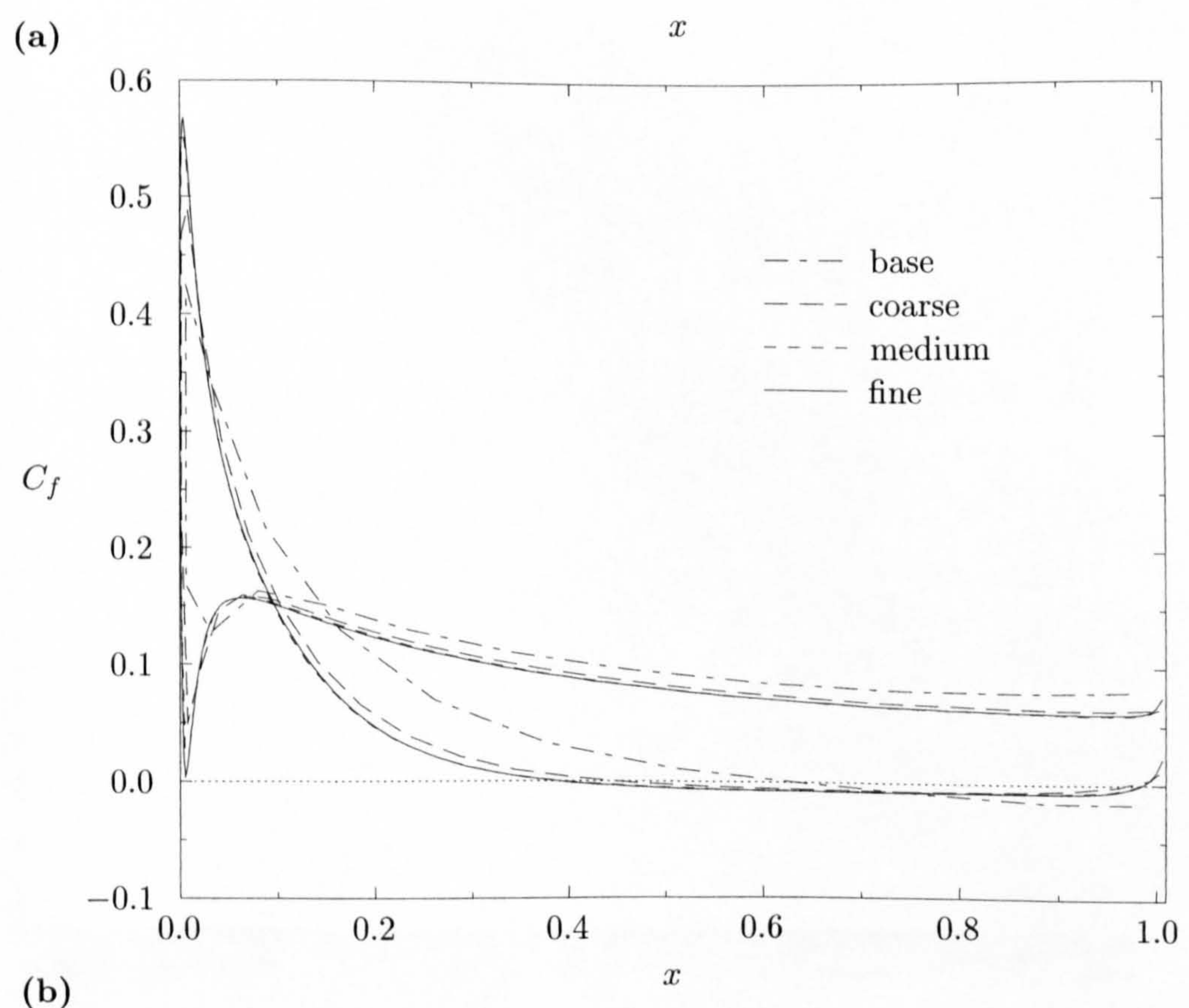
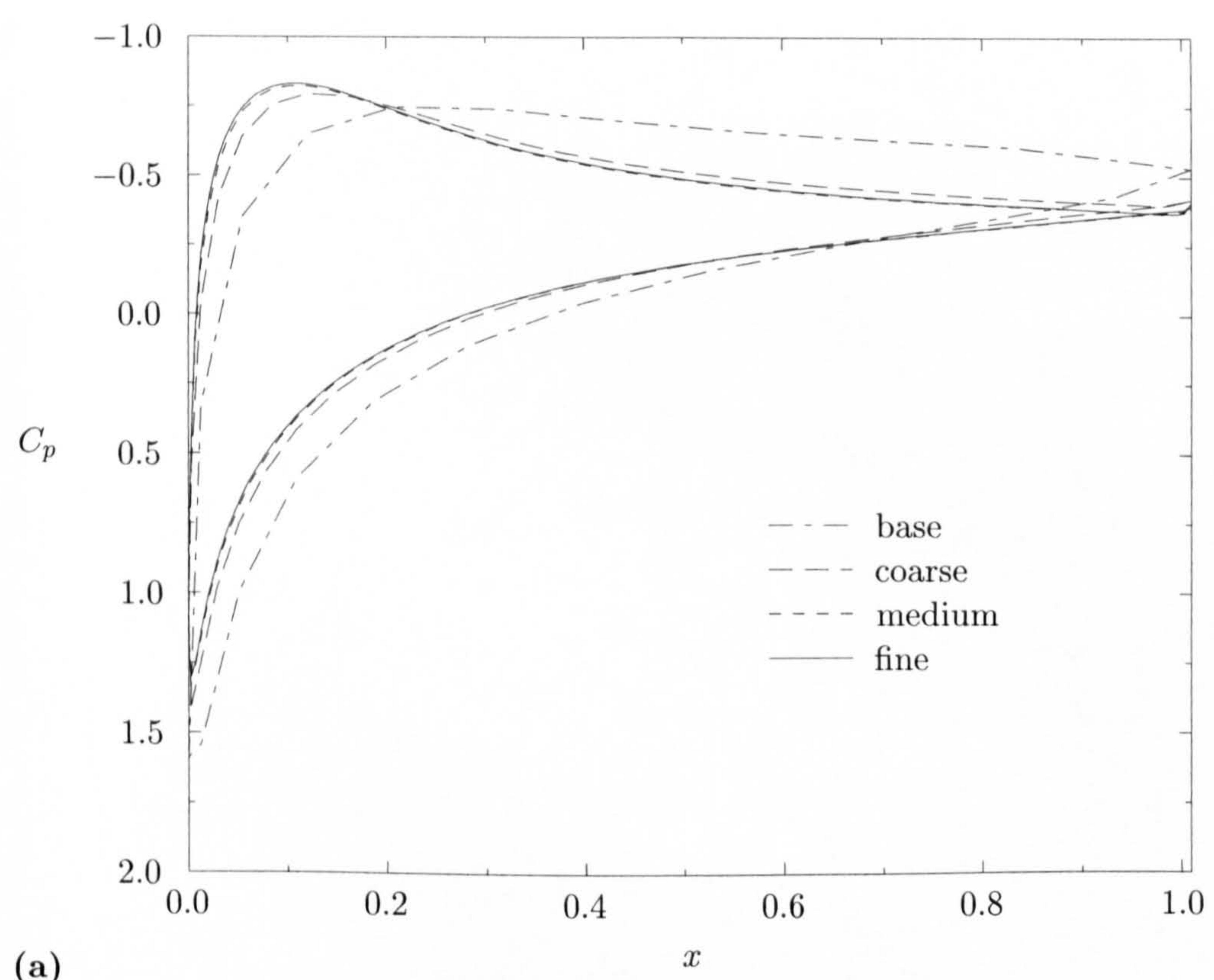


Figure 7.16: Behaviour of (a) pressure coefficient and (b) skin-friction coefficient with grid refinement on quadrilateral grids.

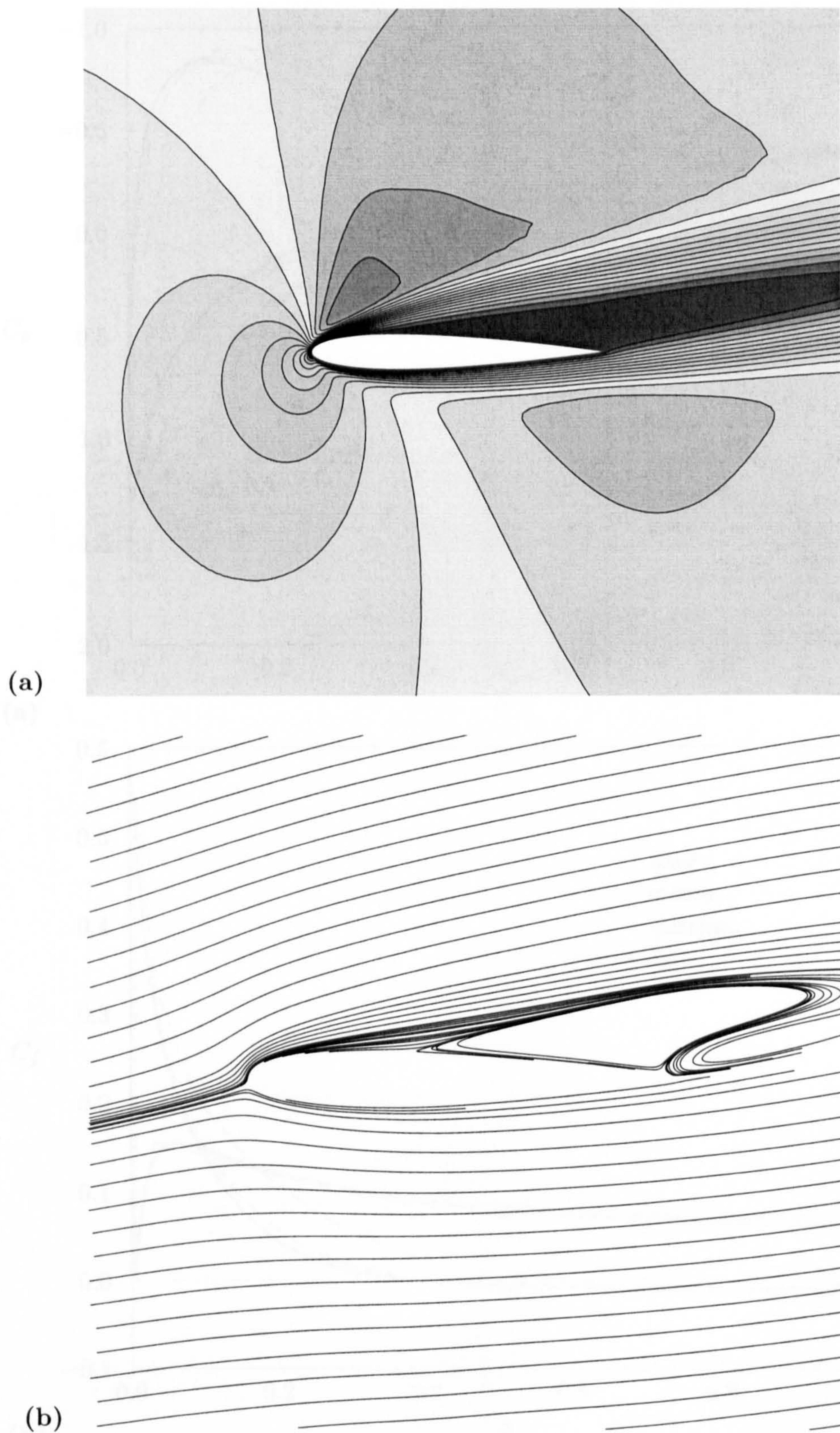
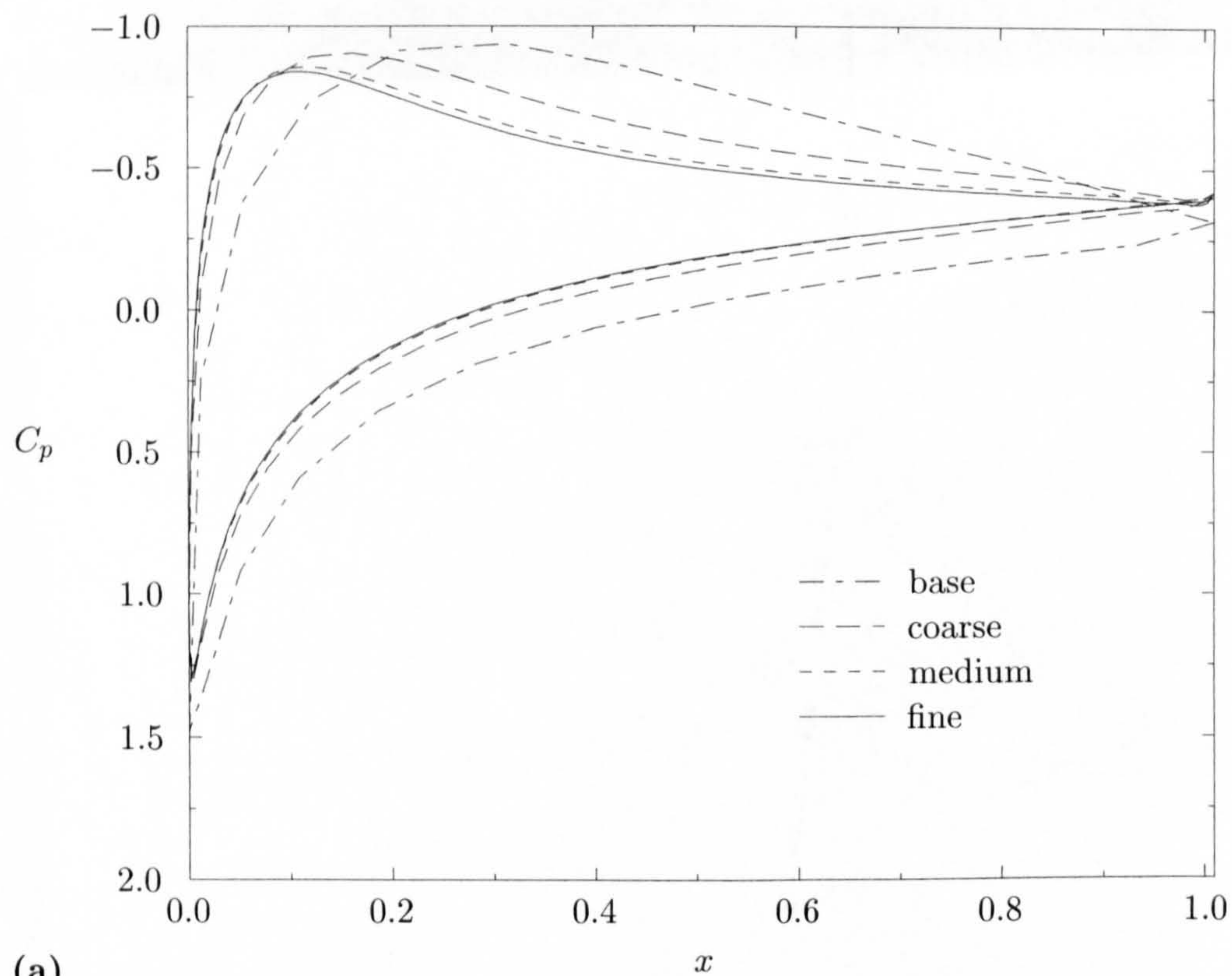
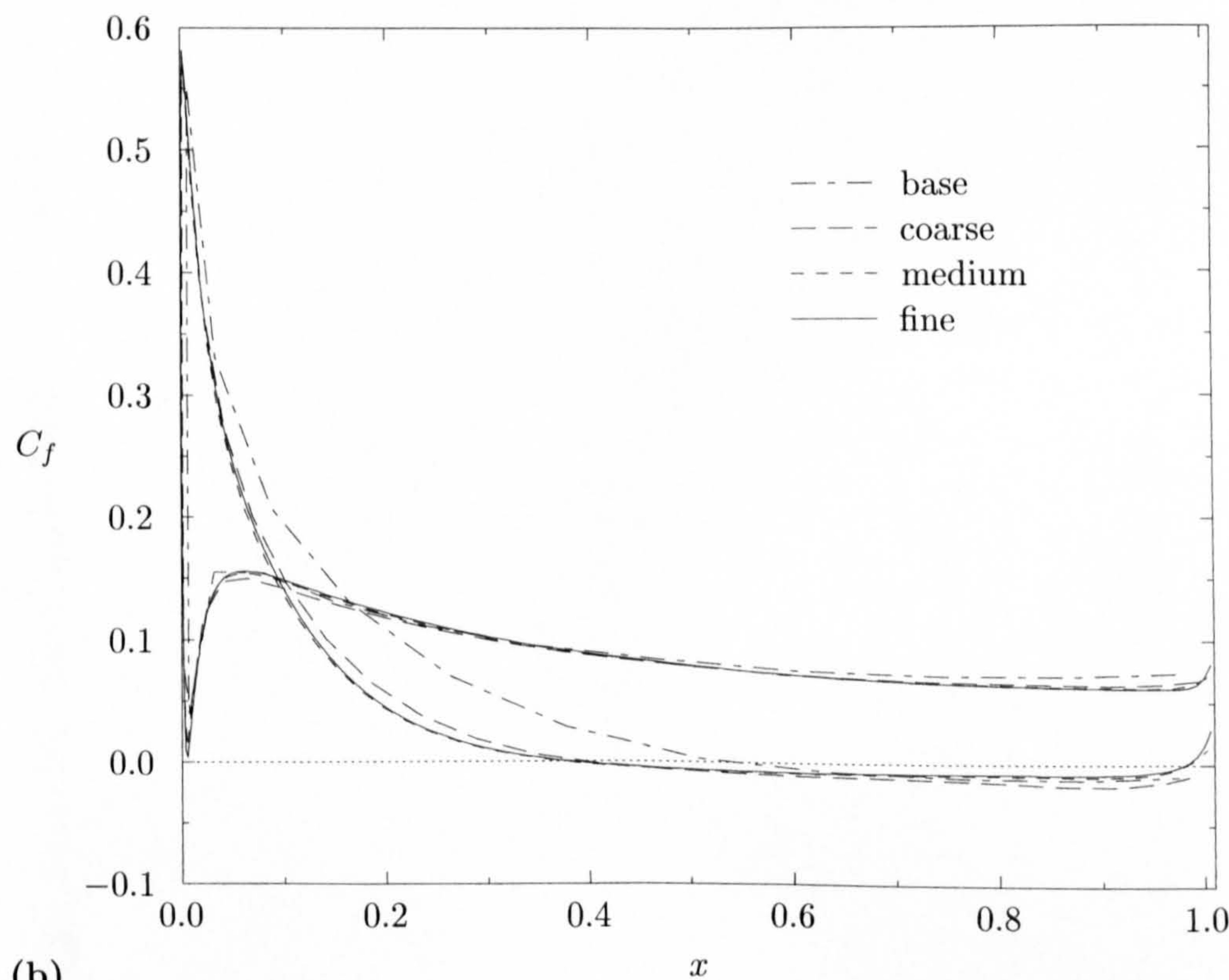


Figure 7.17: (a) Mach contours (0.0,1.110;15) and (b) streamlines with finite-volume discretisation of viscous fluxes on fine level triangular grid.



(a)



(b)

Figure 7.18: Behaviour of (a) pressure coefficient and (b) skin-friction coefficient with grid refinement on triangular grids with finite-volume discretisation of viscous fluxes.

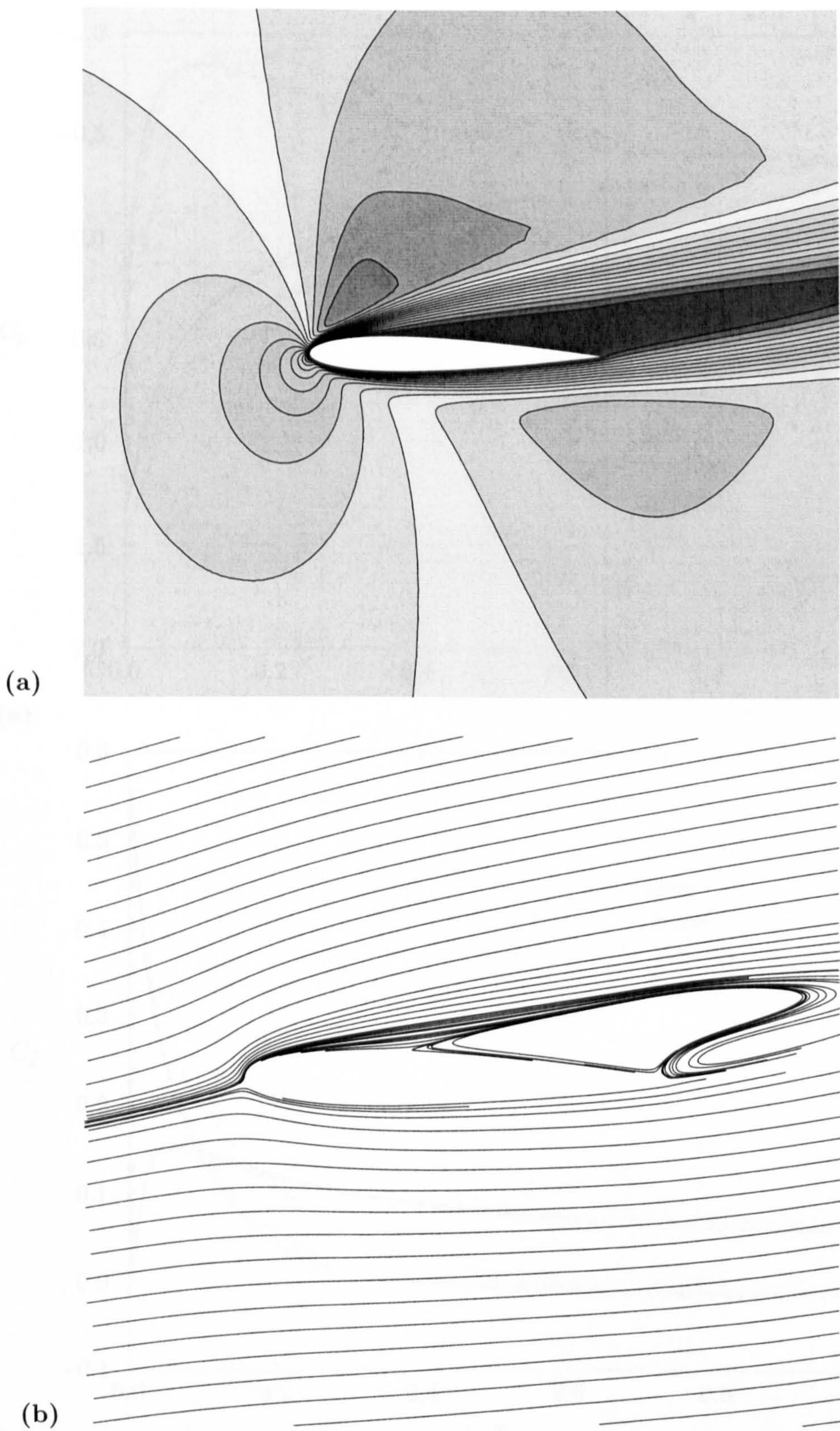


Figure 7.19: (a) Mach number contours (0.0,1.110;15) and (b) streamlines with finite-element discretisation of viscous fluxes on fine level triangular grid.

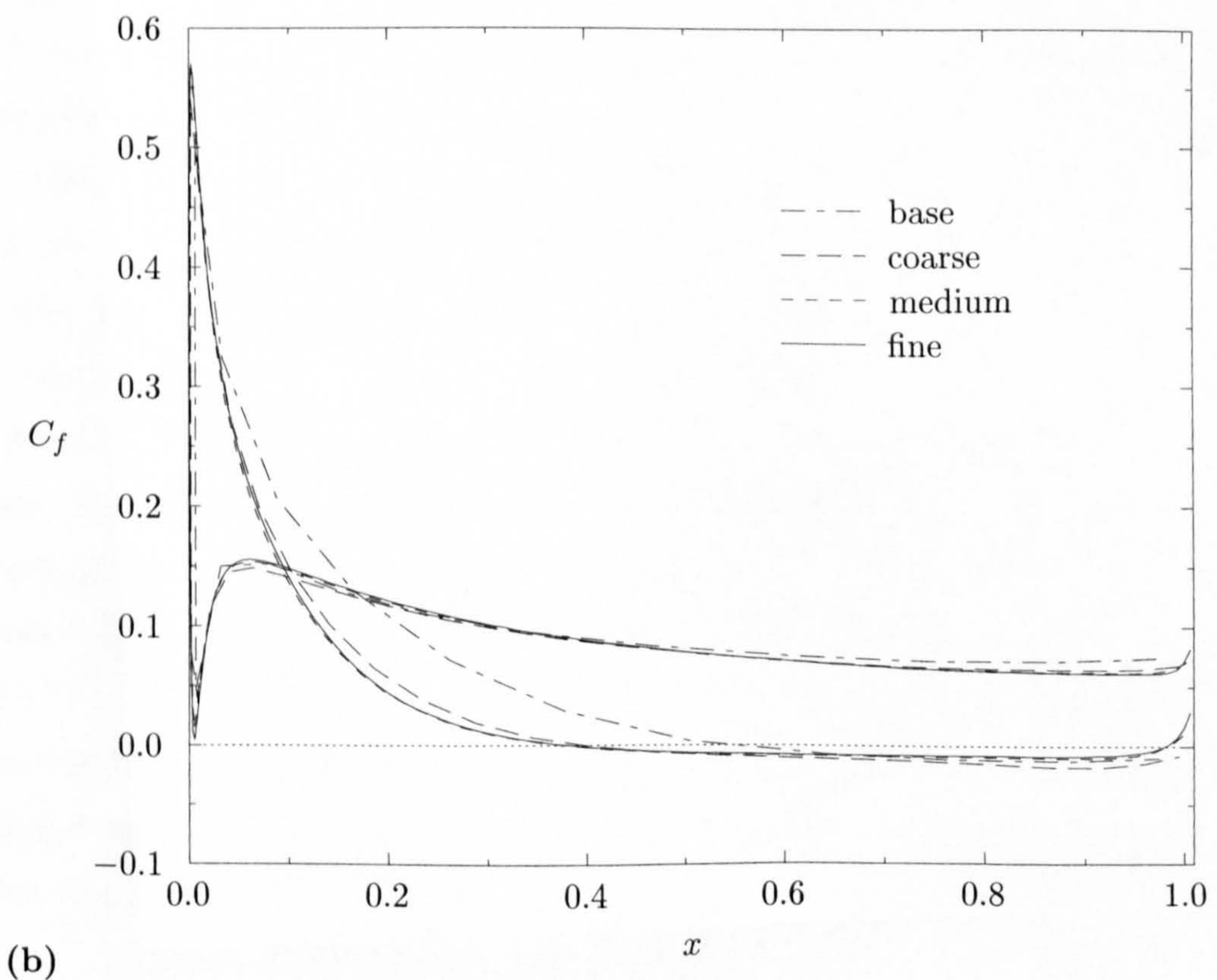
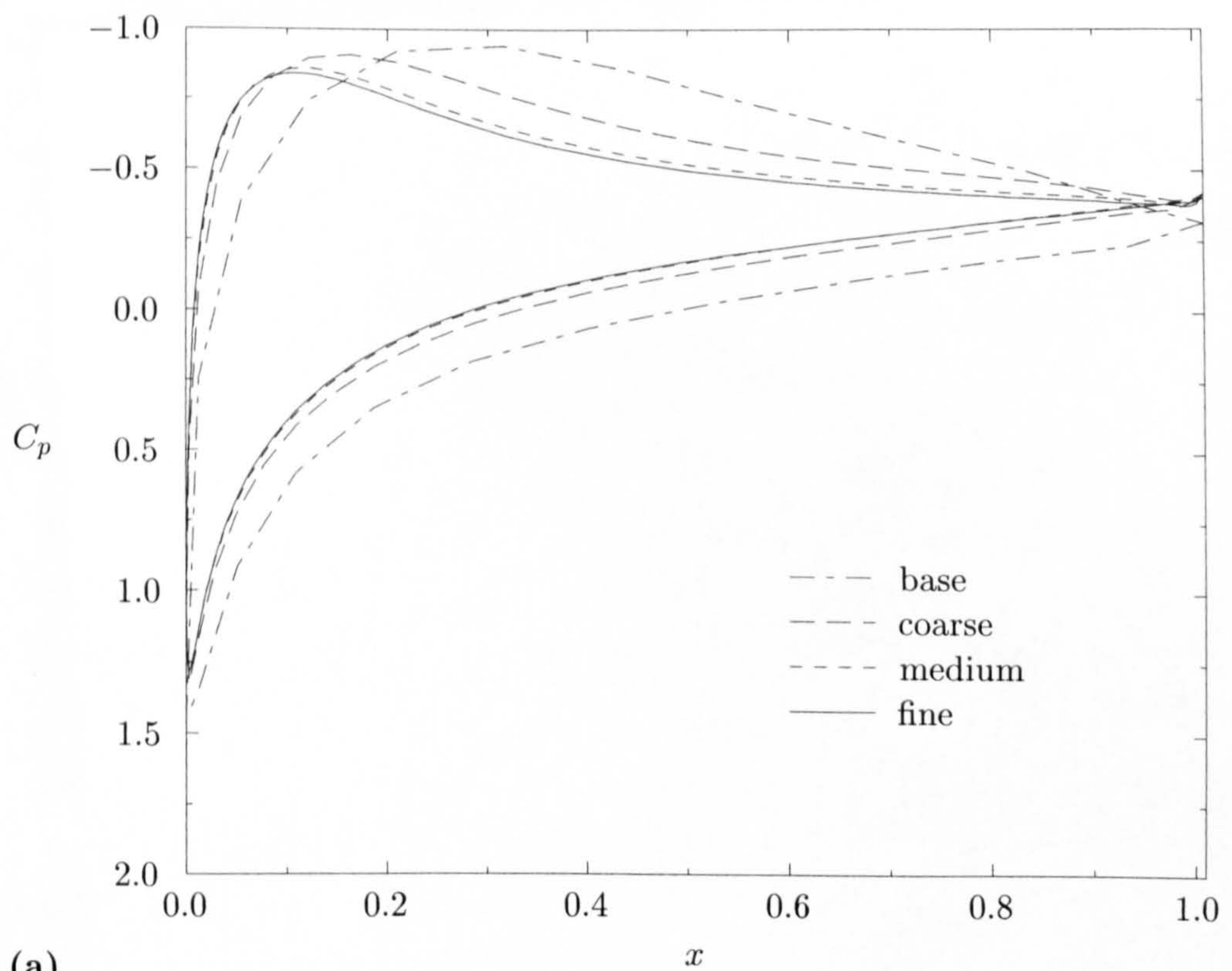


Figure 7.20: Behaviour of (a) pressure coefficient and (b) skin-friction coefficient with grid refinement on triangular grids with finite-element discretisation of viscous fluxes.

reasonable to assume that the results on the finest levels are close to grid independence. It is also of interest to note that the convergence of the lift coefficient on the quadrilateral grids is non-monotone. Such behaviour was observed by other researchers carrying out grid-refinement studies, see, e.g., Zingg et al. [9], and does not indicate numerical anomalies in the present solutions.

3. Whereas the difference between the lift coefficients on the base and fine levels of the quadrilateral grids is much smaller than that of the triangular grids, there are only small differences between the drag coefficients. The explanation for this difference in behaviour may be found in Fig. 7.22. On the coarse and medium grid level, the contribution of the pressure drag on the triangular grids is higher than that on the quadrilateral grid, but is compensated for by a lower contribution of the friction drag.

It is interesting to consider how the third observation concerning the relative importance of pressure and friction drag contributions on the triangular grids is connected to the level of numerical dissipation. Previous results indicated that the level of numerical dissipation was higher on the triangular grids. This seems to be in contradiction to Fig. 7.23, which indicates that separation positions are closer to the trailing edge on coarser grids, on which there is more numerical dissipation. Since the separation positions on the triangular grids are closer to the leading edge, this could be taken to mean that the solutions on the quadrilateral grids are more heavily contaminated by numerical dissipation. That this is not the case may be seen from the observation under Point 3, namely that the difference between the friction drag coefficients on the triangular and quadrilateral grids is not as large as that between the pressure drag coefficients. This is also easily seen from the distribution of the pressure coefficient in Figs. 7.16, 7.18, and 7.20. On the base and coarse levels of the triangular grids, there is a relatively large adverse pressure gradient. By comparison, the adverse pressure gradient on the base and coarse levels of the quadrilateral grid is much smaller. This indicates that the extent of the separation bubble is dominated by the pressure forces.

Assessment of Thin-Shear-Layer Approximation. The performance of the thin-shear-layer approximation is assessed by performing a grid-refinement study on the

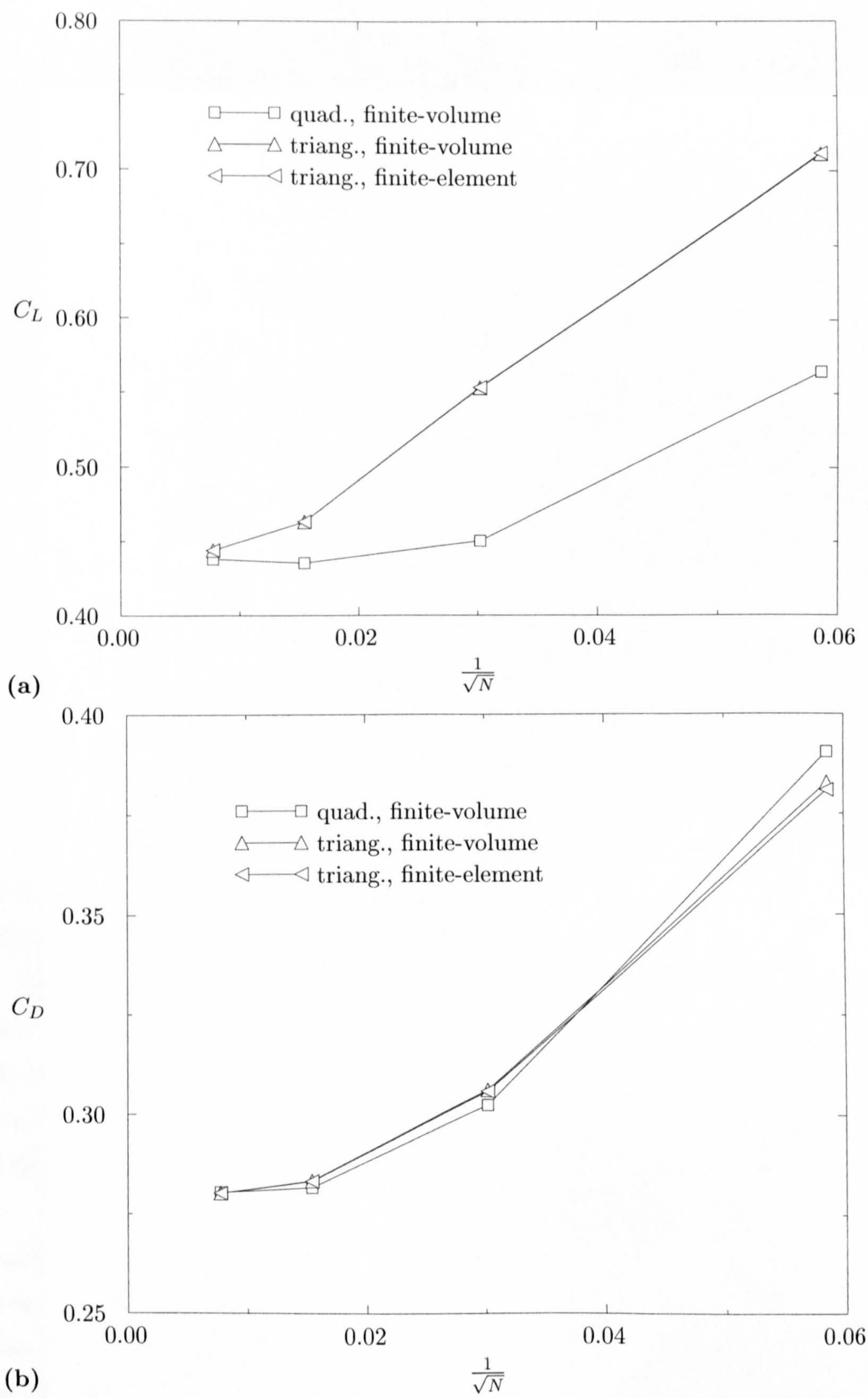


Figure 7.21: Behaviour of (a) lift and (b) drag coefficients with grid refinement for quadrilateral and triangular grids.

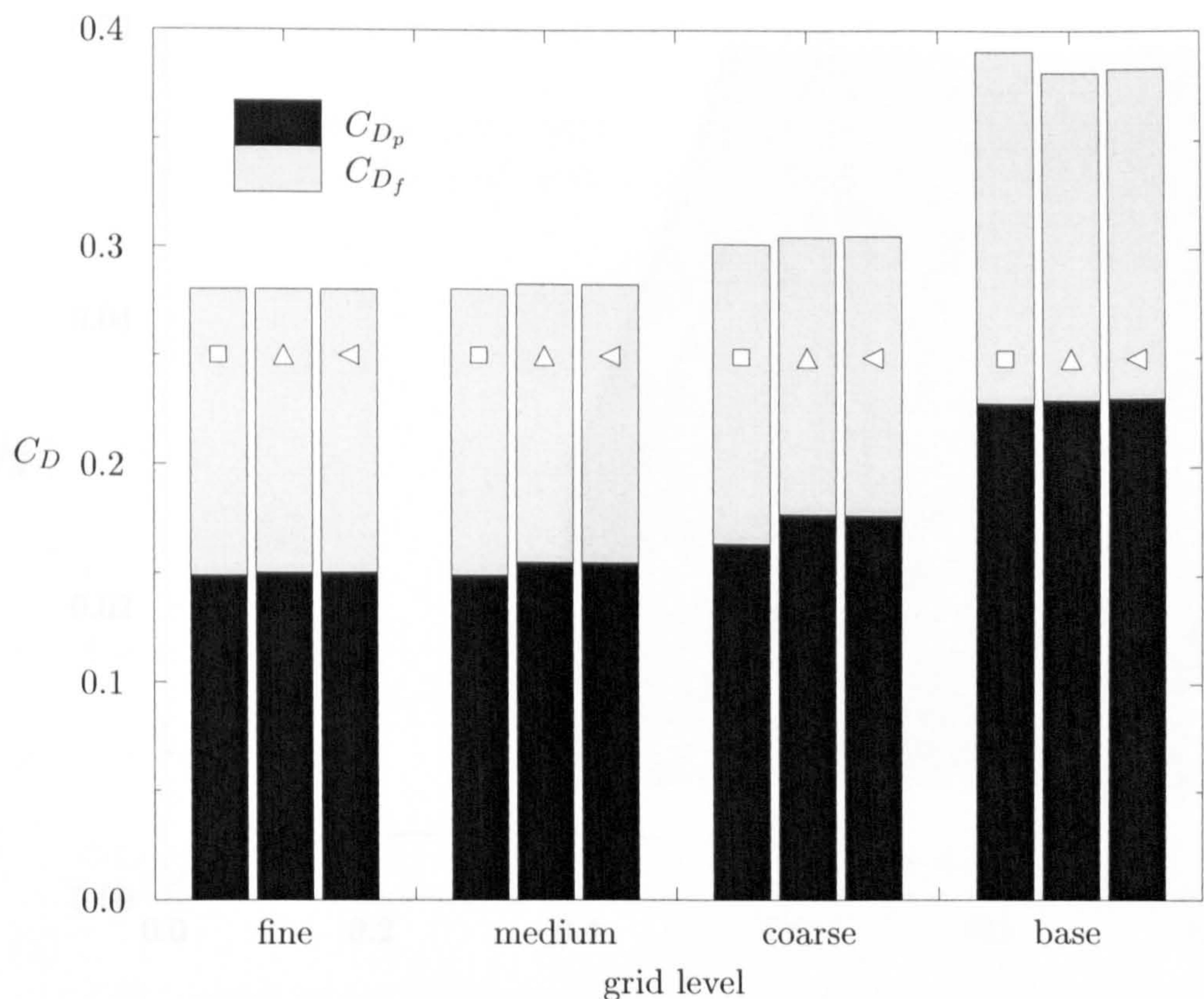


Figure 7.22: Break-up of drag coefficient into pressure and friction drag coefficients with grid refinement for quadrilateral and triangular grids. Legend as shown in Fig. 7.21. C_{Dp} and C_{Df} defined as indicated in Eq. (7.3.1b).

same grids as used above and comparing the results with those obtained for the full viscous fluxes.

Before discussing the results, it must be remarked that the computation of a separated flow at a very low Reynolds number constitutes a very severe test for the thin-shear-layer approximation, as the flow conditions basically invalidate the assumptions made in its derivation. For this reason, the relative importance of the terms appearing in the viscous fluxes will be investigated in detail.

Quadrilateral Grids. The behaviour of the lift and drag coefficients with grid refinement with the thin-shear-layer approximation is compared in Fig. 7.24 to the previously discussed results obtained with the full viscous fluxes. It is seen that the variation of the lift coefficient predicted by the approximate form of the viscous fluxes is very close to that obtained with the full form. For the drag coefficient, agreement is not quite as

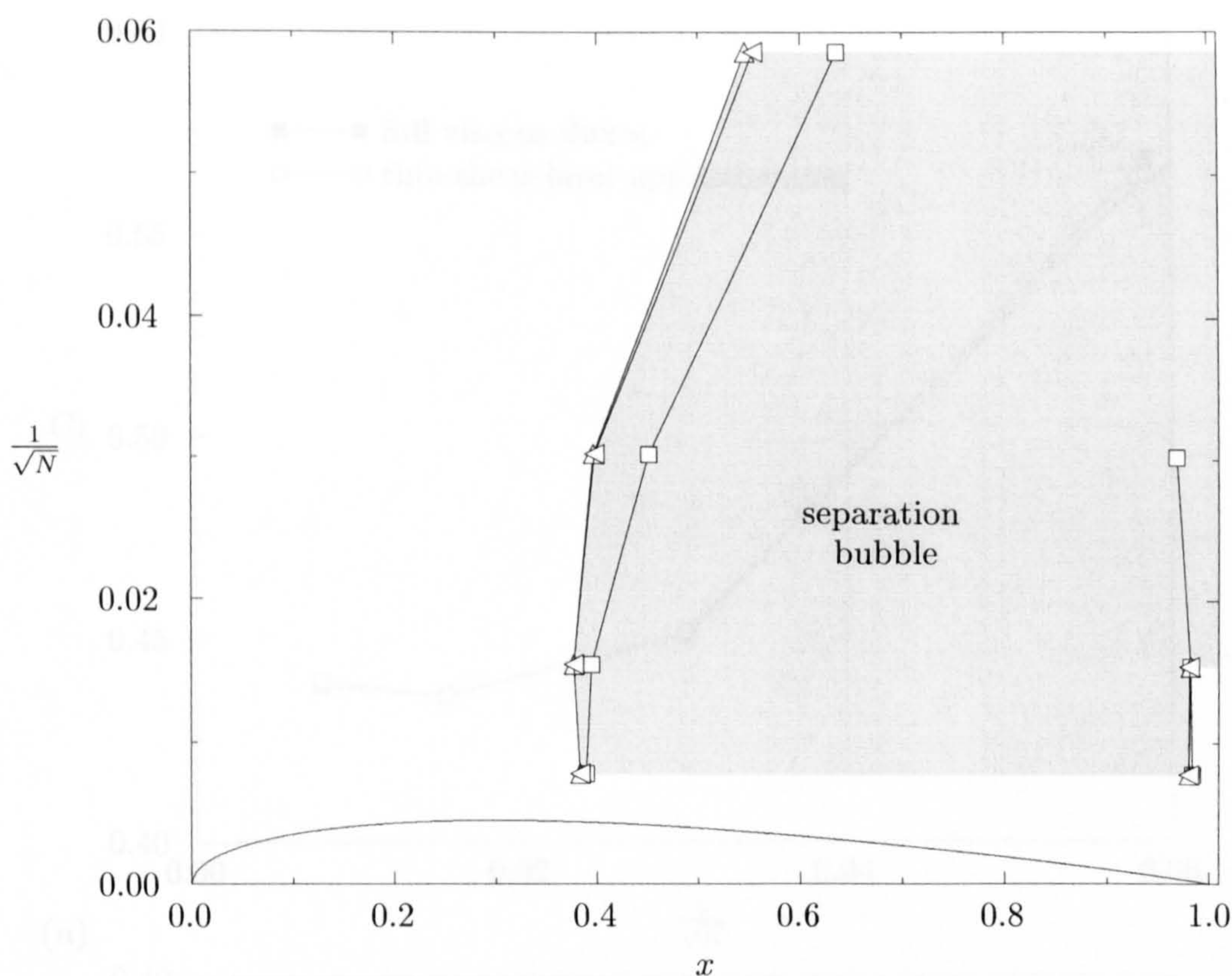


Figure 7.23: Behaviour of separation and reattachment positions with grid refinement for quadrilateral and triangular grids. Legend as shown in Fig. 7.21.

close, but still unexpectedly good.

The reason for the better than expected agreement may be found from Figs. 7.25 and 7.26, which show the relative importance of the three terms in Expressions (4.4.4a) and (4.4.4b) along normals emanating from the upper surface of the aerofoil at $x = 0.2$ and $x = 0.7$, respectively. The former position is about midway between the leading edge and the separation position, and the latter position is within the separation bubble. The variations show clearly that the first terms in Expressions (4.4.4a) and (4.4.4b) are dominant. This explains the good agreement, since the thin-shear-layer approximation developed within the present work treats this term exactly.

The behaviour of the separation and reattachment positions computed with the thin-shear-layer approximation is compared in Fig. 7.27 to that obtained with the full viscous fluxes. Overall agreement is once again surprisingly good.

Triangular Grids. The behaviour of the lift and drag coefficients with grid refinement

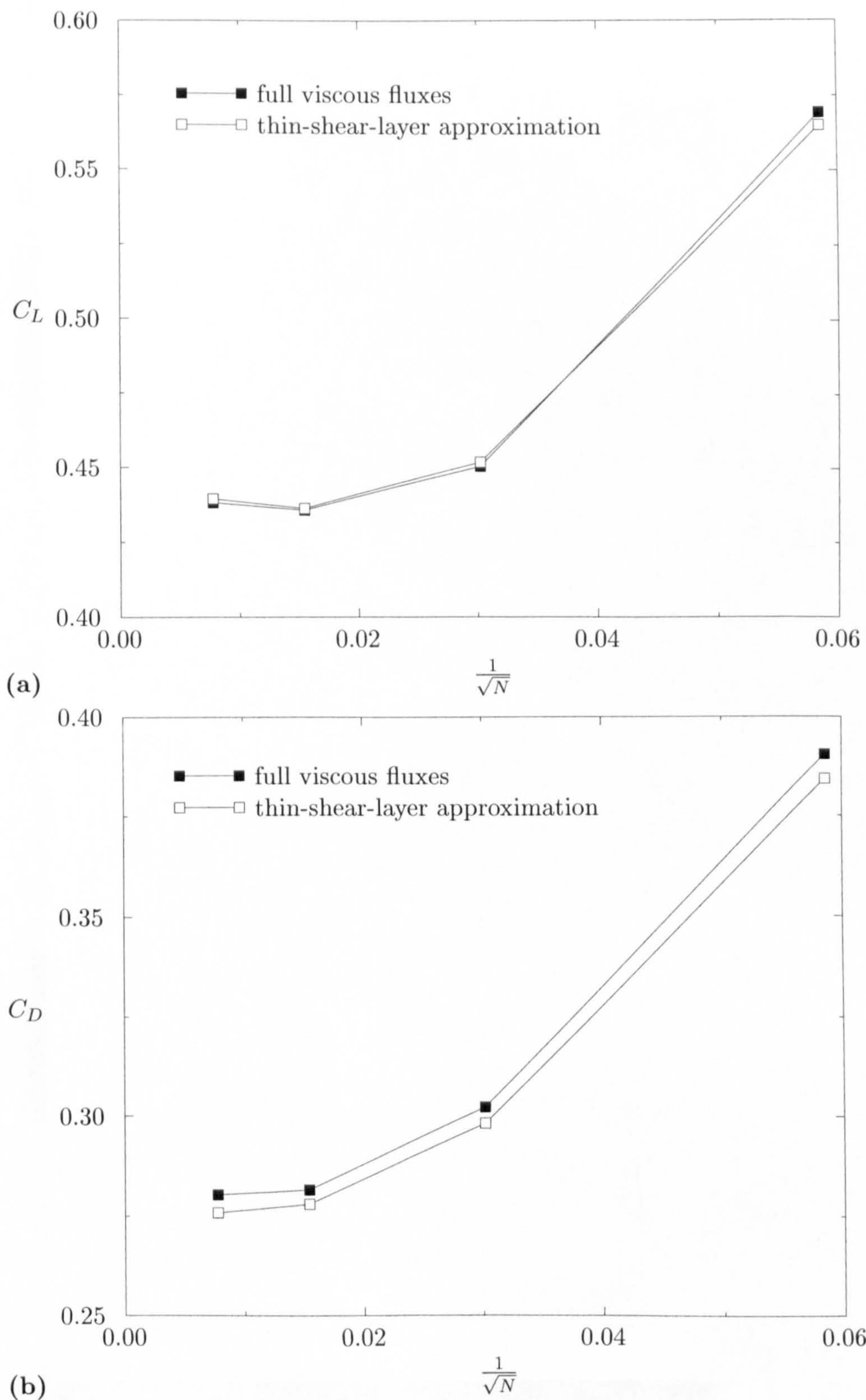


Figure 7.24: Comparison of behaviour of (a) lift and (b) drag coefficients with grid refinement for quadrilateral grids for full viscous fluxes and thin-shear-layer approximation.

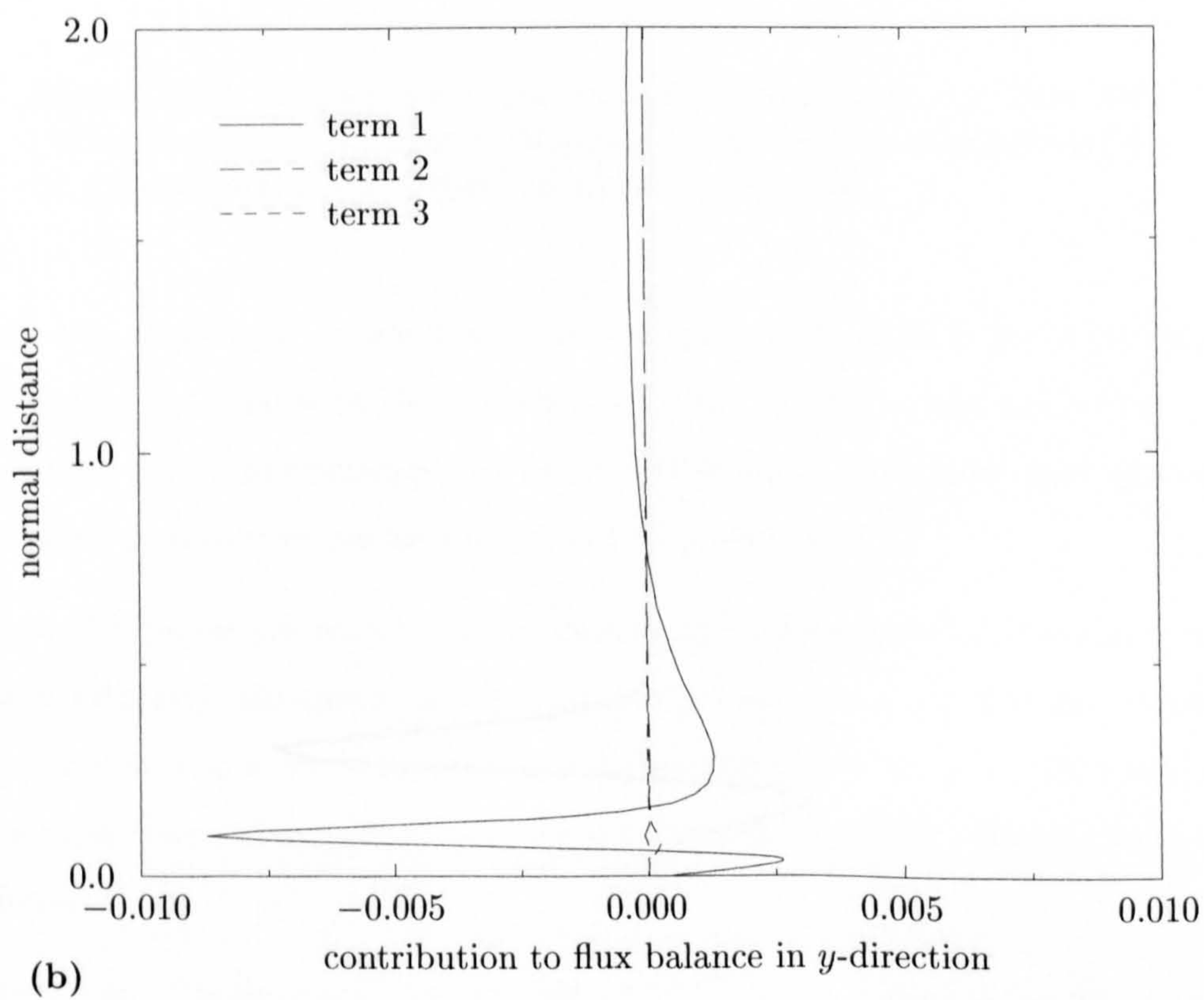
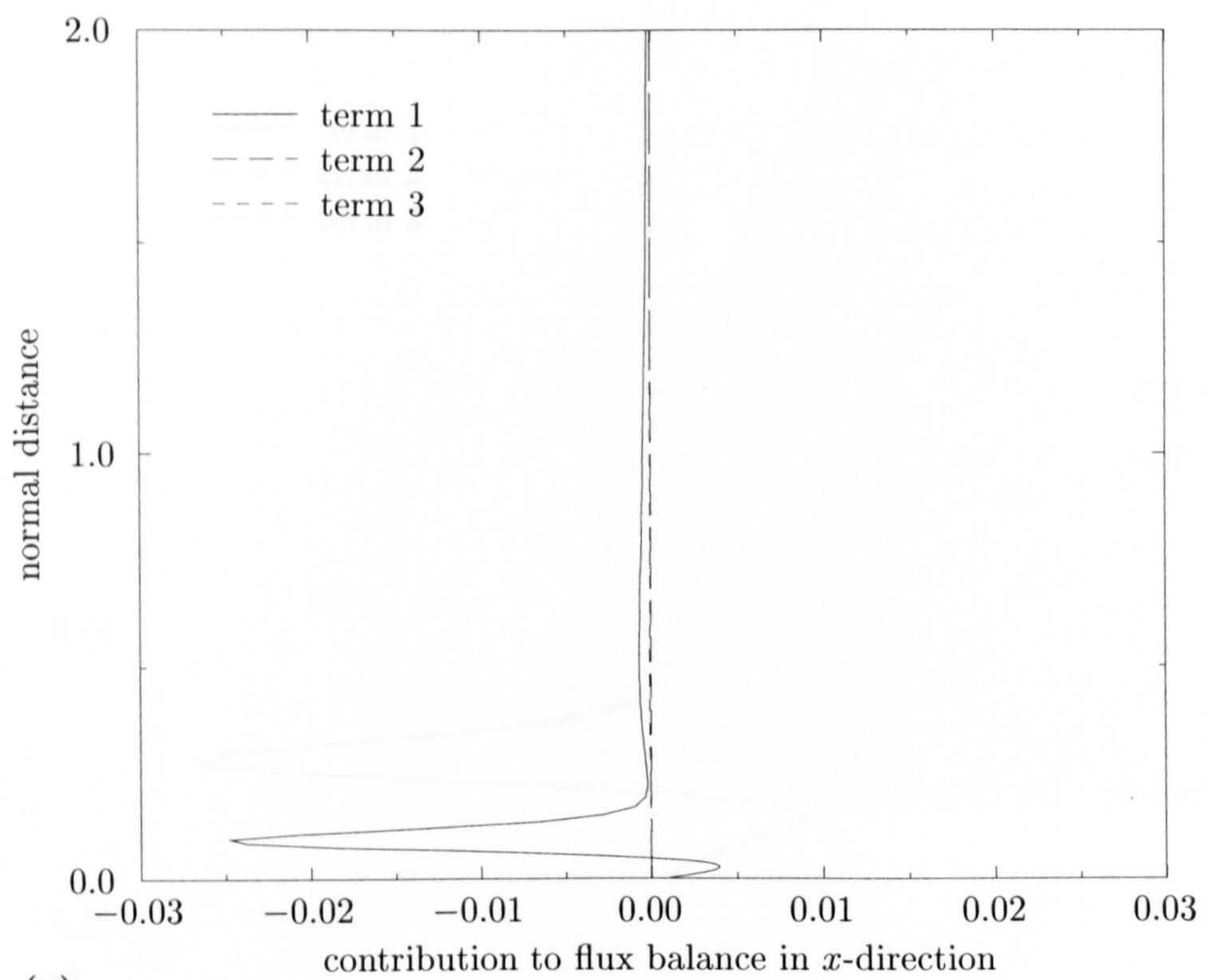


Figure 7.25: Relative importance of terms in (a) Expression (4.4.4a) and (b) Expression (4.4.4b) along normal at $x = 0.2$ on upper surface for fine level quadrilateral grid.

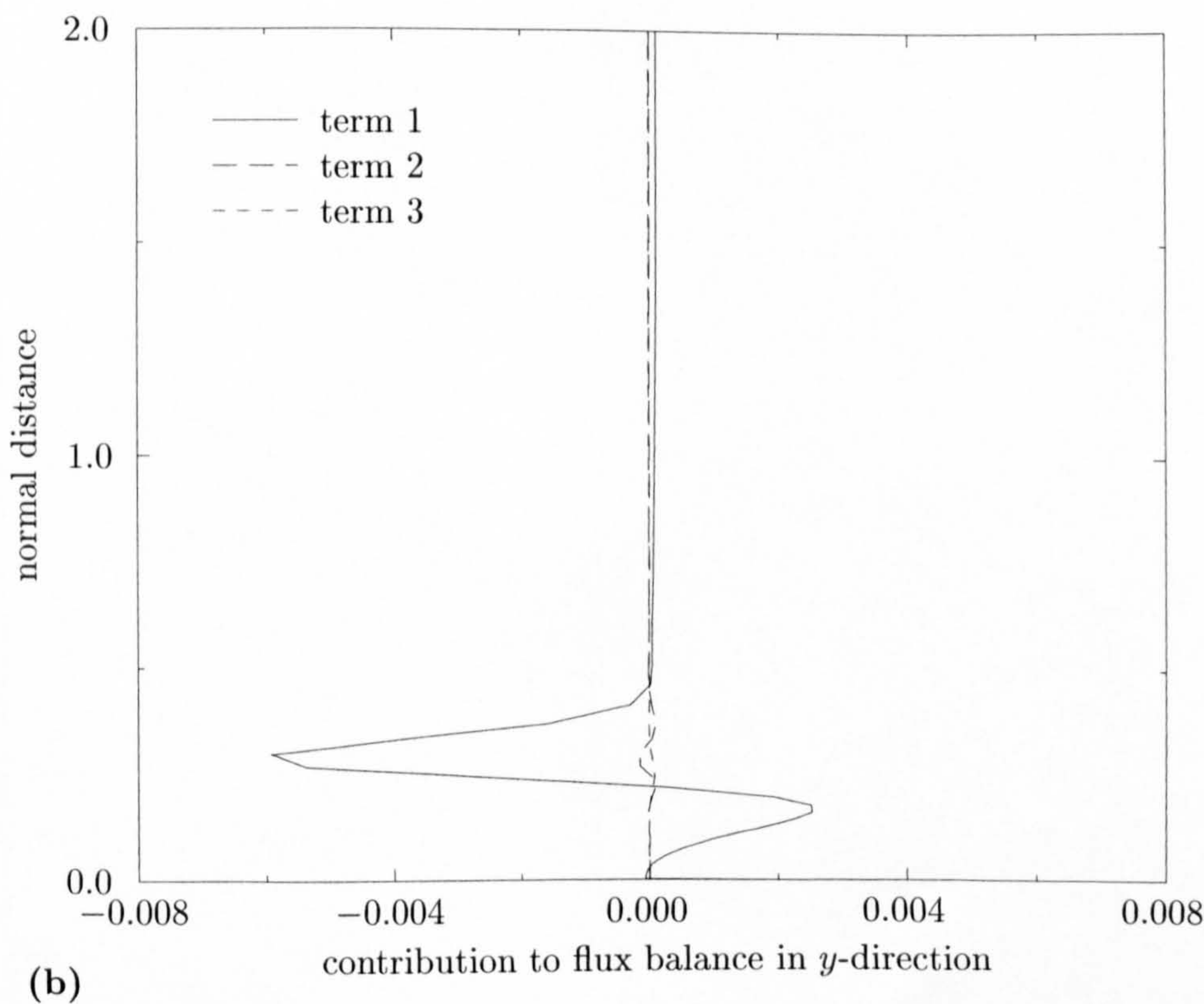
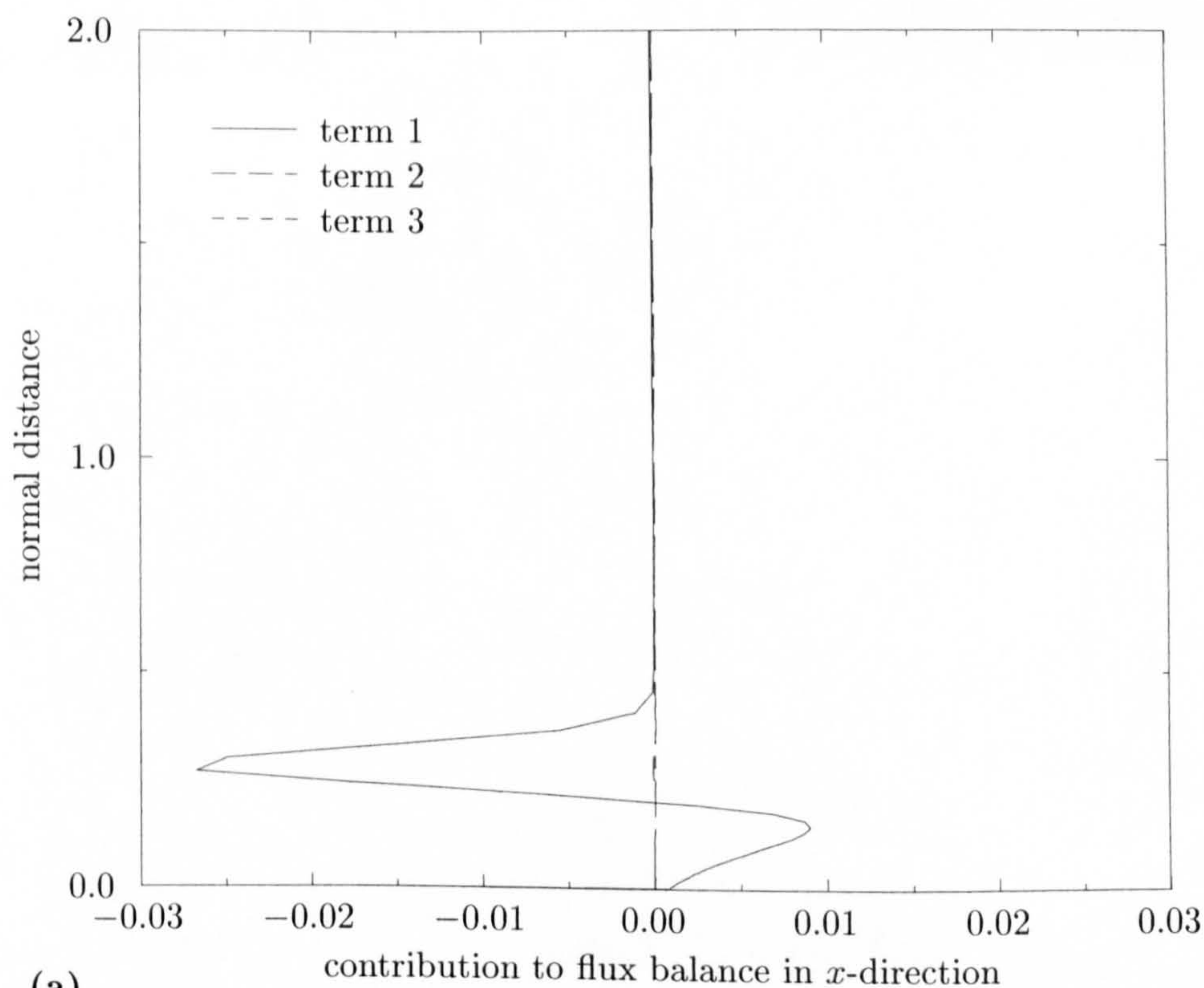


Figure 7.26: Relative importance of terms in (a) Expression (4.4.4a) and (b) Expression (4.4.4b) along normal at $x = 0.7$ on upper surface for fine level quadrilateral grid.

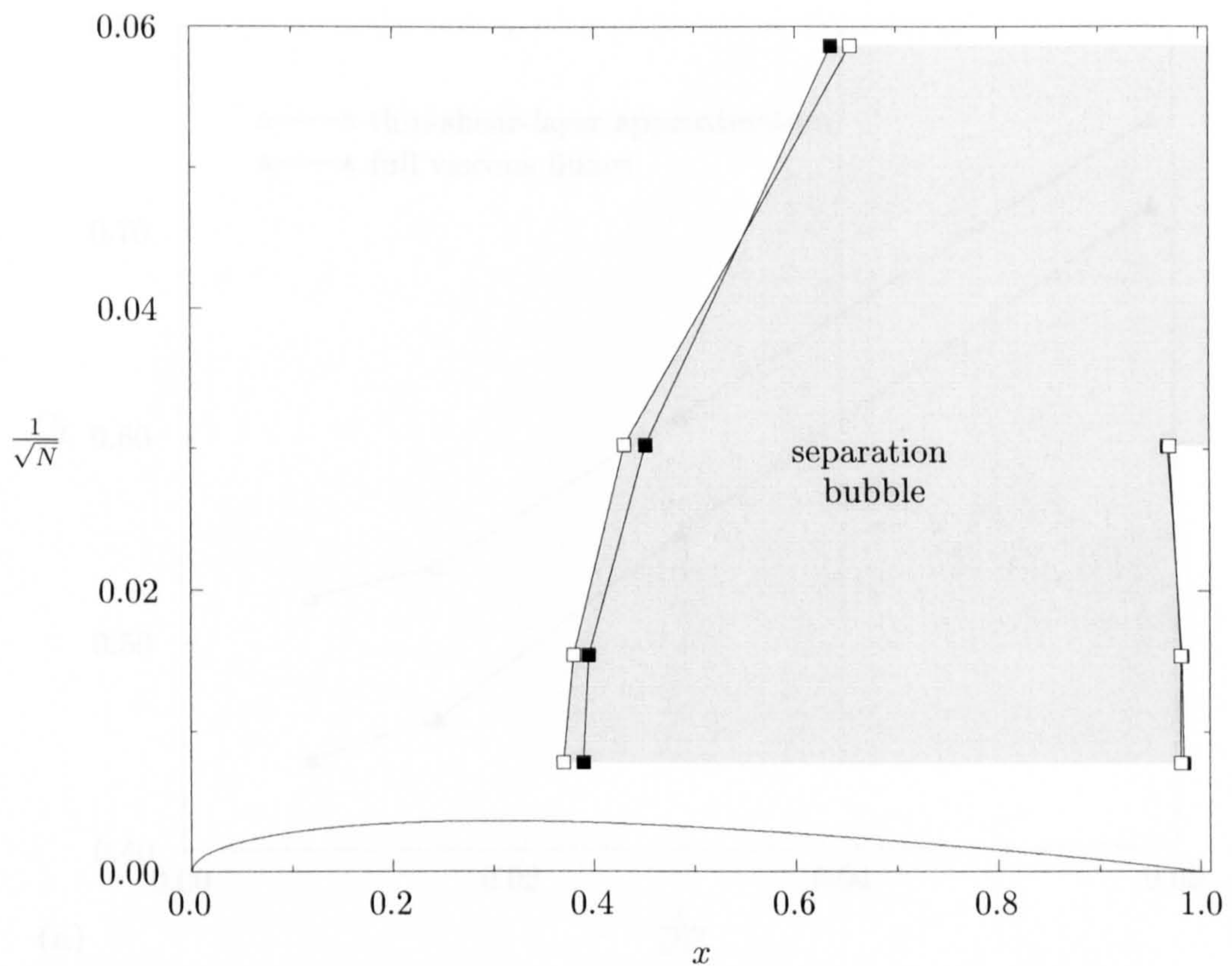


Figure 7.27: Behaviour of separation and reattachment positions with grid refinement for full viscous fluxes and thin-shear-layer approximation on quadrilateral grids. Legend as shown in Fig. 7.24.

with the thin-shear-layer approximation is compared in Fig. 7.28 to the previously discussed results obtained with the full viscous fluxes. In contrast to the results on the quadrilateral grids, the differences are quite large with the thin-shear-layer approximation, leading to higher values for the lift and drag coefficients.

These differences are reflected in the behaviour of the separation and reattachment positions with grid refinement, as depicted in Fig. 7.29. It is seen that the thin-shear-layer approximation leads to separation positions which are considerably closer to the leading edge. The reattachment positions are predicted to be very close to those of the full viscous fluxes.

The reason for the poor performance of the thin-shear-layer approximation was already discussed in the section on the calculations of the laminar boundary layer on a flat plate.

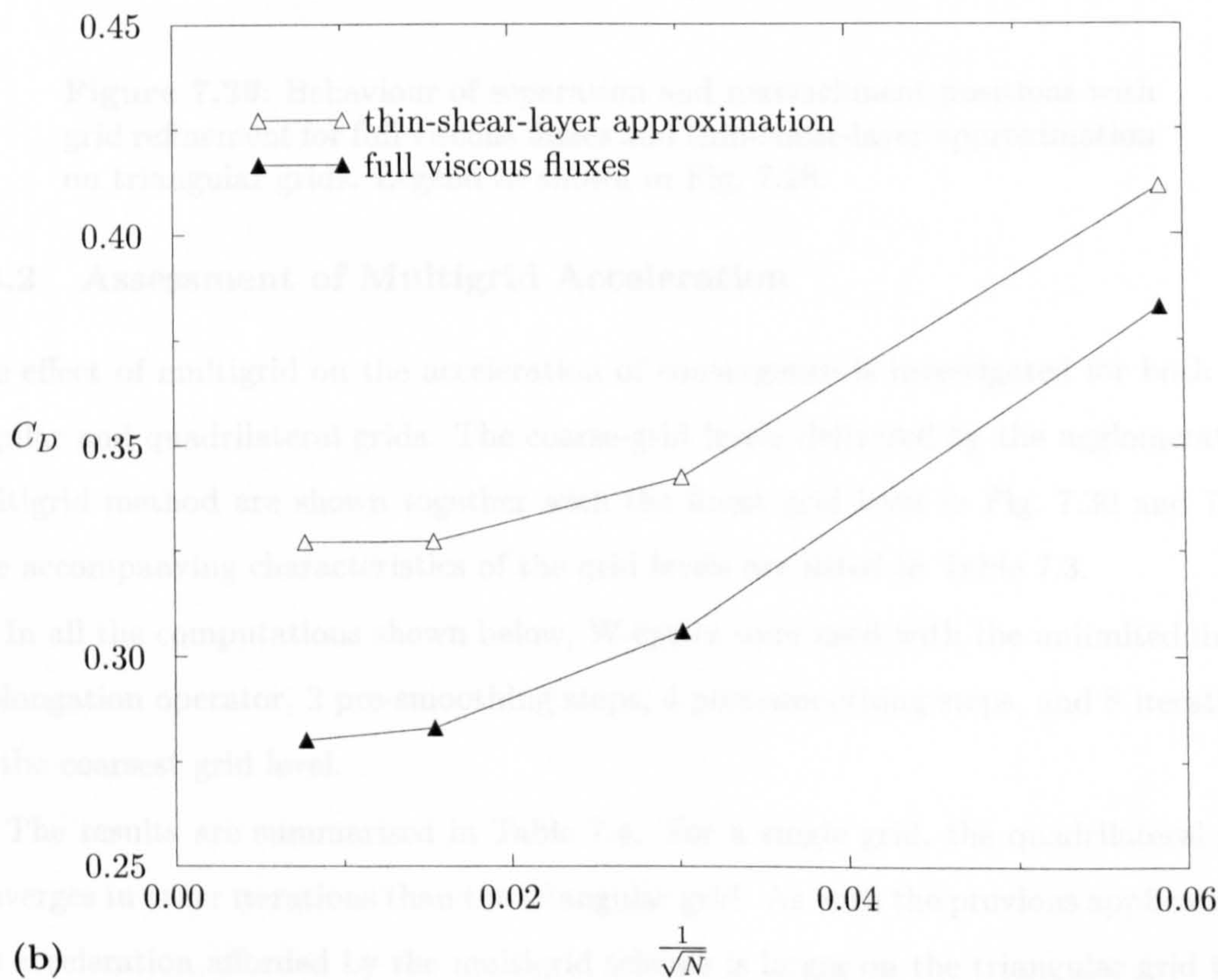
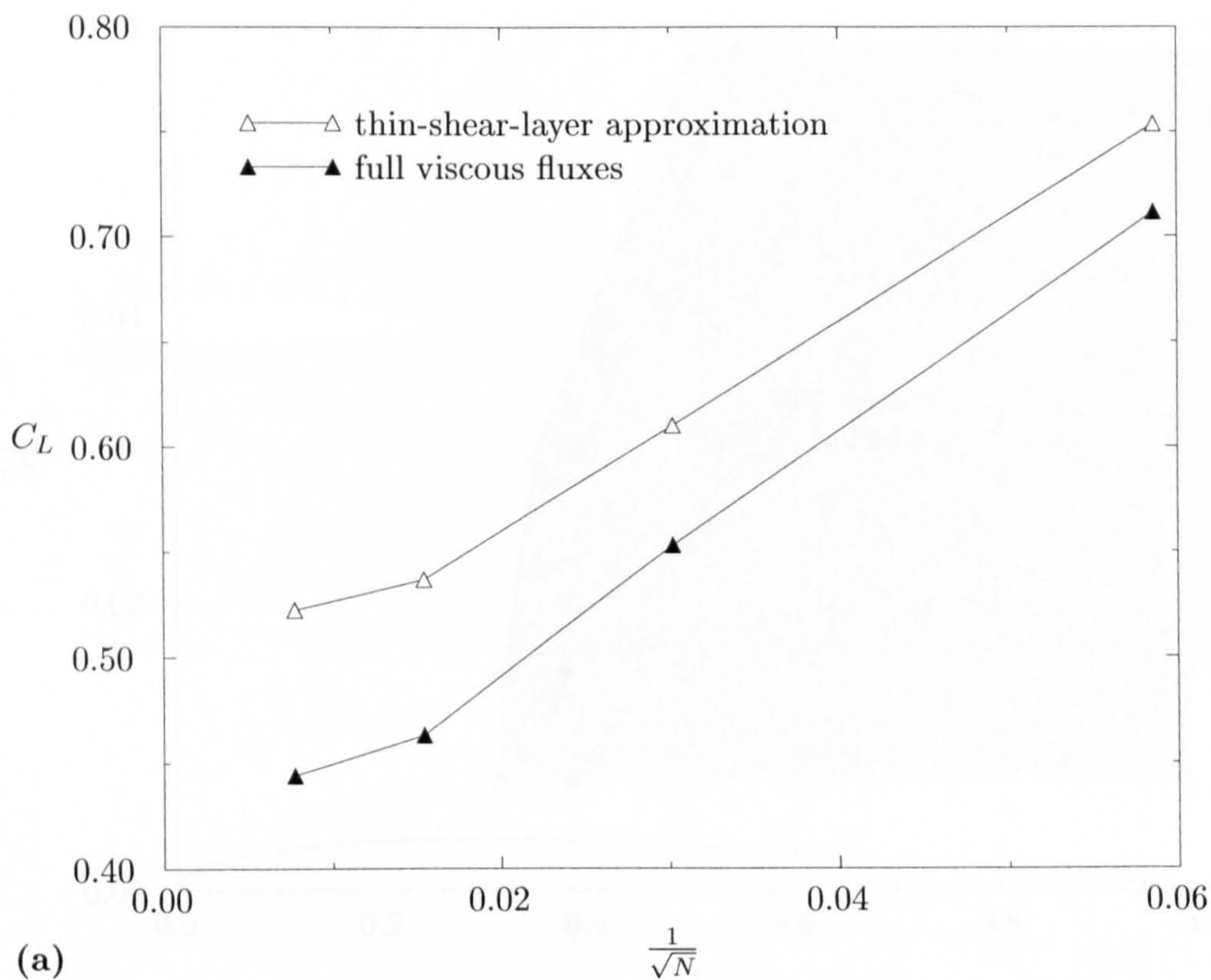


Figure 7.28: Comparison of behaviour of (a) lift and (b) drag coefficients with grid refinement for triangular grids for full viscous fluxes and thin-layer approximation.

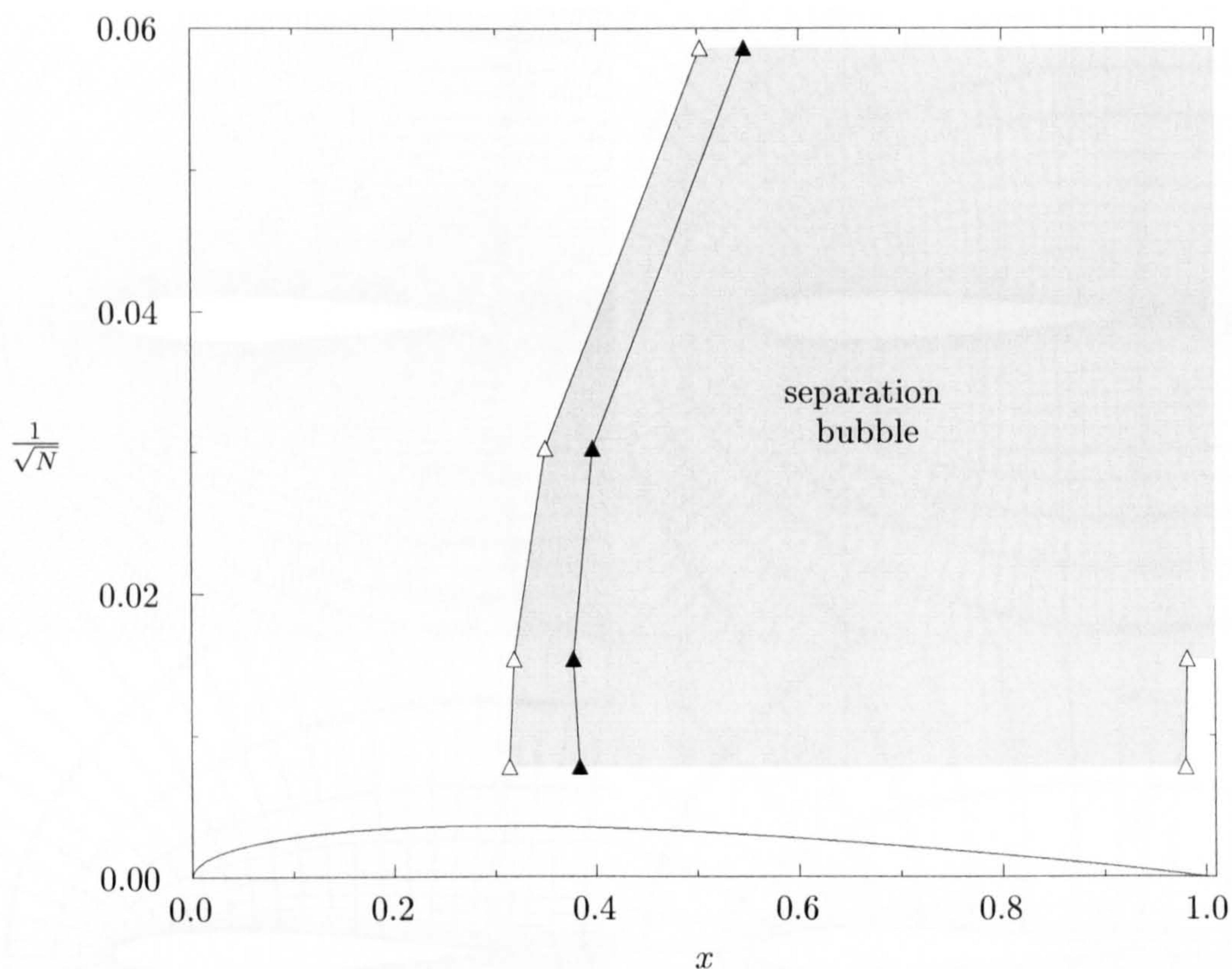


Figure 7.29: Behaviour of separation and reattachment positions with grid refinement for full viscous fluxes and thin-shear-layer approximation on triangular grids. Legend as shown in Fig. 7.28.

7.3.2 Assessment of Multigrid Acceleration

The effect of multigrid on the acceleration of convergence is investigated for both triangular and quadrilateral grids. The coarse-grid levels delivered by the agglomeration multigrid method are shown together with the finest grid level in Fig. 7.30 and 7.31. The accompanying characteristics of the grid levels are listed in Table 7.3.

In all the computations shown below, W-cycles were used with the unlimited linear prolongation operator, 2 pre-smoothing steps, 4 post-smoothing steps, and 8 iterations on the coarsest grid level.

The results are summarised in Table 7.4. For a single grid, the quadrilateral grid converges in fewer iterations than the triangular grid. As with the previous applications, the acceleration afforded by the multigrid scheme is larger on the triangular grid than the quadrilateral grid. This is despite the fact that only four grid levels could be used for the triangular grid. This is surprising, because the characteristics of the coarser

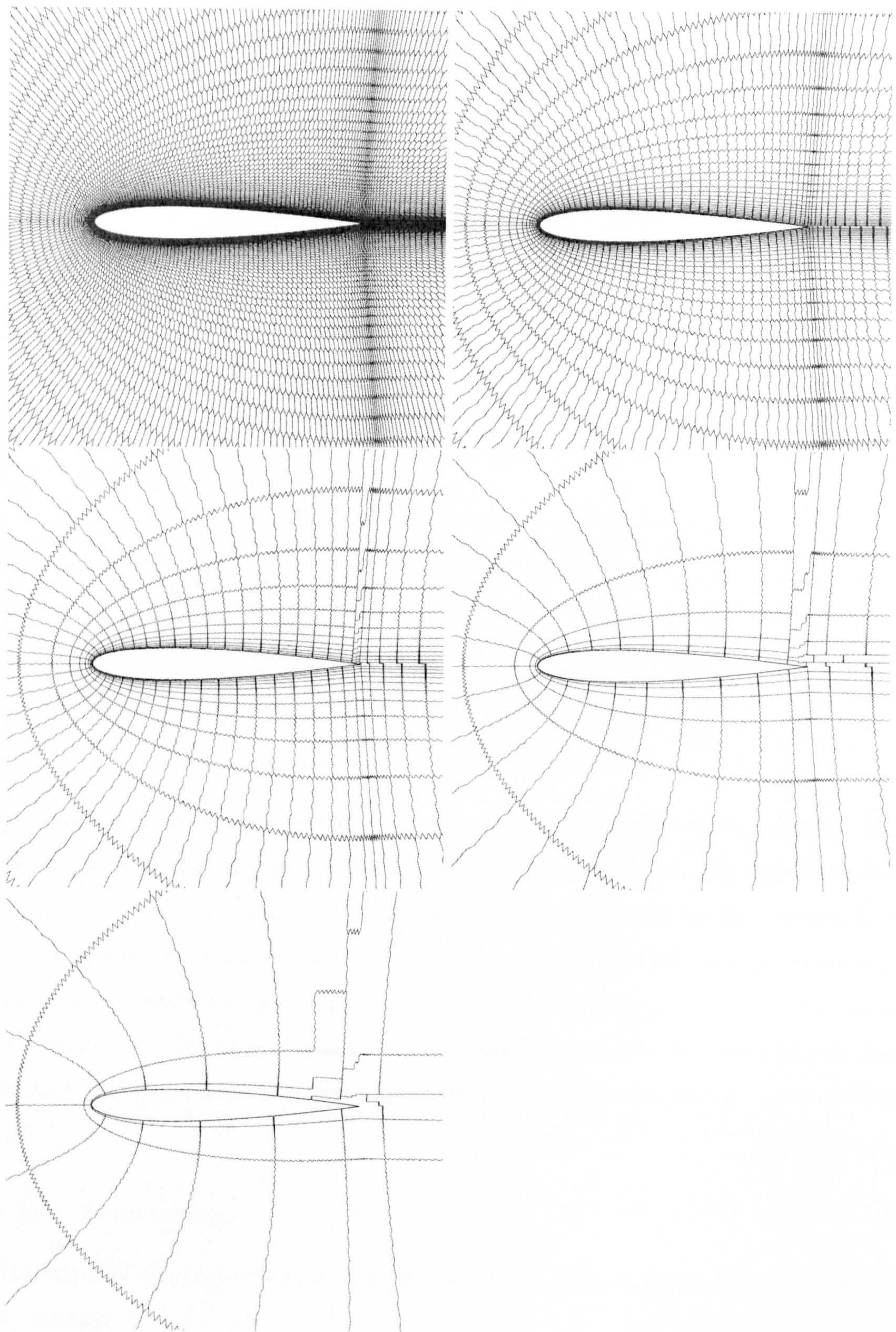


Figure 7.30: The 5 grid levels used in assessment of agglomeration multigrid scheme for laminar flow around NACA 0012 aerofoil on triangular grid.

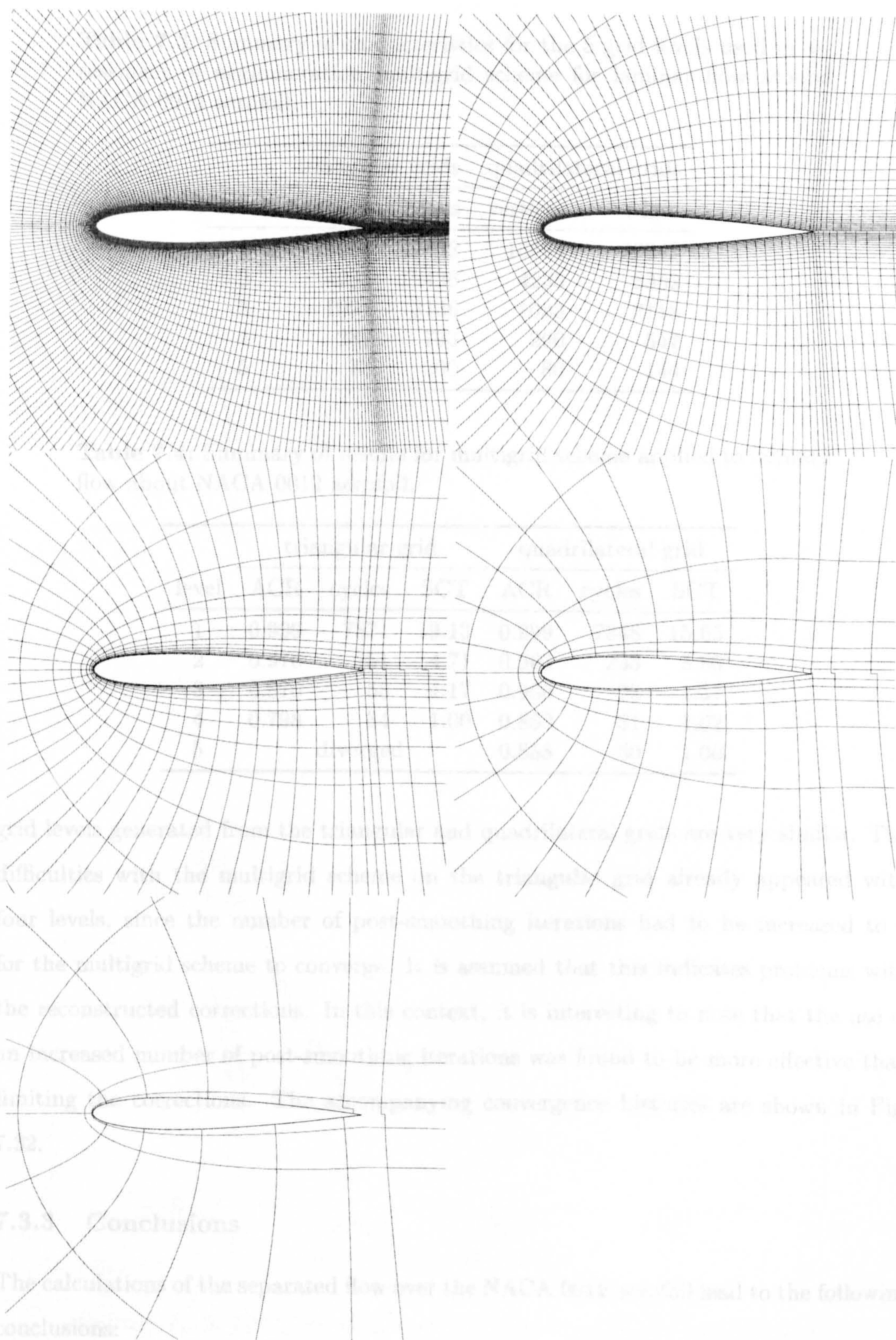


Figure 7.31: The 5 grid levels used in assessment of agglomeration multigrid scheme for laminar flow around NACA 0012 aerofoil on quadrilateral grid.

Table 7.3: Summary of characteristics for the 5 grid levels used in assessment of agglomeration multigrid scheme for laminar flow around NACA 0012 aerofoil.

level	triangular grids		quadrilateral grids	
	vertices	edges	vertices	edges
1	16664	49432	16664	33048
2	4235	12426	4235	8352
3	1091	3136	1093	2118
4	287	793	290	547
5	78	200	80	144

Table 7.4: Summary of results for multigrid scheme applied to laminar flow about NACA 0012 aerofoil.

level	triangular grid			quadrilateral grid		
	ACR	cycles	SCT	ACR	cycles	SCT
1	0.999	7871	19.13	0.999	7348	15.65
2	0.970	251	4.71	0.968	233	3.85
3	0.870	55	1.17	0.900	73	1.37
4	0.798	34	1.00	0.860	51	1.02
5		diverged		0.858	50	1.00

grid levels generated from the triangular and quadrilateral grids are very similar. The difficulties with the multigrid scheme on the triangular grid already appeared with four levels, since the number of post-smoothing iterations had to be increased to 6 for the multigrid scheme to converge. It is assumed that this indicates problems with the reconstructed corrections. In this context, it is interesting to note that the use of an increased number of post-smoothing iterations was found to be more effective than limiting the corrections. The accompanying convergence histories are shown in Fig. 7.32.

7.3.3 Conclusions

The calculations of the separated flow over the NACA 0012 aerofoil lead to the following conclusions:

1. The grid-refinement study revealed that the results on the finest level of the triangular and quadrilateral grids are very similar.

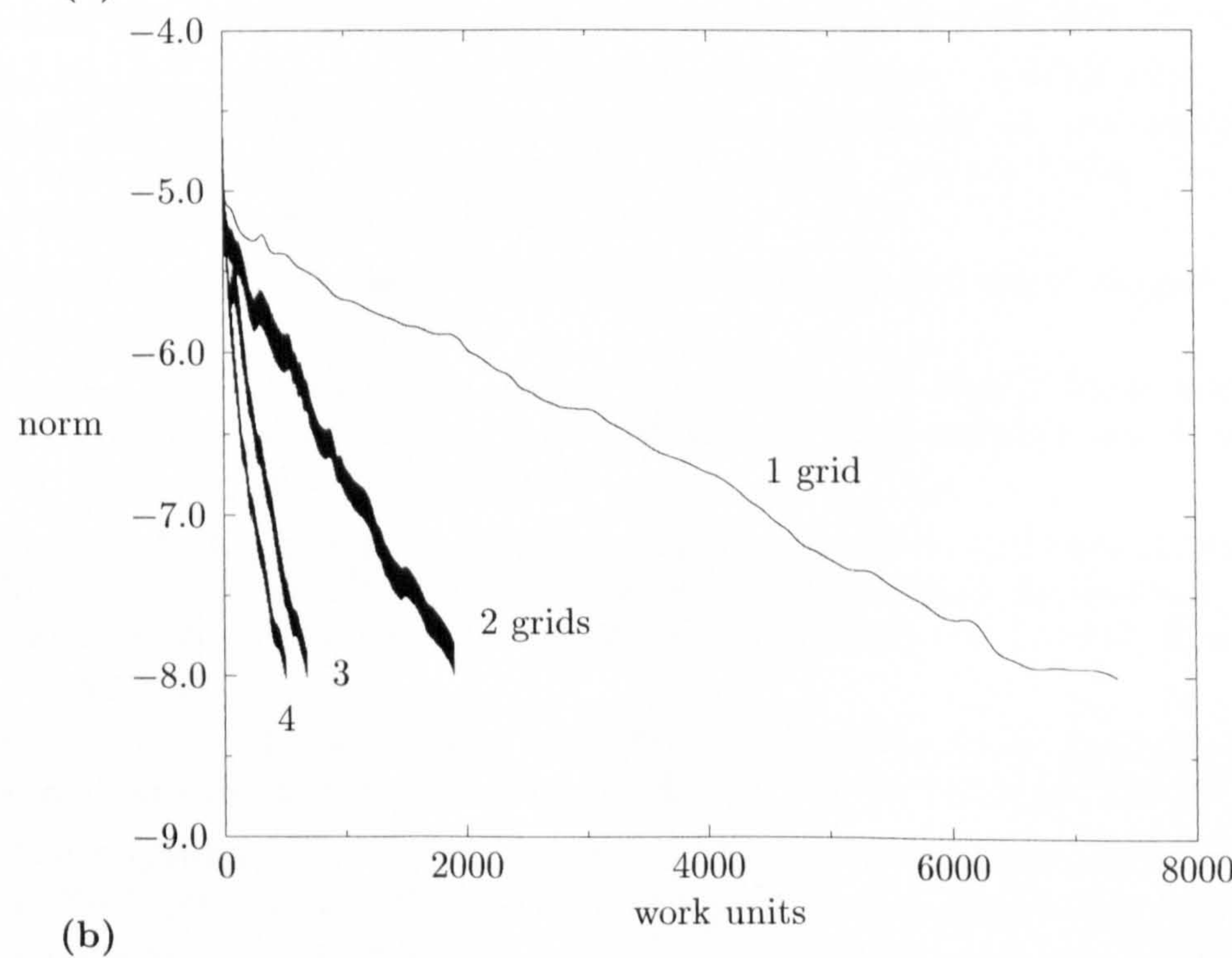
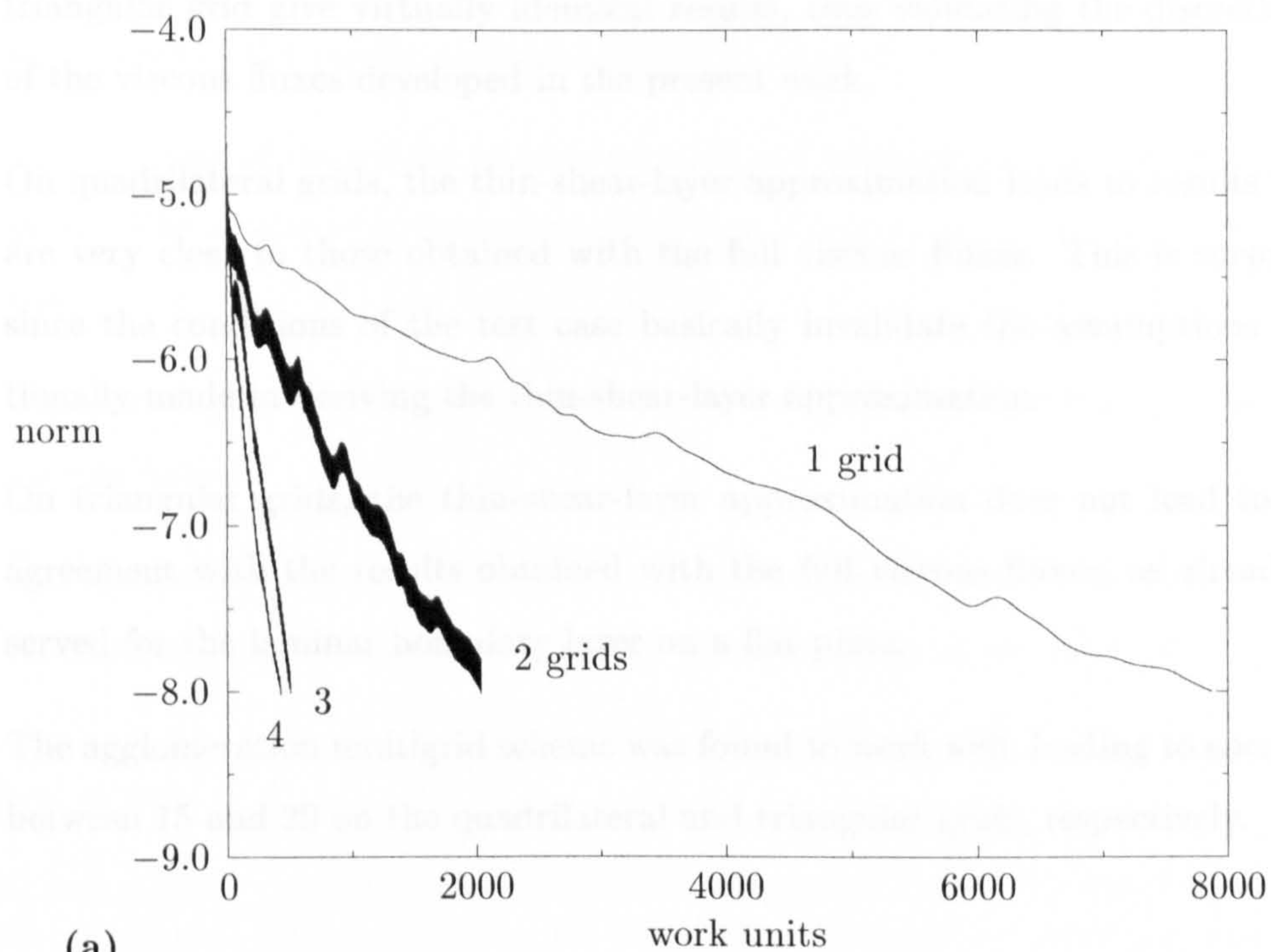


Figure 7.32: Comparison of multigrid convergence on (a) triangular grid and (b) quadrilateral grid for laminar flow about NACA 0012 aerofoil.

2. The finite-volume and finite-element discretisations of the viscous fluxes on the triangular grid give virtually identical results, thus validating the discretisation of the viscous fluxes developed in the present work.
3. On quadrilateral grids, the thin-shear-layer approximation leads to results which are very close to those obtained with the full viscous fluxes. This is surprising, since the conditions of the test case basically invalidate the assumptions traditionally made in deriving the thin-shear-layer approximation.
4. On triangular grids, the thin-shear-layer approximation does not lead to good agreement with the results obtained with the full viscous fluxes, as already observed for the laminar boundary layer on a flat plate.
5. The agglomeration multigrid scheme was found to work well, leading to speed-ups between 15 and 20 on the quadrilateral and triangular grids, respectively.

7.4 Closure

The main points of the results presented in this chapter are:

1. The accuracy of the results on quadrilateral and mixed grids is approximately the same. The solution on the mixed grids was obtained at a lower computational cost.
2. The accuracy on triangular grids is lower than that on quadrilateral grids for viscous flows.
3. The thin-shear-layer approximation gives solutions which are very close to those obtained with the full viscous fluxes on quadrilateral and mixed grids.

References

- [1] Allmaras S.R., *Contamination of Laminar Boundary Layers by Artificial Dissipation in Navier-Stokes Solutions*, in: *Numerical Methods for Fluid Dynamics IV*, Baines M.J. and Morton K.W. (Eds.), Clarendon Press, Oxford, 1993, pp. 443-449
- [2] Batten P., Loyau H., and Leschziner M.A. (Eds.), *ERCOFTAC Workshop on Shock/Boundary-Layer Interaction*, University of Manchester Institute of Science and Technology, Manchester, March 1997; see also: <http://sgp.me.umist.ac.uk/ercoftac97/>
- [3] Blasius H., *Grenzschichten in Flüssigkeiten mit kleiner Reibung*, Z. Angew. Math. Phys., Vol. 56, pp. 1-37, 1908
- [4] Bristeau M.O., Glowinski R., Periaux J., and Viviani H. (Eds.), *Numerical Simulation of Compressible Navier-Stokes Flows*, Notes on Numerical Fluid Mechanics, Vol. 18, Vieweg, Braunschweig, 1987
- [5] Khawaja A., Kallinderis Y., Irmisch S., Lloyd J., Walker D., and Benz E., *Adaptive Hybrid Grid Generation for Turbomachinery and Aerospace Applications*, AIAA Paper 99-0916, 37th AIAA Aerospace Sciences Meeting and Exhibit, Reno, NV, January 1999
- [6] MacCormack R.W. and Candler G.V., *The Solution of the Navier-Stokes Equations using Gauss-Seidel Line Relaxation*, Comp. Fl., Vol. 17, No. 1, pp. 135-150, 1989
- [7] Venkatakrishnan V., *Viscous Computations Using a Direct Solver*, Comp. Fl., Vol. 18, No. 2, pp. 191-204, 1990; see also: Corrigendum, Vol. 18, No. 3, p. I, 1990
- [8] White F.M., *Viscous Fluid Flow*, McGraw-Hill, 2nd Ed., 1991
- [9] Zingg D.W., De Rango S., Nemec M., and Pulliam T.H., *Comparison of Several Spatial Discretisations for the Navier-Stokes Equations*, AIAA Paper 99-3260, 14th Computational Fluid Dynamics Conference, Norfolk, VA, June/July 1999

Chapter 8

Application of Method to Turbulent Flows

The numerical method is applied to turbulent flows on triangular, quadrilateral, and mixed grids. Two cases are computed, both of which entail shock-wave/boundary-layer interactions. The first test case involves the transonic flow over a bump in a channel. The second test case considers the transonic flow about a supercritical aerofoil. For both cases, good agreement is obtained between the computational results and experimental data.

8.1 Introduction

The final computations to be carried out deal with turbulent flows. The two cases considered involve interactions of turbulent boundary layers with shock waves in the flows over a bump in a channel and past a supercritical aerofoil. These so-called shock-wave/boundary-layer interactions are highly important in many industrial applications. Their significance stems from the steep rise in pressure and temperature through the shock wave, which leads to rapid thickening, and possibly separation, of the boundary layer as well as to high heat-transfer rates.

The most prominent example of shock-wave/boundary-layer interaction is the flow past the wing of a transport aircraft at cruise conditions, see, e.g., Fig. 1.1(b). This particular problem received a lot of attention in the 1960's because the drag divergence caused by boundary-layer separation at high cruise speeds prevented economical operation of transport aircraft. The resolution of this problem was the supercritical aerofoil developed by Richard Whitcomb at NASA Langley in 1965. However, Délerly [6] pointed out that there are many other areas, such as intakes, nozzles, turbomachinery blading, missiles, and spacecraft, which ensure that shock-wave/boundary-layer interaction is

still very important today.

The main challenge in computing shock-wave/boundary-layer interaction is the correct prediction of the interaction strength. The burden of meeting this challenge rests mainly with the turbulence models. Given the known limitations of simple turbulence models, such as the Spalart-Allmaras [18] model employed in the present work, the goal of computing the two cases is to attain the same level of agreement as that reached in previous applications of the Spalart-Allmaras turbulence model.

The relevance of the flow over a bump in a channel—apart from intakes of high-speed aircraft—is that this geometrical configuration resembles an aerofoil suction side, an afterbody, or a propulsive nozzle.

8.2 ONERA Bump Case C

The first test case for turbulent flow is the transonic flow over a bump in a channel investigated experimentally by Détery et al. [7]. The geometry of the bump and channel is shown in Fig. 8.1. The main feature of the test case is the extended separation region caused by the strong interaction of the boundary layer with the shock wave. As is characteristic of strong interactions of shock waves with turbulent boundary layers, the shock wave resembles the Greek letter λ , and is thus usually referred to as a λ -shock, see Ackeret et al. [1].

The test case of Détery et al. was used in numerous projects and workshops, most notably in the EUROVAL [15] and ETMA projects [8], and recently in an ERCOFTAC workshop [3].

The boundary conditions used in the present computations are shown in Fig. 8.1. The channel walls are taken as adiabatic. The outlet static pressure is not chosen to be the same as the experimental value. Rather, the outlet static pressure was specified such that the computed position of the shock wave coincided with its experimental position. The reasoning behind this commonly employed procedure is that the identical shock locations allow the solution in the separation and recovery regions to be compared with the experimental data. Further justification for not matching the experimental static pressure at the outlet is that the two-dimensional computation cannot take into account the influence of the channel side walls in the experiment.

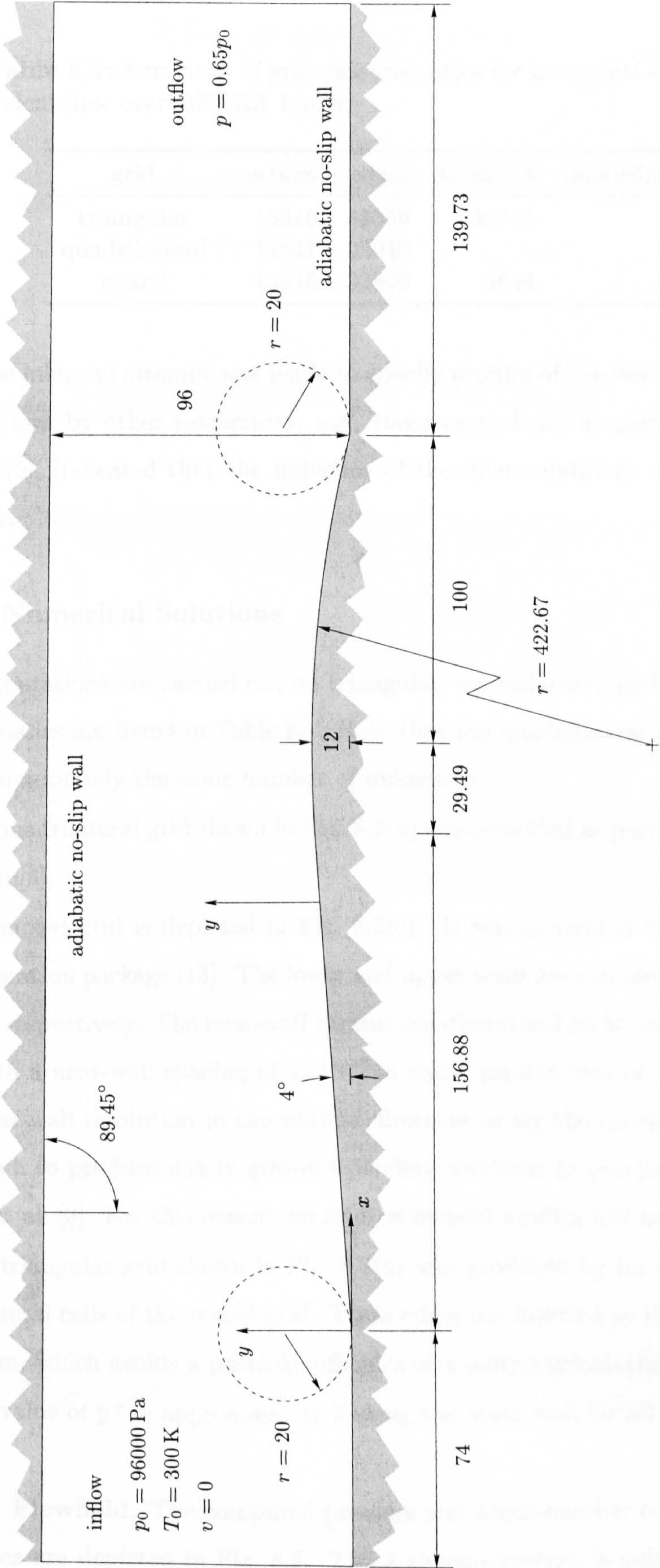


Figure 8.1: Solution domain and boundary conditions for ONERA bump. All dimensions in millimetres.

Table 8.1: Summary of grid characteristics for numerical study of turbulent flow over ONERA bump.

grid	vertices	edges	triangles	quadrilaterals
triangular	15616	46359	30744	–
quadrilateral	14641	29040	–	14400
mixed	15616	32809	3644	13550

At the inlet, no attempt was made to specify profiles of the flow variables. Previous computations by other researchers, e.g., those carried out as part of the EUROVAL project [15], indicated that the influence of the inlet conditions on the solution was negligible.

8.2.1 Numerical Solutions

The computations are carried out on triangular, quadrilateral, and mixed grids. Their characteristics are listed in Table 8.1. Note that the quadrilateral and the mixed grids have approximately the same number of unknowns.

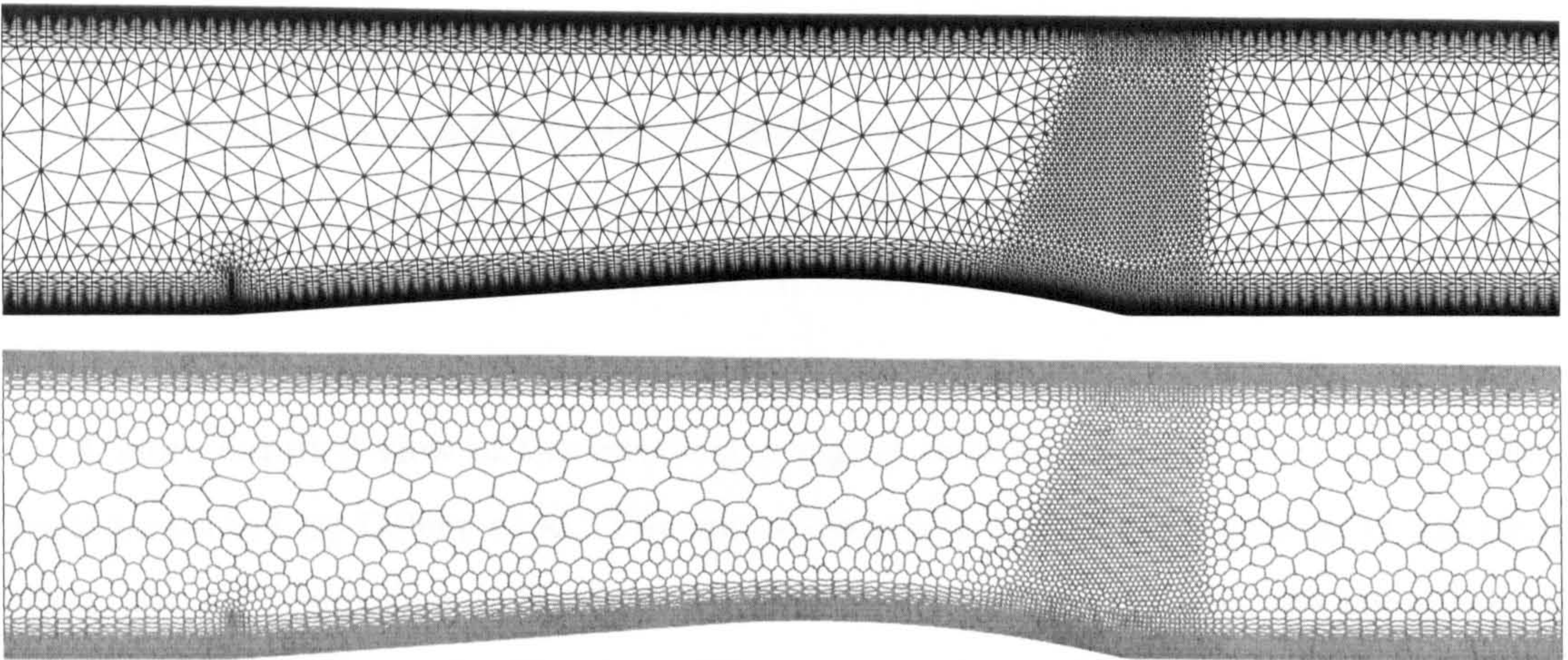
The quadrilateral grid shown in Fig. 8.2(b) was provided as part of the ERCOFTAC workshop [3].

The mixed grid is depicted in Fig. 8.2(c). It was generated with the CENTAUR grid-generation package [13]. The lower and upper walls are represented by 148 and 125 vertices, respectively. The near-wall regions are discretised by 50 layers of quadrilateral cells, with a near-wall spacing of $2 \cdot 10^{-6}$ m and a growth rate of 1.15. This gives the same near-wall resolution in the normal direction as for the quadrilateral grid, which was shown to produce nearly grid-independent solutions in previous studies, see, e.g., Batten et al. [3]. For this reason, no grid-refinement studies will be shown here.

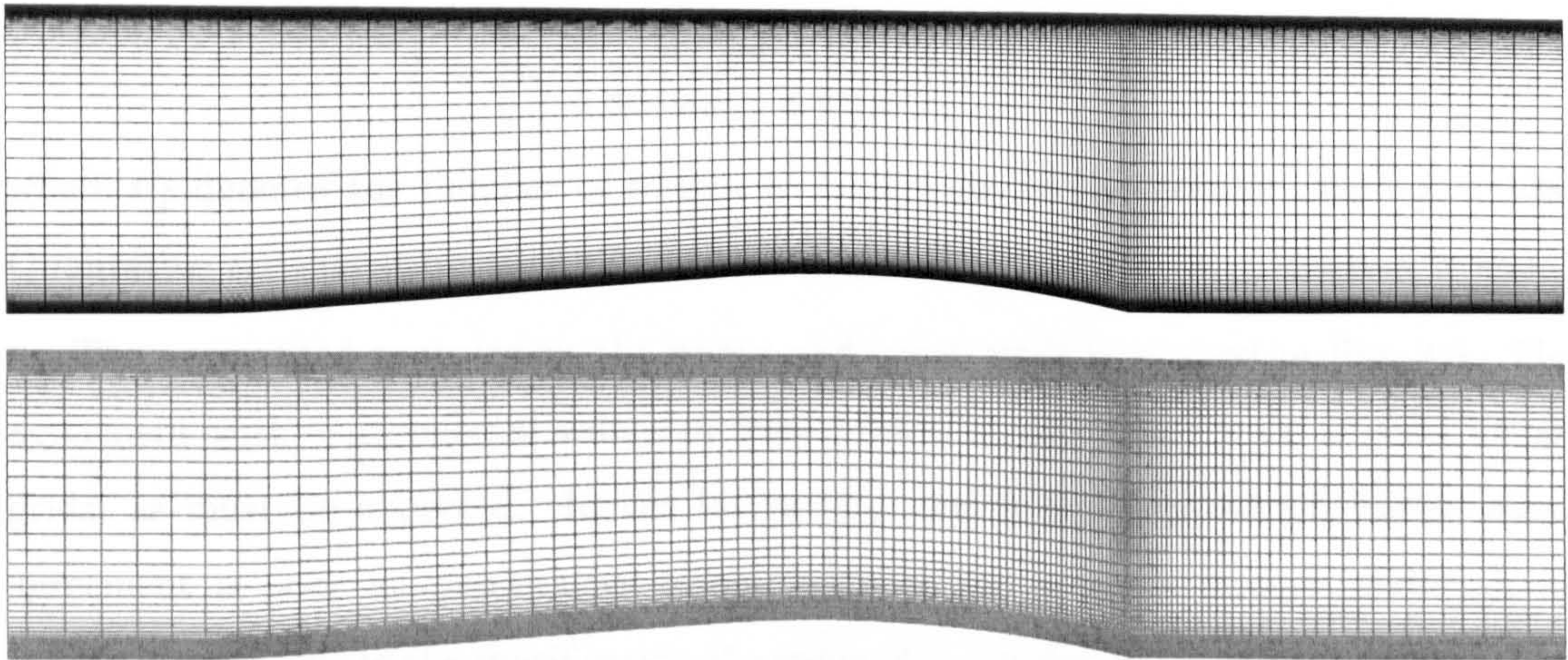
The triangular grid shown in Fig. 8.2(a) was produced by inserting edges into the quadrilateral cells of the mixed grid. These edges are inserted so that their orientation is random, which avoids a possible influence of a unique orientation on the results.

The value of y^+ is approximately 2 along the lower wall for all grids.

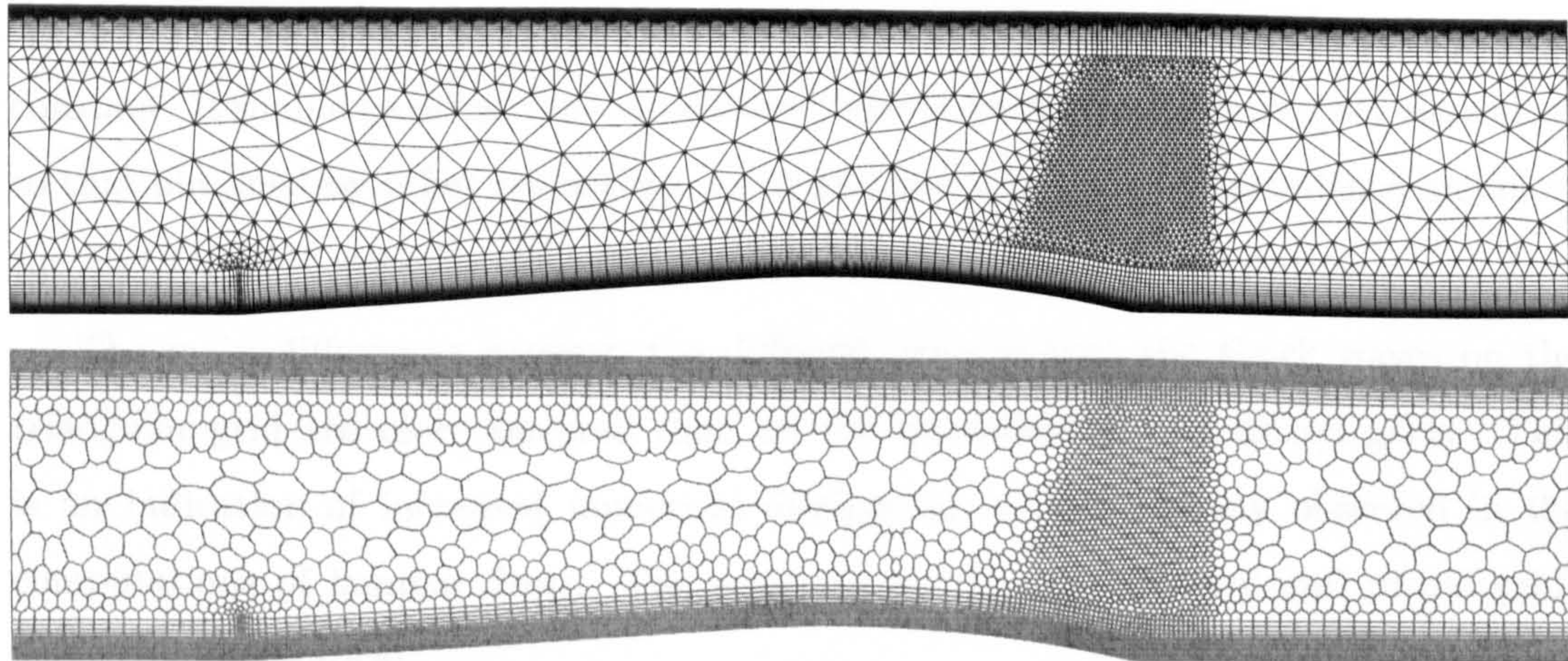
Overall Flowfield. The computed pressure and Mach-number contours on the three grid types are depicted in Fig. 8.3. The λ shock-structure is quite weak, in contrast



(a)



(b)



(c)

Figure 8.2: (a) Triangular, (b) quadrilateral, and (c) mixed grids used for computation of turbulent flow over ONERA bump.

to that in the experiment. The lack of the second leg of the λ -shock was observed in previous simulations with the Spalart-Allmaras turbulence model, see, e.g., the ERCOFTAC workshop [3], and with many other turbulence models. The rapid thickening of the boundary layer following the interaction with the shock wave is apparent from Fig. 8.3.

A more detailed view of the interaction region may be obtained from the interferogram presented by Délery et al. The comparison of a numerically generated interferogram, see, e.g., Samtaney [17], of the solution on the mixed grid with the experimental interferogram is shown in Fig. 8.4. The numerical interferogram was generated by plotting the integer quantity I_i , given by

$$I_i = \left\lfloor n_f \left(\frac{\rho_i - \min_i \rho_i}{\max_i \rho_i - \min_i \rho_i} \right) + \frac{1}{2} \right\rfloor \bmod 2,$$

where n_f denotes the number of fringes to be drawn; in the present case $n_f = 128$. Qualitative agreement between the numerical and experimental interferogram is good.

The normalised pressure on the upper and lower walls is plotted in Fig. 8.5. The agreement with experimental values in front of and at the shock wave is good for all grids, as must be expected. In the interaction region and beyond the shock wave, agreement is poor in quantitative terms, because the pressure is over-predicted, as indeed it must, due to the specification of a value of the outlet static pressure higher than in the experiment. In qualitative terms, however, agreement is good, in the sense that the difference between the numerical solution and experimental values is approximately constant. It should be noted that the quality of the present solution is roughly equivalent to that obtained by other researchers using the Spalart-Allmaras turbulence model at the ERCOFTAC workshop [3], who also specified $p = 0.65p_0$ at the outlet.

The main differences between the different grids is that the shock waves on the triangular grid are more smeared than on the quadrilateral and mixed grids. This is an indication of increased numerical dissipation, as was already observed in the computations of laminar flows. The solutions on the quadrilateral and mixed grids are virtually identical.

For completeness, the numerically computed separation and re-attachment positions on the lower walls are compared with the experimental positions in Table 8.2. It is seen that the predicted location of the separation point is approximately correct. This is

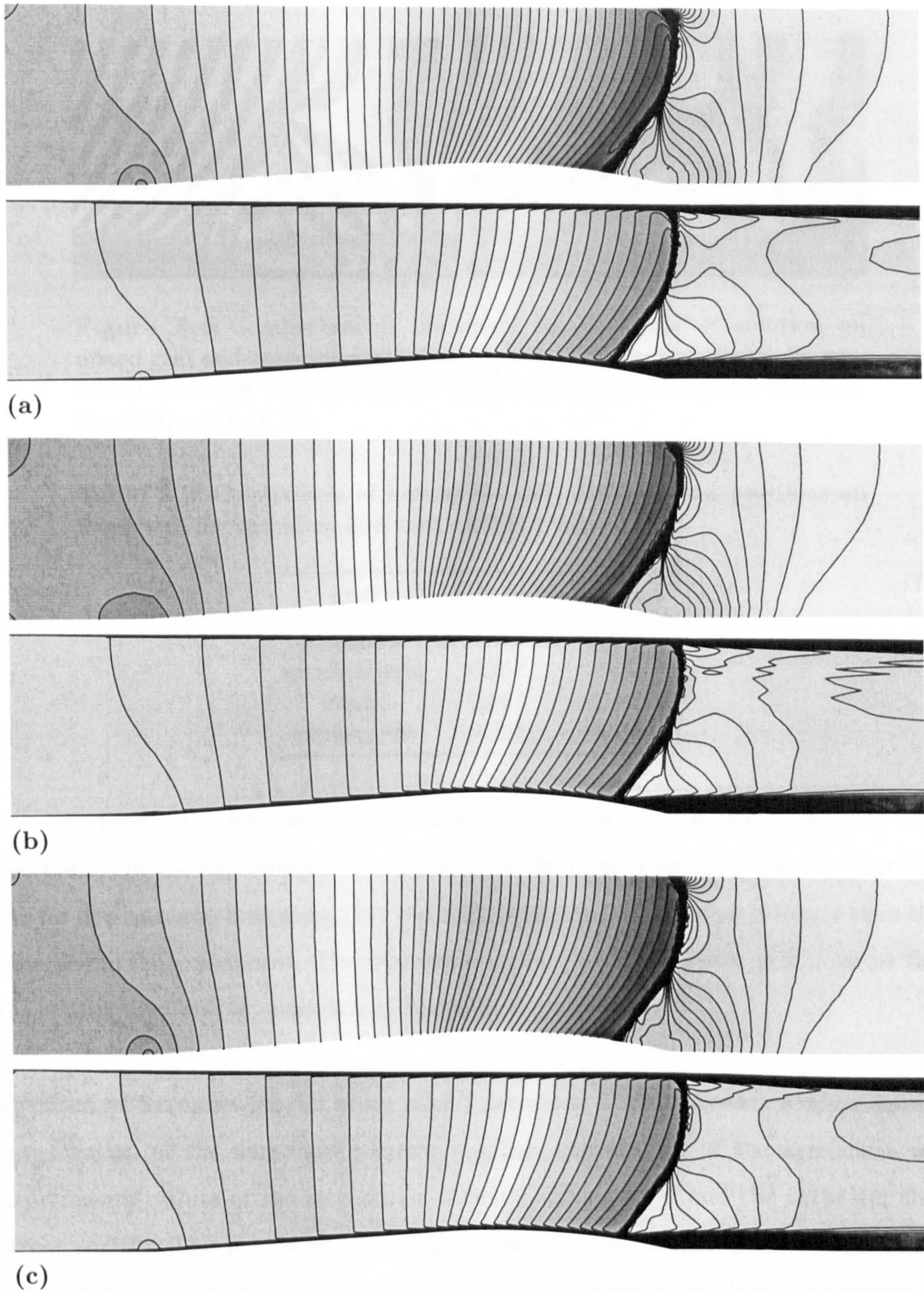


Figure 8.3: Pressure and Mach number contours for turbulent flow over ONERA bump. (a) Pressure contours (0.340,0.796;41) and Mach number contours (0.000,1.368;41) for triangular grid, (b) pressure contours (0.324,0.792;41) and Mach number contours (0.000,1.374;41) for quadrilateral grid, and (c) pressure contours (0.323,0.809;41) and Mach number contours (0.000,1.377;41) for mixed grid.

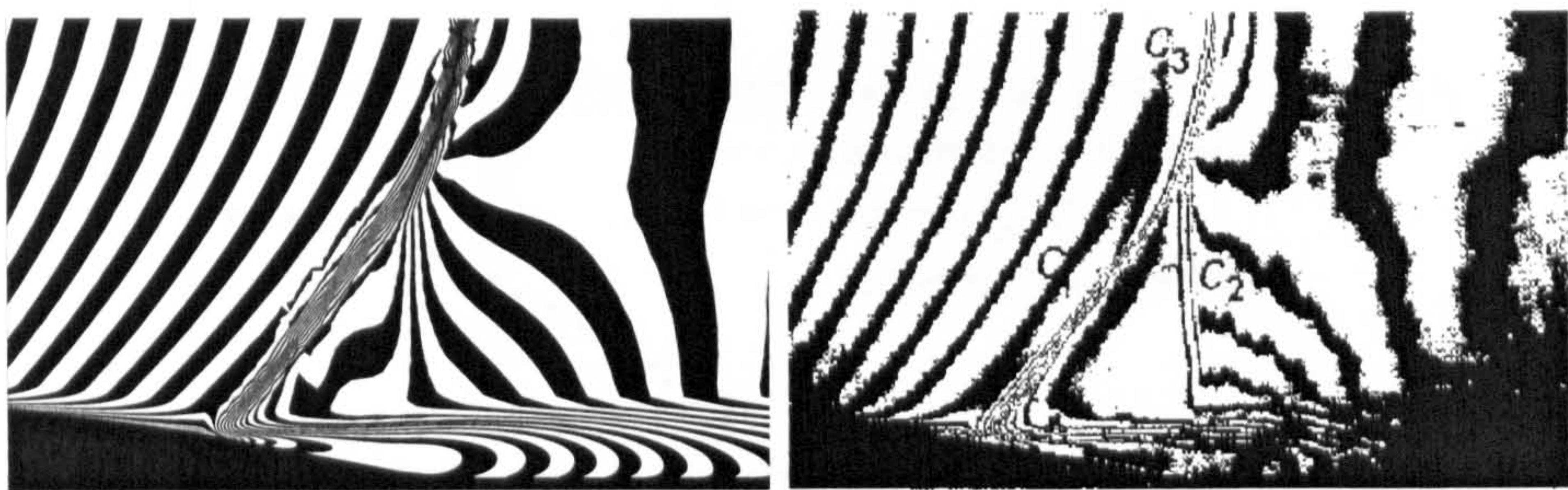


Figure 8.4: Comparison of numerical interferogram of solution on mixed grid and experimental interferogram of interaction region for turbulent flow over ONERA bump. Experimental interferogram obtained from Détery et al. [7].

Table 8.2: Comparison of separation and re-attachment positions on lower wall for turbulent flow over ONERA bump.

grid	x_{sep} (m)	x_{att} (m)
triangular	0.255	0.349
quadrilateral	0.257	0.345
mixed	0.257	0.345
experiment	0.263	0.325

not surprising, since separation is determined by the shock wave, which is in the same position as in the experiment. The position of the re-attachment point on all grids is too far downstream, indicating that the computed separation region is longer than that observed in the experiment. The separation region on the triangular grid is larger than those computed on the quadrilateral and mixed grids.

Profiles of Streamwise Velocity and Turbulent Shear Stress. A more detailed investigation of the numerical solution requires examination of the agreement with experimental values of the streamwise velocity component u and the turbulent shear stress $-u''v''$. The results of the computations will be compared with experimental values at the four stations indicated in Fig. 8.6. In this figure, the four stations and the extent of the separation bubble in the experiment are superimposed on the computed Mach number contours on the mixed grid in order to show the comparison in relation to the overall flowfield. Thus, the first two stations are within the separation region, the third just beyond the re-attachment point and the fourth further downstream.

The comparison of the u -velocity profiles at $x = 0.27$ m and $x = 0.29$ m shown in

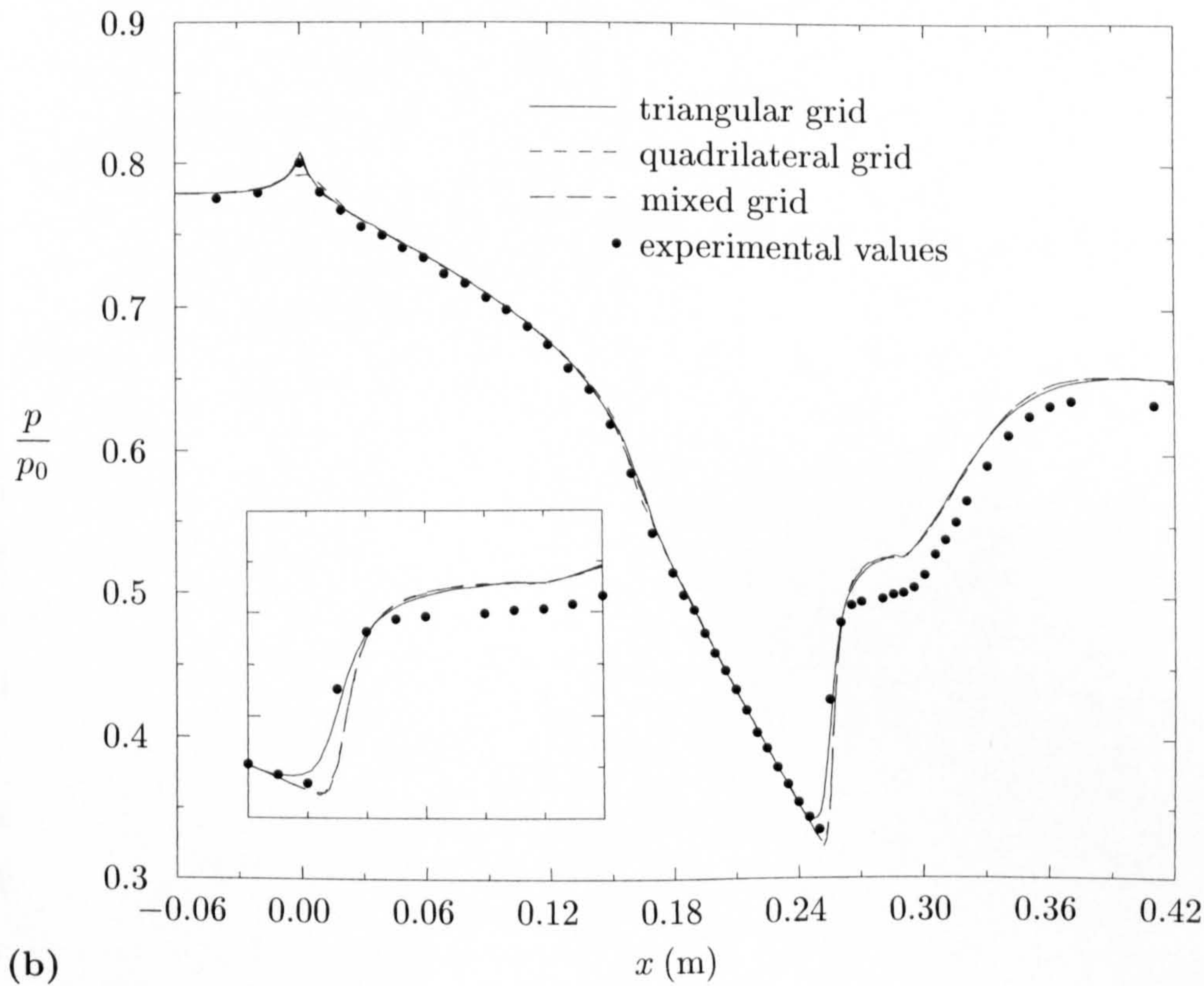
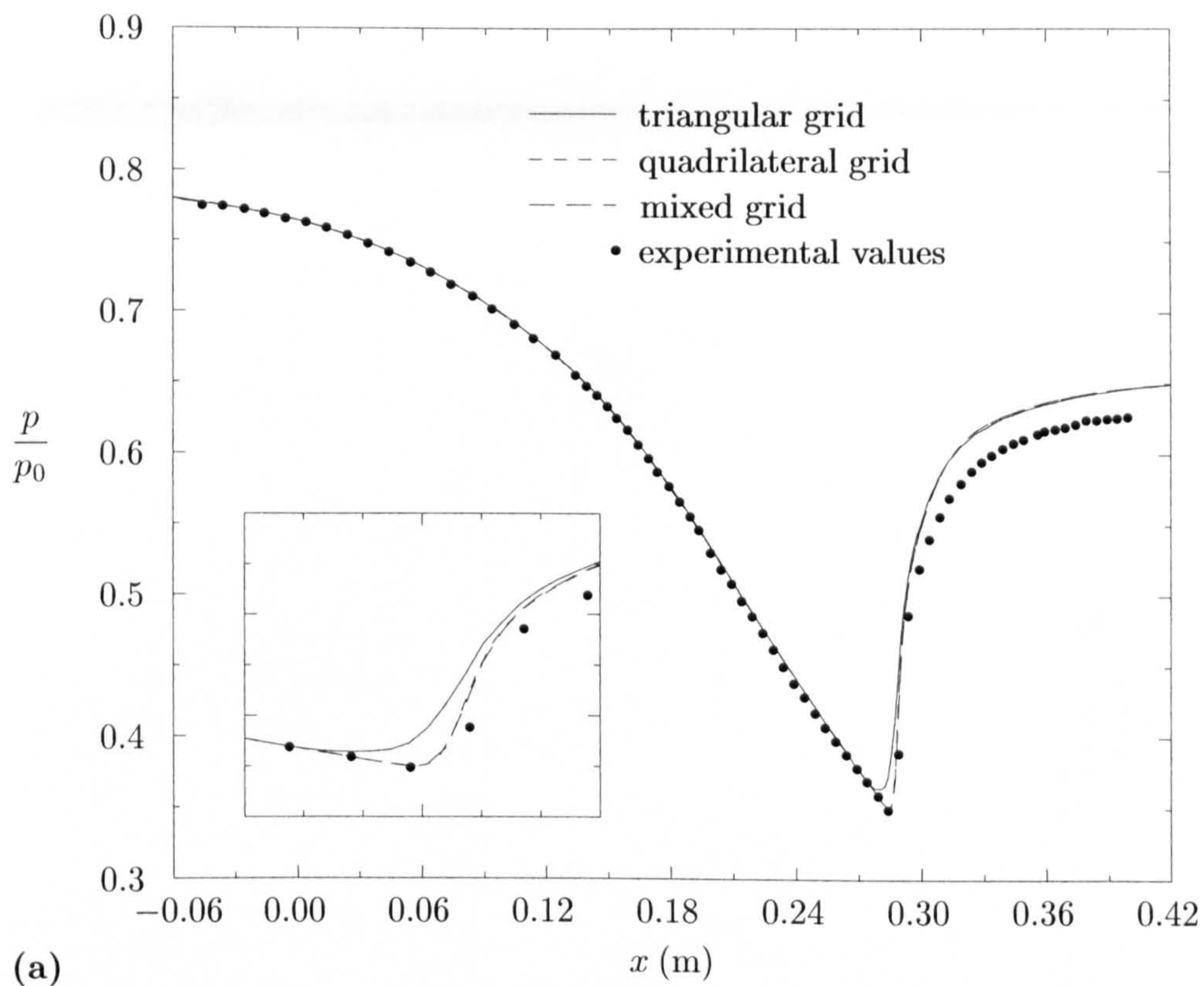


Figure 8.5: Comparison of numerical solution with experimental values of normalised pressure on (a) upper and (b) lower walls for ONERA bump. Insets show close-up view of interaction regions.

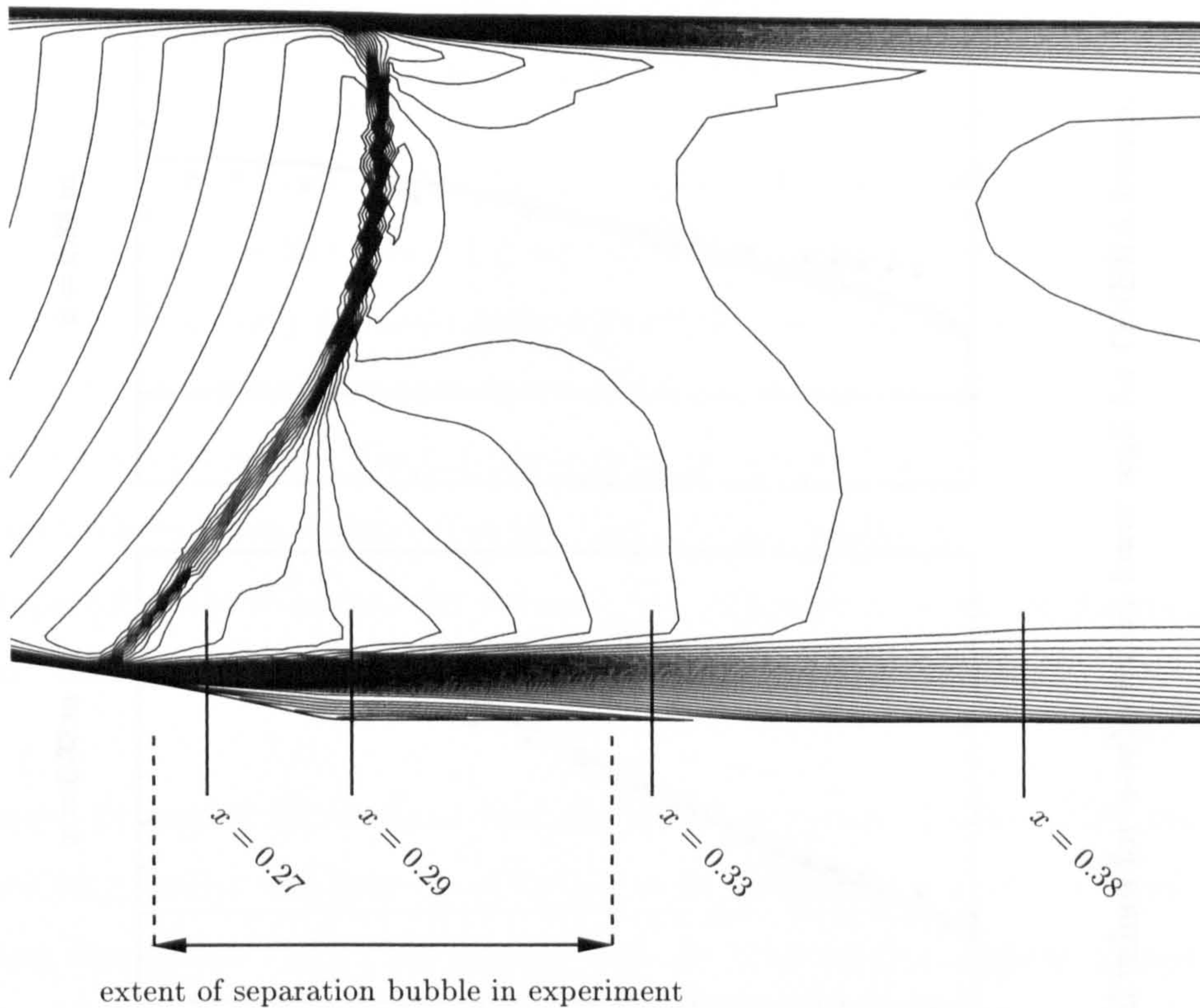


Figure 8.6: Locations of comparisons of numerical solution for u -velocity profiles and turbulent shear stress with experimental values superimposed on computed Mach number contours on mixed grid for ONERA bump.

Figs. 8.7 demonstrate that the computations predicts too thin a recirculation region, which is consistent with the under-predicted strength of the interaction of the boundary layer with the shock wave. It is noted that the computed boundary-layer thickness and the computed magnitude of the maximum reverse velocity are approximately correct at $x = 0.27$ m and $x = 0.29$ m. The velocity profiles on the triangular grid show a slightly larger reverse velocity at $x = 0.27$ m and $x = 0.29$ m and a larger recirculation bubble, which is consistent with the slightly earlier separation point. Figure 8.7 confirms that the extent of the separation region is over-predicted as the numerical solutions at $x = 0.33$ m still exhibits a small negative velocity. This over-prediction affects the agreement at $x = 0.38$ m, where the computations significantly underestimate the near-wall streamwise velocity component.

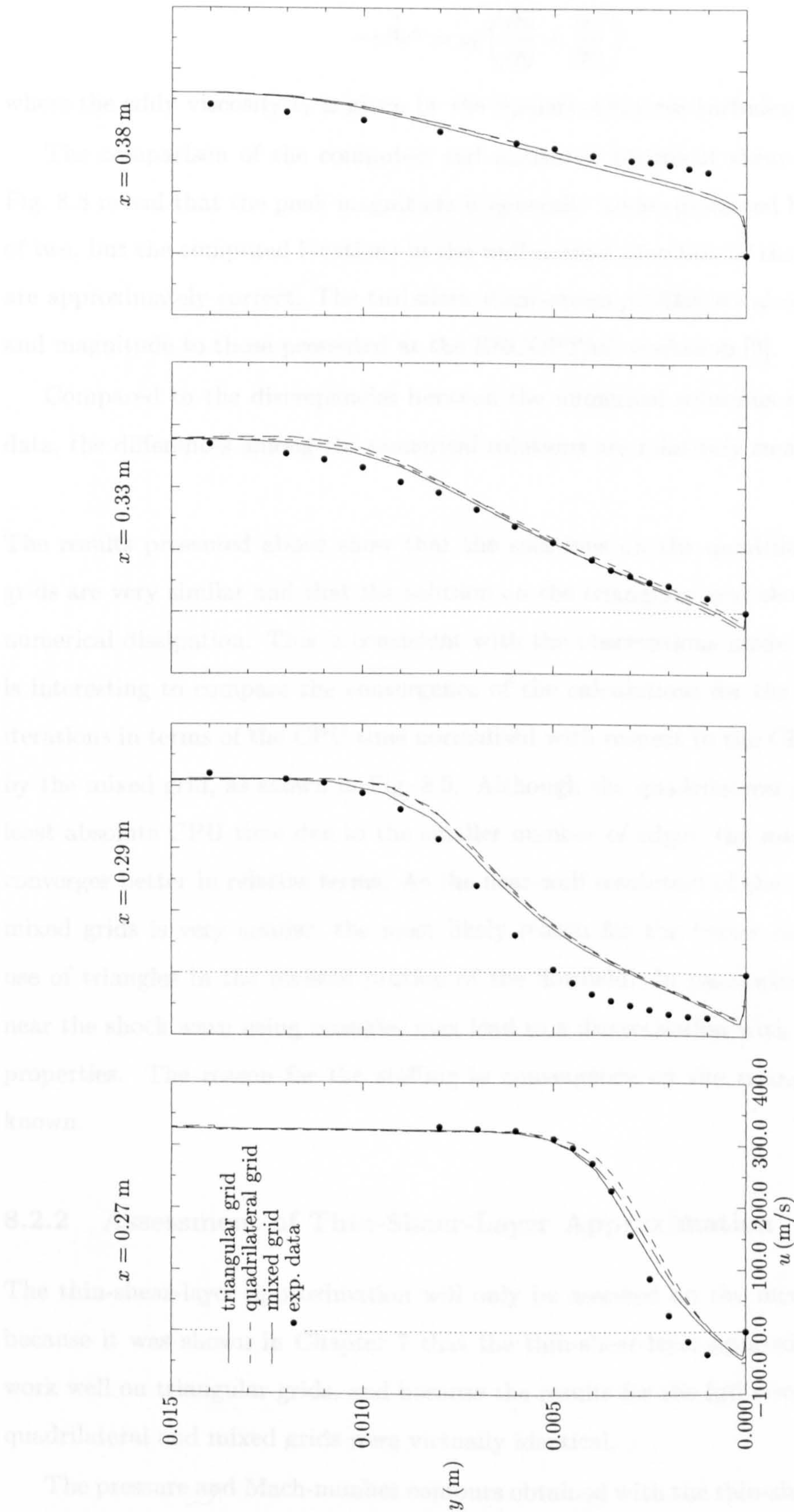


Figure 8.7: Comparison of numerical solutions and experimental values for u -velocity on lower wall for ONERA bump.

The turbulent shear stress is computed from Eq. (2.4.14),

$$-u'v'' = \nu_t \left(\frac{\partial \tilde{u}}{\partial y} + \frac{\partial \tilde{v}}{\partial x} \right),$$

where the eddy viscosity ν_t is given by the Spalart-Allmaras turbulence model.

The comparison of the computed and measured turbulent shear-stress profiles in Fig. 8.8 reveal that the peak magnitude is generally under-predicted by about a factor of two, but the computed locations in the wall-normal direction of the peak magnitude are approximately correct. The turbulent shear-stress profiles are also similar in shape and magnitude to those presented at the ERCOFTAC workshop [3].

Compared to the discrepancies between the numerical solutions and experimental data, the differences among the numerical solutions are relatively small.

The results presented above show that the solutions on the quadrilateral and mixed grids are very similar and that the solution on the triangular grid shows signs of more numerical dissipation. This is consistent with the observations made in Chapter 7. It is interesting to compare the convergence of the calculations for the same number of iterations in terms of the CPU time normalised with respect to the CPU time required by the mixed grid, as shown in Fig. 8.9. Although the quadrilateral grid required the least absolute CPU time due to the smaller number of edges, the mixed grid actually converges better in relative terms. As the near-wall resolution of the quadrilateral and mixed grids is very similar, the most likely reason for the better convergence is the use of triangles in the inviscid portion of the flowfield. In particular, the refinement near the shock wave using triangles may lead to a discretisation with better numerical properties. The reason for the stalling in convergence on the triangular grid is not known.

8.2.2 Assessment of Thin-Shear-Layer Approximation

The thin-shear-layer approximation will only be assessed on the mixed grid. This is because it was shown in Chapter 7 that the thin-shear-layer approximation does not work well on triangular grids, and because the results for the full viscous fluxes on the quadrilateral and mixed grids were virtually identical.

The pressure and Mach-number contours obtained with the thin-shear-layer approx-

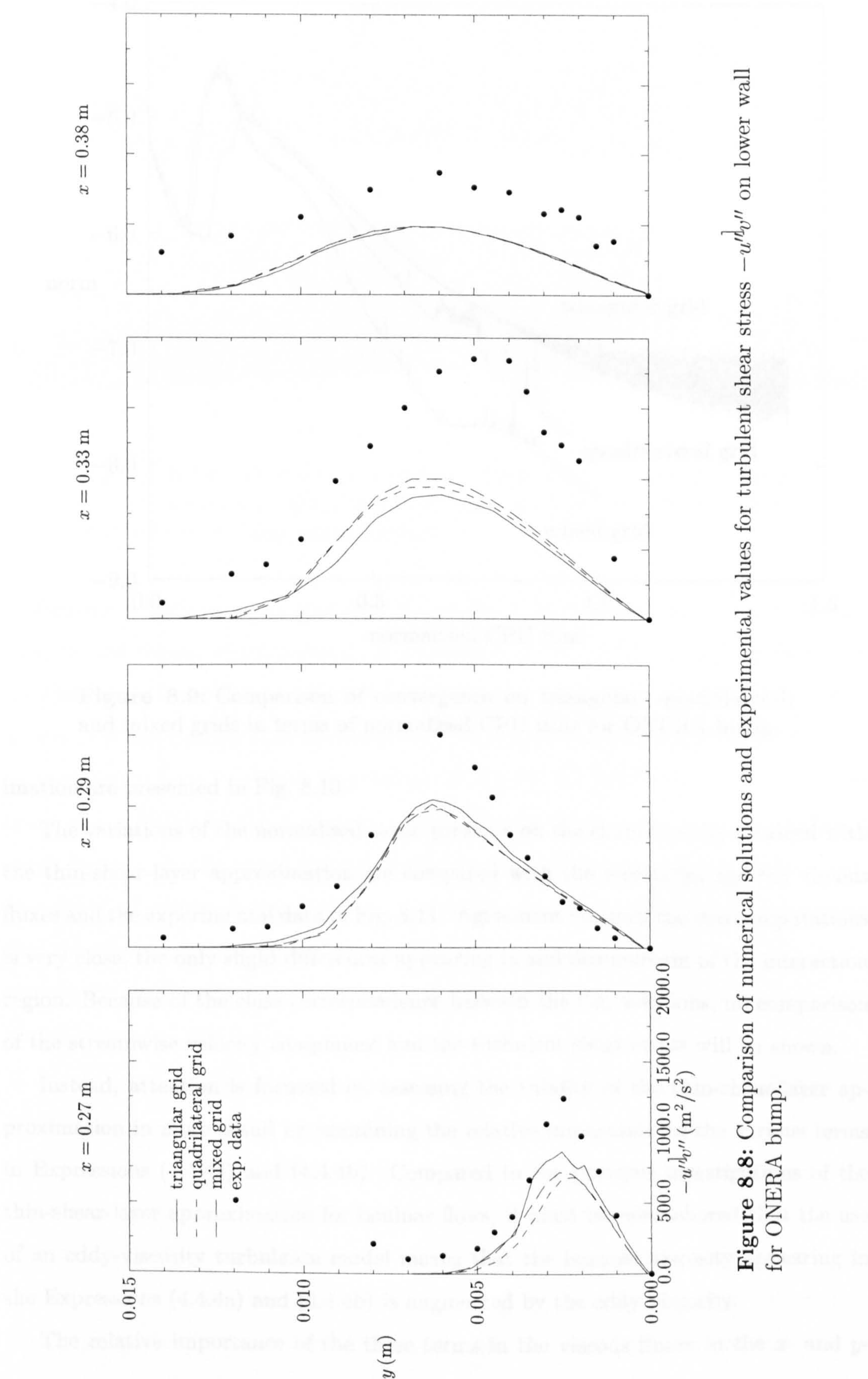


Figure 8.8: Comparison of numerical solutions and experimental values for turbulent shear stress $-u''v''$ on lower wall for ONERA bump.

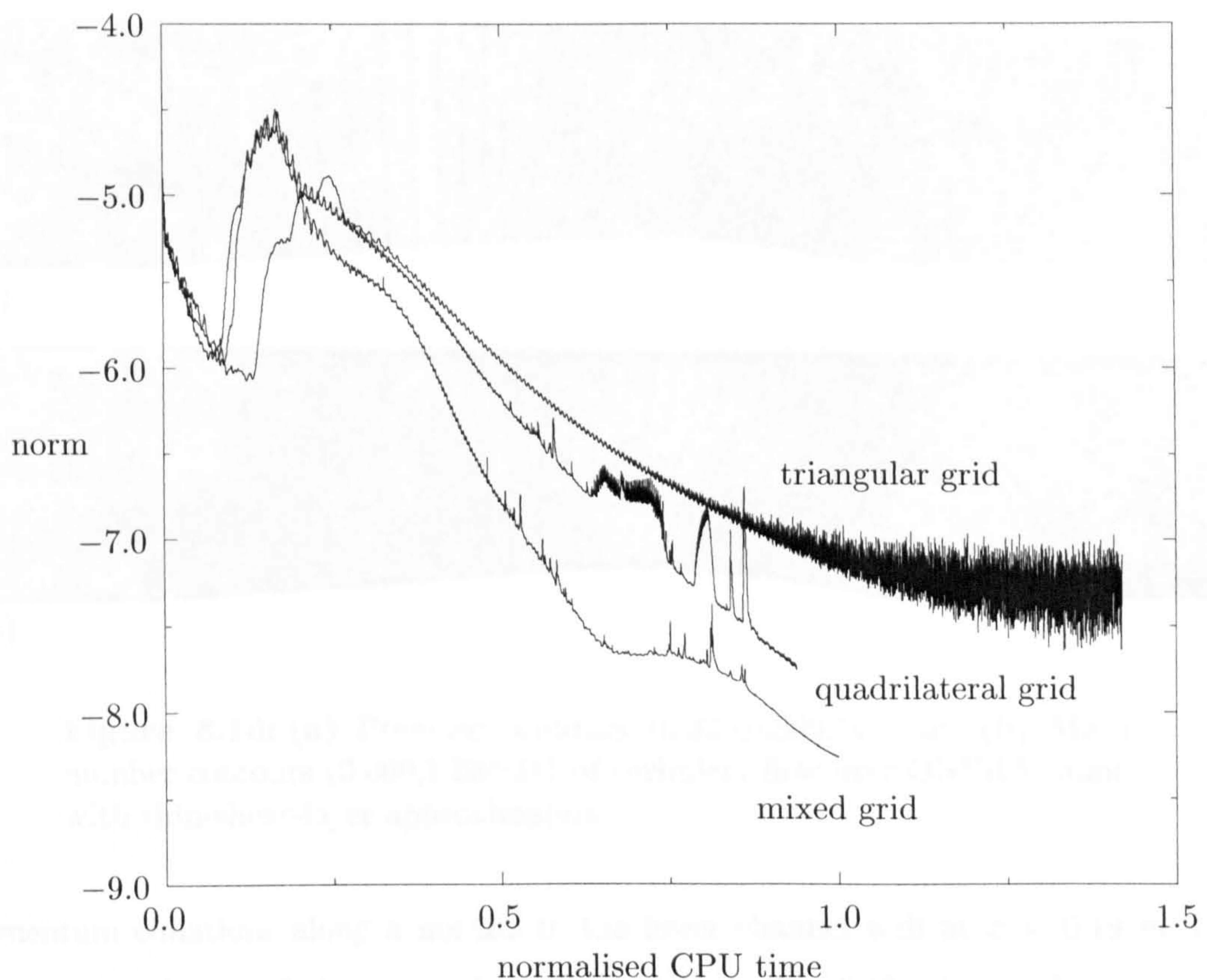


Figure 8.9: Comparison of convergence on triangular, quadrilateral, and mixed grids in terms of normalised CPU time for ONERA bump.

imation are presented in Fig. 8.10.

The variations of the normalised static pressure on the channel walls obtained with the thin-shear-layer approximation are compared with the results for the full viscous fluxes and the experimental data in Fig. 8.11. Agreement between the two computations is very close, the only slight differences appearing in and downstream of the interaction region. Because of the close correspondence between the two solutions, no comparison of the streamwise velocity component and the turbulent shear stress will be shown.

Instead, attention is focussed on assessing the validity of the thin-shear-layer approximation in more detail by examining the relative importance of the various terms in Expressions (4.4.4a) and (4.4.4b). Compared to the previous investigations of the thin-shear-layer approximation for laminar flows, it must be remembered that the use of an eddy-viscosity turbulence model means that the laminar viscosity appearing in the Expressions (4.4.4a) and (4.4.4b) is augmented by the eddy viscosity.

The relative importance of the three terms in the viscous fluxes in the x - and y -

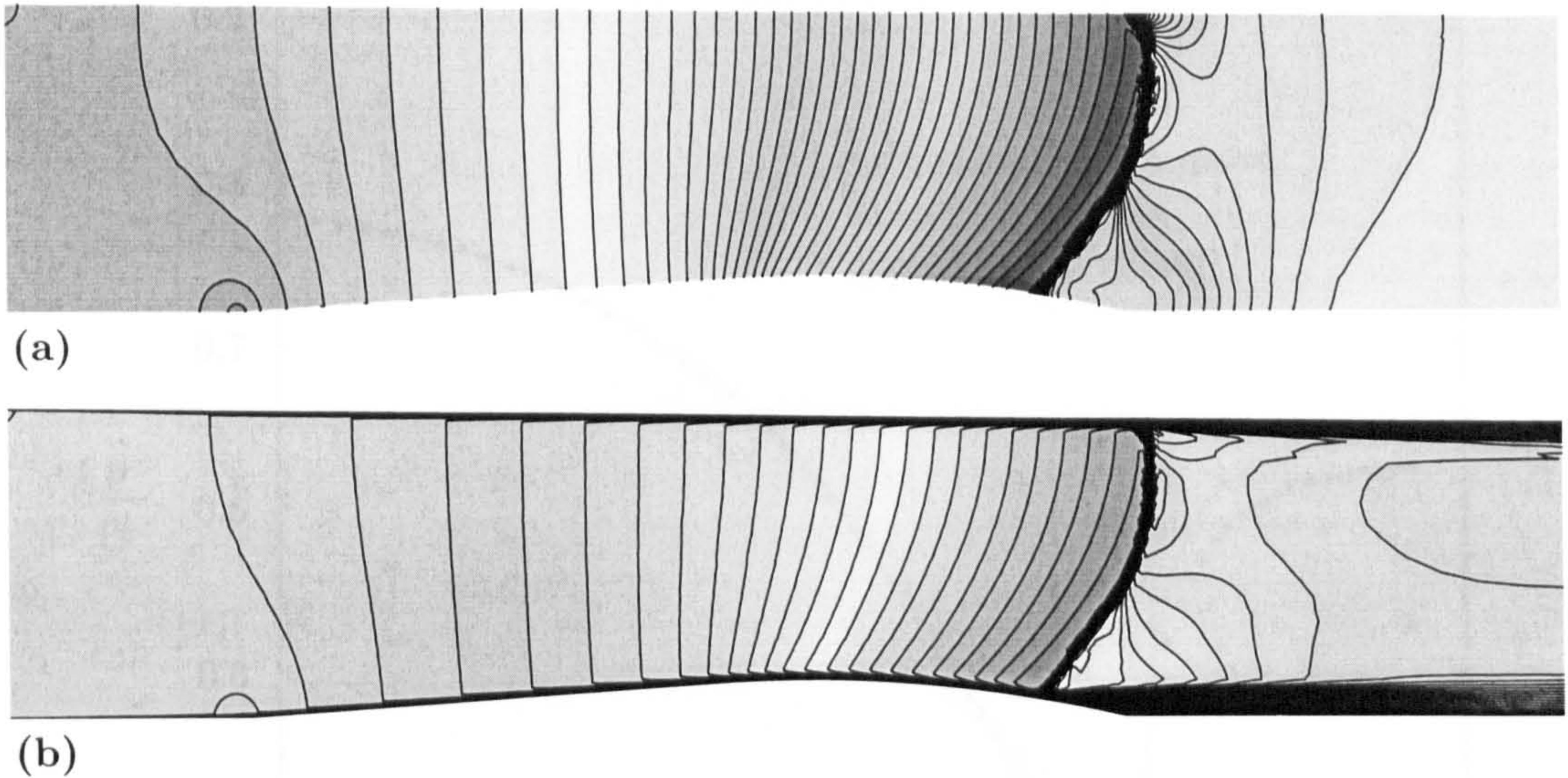


Figure 8.10: (a) Pressure contours (0.320,0.809;41) and (b) Mach number contours (0.000,1.384;41) of turbulent flow over ONERA bump with thin-shear-layer approximation.

momentum equations along a normal to the lower channel wall at $x = 0.19$ m, i.e., close to the throat of the channel, is illustrated in Fig. 8.12. It can be seen that approximating term 2 and neglecting term 3 in the x -momentum equations is justified as term 1 is much larger than the other two over the whole boundary layer. Conversely, approximating term 2 in the y -momentum equation is not justified as it is of the same order of magnitude as the first term. Neglecting the third term may be regarded as valid. It must also be noted that the terms in the y -momentum equation are roughly two orders of magnitude smaller than those in the x -momentum equation. This means that the effect of approximating the second term are probably insignificant, which would explain the excellent agreement between the full viscous fluxes and the thin-shear-layer approximation at $x = 0.19$ m.

A more severe test of the thin-shear-layer approximation is the assessment of the relative importance of the various terms at $x = 0.27$, i.e., in the interaction region. As revealed by Fig. 8.13, the first term in Expression (4.4.4a) clearly outweighs the other two, so that the assumptions underlying the thin-shear-layer approximation are corroborated. By contrast, the third term in Expression (4.4.4b) is the largest over the whole of the boundary layer, indicating that its neglect cannot be justified. The importance of the third term together with the increased importance of the y -

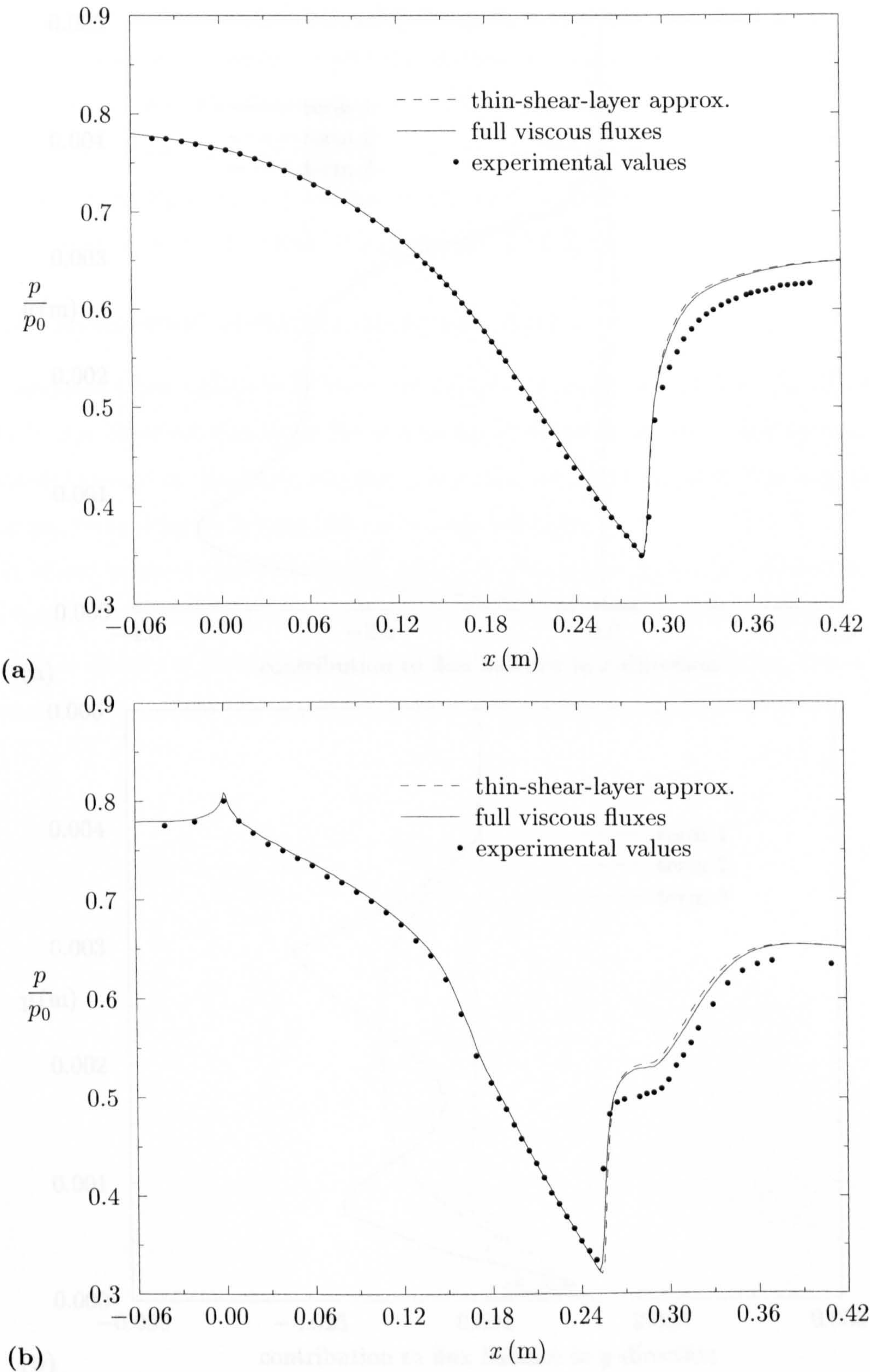
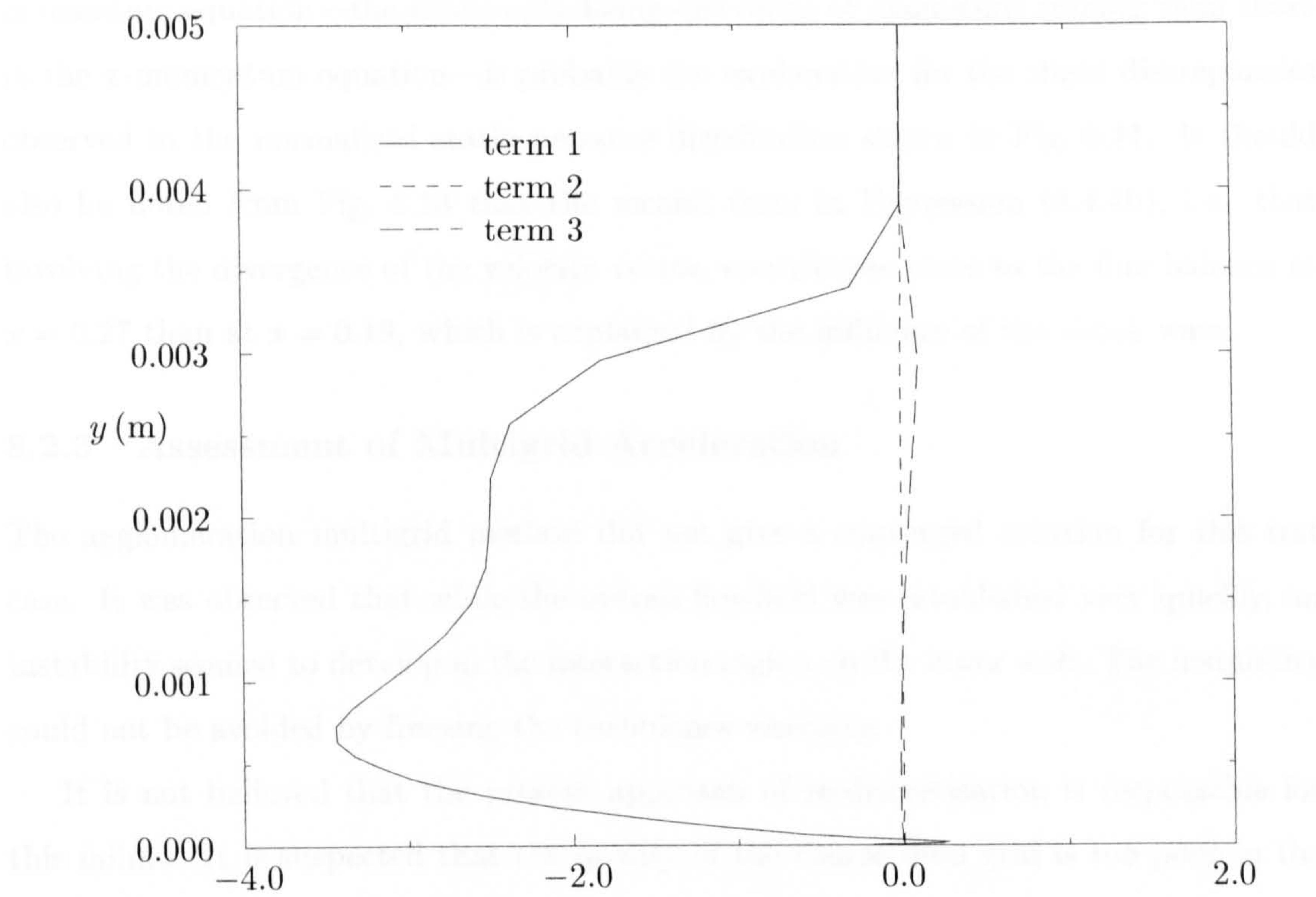
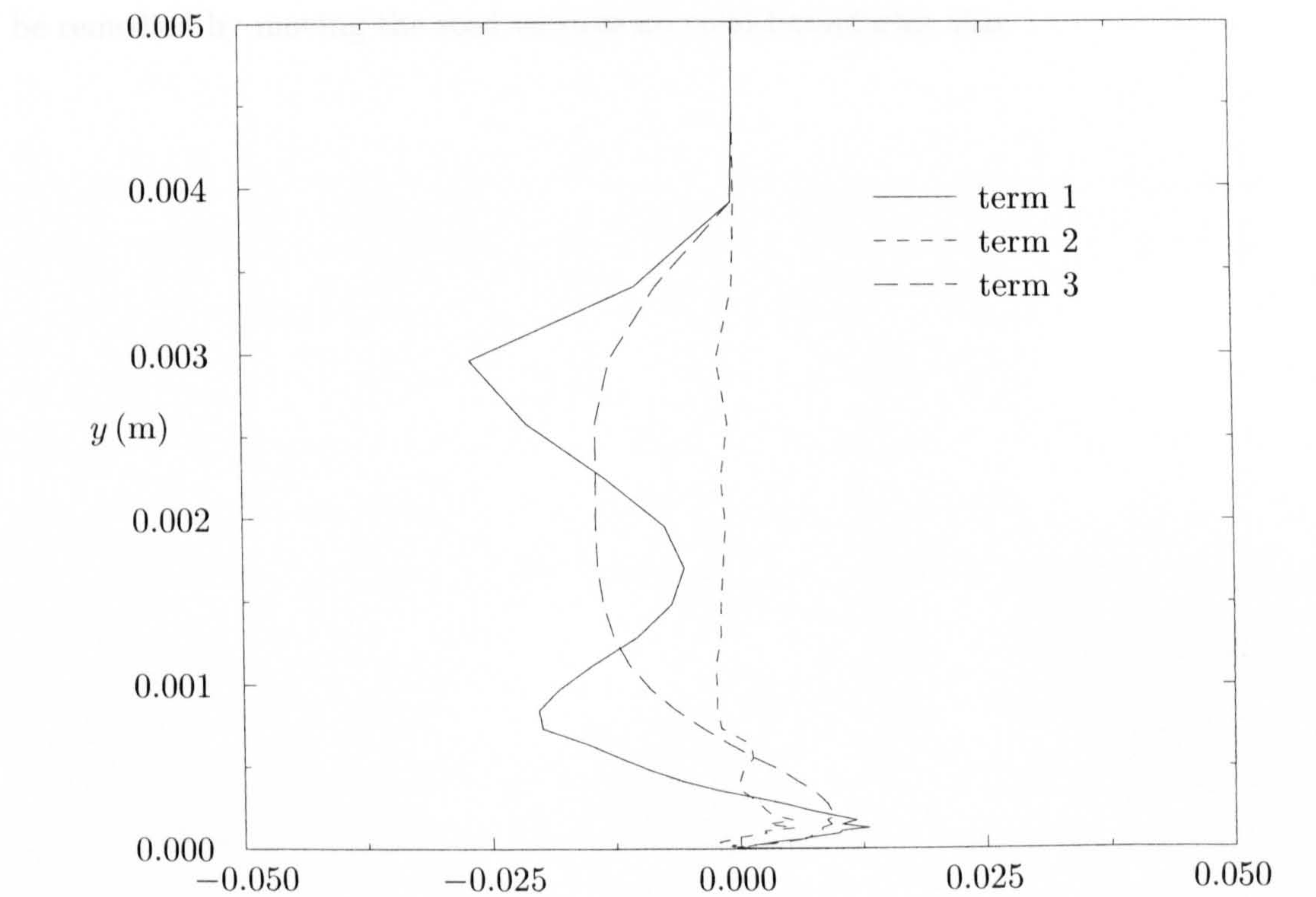


Figure 8.11: Comparison of numerical solution with experimental values of normalised pressure on (a) upper and (b) lower walls for ONERA bump.



(a)



(b)

Figure 8.12: Relative importance of terms in (a) Expression (4.4.4a) and (b) Expression (4.4.4b) along normal at $x = 0.19$ to solid wall.

momentum equation—the terms only being one order of magnitude smaller than those in the x -momentum equation—is probably the explanation for the slight discrepancies observed in the normalised static pressure distribution shown in Fig. 8.11. It should also be noted from Fig. 8.13 that the second term in Expression (4.4.4b), i.e., that involving the divergence of the velocity vector, contributes more to the flux balance at $x = 0.27$ than at $x = 0.19$, which is explained by the influence of the shock wave.

8.2.3 Assessment of Multigrid Acceleration

The agglomeration multigrid method did not give a converged solution for this test case. It was observed that while the overall flowfield was established very quickly, an instability seemed to develop in the interaction region on the lower wall. The instability could not be avoided by freezing the turbulence viscosity.

It is not believed that the present approach of re-discretisation is responsible for this failure. It is suspected that the quality of the coarse dual grid is too poor in the immediate vicinity of the solid walls on account of the high grid stretching. This could be remedied by moving the seed vertices on solid boundaries also.

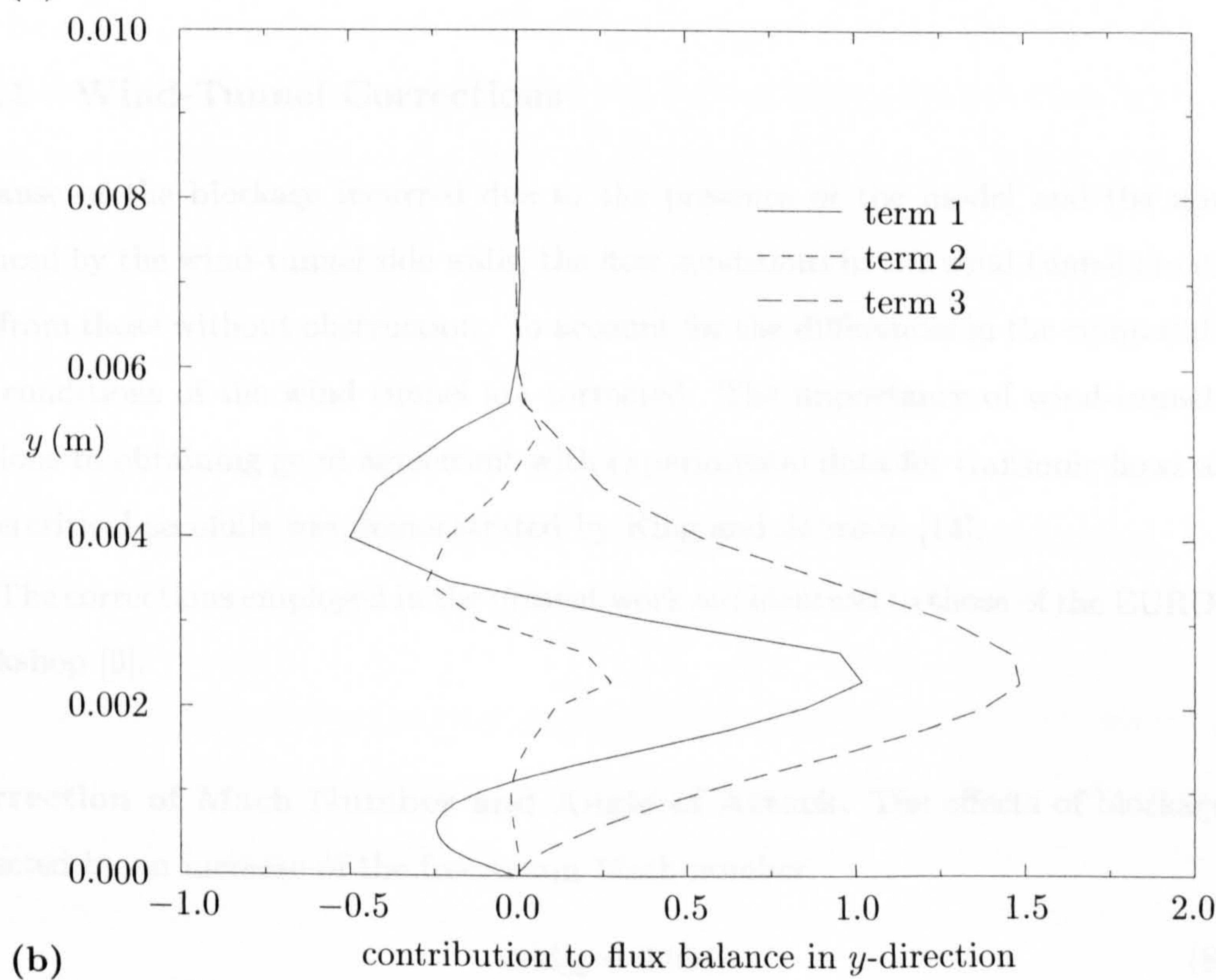
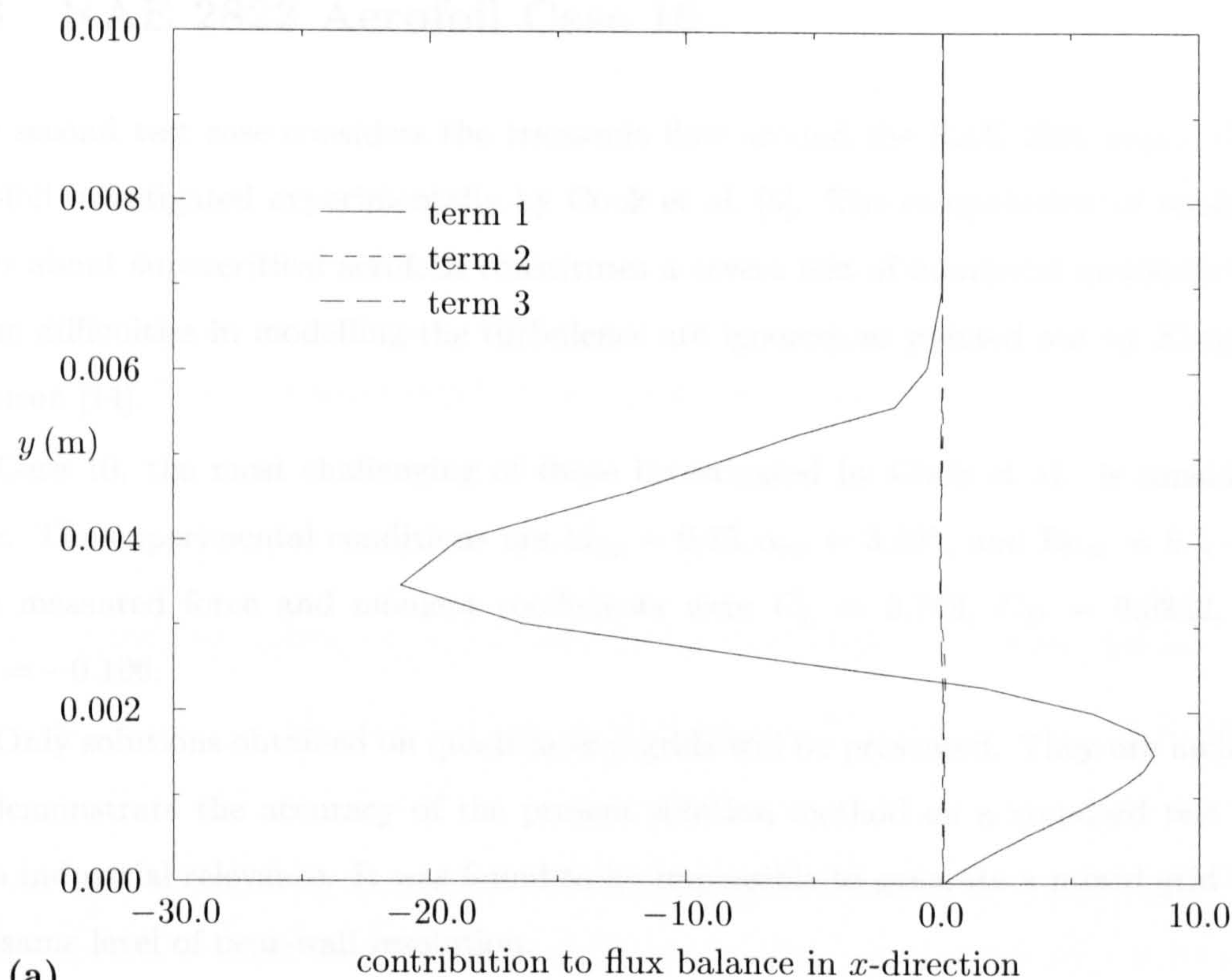


Figure 8.13: Relative importance of terms in (a) Expression (4.4.4a) and (b) Expression (4.4.4b) along normal at $x = 0.27$ to solid wall.

8.3 RAE 2822 Aerofoil Case 10

The second test case considers the transonic flow around the RAE 2822 supercritical aerofoil investigated experimentally by Cook et al. [5]. The computation of transonic flows about supercritical aerofoils constitutes a severe test of numerical methods, even if the difficulties in modelling the turbulence are ignored, as pointed out by King and Johnson [14].

Case 10, the most challenging of those investigated by Cook et al., is considered here. The experimental conditions are $M_\infty = 0.75$, $\alpha_\infty = 3.19^\circ$, and $Re_\infty = 6.2 \cdot 10^6$. The measured force and moment coefficients were $C_L = 0.743$, $C_D = 0.0242$, and $C_M = -0.106$.

Only solutions obtained on quadrilateral grids will be presented. They are included to demonstrate the accuracy of the present solution method on a standard test case with industrial relevance. It was found to be impossible to generate a mixed grid with the same level of near-wall resolution.

8.3.1 Wind-Tunnel Corrections

Because of the blockage incurred due to the presence of the model and the upwash induced by the wind-tunnel side walls, the flow conditions in the wind tunnel are different from those without obstruction. To account for the differences in the computations, the conditions of the wind tunnel are corrected. The importance of wind-tunnel corrections to obtaining good agreement with experimental data for transonic flows about supercritical aerofoils was demonstrated by King and Johnson [14].

The corrections employed in the present work are identical to those of the EUROVAL workshop [9].

Correction of Mach Number and Angle of Attack. The effects of blockage are reflected by an increase of the freestream Mach number,

$$\Delta M_\infty = 0.004. \quad (8.3.1)$$

To take into account the wall-induced upwash, the experimental angle of attack and the aerofoil contour are modified. The angle of attack is changed by adding the

correction

$$\Delta\alpha = \frac{c}{h} \left[C_L \delta_0 + \frac{\delta_1 c}{\beta h} \left(\frac{C_L}{4} + C_M \right) \right], \quad (8.3.2)$$

where c/h is the ratio of chord length to height of the wind tunnel given by 0.25, and β is the Prandtl-Glauert parameter defined by Eq. (3.11.24), evaluated at the corrected Mach number. Furthermore, δ_0 and δ_1 are empirical parameters taking the values -0.0654 and 0.1754 , respectively.* With these values, the correction to the angle of attack is

$$\Delta\alpha = -0.62^\circ. \quad (8.3.3)$$

As a result, the corrected experimental parameters used in the computations are,

$$M_\infty = 0.754, \alpha_\infty = 2.57^\circ, \text{Re}_\infty = 6.2 \cdot 10^6. \quad (8.3.4)$$

Correction of Aerofoil Contour. The measured aerofoil contour tabulated by Cook et al. exhibits a slight irregularity at the trailing edge. The irregularity is removed by eliminating the point at the trailing edge and extrapolating the upper and lower ordinates to $x = 1.0$. The resulting thin but finite trailing-edge thickness is removed by an upward adjustment of the lower surface over $0.4 \leq x \leq 1.0$, which is smoothly blended to zero at $x = 0.4$. This modification is due to Benton [4].

Following this modification, the aerofoil contour is modified by adding a camber correction to the lower and upper surfaces,

$$\frac{\Delta y}{c} = \frac{\delta_1 C_L}{2\beta} \left(\frac{c}{h} \right)^2 \frac{x}{c} \left(1 - \frac{x}{c} \right). \quad (8.3.5)$$

Substituting the relevant values into Eq. (8.3.5) gives, to three decimal places,

$$\frac{\Delta y}{c} = 0.006 \frac{x}{c} \left(1 - \frac{x}{c} \right). \quad (8.3.6)$$

Unfortunately, the corrected parameters and profile are not unique in that several combinations of the corrected freestream Mach number, angle of attack, and profile coordinates can be found in the literature. Furthermore, Spalart and Allmaras [18] corrected the Mach number only, and varied the angle of attack to give the value of the lift

*It is noted that these values differ from those originally quoted by Cook et al. The differences arise because later investigations with a viscous-inviscid interaction code (assumed to be capable of predicting the pressure distribution on the lower surface correctly) showed better agreement with the experiment when the modified values were used [19,20].

coefficient observed in the experiment (they found that $\alpha_\infty = 2.52^\circ$).

While the existence of several sets of parameters and profiles is unsatisfactory, this is probably not a serious issue. An investigation by Bardina et al. [2] demonstrated that the influence of changes in the angle of attack of $\pm 10\%$ with a given turbulence model was smaller than that of the turbulence model for a given angle of attack. This conclusion was also reached from the results of calculations with the present solution method.

8.3.2 Numerical Solution

The quadrilateral grid depicted in Fig. 8.15 is used. It consists of 31120 vertices, 61840 edges, and 30720 cells. The aerofoil surface is represented by 256 vertices. The first grid points are located at a distance of $1 \cdot 10^{-6}$ chord lengths from the aerofoil surface. This gives an average value of y^+ of about unity along both the upper and lower surfaces. The freestream boundary is located at between 12 – 20 chord lengths from the leading edge of the aerofoil. The grid was kindly provided by Dr. Laurence Wigton [22] to conform to the same corrected profile as the EUROVAL grid. Transition was imposed at $x/c = 0.03$ using the dedicated source term of the Spalart-Allmaras turbulence model.

Overall Flowfield. The computed distribution of the pressure coefficient is shown in Fig. 8.17(a). The agreement with experimental values is generally good with the exception of the under-prediction of the suction peak, and the location of the shock wave, which is placed too far aft. Although these discrepancies are often observed for this test case, see, e.g., Holst [11], they are nevertheless disappointing, since Spalart and Allmaras [18] obtained better agreement with experimental values at approximately the same angle of attack and on a very similar grid.[†] Simulations by other authors, e.g., Rumsey and Vatsa [16], Bardina et al. [2], Wang et al. [21], and Kalitzin [12], all obtained solutions similar to the present one.

The corresponding distribution of the skin-friction coefficient is depicted in Fig. 8.17(b). On the upper surface, the level of skin friction is approximately correct. An

[†]The aerofoil contour used in the computations of Spalart and Allmaras differed slightly from the present one on the lower surface and at the trailing edge, but had the same relative grid-point distribution.

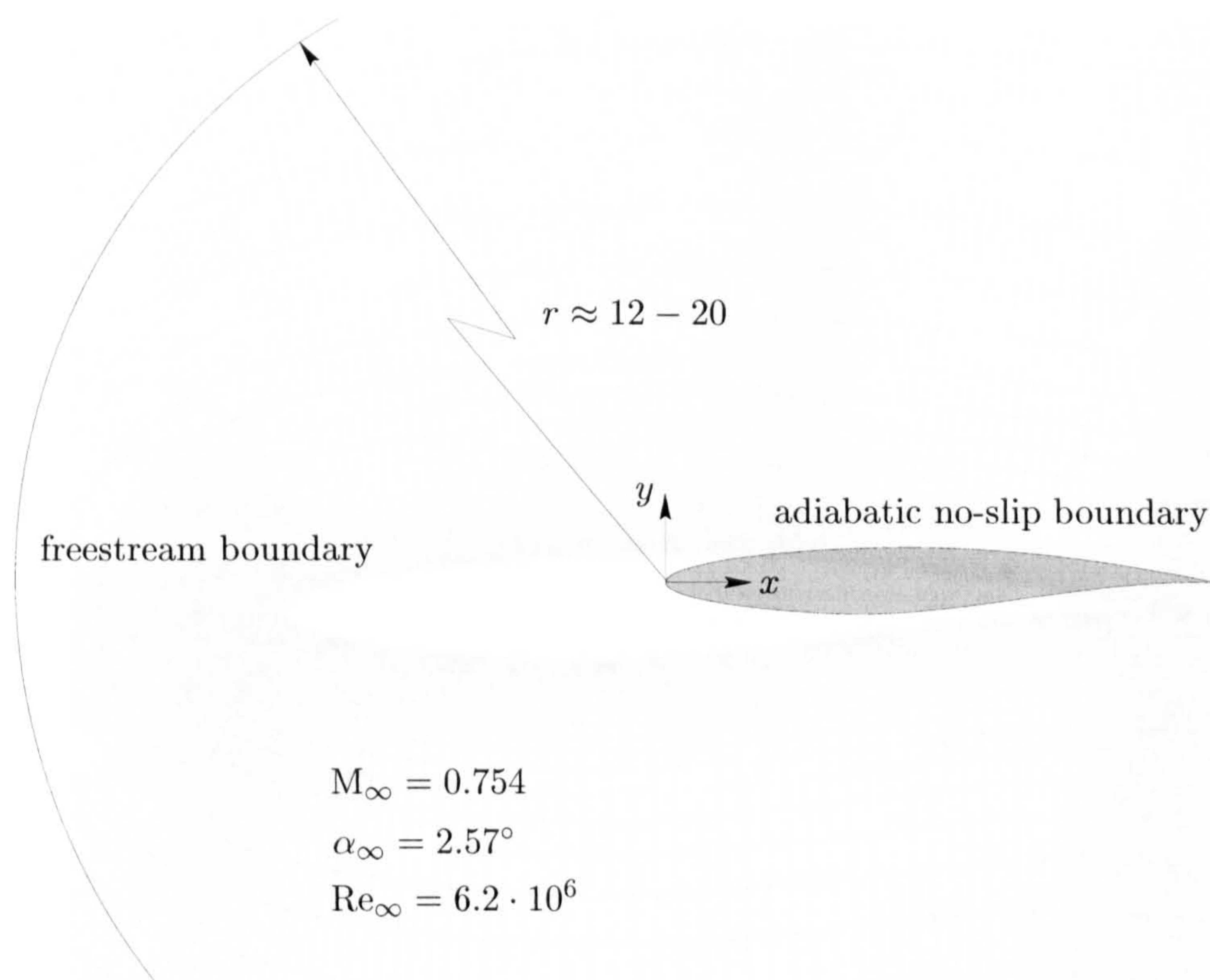


Figure 8.14: Solution domain and boundary conditions for RAE 2822 aerofoil.

interesting feature, exhibited by nearly all simulations carried out so far using the Spalart-Allmaras model, is that the flow does not re-attach following the shock-induced separation. The strong variations of the skin-friction coefficient near the trailing edge is caused by misalignment of the flow direction and the angle of the grid lines, as shown by Haase [10].

The computed lift, drag, and moment coefficients are 0.767, 0.0271, and -0.114 .

Profiles of Streamwise Velocity. The comparison of the computed u -velocity with experimental data on the upper surface will be carried out at the stations indicated in Fig. 8.18. As may be seen from Fig. 8.19, the agreement is good up to $x/c = 0.498$, with the exception of the position $x/c = 0.179$. At the station $x/c = 0.574$, the discrepancy between the computed and experimental velocity profiles is due to the error in the prediction of the shock location. The following three positions demonstrate that while the general shape of the velocity profile is predicted correctly, a thin separation region remains, as already discussed above.

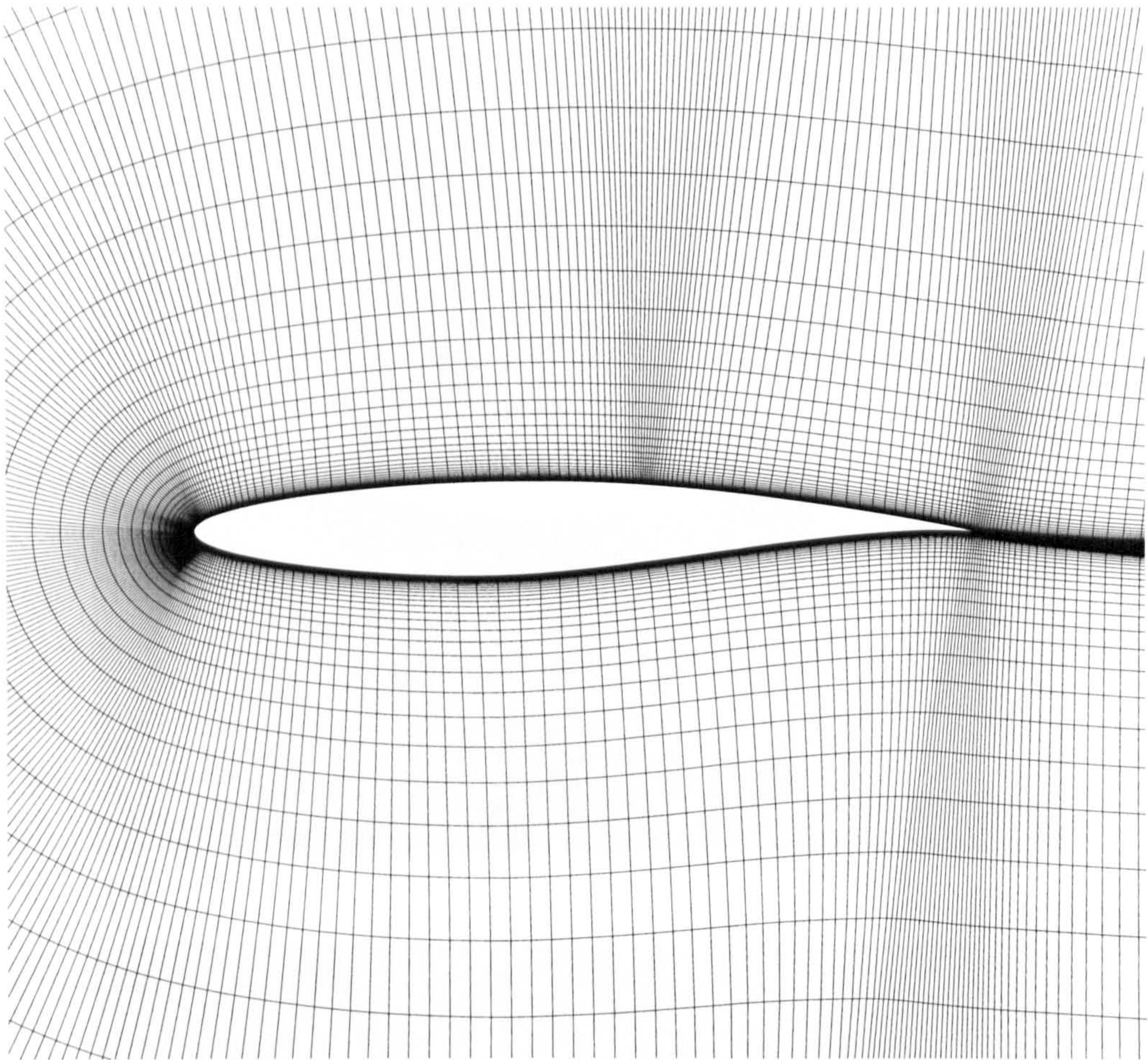
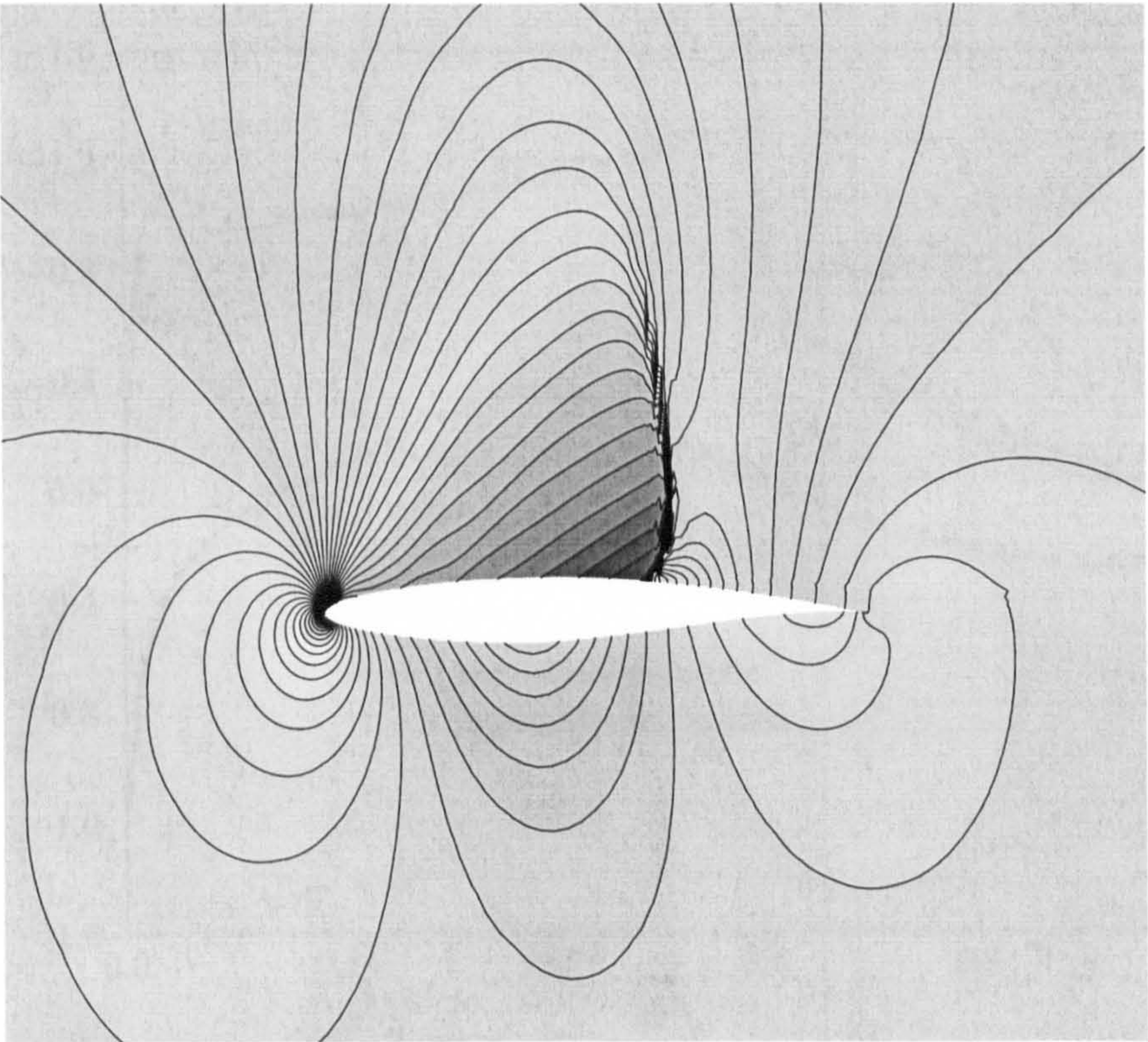


Figure 8.15: Primal grid used for computation of turbulent flow past RAE 2822 aerofoil.

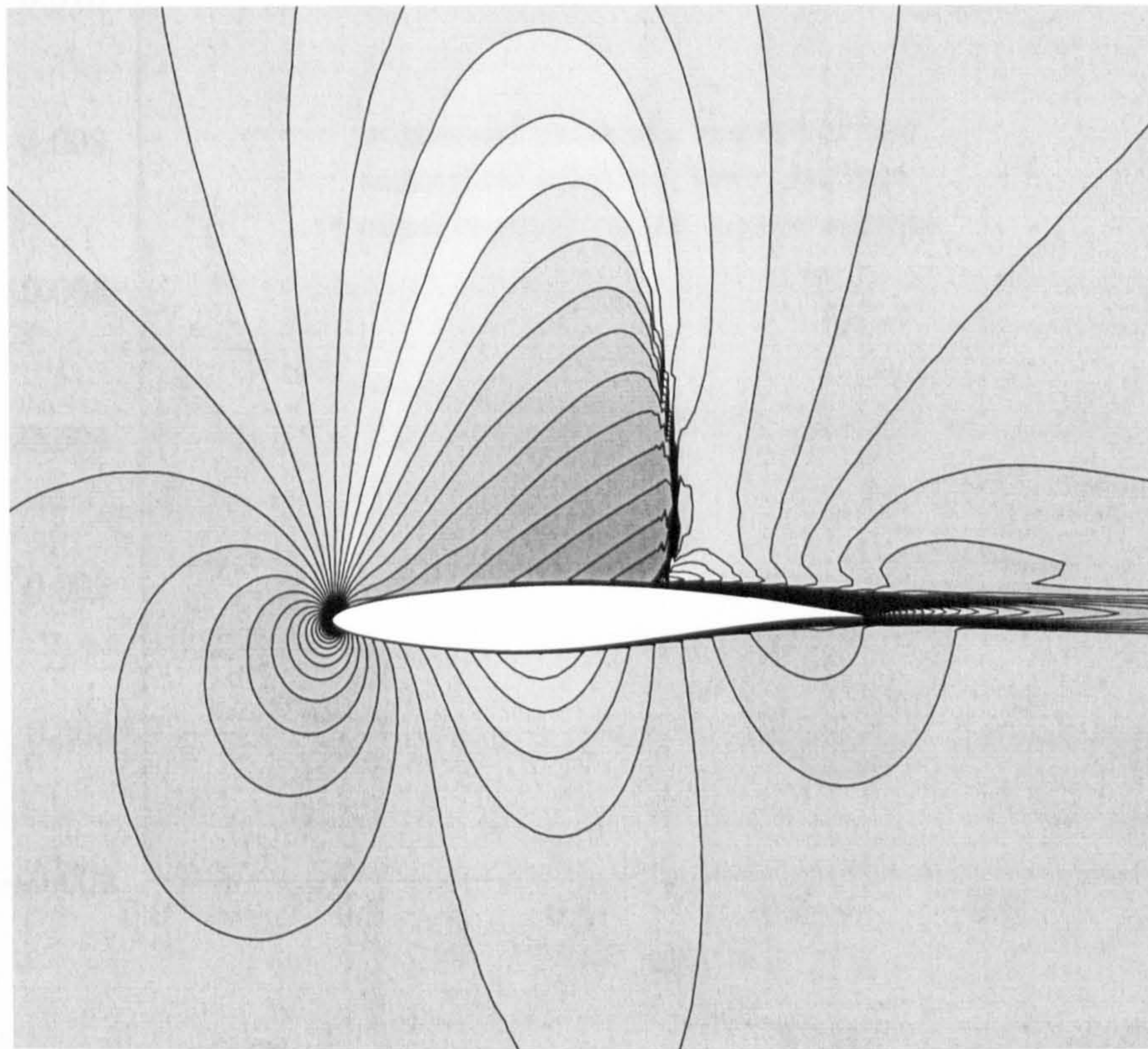
Figure 8.20 demonstrates the effect of the dedicated source term of the Spalart-Allmaras source term for the simulation of transition. This is done by comparing the profiles of the normalised velocity tangential to the aerofoil surface at $x/c = 0.01$ and $x/c = 0.1$. The change from a laminar to a turbulent boundary layer profile can be seen clearly. The inset shows the so-called turbulence index defined by Spalart and Allmaras [18], which is equal to zero in laminar regions and assumes a value close to unity in turbulent regions.

8.3.3 Assessment of Thin-Shear-Layer Approximation

The pressure and skin-friction coefficient obtained using the thin-shear-layer approximation are compared with the results of the full viscous fluxes in Fig. 8.21. As can be seen the agreement is very close, with the exception of the separation region where



(a)



(b)

Figure 8.16: (a) Pressure contours (0.340,1.043;41) and (b) Mach number contours (0.000,1.233;41) for turbulent flow past RAE 2822 aerofoil.

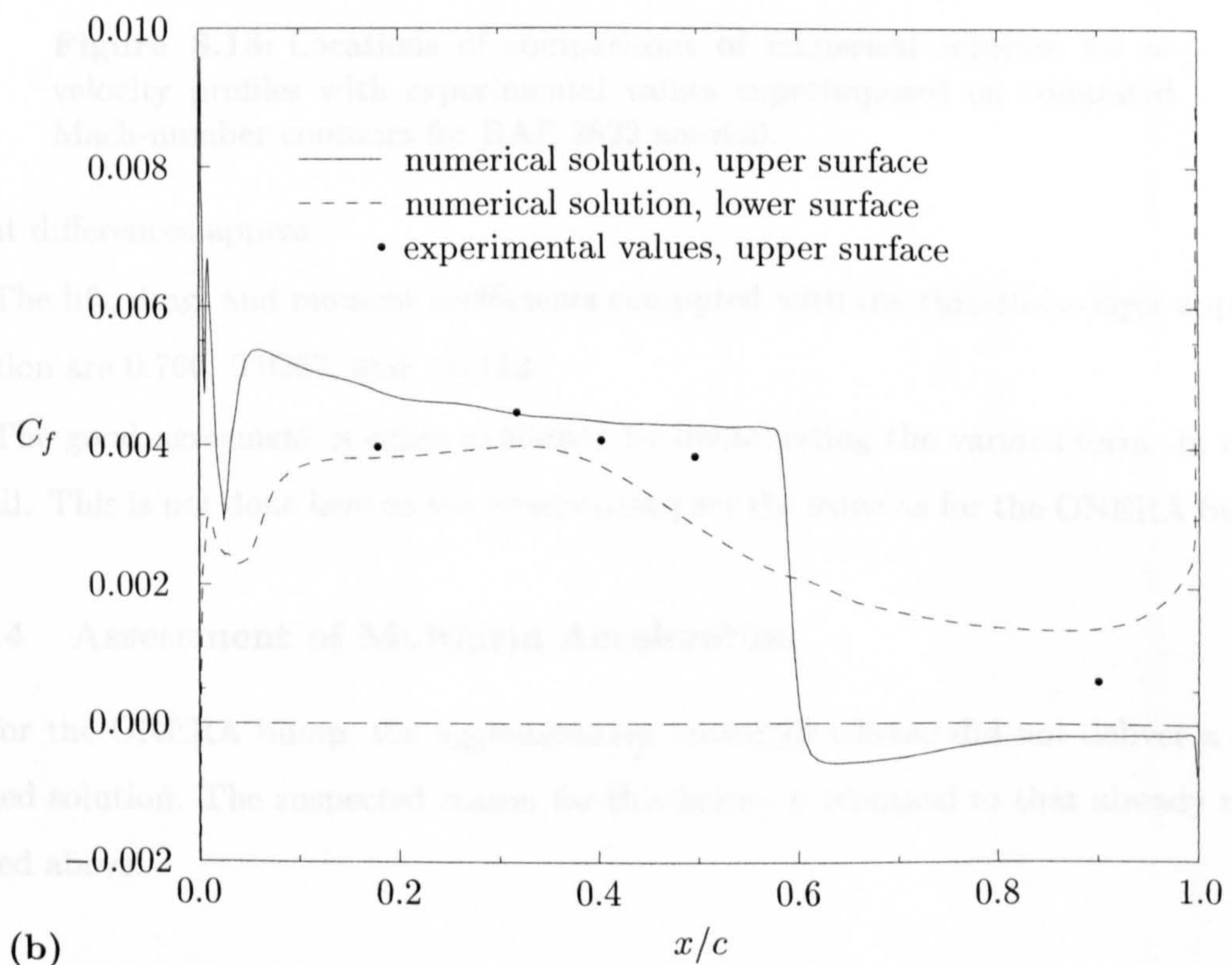
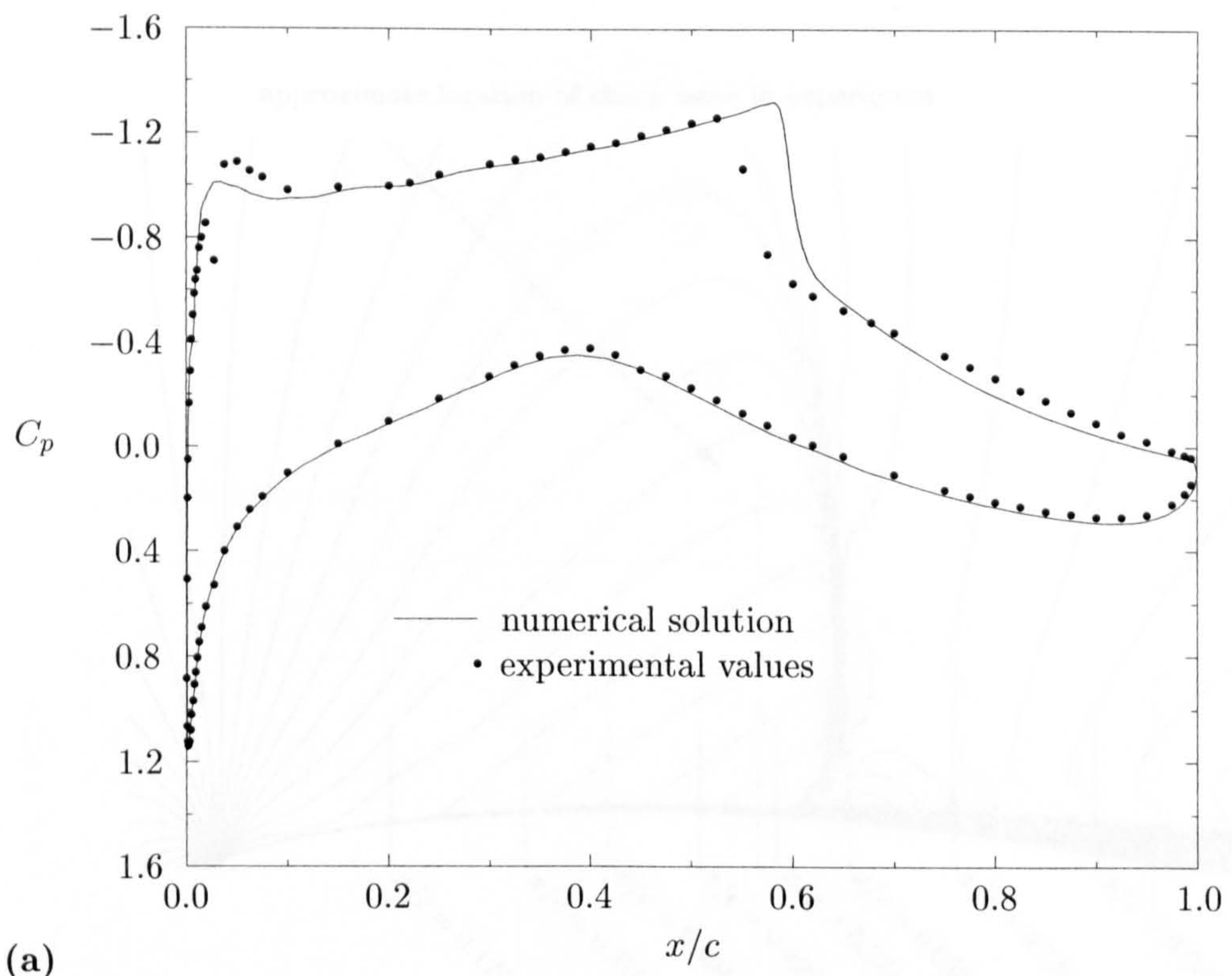


Figure 8.17: Comparison of numerical solution with experimental values of (a) pressure and (b) skin-friction coefficient for RAE 2822 aerofoil.

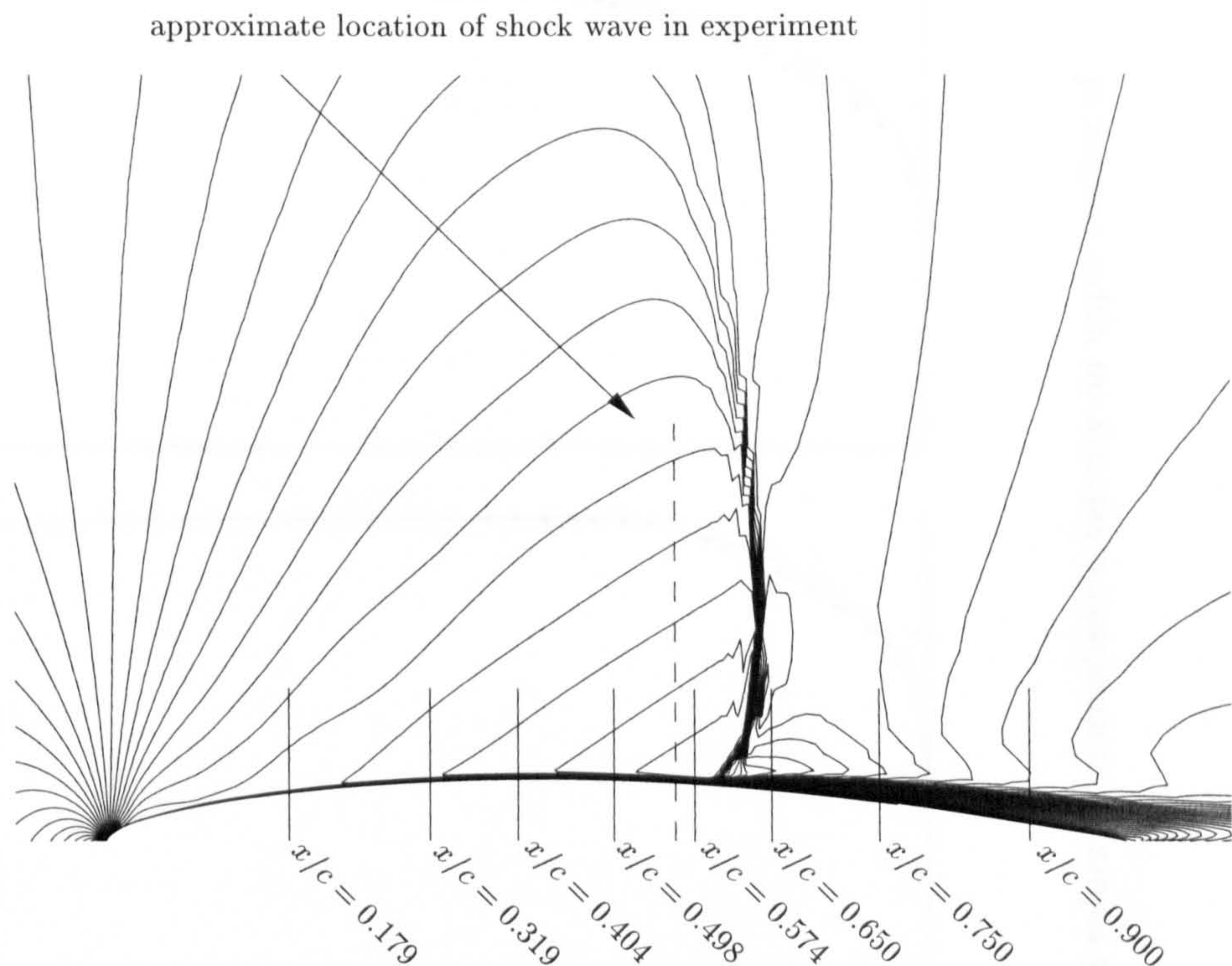


Figure 8.18: Locations of comparisons of numerical solution for u -velocity profiles with experimental values superimposed on computed Mach-number contours for RAE 2822 aerofoil.

slight differences appear.

The lift, drag, and moment coefficients computed with the thin-shear-layer approximation are 0.760, 0.0267, and -0.112 .

The good agreement is again explained by investigating the various terms in more detail. This is not done here as the observations are the same as for the ONERA bump.

8.3.4 Assessment of Multigrid Acceleration

As for the ONERA bump, the agglomeration multigrid scheme did not deliver a converged solution. The suspected reason for this failure is identical to that already mentioned above.

8.4 Conclusions

The computations described in this Chapter lead to the following conclusions:

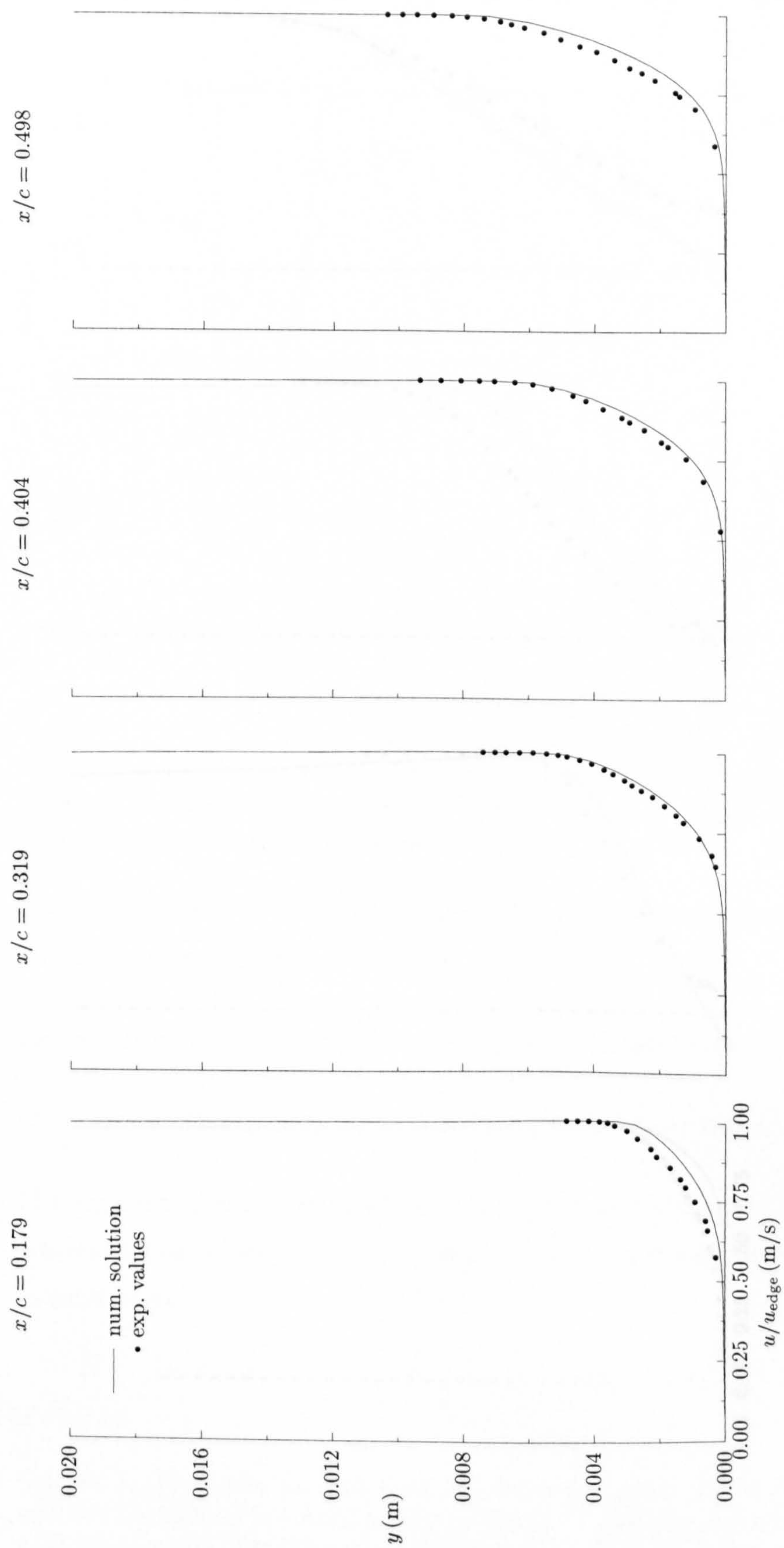


Figure 8.19: Comparison of numerical solutions and experimental values for normalised u -velocity on upper surface of RAE 2822 aerofoil.

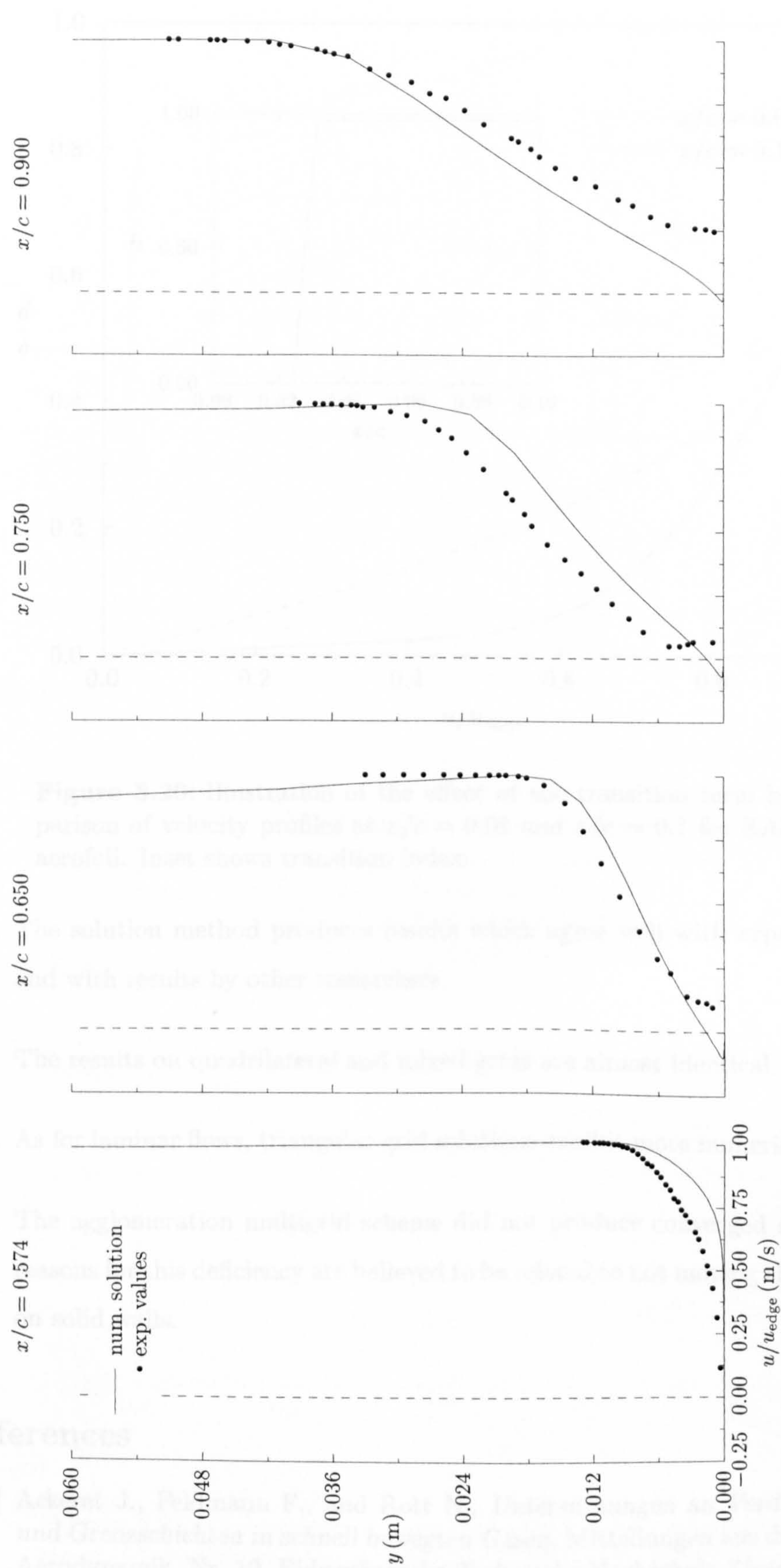


Figure 8.19 (continued): Comparison of numerical solutions and experimental values for normalised u -velocity on upper surface of RAE 2822 aerofoil. Note the change of scale of the abscissa.

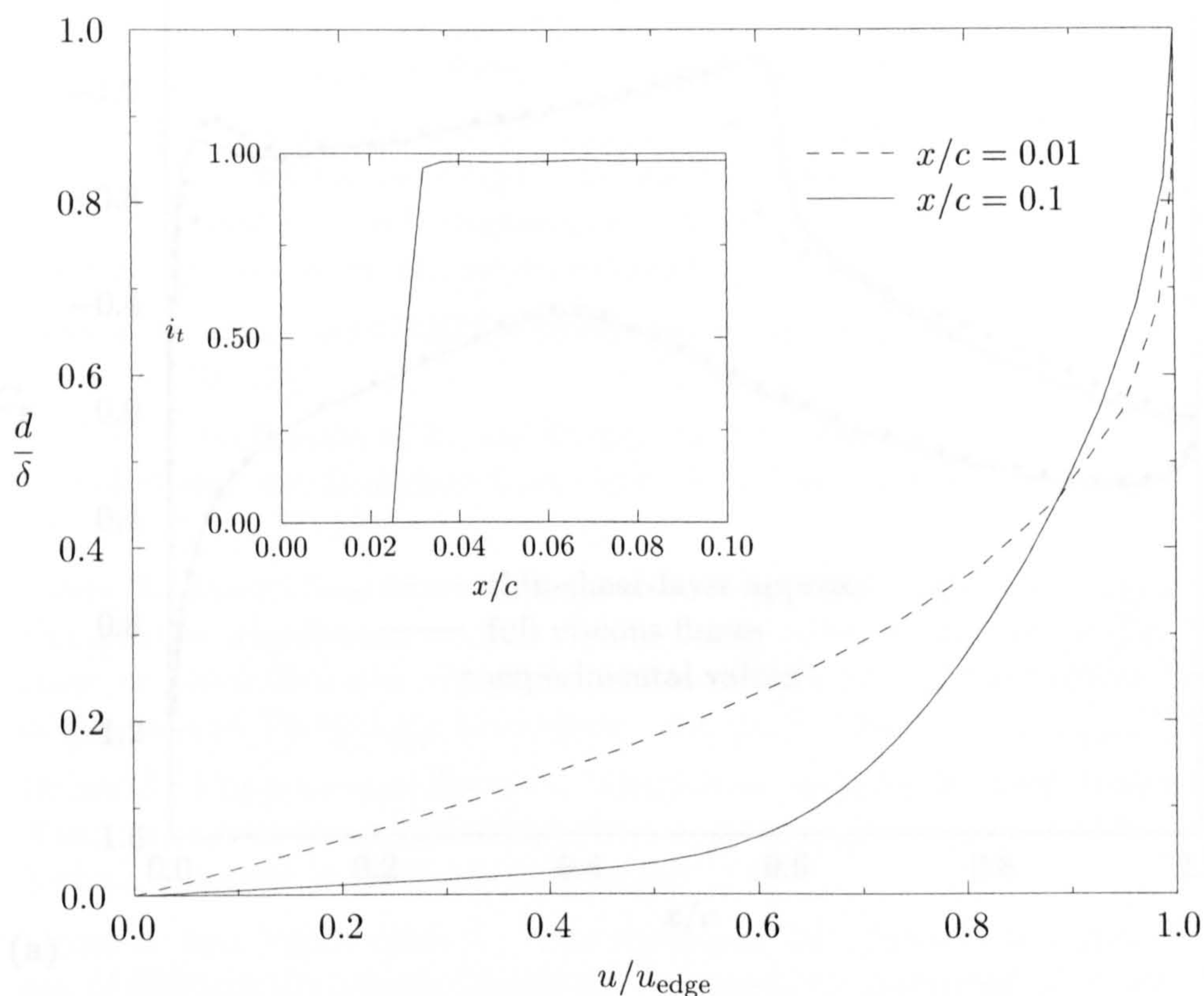
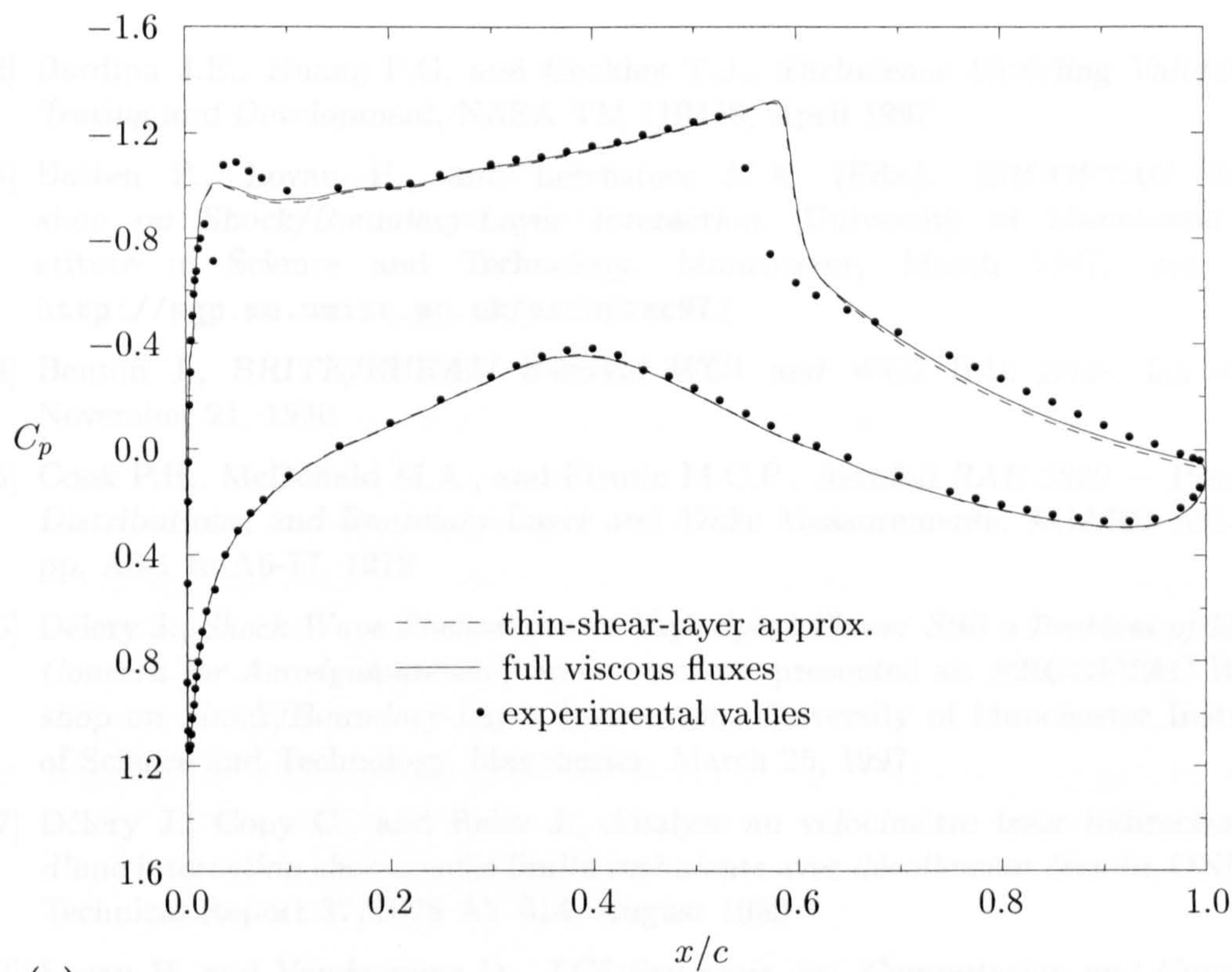


Figure 8.20: Illustration of the effect of the transition term by comparison of velocity profiles at $x/c = 0.01$ and $x/c = 0.1$ for RAE 2822 aerofoil. Inset shows transition index.

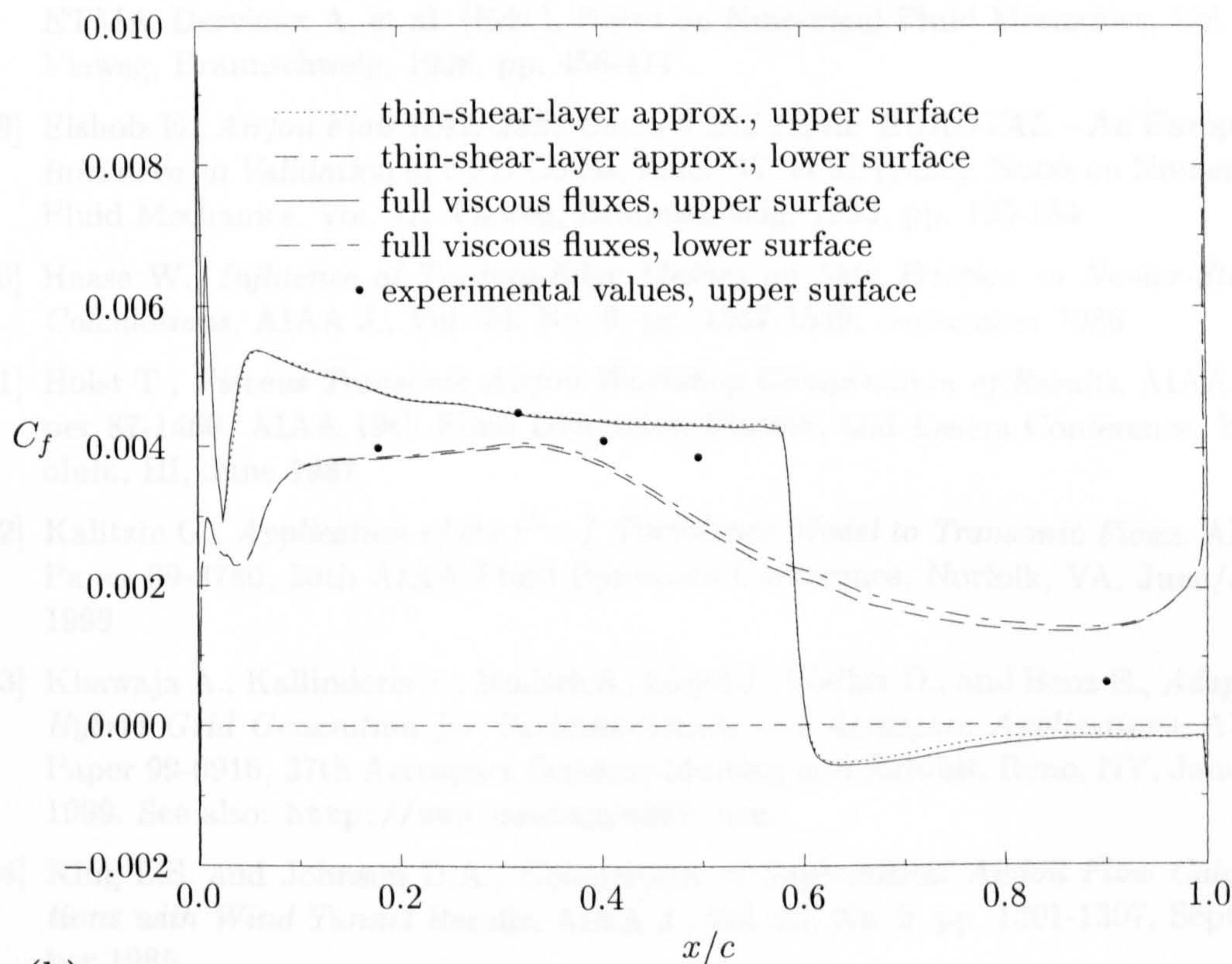
1. The solution method produces results which agree well with experimental data and with results by other researchers.
2. The results on quadrilateral and mixed grids are almost identical.
3. As for laminar flows, triangular-grid solutions exhibit more numerical dissipation.
4. The agglomeration multigrid scheme did not produce converged solutions. The reasons for this deficiency are believed to be related to not moving the seed vertices on solid walls.

References

- [1] Ackeret J., Feldmann F., and Rott N., *Untersuchungen an Verdichtungsstößen und Grenzschichten in schnell bewegten Gasen*, Mitteilungen aus dem Institut für Aerodynamik, Nr. 10, Eidgenössische Technische Hochschule Zürich, 1946



(a)



(b)

Figure 8.21: Comparison of numerical solution with experimental values of (a) pressure and (b) skin-friction coefficient for RAE 2822 aerofoil.

- [2] Bardina J.E., Huang P.G. and Coakley T.J., *Turbulence Modeling Validation, Testing and Development*, NASA TM 110446, April 1997
- [3] Batten P., Loyau H., and Leschziner M.A. (Eds.), *ERCRAFTAC Workshop on Shock/Boundary-Layer Interaction*, University of Manchester Institute of Science and Technology, Manchester, March 1997; see also: <http://sgp.me.umist.ac.uk/ercraftac97/>
- [4] Benton J., *BRITE/EURAM EuroVal WG1 and WG2 BAe grids*, fax dated November 21, 1990
- [5] Cook P.H., McDonald M.A., and Firmin M.C.P., *Aerofoil RAE 2822 — Pressure Distributions, and Boundary Layer and Wake Measurements*, AGARD AR-138, pp. A6-1 to A6-77, 1979
- [6] Détery J., *Shock Wave Phenomena in High Speed Flows: Still a Problem of Major Concern for Aerodynamicists!*, Invited lecture, presented at: *ERCRAFTAC Workshop on Shock/Boundary-Layer Interaction*, University of Manchester Institute of Science and Technology, Manchester, March 25, 1997
- [7] Détery J., Copy C., and Reisz J., *Analyse au vélocimètre laser bidirectionnelle d'une interaction choc-couche limite turbulente avec décollement étendu*, ONERA Technical Report 37/7078 AY 014, August 1980
- [8] Loyau H. and Vandromme D., *TC5 Synthesis*, in: *Computation and Comparison of Efficient Turbulence Models for Aeronautics — European Research Project ETMA*, Dervieux A. et al. (Eds.), Notes on Numerical Fluid Mechanics, Vol. 65, Vieweg, Braunschweig, 1998, pp. 456-471
- [9] Elsholz E., *Airfoil Flow RAE-2822 Cases 9 and 10*, in: *EUROVAL — An European Initiative on Validation of CFD Codes*, Haase W. et al. (Eds.), Notes on Numerical Fluid Mechanics, Vol. 42, Vieweg, Braunschweig, 1993, pp. 125-184
- [10] Haase W., *Influence of Trailing-Edge Meshes on Skin Friction in Navier-Stokes Calculations*, AIAA J., Vol. 24, No. 9, pp. 1557-1559, September 1986
- [11] Holst T., *Viscous Transonic Airfoil Workshop Compendium of Results*, AIAA Paper 87-1460, AIAA 19th Fluid Dynamics, Plasma, and Lasers Conference, Honolulu, HI, June 1987
- [12] Kalitzin G., *Application of the $v^2 - f$ Turbulence Model to Transonic Flows*, AIAA Paper 99-3780, 30th AIAA Fluid Dynamics Conference, Norfolk, VA, June/July 1999
- [13] Khawaja A., Kallinderis Y., Irmisch S., Lloyd J., Walker D., and Benz E., *Adaptive Hybrid Grid Generation for Turbomachinery and Aerospace Applications*, AIAA Paper 99-0916, 37th Aerospace Sciences Meeting and Exhibit, Reno, NV, January 1999. See also: <http://www.centaurosoft.com>
- [14] King L.S. and Johnson D.A., *Comparison of Supercritical Airfoil Flow Calculations with Wind Tunnel Results*, AIAA J., Vol. 23, No. 9, pp. 1301-1307, September 1985
- [15] Leschziner M.A., *ONERA Bumps A and C*, in: *EUROVAL — An European Initiative on Validation of CFD Codes*, Haase W. et al. (Eds.), Notes on Numerical Fluid Mechanics, Vol. 42, Vieweg, Braunschweig, 1993, pp. 185-265

- [16] Rumsey C.L. and Vatsa V.N., *Comparison of the Predictive Capabilities of Several Turbulence Models*, J. Aircraft, Vol. 32, No. 3, pp. 510-514, May-June 1995
- [17] Samtaney R., *Visualisation, Extraction, and Quantification of Discontinuities in Compressible Flows*, Technical Report NAS-99-002, NASA Ames Research Center, March 1999
- [18] Spalart P.R. and Allmaras S.R., *A One-Equation Turbulence Model for Aerodynamic Flows*, La Recherche Aéronautique, No. 1, pp. 5-21, 1994
- [19] Tattersall P., *Wind tunnel corrections for RAE 2822 aerofoil*, letter dated January 21, 1997
- [20] ———, *RAE 2822 Aerofoil*, fax dated July 22, 1999
- [21] Wang Q., Massey S.J., Abdol-Hamid K.S., and Frink N., *Solving Navier-Stokes Equations with Advanced Turbulence Models on Three-Dimensional Unstructured Grids*, AIAA Paper 99-0156, 37th Aerospace Sciences Meeting and Exhibit, Reno, NV, January 1999
- [22] Wigton L.B., *High Quality Grid Generation Using "Laplacian Sweeps"*, in: *Proc. 4th Int. Symp. on Computational Fluid Dynamics*, University of California, Davis, Vol. II, pp. 1222-1227, September 1991

PART IV

**CONCLUSIONS AND
RECOMMENDATIONS**

Chapter 9

Conclusions and Recommendations

The results are summarised and the achievements and findings presented relative to the objectives formulated in Chapter 1. Subsequently, areas for future work are recommended.

9.1 Summary of Results

9.1.1 Inviscid Flow

For the supersonic free vortex case as well as the flows over a bump in a channel, the solution quality obtained on triangular and quadrilateral grids was found to be similar. The use of Green-Gauss reconstruction was found to be less accurate than least-squares reconstruction.

The triangulation of a quadrilateral grid did not give increased accuracy. For median-dual control volumes, shock waves became smeared. For containment-dual control volumes, the results were virtually identical to the original quadrilateral grid. The larger number of edges leads to increased computational cost by a factor of about 1.5.

The agglomeration multigrid scheme performed very well for the bump and NACA 0012 aerofoil flows. On average, the multigrid scheme seems to work better on triangular grids. This could be an indication of the stronger coupling among the solution variables, rather than evidence of increased numerical dissipation.

9.1.2 Laminar Flow

For the flow over a flat plate, the results on the quadrilateral and mixed grids were in very close agreement with the theoretical solution. This shows that mixed grids can

attain the same accuracy as quadrilateral grids at a lower computational cost. On the triangular grid, the solution exhibited signs of excessive numerical dissipation, which is explained by the control-volume faces being misaligned with the edges of the grid for highly stretched triangular grids.

The thin-shear-layer approximation gave results very close to those of the full viscous fluxes on quadrilateral and mixed grids for the flow over a flat plate. A detailed analysis of the various terms in the viscous fluxes explained the good agreement. The outcome of the analysis was consistent with the heuristic arguments put forward in the derivation of the thin-shear-layer approximation. On triangular grids, the results were in poor agreement with the theoretical solution. This was attributed to the approximation of the gradient at a control-volume face misaligned with the edges of the grid.

The grid-refinement study for the separated flow about the NACA 0012 aerofoil showed that on the finest grid level, the solutions on the triangular and quadrilateral grids are very similar. The thin-shear-layer approximation produced results which were very close to those obtained with the full viscous fluxes. This was regarded as surprising, because the conditions of the test case basically invalidated the assumptions made in deriving the thin-shear-layer assumption. An analysis of the various terms in the viscous fluxes once again explained the good agreement. On the triangular grid, there were marked differences between the results of the thin-shear-layer assumption and the full viscous fluxes, as for the flow over a flat plate.

The agglomeration multigrid scheme was found to work well despite the large separation bubble. This demonstrated that the approach of rediscretising the equations on the coarse grid levels is feasible.

9.1.3 Turbulent Flow

The comparison of triangular, quadrilateral, and mixed grids for the turbulent flow over the ONERA bump showed that the solution quality on quadrilateral and mixed grids is almost identical. The solution on the triangular grid exhibited signs of more numerical dissipation, which is consistent with the findings in Chapter 6.

The solution of the flow past the RAE 2822 aerofoil on a quadrilateral grid demonstrated the present solution method delivers results of equal quality to those presented by other researchers.

The agglomeration multigrid method did not produce converged solutions for the two turbulent test cases. The reason for this deficiency is believed to be due to not moving the seed vertices on the solid boundaries.

9.2 Achievements and Findings

Relative to the objectives of the present work formulated in Section 1.5, the achievements and findings are:

1. The use of several cell types in mixed unstructured grids leads to additional difficulties for the discretisation, but these difficulties can be overcome.
2. The concept of grid-transparency was introduced as a framework for the development of discretisations on mixed grids. A grid-transparent discretisation does not require information on cell types.
3. The discretisation of the viscous fluxes on unstructured grids was investigated in detail. Criteria were developed which assess the quality of the discretisation. The importance of the normal derivative in giving a grid-transparent and positive discretisation was emphasised.
4. Analysis of the viscous terms in the Navier-Stokes equations allowed an approximate form to be developed which is easily discretised and shows similarities to the thin-shear-layer approximation. In contrast to the traditional thin-shear-layer approximation, the approximate form developed in the present work does not require knowledge of the directions normal and tangential to solid boundaries.
5. Mixed unstructured grids produce solutions of equal accuracy to those on quadrilateral grids at lower computational cost.
6. The use of an agglomeration multigrid method with rediscritisation on the coarse grid levels leads to good convergence rates for inviscid and laminar flows. Further work is required to make this approach work for turbulent flows.

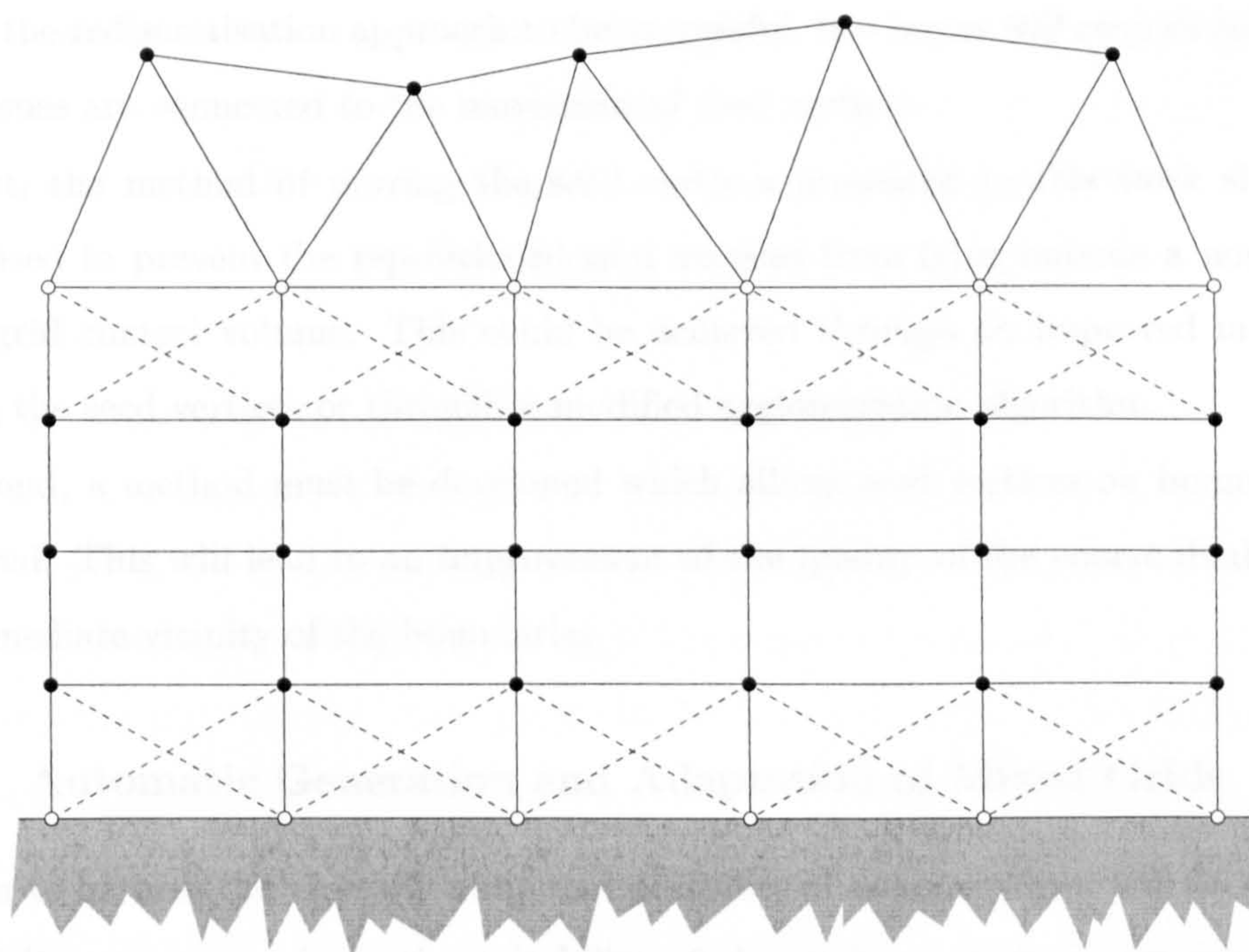


Figure 9.1: Possible use of virtual edges to improve discretisations at interfaces. Virtual edges are shown dashed.

9.3 Recommended Future Work

9.3.1 Development of Solution Methods for Mixed Grids

Spatial Discretisation at Cell-Type Interfaces. One important issue which remains to be addressed is the discretisation at interfaces between cell types. In the present work, no particular problems were encountered, even when shock waves crossed interfaces. However, if the capabilities of mixed grids are to be exploited more fully, e.g., along the lines suggested in Subsection 9.3.2, then cell-type interfaces will become more common and may lead to problems with grid quality. It will therefore be important to investigate discretisation issues at cell-type interfaces more closely.

A possible approach to reduce or eliminate possible problems at the interfaces is the use of virtual edges, as depicted in Fig. 9.1.

Agglomeration Multigrid Based on Rediscretisation. The approach of rediscretising the entire governing equations on the coarse grid levels obtained by agglomeration multigrid should be investigated further.

For the rediscretisation approach to be successful, two issues will require resolution. Both issues are connected to the movement of seed vertices.

First, the method of moving the seed vertices presented in this work should be generalised to prevent the repositioned seed vertices from lying outside a non-convex coarse-grid control volume. This could be achieved through an improved method of moving the seed vertices or through a modified agglomeration algorithm.

Second, a method must be developed which allows seed vertices on boundaries to be moved. This will lead to an improvement of the quality of the coarse dual grids in the immediate vicinity of the boundaries.

9.3.2 Automatic Generation and Adaptation of Mixed Grids

In order to harness the virtually unlimited flexibility of mixed grids, it will be necessary to exploit more aggressively the suitability of the various cell types for representing geometric and flow features. Therefore, it is recommended that future work should focus on the generation and adaptation of mixed grids where the suitable cell types are chosen automatically, as discussed in the subsequent subsections. The discussion concentrates on three dimensions, such that the term 'cell' now refers to a small volume element bounded by triangular and/or quadrilateral faces.

Automatic Generation of Mixed Grids. With the aim of maximising grid quality and minimising the number of cells (for a vertex-based solution method), the automatic generation of mixed grids should be based on a two-pronged approach.

On the one hand, the grid-generation method should recognise automatically those parts of the geometry (i.e., surfaces or volumes) which are best discretised with a given cell type. Since the various cell types are constructed from triangular and quadrilateral faces, the question of which is the best cell type to fill a volume essentially reduces to the question of which is the best face type for covering a surface. To represent a given surface accurately with the minimum the number of faces, it will be useful to employ triangular faces only where the curvature of the surface changes rapidly in more than one direction. If the curvature changes rapidly in only one direction, the use of quadrilateral faces should be considered. An example of a surface where the curvature changes rapidly in only one direction is the leading edge of an aerofoil. The

use of triangular faces to represent the leading edge, as depicted in Fig. 9.2(a), leads to excessive resolution along the leading edge. Furthermore, the arbitrary directions of the edges can lead to serrations or notches in the leading edge. With quadrilateral faces, the leading edge can be represented more economically and accurately, as shown in Fig. 9.2(b).

On the other hand, the grid-generation method should combine suitable cell types judiciously. The present use of quadrilateral/prismatic cells near solid walls to capture shear layers and triangular/tetrahedral cells in the rest of the solution domain is the most obvious example. Future grid-generation methods should take the combined use of cell types a step further. Two possibilities are shown in Fig. 9.3. To prevent the problem of prismatic-tetrahedral grids illustrated in Fig. 1.10, hexahedral cells could be used in the corners, as suggested in Fig. 9.3(a). Care will have to be taken with the use of stretched hexahedra in order to avoid grid-quality problems at cell-type interfaces, as already mentioned in Chapter 1. Flows in pipes could be computed by using grids such as that shown in Fig. 9.3(b), where layers of hexahedra are used on the wall and prisms are used to fill the vicinity of the centre-line.

Automatic Adaptation of Mixed Grids. The aim of future adaptation algorithms should be to achieve maximum resolution with a minimum number of vertices. This is to be accomplished by representing the various flow features by the most suitable cell type.

For example, aligning hexahedra and/or prisms to resolve a shock wave or contact discontinuity, as depicted schematically for two dimensions in Fig. 9.4, leads to fewer cells than employing tetrahedra. With approximate Riemann solvers (such as that of Roe [4] which capture discontinuities with just one interior point), only three layers of hexahedra and/or prisms need to be generated. Van Rosendale [6] demonstrated the effects of grid-alignment on the sharpness of captured shock waves on triangular grids. First steps in the direction of using quadrilateral cells to capture shock waves in an otherwise triangular grid were undertaken by Hwang and Wu [2].

Free shear layers may be captured also by using hexahedra/and or prisms. When capturing wakes behind wings, the merging of the grid layers in the wake and on the fuselage will have to be developed.

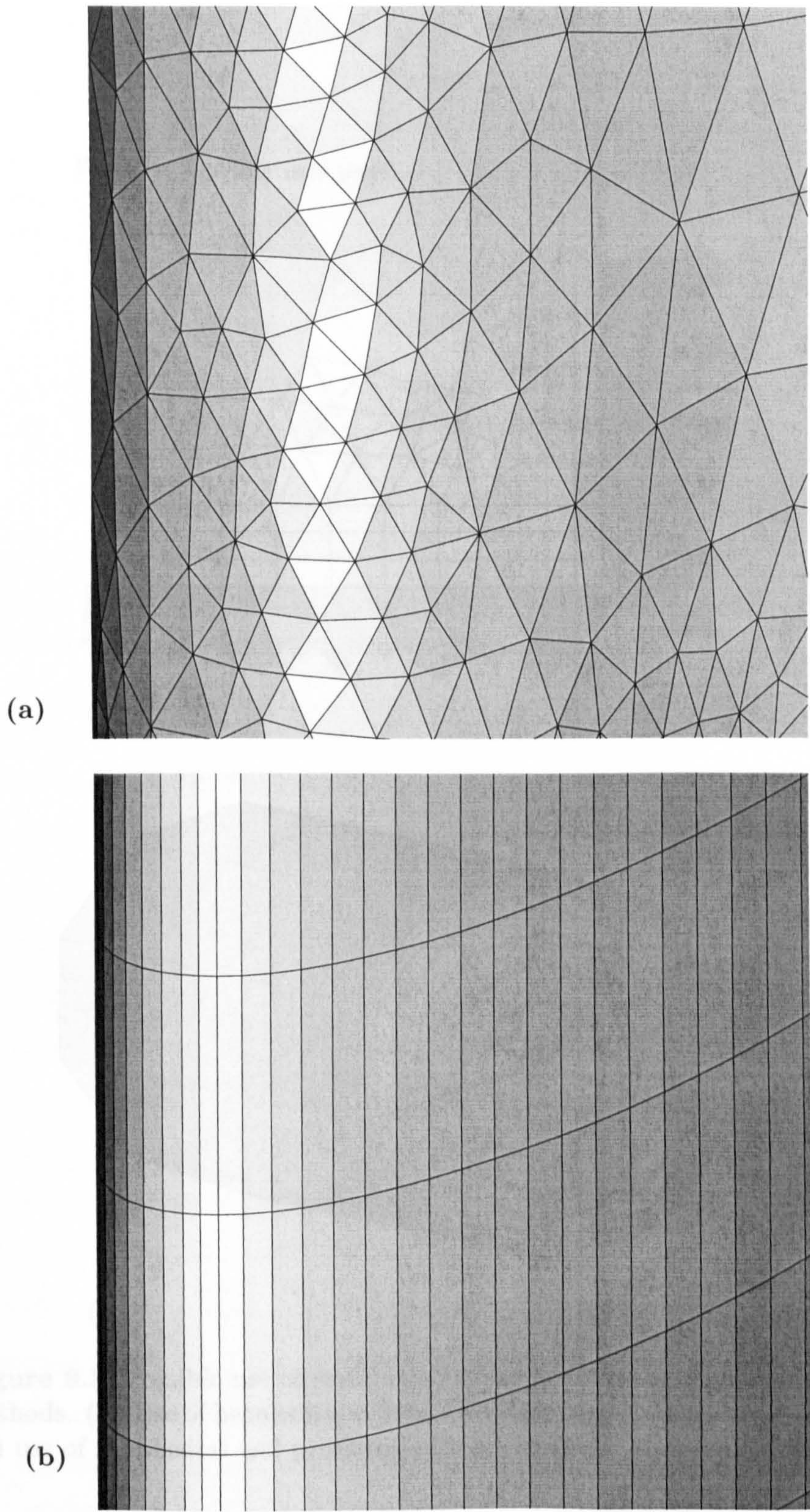
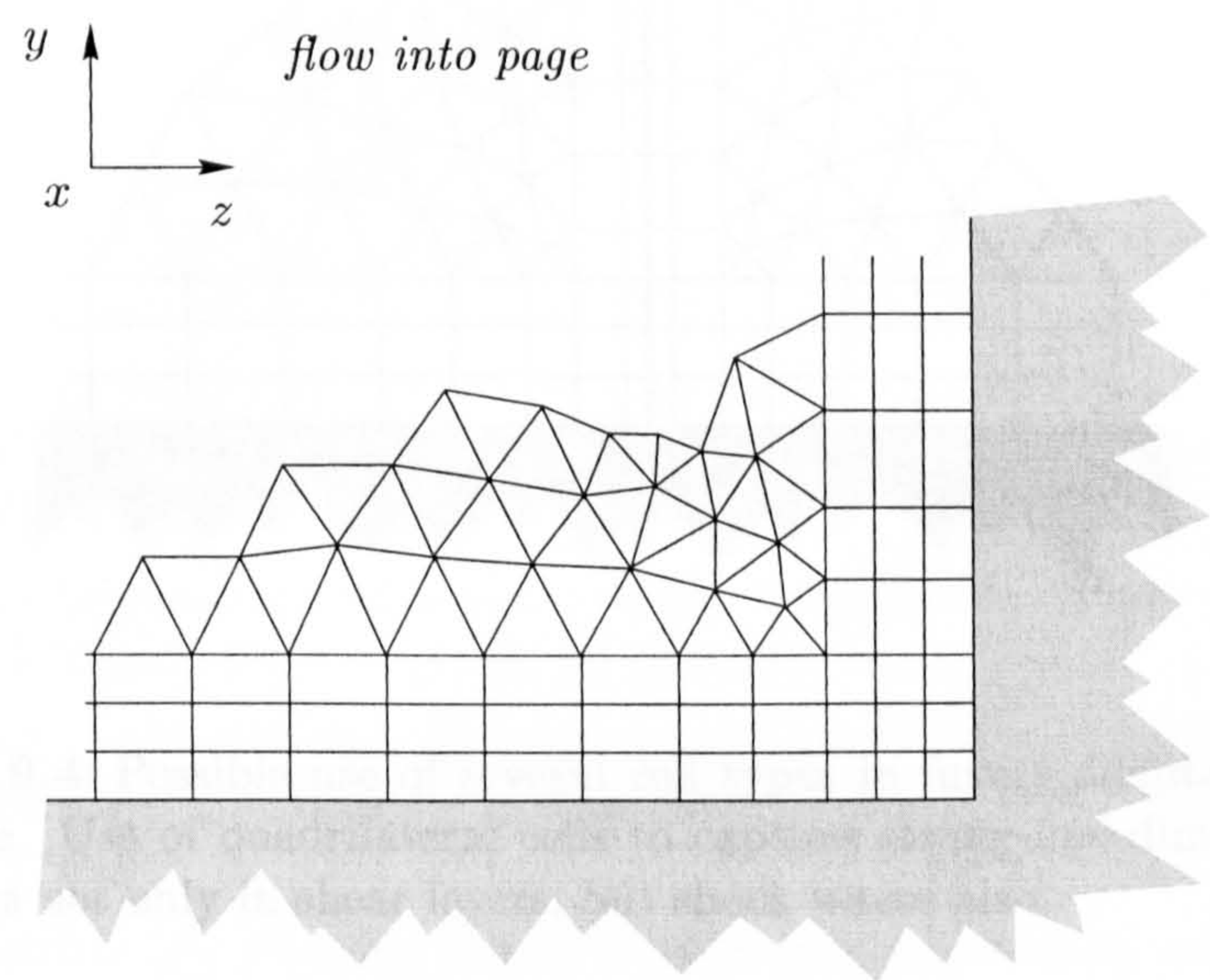
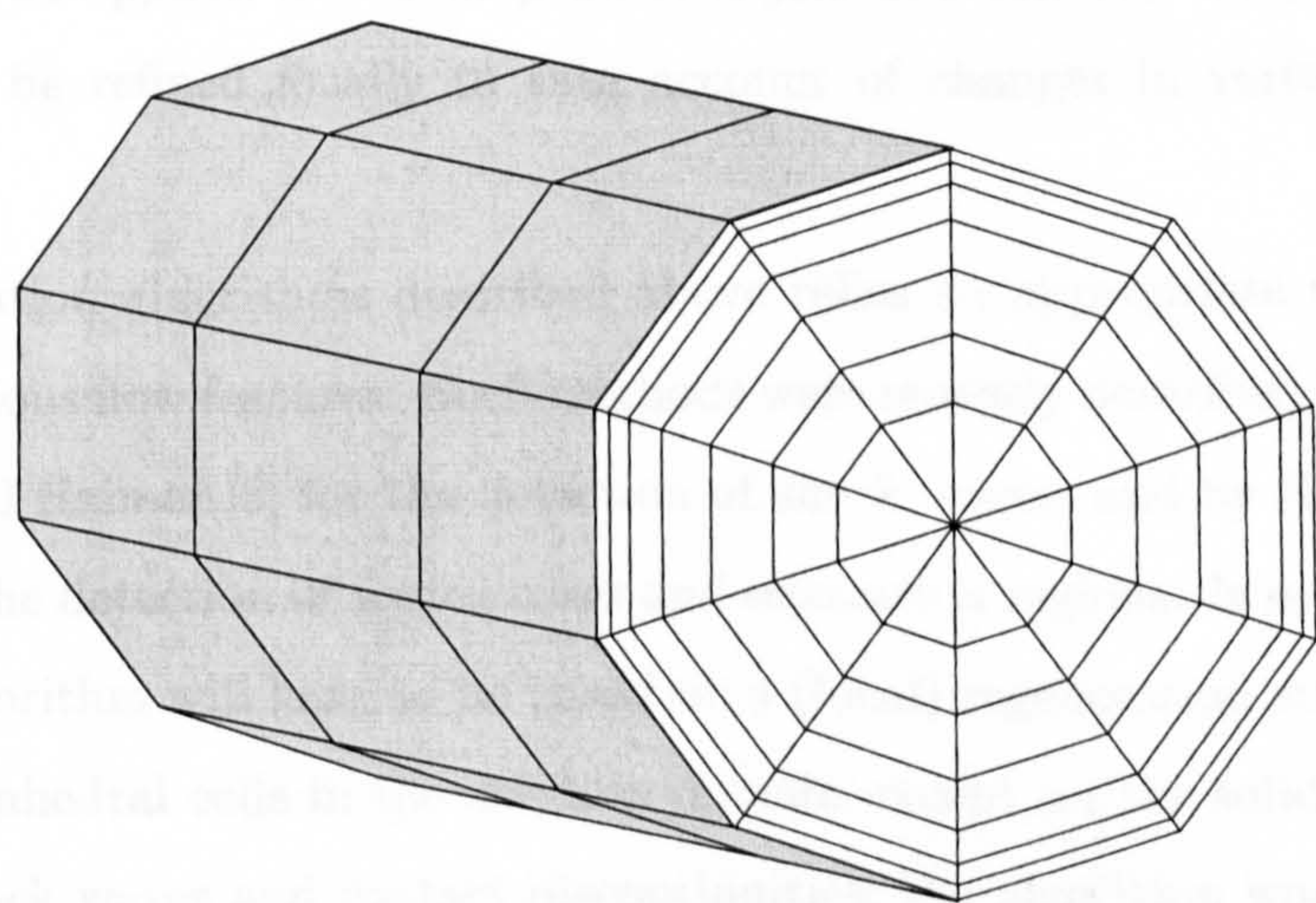


Figure 9.2: Representation of the leading edge of an aerofoil by (a) triangular faces and (b) quadrilateral faces.



(a)



(b)

Figure 9.3: Possible use of several cell types in future grid-generation methods. (a) Use of hexahedral cells to discretise corner geometries, and (b) use of hexahedral and prismatic cells to discretise pipe geometries.

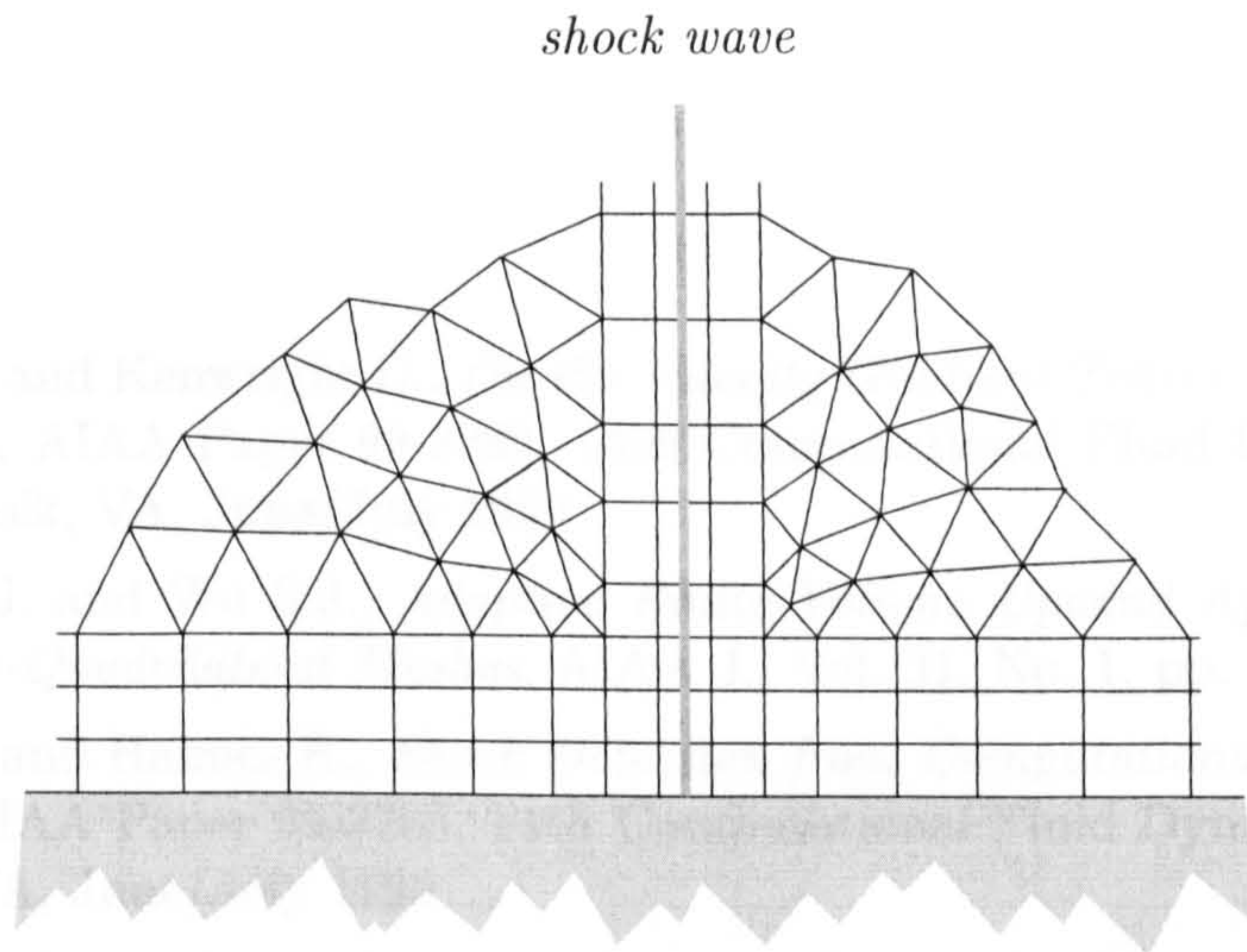


Figure 9.4: Possible use of several cell types in future adaptation algorithms. Use of quadrilateral cells to capture strong one-dimensional gradients not only in shear layers, but shock waves also.

The idea presented above on the use of hexahedra and/or prisms to compute pipe flows may also be applied to the adaptation of jets and vortices. The radial and axial directions can be refined locally to take account of changes in vortex strength, for example.

The adaptation algorithms described above relies on appropriate methods for detecting the various flow features. Such methods were recently described by Samtaney [5] and Lovely and Haines [3] for the detection of shock waves, and by Haines and Kenwright [1] for the detection of vortex cores and separation regions. It is evident that the adaptation algorithm will have to be based on a (local) regeneration strategy, and may start with tetrahedral cells in the solution domain except on the solid boundaries. In the case of shock waves and contact discontinuities, the algorithm would first need to locate the surface on which these lie, and generate on it a grid consisting of quadrilateral and/or triangular faces. From this surface grid, hexahedral and/or prismatic cells may be generated by marching out with more aggressive stretching than usual. In the case of jets and vortices, the centre-line could be used as a marching direction, where the hexahedra and prisms are generated in slices orthogonal to the marching direction.

With the more aggressive use of mixed grids, numerical schemes which do not distinguish between various cell-types such as that developed in the present work will become

essential.

References

- [1] Haimes R. and Kenwright D., *On the Velocity Gradient Tensor and Fluid Feature Extraction*, AIAA Paper 99-3288, 14th Computational Fluid Dynamics Conference, Norfolk, VA, June/July 1999
- [2] Hwang C.J. and Wu S.J., *Adaptive Finite-Volume Upwind Approach on Mixed Triangular-Quadrilateral Meshes*, AIAA J., Vol. 31, No. 1, pp. 61-67, 1993
- [3] Lovely D. and Haimes R., *Shock Detection from Computational Fluid Dynamics Results*, AIAA Paper 99-3285, 14th Computational Fluid Dynamics Conference, Norfolk, VA, June/July 1999
- [4] Roe P.L., *Approximate Riemann Solvers, Parameter Vectors, and Difference Schemes*, J. Comp. Phys., Vol. 43, pp. 357-372, 1981
- [5] Samtaney R., *Visualisation, Extraction, and Quantification of Discontinuities in Compressible Flows*, Technical Report NAS-99-002, NASA Ames Research Center, March 1999
- [6] Van Rosendale J., *Floating Shock Fitting via Lagrangian Adaptive Meshes*, ICASE Report No. 94-89, November 1994